

FROM MOLECULES TO FUNCTIONAL ARCHITECTURE

SUPRAMOLECULAR INTERACTIONS



**EDITED BY
VOLODYMYR I. RYBACHENKO**

FROM MOLECULES TO FUNCTIONAL ARCHITECTURE
SUPRAMOLECULAR INTERACTIONS

Collected research papers

EDITED BY
VOLODYMYR I. RYBACHENKO

Donetsk
«East Publisher House»
2012

УДК 541.1+547
O 80

Reviewers: Opeida I.A. – professor
Grzesiak Piotr – professor

Recommended for printing academic councils of L. Litvinenko Institute Physical Organic and Coal Chemistry National Academy of Science of Ukraine & Faculty of Chemistry Adam Mickiewicz University in Poznań, Poland

O80 From molecules to functional architecture.
Supramolecular interactions [collected research papers]
Edited by V.I. Rybachenko.
Donetsk: «East Publisher House»
Ltd, 2012. – 538 p.

ISBN 978-966-317-155-5

The supramolecular interaction and self-organization of molecules leads to a material and is responsible for their function. The monograph presents various methods for the preparation and use of functional materials.

Супрамолекулярна взаємодія і само-організація молекул призводять до матеріалів і відповідають за їх функції. Монографія представляє різні методи отримання, вивчення і використання функціоналізованих матеріалів.

УДК 541.1+547
O 80
ISBN 978-966-317-155-5

© Collective of authors, 2012

Contents

<i>List of contributors</i>	7
Supramolecular compounds through coordination chemistry – basic strategies	17
<i>Grażyna Bartkowiak, Katarzyna Gawron and Grzegorz Schroeder</i>	
Principles of cation- π interactions in supramolecular chemistry	35
<i>Wojciech Ostrowski and Rafał Frański</i>	
The influence of aggregates of calixarenes and dendrimers on the Protolytic equilibria of dyes in aqueous solution	49
<i>N.A. Vodolazkaya, N.O. Mchedlov-Petrosyan, L.N. Bogdanova, R.V. Rodik and V.I. Kalchenko</i>	
Complexation of triterpene and steroid glycosides with aromatic proteinogenous amino acids	71
<i>Leonid Yakovishin, Vladimir Grishkovets, Anna Kovalenko, Grzegorz Schroeder and Volodymyr Rybachenko</i>	
Functionalized polystyrene beads as carriers in the release studies of tetrapeptides	87
<i>Anna Olejnik, Izabela Nowak and Grzegorz Schroeder</i>	
Description of thermodynamic parameters of formation and dimerization of alkylamides using superposition-additive approach	103
<i>Yu.B. Vysotsky, E.A. Belyaeva, E.S. Fomina and D. Vollhardt</i>	
Self-assembled mesoporous TiO ₂ and its application in photoenergy systems	127
<i>Maciej Zalas</i>	

Monoterpene-derived 1,2-amino alcohols as catalysts precursors for asymmetric reactions	141
<i>Marek P. Krzemiński, Marta Ćwiklińska and Anna Kmieciak</i>	
Recent development in the chemistry of <i>ortho</i> -aminomethylphenylboronic acids	175
<i>Alicja Pawełko, Agnieszka Adamczyk-Woźniak and Andrzej Sporzyński</i>	
Synthesis of pyrazole-based bidentate and tridentate supramolecular ligands	213
<i>Michał Ceglowski and Grzegorz Schroeder</i>	
Mesoporous silicas as carriers in controlled release systems in biomedicine and cosmetics industry	229
<i>Dawid Lewandowski and Grzegorz Schroeder</i>	
Application of transition metals NMR in supramolecular chemistry	269
<i>Błażej Gierczyk</i>	
Cyclodextrins and calyx[n]arenes as inverse phase transfer catalysts	393
<i>Viktor Anishchenko, Volodymyr Rybachenko, Grzegorz Schroeder, Konstantine Chotiy and Andrey Redko</i>	
Role of electronic correlation in the calculations of supramolecular interactions in graphene-like aromatic systems	405
<i>A.F. Dmitruk, O.M. Zarechnaya and I.A. Opeida</i>	
Design of polyfunctional nanosystems based on surfactants and polymers by noncovalent strategy	415
<i>Lucia Zakharova, Elena Zhiltsova, Alla Mirgorodskaya and Alexander Konovalov</i>	

Adsorption behavior, surface dilational rheology and foam stability of mixed sodium humates / cetyltrimethylammonium bromide solutions	455
<i>Svetlana Khil'ko, Volodymyr Rybachenko and Grzegorz Schroeder</i>	
Nanoporous films – model catalysts in the materials gap	473
<i>Izabela Nowak</i>	
Silica surface functionalized by supramolecular systems as effective agent for cesium ions removal	483
<i>Joanna Kurczewska</i>	
Algae and their chelating properties	495
<i>Joanna Fabrowska and Bogusława Łęska</i>	
Decontamination systems on the basis of hydrogen peroxide: Decomposition of ecotoxic substrates	513
<i>Lyubov Vakhitova</i>	

List of contributors

Agnieszka Adamczyk-Woźniak

Warsaw University of Technology
Faculty of Chemistry
Noakowskiego 3
00-664 Warsaw
Poland

Viktor Anishchenko

L.M. Litvinenko Institute of Physical-Organic and Coal Chemistry
National Academy of Science of Ukraine
Department of Spectrochemical Researches
R. Luxemburg 70
81-134 Donetsk
Ukraine

Grażyna Bartkowiak

Adam Mickiewicz University in Poznań
Faculty of Chemistry
Umultowska 89b
61-614 Poznań
Poland

E.A. Belyaeva

Donetsk National Technical University
58 Artema Str.
83000 Donetsk
Ukraine

L.N. Bogdanova

Pharmstandart-Biolik
Pomerki 70
61084, Kharkov
Ukraine

Michał Ceglowski

Adam Mickiewicz University in Poznań
Faculty of Chemistry
Umultowska 89b
61-614 Poznań
Poland

Konstantine Chotiy

L.M. Litvinenko Institute of physical-Organic and Coal Chemistry
National Academy of Science of Ukraine
Department of Spectrochemical Researches
R. Luxemburg 70
81-134 Donetsk
Ukraine

Marta Ćwiklińska

Nicolaus Copernicus University
Faculty of Chemistry
7 Gagarin Street
87-100 Toruń
Poland

A.F. Dmitruk

Litvinenko Institute of Physical Organic Chemistry and Coal Chemistry
National Academy of Sciences of Ukraine
Donetsk 83114
Ukraine

Joanna Fabrowska

Adam Mickiewicz University in Poznań
Faculty of Chemistry
Umultowska 89b
61-614 Poznań
Poland

E.S. Fomina

Donetsk National Technical University
58 Artema Str.
83000 Donetsk
Ukraine

Rafał Frański

Adam Mickiewicz University in Poznań
Faculty of Chemistry
Umultowska 89b
61-614 Poznań
Poland

Katarzyna Gawron

Adam Mickiewicz University in Poznań
Faculty of Chemistry
Umultowska 89b
61-614 Poznań
Poland

Błażej Gierczyk

Adam Mickiewicz University in Poznań
Faculty of Chemistry
Umultowska 89b
61-614 Poznań
Poland

Vladimir Grishkovets

V.I. Vernadsky Taurida National University
Vernadsky Ave., 4
Simferopol, 95007
Crimea
Ukraine

V.I. Kalchenko

Institute of Organic Chemistry
National Academy of Science of Ukraine
Kiev, 02094
Ukraine

Svetlana Khil'ko

L.M. Lytvynenko Institute of Physico-Organic and Coal Chemistry of
Ukrainian National Academy of Sciences
70 R. Luxemburg Street
Donetsk 83114
Ukraine

Anna Kmiecik

Nicolaus Copernicus University
Faculty of Chemistry
7 Gagarin Street
87-100 Toruń
Poland

Alexander Konovalov

State Budgetary-Funded Institution of Science A.E. Arbuzov
Institute of Organic and Physical Chemistry of Kazan Scientific Center
of Russian Academy of Sciences
8, ul. Arbuzova
420088 Kazan
Russia

Anna Kovalenko

Universitetskaya Str., 33
Sevastopol, 99053
Crimea
Ukraine

Marek P. Krzemiński

Nicolaus Copernicus University
Faculty of Chemistry
7 Gagarin Street
87-100 Toruń
Poland

Joanna Kurczewska

Adam Mickiewicz University in Poznań
Faculty of Chemistry
Umultowska 89b
61-614 Poznań
Poland

Dawid Lewandowski

Adam Mickiewicz University in Poznań
Faculty of Chemistry
Umultowska 89b
61-614 Poznań
Poland

Bogusława Łęska

Adam Mickiewicz University in Poznań
Faculty of Chemistry
Umultowska 89b
61-614 Poznań
Poland

N.O. Mchedlov-Petrosyan

Department of Physical Chemistry
V. N. Karazin Kharkov National University
Svoboda sq. 4
61022, Kharkov
Ukraine

Alla Mirgorodskaya

State Budgetary-Funded Institution of Science A.E. Arbuzov
Institute of Organic and Physical Chemistry of Kazan Scientific Center
of Russian Academy of Sciences
Arbuzova 8
420088 Kazan
Russia

Izabela Nowak

Adam Mickiewicz University in Poznań
Faculty of Chemistry
Umultowska 89b
61-614 Poznań
Poland

Anna Olejnik

Adam Mickiewicz University in Poznań
Faculty of Chemistry
Umultowska 89b
61-614 Poznań
Poland

I.A. Opeida

Litvinenko Institute of Physical Organic Chemistry and Coal Chemistry
National Academy of Sciences of Ukraine
Donetsk 83114
Ukraine

Wojciech Ostrowski

Adam Mickiewicz University in Poznań
Faculty of Chemistry
Umultowska 89b
61-614 Poznań
Poland

Alicja Pawelko

Warsaw University of Technology
Faculty of Chemistry
Noakowskiego 3
00-664 Warsaw
Poland

Andrey Redko

L.M. Litvinenko Institute of physical-Organic and Coal Chemistry
National Academy of Science of Ukraine
Department of Spectrochemical Researches
R. Luxemburg 70
81-134 Donetsk
Ukraine

R.V. Rodik

Institute of Organic Chemistry
National Academy of Science of Ukraine
Kiev, 02094
Ukraine

Volodymyr Rybachenko

L.M. Lytvynenko Institute of Physico-Organic and Coal Chemistry
of Ukrainian National Academy of Sciences
70 R. Luxemburg Street
Donetsk 83114
Ukraine

Grzegorz Schroeder

Adam Mickiewicz University in Poznań
Faculty of Chemistry
Umultowska 89b
61-614 Poznań
Poland

Andrzej Sporzyński

Warsaw University of Technology
Faculty of Chemistry
Noakowskiego 3
00-664 Warsaw
Poland

Lyubov Vakhitova

L.M. Litvinenko Institute of Physical Organic Chemistry & Coal
Chemistry
National Academy of Sciences of Ukraine.
R. Luxemburg St. 70
83-114 Donetsk
Ukraine

N.A. Vodolazkaya

Department of Physical Chemistry
V. N. Karazin Kharkov National University
Svoboda sq. 4
61022, Kharkov
Ukraine

D. Vollhardt

Max Planck Institute of Colloids and Interfaces
D-14424 Potsdam/Golm
Germany

Yu.B. Vysotsky

Donetsk National Technical University
58 Artema Str.
83000 Donetsk
Ukraine

Leonid Yakovishin

Universitetskaya Str., 33
Sevastopol, 99053
Crimea
Ukraine

Lucia Zakharova

State Budgetary-Funded Institution of Science A.E. Arbuzov
Institute of Organic and Physical Chemistry of Kazan Scientific Center
of Russian Academy of Sciences
8, ul. Arbuzova
420088 Kazan
Russia

Maciej Zalas

Adam Mickiewicz University in Poznań
Faculty of Chemistry
Umultowska 89b
61-614 Poznań
Poland

O.M. Zarechnaya

Litvinenko Institute of Physical Organic Chemistry and Coal Chemistry
National Academy of Sciences of Ukraine
Donetsk 83114
Ukraine

Elena Zhiltsova

State Budgetary-Funded Institution of Science A.E. Arbuzov
Institute of Organic and Physical Chemistry of Kazan Scientific Center
of Russian Academy of Sciences

Arbuzova 8
420088 Kazan
Russia

Chapter 1

Supramolecular compounds through coordination chemistry – basic strategies

Grażyna Bartkowiak, Katarzyna Gawron and Grzegorz Schroeder
*Adam Mickiewicz University in Poznań, Faculty of Chemistry,
Umultowska 89b, 61-614 Poznań, Poland*

Introduction

In the recent years a rapid development of supramolecular coordination chemistry took place and many new supramolecular complexes based on the metal coordination centers have found their applications in catalysis, as advanced materials for molecular electronics, as molecular receptors used in sensor devices, light-harvesting materials for solar cells and in molecular machines.^{1,2,3} These compounds are of great interest not only due to the variety of their application, but also due to the ease with which many of them can be prepared. The basic methods of the supramolecular coordinative complexes synthesis making use of metal centers with precisely defined coordination numbers and angles and accurately chosen ligands appear often to be simpler and faster when compared to the laborious, multistep organic synthesis.

Supramolecular chemistry has at its disposal not so many reliable, high-yielding reactions in comparison with classical organic chemistry, which provides a lot of proven methods to obtain very strong covalent, mainly carbon-carbon, bonds. Supramolecular compounds are basing on the weak interactions, the same which are often responsible for natural macromolecules formation, i.e. hydrogen bonding, van der Waals forces, dipole-dipole interactions and Coulombic forces. Designing and building of the supramolecular structures with the use of these kinds of interactions is a demanding and challenging task for synthetic chemists. Weak interactions, however, ensure a large degree of supramolecule flexibility and enable conformational changes, which are often needed for specific functions, like spontaneous self-organization and molecular recognition. A great number of weaker interactions leads to the bigger specificity and formation of thermodynamically favoured structures. The entropic and

enthalpic effects involved in large symmetric architectures synthesis are very important and sometimes difficult to predict in advance.

The aim of this work is to show the application of coordination chemistry to the synthesis of supramolecular compounds. Considering the strength of bonds, covalent coordination bonds to the transition metal centers lie between very strong C-C covalent bonds and weak hydrogen bonds or van der Waals interactions, so they can be rated among the intermediate strength bonds. It should be noticed that coordination of metals to heteroatoms forms thermally labile bonds, which gives the possibility to select either a thermodynamic or a kinetic product through the choice of ligands, transition metals, reaction time, temperature and other reaction conditions.

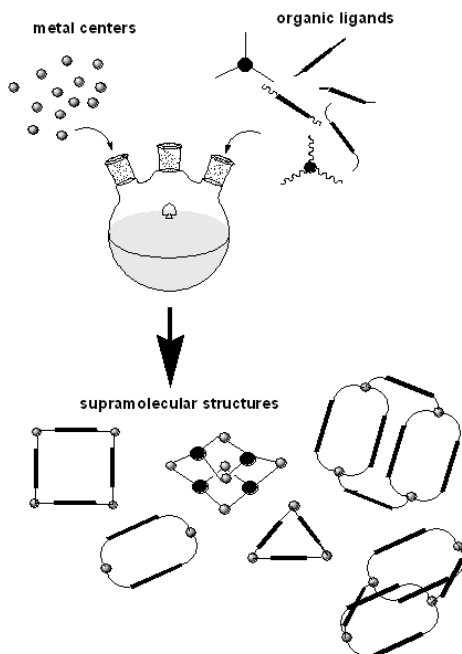


Figure 1. General concept of supramolecular coordination compounds formation, according to.⁴

The detailed literature search allows to specify the main strategies to obtain mesoscopic supramolecular structures by means of coordination chemistry. One can mention hereby three basic strategies:

- making use of directional bonding by metal centers;
- taking advantage of symmetry interactions;
- exploiting of weak metal bonds in coordination complexes.

All three routes mentioned above are based on use of metal centers as building blocks for supramolecular structures.

1. Directional-bonding strategy

The strategy being based on directional bonding treats metal centers as highly-directional corners and gives as results structures forming geometrical shapes, i.e. 2-D systems, like dinuclear macrocycles, molecular triangles, squares, rectangles, hexagons or higher order (3-D) structures, i.e. three-dimensional molecular cages or polyhedra.⁵ The principle of formation of basic two-dimensional structures is shown in Figure 2.

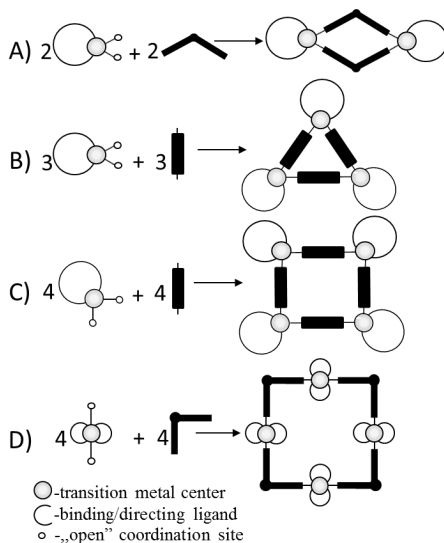


Figure 2. Construction of large structures by the directional-bonding approach.⁴

The main requirements of the directional-bonding approach are:

- access to the rigid precursors, with predefined angles and symmetry proper for the expected product;
- the ratios of the mixed precursors appropriate for the desired outcome.

In practice, many other factors are important and have a great influence on the

experimental results, for instance the solvent choice, the temperature, precursor's concentrations, the order of building blocks introduction, or the rate of mixing of the substrates.⁶

Ways to construct various macrocycles by the directional bonding approach involve selection of metal building blocks with rigorously defined angle between the coordinatively labile sites and a choice of appropriate rigid binding ligands. For example, to construct a dinuclear macrocycle, a metal complex with a 60° angle between the coordinating bonds and a rigid ligand with a 120° kink (see Figure 2A) are needed. A molecular triangle can be assembled using the same metal complex (angle 60°) and a straight linear ligand (Figure 2B). Molecular squares can be obtained by the two alternative ways: using the same, linear ligands and metal centers with coordination sites with 90° angle (Figure 2C) or bonding ligands with a 90° bend and metal complex with a 180° angle between the coordination sites (Figure 2D).

The examples of dinuclear macrocycles formed by use of this strategy are: palladium-ethylenediamine systems (**3**, Figure 3) made by Fujita et al.^{7,8,9},

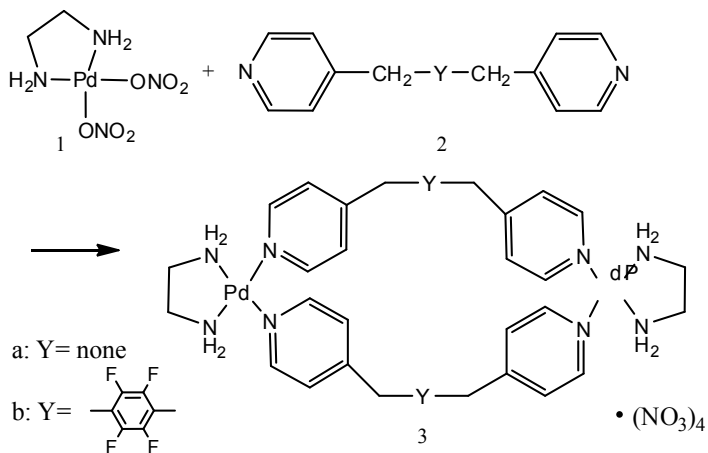


Figure 3. Palladium-ethylenediamine based dinuclear macrocycle

metallomacrocycles containing diazacycloalkanes, prepared by Hosseini et al.¹⁰ (Figure 4) and Yamamoto et al.¹¹ (Figure 5)

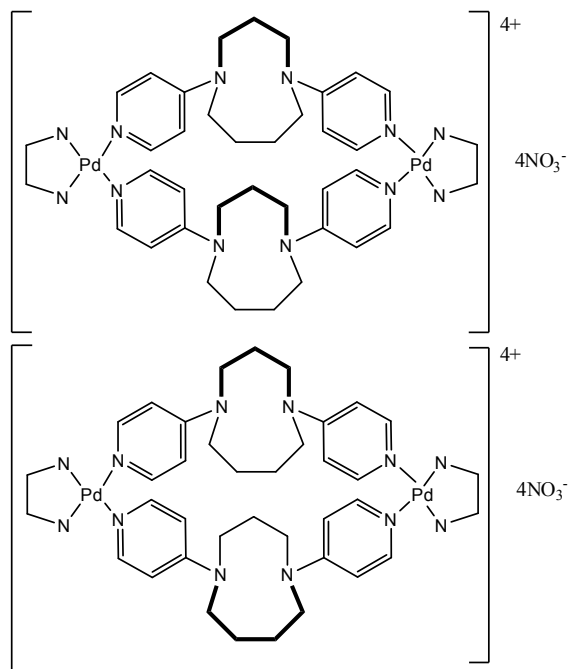


Figure 4. Two possible isomeric metallamacrocycles (top and bottom), containing Pd(II) and ethylenediamine.¹⁰

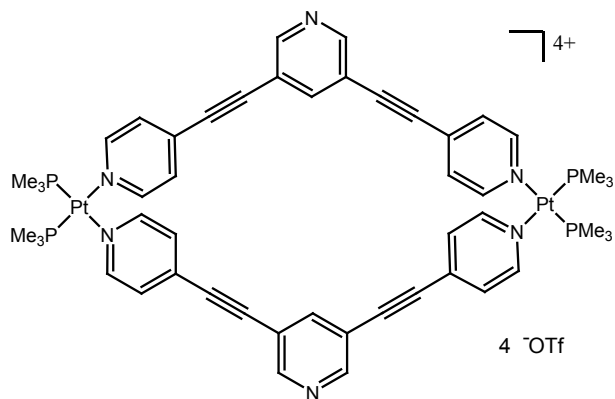


Figure 5. Rhomboid structure assembled using Pt complex and 3,5-bis(4-pyriylethynyl) pyridine ligand¹¹ by directional-bonding approach.

According to the scheme in the Figure 2B there is possible to construct molecular triangles, but the task is difficult, because an ideal triangle would be formed from three rigid linear ligands and three metal centers with 60° angle and there are no appropriate metal complexes (of common coordination numbers) with ideal 60° angle between bonds. However, molecular triangles (relatively rare) are yet reported¹²⁻¹⁶ as obtained by the directional-bonding approach. Less than ideal triangles can be obtained using sufficiently flexible ligands (Figure 6).¹⁸ Examples of this kind of molecules are triangles assembled through coordination to Pd (II)¹⁷, Pt (II)^{18,19} (Figure 6), Mn(III)²⁰, Ru(II)²¹, Cu(II)²², Co²³ and Mo(VI)²⁴.

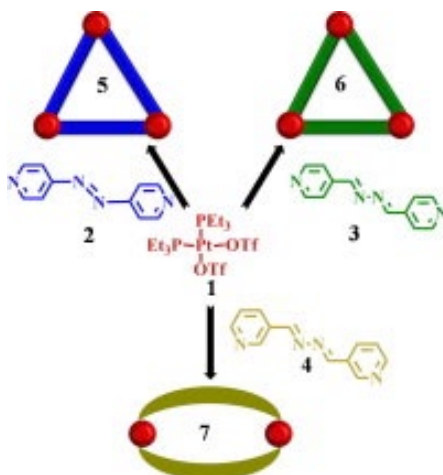


Figure 6. Synthetic routes to the [3+3] molecular triangles **5** and **6** and [2+2] rhomboid **7**.¹⁸

Fujita et al. have reported that molecular triangles are often in equilibrium with molecular squares.¹⁷ Molecular squares are the most widely reported shapes²⁵⁻³⁴ since they are relatively simple to obtain. Among the molecular squares prepared recently particularly interesting one is the architecture made of 4,4'-bipyridine (marked as 4,4'-bipy) and neutral pseudo-square-planar carboplatinum complex [LPt(DMAP)], (H_2L = 2,6-diphenylpyridine, DMAP = 4-dimethylaminopyridine), reported by Lusby et al.³⁰, where the square is assembling in acidic environment and disassembling upon reaction with base. The structure is reassembling when protons are added, so it makes reversible, acid-base switchable system (Figure 7).

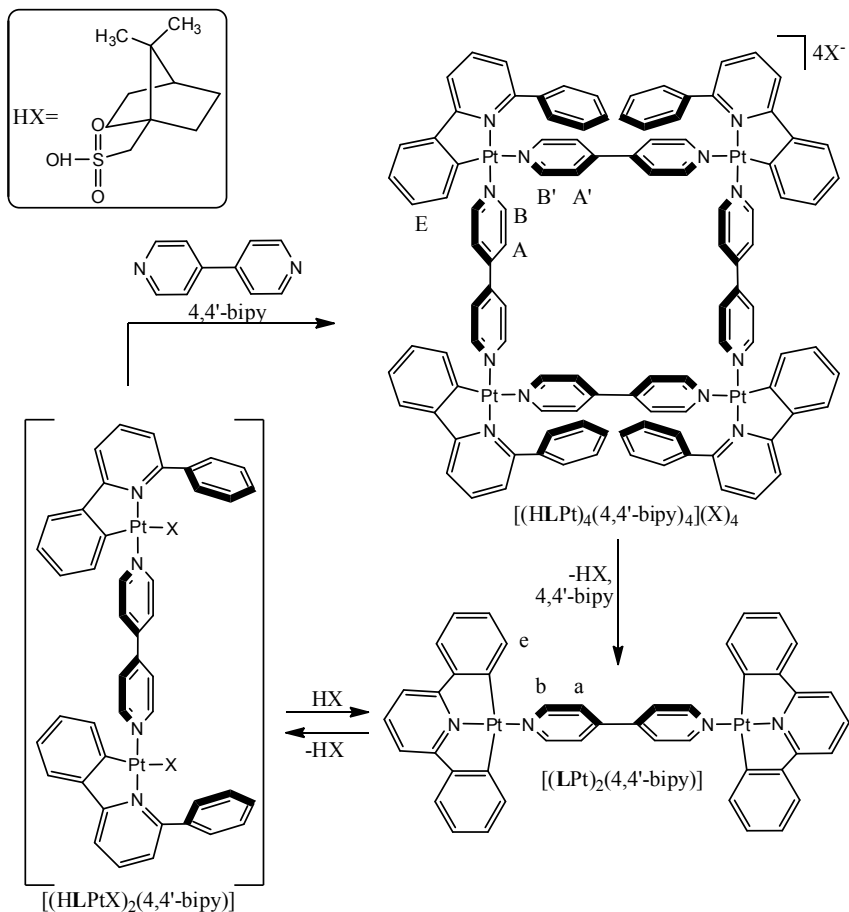


Figure 7. Assembly and disassembly of 2D metallosupramolecular architecture (square)³⁰.

Molecular rectangles cannot be formed in one step, by spontaneous self-assembly, because using a mixture of metal centers (“corners”) and two types of bridging ligands of different length (short and long) only two types of molecular squares are produced (Figure 8) and this process is thermodynamically favored.^{35,36}

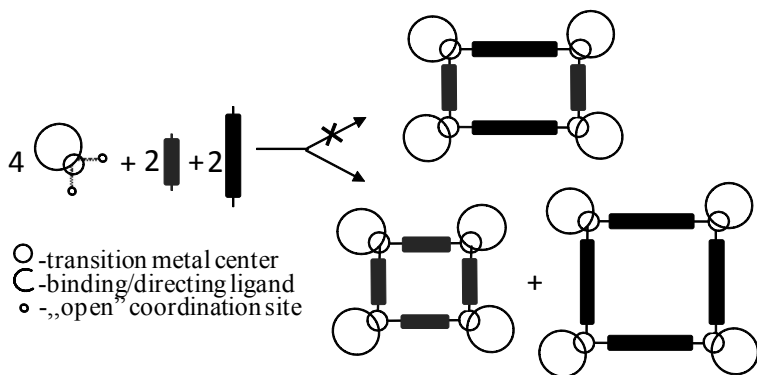


Figure 8. Formation of square structures (rather than rectangles) from the mixture of metal-containing precursors and two kinds of rigid ligands of different length^{35,36}.

Using the directional-bonding approach more complex three-dimensional structures can be obtained, for example molecular cages, presented in Figure 9.

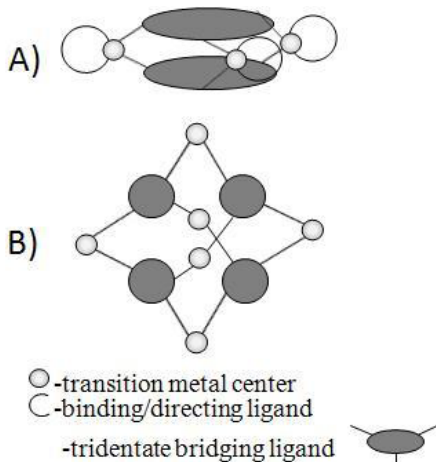


Figure 9. Examples of molecular cages formed from tridentate bridging ligands and transition metal centers according to the directional-bonding strategy.

Directional-bonding strategy has several advantages: the reactions are usually high-yielding and can lead to the wide range of shapes and sizes. They often enable incorporation to the supramolecular structure ligands with desirable

properties. Between the limitations of this approach are: the rigid structures of linking building blocks, which constrain the possibility of conformational changes, so that it makes difficult to form molecular switches and other structures where conformational flexibility is necessary. Other disadvantages of this strategy are: the lack of complexing activity of metallic centers introduced and the termination of certain physical properties (for example luminescence) of building blocks after the complexation process^{37,38,39}.

2. Symmetry-interaction strategy

The approach basing on symmetry-interactions is developed to construct high symmetry coordination clusters. The synthesis involves transition or main group metals without the strongly coordinating ligands as the starting material, which is combined with the multibranching chelating ligands. The formation of supramolecular shapes is stimulated by the strong driving force which consist in the inherent symmetry of the coordination sites on the metal centers. The “symmetry-interaction” term is widely employed by Lehn⁴⁰, Saalfrank⁴¹ and Raymond⁴². The strategy leads to the various macrocyclic structures containing main group or transition metals. Among them dinuclear macrocycles with chelating ligands (Figure 10 A), helicates (Figure 10 B), triple helicates, dinuclear metallocryptands (Figure 10 C), tetrahedral (Figure 11 A) and adamantoid structures (Figure 11 B) are commonly constructed. Important feature in this approach is the careful choice of ligands and metal centers taking into account the orientation of multiple chelation sites to favor the creation of discrete clusters over oligomers or polymers formation.

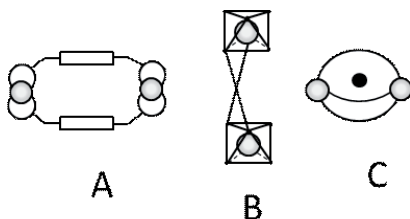


Figure 10. Dinuclear structures prepared by the symmetry-interaction approach.

This approach is quite complicated because many symmetric interactions should be considered, namely:

- metal atom geometry,
- ligand orientation,

- ligand-ligand interactions,
- so it is advisable to use computer modeling to predict target architectures, which could be made of the combinations of given ligands and metals.⁴³

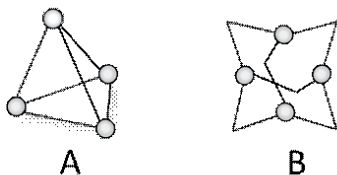


Figure 11. Tetranuclear, three-dimensional structures prepared by the symmetry-interaction approach.

A variety of elegant shapes (helicates, tetrahedral, adamantoids) can be obtained using the symmetry interactions. The limitation of this approach is a “compact” structure of the product, which produces small cavities, which are unable to encapsulate larger guests.

3. Weak-link strategy

The weak-link approach involves combining transition metal centers (without directing ligands) with non-rigid, flexible ligands. As a result, the supramolecular structures are obtained which have coordination sites available for further reactions. As an example may serve the reaction in which hemilabile ligands react with transition metal centers in a bidentate way, forming two kinds of metal-ligand bonds, one stronger than the other, yielding the favored dinuclear complex A⁴⁴ (Figure 12).

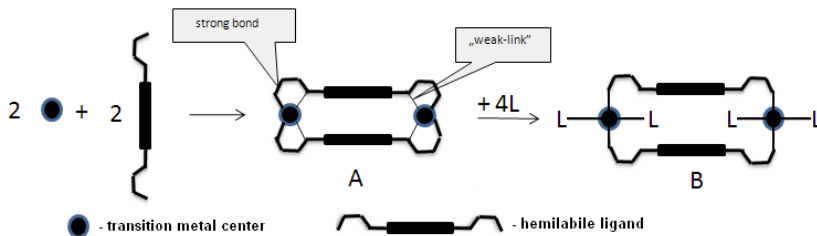


Figure 12. The formation of dinuclear complex A, containing “weak-link” and its conversion to B.

The complex A is formed in very high yield, often quantitatively, and can be isolated from the reaction mixture. Favorable formation of intermediate A can be explained concerning following driving forces:

- the creation of stable, five- or six-member chelate rings;
- the chelation effect of the bidentate ligands, leading to the dinuclear structures;
- the π - π interaction between the moieties (chiefly arene rings), serving as the central binding units in the ligands.

In the next reaction step compound A is added to a ligand L, then weak links are broken and ligands L bind to the free sites at metal centers, replacing the previously bound groups.

The crucial point in this method is the use of hemilabile ligands⁴⁵, i.e. polydentate chelates that contain at least two different types of bonding groups. The first group is strongly bonding to the metal center whereas the other group bonds weakly and can be easily displaced by ancillary bonding ligands or solvent (for example DMSO, acetonitrile) molecules. Typical strong bonding groups contain phosphorus atom as a strong donor (for example the phosphine moiety), while the weak binding groups contain O, N, S or Se atoms (weak donors). The reactions employed in the weak-link approach are chiefly under kinetic rather than thermodynamic control; the thermodynamically favored product can be formed, but it is possible to avoid its formation through the proper reaction conditions because of the high activation barrier.

As an example of weak-link approach application is the formation of a dirhodium compound A (Figure 13) based on a durene (i.e. 2,3,5,6-tetramethylbenzene) ligand at room temperature and its conversion to the more stable form B at elevated temperature. Mononuclear thermodynamic product (“piano-stool” C) can be prohibited from creating due to a relatively high energy barrier.⁴⁶

The transition metal centers in homodimetallic structures formed through weak-link method often remain available for further modification. Such two dinuclear macrocycles can be joined with rigid difunctional ligand to form molecular cylinder (Figure 14).

The main advantages of the weak-link approach are:

- a) a possibility of formation of very sophisticated, 2-D and 3-D, supramolecular structures;
- b) great flexibility and, as a result, wide utility of the architectures obtained,
- c) enabled ligand substitution reaction;
- d) an ability to tailor electronic and steric properties of product.

The frequent thermal instability of the supramolecular structures obtained

according to this approach (a transition from the kinetic to the thermodynamic product) belongs to the limitations of the weak-link method.

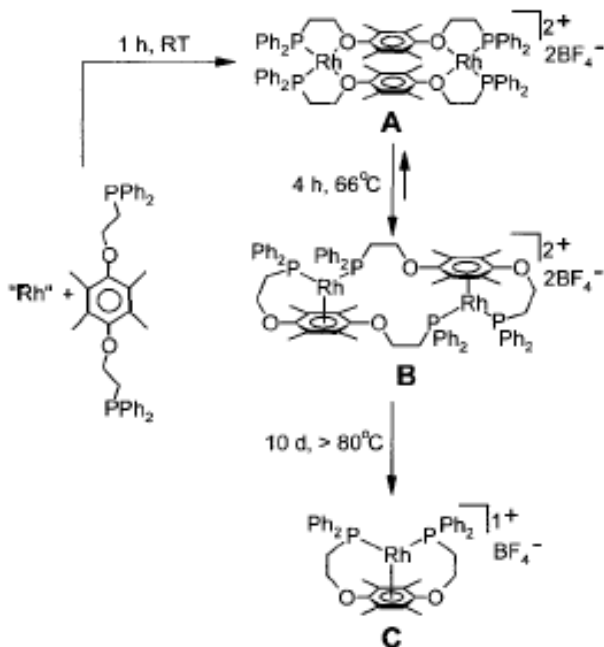


Figure 13. The formation of dinuclear dirhodium complex (A) with durene ligands, its conversion into arene-rhodium structure B and thermodynamic product C at high temperature.⁴⁶

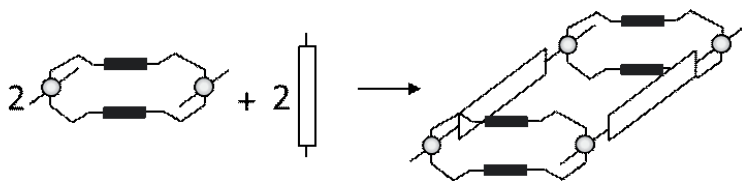


Figure 14. Two macrocycles joined with rigid difunctional ligands into a molecular cylinder.⁴⁷

Summary

Coordination chemistry offers several strategies to obtain supramolecular

assemblies. Metal-ligand interactions, in comparison with other interactions typical for supramolecular compounds (i.e. π - π stacking, hydrogen bonding, van der Waals forces) are much stronger and highly directional. The synthesis via metal coordination shows significant advantages and is usually more efficient than the classical covalent synthesis. Different approaches, presented above, provide rational synthetic routes and yield a variety of architectures and structures possessing interesting properties.

References

1. F. Vögtle; *Supramolecular Chemistry*, Wiley, VCH, New York, 1995.
2. C. S. Lent; Bypassing the transistor paradigm; *Science* **2000**, 288, 1597-1599.
3. V. Balzani, A. Credi, F. M. Raymo, J. F. Stoddart; Artificial Molecular Machines; *Angew. Chem. Int. Ed.* 2000, **39**, 3348-3391.
4. B. J. Holliday, C. A. Mirkin; Strategies for the constitution of supramolecular compounds through coordination chemistry; *Angew. Chem. Int. Ed.* 2001, **40**, 2022 – 2043.
5. P. J. Stang, B. Olenyuk; Self-assembly, symmetry, and molecular architecture. Coordination as the motif in the rational design of supramolecular metallacyclic polygons and polyhedra; *Acc. Chem. Res.* 1997, 30, 502-518.
6. S. R. Seidel, P. J. Stang; High-symmetry coordination cages via self-assembly; *Acc. Chem. Res.* 2002, **35**, 972-983.
7. M. Fujita, S. Nagao, M. Iida, K. Ogata, K. Ogura; Palladium(II)-directed assembly of macrocyclic dinuclear complexes composed of (en)Pd²⁺ and bis(4-pyridyl)-substituted bidentate ligands. Remarkable ability for molecular recognition of electron-rich aromatic guests; *J. Am. Chem. Soc.* 1993, **115**, 1574-1576.
8. M. Fujita, F. Ibukuro, H. Hagihara, K. Ogura, Quantitative self-assembly of a [2]catenane from two preformed molecular rings; *Nature* 1994, **367**, 720-723.
9. M. Fujita, F. Ibukuro, H. Seki, O. Kamo, M. Imanari, K. Ogura; Catenane Formation from Two Molecular Rings through Very Rapid Slippage. A Möbius Strip Mechanism; *J. Am. Chem. Soc.* 1996, **118**, 899-900.
10. R. Schneider, M. W. Hosseini, J.-M. Planeix, A. D. Cian, J. Fischer; Exo-ligands based on two p-aminopyridine interconnection by tuneable alkyl chains: design, synthesis and structural analysis of silver and palladium metallamacrocycles; *Chem. Commun.* 1998, 1625-1626

11. T. Yamamoto, A. M. Arif, P. J. Stang, Dynamic equilibrium of a supramolecular dimeric rhomboid and trimeric hexagon and determination of its thermodynamic constants; *J. Am. Chem. Soc.* 2003, **125** (40), 12309-12317.
12. Y.K. Kryschenko, S.R.Seidel, A.M Arif., P.J.Stang, Coordination-driven self-assembly of pre-designed supramolecular triangles; *J. Am. Chem. Soc.* 2005, **125**, 5193
13. S .J. Lee, A.Hu, W Lin, The first chiral organometallic triangle for asymmetric catalysis; *J. Am. Chem. Soc.* 2002, **124**, 12948-12949.
14. P. S. Mukherjee, N. Das, Y. K Kryschenko., A. M. Arif, P. J. Stang, Design, synthesis, and crystallographic studies of neutral platinum-based macrocycles formed via self-assembly; *J. Am. Chem. Soc.* 2004, **126**, 2464-2473
15. J. Vicente, M. T. Chicote, M. M. Alvarez-Falcon, P. J. Jones, Synthesis and X-ray crystal structure of an anionic heteronuclear metallamacrocyclic triangle; *Chem. Commun.*, **2004**, 2658-2659.
16. P. Teo, L. L. Koh, T. S. A.Hor, Unusual coordination assemblies from platinum(II) thienyl and bithienyl complexes; *Inorg. Chem.*, **42**, 2003, 7290-7296.
17. M. Fujita, O. Sasaki, T. Mitsuhashi, T. Fujita, J. Yazaki, K. Yamaguchi, K. Ogura; On the structure of transition-metal-linked molecular squares; *Chem. Commun.* 1996, 1535-1536.
18. S. Verma, V. Vajpayee, S. M. Lee, H. J. Jung, H. Kim, K.-W. Chi; Effect of ligand flexibility on coordination-driven self-assembly of Pt(II) metallacycles; *Inorg. Chim. Acta* 2012, **387**, 435-440.
19. A. K. Bar, R. Chakrabarty, K.-W. Chi, S. R. Batten, R. P. S. Mukherjee; Synthesis and characterization of heterometallic molecular triangles using ambidentate linker: self-selection of a single linkage isomer; *Dalton Transactions* 2009, **17**, 3222-3229.
20. R. Ingelis, A. D. Katsenis, A. Collins, F. White, C. J. Milios, G. S. Papaefstathiou, E. K. Brechin; Assembling molecular triangles into discrete and infinite architectures; *CrystEngComm* 2010, **12**(7), 2064-2072.
21. E.Zangrando, N.Kulisic, F.Ravalico, I.Bratsos, S.Jedner, M.Casanova, E.Alessio, New ruthenium(II) precursors with the tetradentate sulfur macrocycles tetrathiacyclododecane ([12]aneS₄) and tetrathiacyclohexadecane ([16]aneS₄) for the construction of metal-mediated supramolecular assemblies; *Inorganica Chimica Acta*, 2009, **362** (3), 820-832.
22. J. Heo, Y.-M. Jeon, C. A. Mirkin, Reversible interconversion of

- homochiral triangular macrocycles and helical coordination polymers; *J. Am. Chem. Soc.* 2007, **129** (25), 7712-7713.
23. R. Dreos, G. Nardin, L. Randaccio, P. Siega, G. Tauzher; Self-assembly of cobaloximes and rhodoximes with 3-aminophenylboronic acid: A molecular triangle and a polymer; *Eur. J. Inorg. Chem.* **2002**, (11), 2885-2890.
 24. A.-K. Duhme-Klair, G. Vollmer, C. Mars, R. Fröhlich, Stereoselectivity in the formation of a cyclic trinuclear cis- dioxomolybdenum(VI) complex of a chiral siderophore analogue; *Angew. Chem. Int. Ed.* 2000, **39**(9), 1626-1628.
 25. M. Fujita; Metal-directed self-assembly of two- and three-dimensional synthetic receptors; *Chem. Soc. Rev.* 1998, **27**, 417-425.
 26. D. H. Cao, K. Chen, J. Fan, J. Manna, B. Olenyuk, J. A. Whiteford, P. J. Stang; Supramolecular chemistry and molecular design: Self assembly of molecular squares; *Pure Appl. Chem.* 1997, **69**, 1979-1986.
 27. S. Shanmugaraju, D. Samanta, , B. Gole, , P.S. Mukherjee; Coordination-driven self-assembly of 2D-metallamacrocycles using a shape-selective Pt II 2-organometallic 90° acceptor: Design, synthesis and sensing study; *Dalton Trans.* 2011, **40** (45), 12333-12341.
 28. A. Stephenson, M. D. Ward; Molecular squares, cubes and chains from self-assembly of bis-bidentate bridging ligands with transition metal dications; *Dalton Trans.* 2011, **40** (40),10360-10369.
 29. A. Galstyan, P. J. Sanz Miguel, B. Lippert; A “directed” approach toward a cationic molecular square containing four isonicotinamidate ligands and (4 + 2) (en)Pt II metal entities; *Inorg. Chim. Acta* 2011, **374** (1), 453-460.
 30. P. J. Lusby, P. Müller, S. J. Pike, A. M. Z. Slawin, Stimuli-responsive reversible assembly of 2D and 3D metallosupramolecular architectures; *J. Am. Chem. Soc.* 2009, **131** (45), 16398-16400.
 31. A. Galstyan, P. J. Sanz Miguel, J. Wolf, E. Freisinger, B. Lippert, Discrete Molecular Squares {[*(en)*M(CN)]⁴⁺}₄ Derived from [*(en)*M(CN)₂] (M = Pt II, Pd II) *Eur. J. Inorg. Chem.* 2011 (10), 1649-1656.
 32. K. Halbauer, E.T. Spielberg, A. Sterzik, W. Plass, W. Imhof; Structural and magnetic properties of one-dimensional coordination polymers {*trans*-[Ru(C{triple bond, long}N-*t*Bu)₄(CN)₂]FeX₃]_n vs. molecular squares {*cis*-[Ru(C{triple bond, long}N-*t*Bu)₄(CN)₂]FeX₃]₂ (X = NO₃, Cl); *Inorg. Chim. Acta* 2010, **363** (5), 1013-1020.
 33. H. Arora, F. Lloret, R. Mukherjee; Molecular squares of NiII and CuII: Ferromagnetic exchange interaction mediated by syn-anti carboxylate-

- bridging; *Dalton Trans.* 2009 (44), 9759-9769.
34. H. Kumagai, M. Akita-Tanaka, S. Kawata, K. Inoue, C. J. Kepert, M. Kurmoo; Synthesis, crystal structures, and properties of molecular squares displaying hydrogen and π - π bonded networks; *Cryst. Growth Des.*, 2009, **9** (6), 2734-2741.
 35. R. V. Slone, K. D. Benkstein, S. Belanger, J. T. Hupp, I. A. Guzei, A. L. Rheingold; *Coord. Chem. Rev.* 1998, **171**, 221-243.
 36. K. D. Beckstein, J. T. Hupp, C. L. Stern; Synthesis and characterization of molecular rectangles based upon rhenium thiolate dimmers; *Inorg. Chem.* 1998, **37**, 5404-5405.
 37. P. J. Stang, J. Fan, B. Olenyuk; Molecular architecture via coordination: self-assembly of cyclic cationic porphyrin aggregates via transition-metalbisphosphane auxiliaries; *Chem. Commun.* **1997**, 1453-1454.
 38. C. M. Drain, J.-M. Lehn; Self-assembly of square multiporphyrin arrays by metal ion coordination; *J. Chem. Soc. Chem. Commun.* **1994**, 2313-2315.
 39. R. V. Slone, D. I. Yoon, R. M. Calhoun, J. T. Hupp; Luminescent rhenium/palladium square complex exhibiting excited state intramolecular electron transfer reactivity and molecular anion sensing characteristics; *J. Am. Chem. Soc.* **1995**, **117**, 11813-11814.
 40. P. N. Baxter, J.-M. Lehn, B. O. Kneisel, G. Baum, D. Fenske; The designed self-assembly of multicomponent and multicompartamental cylindrical nanoarchitectures; *Chem. Eur. J.* 1999, **5**, 113- 120.
 41. R. W. Saalfrank, I. Brent, E. Uller, F. Hampel; Template-Mediated Self Assembly of Six- and Eight-Membered Iron Coronates; *Angew. Chem. Int. Ed.* 1997, **36**, 2482-2485.
 42. D. L. Caulder, K. N. Raymond; The rational design of high symmetry coordination clusters; *J. Chem. Soc. Dalton Trans.* **1999**, 1185-1200.
 43. S. Leininger, B. Olenyuk, P. J. Stang; Self-assembly of discrete cyclic nanostructures mediated by transition metals; *Chem. Rev.* 2000, **100**, 853-908.
 44. E. Lindner, A. Bader, Coordination chemistry and catalysis with hemilabile oxygen-phosphorus ligands; *Coord. Chem. Rev.* 1991, **108**, 27.
 45. J. C. Jeffrey, T. B. Rauchfuss; Metal complexes of hemilabile ligands. Reactivity and structure of dichlorobis(o-(diphenylphosphino)anisole) ruthenium(II); *Inorg. Chem.* 1979, **18** (10), 2658-2666.
 46. J. R. Farrell, A. H. Eisenberg, C. A. Mirkin, I. A. Guzei, L. M. Liable-Sands, C. D. Incarvito, A. L. Rheingold, C. L. Stern; *Organometallics*

- 1999, **18**, 4856-4868.
47. J. K. M. Sanders; Supramolecular catalysis in transition; *Chem. Eur. J.* 1998, **4**, 1378-1383.

Chapter 2

Principles of cation- π interactions in supramolecular chemistry

Wojciech Ostrowski and Rafał Frański
*Adam Mickiewicz University in Poznań, Faculty of Chemistry,
Umultowska 89b, 61-614 Poznań, Poland*

1. Introduction

Studies of noncovalent interactions are the basis of issues discussed by the supramolecular chemistry. These binding forces play an important role in structural biology (stabilization of protein and nucleic acids structures) and molecular recognition. To them belong i.a.:

- hydrogen bonds,
- hydrophobic interactions,
- ionic bonds,
- van der Waals forces,
- π interactions.

Among listed, π interactions can be a great tool for drug design, new ligands design, binding sites searching, asymmetric catalysis and conformational analysis. There are certain types of π interactions. The most widely deliberated are cation- π and anion- π . Besides, there are π - π stacking and H- π (CH- π , OH- π , NH- π and similar) [1]. This work focuses on the most widely discussed – forces between cation and π electrons.

2. Cation- π interactions

The first study on cation- π interactions appeared in 1981 [2]. The Kebarle group proved these forces to exist in the gas phase. Their experiments and calculations showed that potassium cation in the gas phase is better stabilized by benzene than by water – obviously opposite situation holds for aqueous phase (see fig. 1). A comparison of binding energies for benzene and alkali metal cations suggests electrostatic model. The highest energy for bond is for Li^+ and decreases in sequence for Na^+ , K^+ and Rb^+ (see tab. 1).

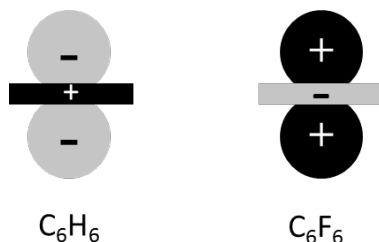


Figure 2. Comparison of quadrupole moments in benzene and hexafluorobenzene.

After successful studies in the gas phase, a logical consequence was an application of acquired knowledge to conditions closer to nature. For that reason research focused on aqueous media. A synthetic receptor has to compete for cation (guest) with water molecules in order to form a host-guest complex. In water cation has solvation shell so a receptor has to bind a guest more strongly than solvent. It is possible thanks to cation- π and another interactions (like hydrophobic). If this process works in the synthetic mode, probably nature uses it equally well in biological recognition. Due to the large amount of relations in water individual interactions are not easy to study. An important role in water solutions plays hydrophobic interaction. In many cases this binding force is so dominant that the others have marginal impact. Solubility is the next problem. Often, for a receptor to be soluble in water, it must have an additional polar groups – usually charged, e.g. carboxyl group. When measuring interactions with cation and receptor, appended groups can make the analysis difficult because they may interact with cation. Up to 1986 most of works had been based on simple aromatics molecules (flat structures). But the Dougherty group decided to investigate hydrophobic cyclophanes with aliphatic molecules. Their studies are the most extensive in terms of cation- π interactions in aqueous media [6]. A discovery of these forces was related to systematic tests of quaternary ammonium salt adamantyltrimethylammonium (ATMA, **1**) with cyclophanes containing different connectors. Monomeric and soluble (through anionic carboxylates) in pH 7-9 structures were chosen as cyclophanes. Also characterized by hydrophobic binding cavity. Binding of ATMA by cyclophanes host was surprising because only few aliphatic molecules had been known at the time to have this ability. Initially, ion-dipole interaction was thought to be responsible for connection. But in course of experiments during which linker in cyclophane was changing, it was discovered that changing from benzene rings (**2**) to cyclohexanes (**3**) in macrocycle decreases dramatically capability of complex formation. It was a

precise evidence that trimethylammonium end of ATMA binds into hydrophobic cavity because of cation- π interactions with benzene rings – the process that had not occurred with cyclohexanes. It also excluded participation of remote carboxylates groups in cation binding. Therefore, benzene is less polarizable than cyclohexane. If interactions with the induced dipole predominates cation- π , host **3** will be better for ATMA than **2**. Following experiments confirmed this theory [7].

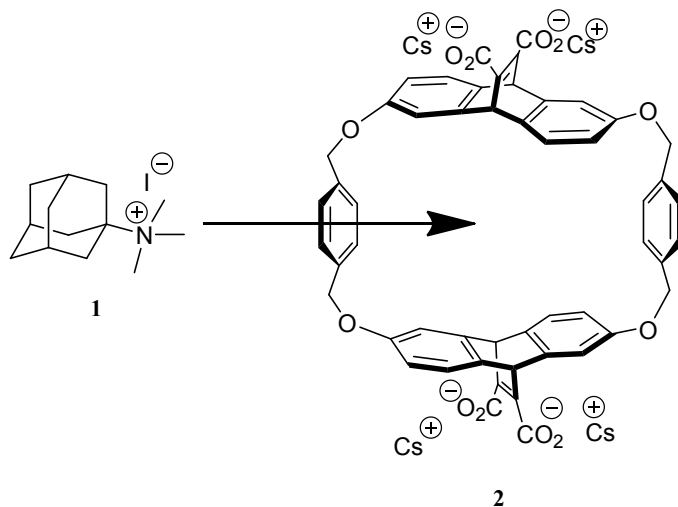


Figure 3. Formation of supramolecule by cation- π interactions.

A comparison of different guests showed that cation of N-methylquinoline is 40-fold better bound than neutral quinolone through host **2** and for **3** the difference is minimal. Electron rich indole is bound by **2** and **3** with similar power – considerably less in comparison to the above-mentioned guests [8]. The replacement of benzene rings by furan (**4**) or thiophene (**5**) caused a reduction of cation binding capacity [9].

What was important from biological point of view, was that acetylcholine interacts with host **2** in the similar way as with natural receptor [10].

The Schneider group synthesized receptors differently than Dougherty. These receptors had charge from quaternary nitrogen atoms (**6**). Good guests for them were arenes (like naphthalene) and nucleosides. In comparison to naphthalene analogues without aromatics, binding energy was substantially higher for aromatic guests. Because hydrophobic properties of these pairs are

comparable, binding must be related with cation- π interactions. In this case, when quaternary nitrogen atoms are replaced by anionic groups (hosts **7** and **8**, see fig. 5), receptors have hydrophobic cavity without charge. Charge was transferred outside the pocket. Obviously, receptors **7** and **8** bind naphthalene worse than **6**. But for aliphatic molecules, which cation- π interactions are not relevant for (main force are hydrophobic), these hosts have parallel attraction [11]. The differences between aromatic or aliphatic guests and positively and negatively charged hosts led to the conclusion: in the case of cation- π interactions existing binding energy increases with the number of phenyl rings in the guest molecule. It was calculated that for every additional ring energy of cation- π force grows by 2 kJ/mol [12].

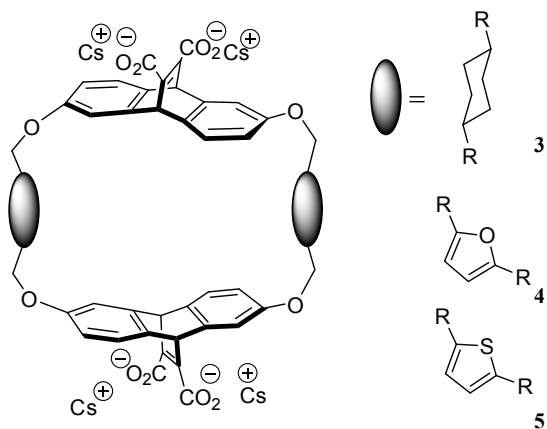


Figure 4. Examples of cyclophanes.

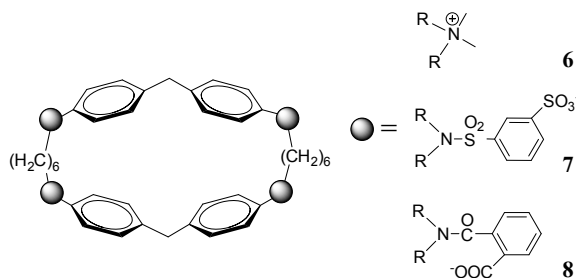


Figure 5. Host with own positive charge (**6**) and with hydrophobic pocket (**7**, **8**).

Selectivity of hosts was the main subject of the Lehn group's work. Also cation- π interactions play significant role in this process. Examined structures of cyclophanes had carboxylates groups increasing the solubility in water. Figure 6 presents three molecules which combine with quaternary ammonium (acetylcholine and related) and iminium ions in 1:1 ratio [13]. As before, Lehn's synthetic hosts are the strongest receptors (**9** and related) for acetylcholine at neutral pH. On the basis of the construction of these pairs it can be assumed that cation- π forces dominate among binding forces but the quantitative measurements are problematic to perform on it [6]. In 1987 J.-M. Lehn and other scientists from USA – D. J. Cram and C. J. Pedersen were awarded the Nobel Prize “for their development and use of molecules with structure-specific interactions of high selectivity” [14].

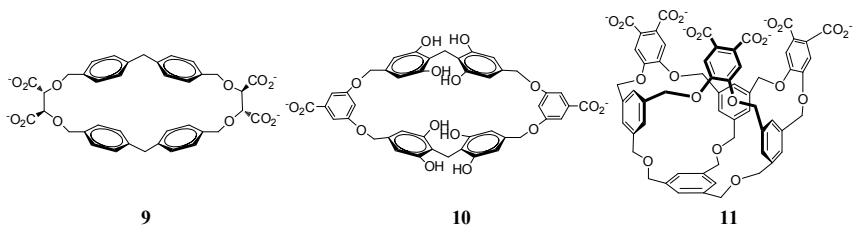


Figure 6. The Lehn group quaternary ammonium ions hosts [6].

Interesting properties can be observed for the two structures synthesized by Schwabacher *et al.* [15]. These molecules have opposite charge. And for **13** negative charge takes active part in binding (situated nearby host's cavity, compare with **7** and **8**). 2,7-Dihydroxynaphthalene and tropolone were complexed 5 times more strongly (in D₂O/CD₃OD 60:40) by the anionic structure. In this example, anion was more prone to the aromatic rings (due to affinity to the positively charged edge of the ring – see fig. 2).

Mass spectrometry is good technique for measurements in the gas phase. Different methods of this technique have been used to investigate interactions. Ion cyclotron resonance (FT-ICR) was the main method for Dunbar *et al.* Their works studied aromatic aminoacids in cooperation with alkali metal ions and determined that K⁺ is bound weaker by Phe, Trp and Tyr aminoacids than Na⁺ [16-17]. CID experiments allowed to calculate bond energies for bis(benzene) and alkali metal ions [18]. Our group uses MS method – electrospray ionization (ESI) to investigate cation- π interactions. This force supports formation of sandwich complex of benzo-crown ethers and alkali metal ions (Na⁺, K⁺, Cs⁺) [19]. Also causes creation of molecular ion (radical cation) of diclofenac

molecule in a presence of Cu^{2+} ion – evidence of the existence of cation- π interactions [20]. Secondary ion mass spectrometry (SIMS) and ESI were used for the experiments with calix[4]arenes (see fig. 8) and metal ions. In case of calix[4]arene having substituent with oxygen (**14**), it was difficult to distinguish how cation- π interactions influence binding. But for structures **15** and **16** with aliphatic substituents, complexes with metals were also observed which means that impact must be significant. As a result of signals for $[\mathbf{16}+\text{Rb}]^+$ and $[\mathbf{16}+\text{Cs}]^+$ being abundant (more than for $[\mathbf{16}+\text{Li}]^+$, $[\mathbf{16}+\text{Na}]^+$ and $[\mathbf{16}+\text{K}]^+$), structure **16** has to form pocket of size ideal for cesium cation [21].

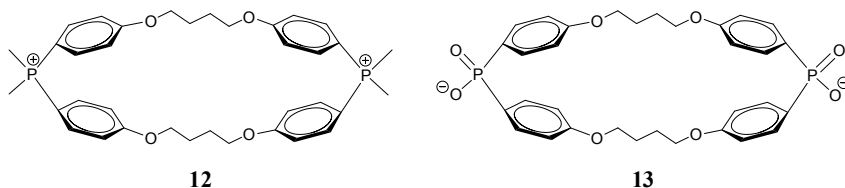


Figure 7. Oppositely charged macrocycles.

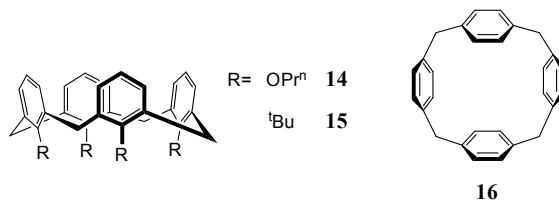


Figure 8. Structures examined by mass spectrometry.

Besides studies in aqueous media, experiments in organic solvents are also interesting because they allow to eliminate unwanted effects which exist in the case of water solutions like hydrophobic force (they are in charge of driving aliphatic guest to cavity, so sometimes influence of cation- π interactions may be obscured). It requires to change the polarity of host molecules, e.g. for the tests in chloroform molecule **2** was esterified to tetramethyl ester. This host binds with strong attraction ATMA (**1**) or methyl quinoline cation. It was also found that neutral molecules like quinoline are not good guests for this host. It suggested that cation- π interaction is critical for the binding [22]. Also structure **11** was esterified to hexamethyl ester by the Lehn group. This ester binds ATMA (**1**) very well in chloroform [23].

Computational studies showed how in the same solvents energy of model

cation- π interaction differs from salt bridge. As an example benzene – methyl ammonium cation (cation- π interactions) and methyl ammonium cation and acetate (as salt bridge) were used. The comparison of interaction energies and solvent dielectric constants is presented in table 2. In the gas phase, obviously, ion pair has a high affinity. It decreases with increasing polarity of solvent, as a consequence of getting better solvation of ions (the same as most other intermolecular interactions). Cation- π interaction still have the same energy in different solvents. As calculated for dielectric constant 22.7, interaction energies for both systems are the same. This value is close to ethanol (see tab. 2) and acetone (20.7). As a result of having better parameters in water than salt, cation- π interactions more often exist on the surface of proteins, where water is always available [24].

Table 2. Interactions energies (kJ/mol) at the SM5.42R/HF/6-31+G* level [24].

solvent	dielectric constant	Benzene-MeNH ₃ ⁺	MeNH ₃ ⁺ -acetate
vacuum	1	-52.3	-525.4
CCl ₄	2.2	-32.7	-223.6
EtOH	24.9	-23.4	-21.8
CH ₃ CN	37.5	-23.4	-15.9
H ₂ O	80.0	-23.0	-9.2

The important factor for binding energy is, as it turned out, a counterion influence. The counterion determines solubility. Series of experiments were performed using cyclophane host (**17**) and tetramethylammonium cation (TMA, **19**) and acetylcholine (**18**) with different anions. CH₃Cl was used as a solvent. In the early investigations of cation- π forces they were not involved in checking the impact of counterion because borate buffer was used in the studies. In these solutions anions are overwhelmed by borate, so counterion effect is neutralized. The results showed that salt is less soluble, the less binding host and guest are. Thus, poorly soluble salts are strongly bound (see tab. 3). In consequence, whole ion pair rather than dissociated cation has to enter the host cavity in CHCl₃ [25].

Apart from cation- π interactions between metal ions, organic cations and π electrons from aromatic systems, described in most of works concerning the subject, these interactions have been also identified in a system with non-aromatic π electrons. This combination creates e.g. acetylene and Ca⁺ (**20**) [26] or ethylene and ammonium cation (**21**) [27]. The Yamada group discovered the presence of these forces in a coordination between a thiocarbonyl group and a pyridinium ring (**22**). Molecule which it was revealed in is shown in fig. 10 (**23**) [28].

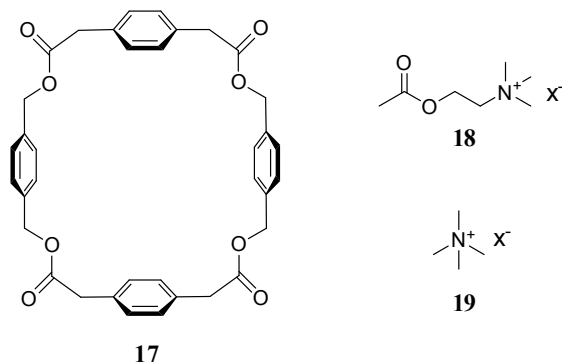


Figure 9. Host and guests in the counterion effect studies.

Table 3. Solubilities (S [mol/L]), standard free energies of binding (ΔG° [kJ/mol]) of complexes TMA and ACh salts with host (17) [25].

tetramethylammonium			acetylcholine		
counterion	ΔG°	S	counterion	ΔG°	S
picrate	-8.35	$1.3 \cdot 10^{-4}$	picrate	-6.33	$6.9 \cdot 10^{-4}$
triflate	-7.68	$7.4 \cdot 10^{-5}$	iodide	-5.99	$4.8 \cdot 10^{-4}$
TFA	-6.05	$2.9 \cdot 10^{-4}$	2,4-DNN	-4.75	$7.8 \cdot 10^{-4}$
chloride	-4.64	$1.1 \cdot 10^{-3}$	bromide	-3.88	$6.4 \cdot 10^{-3}$
acetate	-2.60	$1.1 \cdot 10^{-1}$	chloride	-3.21	$1.0 \cdot 10^{-1}$

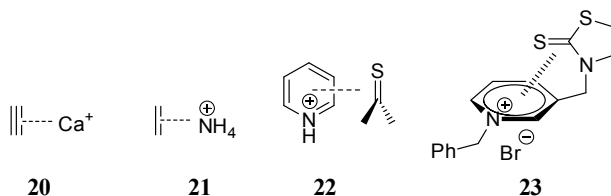


Figure 10. Examples of cation- π interaction with non-aromatic π electrons.

3. Cation- π interactions in synthesis

McCurdy *et al.* proposed to use the **2** host molecule to biomimetic catalysis of alkylation by methyl iodide of a quinoline and similar (the Menshutkin reaction). As well dealkylation by thiocyanate of dimethylphenylsulfonium. During the reaction, host binds the transition state with high efficiency. Stabilization of transition state is fundamental in catalysis of this reaction. It is a consequence of polarizability effect and, naturally, cation- π interactions. Complex of host and

transition state (**24**) is shown schematically in fig. 11. For the same reasons host **2** improves efficiency (10 times) of dealkylation of **25** [29].

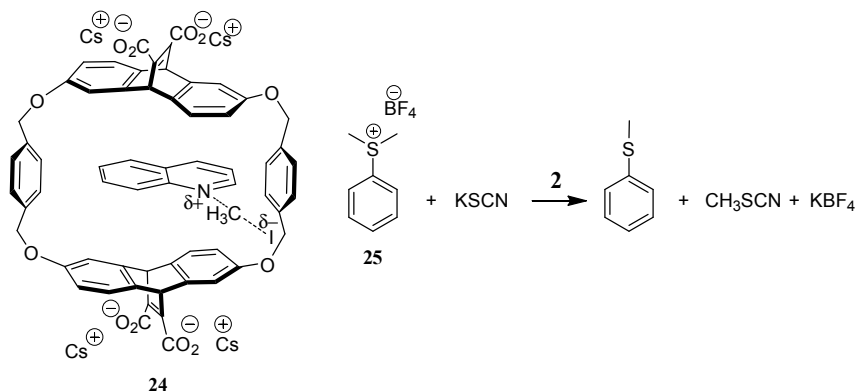


Figure 11. Alkylation and dealkylation with host **2** as the catalyst.

These forces have proved to be a good tool in organic synthesis. Especially in stereoselective reactions where they decide about molecular conformations.

As a result of cation- π forces, diphenylcyclopropane (**26**) is subjected to photoisomerization process. In this reaction with zeolites and alkali metal ions, *trans* isomer turns into *cis* with efficiency of 91% [30].

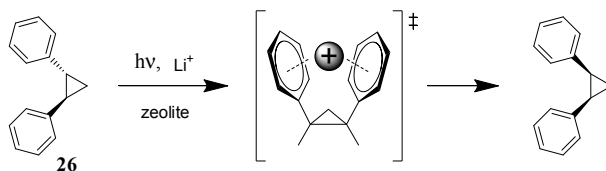


Figure 12. Photoisomerization of diphenylcyclopropane.

Yamada and co-workers proposed a method of synthesis 1,4-dihydropyridines (**27**). Intramolecular cation- π interaction (presented in the fig. 13 in brackets) exists in this process. The reaction proceeds with almost 100% stereoselectivity with 80% efficiency. In the case of cation- π interactions being weak (benzyl is replaced by phenyl), stereoselectivity decreases to ca. 10%. Chiral 1,4-dihydropyridines are required in synthesis of natural products or NADH models [31].

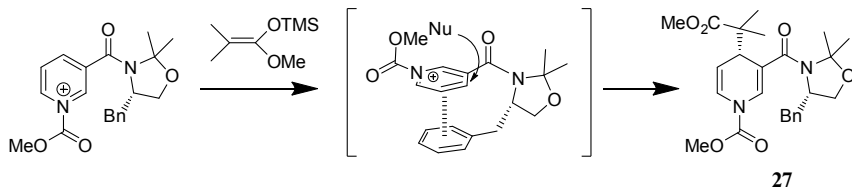


Figure 13. Nucleophilic addition to the pyridinium ring [31].

In the Schmidt reaction an appropriate substituent may determine regioselectivity of this rearrangement. In the example, substrate (**28**) had *iso*-propyl (**29**) or phenyl (**30**) as substituent. In a solution occurs equilibrium (see fig. 14, **32**). If phenyl functions as a substituent, situation is like in the figure 14 (**31**). In the same situation *iso*-propyl stabilizes intramolecular interaction by hydrogen bond. The substituent with phenyl gave products in 64:36 ratio for conformer with cation- π interactions (**34**) while *iso*-propyl resulted in ratio of 88:12 for the opposite (**33**). The best ratio (5:95) was obtained for substrate (**35**) [32].

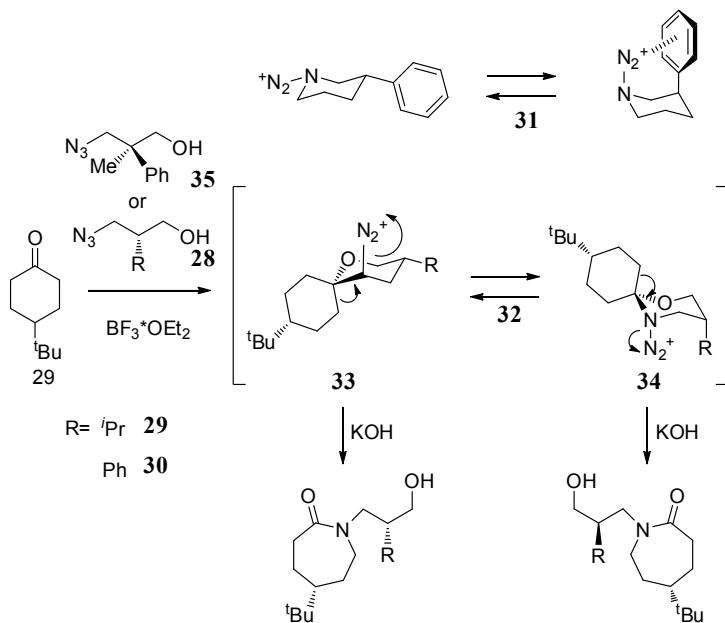


Figure 14. Regioselective rearrangement – the Schmidt reaction [32].

4. Conclusions

It has been presented that cation- π interactions constitute an interesting topic of supramolecular chemistry. Scientists have been intensively involved in the study of these forces in recent years which is demonstrated by two extensive publications [33-34]. The interactions in question bring hope for the development of organic synthesis and chemistry of proteins.

References

1. J. Cheng, X. Luo, X. Yan, Z. Li, Y. Tang, H. Jiang, W. Zhu; Research progress in cation- π interactions. *Sci. China Ser. B-Chem.* 2008, *51*, 709-717.
2. J. Sunner, K. Nishizawa, P. Kebarle; Ion-solvent molecule interactions in the gas phase. The potassium ion and benzene. *J. Phys. Chem.* 1981, *85*, 1814-1820.
3. D. A. Dougherty; Cation- π interactions involving aromatic amino acids. *J. Nutr.* 2007, *137*, 1504S-1508S; discussion 1516S-1517S.
4. G. R. Dennis, G. L. D. Ritchie; Dilute-solution field gradient-induced birefringence and molecular quadrupole moment of benzene. *J. Phys. Chem.* 1991, *95*, 656-660.
5. M. Meot-Ner, C. A. Deakyn; Unconventional ionic hydrogen bonds. 1. $\text{CH}^{\delta+}\cdots\text{X}$. Complexes of quaternary ions with n - and π -donors. *J. Am. Chem. Soc.* 1985, *107*, 469-474.
6. J. C. Ma, D. A. Dougherty; The Cation- π interaction. *Chem. Rev.* 1997, *97*, 1303-1324.
7. T. J. Shepodd, M. A. Petti, D. A. Dougherty; Tight, oriented binding of an aliphatic guest by a new class of water-soluble molecules with hydrophobic binding sites. *J. Am. Chem. Soc.* 1986, *108*, 6085-6087.
8. T. J. Shepodd, M. A. Petti, D. A. Dougherty; Molecular recognition in aqueous media: donor-acceptor and ion-dipole interactions produce tight binding for highly soluble guests. *J. Am. Chem. Soc.* 1988, *110*, 1983-1985.
9. P. C. Kearney, L. S. Mizoue, R. A. Kumpf, J. E. Forman, A. McCurdy, D. A. Dougherty; Molecular recognition in aqueous media. New binding studies provide further insights into the cation- π interaction and related phenomena. *J. Am. Chem. Soc.* 1993, *115*, 9907-9919.
10. D. Dougherty, D. Stauffer; Acetylcholine binding by a synthetic receptor: implications for biological recognition. *Science* 1990, *250*, 1558-1560.
11. H.-J. Schneider, T. Blatter; Modification of hydrophobic and polar

- interactions by charged groups in synthetic host-guest complexes. *Angew. Chem., Int. Ed. Engl.* 1988, 27, 1163-1164.
- H. J. Schneider, T. Schiestel, P. Zimmermann; Host-guest supramolecular chemistry. 34. The incremental approach to noncovalent interactions: coulomb and van der Waals effects in organic ion pairs. *J. Am. Chem. Soc.* 1992, 114, 7698-7703.
 - M. Dhaenens, L. Lacombe, J.-M. Lehn, J.-P. Vigneron; Binding of acetylcholine and other molecular cations by a macrocyclic receptor molecule of speleand type. *J. Chem. Soc., Chem. Commun.* 1984, 1097-1099.
 - http://www.nobelprize.org/nobel_prizes/chemistry/laureates/1987/press.html
 - A. W. Schwabacher, S. Zhang, W. Davy; Directionality of the cation- π effect: a charge-mediated size selectivity in binding. *J. Am. Chem. Soc.* 1993, 115, 6995-6996.
 - V. Ryzhov, R. C. Dunbar, B. Cerda, C. Wesdemiotis; Cation- π effects in the complexation of Na⁺ and K⁺ with Phe, Tyr, and Trp in the gas phase. *J. Am. Soc. Mass Spectrom.* 2000, 11, 1037-1046.
 - A. Gapeev, R. C. Dunbar; Cation- π interactions and the gas-phase thermochemistry of the Na⁺/phenylalanine complex. *J. Am. Chem. Soc.* 2001, 123, 8360-8365.
 - J. C. Amicangelo, P. B. Armentrout; Absolute binding energies of alkali-metal cation complexes with benzene determined by threshold collision-induced dissociation experiments and ab initio theory. *J. Phys. Chem. A* 2000, 104, 11420-11432.
 - R. Frański; Cation- π interactions in gas-phase complexes formed by benzo-crown ethers and alkali metal cations. *Rapid Commun. Mass Spectrom.* 2011, 25, 672-674.
 - W. Ostrowski, K. Linko, R. Frański; Formation of diclofenac molecular ions as the effect of Cu²⁺- π interaction under electrospray ionization mass spectrometry conditions. *Eur. J. Mass Spectrom.* 2012, 18, 43-50.
 - F. Inokuchi, Y. Miyahara, T. Inazu, S. Shinkai; "Cation- π interactions" detected by mass spectrometry; selective recognition of alkali metal cations by a π -basic molecular cavity. *Angew. Chem., Int. Ed. Engl.* 1995, 34, 1364-1366.
 - D. A. Stauffer, D. A. Dougherty; Ion-dipole effect as a force for molecular recognition in organic media. *Tetrahedron Lett.* 1988, 29, 6039-6042.
 - Meric R., Lehn J.-M., Vigneron J.-P. ; Complexation of quaternary

- ammonium cations by a new basket-shaped macrotricyclic cyclophane. *Bull. Soc. Chim. Fr.* 1994, *131*, 579-583.
24. J. P. Gallivan, D. A. Dougherty; A computational study of cation- π interactions vs salt bridges in aqueous media: Implications for protein engineering. *J. Am. Chem. Soc.* 2000, *122*, 870-874.
 25. S. Bartoli, S. Roelens; Binding of acetylcholine and tetramethylammonium to a cyclophane receptor: anion's contribution to the cation- π Interaction. *J. Am. Chem. Soc.* 2002, *124*, 8307-8315.
 26. M. R. France, S. H. Pullins, M. A. Duncan; Spectroscopy of the Ca^+ -acetylene π complex. *J. Chem. Phys.* 1998, *108*, 7049-7051.
 27. M. Meot-Ner, C. A. Deakyne; Unconventional ionic hydrogen bonds. 2. $\text{NH}^+\cdots\pi$ Complexes of onium ions with olefins and benzene derivatives. *J. Am. Chem. Soc.* 1985, *107*, 474-479.
 28. S. Yamada, T. Misono, S. Tsuzuki; Cation- π Interactions of a thiocarbonyl group and a carbonyl group with a pyridinium nucleus. *J. Am. Chem. Soc.* 2004, *126*, 9862-9872.
 29. A. McCurdy, L. Jimenez, D. A. Stauffer, D. A. Dougherty; Biomimetic catalysis of $\text{S}_{\text{N}}2$ reactions through cation- π interactions. The role of polarizability in catalysis. *J. Am. Chem. Soc.* 1992, *114*, 10314-10321.
 30. P. Lakshminarasimhan, R. B. Sunoj, J. Chandrasekhar, V. Ramamurthy; Cation- π interaction controlled selective geometric photoisomerization of diphenylcyclopropane. *J. Am. Chem. Soc.* 2000, *122*, 4815-4816.
 31. S. Yamada, C. Morita; Face-Selective Addition to a cation- π complex of a pyridinium salt: synthesis of chiral 1,4-dihydropyridines. *J. Am. Chem. Soc.* 2002, *124*, 8184-8185.
 32. C. E. Katz, J. Aubé; Unusual tethering effects in the Schmidt Reaction of hydroxyalkyl azides with ketones: cation- π and steric stabilization of a pseudoaxial phenyl group. *J. Am. Chem. Soc.* 2003, *125*, 13948-13949.
 33. A. S. Mahadevi, G. N. Sastry; Cation- π interaction: its role and relevance in chemistry, biology, and material science. *Chem. Rev.* 2012.
 34. S. Yamada; Intramolecular cation- π interaction in organic synthesis. *Org. Biomol. Chem.* 2007, *5*, 2903-2912.

Chapter 3

The influence of aggregates of calixarenes and dendrimers on the protolytic equilibria of dyes in aqueous solution

N.A. Vodolazkaya^a, N.O. Mchedlov-Petrosyan^a, L.N. Bogdanova^b,
R.V. Rodik^c and V.I. Kalchenko^c

^a *Department of Physical Chemistry, V. N. Karazin Kharkov National University, Svoboda sq. 4, 61022, Kharkov, Ukraine*

^b *Pharmstandart-Biolik, Pomerki 70, 61084, Kharkov, Ukraine*

^c *Institute of Organic Chemistry, National Academy of Science of Ukraine, Kiev, 02094, Ukraine*

1. Introduction

Nowadays, the synthesis and application of water-soluble receptor molecules, such as crown ethers, cryptands, calixarenes, dendrimers, etc., belong to the most important tasks of supramolecular chemistry [1]. The solubility in water is usually achieved by attaching ionic groups to the molecules [2–6]. Further interactions of thus modified receptors, in particular calixarenes, with various substrates (either molecules or ions) in aqueous media are usually considered only in terms of "host + guest" association [7–13].

Meanwhile, large cavity-bearing molecules, among them those containing charged groups, are able to form own aggregates (or associates, micelles, clusters) in water [4, 5, 14–24] because of hydrophobic interactions. Therefore apart from "host + guest" supramolecular interactions, micellar effects should be taken into account. The last effects and their influence on the state of compounds dissolved in water are considered in full for the case of well-established micellar solutions of colloidal surfactants [25]. The non-aqueous microenvironment in concert with the interfacial micellar charge display a specific kind of modification of the properties of substrates bound to the micellar pseudophase [25]. However, the corresponding information concerning the supramolecular systems is lacking.

In order to fill a gap in our knowledge of this issue, we conducted a series of systematic studies with cationic calixarenes and dendrimers in aqueous media [26–31]. The brief review given in this chapter is aimed to summarize the main results.

In Figures 1 and 2, the calixarenes and dendrimers examined in our studies are presented. As suitable tools for such a study we used a set of organic dyes: acid-base and solvatochromic indicators and luminophores.

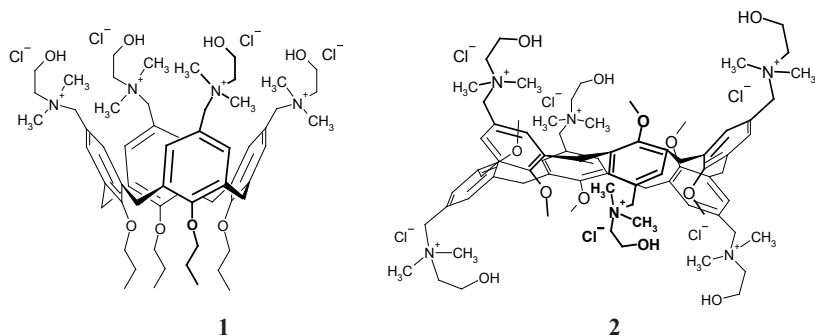


Figure 1. 5,11,17,23-tetrakis(*N,N*-dimethyl-*N*-hydroxyethylammonium)-methylene-25,26,27,28-tetrapropoxy-calix[4]arene tetrachloride (**1**) and 5,11,17,23,29,35-hexakis(*N,N*-dimethyl-*N*-hydroxyethylammoniummethylene)-37,38,39,40,41,42-hexametoxycalix[6]arene hexachloride (**2**) in their most probable conformations.

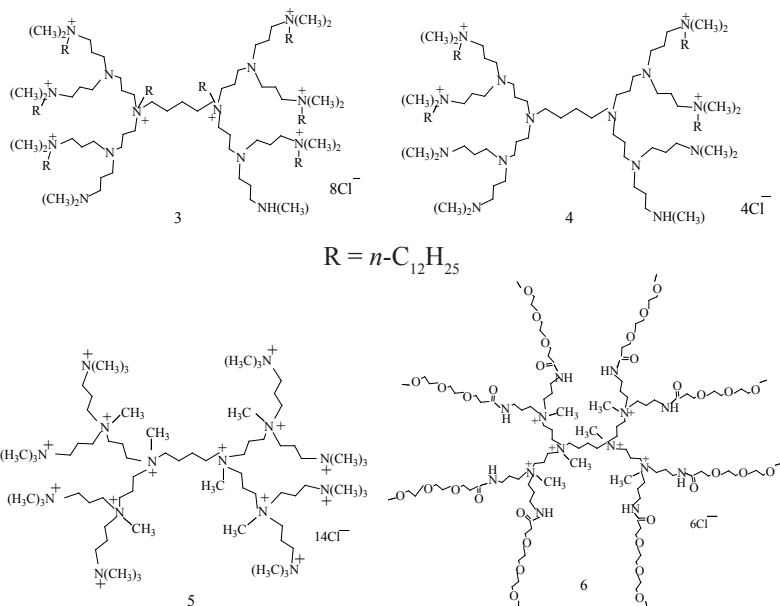


Figure 2. The structure of dendrimers (**3** – $D(8)(\text{CH}_3)_{16}(\text{C}_{12}\text{H}_{25})_8$, **4** – $D(8)(\text{CH}_3)_{16}(\text{C}_{12}\text{H}_{25})_4$, **5** – PMD(8), **6** – IMD8-CO-MPEG).

2. Phenomenological approach: the shift of the acid-base equilibria caused by ionic dendrimers and calixarenes

Indicator dyes are common molecular probes for studying surfactant micelles, droplets of microemulsions, phospholipid liposomes, etc. because of high sensitivity of their spectral and acid-base properties to the nature of the microenvironment [25]. Such dyes were also often used in the research of the properties of receptor molecules [7, 9, 11, 12]. However, in the cited papers the interactions of the receptor cavity with the dye molecule (or ion), i.e., the “host + guest” interactions, have primarily been taken in consideration.

In order to investigate the aqueous solutions of the above calixarenes and dendrimers as media for the acid-base reactions, we utilized over twenty organic dyes [26–31].

For example, the relatively small-sized prolonged indicator molecules are represented by methyl orange (Figure 3). In principle, such species may be docked into the calixarene cavity.

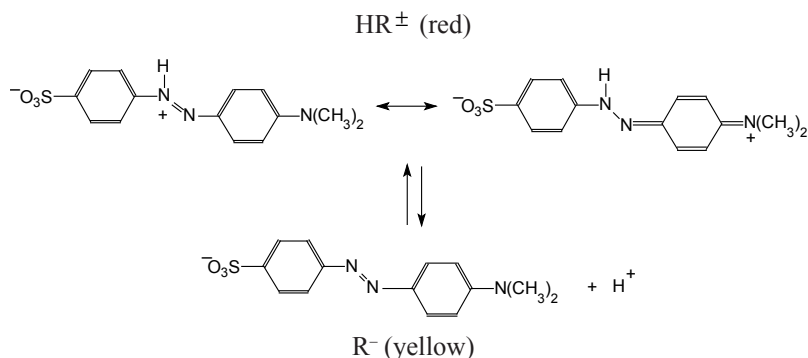


Figure 3. The azo dye methyl orange: the zwitterionic (HR^{\pm}) and anionic (R^-) forms.

The standard acid-base sulfonephthalein indicators phenol red ($X^1 = X^2 = X^3 = H$) and especially its derivatives, such as bromophenol blue, thymol blue, and bromothymol blue (Figure 4), are certainly too large to be involved to high extent into the host cavity, at least in the case of the calixarenes under study [26, 31]. Besides these indicators, methyl yellow, neutral red, four nitrophenols, as well as fluorescein (Figure 5) and its derivatives eosin, rose Bengal B, decylfluorescein, and some other dyes were also involved in the investigation.

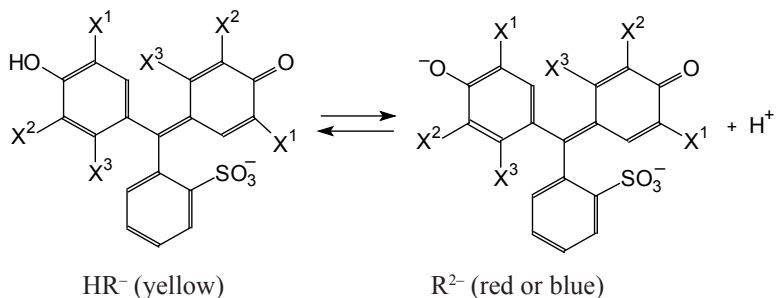


Figure 4. The monoanionic (HR^-) and dianionic (R^{2-}) forms, sulfonephthalein dyes.

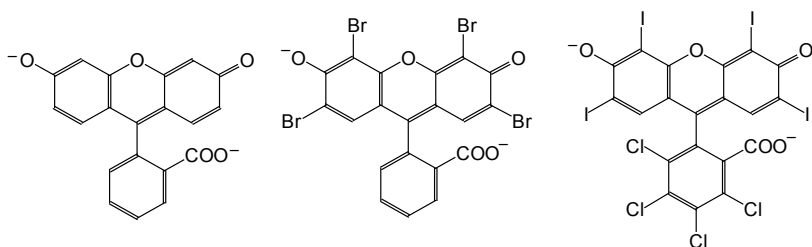


Figure 5. The R^{2-} forms of fluorescein, 2,4,5,7-tetrabromofluorescein (eosin), and 2,4,5,7-tetraiodo-3',4',5',6'-tetrachlorofluorescein (rose Bengal B).

As a key quantitative characteristic, the so-called “apparent” $\text{p}K_a^{\text{app}}$ value of the indicator dye was determined by means of visible spectroscopy accompanied by potentiometric pH determination [25]. Normally, the concentration of indicator dyes in solutions is chosen in the region of 1×10^{-5} M. The concentration of the dendrimer or calixarene was as a rule within the range of 1×10^{-5} to 0.01 M.

In brief, our investigations [26–31] have demonstrated that appearance of cavity-bearing species **1-6** in solution causes the same effects as the introduction of cetyltrimethylammonium bromide (CTAB), *N*-cetylpyridinium chloride (CPC), etc. The $\text{p}K_a^{\text{app}}$ shifts against the $\text{p}K_a$ in water ($\text{p}K_a^{\text{w}}$) are of the same direction and close by value to those registered in micellar solutions of cationic surfactants.

The $\text{p}K_a^{\text{app}}$ values of indicators in solutions of dendrimers [27] are exemplified in Table 1, and some data for calixarene solutions [28] are

compiled in Table 2. The symbols $\text{p}K_a^w$ and $\text{p}K_a^{w*}$ denote the indices of the thermodynamic dissociation constants in water and of the constants at the given ionic strength, I , respectively.

Table 1. The $\text{p}K_a^{app}$ values of different indicator dyes in 1.2×10^{-4} M solutions of dendrimer **3 I** (≈ 0.01 M) and cationic surfactants, CPC and CTAB [27]

Dye ($\text{p}K_a^w$)	$\text{p}K_a^{app}$	$\Delta\text{p}K_a^{app}$	$\Delta\text{p}K_a^{app}$ in surfactant micelles
Bromophenol blue (4.20)	2.19 ± 0.04	-2.01	-(1.94–2.16)
Decylfluorescein (6.31)	4.92 ± 0.03	-1.39	-(1.37–1.39)
Bromothymol blue (7.30)	6.42 ± 0.04	-0.88	-(0.71–0.94)
Thymol blue (9.20)	8.50 ± 0.03	-0.70	-(0.30–0.37)

The medium effects (here: the $\Delta\text{p}K_a^{app} = \text{p}K_a^{app} - \text{p}K_a^w$ values) are governed rather by the charge type of the acid-base couple and the nature of the ionizing group, than by the size of the dye ions and molecules. This strongly resembles the well-documented interaction of dyes with micelles of cationic surfactants [25]. The dependence of the $\text{p}K_a^{app}$ values on the concentration of the receptor molecules and the alteration of the absorption spectra of the equilibrium forms of the indicators as compared with those in water are typified in Figures 6 and 7 respectively.

Such type of dependences and absorption band shifts are also registered for sulfonephthalein indicators in the presence of cationic surfactants.

Hence, the medium effects for a number of indicator dyes in solutions of **1-6**, on the one hand, and in micellar solutions of common cationic surfactants, on the other hand are similar. This allowed deducing that the dyes may interact with the species **1-6** as with cationic micelles. Even more possible seemed to be the formation of positively charged aggregates and the dye + aggregate interactions.

Table 2. The indices of the apparent ionization constants of acid–base indicators in 2.510^{-3} M aqueous solution of calixarene **1**; $I = 0.05$ M (NaCl + buffer) [28]

Indicator	Charge type	pK_a^{w*} (pK_a^w)	pK_a^{app} in 1 solution	ΔpK_a^{app}
Neutral red	A ⁺ B ⁰	6.47 ± 0.04 (6.50)	6.41 ± 0.05	≈ 0
Thymol blue	AB ⁻	1.49 ± 0.01 (1.70)	0.29 ± 0.13^a	-1.41
Methyl orange	AB ⁻	3.21 ± 0.02 (3.40)	1.88 ± 0.05^b	$-1.52 [-2.18]^b$
Methyl yellow	A ⁺ B ⁰	3.06 ± 0.05 (3.25)	2.57 ± 0.04	-0.68
2,4-Dinitrophenol	A ⁰ B ⁻	3.81 ± 0.02 (4.11)	2.88 ± 0.05	$-1.23 [-1.46]^c$
2,6-Dinitrophenol	A ⁰ B ⁻	3.58 ± 0.01 (3.71)	3.24 ± 0.01	-0.47
2,5-Dinitrophenol	A ⁰ B ⁻	5.08 ± 0.02 (5.15)	4.52 ± 0.05	-0.63
4-Nitrophenol	A ⁰ B ⁻	7.07 ± 0.04 (7.15)	7.08 ± 0.12^d	$-0.07 [-0.81]^d$
Bromophenol blue	A ⁻ B ²⁻	4.05 ± 0.02 (4.20)	2.59 ± 0.06^e	$-1.61 [-1.59]^e$
Bromocresol green	A ⁻ B ²⁻	4.85 ± 0.01 (4.90)	4.14 ± 0.05	-0.76
Bromocresol purple	A ⁻ B ²⁻	6.30 ± 0.02 (6.40)	5.51 ± 0.10	-0.89
Bromothymol blue	A ⁻ B ²⁻	7.26 ± 0.02 (7.30)	6.82 ± 0.03	-0.48
Phenol red	A ⁻ B ²⁻	7.97 ± 0.02 (8.00)	7.40 ± 0.06^f	$-0.60 [-0.93]^f$
<i>ortho</i> -Cresol red	A ⁻ B ²⁻	8.25 ± 0.01 (8.46)	7.58 ± 0.04	-0.88
<i>meta</i> -Cresol purple	A ⁻ B ²⁻	8.55 ± 0.01 (8.70)	8.28 ± 0.05	-0.42
Thymol blue	A ⁻ B ²⁻	9.07 ± 0.02 (9.20)	9.14 ± 0.02	-0.06

^a $I > 0.05$ M; ^b at **1** conc. 0.01 M, pK_a^{app} of methyl orange equals 1.22 ± 0.05 ; ^c at **1** conc. 7.5×10^{-3} M, pK_a^{app} of 2,4-dinitrophenol equals 2.65 ± 0.04 ; ^d at **1** conc. 0.01 M, pK_a^{app} of 4-nitrophenol equals 6.34 ± 0.17 ; ^e at **1** conc. 0.01 M, pK_a^{app} of bromophenol blue equals 2.61 ± 0.05 ; ^f at **1** conc. 0.01 M, pK_a^{app} of phenol red equals 7.07 ± 0.01 .

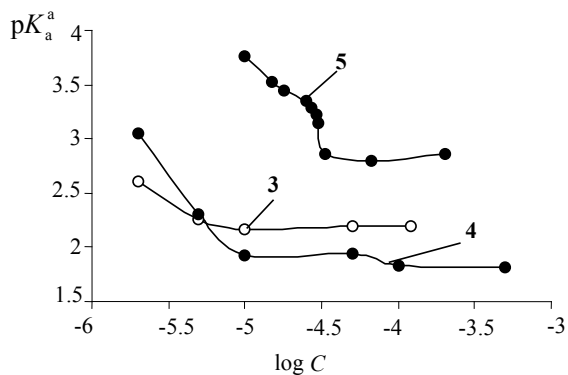


Figure 6. The dependence of bromophenol blue pK_a^a values in solutions of 3, 4, and 5 on logarithm of dendrimer concentration. Dye concentration: 8.5×10^{-6} , 9.0×10^{-6} , and 5.0×10^{-6} M respectively; C_{HCl} varies from 0.001 to 0.01 M. Reprinted from ref. 27 with permission of the American Chemical Society.

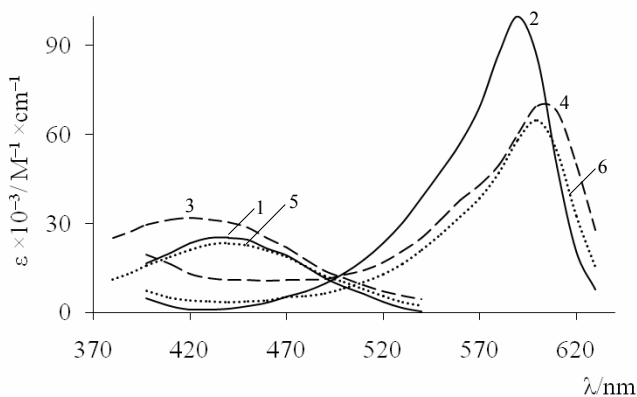


Figure 7. The absorption spectra of bromophenol blue anions HR^- (1, 3, and 5) and R^{2-} (2, 4, and 6) in water (1, 2) and in the presence of $(2.5-5.0) \times 10^{-3}$ M of calixarenes 1 (3, 4) and 2 (5, 6); pH = 8 (2) and 6 (4, 6), $I = 0.05$ M (buffer + NaCl). The spectra (1, 3, and 5) are obtained in the presence of 0.1–0.3 M HCl. Reprinted from ref. 31 with permission of the American Chemical Society.

3. The evidences of the presence of aggregates in aqueous solutions of calixarene and dendrimers

The method of dynamic light scattering (DLS) allows revealing the existence of small aggregates with diameter around 3–4 nm in solutions of compound **1** [28, 29, 31]. For this calixarene, the aggregates are formed only if the concentration exceeds some threshold value. Such behavior strongly resembles the micelle formation of colloidal surfactants, and the abovementioned concentration is in fact the threshold, or critical aggregate concentration (CAC), analogous to the critical micelle concentration (CMC) of amphiphilic surfactants.

The similarity becomes even more expressed by comparing these CAC in solutions with and without addition of indifferent salts. In Figure 8, the intersection of the two straight lines in the intensity data corresponds to the critical aggregate concentration.

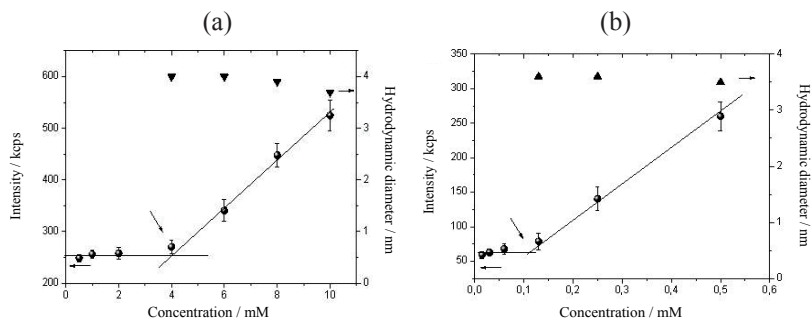


Figure 8. The plots of the intensity of scattered light (in kilo counts per second) and hydrodynamic diameter obtained for the solutions of calixarene **1** prepared in deionized water (a) and in 0.05M NaCl aqueous solution (b) Reprinted from ref. 29.

The threshold values thus obtained are 4×10^{-3} and 1.2×10^{-4} M in pure water and 0.05 M NaCl solution. Such a dramatic decrease in the CAC values emphasizes the similarity between compound **5** and colloidal surfactants. Indeed, the expressed decrease in the CMC values caused by indifferent salts is typical for common ionic amphiphiles, such as CTAB or CPC [25].

The measurements of the electrophoretic potential are also helpful. In the case of calixarene **1** in pure water, the ζ value varies within the range of + (60 to 80) mV [28, 29, 31]. The evident origin of the positive charge is the location of a fraction of Cl^- ions outside the colloidal aggregates. This also underlines the similarity between the calixarene aggregates and micelles of cationic surfactants.

In aqueous solutions of dendrimers **3** and **4**, aggregates of different sizes (5 to 3700 nm) have been detected under acidic and basic conditions, at concentrations similar to those used for the study of the indicator dyes (Table 3) [27]. The diameters of a major component of dendrimer **4** having four *n*-dodecyl chains correspond either to single molecules or to very small aggregates at both pH 10 and 2. On the other hand, dendrimer **3** bearing eight *n*-dodecyl chains is highly aggregated at pH 2 and 10 and show bimodal and trimodal size distributions. The data collected in Table 3 demonstrate that dendrimer **4** exists in water predominantly in the form of small-sized species even at concentrations above the CAC [27].

Table 3. Sizes of dendrimer aggregates in water at 25°C from dynamic light scattering

Dendrimer	C/M	pH	diameter/nm ^a
3	1.20×10^{-4}	2.0	293 (88%), 4900 (11%)
3	1.20×10^{-4}	10.0	64 (32%), 302 (32%), 3700 (35%)
4	5.09×10^{-4}	2.0	5 (major), 196 (minor)
4	5.09×10^{-4}	10.0	4.5 (major), 290 (minor)

^a Size distribution by volume percent. Size was not calibrated, and relative volumes were unreliable for the 5 nm diameter particles. Reprinted from ref. 27 with permission of the American Chemical Society.

In the case of calixarenes, we also observed a significant dependence of aggregate properties on compound structure. The dramatic difference between the aqueous solutions of calixarenes **1** and **2** consists in the size of the aggregates. Indeed, the particles of the six-member calixarene are much larger. Their size varies within the range of $\approx 10^2$ to $\approx 10^3$ nm (Figure 9).

Such difference is probably caused first of all by the character of major conformations of the calixarenes (cone for compound **1** and 1,3,5-alternate for **2**). The less expressed hydrophobicity of the alkoxyaryl portion of calixarene **2** as compared that of compound **1** should be also taken into account.

The histogram for this polydisperse system is typified in Figure 9; for nine C_{calix} values from 1×10^{-4} to 0.01 M, the picture is similar in outline. Note, that the rather large particles of calixarene **2** as 1,3,5-alternate already exist in extremely diluted solutions (about 1×10^{-5} M) of this calixarene. Thus, it is difficult to reveal any distinct CAC value.

At the same time, the electrophoretic study of solutions of calixarene **2** in pure water demonstrated the existence of particles possessing positive charge, with the electrokinetic potential (zeta potential) value $\zeta = +(41-50)$ mV

lower as compared with that of calixarene **1** aggregates: +(60–80) mV. The ill-expressed decrease in ζ at higher C_{calix} values (insert in Figure 9) should be explained by the screening of the interfacial charge of the aggregates by the Cl^- ions, because the concentration of the latter in the bulk increases along with the increase in C_{calix} , a phenomenon well known for ionic surfactant micelles [25, 31] (“negative adsorption”).

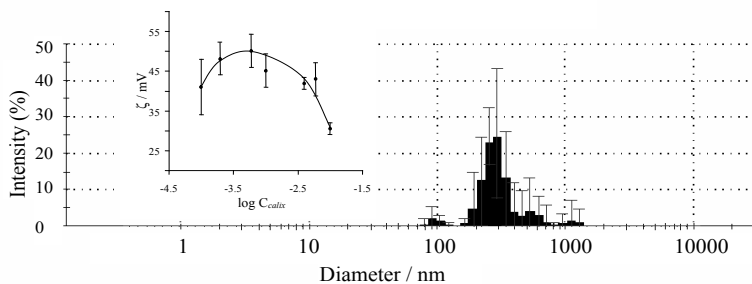


Figure 9. The DLS data: the size distribution by scattering intensity in aqueous solutions of calixarene **2**, $C_{\text{calix}} = 4 \times 10^{-3}$ M, 25 °C. The insert demonstrates the variations of the electrokinetic potential along with the concentrations of calixarene **2**. Reprinted from ref. 31 with permission of the American Chemical Society.

The transmission electron microscopy (TEM) data obtained within the wide concentration range of the colloidal systems confirm the polydisperse character and (in outline) the size of the calixarene aggregates studied (Figure 10).

It is evident, that the particles formed by calixarene **2** consist of primary aggregates, which are rather isometric than prolonged ones, with diameter ca. 15–40 nm (Fig. 10*a,b*). The particulates are amorphous. The formation of some part of secondary aggregates as a result of water evaporation during the sample preparation for the TEM experiments also cannot be excluded. However, just the secondary aggregates shown in Figure 10*a* (several typical examples from a much larger body of data) get the size range estimated by the DLS method. From such a picture, it can be deduced that the aggregates are in fact clusters of neutral salt molecules, i.e., six-charged cations with six chloride anions. Only the interfacial Cl^- ions can leave the aggregates, thus causing their positive charge. This hypothesis was supported by the measurements with the Cl^- -selective electrode [31].

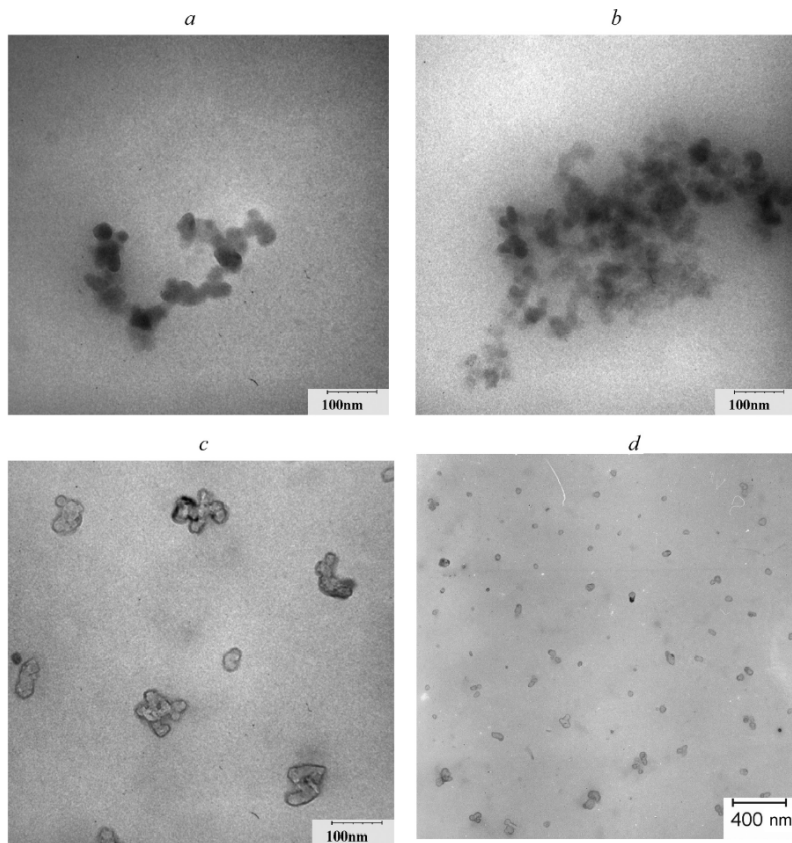


Figure 10. Typical electron micrographs of the aggregates of calixarenes **2** (**a**, **b**) and **1** (**c**, **d**). The images **a** and **b** refer to the dried aqueous solutions (0.001 M); the images **c** and **d** were obtained using the 0.004 M solutions of calixarene **1** contrasted by rose Bengal B. Reprinted from ref. 31 with permission of the American Chemical Society.

The differences in the behavior of calixarenes **1** and **2** probably originate from the peculiarity of their conformations. For calixarene **1** the cone, or, more precise, a dynamic equilibrium between two equivalent conformations of a pinched cone is typical. Its spatial structure investigated with molecular mechanic computations (MM+) [26] revealed that in vacuum two distal rings are almost parallel. Two other rings are almost orthogonal. Distances between distal N-atoms are equal to 0.59 and 1.37 nm, neighboring N-atoms are located

at 0.73 nm.

In contrast, the six-member calixarene **2** is conformationally mobile, and in its solutions the free rotation of the aromatic rings around the bonds with the $-\text{CH}_2-$ groups takes place, resulting in 1,3,5-alternates. For solutions of **2** in DMSO, it was proved by a sole spread signal at 3.98 ppm of methylene protons in ^1H NMR spectrum in DMSO [31]. In the crystal state, the 1,3,5-alternate conformation is also energetically more beneficial as compared with the cone or partial cone conformations [31].

Spatial structure of calixarene **2** in vacuum was studied by the molecular mechanic computations (MM+) method. Calixarene exists in a centrosymmetrical 1,3,5-alternate conformation. Three pairs of distal rings are allocated in almost antiparallel directions; corresponding dihedral angles are 28.6° , 17.95° and 3.93° . Two ammonium moieties are partly incorporated in the cavity of the macrocycle, distances between N-atoms are within 0.53 to 1.53 nm [31].

Recently [31], we compared our data with the results of other research groups devoted to the aggregates formed by cationic [6, 15, 17, 20, 32, 33] and anionic [4, 34] calixarenes.

4. The origin of the medium effects in aqueous solutions of cationic calixarenes and dendrimers

On the whole, the introduction of cationic calixarenes and dendrimers into the aqueous buffered solutions of the indicator dyes leads to their $\text{p}K_a^{\text{app}}$ decrease. In addition to Tables 1 and 2, some data for most common indicator dyes are exemplified in Table 4.

Analogous effects at the transfer from water to calixarenes and dendrimers solutions were also recorded for other indicators. It confirms the colloid character of the systems under study and demonstrates the great significance of micellar effects in supramolecular systems.

The difference $\text{p}K_a^{\text{app}}$ values and the values in water can be expressed through the transfer activity coefficients from water to pseudophase, or dispersed phase, ${}^w\gamma^m$, and electrical potential, Ψ [25]:

$$\Delta\text{p}K_a^{\text{app}} = \text{p}K_a^{\text{app}} - \text{p}K_a^w = \log \frac{{}^w\gamma_{\text{R}}^m}{{}^w\gamma_{\text{HR}}^m} - \frac{\Psi F}{2.302 RT} \quad (1)$$

The positive ζ and, correspondingly, Ψ values of the colloidal systems explain the increase in the “apparent” acidic strength documented in Tables 1,

2, and 4. At that, the six-member calixarene displays a less expressed influence on the protolytic equilibria. This is in line with the fact that the ζ values for aggregates of compound **2** are \approx (20–30) mV lower as compared with those of **1**.

Table 4. The $\text{p}K_a^{\text{app}}$ values [$\pm(0.01$ to $0.07)$] of different indicator dyes in aqueous solutions of calixarenes and dendrimer **3**, 25 °C

System ^a	$\text{p}K_a^{\text{app}}$ [$\log(K_a^{\text{app}} / K_a^{\text{w*}})$]			
	Phenol red	Bromophenol blue	Bromothymol blue	Methyl orange
Water, $I = 0.05$ M	7.97	4.05	7.26	3.21
Calixarene 1	7.40 [0.57]	2.59 [1.46]	6.82 [0.44]	1.88 [1.33]
Calixarene 2	7.66 [0.31]	2.90 [1.15]	–	2.64 [0.57]
Dendrimer 3	–	2.19 [1.86]	6.42 [0.84]	–
Micellar solution of cationic surfactants	7.08 ^b [0.89]	2.83 ^c [1.22]	6.36 ^b [0.90]	1.00 ^c [2.21]

^a Conc. of calixarenes: 2.5×10^{-3} M, $I = 0.05$ M; conc. of dendrimer **3**: 1.2×10^{-4} M (the CAC value is 9.0×10^{-5} M), $I = 0.01$ M; the $\text{p}K_a^{\text{app}}$ values are determined in buffer or HCl + NaCl solutions; ^b CPC: 0.003 M, $I = 0.05$ M (buffer + KCl). ^c CTAB: 0.003 M, $I = 0.05$ M (buffer or HCl + KBr).

Note, that the $\Delta\text{p}K_a^{\text{app}}$ values are quite different for different charge types of acid-base couples, for the indicators of different structure, or even for sulfonephthaleins bearing dissimilar substituents. This differentiating impact of aggregates of compounds **1–6** on the strength of organic acids underlines the similarity with micelles of cationic surfactants [25].

However, such differentiating action of the pseudophase may be also of “trivial” nature [25]. In other words, it may be caused not by the influence of the microenvironment, but by the incomplete binding of the equilibrium species of the indicators to the aggregates.

The completeness of binding of the dye species may be estimated either by using the dependences of $\text{p}K_a^{\text{app}}$ (or $\Delta\text{p}K_a^{\text{app}}$) on the concentration of calixarenes (dendrimers) or by the character of alteration of absorption (emission) spectra under the same conditions. As a rule, the curves of $\text{p}K_a^{\text{app}}$ vs. C_{calix} or C_{dendr} reach the plateau [26–28, 31], as it is exemplified in Figure 6. For instance, in solutions of **1** the concentration $C_{\text{calix}} = 2.5 \cdot 10^{-3}$ M is enough for obtaining stable $\text{p}K_a^{\text{app}}$ values for the majority of dyes. Only for several more hydrophilic indicators,

constant values are fixed at higher calixarene concentrations (Table 2), etc.

Similar conclusions were deduced from the electronic spectra [26–29, 31]. The hypso- or bathochromic shifts of the absorption bands of the equilibrium species are of the same sign as on going from water to surfactant solutions (at $C > \text{CMC}$) or to organic solvents.

Hence, the medium effects in **1-6** solutions should be attributed to the influence of the microenvironment within the pseudophase of the positively charged aggregates.

5. Possible mechanisms of dye + calixarene association

Though the inclusion of smaller species into six-member calixarenes is well documented (as example, the system calix[6]arene hexasulfonate + 4-nitrophenol can be proposed [13]), the cage of calixarene **2** is unable to admit the whole bromophenol blue ion. Even more so, it refers to the case of calixarene **1** [26, 31]. Some possible interaction schemes are given in Figure 11. Such kinds of associates can represent the state of the dye species fixed at the colloidal aggregates of calixarene **2**.

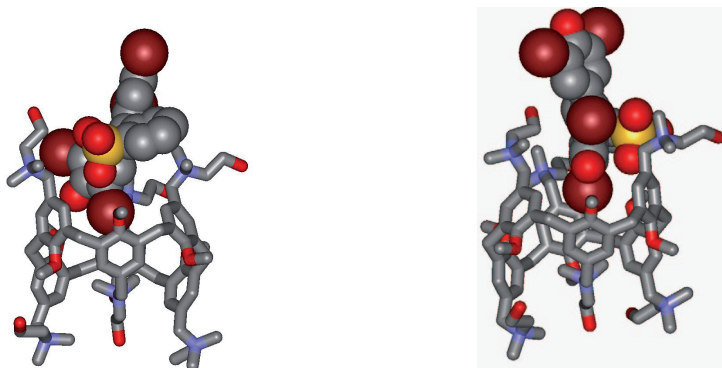


Figure 11. The possible complexes of bromophenol blue dianion, R^{2-} , with the cavity of calix[6]arene **2** (the structures are obtained using the program HyperChem 8.0 Evaluation and WebLabViewer 3.5). Reprinted from ref. 31 with permission of the American Chemical Society.

In the case of the prolonged molecule (or ion) of methyl orange, the complete docking into the cage of **2** is quite possible [31]. However, this is an exception within the set of dyes used in our studies. More probable is a partial penetration

of the dye species into the calixarene cavity or even formation of exo complexes. In Figure 12, two from a number of possible positions of 4-nitrophenol in its R^- form, fixed by a small aggregate of a four-member calixarene **1**, are schematically presented. Analogous endo and exo complexes have been constructed earlier for the R^{2-} anion of bromophenol blue [31].

Attempts to directly detect the interaction between cationic calixarene **1** and bromophenol blue were made by ^1H NMR spectroscopy by using a concentration range sufficiently higher than that for UV-vis spectroscopy. Unfortunately, these studies were hindered by the undesirable effect of precipitation [31].

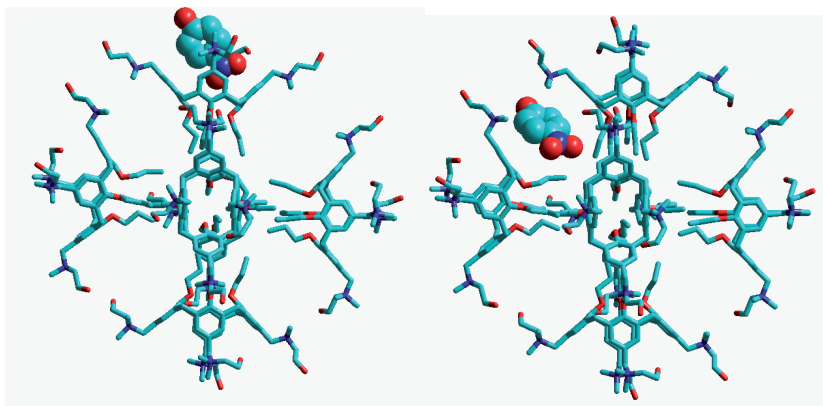


Figure 12. Endo (a) and exo (d) complexes of calixarene **1** aggregates with the anion of 4-nitrophenol. (the structures are obtained using the program HyperChem 7.5 Evaluation) Reprinted from ref. 31.

In the case of dendrimers, the dye species may be located in the voids of the branchy structures. Interestingly, compound **5** exerts a less expressed influence on the acid-base equilibrium of the dyes, as compared with those of **3** and **4** (Figure 6). The main reason may be the absence of *n*-dodecyl chains in its molecule.

6. The peculiarities of some physico-chemical processes in solutions containing aggregates of compounds 1-6

Within the course of our studies [26–31], we have found a number of chemical processes that demonstrate either the similarity of distinction between the calixarene and dendrimer aggregates, on the one hand, and common sphere-shaped micelles of cationic surfactants, on the other hand. Some of them are

briefly considered below.

The peculiar of methyl orange behavior. It is well known, that in the presence of small amounts of cationic surfactants, far below the CMC value, the absorption band of the anionic species of methyl orange (Figure 3) in water ($\lambda_{\max} = 462\text{--}463\text{ nm}$) undergoes a dramatic hypsochromic shift up to $360\text{--}370\text{ nm}$ [35, 36]. This effect was explained in terms of mixed dye–surfactant micelles, where the azo dye exists in form of dimers with parallel orientation of chromophores [36]. At elevated surfactant concentrations, the band shifts toward $420\text{--}430\text{ nm}$, indicating the existence of single R^- ions of the dye fixed in the micellar pseudophase (sole dye ion per micelle).

The displacement of the band to the UV-region is typical for the diluted (7.5×10^{-5} to $2.5 \times 10^{-4}\text{ M}$) aqueous solutions of calixarene **1** [28], and from this viewpoint the calixarene **1** behaves in aqueous solutions like a cationic surfactant. Contrary to it, such a “dimeric” band in the UV portion of the spectrum was not registered in the case of calixarene **2** within the whole concentration range examined, from 1×10^{-5} to 0.01 M [31]. This is in line with the existence of aggregated calixarene species even at the extremely low concentrations of **2**, deduced from the DLS data. Another explanation of the absence of this indicative UV band in diluted solutions of may be the aforementioned complete penetration of the prolonged dye ion into the six-member cage of calixarene **2**. In principle, such docking can preserve the dye–dye interaction.

Interaction of dendrimers with fluorescein. Fluorescein dianion R^{2-} (Figure 5) can be protonated to form monoanion, neutral molecule, and cation. The state of the three-step ionization equilibrium in water $H_3R^+ \rightleftharpoons H_2R \rightleftharpoons HR^- \rightleftharpoons R^{2-}$ is shifted on introducing dendrimers **3** and **4** in the same direction as in micellar solutions of cationic surfactants, and the R^{2-} absorption band is also red-shifted by ca. 10 nm as compared to aqueous media [27].

The neutral species, H_2R , is known to be an equilibrium mixture of three tautomers: zwitter-ion, quinonoid, and colorless lactone (Figure 13).

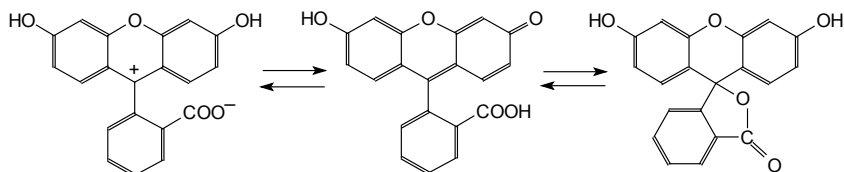


Figure 13. Zwitter-ionic, quinonoidal, and lactonic tautomers of fluorescein.

In micellar media, a drop of molar absorptivity is usually registered because

of shift of tautomeric equilibria: the zwitter-ion and quinoid tautomers convert into the colorless lactone. This effect was also registered in dendrimer solutions [27]. Surprisingly, dendrimer **4**, having a smaller number of hydrocarbon tails and possessing a higher CAC value as compared with dendrimer **3**, displays a more “micellar-like” influence on tautomeric equilibrium of fluorescein. This may be caused by a higher aggregation numbers of the less hydrophobic dendrimer **4**.

Investigation of aggregates using solvatochromic pyridinium-*N*-phenolate dyes. We also examined the behavior of two solvatochromic pyridinium-*N*-phenolate dyes, the so-called Reichardt’s dyes (Figure 14), which can also serve as useful acid-base indicators in organized solutions.

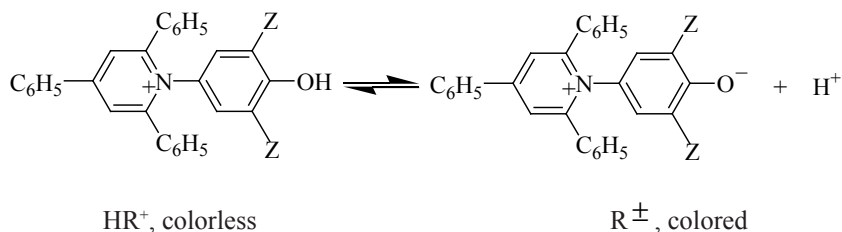


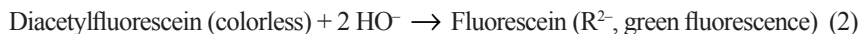
Figure 14. Cationic and zwitter-ionic forms of pyridinium-*N*-phenolate dyes ($Z = C_6H_5$; Cl ; $pK_a^w = 8.64$ and 4.78 respectively).

The standard dye ($Z = C_6H_5$) in its colored form, R^\pm , possesses $\lambda_{max} = 453$ nm in water [37], while in micelles of cationic surfactants is ca. 530–540 nm [37]. Analogous shift has been reported by Pan and Ford for the dendrimer of high generation, which forms in fact “unimolecular” micelles in water [38]. However, neither in solutions of low generation dendrimers **3-6** nor in the presence of aggregates of calixarenes **1** and **2** such effects were observed. For the chloro derivative in solutions of compound **3**, the λ_{max} value is 408 nm (in water: 412 nm) [27]. The pK_a^{app} value appeared to be even somewhat higher than in water ($\Delta pK_a^{app} = +0.3$), while in cationic micelles $\Delta pK_a^{app} = -1.0$, and the λ_{max} value is 465 nm [27]. Probably, the cationic species HR^+ are practically not bound by the dendrimer.

Thus, these solvatochromic dyes testify rather against the similarity between the aggregates of **1-6** and common cationic surfactant micelles.

Kinetic experiments. A preliminary decision may be made that the kinetic data also allow distinguishing between the aggregates of **1-6** and the micelles of cationic colloidal surfactants. For instance, the influence of dendrimer **3** on

the rate of the hydrolysis reaction of diacetylfluorescein shows that the local HO^- concentration in dendrimer is much lower than in the Stern layer of cationic micelles, where the rate of the same reaction is much higher:



On the other hand, cetyltrimethylammonium bromide micelles protect the fading of the bromophenol blue R^{2-} anion at pH around 12 (Figure 15)

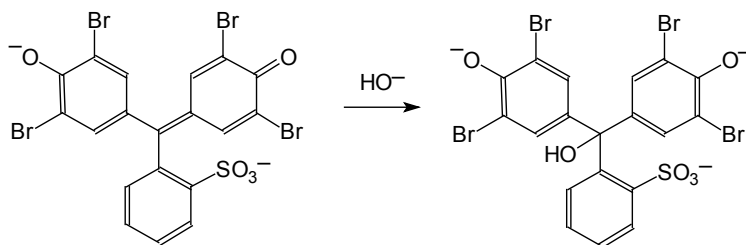


Figure 15. The conversion of the blue dianion R^{2-} to the colorless trianion ROH^{3-} as a result of the nucleophilic attack of the HO^- ion.

However, the dye fades in solutions of dendrimer **3** and of calixarene **1** and **2** just as in water.

7. Concluding remarks

In aqueous solution, cationic calixarenes and low generation dendrimers readily form positively charged aggregates. The size varies from 3–4 nm to $\approx 10^3$ nm, depending on the molecular structure. Large aggregates of calixarene **2** consist of primary ones, being at least one order of magnitude smaller. The positive charge of the particles is confirmed both by the electrokinetic measurements (e.g., for calixarenes ζ varies from +41 to +80 mV) and their influence on the $\text{p}K_a$ values of a set of indicator dyes.

The aggregates markedly influence the absorption spectra and tautomerism of the dyes. The effects displayed by both calixarene and dendrimer aggregates resemble in outline those typical for micellar solutions of cationic surfactants. However, the agreement is far from being complete. For example, some kinetic data allow distinguishing between the aggregates under study and the common micelles of colloidal surfactants. Similar likeness with some specific differences was also stated between cationic surfactant modified silica nanoparticles [39]

and spherical polymeric polyelectrolyte brushes on the one hand and micelles of cationic amphiphiles on the other hand [40].

Concluding, on using ionic calixarenes and dendrimers in aqueous media, not the inclusion phenomena solely, but also micellar effects of colloidal aggregates should be taken into account.

Acknowledgments

We are grateful to Professor Warren T. Ford and A. A. Dissanayake, Oklahoma State University, USA, and Dr. E. Yu. Bryleva, Scientific-Technological Complex “Institute for Single Crystals”, Kharkov, Ukraine for the mutual study of dendrimers [27]. We thank Dr. L. V. Kutuzova, Fakultät Angewandte Chemie, Hochschule Reutlingen, Germany and our Ukrainian colleagues Dr. Science (Chemistry) V. I. Boyko, Drs. A. B. Drapaylo, S. I. Miroshnichenko, A. P. Kryshstal, A. G. Yakubovskaya, Ph.D. student T. A. Cheipesh and former student O. Yu. Soboleva, who participated in the different stages of the above research.

References

1. *Encyclopedia of Supramolecular Chemistry*. J. L. Atwood, J. W. Steed (Eds.) Taylor & Francis, 2004.
2. Sgarlata, C.; Bonaccorso, C.; Gulino, F. G.; Zito, V.; Arena, G.; Sciotto, D. *New J. Chem.* **2009**, *39*, 991–997.
3. Rodik, R. V.; Boyko, V.I.; Kalchenko, V.I. *Current Medicinal Chemistry* **2009**, *16*, 1630–1655.
4. Morozova, J. E.; Kazakova, E. Kh.; Mironova, D. A.; Shalaeva, Y. V.; Syakaev, V. V.; Makarova, N. A.; Konovalov, A. I. *J. Phys. Chem. B*, **2010**, *114*, 13152–13158.
5. Suwinska, K.; Lesnievska, B.; Wszelaka-Rylik, M.; Straver, L.; Jebors, S.; Coleman, A.W. *Chem. Comm.* **2011**, *41*, 8766–8768.
6. Rodik, R. V.; Klymchenko, A. S.; Jain, N.; Miroshnichenko, S. I.; Richert, L.; Kalchenko, V. I.; Mély, Y. *Chemistry – A Eur. J.* **2011**, *17*, 5526–5538.
7. Zhang, Y.; Pham, T. H.; Sánchez Pena, M.; Agbaria, R. A.; Warner, I. M. *Applied Spectrosc.* **1998**, *52*, 952–957.
8. Shi, Y.; Schneider, H.-J. *J. Chem. Soc., Perkin Trans. 2*, **1999**, 1797–1803.
9. Liu, Y.; Chen, Y.; Li, L.; Huang, G.; You, C.-C.; Zhang, H.-Y.; Wada, T.; Inoue, Y. *J. Org. Chem.* **2001**, *66*, 7209–7215.
10. Zhang, Y.; Cao, W. *New J. Chem.* **2001**, *25*, 483–486.

11. Liu, Y.; Han, B.-H.; Chen, Y.-T. *J. Org. Chem.* **2000**, *65*, 6227–6230.
12. Liu, Y.; Han, B.-H.; Chen, Y.-T. *J. Phys. Chem. B*, **2002**, *106*, 4678–4687.
13. Kunsági-Máte, S.; Szabo, K.; Lemli, B.; Bitter, I.; Nagy, G.; Kollár, L. *Thermochim. Acta* **2005**, *425*, 121–126.
14. Da Silva, E.; Lazar, A. N.; Coleman, A. W. *J. Drug. Sci. Tech.* **2004**, *14*, 3–20.
15. Rehm, M.; Frank, M.; Schatz, J. *Tetrahedron Lett.* **2009**, *50*, 93–96.
16. Shinkai, S.; Mori, S.; Koreishi, H.; Tsubaki, T.; Manabe, O. *J. Am. Chem. Soc.* **1986**, *108*, 2409–2416.
17. Arimori, S.; Nagasaki, T.; Shinkai, S. *J. Chem. Soc., Perkin Trans. 1*, **1993**, 887–889.
18. Lee, M.; Lee, S. J.; Jiang, L. H. *J. Am. Chem. Soc.* **2004**, *126*, 12724–12725.
19. Amirov, R.; Nugaeva, Z. T.; Mustafina, A. R.; Fedorenko, S. V.; Morozov, V. I.; Kazakova, E. Kh.; Habicher, W. D.; Kononov, A. I. *Colloids Surf. A* **2004**, *240*, 35–43.
20. Ukhatskaya, E. V.; Kurkov, S. V.; Matthews, S.E.; El Fagui, A.; Amiel, C.; Dalmas, F.; Loftsson, T. *Intern. J. Pharm.* **2010**, *402*, 10–19.
21. Nakai, T.; Kanamori, T.; Sando, S.; Aoyama, Y. *J. Am. Chem. Soc.* **2003**, *125*, 8465–8475.
22. Kellermann, M.; Bauer, W.; Hirsch, A.; Schade, B.; Ludwig, K.; Böttcher, C. *Angew. Chem. Int. Ed.* **2004**, *43*, 2959–2962.
23. Becherer, M.; Schade, B.; Böttcher, C.; Hirsch, A. *Chem. Eur. J.* **2009**, *15*, 1637–1648.
24. Jäger, C.M.; Hirsch, A.; Schade, B.; Ludwig, K.; Böttcher, C.; Clark, T. *Langmuir* **2010**, *26*, 10460–10466.
25. Mchedlov-Petrossyan, N. O. *Pure Appl. Chem.* **2008**, *80*, 1459–1510.
26. Mchedlov-Petrossyan, N. O.; Vilkovala, L. N.; Vodolazkaya, N. A.; Yakubovskaya, A. G.; Rodik, R. V.; Boyko, V. I.; Kalchenko, V. I. *Sensors* **2006**, *6*, 962–977.
27. Mchedlov-Petrossyan, N. O.; Bryleva, E. Yu.; Vodolazkaya, N. A.; Dissanayake, A. A.; Ford, W. T. *Langmuir* **2008**, *24*, 5689–5699.
28. Mchedlov-Petrossyan, N. O.; Vodolazkaya, N. A.; Vilkovala, L. N.; Soboleva, O. Yu.; Kutuzova, L. V.; Rodik, R. V.; Miroshnichenko, S. I.; Drapaylo, A. B. *J. Mol. Liquids* **2009**, *145*, 197–203.
29. Mchedlov-Petrossyan, N. O.; Bogdanova, L. N.; Rodik, R. V.; Vodolazkaya, N. A.; Kutuzova, L. V.; Kalchenko, V. I. *Rep. Nat. Acad. Sci. Ukraine* **2010**, No. 3, 148–153.

30. Mchedlov-Petrosyan, N. O. *Voprosy Khimiyi i Khimicheskoi Tekhnologii (The Questions of Chemistry and Chemical Technology)* **2011**, No. 4 (2), 82–84.
31. Mchedlov-Petrosyan, N. O.; Vodolazkaya, N. A.; Rodik, R. V.; Bogdanova, L. N.; Cheipesh, T. A.; Soboleva, O. Yu.; Kryshtal, A. P.; Kutuzova, L. V.; Kalchenko, V. I. *J. Phys. Chem. C* **2012**, *116*, 10245–10259.
32. Arimori, S.; Nagasaki, T.; Shinkai, S. *J. Chem. Soc., Perkin Trans. 2*, **1995**, 679–683.
33. Shahgaldian, P.; Sciotti, M. A.; Pieleś, U. *Langmuir*, **2008**, *24*, 8522–8526.
34. Arimura, T.; Kawabata, H.; Matsuda, T.; Muramatsu T.; Satoh H.; Fujio K.; Manabe, O.; Shinkai, S. *J. Org. Chem.*, **1991**, *56*, 301–306.
35. Quadrifoglio, F.; Crescenzi, V. *J. Colloid Interface Sci.* **1971**, *35*, 447–459.
36. Reeves, R. L.; Harkaway, S. A. in: *Micellization, solubilization, and microemulsions*, K. L. Mittal (Ed.), Russian transl. Mir, Moscow, 1980.
37. Reichardt, C.; Welton, T. *Solvents and Solvent Effects in Organic Chemistry*; Wiley–VCH: Weinheim, 2011.
38. Pan, Y.; Ford, W. T. *Macromolecules* **2000**, *33*, 3731–3738.
39. Bryleva, E. Yu.; Vodolazkaya, N. A.; Mchedlov-Petrosyan, N. O.; Samokhina, L. V.; Matveevskaya, N. A.; Tolmachev, A. V. *J. Colloid Interface Sci.* **2007**, *316*, 712–722.
40. Vodolazkaya, N. A.; Mchedlov-Petrosyan, N. O.; Bryleva, E. Yu.; Biletskaya, S. V.; Schrunner, M.; Kutuzova, L. V.; Ballauff, M. *Functional Materials* **2010**, *17*, 470–476.

Chapter 4

Complexation of triterpene and steroid glycosides with aromatic proteinogenous amino acids

Leonid Yakovishin¹, Vladimir Grishkovets², Anna Kovalenko¹,
Grzegorz Schroeder³ and Volodymyr Rybachenko⁴

¹*Sevastopol National Technical University, Universitetskaya Str., 33,
Sevastopol, 99053, Crimea, Ukraine;*

²*V.I. Vernadsky Taurida National University, Vernadsky Ave., 4,
Simferopol, 95007, Crimea, Ukraine*

³*Adam Mickiewicz University in Poznań, Faculty of Chemistry,
Umultowska 89b, 61-614 Poznań, Poland*

⁴*L.M. Litvinenko Institute of Physical Organic and Coal Chemistry NAS
of Ukraine, R. Luxemburg 70, 83114 Donetsk, Ukraine*

One possible method for reducing therapeutic doses of drugs, increasing their solubility, and expanding the spectrum of biological activity is to form clathrates with plant saponins [1]. This approach has already been examined for glycyrrhizic acid (3-*O*-β-*D*-glucuronopyranosyl-(1®2)-*O*-β-*D*-glucuronopyranoside of glycyrrhetic acid, Fig. 1), the main triterpene saponin of licorice roots *Glycyrrhiza glabra* L. (Fabaceae) [1–3].

Triterpene glycosides α-hederin (hederagenin 3-*O*-α-*L*-rhamnopyranosyl-(1®2)-*O*-α-*L*-arabinopyranoside, glycoside **1**, Fig. 2) and hederasaponin C (hederagenin 3-*O*-α-*L*-rhamnopyranosyl-(1®2)-*O*-α-*L*-arabinopyranosyl-28-*O*-α-*L*-rhamnopyranosyl-(1®4)-*O*-β-*D*-glucopyranosyl-(1®6)-*O*-β-*D*-glucopyranoside, glycoside **2**, Fig. 2) are suggested as perspective complexing agents [4–10]. Glycosides **1** and **2** were discovered in representatives of most species of the ivy genus *Hedera* L. (Araliaceae), in which they are dominant saponins [11].

Glycosides **1** and **2** were isolated from *Hedera helix* L. [12, 13], *H. canariensis* Willd. [14], *H. taurica* Carr. [15, 16], *H. nepalensis* C. Koch. [17], *H. rhombea* Bean. [18], *H. caucasigena* Pojark. [19, 20], *H. scotica* A. Cheval. [21] and *H. colchica* C. Koch. [22, 23]. Glycoside **2** was extracted from *H. pastuchovii* G. Woron. [24, 25].

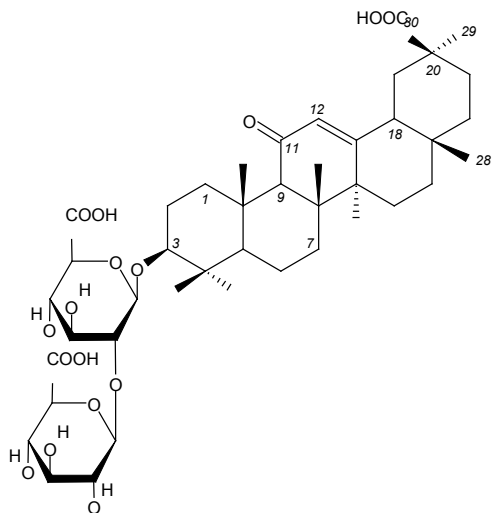


Figure 1. Glycyrrhizic acid.

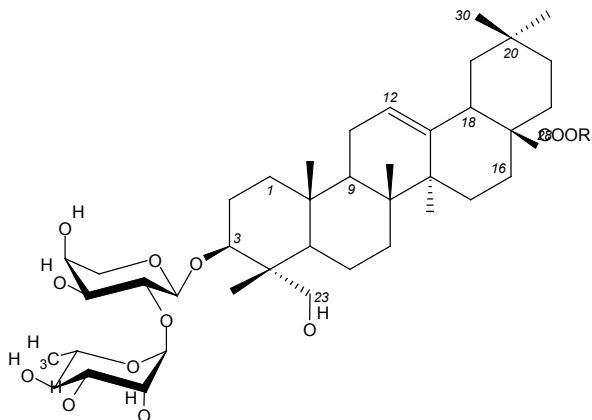


Figure 2. Glycosides **1** (α -hederin; $R=H$) and **2** (hederasaponin C; $R=-\beta\text{Glc}_p-(6-1)-\beta\text{Glc}_p-(4-1)-\alpha\text{Rha}_p$).

Glycosides **1** and **2** are included in the well-known drugs for treating coughs, Hedelix and Prospan, composed of *H. helix* leaves [11, 26]. Glycoside **2** (precursor of glycoside **1**) is the dominant glycoside of ivy leaves [11]. Herewith,

the main therapeutic effect of ivy medicines is determined by the presence of glycoside **1**. Glycoside **1** inhibits the inactivation of β_2 receptors in the lungs and bronchus [27].

Besides, the complexes of steroid glycosides of the spirostan type neotigogenin bioside (neotigogenin 3-*O*- β -*D*-glucopyranosyl-(1 \rightarrow 4)-*O*- β -*D*-galactopyranoside, Fig. 3), neotigogenin trioside (neotigogenin 3-*O*- β -*D*-glucopyranosyl-(1 \rightarrow 4)-*O*- β -*D*-glucopyranosyl-(1 \rightarrow 4)-*O*- β -*D*-galactopyranoside, Fig. 3) and petunioside D (capsicoside B₁, gitogenin 3-*O*- β -*D*-glucopyranosyl-(1 \rightarrow 4)-*O*- β -*D*-galactopyranoside, Fig. 4) were prepared with amino acids, nucleosides and adenosine-5-monophosphate [28–34]. Glycosides were isolated from seeds of tomato *Lycopersicon esculentum* Mill. (Solanaceae) and petunia *Petunia hybrida* Hort. (Solanaceae) [35]. Capsicoside B₁ (petunioside D) was isolated for the first time from the roots of the red pepper *Capsicum annuum* L. (Solanaceae) [36].

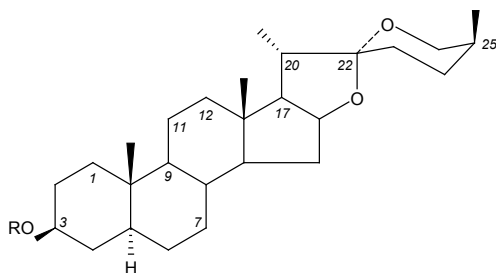


Figure 3. Neotigogenin glycosides ($R = \beta\text{Glc}_p-(1\rightarrow4)-\beta\text{Gal}_p$, $\beta\text{Glc}_p-(1\rightarrow4)-\beta\text{Glc}_p-(1\rightarrow4)-\beta\text{Gal}_p$).

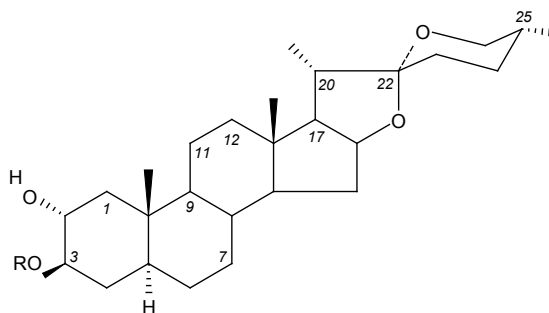


Figure 4. Petunioside D (capsicoside B₁; $R = \beta\text{Glc}_p-(1\rightarrow4)-\beta\text{Gal}_p$).

Complexes of the cardiac glycosides digoxin (Fig. 5) and K-strophanthin- β (Fig. 6) with amino acids and ternary complexes containing in addition Ca^{2+} and Mg^{2+} were prepared [37]. The compounds were characterized by NMR and UV spectroscopy. Digoxin is contained in *Digitalis lanata* Ehrh. (Scrophulariaceae) [38]. K-strophanthin- β was isolated from seeds of *Strophanthus Kombe* Oliver (Apocynaceae) [38].

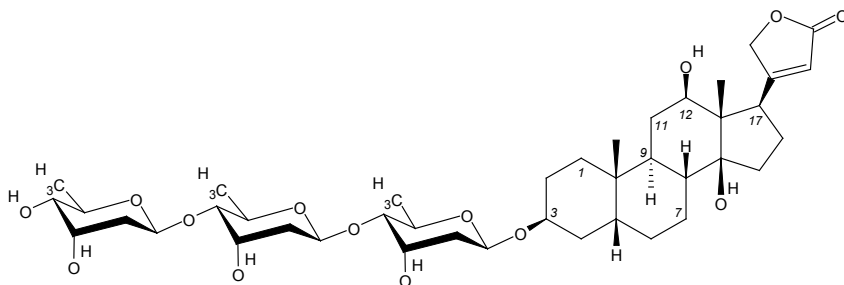


Figure 5. Digoxin.

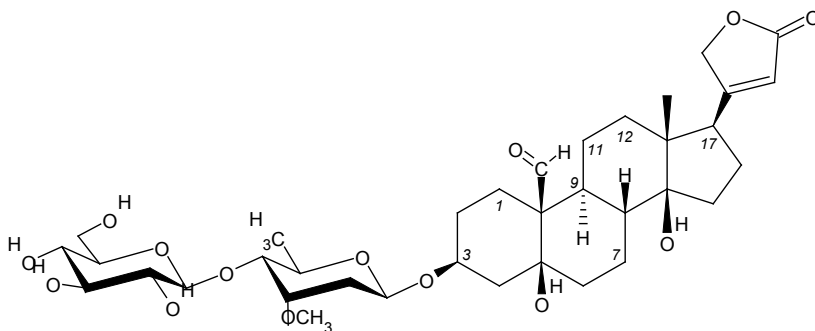


Figure 6. K-strophanthin- β .

1. Complexes with *L*-phenylalanine

The complexes of amino acid *L*-phenylalanine (**Phe**, Fig. 7) with cardiac glycosides K-strophanthin- β (Fig. 6) and digoxin (Fig. 5) as well as triple complexes including Ca^{2+} and Mg^{2+} cations were prepared [37]. The complexes of K-strophanthin- β with **Phe**, *L*-tyrosine (**Tyr**, Fig. 7), and *L*-tryptophan (**Trp**, Fig. 7) are deduced to have almost equal stability constants. The complex of **Phe** and digoxin is less stable than the **Tyr** complex. Triple complexes **Phe**-glycoside-

Me^{2+} are more stable than double ones. Stability constants of complexes have been defined by the method of spectrophotometric titration.

The authors of [37] explain the durability of complexes by different polarity of steroid glycosides (strophanthin is a polar glycoside, whereas digoxin is a non-polar one).

The complexation of **Phe** with steroid glycosides was investigated by the ^{252}Cf fission-product ionization time-of-flight plasma-desorption mass spectrometry [28–32]. Herewith, neotigogenin bioside and petunioside D (gitogenin bioside) were shown to make stable complexes and neotigogenin trioside to interact with **Phe** moderately. All the complexes had 1:1 composition. For them the mass spectrometry peaks $[\text{M}^{\text{glycoside}}+\text{M}^{\text{Phe}}+\text{H}]^+$ and $[\text{M}^{\text{glycoside}}+\text{M}^{\text{Phe}}+\text{K}]^+$ were found.

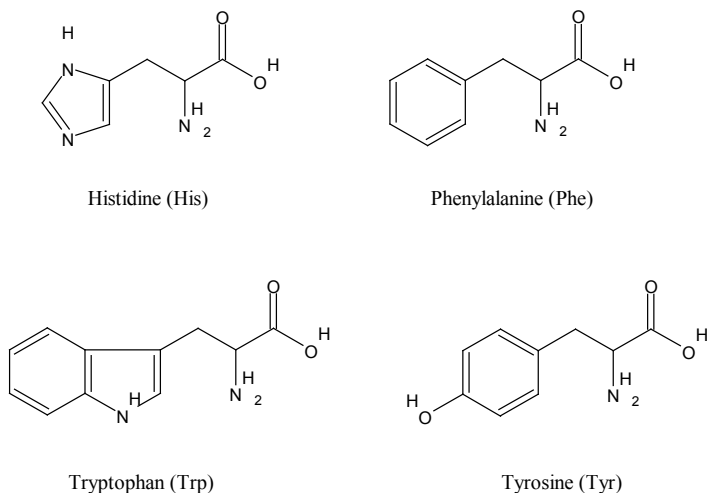


Figure 7. Aromatic amino acids.

The presence of intermolecular interactions between **Phe** and glycosides **1** and **2** (Fig. 2) was found out by the UV-spectrometry. As the glycosides **1** and **2** concentrations increases at constant **Phe** concentration, the optical density of their solutions increases as well (hyperchromic effect) (Fig. 8). The complexes composition was determined by the method of isomolar series [39]. This method gave a molar ratio ~ 1.0 , which corresponded to a 1:1 glycoside–**Phe** complex.

Formation of complexes of analogous composition between **Phe** and glycosides **1** and **2** was recently confirmed using electrospray-ionization mass spectrometry (ESI-MS) [40]. It was established that the glycoside **1** and

Phe in negative-ion mode formed the complex $[M^1+M^{\text{Phe}}-H]^-$. Peaks for four molecular complexes $[M^1+M^{\text{Phe}}+H]^+$, $[4M^1+2M^{\text{Phe}}+2H]^{2+}$, $[5M^1+M^{\text{Phe}}+2H]^+$ и $[5M^1+2M^{\text{Phe}}+2H]^{2+}$ in addition to peaks belonging to **Phe** and glycoside **1** self-associates and their adducts with Na^+ and K^+ were observed in the positive-ion mass spectrum (Fig. 9). The ratio of intensities of the peaks for the four molecular complexes was 174.8:6.8:1.2:1.0.

The negative-ion mass spectrum contained a peak for the complex $[M^2+M^{\text{Phe}}-H]^-$, the intensity of which was 1.5 times greater than that of the $[M^1+M^{\text{Phe}}-H]^-$ peak. In positive-ion mode, complexation of **2** and **Phe** was not observed. Thus, complexes with a glycoside:**Phe** 1:1 molar ratio were the most stable.

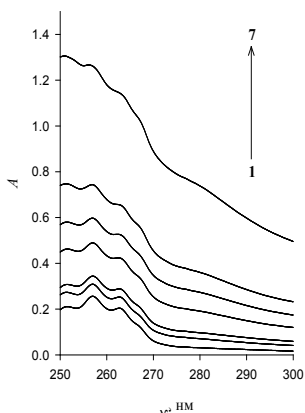


Figure 8. UV spectra of **Phe** aqueous solutions ($10^{-4} M = \text{const}$) with different concentrations of glycoside **1**: 0 M (1), $0.50 \times 10^{-4} M$ (2), $10^{-4} M$ (3), $0.25 \times 10^{-3} M$ (4), $0.50 \times 10^{-3} M$ (5), $0.75 \times 10^{-3} M$ (6), and $10^{-3} M$ (7).

Allelopathic activity of saponins has been known for a long time [41–44]. The influence of **Phe**, of glycosides **1** and **2**, and of their complexes on the germination of *Avena sativa* L. (Poaceae or Gramineae) seeds was recently studied [39]. Herewith, it was shown that as the 72-hours period (after the seeds cultivation with glycoside–**Phe** mixtures) passed, the germination was better than of those held in solutions of individual glycosides. The length of roots and sprouts of the seeds, cultivated by the above-mentioned mixtures, appeared to be maximum as well.

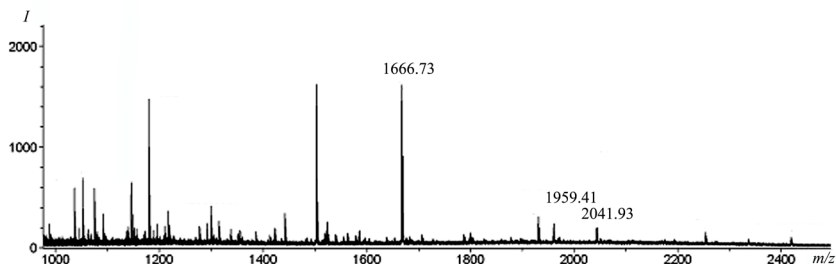


Figure 9. Portion of the positive-ion mass spectrum of a mixture of glycoside **1** with **Phe** (peaks for ions $[4M^1+2M^{\text{Phe}}+2H]^{2+}$ (m/z 1666.73), $[5M^1+M^{\text{Phe}}+2H]^+$ (m/z 1959.41), and $[5M^1+2M^{\text{Phe}}+2H]^{2+}$ (m/z 2041.93)).

Consequently, the interaction between **Phe** and glycosides **1**, **2** results in the compounds improving seeds' germination, size of roots and sprouts. In such a way, the complexation products are less toxic than individual glycosides.

2. Complexes with *L*-tyrosine

The complexes of *L*-tyrosine (**Tyr**, Fig. 7) with glycosides K-strophanthin- β (Fig. 6) and digoxin (Fig. 5) as well as triple complexes including Ca^{2+} and Mg^{2+} have been prepared [37]. Complexes of K-strophanthin- β with **Trp**, **Phe** and **Tyr** have almost equal stability constants. The complex of **Tyr** and digoxin greatly stands out for its stability among complexes of other aromatic amino acids ($K_s=245\pm 10 \text{ M}^{-1}$).

The complexation of **Tyr** with neotigogenin and gitogenin glycosides (Fig. 3 and 4) was studied by the time-of-flight plasma desorption mass spectrometry with ionization by ^{252}Cf fission fragments [28–32]. Herewith, neotigogenin bioside and trioside were shown to make unstable complexes and gitogenin bioside (petunioside D) to interact with **Tyr** moderately.

The veterinary preparation “Clatiram”, being the complex of glycyrrhizic acid (basic triterpene glycoside from licorice roots; Fig. 1) with prostaglandin cloprostenol (Fig. 10) [45] and **Tyr**, was patented [1, 2]. It is used for the regulation of animals' reproductive function.

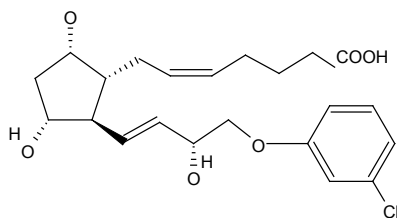


Figure 10. Cloprostenol.

Complexation of **Tyr** with triterpene glycosides **1** and **2** was also studied using electrospray ionization mass spectrometry [46]. For the mixture of glycoside **1** and **Tyr** in the negative-ion mode the peak of $[M^1+M^{\text{Tyr}}-H]^-$ ion with m/z 930.5 corresponding to 1:1 complex formation. In mass spectrum of positive ions the peaks of three molecular complexes $[M^1+M^{\text{Tyr}}+H]^+$, $[2M^1+M^{\text{Tyr}}+H]^+$ and $[3M^1+M^{\text{Tyr}}+H]^+$ were observed (Fig. 11). The ratio of these peaks intensities is 632:28:1.

In the negative-ion mode the complexes of glycoside **2** with **Tyr** are not registered. But in the negative-ion mode the peaks of $[M^2+M^{\text{Tyr}}+H]^+$ and $[3M^2+2M^{\text{Tyr}}+H]^+$ corresponding to complexes of 1:1 and 3:2 composition relatively. The intensities of the peaks have 24:1 ratio. It indicates the dominance of equimolar composition complex.

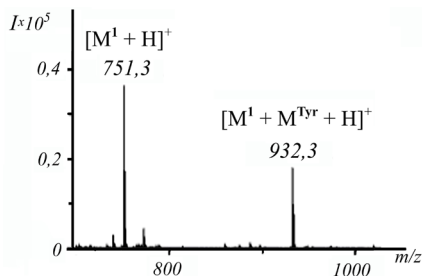


Figure 11. Portion of the positive-ion mass spectrum of a mixture of glycoside **1** with **Tyr**.

By the method of isomolar series **Tyr** was deduced to make 1:1 and 2:3 complexes with glycosides **1** and **2** in aqueous solutions respectively. Intermolecular interaction was shown to result in hyperchromic effect and bathochromic shift [47].

Bidesmosidic triterpene glycosides are known to have low toxicity because of the absence of free carboxyl group in their aglicones. On the contrary,

glycosides with a free (non-glycosylated) carboxyl group are quite active [48]. The ichthyotoxicity of complexes and their components was studied for *Poecilia sphenops* [47]. It was found out that the activity of **1-Tyr** and **2-Tyr** complexes is almost identical to the one of individual glycosides.

The toxic activity of triterpene glycosides results in plants' development suppression [41–44]. In the article [46] the study of the influence of glycosides **1** and **2, Tyr** and of their complexes on the germination and development of *Avena sativa* L. sprouts was reported. The mixture of glycoside **1** and **Tyr** was determined to suppress germination and to limit sprout length most of all after 72 hours. The seeds cultivated by the **2-Tyr** complex and by individual glycoside **2** solution have similar germination. The length of sprouts in case of complex cultivation is almost equal to that of control ones and of those held in **Tyr** solution.

3. Complexes with *L*-tryptophan

The complexation of *L*-tryptophan (**Trp**; Fig. 7) with neotigogenin and gitogenin glycosides (Fig. 3 and 4) was studied by the time-of-flight plasma desorption mass spectrometry with ionization by ^{252}Cf fission fragments [28–32]. Nevertheless, **Trp** does not make complexes with neotigogenin bioside and trioside, though making them with gitogenin bioside (petunioside D).

The complexes of cardiac glycosides digoxin and K-strophanthin- β with amino acids and triples including Ca^{2+} and Mg^{2+} were prepared [37]. The compounds were characterized by NMR- and UV-spectrometry methods. The digoxin–asparagine complex was shown to have the highest durability among binary complexes ($K_s = 355 \pm 17 \text{ M}^{-1}$). Stability constants of strophanthin–**Trp** and digoxin–**Trp** complexes are 5.5 and 2.2 times less respectively.

By the method of isomolar series, **Trp** was deduced to make 1:1 complexes with triterpene glycosides **1** and **2** in aqueous solutions [49]. Intermolecular interaction was shown to result in hyperchromic effect. In case of complexation of **Trp** with bidesmosidic glycoside **2** a faint bathochromic shift was also observed.

In [50] molecular complexation of **Trp** with glycosides **1** and **2** was studied by the method of electrospray-ionization mass spectrometry for the first time. In mass spectrum of the mixture of **Trp** and glycoside **1**, the peaks of complexes $[\text{M}^1 + \text{M}^{\text{Trp}} + \text{H}]^+$, $[4\text{M}^1 + 2\text{M}^{\text{Trp}} + 2\text{H}]^{2+}$ and $[3\text{M}^1 + \text{M}^{\text{Trp}} + 2\text{H}]^{2+}$ with intensities ratio 115:4:1 were found. In the spectrum of glycoside **1**–**Trp** mixture (negative-ion mode) the $[\text{M}^1 + \text{M}^{\text{Trp}} - \text{H}]^-$ ion was identified. Its peak intensity is 5.87 %, which is 11 times less than the main peak of $[\text{M}^{\text{Trp}} - \text{H}]^-$.

Complexation of glycoside **2** with **Trp** was not observed in spectrum of the positive-ion mode. But in the negative-ion mode there was the low intensity

peak of the complex $[M^2+M^{Trp}-H]^-$. Glycoside **1** forms complex of the same molar ratio, with its peak intensity being 15 times higher.

Allelopathic activity of **Trp** complexes with glycosides **1** and **2** was studied [50]. Suppression of the germination of *Avena sativa* L. seeds was observed both in the mixtures of **Trp** and glycosides **1** and **2**. The mixture **Trp**–glycoside **1** is most suppresses of the germination. The germination in the latter case appeared to be 2 times less than in control case.

4. Complexes with *L*-histidine

Triterpene glycoside **1** (Fig. 2) and *L*-histidine (**His**; Fig. 7) make complexes of 1:1 and 2:1 compositions. It is proved by the presence of ions $[M^1+M^{His+H}]^+$ and $[2M^1+M^{His+H}]^+$ peaks in mass spectrum (electrospray ionization) [51]. The ratio of peaks intensities is 20:1. In mass spectrum (negative-ion mode) of glycoside **1** and **His**, the peak of the complex $[M^1+M^{His}-H]^-$ ion with intensity of 3.41 % was observed.

Glycoside **2** (Fig. 2) makes complexes with **His** of the same compositions 1:1 and 2:1 [51]. For them the peaks of $[M^2+M^{His+H}]^+$, $[M^2+M^{His+K}]^+$, $[M^2+M^{His+Na}]^+$ and $[2M^2+M^{His+K}]^+$ with 7:2:2:1 intensities ratio appeared. The most stable complex was the one between glycoside **2** and **His** in the negative-ion mode. Its ion $[M^2+M^{His}-H]^-$ (m/z 1374.7) peak intensity was 28.16 %. This value is the highest one among those of complexes of glycosides **1** and **2** prepared with some drugs [5, 52–54] and aromatic amino acids [40, 46, 50] earlier.

In [50] a hypothesis for the formation of structure with internal cavity (Fig. 12) in the glycoside **2** molecule was put forward. In such a cavity the guest molecule can site. **His** molecule has got the smallest size among aromatic proteinogenous amino acids, that is why it penetrates deeper into the cavity of glycoside **2** and interacts more efficiently with it.

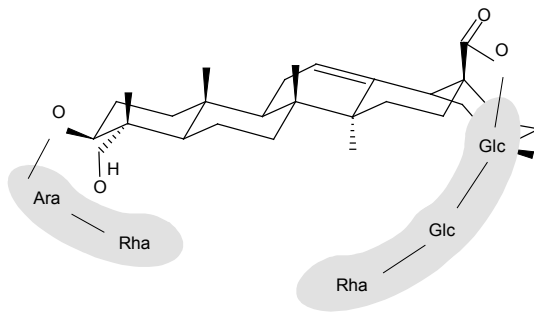


Figure 12. Schematic representation of glycoside **2** internal cavity.

In such a way, complexes of other aromatic proteinogenous amino acids with glycoside **2** [40, 46, 50] proved to be less stable. More durable boundaries can be explained with the structural peculiarities of imidazole ring resulting in the polarity of **His** and its faint basic properties. **Tyr** is one of hydrophilic neutral amino acids. **Phe** and **Trp** are, on the contrary, amino acids with hydrophobic lateral group. The **Trp** molecule, being the largest one among other aromatic proteinogenous amino acids, can not place itself in the cavity efficiently. That is why the complex of glycoside **2** with **Trp** turned to be less stable than that with other aromatic amino acids of analogical composition [50].

Glycoside **2** is bonded to NH_3^+ of the amino acids through hydrogen bonds to OH groups of monosaccharide units and $\text{N}^+\dots\text{OH}$ ion-dipole interactions. Hydrophobic interactions of the amino acids aromatic ring with the nonpolar aglycon (hederagenin) of the glycosides **1** and **2** may also occur.

By means of IR spectrometry a zwitter-ion form of amino acids $\text{RCH}(\text{NH}_3^+)\text{COO}^-$ was shown to interact with glycoside carboxyl in intermolecular complexes of hydrophilic (including **His**) and aliphatic amino acids and glycoside **1** [55, 56]. Earlier it was discovered that complexation of amino acids with some oxygenated macrocyclic ligand, including those of carbohydrate nature (α - and β -cyclodextrins), takes place due to hydrogen bounds formation and to the presence of electrostatic forces between the NH_3^+ group and donor oxygen atoms [57, 58]. Taking it into account, we can assume NH_3^+ group of zwitter-ion form of **His** (**Phe**, **Tyr**, **Trp**) form a hydrogen bound with CO group of glycoside **1** carboxyl $\text{NH}_3^+\dots\text{O}=\text{C}$.

The influence of glycosides **1** and **2** complexes with **His** on the *Avena sativa* L. seeds germination was examined [51]. The germination of seeds, cultivated by the mixtures of glycosides **1**, **2** and **His**, proved to be better than of those held in individual glycosides. Consequently, the complexes are less toxic than individual glycosides. The germination of seeds held in **His** solution turned out to be the same as of those affected by complexes and as control ones. The length of roots and sprouts of germinates, affected by the complexes, changed less than of those held in glycosides.

Unlike triterpene glycosides **1** and **2**, a number of steroid glycosides were not observed to complexation with **His** [28–32]. This fact had been previously proved by time-of-flight plasma desorption mass spectrometry with ionization by ^{252}Cf fission fragments.

Thus, for amino acids **Phe**, **Tyr**, **Trp**, **His** and triterpene glycosides **1** and **2** the complexes of 1:1 composition are most typical. Analogical principle has been deduced for the complexes of **Phe**, **Tyr** and **Trp** with steroid glycosides.

References

1. Tolstikova T.G., Tolstikov A.G., Tolstikov G.A. On the way to low-dose drugs, *Vestn. Ross. Acad. Nauk*, 2007, Vol. 77, P. 867–874.
2. Tolstikov G.A., Baltina L.A., Grankina V.P., Kondratenko R.M., Tolstikova T.G. Licorice: biodiversity, chemistry and application in medicine, Novosibirsk: Geo, 2007, 311 p.
3. Tolstikova T.G., Khvostov M.V., Bryzgalov A.O. The complexes of drugs with carbohydrate-containing plant metabolites as pharmacologically promising agents, *Mini-Rev. Med. Chem.*, 2009, Vol. 9, P. 1317–1328.
4. Yakovishin L.A., Borisenko N.I., Rudnev M.I., Vetrova E.V., Grishkovets V.I. Self-association and complexation of triterpene glycosides and cholesterol, *Chem. Nat. Comp.*, 2010, Vol. 46, No. 1, P. 49–52.
5. Lekar A.V., Vetrova E.V., Borisenko N.I., Yakovishin L.A., Grishkovets V.I. Electrospray-ionization mass spectrometry of mixtures of triterpene glycosides with paracetamol, *J. Appl. Spectr.*, 2010, Vol. 77, No. 5, P. 615–618.
6. Yakovishin L.A. Molecular complexation of the triterpene glycoside hederasaponin C and caffeine in aqueous solution, *Chem. Nat. Comp.*, 2010, Vol. 46, No. 5, P. 746–749.
7. Lekar' A.V., Vetrova E.V., Borisenko N.I., Yakovishin L.A., Grishkovets V.I. Mass spectrometry of triterpene glycosides molecular complexation with purine bases of nucleic acids, *Rus. J. Bioorgan. Chem.*, 2011, Vol. 37, No. 5, P. 609–613.
8. Yakovishin L.A. Molecular complex's formation of the triterpene glycoside α -hederin with caffeine in aqueous solution, *Ukr. Bioorg. Acta*, 2010, Vol. 8, No. 1, P. 42–46.
9. Yakovishin L.A., Yarovoy I.R., Belash D.Yu. Supramolecular complex of the triterpene glycoside hederasaponin C and sildenafil citrate, *Ukr. Bioorg. Acta*, 2011, Vol. 9, No. 1, P. 41–45.
10. Yakovishin L.A., Grishkovets V.I., Belash D.Yu., Yarovoy I.R. Molecular complexation of ivy and licorice saponins with some drugs of aromatic nature, *Sci. Not. V.I. Vernadsky Taurida Nat. Univ., ser. Biol. Chem.*, 2011, Vol. 24 (63), No. 3, P. 4–10.
11. Hostettmann K., Marston A. Saponins, Cambridge: Cambridge University Press, 1995, 548 p.
12. Elias R., Diaz-Lanza A.M., Vidal-Ollivier E., Balansard G., Faure R., Babadjamian A. Triterpenoid saponins from the leaves of *Hedera helix*, *J. Nat. Prod.*, 1991, Vol. 54, P. 98–103.

13. Grishkovets V.I., Kondratenko A.E., Tolkacheva N.V., Shashkov A.S., Chirva V.Ya. Triterpene glycosides of *Hedera helix* I. The structures of glycosides L-1, L-2a, L-2b, L-3, L-4a, L-4b, L-6a, L-6b, L-6c, L-7a, and L7-b from the leaves of common ivy, Chem. Nat. Comp., 1994, Vol. 30, No. 6, P. 689–692.
14. Grishkovets V.I., Sidorov D.Yu., Yakovishin L.A., Arnautov N.N., Shashkov A.S., Chirva V.Ya. Triterpene glycosides of *Hedera canariensis* I. Structures of glycosides L-A, L-B₁, L-B₂, L-C, L-D, L-E₁, L-G₁, L-G₂, L-G₃, L-G₄, L-H₁, L-H₂, and L-I₁ from the leaves of *Hedera canariensis*, Chem. Nat. Comp., 1996, Vol. 32, No. 3, P. 360–365.
15. Shashkov A.S., Grishkovets V.I., Loloyko A.A., Chirva V.Ya. Triterpene glycosides of *Hedera taurica* I. Structure of tauroside E from the leaves of *Hedera taurica*, Chem. Nat. Comp., 1987, Vol. 23, No. 3, P. 299–302.
16. Grishkovets V.I., Tolkacheva N.V., Shashkov A.S., Chirva V.Ya. Triterpene glycosides of *Hedera taurica* IX. Structures of tauroside G₁, G₂, G₃, H₁, and H₂ from the leaves of Crimean ivy, Chem. Nat. Comp. 1992, Vol. 28, No. 5, P. 455–460.
17. Kizu H., Kitayama S., Nakatani T., Tomimori T., Namba T. Studies on nepalese crude drugs III. On the saponins of *Hedera nepalensis* K. Koch., Chem. Pharm. Bull., 1985, Vol. 33, P. 3324–3329.
18. Shimizu M., Arisawa M., Morita N., Kizu H., Tomimori T. Studies of the constituents of *Hedera rhombea* Bean. I. Glycosides of hederagenin, Chem. Pharm. Bull., 1978, Vol. 26, P. 655–659.
19. Dekanosidze G.E., Pkheidze T.A., Kemertelidze E.P. Research of triterpene glycosides from caucasian ivy, Soobshch. Akad. Nauk Gruz. SSR (pharmacochemistry), 1970, Vol. 60, No. 2, P. 349–352.
20. Grishkovets V.I. Triterpene glycosides from *Hedera caucasigena* leaves, Chem. Nat. Comp., 1999, Vol. 35, No. 6, P. 688–689.
21. Grishkovets V.I. Triterpene glycosides from *Hedera scotica* leaves, Chem. Nat. Comp., 1999, Vol. 35, No. 6, P. 690–691.
22. Dekanosidze G.E., Kemertelidze E.P. Kalopanax-saponin B from *Hedera colchica*, Chem. Nat. Comp., 1980, No. 2, P. 259.
23. Mshvildadze V., Elias R., Faure R., Debrauwer L., Dekanosidze G., Kemertelidze E., Balansard G. Triterpenoid saponins from berries of *Hedera colchica*, Chem. Pharm. Bull., 2001, Vol. 49, P. 752–754.
24. Iskenderov G.B. Triterpene glycosides of *Hedera pastuchovii*, Pharmacia, 1971, Vol. 20, No. 4, P. 27–30.
25. Mshvildadze V., Elias R., Faure R., Rondeau D., Debrauwer L., Dekanosidze G., Kemertelidze E., Balansard G. Triterpenoid saponins

- from the leaves of *Hedera pastuchowii*, Chem. Pharm. Bull., 2004, Vol. 52, P. 1411–1415.
26. Zuzuk B.M., Kutsik R.V., Zuzuk L.I. Ivy *Hedera helix* L., Provizor, 2003, No. 12, P. 13–14.
 27. Sieben A., Prenner L., Sorkalla T., Wolf A., Jakobs D., Runkel F., Haberlein H. α -Hederin, but not hederacoside C and hederagenin from *Hedera helix*, affects the binding behavior, dynamics, and regulation of β_2 -adrenergic receptors, Biochemistry, 2009, Vol. 48, No. 15, P. 3477–3482.
 28. Pilipenko V. V., Aksyonov S. A., Kalinkevich A. N., Sukhodub L. F. PDMS study of the steroid glycosides interaction with amino acids, Biopolym. Cell, 2000, Vol. 16, No. 3, P. 212–219.
 29. Pilipenko V.V., Sukhodub L.F., Aksyonov S.A., Kalinkevich A.N., Kintia P.K. ^{252}Cf Plasma desorption mass spectrometric study of interactions of steroid glycosides with amino acids, Rapid Commun. Mass Spectrom., 2000, Vol. 14, P. 819–823.
 30. Pilipenko V.V., Sukhodub L.F. Mass spectrometry study of plant steroid glycosides and their interactions with biomolecules, Biopolym. Cell, 2002, Vol. 18, No. 2, P. 139–141.
 31. Sukhodub L.F., Kalinkevich A.N. Plant steroid glycosides and their complexation with biomolecules (mass-spectrometry data), J. Acad. Medic. Sci. Ukr., 2009, Vol. 15, No. 2, P. 225–245.
 32. Pilipenko V.V., Sukhodub L.F. Mass spectrometry study of complexation of steroid glycosides with amino acids, Vis. Kharkov. Univer.: Biophys. Bull., 2004, No. 1–2, P. 131–137.
 33. Pilipenko V.V., Sukhodub L.F., Kalinkevich A.N. PDMS study of interactions of steroid glycosides with nucleoside and nucleotide, Vis. Kharkov. Univer.: Biophys. Bull., 2001, No. 2(9), P. 103–109.
 34. Pilipenko V.V., Aksyonov S.A., Kalinkevich A.N., Sukhodub L.F. ^{252}Cf Plasma desorption mass spectrometric study of interactions of steroid glycosides with nucleosides, Vis. Kharkov. Univer.: Biophys. Bull., 1999, No. 3, P. 56–62.
 35. Shvets S.A., Naibi A.M., Kintya P.K., Shashkov A.S. Steroid glycosides from the seeds of *Petunia hybrida*. Structures of petuniosides B, D, and F, Chem. Nat. Comp., 1995, Vol. 31, No. 3, P. 328–331.
 36. Gutsu E.V., Kintya P.K., Shvets S.A., Lazur'evskii G.V. Steroid glycosides of the roots of *Capsicum annuum*. I. The structure of capsicosides A₁, B₁, and C₁, Chem. Nat. Comp., 1986, Vol. 22, No. 6, P. 661–664.

37. Gorchakova N.A., Samarskaya T.G., Samarsky V.A., Lezina G.G., Grischenko L.I., Babak V.V. Complexation of cardiac glycosides with amino acids and alkaline earth metals, *Eksp. Klin. Farmakol.*, 1992, Vol. 55, No. 2, P. 106–109.
38. Dewick P.M. *Medicinal natural products. A biosynthetic approach*, 2nd Ed., John Wiley & Sons, Chichester, 2002, 507 p.
39. Yakovishin L.A., Grishkovets V.I., Sergienko U.I., Korzh E.N. Molecular complexation of triterpene glycosides with *L*-phenylalanine in water solutions, *Sci. Notes of Taurida V.I. Vernadsky Nat. Univ., ser. Biol. Chem.*, 2010, Vol. 23 (62), No. 3, P. 255–261.
40. Lekar A.V., Vetrova E.V., Borisenko N.I., Yakovishin L.A., Grishkovets V.I., Borisenko S.N. Electrospray ionization mass spectrometry of mixtures of triterpene glycosides with *L*-phenylalanine, *J. Appl. Spectr.*, 2011, Vol. 78, No. 4, P. 501–505.
41. Anisimov M.M., Chirva V.Ya. About of the biological role of triterpene glycosides, *Usp. Sovrem. Biol.*, 1980, Vol. 6, No. 3, P. 351–364.
42. Waller G.R., Jurzysta M., Trohne R.L.Z. Root saponins from alfalfa (*Medicago sativa* L.) and their allelopathic activity on weeds and wheat, *Allelopathy J.*, 1995, Vol. 2, No. 1, P. 21–30.
43. Oleszek W., Jurzysta M. The allelopathic potential of alfalfa root medicagenic acid glycosides and their fate in soil environments, *Plant Soil*, 1987, Vol. 98, P. 67–80.
44. Wyman-Simpson C.L., Waller G.R., Jurzysta M., McPherson J.K., Young C.C. Biological activity and chemical isolation of root saponins of six cultivars of alfalfa (*Medicago sativa* L.), *Plant Soil*, 1991, Vol. 135, P. 83–94.
45. Colazo M.G., Mart´inez M.F., Kastelic J.P., Mapletoft R.J. Effects of dose and route of administration of cloprostenol on luteolysis, estrus and ovulation in beef heifers, *Anim. Reprod. Sci.*, 2002, Vol. 72, P. 47–62.
46. Yakovishin L.A., Lekar A.V., Vetrova E.V., Borisenko N.I., Borisenko S.N., Grishkovets V.I. Molecular complexes of the triterpene glycosides with *L*-tyrosine and their biological activity, *Biopolym. Cell*, 2012, Vol. 28, No. 1, P. 62–67.
47. Yakovishin L.A., Grishkovets V.I., Sergienko U.I., Dovgy I.I. Molecular complexation of triterpene glycosides with *L*-tyrosine in aqueous solutions, *Sci. Notes of Taurida V.I. Vernadsky Nat. Univ., ser. Biol. Chem.*, 2011, Vol. 24 (63), No. 1, P. 232–238.
48. Podolak I., Galanty A., Sobolewska D. Saponins as cytotoxic agents: a

- review, *Phytochem. Rev.*, 2010, Vol. 9, P. 425–474.
49. Yakovishin L.A., Grishkovets V.I., Epishina N.V., Kurtametov I.S. Molecular complexation of the triterpene glycosides with tryptophan in water solutions, *Sci. Notes Taurida V.I. Vernadsky Nat. Univ., ser. Biol. Chem.*, 2010, Vol. 23 (62), No. 2, P. 270–275.
 50. Yakovishin L.A., Lekar A.V., Borisenko S.N., Vetrova E.V., Borisenko N.I., Grishkovets V.I. Molecular complexation of ivy saponins with *L*-tryptophan, *Khimiia rastitel'nogo syr'ia*, 2011, No. 4, P. 65–70.
 51. Yakovishin L.A., Lekar A.V., Vetrova E.V., Borisenko N.I., Grishkovets V.I. Molecular complexes of triterpene glycosides with *L*-histidine and their biological activity, *Biopolym. Cell*, 2011, Vol. 27, No. 4, P. 300–305.
 52. Lekar A.V., Yakovishin L.A., Borisenko S.N., Vetrova E.V., Borisenko N.I., Grishkovets V.I. Electrospray ionization mass spectrometry of mixtures of triterpene glycosides with acetylsalicylic acid (aspirin), *Sci. Notes Taurida V.I. Vernadsky Nat. Univ., ser. Biol. Chem.*, 2012, Vol. 25 (64), No. 3, P. 291–297.
 53. Lekar A.V., Yakovishin L.A., Borisenko S.N., Vetrova E.V., Borisenko N.I. Complexation of antibiotic levomycetin (chloroamphenicol) with α -hederin and hederasaponin C under the conditions of electrospray ionization, *J. Analytic. Chem.*, 2011, Vol. 66, No. 14, P. 1437–1440.
 54. Lekar A.V., Vetrova E.V., Borisenko N.I., Yakovishin L.A., Grishkovets V.I. Mass spectrometry research of molecular complexation plant glycosides with streptocid (sulfanilamide), *Khimiia rastitel'nogo syr'ia*, 2011, No. 2, P. 103–106.
 55. Yakovishin L.A., Grishkovets V.I., Rubinson M.A., Korzh E.N. The complex's formation of triterpene glycoside α -hederine with hydrophilic proteinogenous amino acids, *Sci. Notes Taurida V.I. Vernadsky Nat. Univ., ser. Biol. Chem.*, 2009, Vol. 22 (61), No. 1, P. 208–213.
 56. Yakovishin L.A., Rubinson M.A. Molecular complexes of the triterpene glycoside α -hederine with aliphatic proteinogenous amino acids, *Ukr. Bioorg. Acta*, 2009, Vol. 7, No. 1, P. 32–35.
 57. Terekhova I.V., Kulikov O.V., Agafonov A.V., Volume changes on complex formation of 18-crown-6 with amino acids in aqueous solutions, *Rus. J. Gen. Chem.*, 2003, Vol. 73, No. 2, P. 312–314.
 58. Kulikov O.V. Thermodynamics of formation of molecular complexes in aqueous solutions of amino acids, peptides, nucleic bases and macrocyclic compounds, Author's abstr. of a doctoral dissertation in chem. sci., Ivanovo, 2005, 36 p.

Chapter 5

Functionalized polystyrene beads as carriers in the release studies of tetrapeptides

Anna Olejnik, Izabela Nowak and Grzegorz Schroeder
*Adam Mickiewicz University in Poznań, Faculty of Chemistry,
Umultowska 89b, 61-614 Poznań, Poland*

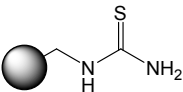
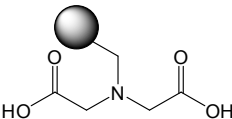
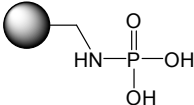
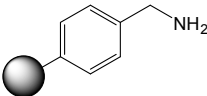
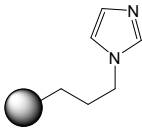
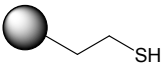
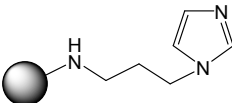
Introduction

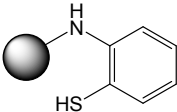
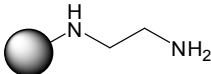
Nanotechnology has developed tremendously in the past decade and was able to create many new materials with a vast range of potential applications. Some of those innovative materials are promising to reduce environmental pollution. The surfaces of these hybrid nanomaterials have different functional groups capable of interacting with biological molecules such as peptides or proteins. The biological activity of the functionalized materials is determined by two processes: formation and dissociation of supramolecular complex between functional groups on the surface of the material and biological molecules. The risk that nano-particles may pose to human and environment health is not yet fully understood. The precautionary principle therefore suggests keeping environmental release of nano-particles minimal until their fate and toxicity is better understood. Examination of these two processes: formation and dissociation of supramolecular complex allows full and credible interpretations of interaction of functional materials on biological systems.

Release testing is used to quantify the amount and extent of drug release from solid and semisolids dosage forms. These tests are routinely applied in Quality Control (QC) and Research & Development (R&D) Laboratories. Usually, the studies are focused on estimation of the active compound release in respect to *in vivo* performance of the drug product. The controlled release system exhibits various advantages, such as enhancement of the drug efficiency and toxicity reduction [1]. Recently, considerable development in different methods for delivery of bioactive compounds using various polymeric materials as carriers has been observed [2]. Generally, active compounds are introduced into polymer matrix by different techniques such as direct compression, wet granulation or

mechanical mixing [3]. QuadraPure™ scavengers are functionalized macroporous or microporous polystyrene-based resin beads widely used in the removal and economic recovery of precious metal contamination from products and organic or aqueous process streams [4,5,6]. All QuadraPure™ metal scavengers were purchased from Sigma-Aldrich. Chemical structure of QuadraPure™ reservoirs and their characterization are summarized in Table 1.

Table 1. QuadraPure® structure and characterization.

QuadraPure Type	Description	Structure
TU	Macroporous 400-600 µm particle size	
IDA	Macroporous 350-750 µm particle size	
AMPA	Macroporous 350-750 µm particle size	
BZA	Macroporous 400-1100 µm particle size	
BDZ	Macroporous 400-750 µm particle size	
DET	Macroporous 450-650 µm particle size	
IMDAZ	Microporous 100-400 µm particle size	

MPA	Microporous 100-400 μm particle size	
AEA	Microporous 100-400 μm particle size	

The polystyrene beads are monodisperse and exhibit relatively low swelling in organic solvents (up to 30%). It is known that QuadraPure™ cartridges demonstrate excellent clean-up in comparison with traditional methods for metal removal [7]. On the other hand, the pre-treatment of polystyrene beads with a nonpolar organic solvent is the key for the generation of mechanically robust tablets consisting of neat functionalized polystyrene beads alone or in combination with solid reagents or catalysts [8]. Polystyrene beads have also been used as controlled release carriers for liquid biocides, added before copolymerization [9].

Herein, we demonstrate the novel practical benefit of functionalized polystyrene beads which can be applied in release studies of low molecular peptides. It is well known that peptides exhibit low bioavailability after oral administration and have short biological half-lives in plasma [10]. Therefore, it is important to design a new delivery system for these compounds.

In order to understand the release behaviour of three tetrapeptides (AcPPYL – Ac-Pro-Pro-Tyr-Leu, AcYPPF – Ac-Tyr-Pro-Phe-Phe, AcQDVH – Ac-Gln-Asp-Val-His) several kinds of polystyrene beads with different pore sizes and functional groups have been studied. The formation and release of peptides is tested scavengers following method.

The appropriate QuadraPure™ were added to the peptide solution and left in drier at 35°C for 24 hours. When ethanol was completely evaporated, the QuadraPure™ materials containing peptide were placed in the Enhancer cell. (In order to maintain appropriate experiment conditions and steady surface area the QuadraPure™ the scavengers were sandwiched between two porous synthetic nets). In vitro release studies were performed with the use of an USP Apparatus 2 (Varian Vankel 7010). The receiving medium was chosen depending on the solubility of the compound examined. When the active compound was AcPPYL, potassium phosphate buffer at pH 5.8 was used, however for AcYPPF and AcQDVH, the use of hydro-alcoholic solutions as receptor media was required (1:1 ethanol/ potassium phosphate buffer at pH 5.8). The medium (200 ml) was

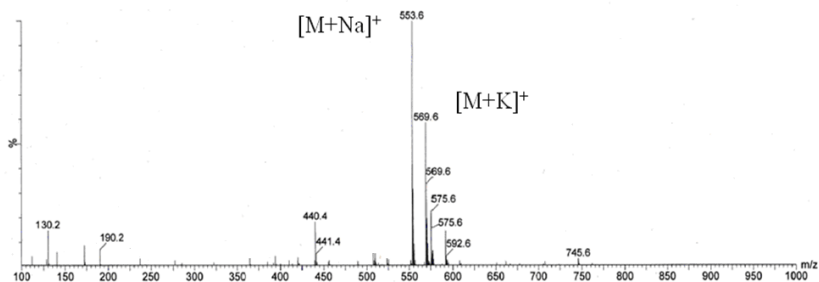
maintained at $32.0^{\circ}\text{C} \pm 0.5^{\circ}\text{C}$ and stirred at 100 rpm. The samples were filtered through $35\ \mu\text{m}$ HDPE Full-Flow filters and the concentration of the dissolved peptide was spectrometrically monitored at 276 nm for AcPPYL, 275 nm for AcYPFF and at 260 nm for AcQDVH. The absorbance of the sample aliquots was used to assess the amount of compound release at each time point. In addition, the reference standard solutions of each peptide were prepared in the appropriate receptor fluid in order to generate the standard curve of absorbance versus concentration. Kinetic measurements were performed to determine the release rate constant in given conditions. The rate constant (k) and the peptide half-release time were determined from kinetics curves by the Gugenheim method [11].

In this study two ranges of QuadraPure[®] macroporous and microporous scavengers were applied. They were different not only in the particle size but they also had various functional groups attached to polystyrene such as thiourea (TU), imino diacetate (IDA), aminomethyl phosphonic acid (AMPA), benzyl amine (BZA), imidazole (BDZ), thiol (DET), imidazol-1-yl propyl amine (IMDAZ), mercaptophenyl amine (MPA), aminoethyl amine (AEA). These functional groups are responsible for the specific properties of the above mentioned molecules. Functional groups such as thiol, amine, imidazole are nucleophilic and thanks to their lone pair of electrons they are readily accessible.

Table 2 presents the chemical structure and the molecular weight of three N-terminal acetyl-tetrapeptides tested in the release studies. The molecular weight was determined by MS MALDI technique. In Fig.1 the mass spectrum of AcPPYL (MW:530.6) is presented. The positive ion mode spectrum of AcPPYL shows a molecular ion with associated sodium $[\text{M}+\text{Na}]^{+}$ at m/z 553.6 and a molecular ion with associated potassium $[\text{M}+\text{K}]^{+}$ at m/z 569.6. A similar pattern was also observed for AcYPFF in Fig.2 whose spectrum shows a molecular ion associated with sodium $[\text{M}+\text{Na}]^{+}$ at m/z 636.6 and a molecular ion associated with potassium $[\text{M}+\text{Na}]^{+}$ at m/z 653.6. In Fig.3 the signals at m/z 540.5 $[\text{M}+\text{H}]^{+}$, m/z 562.5 $[\text{M}+\text{Na}]^{+}$ and m/z 578.5 provided specific evidence for the identification of AcQDVH (MW:539.5).

Table 2. Tetrapeptide chemical structure and molecular weight.

Tetrapeptide	Chemical structure	MW
AcPPYL		530.6
AcYPPF		614.6
AcQDVH		539.5


 Figure 1. MALDI-TOF Mass spectrum of *Ac-Pro-Pro-Tyr-Leu* (MW: 530.5).

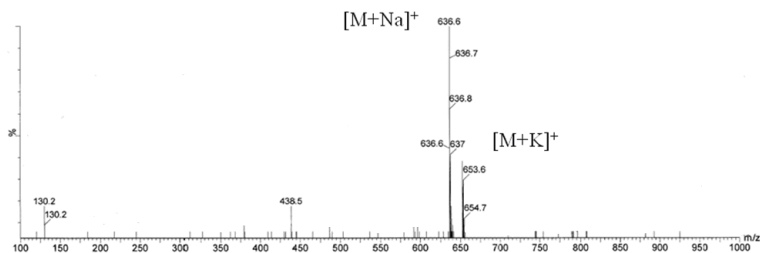


Figure 2. MALDI-TOF Mass spectrum of Ac-Tyr-Pro-Phe-Phe (MW: 614.6).

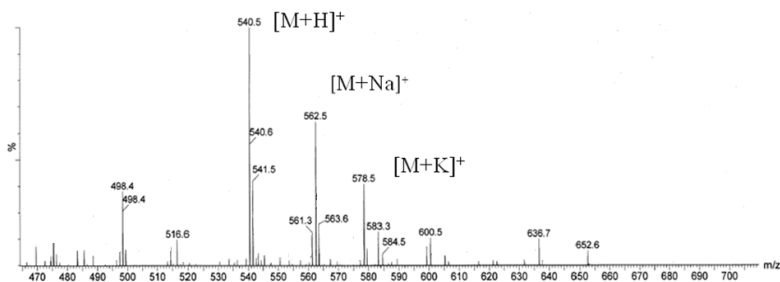


Figure 3. MALDI-TOF Mass spectrum of Ac-Gln-Asp-Val-His (MW: 539.5).

In vitro release of Ac-Pro-Pro-Tyr-Leu

Figs. 4 and 5 show the amount of released AcPPYL from macroporous and microporous particles as a function of time. Within the 10-h period, the amount of AcPPYL released from AMPA, IDA, DET, BDZ, BZA and TU-modified scavengers reached 99.8 %, 99.5%, 86.6%, 80.8%, 56.7%, and 39.4%, respectively. Comparison of the six release profiles indicates that the AcPPYL release rate is determined by the type of functional groups of the macroporous material. The release rate depends on the number of nitrogen atoms with free electron pair. The release profiles of AcPPYL from microporous materials are shown in Fig. 5. The amount of AcPPYL released from AEA, MPA and IMDAZ reached 97.7%, 90.3% and 26.6%, respectively.

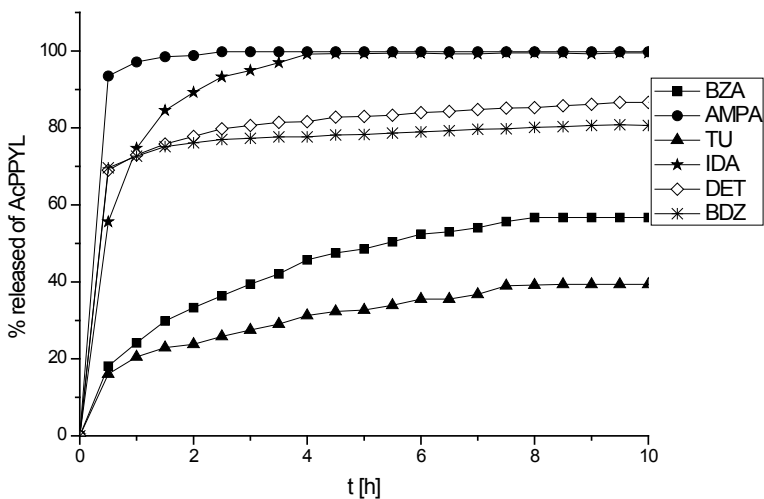


Figure 4. The release profiles of AcPPYL from various functionalized macroporous polystyrene beads.

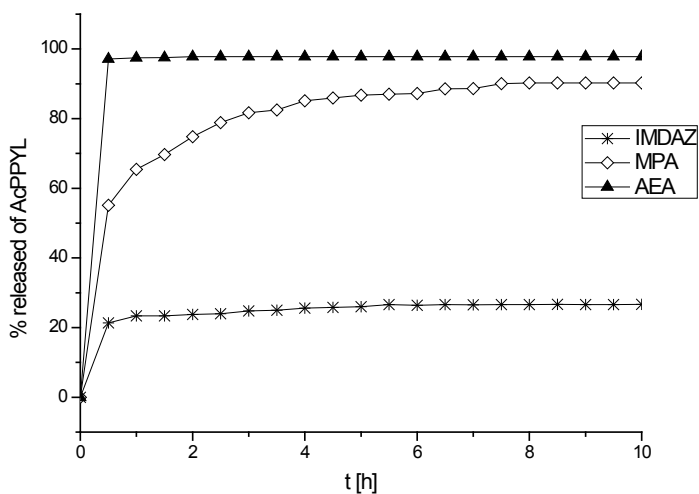


Figure 5. The release profiles of AcPPYL from various functionalized microporous polystyrene beads.

Table 3. Rate constant and half-release time of AcPPYL from various micro- and macroporous reservoirs.

		k [h ⁻¹]	t _{1/2} [h]
	BZA	0.44	5.50
	AMPA	1.36	0.25
macroporous	TU	1.08	-
	IDA	0.99	0.50
	DET	0.84	0.25
	BDZ	1.46	0.25
	IMDAZ	1.82	-
microporous	MPA	0.91	0.25
	AEA	0.60	0.25

Table 3 presents the tetrapeptide AcPPYL rate constant and half-release time from various micro- and macroporous reservoirs. In case of macroporous materials the rate of release calculated from the Gugenheim's method is the highest for BDZ (1.46) and the lowest for BZA (0.44) where the half amount of peptide was released only after 5.50 h. However, the results were different for AMPA, DET and BDZ functionalized scavengers because after 0.25 h even more than 50% was released. In the Fig.6 the mass spectrum of AcPPYL before and after the experiment is presented. It was proven that in case of AMPA no signal of peptide was detected after the release test, so the functional group – aminomethyl phosphonic acid – was not bound to AcPPYL. Furthermore, the results indicated that there were strong interactions between scavenger with thiourea functional group (TU) and AcPPYL because even after 24 h the 50% of the peptide was not released. The similar pattern was observed also in case of microporous IMDAZ. The data in the Fig. 7 provided the evidence that even after 24 h the peptide was still interacting with IMDAZ functional group (imidazol-1-yl propyl amine) because the signal of the peptide was detected. It should be mentioned that the experiment was carried out in potassium phosphate buffer so this is the reason why molecular ion with an associated potassium [M+K]⁺ could be observed.

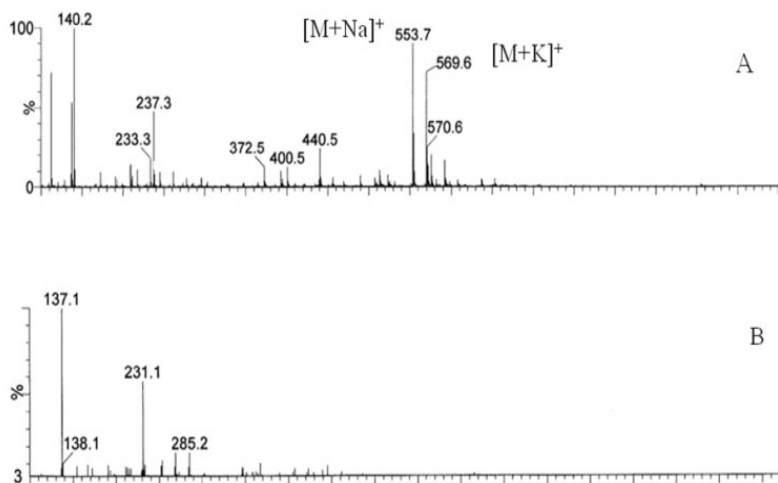


Figure 6. MALDI-TOF Mass spectrum of Ac-Pro-Pro-Tyr-Leu (MW: 530.5) before (A) and after (B) the release from AMPA-functionalized beads.

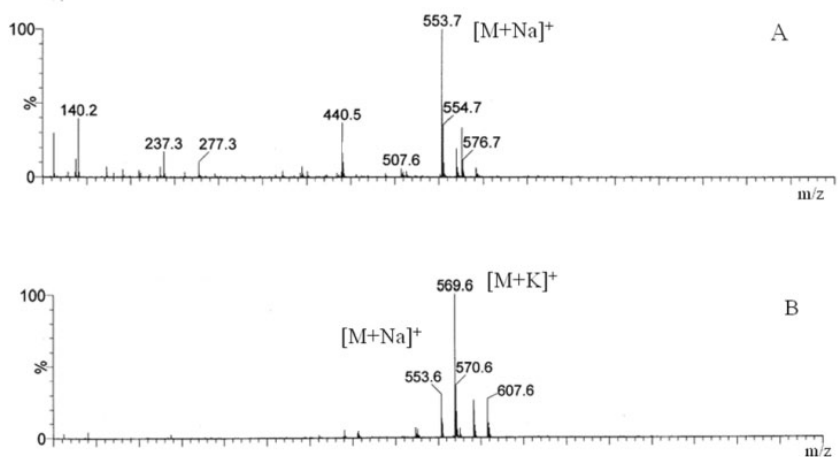


Figure 7. MALDI-TOF Mass spectrum of Ac-Pro-Pro-Tyr-Leu (MW: 530.5) before (A) and after (B) the release from IMDAZ-functionalized beads.

In vitro release of Ac-Tyr-Pro-Phe-Phe (AcYPPF)

Figs. 8 and 9 present the release profiles of AcYPPF from functionalized macroporous and microporous particles. After 10 h, the amount of AcYPPF released from AMPA, IDA, DET, BZA, BDZ and TU functionalized macroporous beads reached 98.3 %, 89.9%, 88.9%, 88.3%, 68.5% and 66.4%, respectively (Fig. 8). The results show that AcYPPF release rate is determined by the kind of the functional group of macroporous material. The release rate decreases when the amount of free NH_2 increases. The release profiles of AcYPPF from functionalized microporous materials are demonstrated in Fig. 9. The release amount of AcYPPF from AEA, MPA and IMDAZ functionalized beads reached 99.1 %, 75.3% and 39.0%.

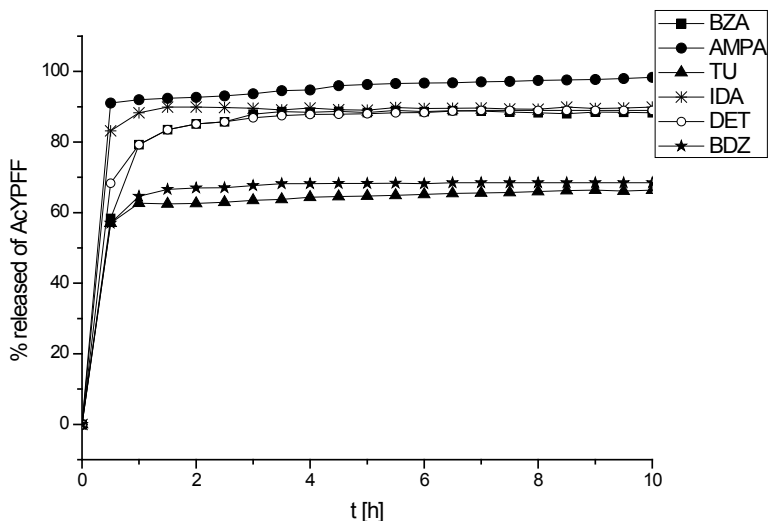


Figure. 8. The release profiles of AcYPPF from various functionalized macroporous polystyrene beads.

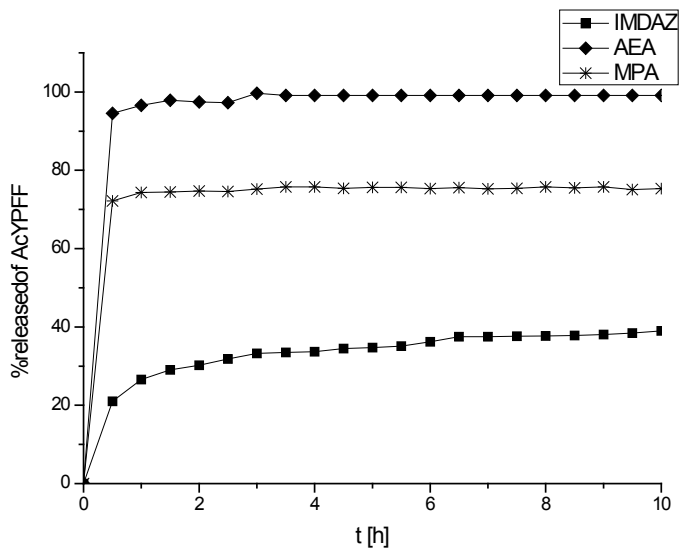


Figure 9. The release profiles of AcYPPFF from various functionalized microporous polystyrene beads.

Table.4. Rate constant and half-release time of AcYPPFF.

		k [h ⁻¹]	t _{1/2} [h]
macroporous	BZA	2.40	0.25
	AMPA	5.09	0.25
	TU	6.58	0.50
	IDA	4.13	0.25
	DET	2.28	0.50
	BDZ	2.82	0.50
	IMDAZ	1.76	-
microporous	MPA	6.27	0.25
	AEA	2.62	0.25

The calculated rate constant and half-release time of AcYPPFF are gathered in Table 4. The highest k was determined for TU (6.58 h⁻¹) and the lowest for DET (2.28 h⁻¹). Moreover, for TU (thiourea), DET (thiol) and BDZ (imidazole)

the half-release time was 0.50 h. In case of microporous beads modified with IMDAZ even after 24 h only 40 % of the peptide was released. The lowest rate constant was indicated for IMDAZ (1.76) and the highest for MPA (6.27).

In vitro release of Ac-Gln-Asp-Val-His (AcQDVH)

The data in Figs. 10 and 11 demonstrates the differences in release profiles of AcQDVH from macroporous and microporous functionalized particles. After 24 h the amount of AcQDVH released from TU, IDA, AMPA, DET, BZA, BDZ functionalized macroporous beads reached 99.8 %, 98.9%, 96.0%, 73.2%, 72.9%, 53.9%, respectively (Fig. 10). These results also proved that the release rate is strongly determined by the type of functional group attached to the macroporous materials. The release profiles of AcQDVH from various functionalized microporous materials are demonstrated in Fig. 11. The release amount of AcQDVH from modified with MPA, AEA and IMDAZ microporous solids reached 92.9 %, 85.2 %, 78.4%, respectively.

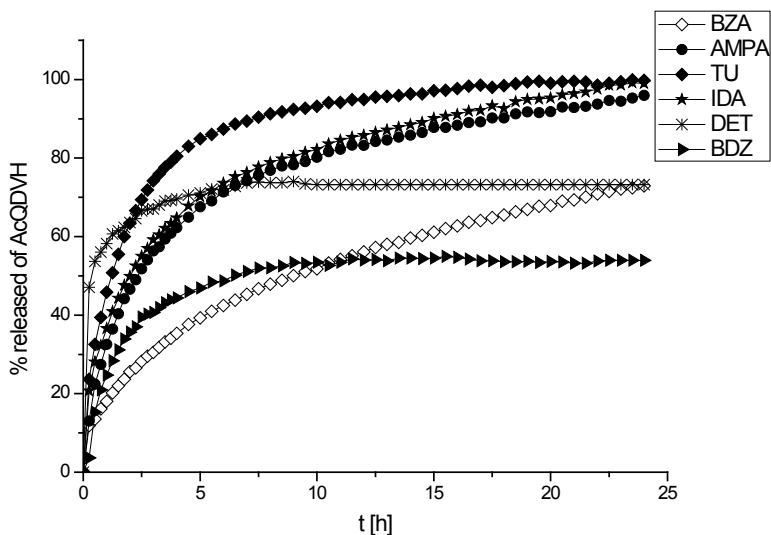


Figure 10. The release profiles of AcQDVH from various functionalized macroporous polystyrene beads.

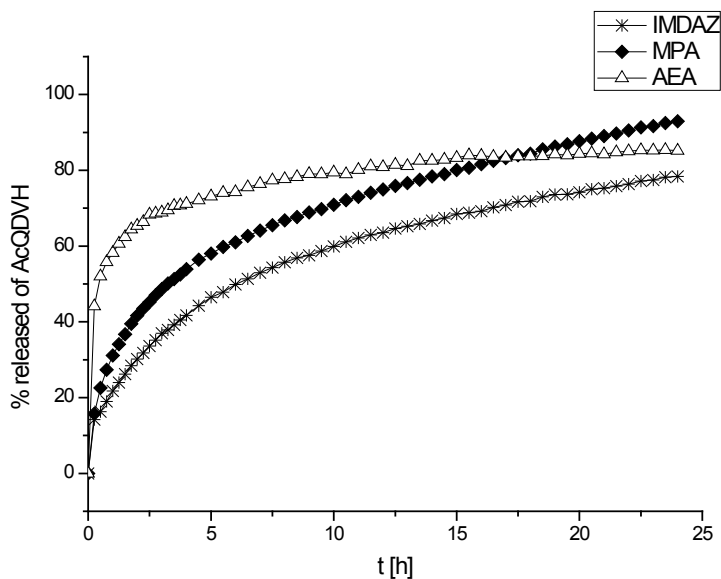


Figure 11. The release profiles of AcQDVH from various functionalized microporous polystyrene beads.

Table.5. Rate constant and half-release time of AcQDVH.

		k [h ⁻¹]	t _{1/2} [h]
macroporous	BZA	0.28	9.00
	AMPA	0.38	2.50
	TU	0.57	1.25
	IDA	0.47	2.00
	DET	0.51	0.50
	BDZ	0.74	6.50
microporous	IMDAZ	0.34	6.25
	MPA	0.40	3.25
	AEA	0.78	0.50

In the Table 5 the data concerning rate constant and half-release time of AcQDVH can be found. It was calculated that in case of peptide released from

macroporous k was the highest for BDZ (imidazole) 0.74 h^{-1} and the lowest for BZA (benzyl amine) 0.28 h^{-1} . Moreover, the half-release time for those materials was respectively 6.5 h and 9.0 h. It should be mentioned that also in this case, microporous functionalized beads IMDAZ strongly interacted with peptide, because the half-release time was 6.25 h.

This work had demonstrated the new ability of polystyrene beads modified with functional groups that can be successfully used as a reservoir for the storage and controlled release of tetrapeptides. Geometrical features, such as bead size and pore architecture of polystyrene beads were found to govern the loading efficiency and in vitro drug release kinetics. Generally, the smaller resin beads offering more surface area have shown quick exchange of tetrapeptides due to shorter diffusion path length. Whereas, the larger beads, have more diffusional path length leading to sustained release.

Depending on the needs, the appropriate QuadraPure™ can be chosen to design and carry out the specifically controlled release experiments. If the purpose is to storage or prolong the release of the peptide, the microporous IMDAZ (with imidazol-1-yl propyl amine as functional group) was determined to be the ideal solution for all tested peptides. However, macroporous TU functionalized beads (with tiourea as functional group) were appropriate for AcPPYL and AcYPPF storage, whereas for AcQDVH macroporous particles modified with BDZ- (with imidazole as functional group) were better material for this purpose. The research also proved that AMPA with aminomethyl phosphonic acid and AEA with aminoethyl amine are not strongly bond to peptide.

Acknowledgments

The authors would like to thank the Polish Ministry of Science and Higher Education for the financial support (N N204 403040; 2011-012)

References

1. Uhrich, K. E.; Cannizzaro, S. M.; Langer, R. S.; Shakesheff, K.M. Polymeric Systems for Controlled Drug Release, *Chem. Rev.* 1999, 99, 3181–3198.
2. Langer, R. S.; Peppas, N. A. Chemical and physical structure of polymerases Carriers for controlled release of bioactive agents: a review *J. Macromol. Sci., Rev. Macromol. Chem. Phys.* 1983, C23, 61-126.
3. Xu, W.; Gao, Q.; Xu, Y.; Wu, D.; Sun, Y.; Shen, W.; Deng, F.; Controllable release of ibuprofen from size-adjustable and surface hydrophobic mesoporous silica spheres *Powder Technology* 2009, 191,

- 13–20.
4. QuadraPure resins are available from Sigma-Aldrich at research-scale amounts, and in bulk quantities and cartridge format from Reaxa Ltd., Manchester, U.K. (www.reaxa.com).
 5. Richardson, J. M.; Jones, C.W.; Poly(4-vinylpyridine) and Quadrapure TU as Selective Poisons for Soluble Catalytic Species in Palladium-Catalyzed Coupling Reactions – Application to Leaching from Polymer-Entrapped Palladium, *Adv. Synth. Catal.* 2006, 348, 1207 – 1216.
 6. Nikbin, N.; Ladlow, M.; Ley, S. V. Continuous flow ligand-free Heck reactions using monolithic Pd [0] nanoparticles, *Org. Process Res. Dev.* 2007, 11, 458–462.
 7. Hinchcliffe, A.; Hughes, C.; Pears, D. A.; Pitts, M. R., QuadraPure Cartridges for Removal of Trace Metal from Reaction Mixtures in Flow, *Org. Process Res. Dev.* 2007, 11, 477–481.
 8. Ruhland, T., Holm, P. Andersen, K., Tablets of functionalized polystyrene beads alone and in combination with solid reagents or catalysts. Preparation and applications in parallel solution and solid phase synthesis, *J. Comb. Chem.* 2003, 5, 842–850.
 9. Iconomopoulou, S. M.; Andreopoulou, A. K.; Soto, A.; Kallitsis, J. K.; Voyiatzis, G.A. Incorporation of low molecular weight biocides into polystyrene-divinyl benzene beads with controlled release characteristics, *J Control Release.* 2005, 102, 223–233.
 10. Lee H. J., Biopharmaceutical properties and pharmacokinetics of peptide and protein drugs, in: M.D. Taylor, G.L. Amidon (Eds.), *Peptide-based Drug Design Controlling Transport and Metabolism*, American Chemical Society, Washington, 1995, pp. 69–91.
 11. Schwetlick, K.; *Kinetische Methoden zur Untersuchung von Reaktionsmechanismen*, VEB Deutscher Verlag der Wissenschaften Berlin 1971, E.A. Guggenheim, *Phil. Mag.*, 2 (7), 538, 1926.

Chapter 6

Description of thermodynamic parameters of formation and dimerization of alkylamides using superposition-additive approach

Yu.B. Vysotsky¹, E.A. Belyaeva¹, E.S. Fomina¹ and D. Vollhardt²

¹*Donetsk National Technical University, 58 Artema Str.,*

83000 Donetsk, Ukraine,

²*Max Planck Institute of Colloids and Interfaces,*

D-14424 Potsdam/Golm, Germany

The superposition-additive approach (SAA) is theoretically based on the postulate about the way in which atoms exist in molecules [1]. Nowadays this postulate is getting more widespread. Initially this approach was developed for description of electronic structure and physicochemical properties of conjugated systems [2]. Later SAA was applied for calculation of thermodynamic parameters of formation and atomization of conjugated systems, their dipole electric polarizabilities, molecular diamagnetic susceptibilities, π -electronic ring current etc. [3]. Although calculations according different additive schemes were done before, still they did not account the properties of molecular graphs [4-6].

In our previous study [7, 8] superposition-additive approach was exploited for description of thermodynamic parameters of formation and clusterization of monosubstituted alkanes which possess amphiphilic properties and are capable of monolayer formation at the interface. Implementation of this approach enables to reproduce the values of thermodynamic parameters of formation and clusterization of five surfactant classes (fatty alcohols, saturated and monoionic carboxylic acids, thioalcohols, amines) in condensed state quite accurately. It is also applicable for calculation of the thermodynamic parameters of phase transition for mentioned compounds. The introduction of the superposition-additive approach offers a new and unique possibility to obtain parameters which are unknown for some members of homologous surfactant series in the case that corresponding experimental or theoretically calculated parameters (for example, thermodynamic parameters at the formation of aggregates) are available for

other members of the homologous series. Also it suggests the option to calculate the thermodynamic parameters in the case that corresponding values for other classes of surfactants are available. In this connection it is of interest to apply SAA to multisubstituted alkanes, e.g. alkylamides. Thermodynamic parameters of them could be considered as a sum of the corresponding parameters for monosubstituted alkanes: carboxylic acids, amines and alcohols.

The objective of the present work is to obtain the thermodynamic parameters of formation and dimerization for aliphatic amides $C_nH_{2n+1}CONH_2$ ($n=6-16$) at air/water interface under standard condition as a first stage of their clusterization process.

1. Theoretical background of the superposition-additive approach

As it was noted above the superposition-additive approach (SAA) is theoretically based on the postulate about the way in which atoms exist in molecules [1]. According to this postulate, each atom in a molecule retains its individuality in various chemical combinations (i.e., in various molecules). This refers to transferability of atomic patterns. In addition, the atomic values, being summed over all atoms in the molecule, yield the molecular average so that the corresponding molecular characteristics are additive. The above presumption about the way in which atoms exist in molecules is the background for various additive schemes [1]. The main idea of the superposition-additive approach is based on the transferability of atomic properties and the additivity of molecular properties. The essence of the procedure is the assumption that when two molecular graphs are virtually superimposed (atoms of one molecule coincide spatially with corresponding atoms of the other molecule), the properties of the constituent atoms remain unchanged. Then, if the same superposition can be constructed in two different ways, each involving two entities (molecules, ions, radicals, clusters), it become possible to calculate the structure and properties of one of these entities, provided the structure and properties of the remaining three entities are known.

This principle is graphically illustrated in Fig. 1. The molecules (1), (2), (4) and (5) are the structures which involve the alkyl chain and the functional groups X, Y and Z (these groups can be the same or different). The structure (3) is the result of the superposition of the structures (1) and (2), and also of the structures (4) and (5). As these two superpositions lead to the same result, the properties of any of the four molecules could be expressed as the algebraic sum of the corresponding properties of three other molecules. Thus, for example, to calculate any thermodynamic parameter of the molecule (4) one has to add the corresponding values for the molecules (1) and (2) and to subtract the value of

the molecule (5).

In ref. [7] the superposition-additive approach was implemented for the description of the thermodynamic parameters of formation and clusterization of monosubstituted alkanes which possess amphiphilic structure and are capable of monolayer formation at the air/water interface. This approach allows reasonably accurate reproducing thermodynamic parameters of formation and clusterization of alkanes, fatty alcohols, carboxylic acids, thioalcohols, amines and *cis*-unsaturated carboxylic acids and parameters of their phase transition, as well. It should be mentioned that SAA enables the description of thermodynamic parameters of formation not only for monosubstituted alkanes but also amphiphiles having two functional groups, e.g. α -amino acids. Thus, in the framework of the regarded approach the values of the thermodynamic parameters of formation of aliphatic α -amino acids could be expressed as the sum of the corresponding parameters of carboxylic acids and amines after subtraction of alkanes.

As opposed to the mentioned above, it is impossible to apply this scheme to the case of α -amino acids clusterization. This is stipulated by the structural inequalities of α -amino acid monolayers and monolayers of amines, carboxylic acids and alkanes. They have a different number of intermolecular $\text{CH}\cdots\text{HC}$ interactions per one monomer of the 2D cluster. Consequently, it leads to impossibility of their superimposition in the monolayers of the considered amphiphiles. As a result, the main requirement of superposition-additive approach (virtual superimposition of the considered molecular graphs) is not implemented.

The structure of alkylamide aggregates up to its monolayers built on the basis of the most energetically preferred Monomer 2 (see ref. [9]) agrees reasonably well with the corresponding structures of homologous amines, carboxylic acids and alcohols studied earlier. There are an equal number of intermolecular $\text{CH}\cdots\text{HC}$ interactions per one monomer of their dimers. This ensures a maximal region of superimposition of the molecular graphs for the regarded compounds. In this connection it is interesting to apply the regarded approach to the description of thermodynamic parameters of formation and dimerization of aliphatic amides because the increment of the functional amide group in the values of these parameters can be considered as a total increment of the functional groups of amines and carboxylic acids after subtraction of alcohols.

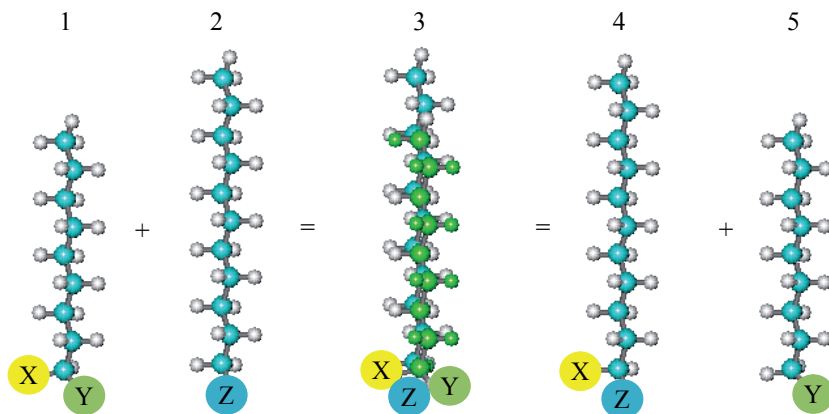


Figure 1. Generalized superposition-additive scheme for the calculation of thermodynamic parameters of monomers of substituted alkanes.

As in the case of refs. [7, 8], the physicochemical characteristics involved in the superposition-additive approach can either be those calculated by the semiempirical quantum-chemical PM3 method or those obtained from the experiment [10-12]. Both options are utilized in the present work. The calculated results according to the superposition-additive schemes (SAS) for alkylamides are listed in corresponding tables. In these tables, the column “SAS Scheme № (cal)” lists the values estimated by SAS using the corresponding parameters that were previously determined by PM3 calculations listed in the “Direct Calculation” column. In the “SAS Scheme № (exp)” column the values are shown which were estimated by SAS from the available experimental data [10-12] listed in the “Experiment” column.

In our previous study [7] devoted to the application of the superposition-additive approach for the description of the thermodynamic parameters of formation and clusterization of monosubstituted alkanes we regarded different SAS, which exploited the values of the corresponding parameters referred both to one class of compounds and several classes as well (three in the case of α -amino acids). In the present study for alkylamides we regard only the most interesting SAS which exploit the data for the three surfactant classes carboxylic acids, amines and alcohols, where $X \neq Y \neq Z$ (see Fig.1). But at first we illustrate the application of the simplest SAS (where $X=Y$) to calculation of the required parameters for the monosubstituted alkanes: carboxylic acids, amines and alcohols (see Fig.2).

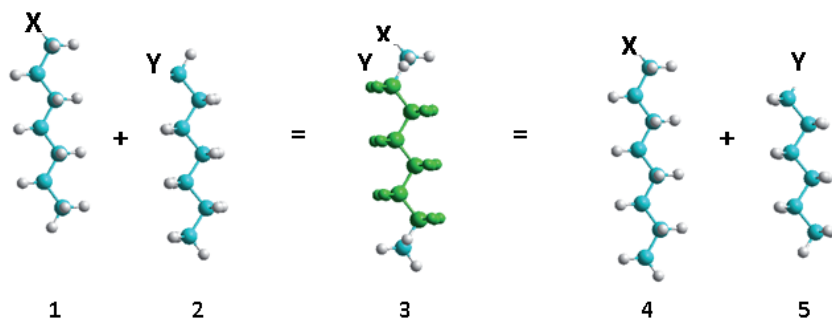


Figure 2. Superposition-additive scheme for calculation of thermodynamic parameters of individual molecules of substituted alkanes (X and Y – schematic definition of the functional groups).

2. Thermodynamic parameters of formation of individual molecules of saturated alcohols, carboxylic acid, amines and amides

It was shown in the refs. [7, 8] that the most useful superposition-additive schemes are those in which the maximal overlapping of the molecular graphs is present. So, for calculation of the thermodynamic parameters of monomer formation for alcohols, carboxylic acids and amines in gas phase will exploit the next scheme which has the region of the molecular graphs overlapping equal to $C_{n-2}H_{2n-4}$. This scheme is expressed as:

$$\text{SAS 1: } A(C_n H_{2n+1} X) = A(C_{n-1} H_{2n-1} X) + A(C_{n-1} H_{2n-1} Y) - A(C_{n-2} H_{2n-3} Y) \quad (1)$$

where A is the thermodynamic parameter (absolute entropy, enthalpy or Gibbs energy of the formation of the compound from elementary substances at normal conditions ($T = 298.15 \text{ K}$); n is the number of atoms in the alkyl chain; X and Y stand for the functional groups, e.g. OH for alcohols, NH_2 for amines, COOH for carboxylic acids (see Fig. 2).

To calculate the thermodynamic parameters of a molecule using SAS 1, containing n carbon atoms in the alkyl chain, one should add the corresponding parameters of two molecules with $(n - 1)$ carbon atoms in the chain, and subtract the corresponding parameter of the molecule with $(n - 2)$ carbon atoms in the chain.

If X and Y are the same, this means that the parameters which correspond to one class of compounds are used in the calculations. In the SAS 1 calculations the experimental values of enthalpy of formation, absolute entropy and Gibbs'

energy of formation [13-20] for saturated alcohols, amines, carboxylic acids related parameters calculated previously in the framework of the quantum chemical semiempirical PM3 method [21-23] were used. Note that entropy and Gibbs' energy of the studied molecules determined earlier [21-32] assuming the free rotation of the methylene fragments within the molecules were used in the calculations. The parameters calculated by SAS 1 (enthalpy of monomer formation $\Delta H_{298, \text{mon}}^0$, absolute entropy $S_{298, \text{mon}}^0$ and Gibbs' energy of monomer formation $\Delta G_{298, \text{mon}}^0$) with $X = Y$ for alcohols, amines, carboxylic acids are listed in Table 1.

The standard deviations of the values calculated by SAS 1 with $X = Y$ from the values determined using the PM3 method and from the corresponding experimental values for all the compound classes considered, and also the standard deviations between the PM3 values and the experimental data are shown in Table 2.

It is seen that the SAS 1 yields quite good results for both the calculated and the experimental values. The fact that the standard deviations between the PM3 values [21-23] and the experimental data are somewhat higher could be possibly ascribed to the deficiencies in the PM3 parameterisation. Note that the proposed superposition-additive scheme reproduces both the experimental and calculated thermodynamic parameters better than the PM3 method reproduces the experimental parameters.

It is known [2, 3] that it is possible to use reasonably the quite wide range of superposition-additive schemes. However, the best results can be obtained in the framework of schemes having maximal superimposition of the molecular graphs. Therefore, we consider the scheme (see Fig.3) with maximal mutual overlap of the alkyl chains ($C_n H_{2n+1}$):

$$\text{SAS 2: } A(C_n H_{2n+1} [XZ]) = A(C_n H_{2n+1} [XY]) + A(C_{n-2} H_{2n-5} Z) - A(C_{n-2} H_{2n-5} Y), \quad (2)$$

where A is the thermodynamic parameter (absolute entropy, enthalpy or Gibbs energy of the formation of the compound from elementary substances) at normal conditions ($T = 298.15 \text{ K}$); n is the number of atoms in the alkyl chain; X , Y and Z define schematically the structural fragments of the functional groups, e.g. $[XY] = \text{COOH}$ for carboxylic acids, $Y = \text{OH}$ for alcohols, $Z = \text{NH}_2$ for amines, $[XZ] = \text{CONH}_2$ for amides.

This scheme is illustrated graphically in Fig. 1. Here, the functional COOH group of carboxylic acids can be represented as a combination of the ketonic $\text{C}=\text{O}$ group and the hydroxyl OH group of alcohols, whereas the functional amide group CONH_2 can be represented as a combination of the ketonic $\text{C}=\text{O}$

group and the amine NH_2 group. Note that the simplest superposition scheme for calculation of thermodynamic parameters of the alkylamide formation can be the following scheme: 'amide = aldehyde + amine – alkane'. However, this scheme cannot be exploited because of the presence of p - π conjugation of the lone-electron pair of nitrogen atom and π -electrons of carbonyl oxygen atom in the hydrophilic head group of amide and its absence in aldehyde. At the same time, carboxylic acids have such conjugation between the lone-electron pair of hydroxyl oxygen atom and π -electrons of carbonyl oxygen atom. As a result, the π -electronic system realized in the compounds described above provides planarity of the regarded atomic groups. This enables maximal superimposition of the molecular graphs in case of using the next scheme: 'amide = carboxylic acid + amine – alcohol' due to planar structure of functional groups for the two classes of amphiphiles used in this scheme and the pyramidal structure of the two others.

Consider now the methodology of the calculation in the framework of the superposition-additive scheme 1 in detail. To calculate the thermodynamic parameters of amide molecule, containing n carbon atoms in the alkyl chain, one should use the parameters of monomer molecules of three other regarded classes of amphiphiles with the same number (n) of carbon atoms in their alkyl chains. For example, to calculate the thermodynamic parameter for octylamide one should add the values of the corresponding parameter (enthalpy, entropy or Gibbs' energy) for octanoic acid and octylamine and subtract from the calculated sum the corresponding thermodynamic parameter of octanol.

Table 1. Comparison of the thermodynamic parameters calculated within SAS 1 ($X=Y$) and SAS 2 ($X\neq Y\neq Z$) with the corresponding results of the direct calculations and experimental data

System	SAS 1 (cal)		Experiment [10-12, 14]		SAS 1 (exp)		$S_{298}^0, J/(mol\cdot K)$		SAS 1 (cal)		Experiment [10-12, 14]		SAS 1 (exp)		$\Delta G_{298}^0, kJ/mol$	
	Calculation	(exp)	Calculation	(exp)	Calculation	(exp)	Calculation	(exp)	Calculation	(exp)	Calculation	(exp)	Calculation	(exp)	Calculation	(exp)
Carboxylic acids																
$C_6H_{13}COOH$	-535,49	-533,70	-536,20	-536,20	504,72	480,00	480,00	480,00	504,72	480,00	480,00	480,00	480,00	-333,11	-335,61	
$C_7H_{15}COOH$	-558,16	-560,50	-556,00	-556,00	543,58	519,00	520,00	520,00	543,58	519,00	520,00	520,00	-330,93	-326,72		
$C_8H_{17}COOH$	-580,83	-575,80	-577,30	-577,30	582,44	560,00	559,00	559,00	582,44	560,00	559,00	559,00	-317,84	-319,04		
$C_9H_{19}COOH$	-603,50	-598,60	-594,30	-594,30	622,17	598,00	599,00	599,00	622,17	598,00	599,00	599,00	-311,36	-307,36		
$C_{10}H_{21}COOH$	-626,18	-611,30	-614,60	-614,60	663,48	639,00	638,00	638,00	663,48	639,00	638,00	638,00	-295,67	-298,67		
$C_{11}H_{23}COOH$	-648,85	-634,90	-640,00	-640,00	701,35	677,00	677,00	677,00	701,35	677,00	677,00	677,00	-285,56	-289,99		
$C_{12}H_{25}COOH$	-671,54	-665,40	-660,20	-660,20	742,99	716,80	716,80	716,80	742,99	716,80	716,80	716,80	-291,74	-286,60		
$C_{13}H_{27}COOH$	-694,21	-680,40	-683,00	-683,00	778,91	756,60	756,60	756,60	778,91	756,60	756,60	756,60	-278,00	-279,82		
$C_{14}H_{29}COOH$	-716,90	-705,80	-699,00	-699,00	819,96	791,00	791,00	791,00	819,96	791,00	796,00	796,00	-273,04	-267,73		
$C_{15}H_{31}COOH$	-739,56	-739,54	-715,00	-723,00	858,10	838,00	838,00	838,00	858,12	838,00	833,00	833,00	-255,64	-262,15		
$C_{16}H_{33}COOH$		-747,00	-743,00			870,00	870,00	870,00			874,00	874,00	-256,58	-253,77		
Alcohols																
$C_6H_{13}OH$			-319,62				441,50				441,50				-138,10	
$C_7H_{15}OH$	-358,61		-334,85		434,38		480,45		434,38		480,45			-103,82	-124,33	
$C_8H_{17}OH$	-381,28	-350,08	-357,06		467,15	519,40	519,40		467,15	519,40	519,40		-110,57	-117,55		
$C_9H_{19}OH$	-403,96	-379,28	-386,89		499,03	499,00	558,35		499,00	558,35	558,35		-110,77	-118,39		
$C_{10}H_{21}OH$	-426,64	-416,73	-403,25		530,84	531,53	597,31		530,84	597,31	597,31		-119,22	-105,75		

$C_{11}H_{23}OH$	-449,32	-449,32	-419,61	-422,21	564,06	563,14	636,26	636,26	-70,75	-70,48	-93,11	-95,71
$C_{12}H_{25}OH$	-472,00	-472,00	-441,16	-442,83	594,75	600,12	675,21	675,21	-61,98	-63,57	-85,66	-87,34
$C_{13}H_{27}OH$	-494,67	-494,67	-463,46	-463,46	637,09	626,65	714,17	712,83	-56,66	-53,56	-78,97	-78,57
$C_{14}H_{29}OH$	-517,37	-517,37	-484,09	-484,09	653,19	660,86	750,44	751,78	-43,55	-45,83	-69,80	-70,20
$C_{15}H_{31}OH$	-540,05	-540,05	-504,72	-504,67	695,07	691,25	790,73	790,73	-38,11	-36,96	-61,83	-61,78
$C_{16}H_{33}OH$	-562,73	-562,73	-525,26	-525,26	721,64	724,43	829,69	829,69	-28,10	-28,93	-53,37	-53,37
Amines												
$C_2H_5NH_2$		ΔH_{298}^0 , kJ/mol		S_{298}^0 , J/(mol·K)		ΔG_{298}^0 , kJ/mol		S_{298}^0 , J/(mol·K)		ΔG_{298}^0 , kJ/mol		
$C_3H_7NH_2$		-74,78	-71,33	-70,50	328,23	326,30	324,20	324,20	43,58	41,38	42,83	37,32
$C_4H_9NH_2$		-97,47	-93,85	-92,00	367,63	363,60	363,00	363,00	51,82	48,35	50,38	50,38
$C_5H_{11}NH_2$		-120,17	-113,50	-113,00	407,04	407,31	401,80	402,00	60,06	60,03	57,92	58,36
$C_6H_{13}NH_2$		-142,76	-134,00	-133,30	446,99	446,81	441,00	443,10	68,24	68,27	66,34	66,42
$C_7H_{15}NH_2$		-165,46	-153,60	-153,00	486,30	486,10	484,20	480,00	76,51	76,57	74,47	76,33
$C_8H_{17}NH_2$		-188,13	-172,70	-174,60	525,38	525,20	516,90	512,80	84,87	84,92	86,24	85,56
$C_9H_{19}NH_2$		-210,82	-196,20	-195,20	564,30	564,85	545,60	561,10	93,27	93,10	94,79	91,17
$C_{10}H_{21}NH_2$		-233,50	-215,80	-215,80	604,50	604,09	609,40	600,40	101,29	101,41	96,78	99,46
$C_{11}H_{23}NH_2$		-256,18	-236,40	-236,00	643,33	642,63	639,70	638,00	109,72	109,92	107,76	108,66
$C_{12}H_{25}NH_2$		-278,86	-256,20	-256,00	681,18	682,21	675,60	678,00	118,44	118,13	117,86	117,35
Amides												
	SAS 2	Direct	SAS 2	Experiment	SAS 2	Direct	SAS 2	Experiment	SAS 2	Direct	SAS 2	Experiment
	(cal)	Calculation	(exp)	[10-12, 14]	(cal)	Calculation	(exp)	[10-12, 14]	(cal)	Calculation	(exp)	[10-12, 14]
CH_3CONH_2	-	-	-211,0	-238,3	-	-	-	-	-	-	-	-
		ΔH_{298}^0 , kJ/mol		S_{298}^0 , J/(mol·K)		ΔG_{298}^0 , kJ/mol		S_{298}^0 , J/(mol·K)		ΔG_{298}^0 , kJ/mol		

$C_2H_3CONH_2$	-	-259.1	-252.3	-	-	-	-	-	-	-	-	-	-
$C_3H_7CONH_2$	-	-275.5	-261.0	-	-	-	-	-	-	-	-	-	-
$C_4H_9CONH_2$	-	-294.2	-290.2	-	-	-	-	-	-	-	-	-	-
$C_5H_{11}CONH_2$	-	-321.0	-324.3	-	-	-	-	-	-	-	-	-	-
$C_6H_{13}CONH_2$	-	-323,56	-340.6	-	-	-	-	-	-	-	-	-	-
$C_7H_{15}CONH_2$	-346,24	-362,8	-362,7	484,31	483,53	-	-	-	-	-87,22	-86,97	-	-
$C_8H_{17}CONH_2$	-368,93	-368,92	-	516,25	515,83	-	-	-	-	-78,81	-78,65	-	-
$C_9H_{19}CONH_2$	-391,60	-391,60	-	548,02	547,26	-	-	-	-	-70,35	-70,10	-	-
$C_{10}H_{21}CONH_2$	-414,28	-414,27	-	579,87	579,45	-	-	-	-	-61,92	-61,76	-	-
$C_{11}H_{23}CONH_2$	-436,97	-436,96	-	611,77	610,49	-	-	-	-	-53,50	-53,08	-	-
$C_{12}H_{25}CONH_2$	-459,65	-459,64	-	642,37	642,46	-	-	-	-	-44,69	-44,69	-	-
$C_{13}H_{27}CONH_2$	-482,33	-482,31	-	668,79	671,93	-	-	-	-	-34,65	-35,54	-	-
$C_{14}H_{29}CONH_2$	-505,00	-505,00	-	706,01	705,78	-	-	-	-	-27,80	-27,71	-	-
$C_{15}H_{31}CONH_2$	-527,65	-527,68	-	733,88	736,33	-	-	-	-	-18,15	-18,89	-	-
$C_{16}H_{33}CONH_2$	-550,31	-550,36	-	767,68	768,22	-	-	-	-	-10,28	-10,47	-	-

Table 2. Standard derivations of the thermodynamic parameters of formation for saturated alcohols, amines, carboxylic acids and amides calculated within SAS 1($X=Y$) and SAS 2($X\neq Y\neq Z$) from results of the direct calculations and experimental data, N is sampling amount

System	ΔH_{298}^0 kJ/mol	S_{298}^0 J/(mol·K)	ΔG_{298}^0 kJ/mol	N
SAS (cal) - Direct Calculation				
Alcohol	0.004	5.26	1.56	8
Amine	0.02	0.53	0.15	8
Carboxylic acid	0.01	1.22	0.37	8
Amide	0.01	1.97	0.66	10
SAS (exp) - Experiment				
Alcohol	5.75	0.63	5.76	9
Amine	1.00	6.11	1.78	10
Carboxylic acid	4.86	2.21	4.43	17
Amide	8.26	-	-	5
Direct Calculation – Experiment				
Alcohol	27.71	6.95	28.18	11
Amine	14.19	5.81	1.38	11
Carboxylic acid	10.78	24.45	8.32	11
Amide	6.31	-	-	5

The results of calculation of thermodynamic parameters within the SAS 2 is listed in Table 1. The experimental data regarding the standard thermodynamic characteristics of the formation of alkylamides are very scarce and are available only for enthalpy of formation. So there are results only for enthalpy as an example in Table 1.

It should be mentioned that the superposition-additive approach cannot account the intramolecular interaction between the oxygen of the carbonyl group and the amino group in the amide molecule when superimposing the molecular structures of amine, carboxylic acid and alcohol. This causes a systematic error of the description of enthalpy, entropy and Gibbs' energy of the amide formation. This means these values for regarded scheme 2 was 12.98 kJ/mol, 8.17 J/(mol·K) and 15.81 kJ/mol, respectively in comparison to the data obtained by direct calculation using the PM3 method. For experimental data this error was calculated to be 32.45 kJ/mol. In the case of comparison data for experimental and directly calculated values of the formation enthalpy the systematic error was found to be 16.43 kJ/mol. The account of the mentioned errors reduces

significantly the values of these standard deviations (the corrected values are listed in Table 2).

3. Thermodynamic parameters of dimer formation of saturated alcohols, carboxylic acid, amines and amides

With regard to the application of the proposed approach to the van der Waals molecules and clusters, it should be kept in mind that, in contrast to the individual monomers, these systems involve also intermolecular interactions. It is evident from Fig. 3 that the application of the schemes similar to SAS 1 which involve two terms of the $(n + 1)$ -th order and one term of the $(n + 2)$ -th order to clusters is incorrect.

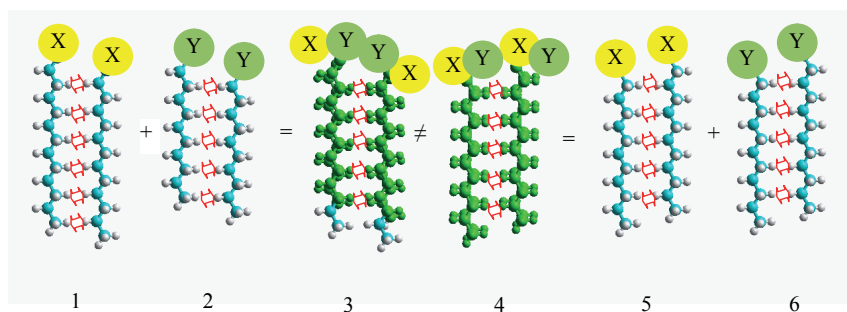


Figure 3. Deficient superposition-additive scheme which **can not** be used for the calculations of the parameters of clusters of substituted alkanes with constant m .

In fact, structure 3 in Fig. 4 is the superposition of the structures 1 and 2, while structure 4 is obtained by the superposition of structures 5 and 6. It is seen from this Figure that the areas of superposition in these structures are different: $C_{20}H_{40}$ and $C_{22}H_{46}$ for the structures 3 and 4, respectively. One can superpose the structures to obtain equal superposition areas ($C_{20}H_{40}$). However, this configuration does not yield the superposition of the relevant intermolecular $CH \cdots HC$ interactions, and thus contradicts the main idea of the superposition-additive approach which requires complete matching of the superimposed areas. One should use the clusters with the same parity (even or odd, respectively) of carbon atoms number in the alkyl chain to construct the configuration which ensure the complete superposition of molecular graphs and intermolecular $CH \cdots HC$ interactions for the cluster with even (or odd) number of carbon atoms in the alkyl chain.

Figure 4 illustrates SAS 2 used to calculate the thermodynamic parameters

of formation and clusterization of van der Waals molecules. In this SAS the number of molecules in a cluster m is the same (i.e. these molecules are dimers, so $m = 2$), and the number of carbon atoms in the alkyl chain n was varied from 6 to 16. For example, to calculate the thermodynamic parameters of dimerization of dodecanol, one should add the corresponding values for two dimers of decanol, and subtract the corresponding value for octanol. In formal terms, SAS 3 is expressed as:

$$\text{SAS 3: } A(\text{C}_n\text{H}_{2n+1}\text{X})_2 = A(\text{C}_{n+2}\text{H}_{2n+5}\text{X})_2 + A(\text{C}_{n+2}\text{H}_{2n+5}\text{Y})_2 - A(\text{C}_{n+4}\text{H}_{2n+9}\text{Y})_2 \quad (3)$$

where A is the thermodynamic parameter of cluster formation or dimerization; n is the number of carbon atoms in the alkyl chain of the corresponding monomer.

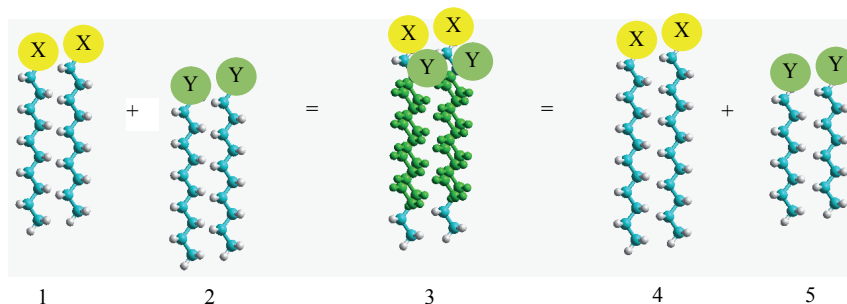


Figure 4. The superposition-additive scheme SAS 2 for the calculations of the parameters of clusters of substituted alkanes with constant m .

In our previous papers [21-23] the thermodynamic parameters of formation and dimerization *per one monomer* were listed. These parameters can directly be used in SAS 3 because all terms in Eq. (3) can be divided by 2 for dimers. Enthalpies of formation and absolute entropies of the clusters of alcohols, thioalcohols, amines and *cis*-unsaturated carboxylic acids calculated by SAS 2 are listed in Table 3 ($\Delta H_m/m$ and S_m/m are enthalpy and entropy of formation *per one monomer*); the standard deviations of the calculated values from the Direct Calculation results are summarized in Table 4.

The errors related to the enthalpies of dimers formation are lower than those related to the enthalpies of formation of monomers. This should be attributed to the fact that in the former case the domain of mutual superposition of the structures is larger. At the same time, for the absolute entropy the standard deviation for the dimers formation is higher than that for the monomers. This is

because the studied structures are more complicated and, therefore, less ordered as compared with the monomers.

Table 3. Comparison of the thermodynamic parameters of dimer formation calculated within SAS 3 ($X=Y$) and SAS 4 ($X\neq Y\neq Z$) with the corresponding results of the direct calculations

System	SAS 3 (cal)	Direct Calculation	SAS 3 (cal)	Direct Calculation
Alcohols	$\Delta H_m/m$, kJ/mol		S_m/m , J/mol·K	
$C_6H_{13}OH$		-351.85		329.07
$C_7H_{15}OH$		-375.74		360.79
$C_8H_{17}OH$		-402.38		389.86
$C_9H_{19}OH$		-426.30		415.27
$C_{10}H_{21}OH$	-452.91	-452.92	450.65	440.08
$C_{11}H_{23}OH$	-476.85	-476.86	469.75	472.93
$C_{12}H_{25}OH$	-503.47	-503.48	490.29	498.86
$C_{13}H_{27}OH$	-527.42	-527.42	530.58	526.82
$C_{14}H_{29}OH$	-554.03	-554.04	557.65	550.39
$C_{15}H_{31}OH$	-577.99	-577.99	580.72	579.92
$C_{16}H_{33}OH$	-604.60	-604.60	601.92	607.14
Amines	$\Delta H_m/m$, kJ/mol		S_m/m , J/(mol·K)	
$C_6H_{13}NH_2$		-153,02		330,72
$C_7H_{15}NH_2$		-176,94		356,94
$C_8H_{17}NH_2$		-203,56		381,38
$C_9H_{19}NH_2$		-227,49		408,12
$C_{10}H_{21}NH_2$	-254,10	-253,98	432,05	434,65
$C_{11}H_{23}NH_2$	-278,05	-278,06	459,31	458,78
$C_{12}H_{25}NH_2$	-304,39	-304,52	487,92	484,31
$C_{13}H_{27}NH_2$	-328,63	-328,63	509,44	509,97
$C_{14}H_{29}NH_2$	-355,07	-355,09	533,97	534,68
$C_{15}H_{31}NH_2$	-379,19	-378,49	561,16	571,93
$C_{16}H_{33}NH_2$	-405,66	-405,65	585,04	586,21

Carboxylic acids	$\Delta H_m/m$, kJ/mol		S_m/m , J/(mol·K)	
C ₆ H ₁₃ COOH		-550,58		375,44
C ₇ H ₁₅ COOH		-574,60		396,23
C ₈ H ₁₇ COOH		-601,00		425,73
C ₉ H ₁₉ COOH		-624,96		450,96
C ₁₀ H ₂₁ COOH	-651,43	-651,50	476,03	476,01
C ₁₁ H ₂₃ COOH	-675,32	-675,46	505,69	501,39
C ₁₂ H ₂₅ COOH	-701,99	-702,02	526,29	526,12
C ₁₃ H ₂₇ COOH	-725,95	-725,95	551,81	551,91
C ₁₄ H ₂₉ COOH	-752,54	-752,55	576,22	576,58
C ₁₅ H ₃₁ COOH	-776,45	-776,49	602,43	603,26
C ₁₆ H ₃₃ COOH				
Amides	SAS 4 (cal)	Direct Calculation	SAS 4 (cal)	Direct Calculation
	$\Delta H_m/m$, kJ/mol		S_m/m , J/(mol·K)	
C ₆ H ₁₃ CONH ₂		-337,54		376,28
C ₇ H ₁₅ CONH ₂	-362.76	-361,30	412.98	396,59
C ₈ H ₁₇ CONH ₂	-386.81	-387,91	428.28	425,92
C ₉ H ₁₉ CONH ₂	-413.20	-411,73	453.15	448,47
C ₁₀ H ₂₁ CONH ₂	-437.17	-438,38	479.71	476,51
C ₁₁ H ₂₃ CONH ₂	-463.56	-462,20	506.49	501,45
C ₁₂ H ₂₅ CONH ₂	-487.67	-488,73	523.14	529,29
C ₁₃ H ₂₇ CONH ₂	-514.08	-512,70	547.47	554,16
C ₁₄ H ₂₉ CONH ₂	-538.17	-539,25	570.96	578,65
C ₁₅ H ₃₁ CONH ₂	-564.61	-563,22	596.77	603,34
C ₁₆ H ₃₃ CONH ₂	-588.00	-589,79	631.16	628,41

As it was shown in previous paragraph the values of thermodynamic parameters of amide formation can be calculated in the framework of superposition-additive approach using corresponding values for carboxylic acids, alcohols and amines. That enables us to apply this approach to calculation of thermodynamic parameters of formation and clusterization for small amide

aggregates, dimers in particular. To provide the maximal molecular graphs overlapping of compounds involved we use the next scheme:

$$\text{SAS 4: } A(\text{C}_n\text{H}_{2n+1}[\text{XZ}])_m/m = A(\text{C}_n\text{H}_{2n+1}[\text{XY}])_m/m + A(\text{C}_{n-2}\text{H}_{2n-5}[\text{Z}])_m/m - A(\text{C}_{n-2}\text{H}_{2n-5}[\text{Y}])_m/m, (4)$$

where A is the thermodynamic parameter of formation or dimerization of aggregates; m is the number of monomers in a cluster ($m=2$ for dimers); n is the number of carbon atoms in the alkyl chain of the monomer.

This scheme is illustrated in Fig. 5. As in the case of SAS 1, the thermodynamic parameters of the entities involved in SAS 4 should have the same alkyl chain length n (to obtain maximal molecular graphs overlapping).

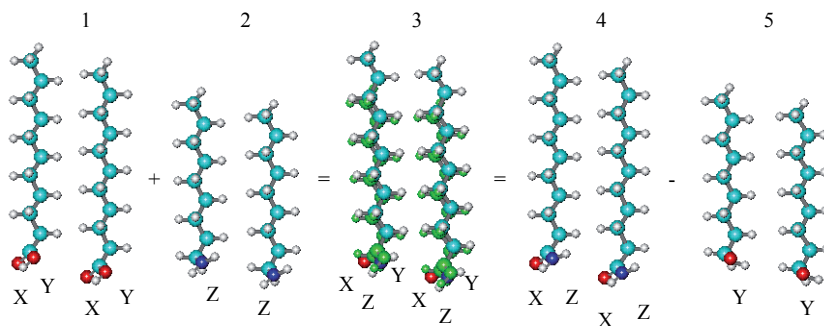


Figure 5. Generalized superposition-additive scheme (SAS 4) for the calculation of the thermodynamic parameters of alkylamide dimers

According to SAS 4 described above, enthalpy and absolute entropy of the formation for alkylamide dimers and their standard errors from the results of the PM3 calculations were calculated (see Table 3, 4). It should be mentioned that the deviations of the thermodynamic parameters of the formation of amide associates are larger than the corresponding values for the monomer formation. This is stipulated by complication of investigated structures that, in its turn, causes a decrease in their order with respect to the monomer structure. In addition, as in the case of monomers, there are systematic errors of the description of the formation of enthalpy, entropy and Gibbs' energy of amide associates. These values were found to be 11.01 kJ/mol and 35.90 J/(mol·K) correspondingly. The account of these errors reduce significantly the value of the standard deviation (corrected values are listed in Table 4).

Table 4. Standard deviations of thermodynamic parameters of formation of dimers calculated by SAS 3 ($X = Y$) and SAS 4 ($X \neq Y \neq Z$) from the values obtained by PM3 method. N is the sampling amount.

System	$\Delta H_m/m$, kJ/mol	S_m/m , J/(mol·K)	N
Alcohols	0.01	6.44	7
Amines	0.27	4.44	7
Acids	0.07	1.80	6
Amides	1.35	7.24	10

4. Thermodynamic parameters of dimerization of saturated alcohols, carboxylic acid, amines and amides

It was shown above that the superposition-additive approach is applicable for the estimation of the thermodynamic parameters of formation of monomers of substituted alkanes and their dimers. Any thermodynamic parameter (ΔA) of dimerization can be calculated as $\Delta A_m^{\text{dim}} = \Delta A_m - m \cdot \Delta A_{298}^0$ ($\Delta H_m^{\text{dim}}/m$, $\Delta S_m^{\text{dim}}/m$ and $\Delta G_m^{\text{dim}}/m$ are enthalpy, entropy and Gibbs' energy of dimerization *per one monomer*), where $m=2$ for dimers. Therefore it is expected that these parameters can be calculated within a sufficient degree of accuracy in the framework of this approach. To verify this supposition, SAS 3 was applied accordingly to the dimers of monosubstituted alkanes.

The dimerization energies per one monomer for alcohols, amines and carboxylic acids calculated by SAS 3 using the parameters for one class of compounds ($X = Y$) are listed in Table 5. For all these classes of compounds, the thermodynamic parameters calculated using the superposition-additive approach agree well with the values determined earlier [21-23] by Direct Calculations. Corresponding standard deviations are summarized in Table 6.

The dimerization energies per one monomer for aliphatic amides were calculated in the frameworks of SAS 4 using the parameters for three classes of surfactants: carboxylic acids, amines and alcohols ($X \neq Y \neq Z$). The results of the calculation of enthalpy, entropy and Gibbs' energy of clusterization per one monomer of the amide cluster according to SAS 4 are listed in Table 5. As in the case of thermodynamic parameters of monomer and dimer formation described above, the calculated values of the thermodynamic parameters of dimerization have a systematic error. This is probably stipulated by incomplete molecular graphs overlapping of the structures involved in this scheme. The latter, in its turn, can be drawn by the impossibility to represent the intermolecular interactions of the hydrophilic head groups in the amide associates only as a simple combination of the corresponding interactions realized in the clusters of

carboxylic acids, amines and alcohols. The p - π system realized in the functional group of amide molecule differs from that present in carboxylic acids and it is absent in the molecules of amines and alcohols. The impact of such differences can be retraced if one compares the contributions of the functional group interactions to the dimerization Gibbs' energy per one monomer molecule for all compounds involved in SAS 4. Thus, for alcohols, amines, carboxylic acids and amides the values of the regarded contributions were 12.08, 11.65, 14.15 and 14.42 kJ/mol, respectively. It is clearly seen that the contributions for the two last compounds (carboxylic acids and amides), having a close structure of the functional group, are quite approximate and differ within the statistical error from the two other. The increments of the intermolecular $CH\cdots HC$ interactions are practically the same for the different classes of amphiphiles [21-28], but the increments of the interactions realized between structurally different functional groups of amphiphiles are different. This causes the systematic errors of the description of the thermodynamic parameters of clusterization for associates of different dimensions up to infinite 2D films. Mentioned systematic error was found to be 1.45 kJ/mol for dimerization enthalpy, 18.78 J/(mol·K) for entropy and 4.26 for Gibbs' energy. The corrected values of the thermodynamic parameters of amide dimerization with account of mentioned systematic errors are listed in Table 8. Standard deviations of thermodynamic parameters of amide dimerization calculated using SAS 4 from the directly obtained values are listed in Table 6.

Table 5. Comparison of the thermodynamic parameters of dimerization calculated within SAS 3 ($X = Y$) and SAS 4 ($X \neq Y \neq Z$) with the corresponding results of the direct calculations

System	SAS 3 (cal)	Direct Calculation	SAS 3 (cal)	Direct Calculation	SAS 3 (cal)	Direct Calculation
Alcohols	$\Delta H_m^{\text{dim}}/m$, kJ/mol		$\Delta S_m^{\text{dim}}/m$, J/mol·K		$\Delta G_m^{\text{dim}}/m$, kJ/mol	
$C_6H_{13}OH$		-15,91		-73,11		5,88
$C_7H_{15}OH$		-17,13		-73,59		4,80
$C_8H_{17}OH$		-21,09		-77,30		1,94
$C_9H_{19}OH$		-22,33		-83,73		2,62
$C_{10}H_{21}OH$	-26,28	-26,28	-81,48	-91,45	-1,99	0,97
$C_{11}H_{23}OH$	-27,54	-27,54	-93,87	-90,21	0,43	-0,65
$C_{12}H_{25}OH$	-31,47	-31,48	-105,61	-101,25	0,00	-1,31
$C_{13}H_{27}OH$	-32,74	-32,74	-96,70	-99,83	-3,92	-2,99

$C_{14}H_{29}OH$	-36,68	-36,67	-111,06	-110,47	-3,58	-3,75
$C_{15}H_{31}OH$	-37,94	-37,94	-109,45	-111,33	-5,33	-4,76
$C_{16}H_{33}OH$	-41,86	-41,87	-119,69	-117,29	-6,19	-6,92
Amines	$\Delta H_m^{dim}/m$, kJ/mol		$\Delta S_m^{dim}/m$, J/mol·K		$\Delta G_m^{dim}/m$, kJ/mol	
$C_6H_{13}NH_2$		-16,03		-75,38		6,44
$C_7H_{15}NH_2$		-17,26		-81,63		7,07
$C_8H_{17}NH_2$		-21,21		-89,50		5,47
$C_9H_{19}NH_2$		-22,45		-95,14		5,90
$C_{10}H_{21}NH_2$	-26,39	-26,26	-103,61	-100,57	4,49	3,71
$C_{11}H_{23}NH_2$	-27,65	-27,66	-108,65	-108,21	4,73	4,59
$C_{12}H_{25}NH_2$	-31,31	-31,44	-111,64	-114,17	1,96	2,59
$C_{13}H_{27}NH_2$	-32,86	-32,86	-121,28	-121,48	3,28	3,34
$C_{14}H_{29}NH_2$	-36,62	-36,64	-127,78	-127,69	1,46	1,42
$C_{15}H_{31}NH_2$	-38,07	-37,36	-134,75	-123,77	2,09	-0,48
$C_{16}H_{33}NH_2$	-41,84	-41,83	-141,20	-139,08	0,25	-0,39
Carboxylic acids	$\Delta H_m^{dim}/m$, kJ/mol		$\Delta S_m^{dim}/m$, J/mol·K		$\Delta G_m^{dim}/m$, kJ/mol	
$C_6H_{13}COOH$		-15,10		-80,81		8,99
$C_7H_{15}COOH$		-16,44		-91,71		10,89
$C_8H_{17}COOH$		-20,19		-94,28		7,91
$C_9H_{19}COOH$		-21,47		-100,18		8,38
$C_{10}H_{21}COOH$	-25,28	-25,34	-107,75	-107,93	6,83	6,82
$C_{11}H_{23}COOH$	-26,50	-26,73	-108,64	-112,13	5,87	6,68
$C_{12}H_{25}COOH$	-30,49	-30,52	-121,58	-121,04	5,74	5,55
$C_{13}H_{27}COOH$	-31,99	-31,76	-124,08	-124,97	4,98	5,48
$C_{14}H_{29}COOH$	-35,70	-35,71	-134,15	-133,58	4,28	4,09
$C_{15}H_{31}COOH$	-36,79	-36,99	-137,81	-136,99	4,27	3,83
$C_{16}H_{33}COOH$						

Amides	SAS 3	Direct	SAS 3	Direct	SAS 3	Direct
	(cal)	Calculation	(cal)	Calculation	(cal)	Calculation
	$\Delta H_m^{\text{dim}}/\text{m}$, kJ/mol		$\Delta S_m^{\text{dim}}/\text{m}$, J/mol·K		$\Delta G_m^{\text{dim}}/\text{m}$, kJ/mol	
$C_6H_{13}CONH_2$		-13.95		-74.89		8.37
$C_7H_{15}CONH_2$	-15.11	-15.04	-75.20	-86.91	10.00	10.86
$C_8H_{17}CONH_2$	-18.87	-18.98	-83.54	-89.45	8.73	7.67
$C_9H_{19}CONH_2$	-20.14	-20.13	-93.60	-98.94	10.46	9.36
$C_{10}H_{21}CONH_2$	-24.01	-24.10	-100.56	-102.44	8.66	6.43
$C_{11}H_{23}CONH_2$	-25.25	-25.24	-102.46	-109.26	7.98	7.32
$C_{12}H_{25}CONH_2$	-29.19	-29.09	-120.26	-112.03	9.35	4.30
$C_{13}H_{27}CONH_2$	-30.27	-30.38	-119.10	-119.39	7.92	5.20
$C_{14}H_{29}CONH_2$	-34.39	-34.25	-136.44	-126.29	8.97	3.39
$C_{15}H_{31}CONH_2$	-35.51	-35.54	-135.43	-133.23	7.55	4.16
$C_{16}H_{33}CONH_2$		-39.42		-138.90		1.97

Table 6. Standard derivations of the thermodynamic parameters of dimerization of saturated alcohols, amines, carboxylic acids and amides calculated within SAS 3 ($X=Y$) and SAS 4 ($X \neq Y \neq Z$) from results of the direct calculations, N is sampling amount

System	$\Delta H_m^{\text{dim}}/\text{m}$, kJ/mol	$\Delta S_m^{\text{dim}}/\text{m}$, J/(mol·K)	$\Delta G_m^{\text{dim}}/\text{m}$, kJ/mol	N
Alcohol	0.01	4.65	1.38	11
Amine	0.28	4.49	1.07	11
Carboxylic acid	0.16	1.54	0.44	10
Amides	0.09	6.88	2.04	10

Summarizing, different superposition-additive schemes have been applied to calculate the thermodynamic parameters of formation and dimerization of different classes of amphiphilic compounds. Enthalpy, entropy and Gibbs' energy of formation and dimerization of aliphatic amides can be obtained as a sum of corresponding parameters for carboxylic acids and amines after subtraction of alcohols.

Conclusion

Summarizing, present work shows that superposition-additive approach can

be applied for calculation of the thermodynamic parameters of formation and dimerization for mono- and disubstituted alkanes. Thus, enthalpy, entropy and Gibbs' energy of formation and dimerization of aliphatic amides can be obtained as a sum of corresponding parameters for carboxylic acids and amines after subtraction of alcohols.

It should be noted that for the description of the thermodynamic parameters of van der Waals molecules and clusters, those schemes should be used which ensure the correct account for intermolecular $\text{CH}\cdots\text{HC}$ interactions. This requirement imposes certain restrictions on the superimposed structures as compared with the structures used in the additive method: in the superposition-additive method the correct configuration should ensure the matching of the molecular graphs and the relevant intermolecular $\text{CH}\cdots\text{HC}$ interactions. In particular, for the description of van der Waals molecules and clusters of homologous series of surfactants with even or odd number of carbon atoms in the alkyl chain, the structures should be used with the same parity of the carbon atoms number in the superimposed constituents.

Another point should be mentioned that the calculated values of the thermodynamic parameters of amide formation and dimerization possess a systematic error. It could be stipulated by incomplete molecular graphs overlapping of the structures involved in considered schemes. This in its turn can be stipulated by the impossibility to represent the intermolecular interactions of the hydrophilic head groups in the amide associates only as a simple combination of the corresponding interactions realized in the associates of carboxylic acids, amines and alcohols. The p - π system realized in the functional group of amide molecule differs from that present in carboxylic acids and it is absent in the molecules of amines and alcohols. But account of found systematic error enables one to calculate accurately the values of thermodynamic parameters of alkylamide formation and dimerization. This gives one more proof that proposed SAA enable to estimate the parameters for different aggregates up to monolayer in the case when the amphiphiles in question are uncommon or lack the required experimental data from the corresponding data concerned more widespread surfactants as in the case of aliphatic amides.

References

1. Bader, R. F. W. Atoms in molecules. A quantum theory. Oxford: Clarendon Press, 2001.
2. Vysotskii, Yu. B., Zaikovskaya, Ya. V., Solonskii, I. N. Quantum-chemical interpretation of cyclization and recyclization reactions. 24. Superposition-additive approach. Russian Journal of Organic

- Chemistry. – 2001. – Vol. 37. – P. 101-118.
3. Vysotsky, Yu. B., Bryantsev, V.S. Calculation of Thermo-Chemical Properties of Conjugated Radicals. *International Journal of Quantum Chemistry*. – 2004. – Vol. 96. –P. 123-35.
 4. Davis, M.I., Douheret, G. Group contributions to the thermodynamic properties of cluster formation by non-ionic amphiphiles in their aqueous mixtures. *J. Chem. Soc. Faraday Trans.* – 1998. – Vol. 94. – P. 2389-2394.
 5. Hoiland, H., Vikingstad, E. Partial Molal Volumes and Additivity of Group Partial Molal Volumes of Alcohols in Aqueous Solution at 25 and 35 degrees C. *Acta Chem. Scand.*- 1976. – Vol. 30 A. – P. 182-186.
 6. Zhuo, S., Wei, J., Si, W., Ju, G. J. Is there any group additive rules in the calculation of electron correlation energies of long straight chain alkane molecules? *J. Chem. Phys.* – 2004. – Vol. 120. – P. 2575-2580.
 7. Vysotsky, Yu.B., Belyaeva, E.A., Fomina, E.S., Vasylyev, A.O., Vollhardt, D., Fainerman, V.B., Aksenenko, E.V., Miller, R. Superposition-additive approach in the description of thermodynamic parameters of formation and clusterization of substituted alkanes at the air/water interface. *J. Coll. Int. Sci.* – 2012. – Vol. 387. – P. 162-174
 8. Vysotsky, Yu.B., Belyaeva, E.A., Vasylyev, A.O., Fainerman, V.B., Aksenenko, E.V., Vollhardt, D., Miller, R. Superposition-additive approach: Thermodynamic parameters of monosubstituted alkanes. *Colloids and Surfaces A: Physicochem. Eng. Asp.* – 2012. – Vol. 413 – P. 303-306.
 9. Vysotsky, Yu.B., Fomina, E.S., Miller, R. Thermodynamic aspects of 2D cluster formation of aliphatic amides at the air/water interface in the PM3 approximation. *Abstracts MACC-4, Lviv.* – 2011. – P. 83.
 10. Stull, D. R.; Westrum, E. F., Jr.; Sinke, G. C. *The Chemical Thermodynamics of Organic Compounds*; John Wiley & Sons: New York, 1969.
 11. Dean, J. *Lange's handbook of chemistry*; McGRAV-HILL, INC.: N.-Y., 1999. – 1291 p.
 12. Pedley, J. B., Naylor, R. D., Kirby, S. P. *Thermochemical Data of Organic Compounds*, 2nd ed.; Capman and Hall: New-York. – 1986.
 13. Vollhardt, D., Fainerman, V.B. Characterisation of phase transition in adsorbed monolayers at the air/water interface *Adv. Interface Sci.* – 2010. – Vol. 154. – P. 1-19.
 14. Daubert, T.E., Danner, R.P., Sibul, H.M., Stebbins, C.C. *Physical and Thermodynamic Properties of Pure Chemicals: Data Compilation*, Part

- 1–Part 5, Taylor & Francis, Pennsylvania, 1998. – 9860 p.
15. Stull, D. R., Westrum Jr., E. F., Sinke, G.C. The Chemical Thermodynamics of Organic Compounds, John Wiley and Sons, N-Y. - 1969. –536 p.
 16. Alberty, R.A., Gehrig, C.A. Standard Chemical Thermodynamic Properties of Alkene Isomer Groups J. Phys. Chem. Ref. Data. – 1985. –Vol. 14. – P. 803-820.
 17. John A.D. Lange’s Handbook of Chemistry, McGraw-Hill Inc., N.-Y. - 1999. - 51 p.
 18. Davidovits, P., Kolb, C. E., Williams, L. R., Jayne, J. T., Worsnop, D. R. Mass Accommodation and Chemical Reactions at Gas–Liquid Interfaces. Chem. Rev.- 2006. – Vol. 106. – P. 1323-1354.
 19. Mundy, C.J., Kuo, I.-F.W. First-Principles Approaches to the Structure and Reactivity of Atmospherically Relevant Aqueous Interfaces. Chem. Rev. – 2006. – Vol. 106. – P. 1282-1304.
 20. Helgaker, T. Ab Initio Methods for the Calculation of NMR Shielding and Indirect Spin–Spin Coupling Constants. Chem. Rev. – 1999. – Vol. 99. – P. 293-352.
 21. Vysotsky Yu. B., Bryantsev V. S., Fainerman V. B., Vollhardt D. Thermodynamics of 2D Cluster Formation of Odd n-Alcohols at the Air/Water Interface // J. Phys. Chem. B. – 2002. - Vol. 106. - P.11285-11294.
 22. Vysotsky Yu. B., Muratov D. V., Boldyreva F. L., Fainerman V. B., Vollhardt D., Miller R. Quantum Chemical Analysis of the Thermodynamics of 2D Cluster Formation of n-Carboxylic Acids at the Air/Water Interface. J. Phys. Chem. B. - 2006. - Vol. 110 - P. 4717-4730.
 23. Vysotsky Yu. B., Belyaeva E. A., Fainerman V. B., Aksenenko E.V., Vollhardt D., Miller R. Quantum Chemical Analysis of the Thermodynamics of 2-Dimensional Cluster Formation of Alkylamines at the Air/Water Interface J. Phys. Chem. C. – 2007. - V. 111, № 42. - P. 15342 – 15349.
 24. Vysotsky Yu. B., Bryantsev V. S., Fainerman V. B., Vollhardt D., Miller R. Quantum Chemical Analysis of Thermodynamics of the Two-Dimensional Cluster Formation at the Air/Water Interface J. Phys. Chem. B. – 2002. - Vol. 106. - P. 121-131.
 25. Vysotsky Yu.B., Belyaeva E.A., Fainerman V. B., Vollhardt D., Miller R. Quantum Chemical Analysis of Thermodynamics of 2D Cluster Formation of n-Thioalcohols at the Air/Water Interface J. Phys. Chem. C. – 2007. - V. 111. - P. 5374-5381.

26. Vysotsky Yu. B., Belyaeva E. A., Fainerman V. B., Aksenenko E.V., Vollhardt D., Miller R. Thermodynamics of the Clusterization Process of Cis Isomers of Unsaturated Fatty Acids at the Air/Water Interface J. Phys. Chem. B. – 2009. - V. 113, № 13. – P. 4347 – 4359.
27. Vysotsky Yu. B., Fomina E.S., Belyaeva E. A., Fainerman V. B., Aksenenko E.V., Vollhardt D., Miller R. Quantum-chemical analysis of thermodynamics of two-dimensional cluster formation of α -amino acids at the air/water interface J. Phys. Chem. B. – 2009. - V. 113. – P. 16557 – 16567.
28. Vysotsky Yu. B., Belyaeva E. A., Fomina E. S., Fainerman V. B., Aksenenko E. V., Vollhardt D., Miller R.. Superposition-additive approach: thermodynamic parameters of clusterization of monosubstituted alkanes at the air/water interface. Phys. Chem. Chem. Phys. – 2011. – Vol. 13. – P. 20927–20932.

Chapter 7

Self-assembled mesoporous TiO₂ and its application in photoenergy systems

Maciej Zalas

*Adam Mickiewicz University in Poznań, Faculty of Chemistry,
Umultowska 89b, 61-614 Poznań, Poland*

1. Introduction

According to the classification of the International Union of Pure and Applied Chemistry (IUPAC) the mesoporous materials are those with pore sizes between 2 and 50 nm [1]. Intensive investigation of mesoporous materials has been initiated by the first synthesis of ordered silica materials reported by Kuroda et. al. and Mobil Oil Corporation in the early 1990's [2, 3]. The applications of mesoporous materials in various fields such as production of green energy, optics, medicine, electronics or medicine are strongly connected with their very good host properties for bulky molecules, high surface area, uniform and tunable pore sizes and various morphologies and compositions [4]. Mesoporous materials based on transition metal oxides mesoporous materials have been simultaneously developed to to combine the advantages of mesoporous structure with the electronic and optic properties of transition metals oxides [4]. Titanium dioxide (TiO₂, titania) is admittedly one of the most intensively studied mesoporous material [4-6]. As it is relatively chemically inert and environmental friendly, TiO₂ has been widely used in industry as a pigment, in sunscreens, paints, ointments, toothpaste etc. since the beginning of the 20th century, when its commercial production began. When, in 1972, Fujishima and Honda discovered the phenomenon of photocatalytic water splitting over the titania electrodes [7], enormous potential to apply TiO₂ in such areas as photocatalysis, photovoltaics, photo and/or electrochromics and sensor construction has been recognized [5].

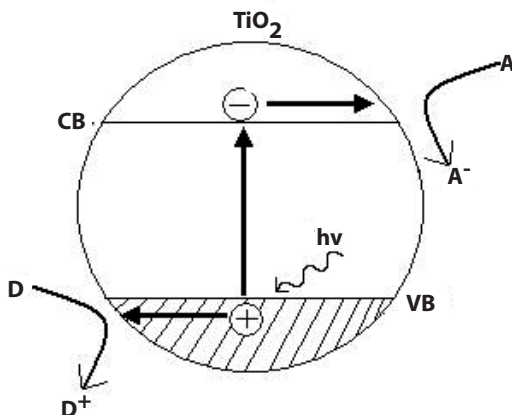


Figure 1. Schematic presentation of the basic processes in the photocatalytic activity of the TiO_2 .

The basic mechanism of the photocatalytic process, which occurs on TiO_2 surface, can be easily explained (see Fig. 1) [8]. At the beginning, a light photon with energy greater than the bandgap of titania is absorbed, thereupon the electrons are promoted from the valence band (VB) to the conduction band (CB) creating electron-positive hole pairs. The electrons and positive holes migrate to the titania surface and react with the species adsorbed on this surface to decompose them. The photodecomposition processes, taking place on the TiO_2 surface during the photocatalytic process, usually involve one or more intermediate species or radicals such as $\cdot\text{OH}$, O_2^- , H_2O_2 or O_2^- . These species are important substrates for processes such as photodegradation of various water pollutants, photocatalytic organic and inorganic synthesis, photocatalytic water decomposition, photocatalytic killing bacteria or even tumor cells killing in light-induced TiO_2 supported cancer treatment [5, 8]. The efficiency of TiO_2 photocatalytic activity depends on the catalyst surface area and crystallinity. The larger the surface area, the higher the photocatalytic activity of the material, but large surface area increases surface defects concentration, which increases the electron-hole recombination process and this, in consequence, decreases the photocatalytic process rate. To decrease the surface and bulk defects concentration, a higher crystallinity of TiO_2 material is needed, high crystallinity is usually obtained upon high temperature treatment, which leads to aggregation of small nanoparticles and to a decrease in the surface area, so the synthesis of the photocatalysts must be a compromise between these conditions.

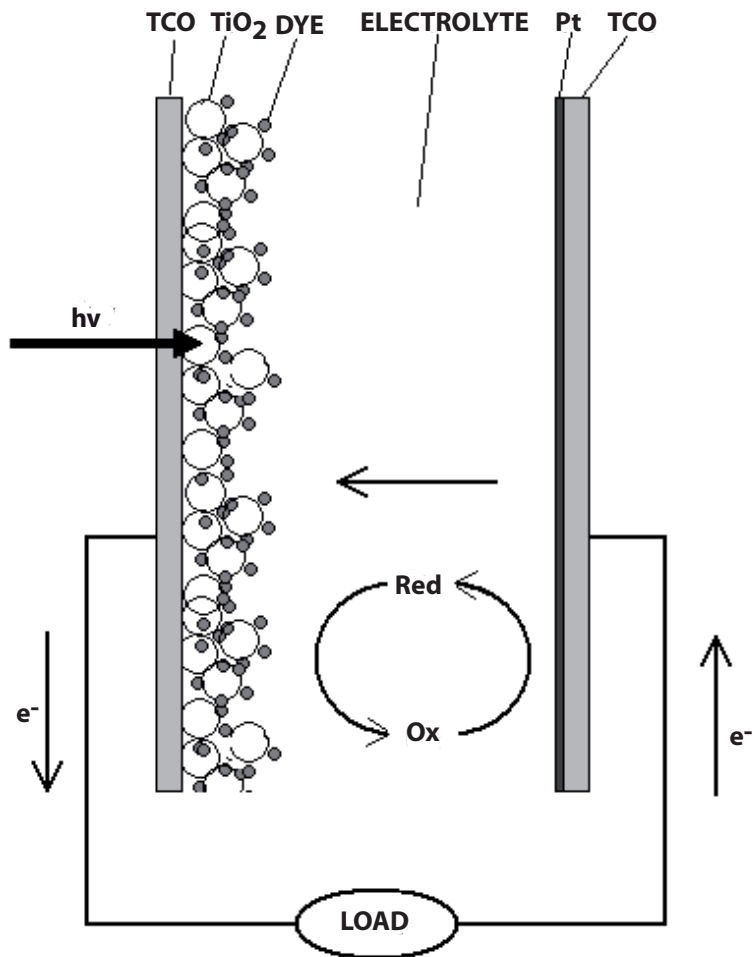


Figure 2. Schematic presentation of the principle rules of the DSSC working mechanism.

Almost two decades after the Fujishima's and Honda's discovery of photocatalytic water splitting over the titania electrodes, O'Regan and Grätzel have presented the first highly efficient dye sensitized solar cell (DSSC) [9]. The device made by O'Regan and Grätzel is based on a mesoporous titania electrode sensitized with a ruthenium dye to convert energy of incident light to electricity with efficiencies around 7-8 %. Typical DSSC is build with two sheets of tin

conducting oxide (TCO) coated glass, one of which, so called working electrode, is covered by the mesoporous electrode, mostly made of nanocrystalline TiO_2 , sensitized with an organic dye (mostly ruthenium complexes). The second TCO glass sheet, the so-called counter electrode, is covered by a thin layer of platinum. These two electrodes are arranged in a sandwich cell and the space between them is filled with a liquid electrolyte containing I^-/I_3^- redox pair solution in organic solvent(s) [10]. The principle mechanism of the DSSC working cycle is straightforward (see Figure 2) and may be described with five steps electron movement. The first step is the excitation of an electron from the ground to the excited state of the dye molecule by a photon of incident light. Next, the excited electron is injected from the dye molecule into the conducting band of the mesoporous semiconducting electrode, afterwards the electron is transported across the mesoporous electrode and external circuit into the counter electrode. Now electron reduces the oxidized form of the redox couple in the electrolyte and as the last step, the reaction between the reduced form of the redox mediator and the oxidized dye molecule occurs thereupon the ground state of the dye molecule and oxidized form of the redox couple are restored and DSSC working cycle is closed [10-12]. In the ideal system the whole process takes place without consumption or permanent transformation of any chemical species and theoretically it can occur until illumination is present.

2. Synthesis of the mesoporous TiO_2

The typical synthesis of the mesoporous titania (see Fig. 3), similarly to the synthesis of mesoporous silica, requires the application of a surfactant as a structure-directing agent and a titania source [4]. The greatest problem in the synthesis, is the natural tendency of typical titania precursors, such as titanium alkoxides or titanium tetrachloride, to very rapid hydrolysis, which results in uncontrolled precipitation of TiO_2 without formation of mesopores, so a careful control of synthesis conditions is critical to obtain the expected material. The use of neutral amine surfactants to control a $\text{Ti}(\text{OPr})_4$ hydrolysis rate during the synthesis of 2D hexagonal mesoporous titania, applied by Ulagappan et al. [13], or addition of bidentate ligands to the synthesis mixture to modify the reactivity of titania precursors proposed by Froba and his co-workers to obtain ordered mesostructured titania [14], or application of novel, more stable titania precursors presented by Niessen et al. [15] to obtain MCM-41 titania analogues are exemplary approaches which lead to more predictable and controllable behavior of titania precursors and in consequence to the successful synthesis of mesoporous titania.

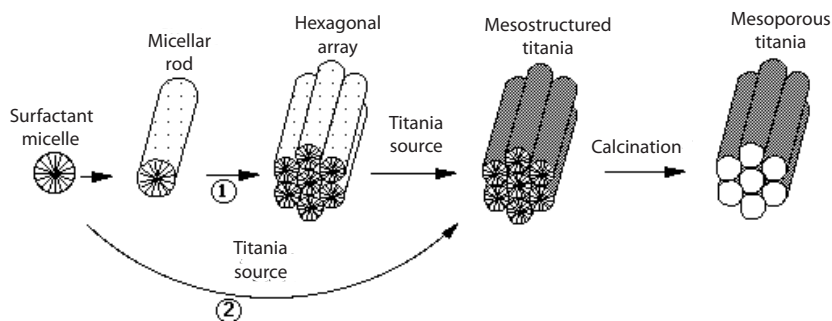


Figure 3. Schematic synthesis route of the mesoporous TiO_2 [16].

Over the last two decades, a number of groups have developed the methods for successful mesoporous titania synthesis by controlling such parameters as ageing conditions, pH of the precursor solution, the type of templating agent applied or calcination temperature. Most of the methods give well defined 2D or 3D ordered mesoporous titania bulks, films or nanoparticles. Ogawa has been the first to propose the preparation of mesoporous films via solvent evaporation method [17] (the so-called evaporation-induced self-assembly method), which because of its convenience has become most widely applied [4]. In a typical procedure the coating solution includes ethanol as a solvent, basic or acidic inorganic hydrolysis stabilizers and a templating agent. Titania precursor is spread on the coated surface and the hydrolysis/condensation of the titania precursor takes place when ethanol is evaporated in mild temperature conditions. The templating agent is removed from the obtained mesostructured material via calcination or solvent extraction [18]. The method based on inverse opal titania materials preparation was also studied [5]. A typical version of this method has been proposed by Carbajo et al. [19], who prepared a hierarchically 3D-ordered meso/macroporous TiO_2 materials using the so-called latex arrays as a templates. The arrays were prepared via copolymerization of styrene with different acrylic acid derivatives, long term dialyzing against water and finally evaporation of the solvent. The isopropanolic solution of $\text{Ti}(\text{OPr})_4$ was introduced by capillary forces into the arrays and hydrolyzed in air at room temperature. Finally the template was removed by calcination. The material obtained has a system of pores including macropores being replicas of latex particles, pore structures inside the macropores walls and a network of macro-mesopores made of the octahedral and tetrahedral holes in the partly mineralized template. The

solvothermal (including hydrothermal) methods have been widely applied for preparation of mesoporous titania nanoparticles of various shapes and porosities [4]. The hydrothermal treatment as a synthetic route to obtain mesoporous titania nanoparticles has been found to have effective influence on the physical properties, particularly crystal composition, crystallinity, thermal stability, surface area, pore size distribution and photocatalytic activity of the mesoporous titania [20]. The combination of sol-gel process with solvothermal treatment may lead to formation of TiO_2 beads of high surface areas, tunable pore sizes and walls build of well-crystallized anatase phase [21, 22]. By spraying the precursor solution containing the template and inorganic pH regulators, into a hot chamber it is possible to get spherical and well ordered mesoporous nanoparticles. The main mechanism of this process, analogously to that in the method described above, is the evaporation-induced self-assembly of the droplets [23].

An interesting method seems to be the ultrasound assisted synthesis of mesoporous titania materials. Wang et al. have prepared the mesoporous TiO_2 of high surface area using ultrasound irradiation of the $\text{Ti}(\text{OPr})_4$ solution with octadecylamine as a templating agent [24]. More interesting in the ultrasound assisted synthetic methods is the work published by Yu et al, who first synthesised mesostructured TiO_2 titania without any templates [25]. Literature gives a few single reports about successful synthesis of mesoporous titania without using templating material. Qi et al. have obtained well-crystallized anatase with disordered mesoporous structure, using only titanium precursor in ethanolic solution and distilled water [26]. Mesoporous titania with crystalline framework obtained via controlled hydrolysis of titanium(IV) n-butoxide in the presence of a small amount of nitric acid as a catalyst at room temperature has been presented by Liu et. al [27]. The as-prepared material exhibited a nanoporous and amorphous structure and its further temperature treatment led to formation of well-crystallized anatase with disordered mesoporous structure. Simultaneous formation of macro and mesopores in sponge-like structures has been further reported [28-30]. Such structures were in general obtained via dropwise addition of titanium precursor to deionized water or a water solution of a weak inorganic acid and calcination of the obtained precipitate after various ageing times. Raveendran et.al. have been the first to report a short range ordered mesoporous anatase, with spherical morphology, prepared via template-free method [31]. The ordered structure was obtained via hydrolysis of titanium(IV) n-butoxide in ethyl acetate media after addition of a small amount of water. Numerous template-free mesoporous titania materials have been applied as active photocatalysts [29, 30, 32, 33] or electrode materials in DSSCs [34-36]. The template free synthesis of the mesoporous materials seems to be worth of further investigation, when

taking into regard of the fact that it is environmentally friendly, cheaper and often needs milder synthesis conditions.

3. Photocatalytic applications of mesoporous TiO₂

The photocatalytic applications of mesoporous titania may be divided into three main groups: photocatalysis in organic synthesis, photocatalytic oxidation of water/air pollutants and photocatalytic water splitting [5, 37], but the latter two have been most intensively studied because of their potential applications in environmental friendly devices. To prepare mesoporous TiO₂ many organic and inorganic compounds such as surfactants, triblock copolymers, acids and bases have been used. In most attempts well-defined mesoporous titania with amorphous walls were obtained, but the photocatalytic activity of such materials was rather poor [4, 5]. As mentioned above, an effective method achieve high photocatalytic activity is preparation of mesoporous titania of high specific surface area and well-crystallized anatase walls. The simplest procedure to obtain well-crystallized TiO₂ is the high temperature treatment, however, the calcination results in distortion or total destruction of mesopores framework and reduction of the surface area, so in fact it gives no improvement in the photocatalytic activity of the material [38]. This situation poses a great challenge to find away of synthesis of mesoporous titania with well crystallized anatase walls and still large surface area.

Well crystallized titania with mesoporous structure has been successfully prepared by Peng et al. [39]. The as synthesized material obtained by hydrothermal procedure and drying at 120 °C shows well crystallized anatase phase with a well defined short range ordered mesoporous structure which was stable under temperature treatment up to 800 °C. The nanoparticles synthesized in this procedure showed a high photocatalytic activity in Rhodamine B oxidation process. The overall efficiency of the photooxidation process on the material calcined at 400 °C was 97 %, while the efficiency of the same process in the same conditions performed with the application of a commercial catalyst Degussa P25 was only 60 %. Beyers et al. have shown that post-synthesis treatment of the mesostructured titania with ammonia or hydrochloric acid solution increased its thermal stability [40]. These authors have prepared two mesoporous materials using hexadecylamine or cetyl trimethylammonium bromide as surfactant-directing and pore-forming agents. The post-synthesis treatment with an acidic or basic medium gave the material of much better crystallized titania wells and higher surface area than those of untreated samples, moreover, the photocatalytic activity in the Rhodamine 6G oxidation process was much higher when post-synthesis treated materials were used as photocatalysts. About 10

times increase in the efficiency in the photocatalytic water splitting reaction was obtained by Hartman et al. when mesoporous anatase TiO_2 was compared with nonporous TiO_2 nanoparticles prepared in similar conditions [38]. A mesoporous titania photocatalyst very active in the photocatalytic water decomposition was prepared by hydrothermal method using titanium butoxide as a starting material and acetylacetone as a nonstandard templating agent, by Jitputti et al. [41]. This material shows a thermal stability of the mesoporous structure up to 500 °C, and its photocatalytic activity was up to 4 times better than that of the commercial ST-01 Ishihara TiO_2 . The typically template-free synthesized mesoporous titania was first tested by Yu and his coworkers in the photocatalytic degradation of acetone [30]. The as prepared material showed no photocatalytic activity and poor crystallinity and porosity, but the material calcined at 400 °C showed the almost 20 % better activity than that of Degussa P25 powder. The use of various metals or nonmetals as dopants of mesoporous titania may lead to better thermal stability and higher photocatalytic activity of the materials obtained [4, 5]. An example may be the above mentioned material synthesized by Peng et al. [39]. After incorporation of lanthanum ions into the reaction mixture the material obtained shows much higher photoactivity than the undoped material [42]. On the other hand, the N-doped TiO_2 shows much higher activity in the methylene blue photodecomposition process when compared with that of undoped material [43]. Generally it can be assumed that introduction of N atoms in small amount into the TiO_2 structure leads to the activation of the material in the visible light region.

4. Photoelectric applications of mesoporous TiO_2

Dye sensitized solar cells had been investigated long before O'Regan and Grätzel presented their high-effective device [10]. Initially TiO_2 with smooth surface was used as anode material and, in consequence, low dye adsorption took place, which led to the efficiencies not reaching 1 %. The critical discovery was the application of nanocrystalline mesoporous TiO_2 as an electrode material, which resulted in over 1000 times increase in the dye load and almost 10 times better photoconversion performance in the O'Regan and Grätzel cell [9, 10]. Since this publication, the annual publication rate of papers dealing with various aspects of DSSCs rose exponentially reaching over 1500 papers in 2011 [44]. Much more than half of these publications were concerned with synthesis and application of mesoporous TiO_2 . For almost 15 years the basic material used to prepare semiconducting mesoporous electrode was randomly ordered TiO_2 , but since 2005 when Zukalová et al. reported that DSSCs electrode material prepared of organized mesoporous titania film shows solar energy conversion efficiency

enhanced by about 50% when compared with non-ordered ones [45], the interest in synthesis and application in DSSCs of well-ordered mesoporous titania has increased significantly. Lancelle-Beltran et al. have presented the self-assembly mesoporous titania thin films for DSSC applications [46]. The films exhibit a high porous volume and large surface area. The measurements executed by the authors revealed that the crystallization and diffuse sintering of TiO₂ and, in consequence, formation of the anatase phase occur simultaneously during the curing of the film at temperatures between 400 and 500 °C. The photoconversion efficiencies obtained with the use of the presented films as electrode materials in DSSC were very promising. Thick titania mesoporous films with highly ordered orthorhombic pore organization synthesized via supramolecular templated route have been presented and used as photoanodes in high performance DSSCs by Zhang et al. [47]. The highly crystallized films demonstrate very good optical transparency and have highly mesoporosity and uniformity of the mesoporous structure. The maximum light-to-electricity conversion efficiency was equal to 6.02 % and obtained for DSSC with the electrode made of a film of 5.08 μm in thickness. Highly crystalline mesoporous anatase was also obtained through supramolecular self-assembly by Asefa's group [48]. The TiO₂ obtained via hydrolysis of TiOSO₄ assisted by cetyltrimethylammonium bromide as a templating agent was used to prepare photoanodes of DSSCs with high specific surface area and high surface roughness. Presented photoelectrode films show hierarchical macro- and mesoporous structure, which leads to better dye adsorption and electrolyte percolation, combined with improved electron conduction pathways compared to those of the films obtained with commercial Degusa P25 TiO₂. Sodium salicylate was used as a template in highly efficient synthesis of self-assembled mesoporous titania spherical nanoparticles with well-defined crystal morphology by Petra et al. [49]. The material obtained showed mesopores of diameters in the range 2.5-6.5 nm. These authors have reported a drastic enhancement in photoconductivity of the material investigated when sensitizing dye molecules were entrapped inside of the mesopores. This observation was another strong evidence supporting the use of mesoporous titania as an electrode material in DSSCs. The interesting template free synthetic route of the non-ordered porous titania electrodes, using H₂TiO₃ as titania precursor has been presented by Gao and Nagai [35]. The self assembled films were deposited on FTO substrates via soaking in the precursor solution at various temperatures and for different time. The as-prepared materials exhibited amorphous structure, but their post synthetic temperature treatment led to the anatase phase formation. Unfortunately, DSSCs assembled with thus prepared electrodes exhibited relatively low efficiencies, which were probably caused by

poor fill factors. The microwave-assisted hydrothermal template-free synthesis of well crystallized mesoporous TiO_2 was presented by Huang et al. [34]. Stable and water soluble titanium citrate complexes were used as titania precursors. The materials obtained exhibited large surface areas, from the range $217\text{-}323\text{ m}^2\times\text{g}^{-1}$, which depended on hydrothermal procedure temperature. The relatively good photon-to-current conversion efficiencies, reaching 7.1 %, have shown that the template-free mesoporous titania synthesis leads to the materials which can be highly effective when used for electrodes in DSSCs.

5. Conclusions

Mesoporous titania materials may be successfully applied in photoenergy systems. In most cases the use of mesoporous material gives better results than the use of nonporous one. A mesoporous material to be applied in photoenergy systems should show well-defined high porosity, high specific surface area, good crystallinity and a suitable crystallite size. Different synthetic methods have been developed to prepare materials satisfying the above conditions, but there is still enormous demand for more refined methods that could ensure more active suitable materials. From among a number synthetic approaches, very interesting is the template free synthesis of mesoporous materials, when looking through the lens of its environmental friendliness in connection with potentially cheaper way to obtain well defined mesostructured materials caused by elimination of the templates and often softer synthesis conditions. It can be expected that the template free self-assembly methods will be intensively developed and may displace the “traditional” template assisting methods.

Acknowledgments

This work was supported from the funds of Polish National Science Centre, grant No. NN204 023538.

References

1. K.S.W. Sing, D.H. Everett, R.A.W. Haul, L. Moscou, R.A. Pierotti, J. Rouquerol, T. Siemieniewska, Reporting physisorption data for gas/solid systems with special reference to the determination of surface area and porosity (Recommendations 1984), *Pure and Applied Chemistry*, 57 (1985) 603-628.
2. T. Yanagisawa, T. Shimizu, K. Kuroda, C. Kato, The Preparation of Alkyltriinethyllaininonium-Kaneinite Complexes and Their Conversion to Microporous Materials, *Bull. Chem. Soc. Jpn.*, 63 (1990) 988-992.

3. C.T. Kresge, M.E. Leonowicz, W.J. Roth, J.C. Vartuli, J.S. Beck, Ordered mesoporous molecular sieves synthesized by a liquid-crystal template mechanism, *Nature*, 359 (1992) 710-712.
4. J.L. Vivero-Escoto, Y.-D. Chiang, K.C.-W. Wu, Y. Yamauchi, Recent progress in mesoporous titania materials: adjusting morphology for innovative applications, *Science and Technology of Advanced Materials*, 13 (2012) 013003.
5. X. Chen, S.S. Mao, Titanium Dioxide Nanomaterials: Synthesis, Properties, Modifications, and Applications, *Chem. Rev.*, 107 (2007) 2891-2959.
6. G.J.A.A. Soler-Illia, P.C. Angelome, M.C. Fuertes, D. Grosso, C. Boissiere, Critical aspects in the production of periodically ordered mesoporous titania thin films, *Nanoscale*, 4 (2012) 2549-2566.
7. A. Fujishima, K. Honda, Electrochemical Photolysis of Water at a Semiconductor Electrode, *Nature*, 238 (1972) 37-38.
8. M.R. Hoffmann, S.T. Martin, W. Choi, D.W. Bahnemann, Environmental Applications of Semiconductor Photocatalysis, *Chem. Rev.*, 95 (1995) 69-96.
9. B. O'Regan, M. Grätzel, A low-cost, high-efficiency solar cell based on dye-sensitized colloidal TiO₂ films, *Nature*, 353 (1991) 737-740.
10. A. Hagfeldt, G. Boschloo, L. Sun, L. Kloo, H. Pettersson, Dye-Sensitized Solar Cells, *Chem. Rev.*, 110 (2010) 6595-6663.
11. M. Grätzel, Photoelectrochemical cells, *Nature*, 414 (2001) 338-344.
12. M. Grätzel, Dye-sensitized solar cells, *Journal of Photochemistry and Photobiology C: Photochemistry Reviews*, 4 (2003) 145-153.
13. N. Ulagappan, C.N.R. Rao, Mesoporous phases based on SnO₂ and TiO₂, *Chem. Commun.*, (1996) 1685-1686.
14. M. Fröba, O. Muth, A. Reller, Mesostructured TiO₂: ligand-stabilized synthesis and characterization, *Solid State Ionics*, 101-103, Part 1 (1997) 249-253.
15. T.E.W. Nießen, J.P.M. Niederer, T. Gjervan, W.F. Hölderich, Synthesis and characterisation of titanium-containing MCM-41 using (NH₄)₃[Ti(O₂)F₅] as the titanium source, *Microporous Mesoporous Mater.*, 21 (1998) 67-74.
16. A. Corma, From Microporous to Mesoporous Molecular Sieve Materials and Their Use in Catalysis, *Chem. Rev.*, 97 (1997) 2373-2420.
17. M. Ogawa, A simple sol-gel route for the preparation of silica-surfactant mesostructured materials, *Chem. Commun.*, (1996) 1149-1150.
18. C.-W. Wu, T. Ohsuna, M. Kuwabara, K. Kuroda, Formation of

- Highly Ordered Mesoporous Titania Films Consisting of Crystalline Nanopillars with Inverse Mesospace by Structural Transformation, *J. Am. Chem. Soc.*, 128 (2006) 4544-4545.
19. M.C. Carbajo, E. Enciso, M.J. Torralvo, Synthesis and characterisation of macro-mesoporous titania, *Colloids and Surfaces A: Physicochemical and Engineering Aspects*, 293 (2007) 72-79.
 20. D.S. Kim, S.-Y. Kwak, The hydrothermal synthesis of mesoporous TiO₂ with high crystallinity, thermal stability, large surface area, and enhanced photocatalytic activity, *Applied Catalysis A: General*, 323 (2007) 110-118.
 21. D. Chen, F. Huang, Y.-B. Cheng, R.A. Caruso, Mesoporous Anatase TiO₂ Beads with High Surface Areas and Controllable Pore Sizes: A Superior Candidate for High-Performance Dye-Sensitized Solar Cells, *Adv. Mater.*, 21 (2009) 2206-2210.
 22. D. Chen, L. Cao, F. Huang, P. Imperia, Y.-B. Cheng, R.A. Caruso, Synthesis of Monodisperse Mesoporous Titania Beads with Controllable Diameter, High Surface Areas, and Variable Pore Diameters (14–23 nm), *J. Am. Chem. Soc.*, 132 (2010) 4438-4444.
 23. Y. Lu, H. Fan, A. Stump, T.L. Ward, T. Rieker, C.J. Brinker, Aerosol-assisted self-assembly of mesostructured spherical nanoparticles, *Nature*, 398 (1999) 223-226.
 24. Y. Wang, X. Tang, L. Yin, W. Huang, Y. Rosenfeld Hacothen, A. Gedanken, Sonochemical Synthesis of Mesoporous Titanium Oxide with Wormhole-like Framework Structures, *Adv. Mater.*, 12 (2000) 1183-1186.
 25. J. C. Yu, L. Zhang, J. Yu, Rapid synthesis of mesoporous TiO₂ with high photocatalytic activity by ultrasound-induced agglomeration, *New J. Chem.*, 26 (2002) 416-420.
 26. L. Qi, Y. Wang, J. Ma, Synthesis of mesoporous TiO₂ (anatase) in the absence of templates, *Journal of Materials Science Letters*, 21 (2002) 1301-1303.
 27. C. Liu, L. Fu, J. Economy, A simple, template-free route for the synthesis of mesoporous titanium dioxide materials, *J. Mater. Chem.*, 14 (2004) 1187-1189.
 28. A. Collins, D. Carriazo, S.A. Davis, S. Mann, Spontaneous template-free assembly of ordered macroporous titania, *Chem. Commun.*, (2004) 568-569.
 29. H. Fei, Y. Liu, Y. Li, P. Sun, Z. Yuan, B. Li, D. Ding, T. Chen, Selective synthesis of borated meso-macroporous and mesoporous spherical TiO₂

- with high photocatalytic activity, *Microporous Mesoporous Mater.*, 102 (2007) 318-324.
30. J.G. Yu, Y.R. Su, B. Cheng, Template-Free Fabrication and Enhanced Photocatalytic Activity of Hierarchical Macro-Mesoporous Titania, *Adv. Funct. Mater.*, 17 (2007) 1984-1990.
 31. P. Raveendran, M. Eswaramoorthy, U. Bindu, M. Chatterjee, Y. Hakuta, H. Kawanami, F. Mizukami, Template-Free Formation of Meso-Structured Anatase TiO₂ with Spherical Morphology[†], *The Journal of Physical Chemistry C*, 112 (2008) 20007-20011.
 32. P. Xu, J. Lu, T. Xu, S. Gao, B. Huang, Y. Dai, I₂-Hydrosol-Seeded Growth of (I₂)_n-C-Codoped Meso/Nanoporous TiO₂ for Visible Light-Driven Photocatalysis, *The Journal of Physical Chemistry C*, 114 (2010) 9510-9517.
 33. N. Lakshminarasimhan, E. Bae, W. Choi, Enhanced Photocatalytic Production of H₂ on Mesoporous TiO₂ Prepared by Template-Free Method: Role of Interparticle Charge Transfer, *The Journal of Physical Chemistry C*, 111 (2007) 15244-15250.
 34. C.-H. Huang, Y.-T. Yang, R.-A. Doong, Microwave-assisted hydrothermal synthesis of mesoporous anatase TiO₂ via sol-gel process for dye-sensitized solar cells, *Microporous Mesoporous Mater.*, 142 (2011) 473-480.
 35. Y. Gao, M. Nagai, W.-S. Seo, K. Koumoto, Template-Free Self-Assembly of a Nanoporous TiO₂ Thin Film, *J. Am. Ceram. Soc.*, 90 (2007) 831-837.
 36. M. Zalas, G. Schroeder, Template free synthesis of locally-ordered mesoporous titania and its application in dye-sensitized solar cells, *Mater. Chem. Phys.*, 134 (2012) 170-176.
 37. M.A. Fox, M.T. Dulay, Heterogeneous photocatalysis, *Chem. Rev.*, 93 (1993) 341-357.
 38. P. Hartmann, D.-K. Lee, B.M. Smarsly, J. Janek, Mesoporous TiO₂: Comparison of Classical Sol-Gel and Nanoparticle Based Photoelectrodes for the Water Splitting Reaction, *ACS Nano*, 4 (2010) 3147-3154.
 39. T. Peng, D. Zhao, K. Dai, W. Shi, K. Hirao, Synthesis of Titanium Dioxide Nanoparticles with Mesoporous Anatase Wall and High Photocatalytic Activity, *The Journal of Physical Chemistry B*, 109 (2005) 4947-4952.
 40. E. Beyers, P. Cool, E.F. Vansant, Anatase Formation during the Synthesis of Mesoporous Titania and Its Photocatalytic Effect, *The*

- Journal of Physical Chemistry B, 109 (2005) 10081-10086.
41. J. Jitputti, S. Pavasupree, Y. Suzuki, S. Yoshikawa, Synthesis and photocatalytic activity for water-splitting reaction of nanocrystalline mesoporous titania prepared by hydrothermal method, *J. Solid State Chem.*, 180 (2007) 1743-1749.
 42. T. Peng, D. Zhao, H. Song, C. Yan, Preparation of lanthana-doped titania nanoparticles with anatase mesoporous walls and high photocatalytic activity, *J. Mol. Catal. A: Chem.*, 238 (2005) 119-126.
 43. R. Asahi, T. Morikawa, T. Ohwaki, K. Aoki, Y. Taga, Visible-Light Photocatalysis in Nitrogen-Doped Titanium Oxides, *Science*, 293 (2001) 269-271.
 44. L.M. Peter, The Grätzel Cell: Where Next?, *The Journal of Physical Chemistry Letters*, 2 (2011) 1861-1867.
 45. M. Zukalová, A. Zukal, L. Kavan, M.K. Nazeeruddin, P. Liska, M. Grätzel, Organized Mesoporous TiO₂ Films Exhibiting Greatly Enhanced Performance in Dye-Sensitized Solar Cells, *Nano Lett.*, 5 (2005) 1789-1792.
 46. E. Lancelle-Beltran, P. Prené, C. Boscher, P. Belleville, P. Buvat, S. Lambert, F. Guillet, C. Boissière, D. Grosso, C. Sanchez, Nanostructured Hybrid Solar Cells Based on Self-Assembled Mesoporous Titania Thin Films, *Chem. Mater.*, 18 (2006) 6152-6156.
 47. Y. Zhang, Z.B. Xie, J. Wang, Highly efficient dye-sensitized solar cells of thick mesoporous titania films derived from supramolecular templating, *Nanotechnology*, 20 (2009) 505602.
 48. S. Ahmed, A. Du Pasquier, D.P. Birnie, T. Asefa, Self-Assembled TiO₂ with Increased Photoelectron Production, and Improved Conduction and Transfer: Enhancing Photovoltaic Performance of Dye-Sensitized Solar Cells, *ACS Applied Materials & Interfaces*, 3 (2011) 3002-3010.
 49. A.K. Patra, S.K. Das, A. Bhaumik, Self-assembled mesoporous TiO₂ spherical nanoparticles by a new templating pathway and its enhanced photoconductivity in the presence of an organic dye, *J. Mater. Chem.*, 21 (2011) 3925-3930.

Chapter 8

Monoterpene-derived 1,2-amino alcohols as catalysts precursors for asymmetric reactions

Marek P. Krzemiński, Marta Ćwiklińska and Anna Kmiecik
*Nicolaus Copernicus University, Faculty of Chemistry,
7 Gagarin Street, 87-100 Toruń, Poland*

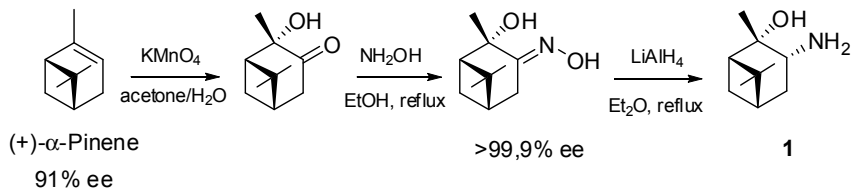
Introduction

Asymmetric synthesis employing chiral catalysts has become one of the most intensively growing field in organic chemistry for the last three decades.¹ Synthesized enantio-enriched or enantiopure products are valuable compounds of biological, medicinal or agrochemical interests. Many optically active naturally occurring compounds, such as amino acids, carbohydrates, alkaloids or terpenes, have been used as chiral building blocks, chiral auxiliaries and/or the source of stereogenic centers. Among them, monoterpenes proved to be very valuable especially as precursors of boron reagents and catalysts. α -Pinene derived reagents were successfully applied to many asymmetric reactions, for example, asymmetric hydroboration and reduction², allylboration³, homologation⁴, ring opening of epoxides⁵, and others⁶. This review covers the synthesis and the use of β -amino alcohols derived from bicyclic monoterpenes. The importance of 1,2-amino alcohols has already been summarized⁷. Herein we present syntheses and essentially catalytic utilizations of β -amino alcohols and their derivatives obtained from α - and β -pinene, 3-carene, and camphor.

Asymmetric reductions with borane/oxazaborolidines

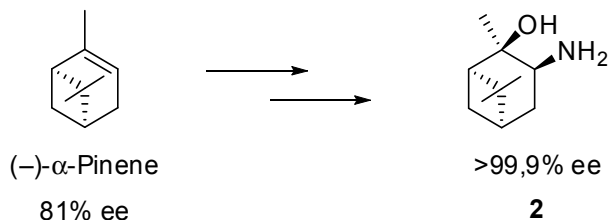
Asymmetric reduction of prochiral ketones with stoichiometric organoboranes² or with borane in the presence of catalytic amount of oxazaborolidines⁸ is one of the simplest method for the preparation of chiral secondary alcohols. In contrast to extensively studied oxazaborolidines obtained from amino acids, for instance, derivatives of 1,1-diphenylprolinol, not many terpene-derived oxazaborolidines are known as catalysts for the reduction of ketones with borane. 3-Amino-2-hydroxypinane was reported for the first

time by Burak and Chabudziński without specifying enantiomeric purity.⁹ However, Masui and Shioiri slightly modified their procedure and they prepared enantiomerically pure (1*S*,2*S*,3*R*,5*S*)-3-amino-2-hydroxypinane (**1**) from (1*R*,5*R*)- α -pinene (Scheme 1).¹⁰



Scheme 1.

α -Pinene was oxidized with potassium permanganate, utilizing the procedure developed by Carlson and Pierce¹¹, followed by the reaction with aqueous hydroxylamine. Optical purity of the oxime was upgraded by fractional crystallization. Lithium aluminum hydride reduction of the oxime gave the expected β -amino alcohol **1**. Applying the same methodology to (–)- α -pinene of 81% ee, Masui synthesized the optically pure opposite enantiomer of the amino alcohol **1** – (1*R*,2*R*,3*S*,5*R*)-3-amino-2-hydroxypinane (**2**) (Scheme 2).

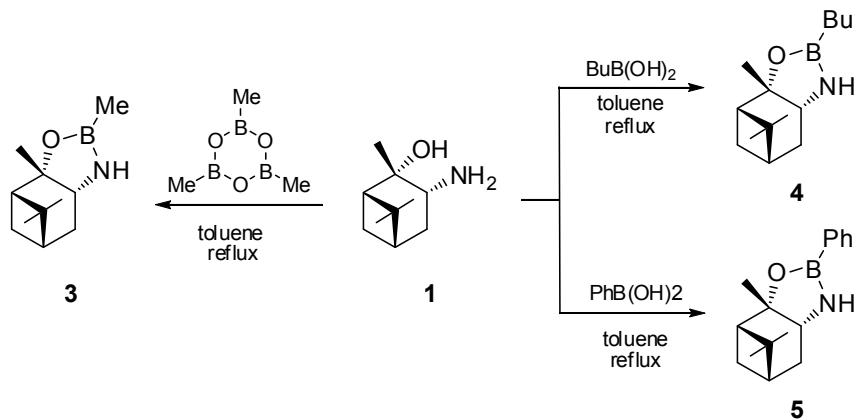


Scheme 2.

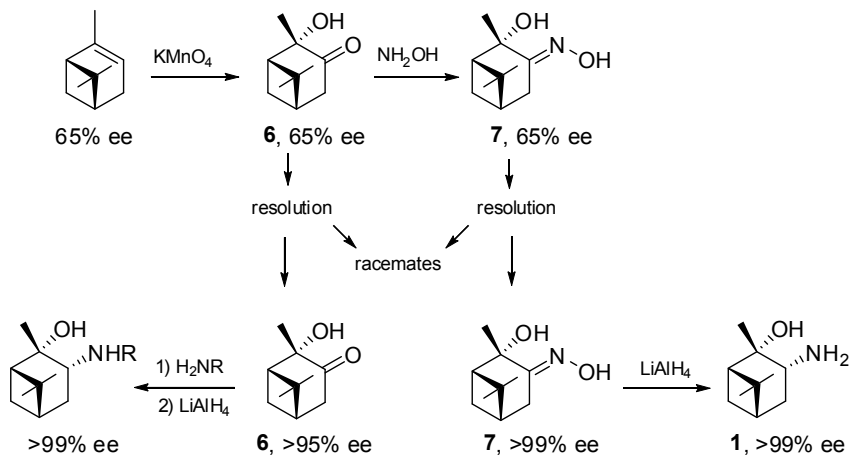
The reaction of 3-amino-2-hydroxypinane **1** with trimethylboroxine, butylboronic acid, or phenylboronic acid was completed in refluxing toluene to give respectively *B*-methyl- **3**, *B*-*n*-butyl- **4**, and *B*-phenyl- **5** oxazaborolidines (Scheme 3). In contrast to other oxazaborolidines usually used as crude compounds in following reactions, oxazaborolidines derived from a volatile α -pinene could be purified by distillation.

Markowicz and co-workers demonstrated a convenient method for the preparation of **1**, and its *N*-derivatives, starting from inexpensive (+)- α -pinene

of low enantiomeric purity (~65%).¹² 2 α -Hydroxy-pinane-3-one **6** of 65% ee could be crystallized from condensed hexane solutions containing 1% v/v of ethylene glycol to give, after seeding, almost enantiomerically pure **6**. Similarly, optical purity of oxime **7** was upgraded utilizing different solubility of the two forms, enantiomer and racemate, in boiling hexane (Scheme 4).



Scheme 3.

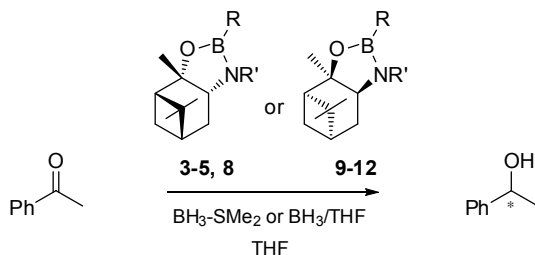


Scheme 4.

Acetophenone is usually selected as a model ketone to test new

oxazaborolidines as catalysts for the asymmetric reduction with borane. Table 1 summarizes reductions of acetophenone catalyzed by variously substituted oxazaborolidines obtained from 3-amino-2-hydroxypinanes **1** and **2**. *B*-Methyl **3** furnished the best results and produced (*S*)-1-phenylethanol in high enantiomeric excess. The standard catalyst loading is 10 mol %, 5 mol % of **3** still catalyzed the reduction with high enantioselectivity. Lowering the catalyst loading to 2 mol % influenced the selectivity and the reaction time. The use of both enantiomers of the catalyst for the reduction of ketone led to both enantiomers of the product alcohol. This can be clearly seen for catalysts **3** and **9**.¹³ *N*-Alkylation in oxazaborolidines **11** and **12** had a profound effect on enantioselectivity to yield nearly racemic 1-phenylethanol.¹⁴

Table 1. Asymmetric reduction of acetophenone with oxazaborolidines derived from **1** and **2**.



	Oxazaborolidine (mol %)		Temp., °C	Time, h	Ee, %	Config.	Ref.
	R	R'					
3 (10)	Me	H	25~30	0,5	91	<i>S</i>	13
3 (10)	Me	H	0~5	2	93	<i>S</i>	13
3 (5)	Me	H	0~5	6	92	<i>S</i>	13
3 (2)	Me	H	0~5	24	87	<i>S</i>	13
4 (10)	Bu	H	0~5	4	92	<i>S</i>	13
5 (10)	Ph	H	0~5	6	91	<i>S</i>	13
8 (10)	H	H	25~30	1	94	<i>S</i>	13
8 (10)	H	H	0~5	2	93	<i>S</i>	13
8 (10)	H	H	0	2	89	<i>S</i>	12
9 (10)	Me	H	0~5	2	93	<i>R</i>	13
10 (10)	H	H	0→rt	1,25	93	<i>R</i>	14

11 (10)	H	<i>i</i> -Pr	0→rt	1,25	24	<i>R</i>	14
12 (10)	H	Bn	0→rt	1,25	3	–	14

The stereochemical outcome of the reaction was explained using well documented mechanism of the CBS (Corey-Bakshi-Shibatta) reduction.^{8b,15} The mechanism implies the coordination of both the ketone and the borane to oxazaborolidine, which allows hydride transfer to take place through chair-like transition state as depicted on Figure 1.

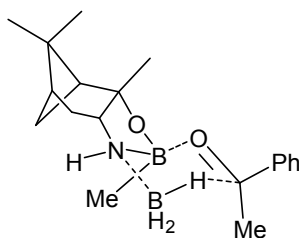
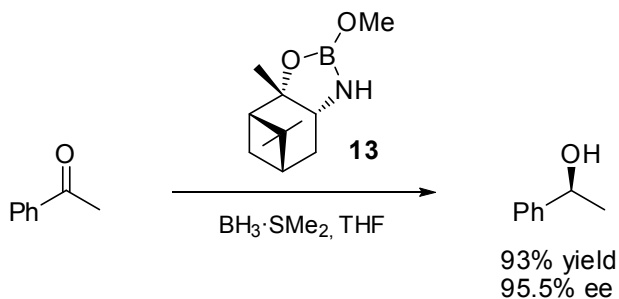


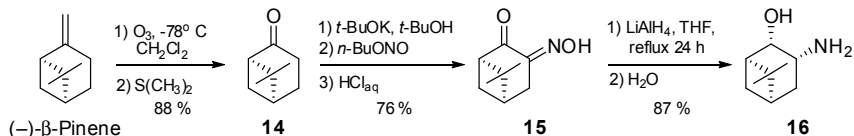
Figure 1.

As a result of model studies and the mechanism of this reduction, Masui and Shioiri introduced *B*-methoxy oxazaborolidine **13** in order to increase Lewis acidity of the boron atom in oxazaborolidine ring.¹⁶ This compound, similarly to other *B*-alkoxy derivatives, was generated prior to the reaction and was used without isolation. The catalyst **13** has shown higher activity in comparison with *B*-H and *B*-Me derivatives giving product alcohols with higher enantiomeric excess (Scheme 5).^{14, 16} Recently, a DFT studies of the whole catalytic cycle in the reduction of acetophenone catalyzed with **13** was published.¹⁷



Scheme 5.

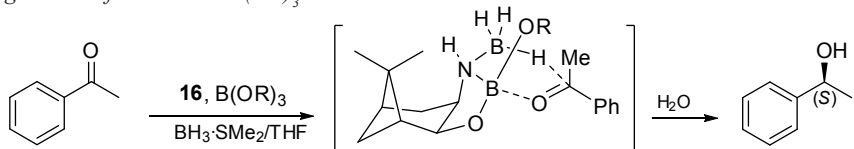
Another readily available bicyclic monoterpene component of turpentine is (–)- β -pinene, which occurs naturally only as (1*S*,5*S*) enantiomer. Krzemiński et al., prepared amino alcohol **16** in three-step synthesis from β -pinene (Scheme 6).¹⁸ Thus, (+)-nopinone (**14**), obtained by ozonolysis of (–)- β -pinene, was converted into ketoxime **15**. Reduction of **15** with lithium tetrahydridoaluminate produced (1*R*,2*S*,3*R*,5*R*)-3-amino-apopinan-2-ol (**16**) in 87 % yield. The structure was confirmed by spectroscopic methods and additionally by crystal structure analysis of its *p*-toluenesulfonamide derivative.¹⁸



Scheme 6.

Amino alcohol **16** was treated with selected trialkyl borates and the corresponding *B*-alkoxy-oxazaborolidines were used directly, without isolation, to catalyze the reduction with borane dimethylsulfide adduct (Table 2).¹⁸

Table 2. Asymmetric reduction of acetophenone with BMS catalyzed by oxazaborolidines generated from **16** and $B(OR)_3$.



Entry	3 (mol%)	R	Temp. (°C)	Product ^b	
				Yield (%) ^c	Ee (%) ^c
1	10	Me	0	98	96
2	10	Me	20	99	97
3	10	<i>i</i> -Pr	0	98	84
4	10	<i>i</i> -Pr	20	97	94
5	10	<i>n</i> -Bu	20	99	98
6	5	Me	20	97	97
7	3	Me	20	98	98
8	1	Me	20	96	92

^a Borane-dimethyl sulfide complex ($BH_3 \cdot S(CH_3)_2$).

^b Configuration was established by comparing the sign of rotation with an authentic sample (Aldrich).

^c Isolated yields after flash chromatography.

^e Enantiomeric excess was established by GC analysis of the 1-phenylethanol on chiral column.

Experiments with oxazaborolidine generated from 10 mol % of **16** and 11 mmol % of B(OMe)₃ proceeded readily to give (*S*)-1-phenylethanol of 97 % ee in 99 % yield (Table 2, entries 1 and 2). Bulkier isopropoxy group on boron atom, when triisopropyl borate was used to generate catalyst, led to a lower enantiomeric excess, especially at 0 °C (entries 3 and 4). Tri-*n*-butyl borate gave similar result to B(OMe)₃ (entry 5). Lower catalysts loadings did not reduce the enantiomeric purity of the 1-phenylethanol (entries 6 and 7). The best reaction conditions, 3 mol % of **16** and B(OMe)₃ at room temperature, were employed for the reduction of the selected alkyl-aryl ketones and the results are presented on Figure 2.

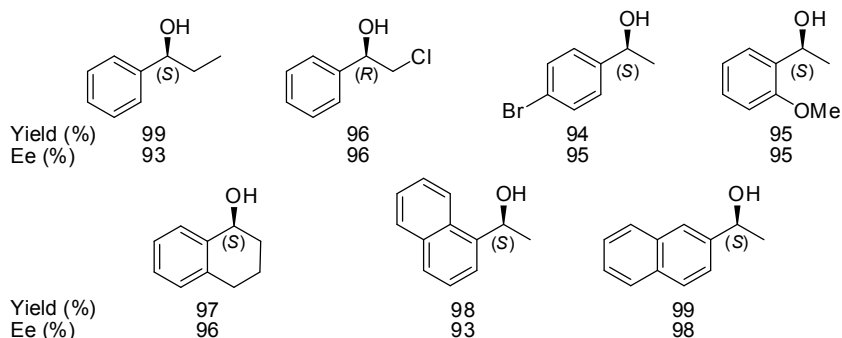
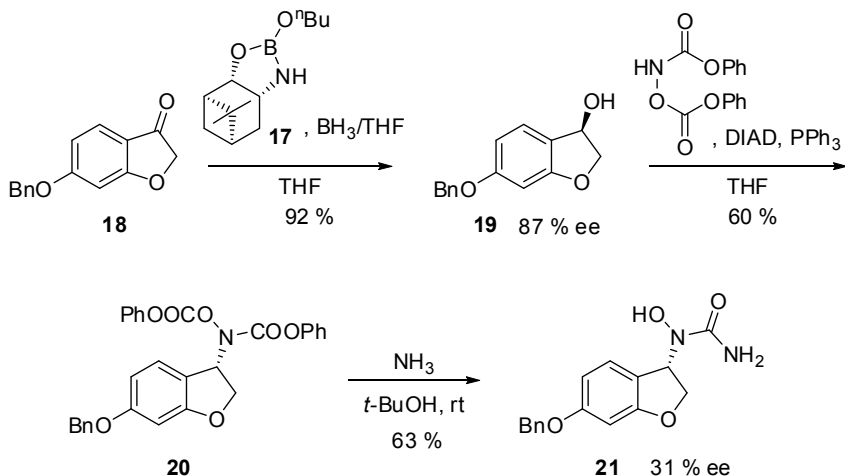


Figure 2.

The extension of this studies was an approach to *N*-hydroxyurea **21** utilizing in a key step the reduction of 6-benzyloxy-2,3-dihydrobenzofuran-3-one (**18**) (Scheme 7).¹⁹ *N*-Hydroxyureas derived from dihydrobenzofuran, and other oxygen and sulfur heterocycles, are 5-lipoxygenase inhibitors exhibiting antiasthmatic, antiallergic and antiinflammatory activities. Oxazaborolidine **17**, prepared from **16** and B(*O-n*-Bu)₃, was more selective than oxazaborolidine from (1*R*,2*S*)-norephedrine giving **19** in 87 % ee.



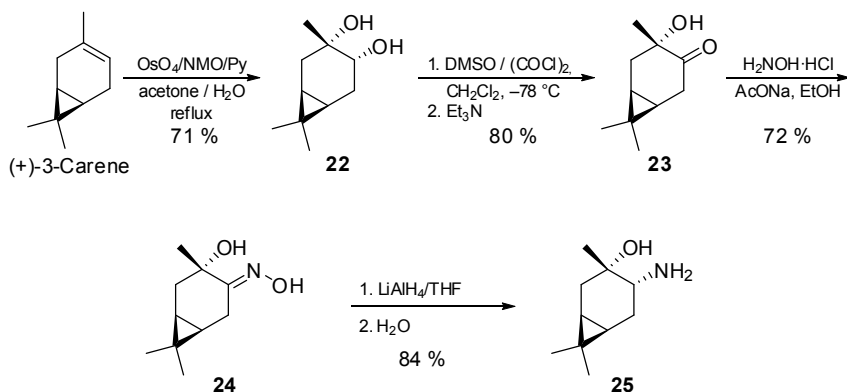
Scheme 7.

Unfortunately, the transformation of **19** to **20** under Mitsunobu conditions, with *N,O*-bis(diphenoxycarbonyl)hydroxylamine, followed by treatment with ammonia proceeded with extensive racemization to give **21** of 31% ee. Attempts to modify reaction conditions by switching to other phosphines instead of triphenylphosphine have not raised the enantiomeric excess of **21**. Presumably, two oxygen atoms attached to aromatic ring exert too strong electron-donating effect leading to partial racemization at the benzylic position.¹⁹

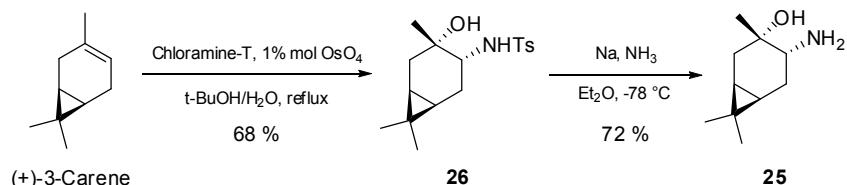
A further constituent of turpentine, (+)-3-carene has already proved to be a powerful chiral auxiliary in hydroboration and allylboration reactions²⁰, as well as a precursor of chiral ligands and reagents.²¹ (1*S*,3*S*,4*R*,6*R*)-4-Aminocaran-3-ol (**25**) was obtained by analogy to the synthesis of amino alcohol **1** in four-step synthesis (Scheme 8). Since 3-carene is more sensitive towards strong oxidants, first, dihydroxylation by osmium tetroxide in the presence of *N*-methylmorpholine *N*-oxide (NMO) as a stoichiometric oxidant was accomplished to give a single stereoisomer of the diol **22**.²² In the next step, diol was oxidized using Swern method to α -hydroxy ketone **23**, which was converted into α -hydroxy oxime **24**. Reduction of the oxime with lithium aluminum hydride gave the expected β -amino alcohol **25** (Scheme 8).

Łączkowski et al., developed a shorter synthesis of **25** utilizing Sharpless aminohydroxylation reaction (Scheme 9).²³ The aminohydroxylation of 3-carene with chloramine-T was conducted in the presence of 1 mol % of osmium

tetroxide producing β -hydroxy-toluenesulfonamide **26**. The increased amount of the osmium catalyst (1 mol %), much higher compared with dihydroxylation reaction (0.2 mol %, Scheme 8), is necessary to achieve a good yield of the hydroxy-amide **26**. The reduction of the sulfonamide with sodium in liquid ammonia gave 4-amino-caran-3-ol **25** in 72 % yield.



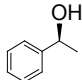
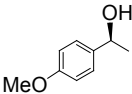
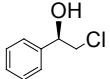
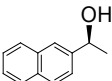
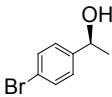
Scheme 8.



Scheme 9.

In contrast to *B*-isopropoxy oxazaborolidine obtained from **16**, which gave lower enantiomeric excess of 1-phenylethanol in reduction of acetophenone (Table 2), (1*S*,3*S*,4*R*,6*R*)-4-amino-caran-3-ol (**25**) in conjunction with triisopropyl borate catalyzed the reduction of the selected ketones to produce alcohols with excellent enantioselectivities (Table 3).²⁴ Alkyl-aryl ketones were reduced with the solution of borane in tetrahydrofuran in the presence of 5 mol % of the catalyst.

Table 3. Reduction of selected ketones with borane catalyzed by oxazaborolidine generated from **25** and $B(O-i-Pr)_3$.

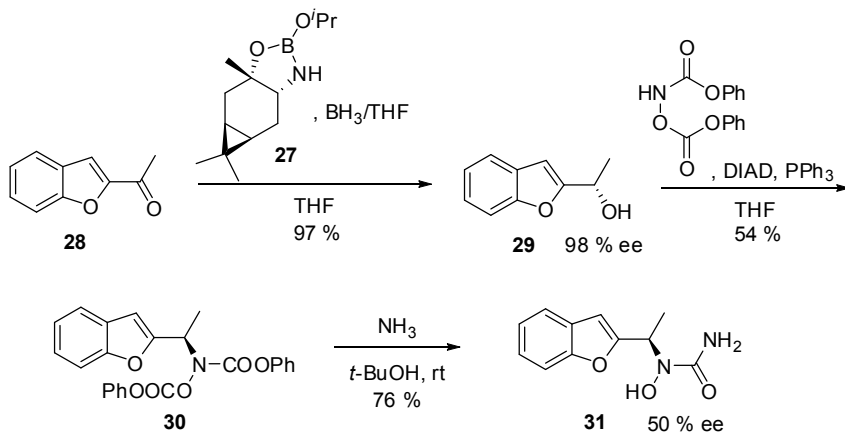
$\text{Ar}-\overset{\text{O}}{\parallel}{\text{C}}-\text{R} \xrightarrow[1\text{eq BH}_3 \cdot \text{THF, THF}]{5\% \text{ mol. } \mathbf{25}, B(O-i-Pr)_3} \text{Ar}-\underset{\text{OH}}{\text{C}}-\text{R}$		
Product	Yield (%)	Ee (%)
	95	98
	93	98
	89	98
	96	99
	95	99

The superior enantioselectivity of the oxazaborolidine **27** was employed in the facile synthesis of the *N*-hydroxyurea **30** (Scheme 10).²⁵ 2-Acetyl-benzofuran **28**, readily prepared from salicylic aldehyde and chloroacetone, was reduced with borane/oxazaborolidine **27**, generated in situ from $B(O-i-Pr)_3$ and **25**, producing (*S*)-1-(benzofuran-2-yl)ethanol **29** with 98 % ee. The other oxazaborolidines, generated from (1*S*,2*R*)-norephedrine and (*S*)-diphenylvalinol, resulted in lower enantiomeric excess of **29**.

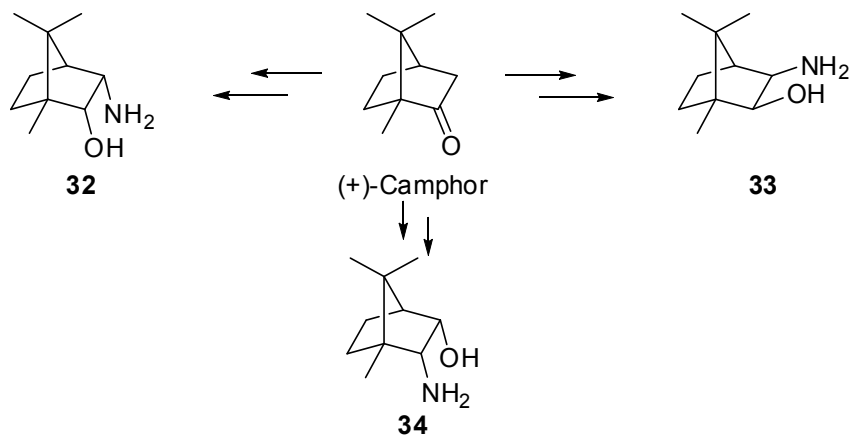
In the following step, **29** reacted with *N,O*-bis(diphenoxycarbonyl) hydroxylamine under Mitsunobu conditions. The substitution product **30** after treatment with liquid ammonia yield *N*-hydroxyurea **31** with 50 % ee (Scheme 10). Unfortunately, a partial racemization was observed, similarly to substitution in **19** (Scheme 7).

Besides α - and β -pinene and 3-carene, camphor belongs to one of the most important chiral auxiliaries. Several β -amino alcohols from camphor were

synthesized²⁶ long time ago, but not many reports describe their applications as ligands or catalysts. Santhi and Rao obtained three isomers, *cis-endo-endo* (**32** and **34**) and *cis-exo-exo* (**33**) amino alcohols using reported procedures (Scheme 11).²⁷



Scheme 10.



Scheme 11.

Amino alcohols **32-34** were subjected to the reaction with borane or trimethyl borate to yield the appropriate catalysts **35-37** (Figure 3).

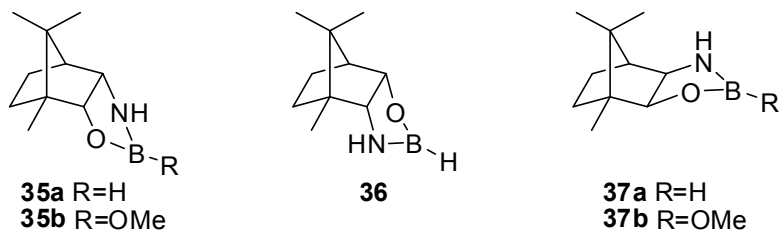


Figure 3.

Oxazaborolidines **35-37** (10 mol %) generated in situ were used in asymmetric reduction of prochiral ketones with borane-dimethylsulfide adduct in tetrahydrofuran at room temperature (Table 4). *B-H* Oxazaborolidine **35a**, obtained from 3-*endo*-aminoborneol **32**, furnished the best enantioselectivities for the reduced ketones. In contrast to previous results, catalyst **35b** gave product alcohols with lower enantiomeric excess. Almost total lack of selectivity was observed for **36**, which was explained based on steric factors. Coordination of borane to the nitrogen in **36** is difficult because of the proximity of the methyl group. Product alcohols with the opposite configuration were received, when the reaction was catalyzed by oxazaborolidine **37** generated from the *cis-exo-exo* amino alcohol **33**.

Table 4. Enantioselective reduction of ketones catalyzed by oxazaborolidines **35-37**.

Ketone	Catalyst	Yield, %	Ee, %	Config.
Acetophenone	35a	84	93	<i>R</i>
	35b	86	78	<i>R</i>
	36	71	2	<i>S</i>
	37a	94	79	<i>S</i>
	37b	70	56	<i>S</i>
Propiophenone	35a	93	86	<i>R</i>
	35b	90	43	<i>R</i>
	36	88	0.7	<i>R</i>
	37a	70	68	<i>S</i>
	37b	83	41	<i>S</i>
1-Tetralone	35a	95	74	<i>R</i>
	35b	97	71	<i>R</i>
	36	81	8	<i>S</i>
	37a	98	63	<i>S</i>
	37b	91	47	<i>S</i>

2-Acetonaphthone	35a	78	90	<i>R</i>
	35b	74	68	<i>R</i>
	36	81	0.9	<i>S</i>
	37a	85	78	<i>S</i>
	37b	63	50	<i>S</i>
2-Octanone	35a	73	85	<i>R</i>
	35b	70	58	<i>R</i>
	36	69	9	<i>S</i>
	37a	88	69	<i>S</i>
	37b	79	62	<i>S</i>

Similarly to previous results for oxazaborolidines **11** and **12** (Table 1), *N*-substituted amino alcohols **38**, **39** and **40** (R = Ph, 1-Napht) (Figure 4), applied for the in situ generation of oxazaborolidines, yielded product alcohols with low enantioselectivities.²⁸

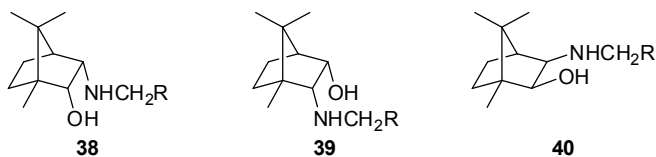
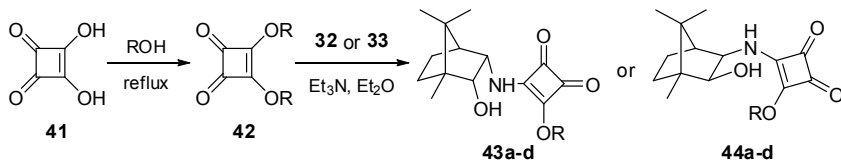


Figure 4.

Xie et al. has utilized squaric acid (**41**) to modify aminoalcohols **32** and **33**.²⁹ Squaric acid **41**, being an aromatic four-membered cyclic compound with highly acidic hydroxyl groups, was converted into diesters **42** by refluxing in corresponding alcohols (**a**: EtOH, **b**: *n*-BuOH, **c**: *n*-C₆H₁₃OH, **d**: *n*-C₈H₁₇OH) (Scheme 12). In the next step, **42** has reacted with *cis*-*endo*-*endo* amino alcohol **32** and the *cis*-*exo*-*exo* amino alcohol **33** to give the corresponding squaramidoalcohols **43** and **44**.



Scheme 12.

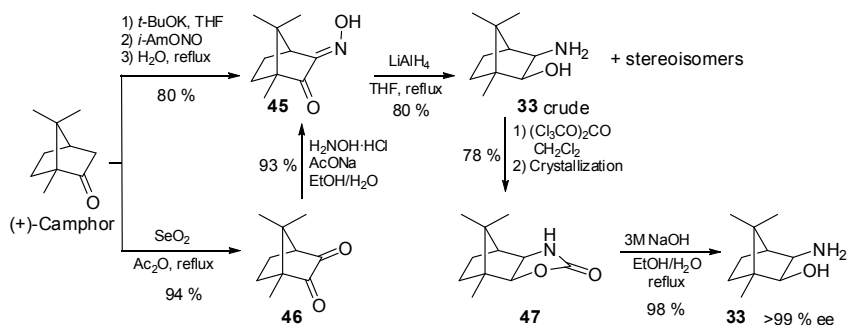
Squaramidoalcohols **43** and **44** were employed to the asymmetric reduction of prochiral ketones with borane. In the optimized reaction conditions, ligands (10 mol % of **43** or **44**) reacted with $\text{BH}_3 \cdot \text{SMe}_2$ (1.2 equiv.) in THF at 0 °C, followed by the addition of ketones carried out at 50 °C. The results are gathered in Table 5. ω -Bromoacetophenone was used to screen the activity of catalysts prepared from ligands **43** and **44**. *cis-endo-endo* Amino alcohol ligands **43** reduced ω -bromoacetophenone with higher enantiomeric excess than ligands **44**. The best ligand **43b** was applied to the reduction of alkyl-aryl ketones with borane. Enantioselectivities were moderate except α -halogenated ketones (Table 5).

Table 5. Asymmetric reduction of prochiral ketones using squaric amino alcohols.

Ketone	Ligand	Yield, %	Ee, %	Config.
ω -Bromoacetophenone	43a		95	<i>S</i>
	43b		99	<i>S</i>
	43c		94	<i>S</i>
	43d	>80	96	<i>S</i>
	44a		77	<i>R</i>
	44b		84	<i>R</i>
	44c		82	<i>R</i>
Acetophenone	43b	82	56	<i>R</i>
Propiophenone	43b	85	51	<i>R</i>
1-Tetralone	43b	87	54	<i>R</i>
2-Acetonaphthone	43b	91	35	<i>R</i>
ω -Chloroacetophenone	43b	81	93	<i>S</i>

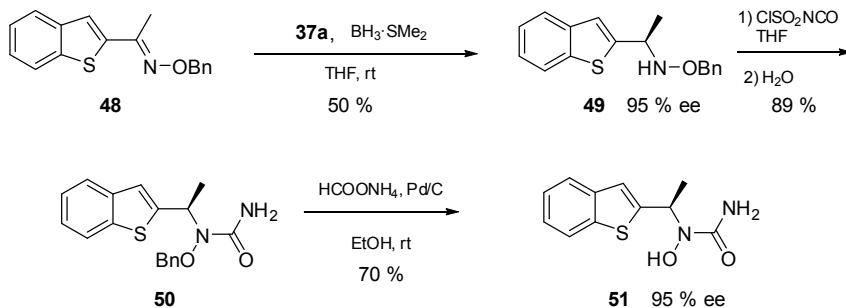
There are some examples of chiral amplification, but in all other asymmetric transformations chiral auxiliaries and catalysts must be optically pure in order to obtain the highest enantioselectivity of the stereoselective reactions. From the results presented above, it can be seen that (+)-camphor derived amino alcohols **32** and **33** were less selective in comparison with amino alcohols obtained from α - and β -pinene. In order to ensure the enantiomeric purity of amino alcohol **33**, Zaidlewicz et al. have developed the synthesis and purification of this compound (Scheme 13).²⁵

Camphoroquinone monooxime obtained either by nitrosation of camphor or oximation of camphoroquinone was a mixture of an *E/Z* isomers. The mixture was isomerized in refluxing water to pure *E*-oxime, and then it was reduced with lithium tetrahydridoaluminate. The crude **33** contained stereoisomeric impurities, which were removed after the formation of oxazolidone **47**. Alkaline hydrolysis furnished enantiomerically pure **33**.



Scheme 13.

Oxime *O*-benzyl ether **48**, readily prepared from 2-acetyl-benzo[*b*]thiophene via oxime and etherification, was reduced with borane/oxazaborolidine **37a** to produce hydroxylamine *O*-benzyl ether **49** with 95 % ee.²⁵ The subsequent reaction with chlorosulfonyl isocyanate gave *N*-benzyloxyurea **50**. (Scheme 14).



Scheme 14.

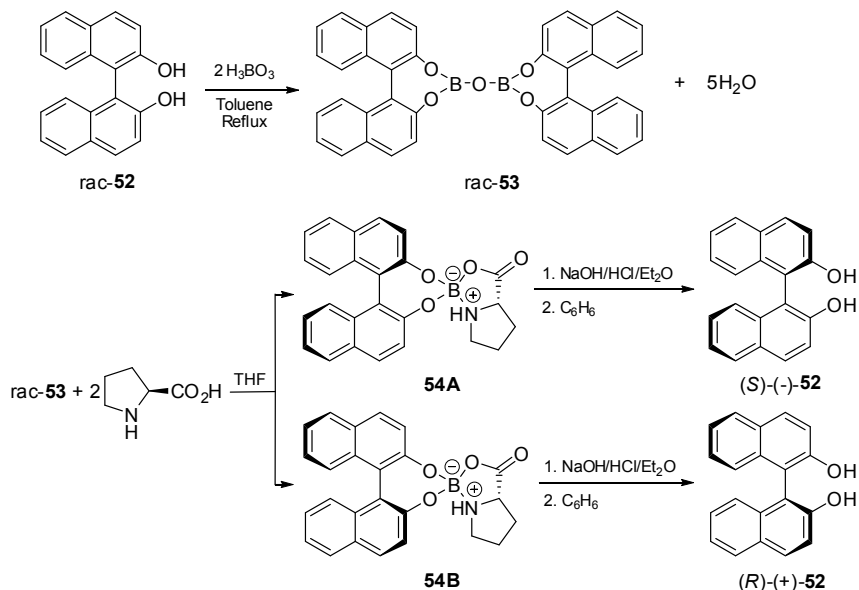
Debonylation of **50** was achieved with ammonium formate in the presence of Pd/C in ethanol. *N*-Hydroxyurea **51** is a chiral equivalent of Zileuton® a commercial anti-asthmatic and anti-inflammatory drug.

Asymmetric reductions with borane/spiroborate esters

Chiral spiroborate esters are a new class of boron compounds exhibiting a great potential as catalysts in modern asymmetric synthesis. What distinguish spiroboranes from well-known oxazaborolidines is an unique structure containing a characteristic O₃BN framework, where B-N bond is a coordinate

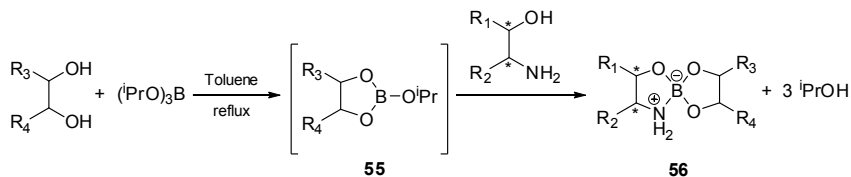
bond that implies a high stability of molecule towards moisture and air. Consequently, spiroboranes are easier to prepare, purify, store, and handle. This fact is a great advantage with respect to other organoborane catalysts, especially oxazaborolidines.

First chiral spiroborate esters were discovered by Shan as a simple and convenient method for the resolution of enantiomers of 1,1'-bi-2-naphthol (**rac-52**).³⁰ Shan and co-workers showed that the addition of racemic binaphthol to boric acid and (*S*)-proline in toluene under reflux conditions leads to obtain two new spiroaminoborate diastereoisomers (**54A** and **54B**), easy to separate, because one of them precipitated (**54A**), whereas the second remained in the solution (**54B**) (Scheme 15).^{30a}



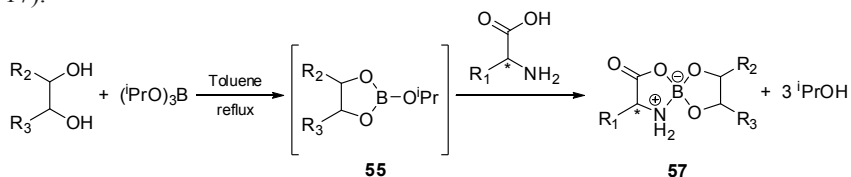
Scheme 15^{30a}.

Recently, two general pathways concerning the synthesis of spiroborate esters have been developed. One of them involves chiral 1,2-amino alcohols used in double transesterification of boric acid ester (Scheme 16).³¹⁻³⁷ What is really important, in the first step a diol is employed to create a 1,3,2-dioxaborolane **55**, which reacts with amino alcohol in toluene under reflux condition. It is necessary to distill out the isopropanol that is formed next to the main product **56**.



Scheme 16.

In the second method, instead of amino alcohol, amino acid is applied (Scheme 17).^{30-31, 38-40}



Scheme 17.

Both approaches lead to spiroborate esters almost quantitatively. Certain modification involving the use of trimethylborate instead 1,3,2-dioxaborolane **55** was proposed by Ortiz-Marciales group.³⁵ As a result also **58** structure-type spiroborane is available, but exists as a dimer (Figure 5).

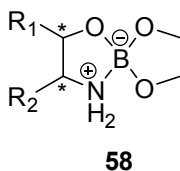


Figure 5.

Spiroborate esters derived from 1,2-amino alcohol as well as amino acid are highly effective and efficient catalysts for the asymmetric borane-mediated reduction of prochiral ketones^{31, 33-36, 41-43}, α -haloketones⁴⁴, and oxime ethers^{32, 39, 45, 46}. They are also successfully utilized in the asymmetric aldol condensation.³⁸ In particular, spiroborate ester synthesized from (S)-1,1-diphenylprolinol and ethylene glycol achieves outstanding stereoselectivity in the reduction of a large variety of arylalkyl and aromatic heterocyclic ketones^{34, 41-43}, comparable in their enantioselectivity to the CBS oxazaborolidine, whereas other, derived

from (S)-1,1-diphenylvalinol and ethylene glycol was found as a perfect catalyst for the asymmetric reduction of arylalkyl and heterocyclic O-benzyl oxime ethers^{32, 45-46}, giving the corresponding enantiopure primary amines and amino ethers. These two compounds were also employed in the syntheses of mexiletine^{43,45} and nicotine⁴⁶, and their analogues – a group of ligand-gated ion channel receptors playing a vital role in many biological processes, for example, neurotransmission. Additionally, because of their Lewis acid-base nature, spiroboranes can be applied as catalysts for other types of reaction, for example, the selective reduction of ketones, esters, and amides using *N,N*-diethylaniline-borane.⁴⁷ Moreover, they are notably useful as synthetic templates for further asymmetric transformations.^{40, 48}

Because nature still inspires a great number of chemists, in this part the attention is focused on a new class of spiroborate esters derived from α -pinene. This system offers an interesting alternative and a great potential for the borane-based catalytic asymmetric synthesis of enantiopure alcohols.

Obtained from (-)- α -pinene, enantiomerically pure (1*R*,2*R*,3*S*,5*R*)-3-amino-pinane-2-ol^{9, 11-12} (**2**) has led to the preparation of terpenyl spiroborate esters **61-66**³⁶, according to Scheme 16, by the reaction with ethylene glycol, propan-1,3-diol, pinacol, catechol, (1*S*,2*S*,3*R*,5*S*)-pinane-2,3-diol⁴⁹, and (1*R*,2*R*,3*S*,5*R*)-pinane-2,3-diol⁴⁹, respectively (Figure 6). Each terpenyl spiroborate ester was formed as a white precipitate with high yield, and indicated an excellent stability after being exposed to air for a short period of time. Furthermore, it could be readily stored under an inert atmosphere for prolonged periods.

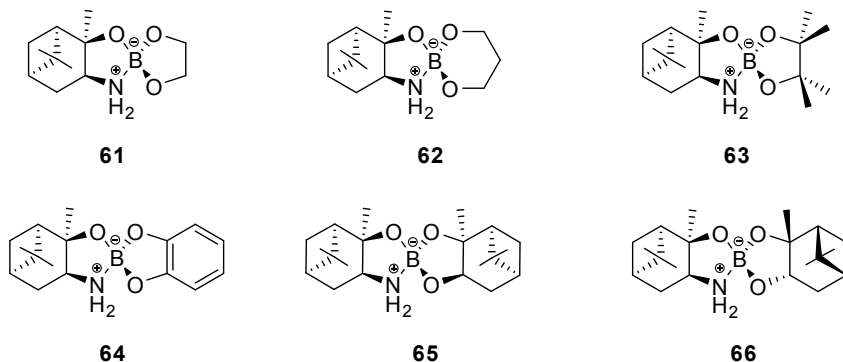


Figure 6.

In all cases ¹¹B NMR spectra recorded in THF-*d*₈ exhibited a characteristic singlet

between 4–12 ppm for the central boron atom that corresponds and confirms a unique O_3BN framework in the molecule of spiroborate ester. However, the presence of minor signals at 16,5 and 14,5 ppm, for **62** and **64** respectively, and for **61**, **63**, **65**, and **66** around 21 ppm, was also noticed. The reason for this phenomenon is the inherence of equilibrium between two co-existing forms: spiroborate and the borate lacking complexation between the nitrogen and boron atoms. Representative properties of terpenyl spiroborate esters **61–66** are summarized in Table 6.

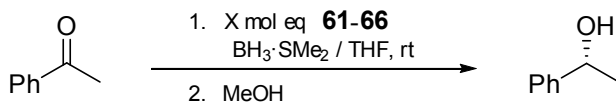
Table 6. Synthesis of terpenyl spiroborate esters **61–66**³⁶.

Spiroborate ester	Yield, %	Mp, °C	¹¹ B NMR ^{ab} , δ ppm	$[\alpha]_D^{20}$
61	84	161-163	8,44	+7,96 (c 1, THF)
62	54	147-150	3,83	-8,33 (c 1, THF)
63	87	221-224	7,26	+2,12 (c 0.9, THF)
64	85	200 (dec)	11,80	+31,8 (c 0.9, THF)
65	45	241-242	8,50	+12,3 (c 0.9, THF)
66	84	220-222	8,34	-14,7 (c 1, THF)

^{a)} Spectra were recorded in THF-*d*₈.

^{b)} Co-existing signals in the ¹¹B NMR spectra and their percentage: **610** (21.5 ppm, 3%), **62** (16,5 ppm, 36%), **63** (20,5 ppm, 8%), **64** (14,1 ppm, 4%), **65** (20,6 ppm, 13%), **66** (20,6 ppm, 45%).

Terpenyl spiroborate esters show a great catalytic activity in the asymmetric borane reduction of prochiral ketones.³⁶ Reduction of acetophenone as a model compound with 1 molar equivalent of borane-dimethyl sulfide adduct and 0,1, 0,05 and 0,01 molar equivalent of **61–66** as the catalyst in dry THF, at room temperature was very fast (<1 h) and always gave the corresponding (*R*)-1-phenylethanol almost quantitatively (Scheme 18, Table 7).



Scheme 18.

Table 7. Borane reduction of acetophenone catalyzed by terpenyl spiroborate esters **61-66**³⁶.

Entry	Cat.	X mol. eq. Cat.	Yield, % ^{a)}	Ee, % ^{b)}	Conf. ^{c)}
1	61	0,10	94	96	<i>R</i>
2	61	0,05	90	93	<i>R</i>
3	61	0,01	93	92	<i>R</i>
4	62	0,10	94	96	<i>R</i>
5	62	0,05	92	81	<i>R</i>
6	62	0,01	92	66	<i>R</i>
7	63	0,10	90	92	<i>R</i>
8	64	0,10	88	7	<i>R</i>
9	65	0,10	86	95	<i>R</i>
10	65	0,05	91	86	<i>R</i>
11	66	0,10	94	90	<i>R</i>
12	66	0,05	90	88	<i>R</i>

^{a)} Isolated yield.

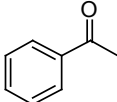
^{b)} Determined by GC analysis on a chiral column, Supelco β -DEX 325TM, 30 m \times 0.25 mm.

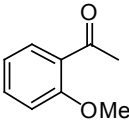
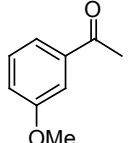
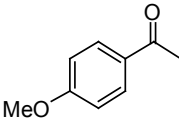
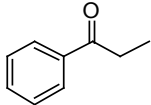
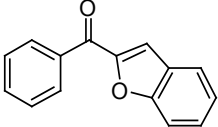
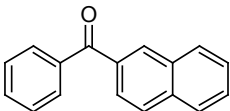
^{c)} The *R* configuration was assigned by comparison of the rotation with the literature data.

As it is presented in Table 7, the best results for this type of reaction indicated spiroborate ester **61**. Even decreasing catalyst loading from 0,1 to 0,01 molar equivalent the enantiomeric excess of the product still remained above 90% (Table 7, entries 1-3). It seems that only the size of the diol moiety and not its chirality is an important factor in these reductions. The change of the diol part in the spiroborate ester molecule did not affect the configuration of the product alcohol. The chiral pinane diols exerted only a small effect on the enantioselectivity of the reduction (Table 7, entries 9-12), whereas applying catechol moiety caused almost total lack of selectivity for the catalyst **64** (Table 7, entry 8).

Further studies have led to employ spiroborate ester **61** in the borane reduction of other prochiral ketones (Table 8).³⁶

Table 8. Borane reduction of prochiral ketones catalyzed by spiroborate ester **61**³⁶.

Entry	Ketone	61 (x eq. mol.)	Yield, % ^{a)}	Ee, %	Conf. ^{d)}
1		0,10	94	96 ^{b)}	<i>R</i>
		0,05	90	93	

2		0,10 0,05	91 92	93 ^{b)} 90	<i>R</i>
3		0,10 0,05	88 93	98 ^{b)} 95	<i>R</i>
4		0,10 0,05	91 97	97 ^{b)} 96	<i>R</i>
5		0,10 0,05	94 93	92 ^{b)} 90	<i>R</i>
6		0,10 0,05	95 91	65 ^{c)} 60	— ^{c)}
7		0,10	87	4 ^{c)}	— ^{c)}

^{a)} Isolated yield.

^{b)} Determined by GC analysis on a chiral column, Supelco β -DEX 325TM, 30 m \times 0,25 mm.

^{c)} Determined by HPLC analysis on a chiral column, Daicel Chiralcel OD-H, 250 mm \times 4.6 mm, 5 μ m.

^{d)} Assigned by comparison of the sign of rotation with literature data.

^{e)} Absolute configuration not determined.

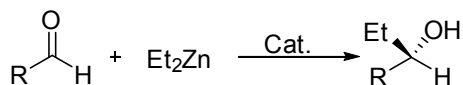
The corresponding optically active alcohols were obtained in excellent yields and with high enantiomeric excess, aside from slightly worse for benzofuran-2-yl-(phenyl)methanol and naphthalen-2-yl(phenyl)methanol (Table 8, entries 6-7).

Further studies concern on the new series of spiroborate esters derived from (1*R*,2*S*,3*R*,5*R*)-3-amino-6,6-dimethylbicyclo[3.1.1]heptan-2-ol (**16**) with

the particular diols: ethylene glycol, 1,4-anhydroerythritol, and cyclopentane-1,2-diol. These compounds offer a great catalytic activity in the enantioselective borane reduction of carbon-oxygen double bonds, but, what is more interesting, they can be also easily applied in the enantioselective borane reduction of carbon-nitrogen double bonds contained in *NH*-, arylalkyl, and cyclic imines, like dihydroisoquinoline systems, giving a number of corresponding optically active amines, among them salsolidine with enantiomeric excesses up to 97% ee.

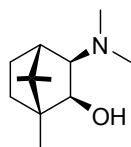
Enantioselective diethylzinc addition to aldehydes

The asymmetric dialkylzinc addition to aldehydes is a useful method to form a new C-C bond and to synthesize chiral secondary alcohols.⁵⁰ This reaction, catalyzed with optically active amino alcohols as effective chiral ligands, was discovered by Oguni et al. in 1983 (Scheme 19).⁵¹

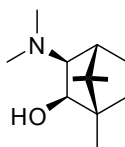


Scheme 19.

However, the first addition of diethylzinc to aldehydes with high enantiomeric excess was reported by Noyori et al. in 1986.⁵² They used (2*S*)-(-)-3-*exo*-(dimethylamino)isoborneol ((-)-DAIB) **67**, derived from natural camphor, as the catalyst to obtain (*S*)-product alcohols with high enantiomeric excess (61-98% ee) (Table 9). When the catalyst was changed to its enantiomer **68**, the addition of diethylzinc to benzaldehyde produced (*R*)-1-phenylpropanol in 98 % ee.⁵³



67 (-)-DAIB



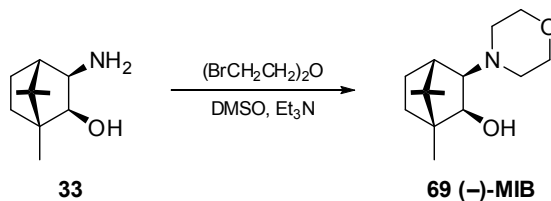
68 (+)-DAIB

Table 9. Enantioselective addition of diethylzinc to aldehydes catalyzed by 2 mol % of **1**.

Aldehyde	Time, h	Yield, %	Ee, % (config.)
Benzaldehyde	6	97	98 (<i>S</i>)
<i>p</i> -Chlorobenzaldehyde	12	86	93 (<i>S</i>)

<i>p</i> -Methoxybenzaldehyde	12	96	93 (<i>S</i>)
<i>E</i> -Cinnamaldehyde	6	81	96 (<i>S</i>)
3-Phenylpropanal	12	80	90 (<i>S</i>)
<i>n</i> -Heptanal	24	81	61 (<i>S</i>)

In 1999 Nugent presented a simple structural modification of DAIB (**67**), (2*S*)-(-)-3-*exo*-morpholinoisoborneol ((-)-MIB) (**69**) obtained in reaction of 3-*exo*-(amino)isoborneol **33** with bis-(bromoethyl)ether (Scheme 20).⁵⁴



Scheme 20.

Like DAIB, MIB catalyzed the enantioselective addition of diethylzinc to aldehydes with high enantiomeric excess (91-99 % ee) (Table 10). The author observed that during reactions detectable amounts of primary alcohols were formed and it depended on the type of aldehyde used: 2% or less for aromatic and primary aliphatic aldehydes, 5% or less for secondary aliphatic aldehydes and 38% for tertiary aldehyde – trimethylacetaldehyde.

Table 10. Enantioselective addition of diethylzinc to aldehydes catalyzed by **69**.

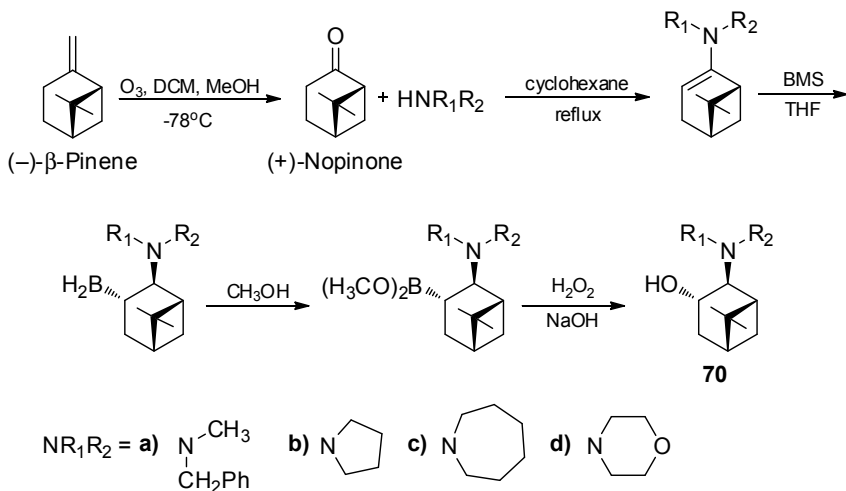
Aldehyde	MIB, %mol	Time, h	Yield, % ^a	Ee, % (config.) ^a
Benzaldehyde	2	3	98	98 (<i>S</i>)
<i>p</i> -Fluorobenzaldehyde	5	3	98	98 (<i>S</i>)
Hexanal	5	3	96	91 (<i>S</i>)
Isobutyraldehyde	5	3	94	99 (<i>S</i>)
2-Ethylbutyraldehyde	5	18	92	99 (<i>S</i>)
Trimethylacetaldehyde	5	24	62	97 (<i>S</i>)

^a Reaction was quenched by addition of Ac₂O which quantitatively converts the intermediate zinc alkoxides to the corresponding acetates

Comparing DAIB and MIB, it can be noted that the enantiomeric excess as well as the yield of diethylzinc addition to aldehydes are similar, but one of the

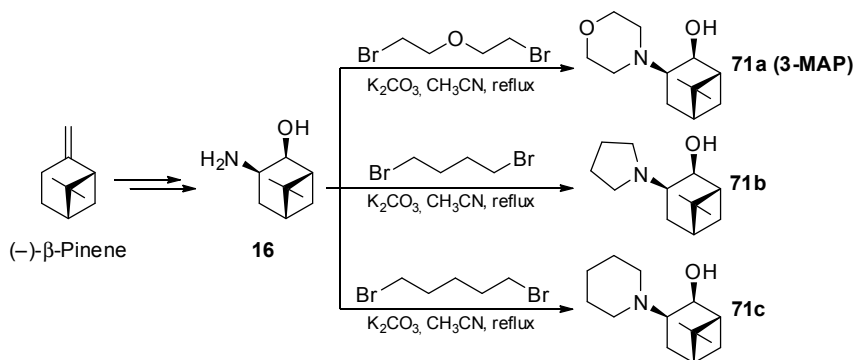
advantages that the crystalline nature of MIB imparts is greater air-stability than DAIB.⁵⁴

The results presented above show that the configuration of product is determined by the configuration of catalyst. In contrast to (–)-camphor, the precursor of (–)-DAIB and (–)-MIB, (+)-camphor occurs naturally. Consequently, exploration of other optically active natural monoterpenes has begun to find new chiral auxiliaries for dialkylzinc addition. One of these compounds with the possibility of wide application as a chiral auxiliaries is pinene. α -Pinene occurs naturally in both enantiomers (+)- and (–)- α -pinene, although (–)- β -pinene is the only natural product. Its derivative, (+)-nopinone is an important precursor to synthesize several amino alcohols, which formally are derived from (–)- β -pinene. Thus, research was carried out on β -amino alcohols from (–)- β -pinene. The application of *trans*- β -amino alcohols as chiral auxiliaries in diethylzinc addition to aldehydes was reported in 1997⁵⁵ and *cis*- β -amino alcohols in 2009⁵⁶. (1*R*,2*S*,3*S*,5*R*)-2-Dialkylamino-6,6-dimethylbicyclo[3.1.1]heptan-3-ols **70a-d** were obtained via the hydroboration/oxidation of the corresponding enamines of (1*R*,5*S*)-(+)-nopinone (Scheme 21).



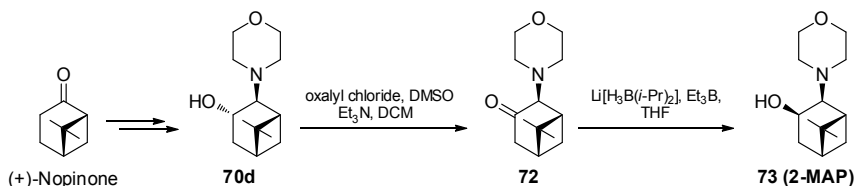
Scheme 21.

Cis-amino alcohols **71a-c** were obtained from amino alcohol **16**¹⁸ by the reaction with proper dibromoalkyl derivatives in the presence of K_2CO_3 in acetonitrile (Scheme 22). By this way authors got diastereoisomeric amino alcohol of **70d** – **71a** (**3-MAP**).



Scheme 22.

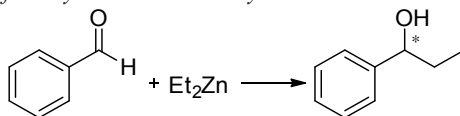
By the appropriate transformation of (+)-nopinone, *trans*-amino alcohol **70d** was prepared, which was oxidized using Swern methodology to obtain α -amino ketone **72**. Reduction of the carbonyl group in **72** with lithium diisopropylaminoborohydride (Li[H₃BN(*i*-Pr)₂], LAB reagent) in the presence of triethylborane greatly increased the reaction stereoselectivity giving amino alcohol **73** (2-MAP), which is a pseudo-enantiomer of **71a** (Scheme 23).



Scheme 23.

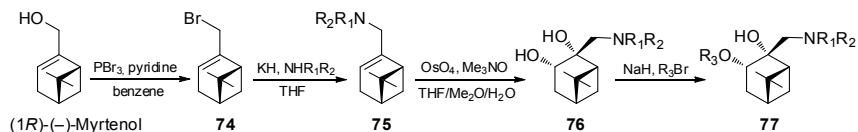
All (-)-β-pinene derivatives were applied in asymmetric diethylzinc addition to benzaldehyde (Table 11). These were utilized catalytically and have shown to be very effective catalysts. When the results from Table 11 are compared, it can be seen that *trans*-amino alcohols are less stereospecific catalysts than *cis*-amino alcohols. Compounds “2-amino-3-ols” **70a-d**, **73** provide the formation of secondary alcohols with *R* configuration, while “3-amino-2-ols” give *S*-alcohols.

Table 11. Addition of diethylzinc to benzaldehyde.



Amino alcohol, %mol	Temp, °C	Yield, %	Ee, %, (config)
70a (10)	0	95	80 (<i>R</i>)
70b (10)	0	95	76 (<i>R</i>)
70c (10)	0	95	70 (<i>R</i>)
70d (10)	0	89	58 (<i>R</i>)
71b (10)	0	99	84 (<i>S</i>)
71c (10)	0	99	87 (<i>S</i>)
71a (10)	0	99	86 (<i>S</i>)
71a (10)	-15 to 0	99	97 (<i>S</i>)
71a (8)	-15 to 0	98	97 (<i>S</i>)
71a (5)	-15 to 0	92	99 (<i>S</i>)
71a (1)	-15 to 0	97	96 (<i>S</i>)
73 (10)	-15 to 0	94	99 (<i>R</i>)

(1*R*)-(-)-Myrtenol has the same type of bicyclic structure as (-)- β -pinene and on its skeleton several β -amino alcohols were built utilizing simple transformations (Scheme 24).⁵⁷ Myrtenol was converted into the myrtenyl bromide **74**, followed by the substitution with potassium amides to tertiary amines **75**. Dihydroxylation gave diols of series **76**, which were further modified to monoethers **77**.



76	a	b	c	d	e	f	g	h	i	j
R₁	Ph	Ph	Ph	Ph	H	H	H	H	H	H
R₂	Me	Et	<i>n</i> -Bu	Ph	Ph	<i>o</i> -MePh	<i>o</i> - <i>n</i> PrPh	<i>o</i> - <i>t</i> PrPh	<i>o</i> - <i>t</i> BuPh	<i>o</i> -MeOPh

77 (R₁=H, R₂=Ph)	a	b	c	d
R₃	Me	Et	<i>n</i> -Pr	<i>n</i> -Bu

Scheme 24.

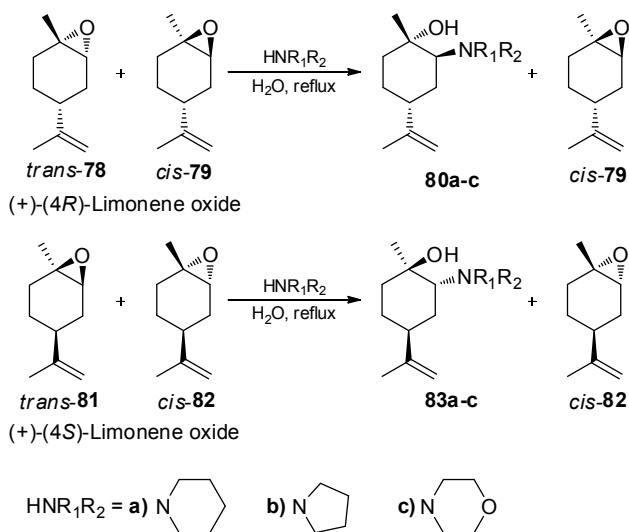
Ligands **76a-j** and **77a-d** were used in the addition of diethylzinc to benzaldehyde. The diol ligands **76a-j** gave (*S*)-1-phenylpropanol with higher yields and higher enantiomeric excess than the monohydroxy ligands **77a-d** (Table 12). Reaction was carried out at room temperature by using 2,2 equiv. of Et₂Zn and 2% mol of chiral auxiliaries. The reactions catalyzed by monohydroxy ligands **77a-d** provided *R* enantiomer of product, whereas that used diols **76a-j** gave (*S*)-1-phenylpropanol.

Table 12. Addition of diethylzinc to benzaldehyde catalyzed by **76** and **77**.

Amino alcohol	Yield, %	Ee, %, config
76a	85	82 (<i>S</i>)
76b	84	82 (<i>S</i>)
76c	83	88 (<i>S</i>)
76d	84	82 (<i>S</i>)
76e	87	37 (<i>S</i>)
76f	81	77 (<i>S</i>)
76g	77	69 (<i>S</i>)
76h	83	86 (<i>S</i>)
76i	84	84 (<i>S</i>)
76j	79	23 (<i>S</i>)
77a	60	9 (<i>R</i>)
77b	73	47 (<i>R</i>)
77c	68	50 (<i>R</i>)
77d	66	46 (<i>R</i>)

Another source of natural chirality is limonene, which is monocyclic monoterpene. (*R*)- and (*S*)-(+)-Limonene are very useful and not expensive precursors of readily available (*R*)- and (*S*)-(+)-limonene oxides. However, epoxidation of the endocyclic double bond has led to 1:1 mixture of *trans*- and *cis*-limonene oxides, which are difficult to separate. It is possible to conduct the epoxide ring opening reaction by secondary amines with water as catalyst to isolate diastereomerically pure β-amino alcohol **80** or **83** and unreacted *cis*-**79** or *cis*-**82** (Scheme 25).⁵⁸ This phenomena is caused by conformational differences in transition states.⁵⁹

β-Amino alcohols derived from (*R*)-(+)-limonene oxide and (*S*)-(+)-limonene oxide were utilized as chiral catalysts in the addition of diethylzinc to benzaldehyde to produce 1-phenyl-1-propanol with good yield and high enantiomeric excess with configuration dependent on the isomer of limonene (Table 13).



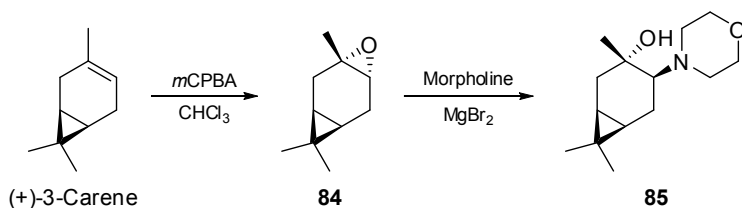
Scheme 25.

Table 13. Diethylzinc addition to benzaldehyde catalyzed by limonene derived β -amino alcohols.

β -Amino alcohol	Yield, %	Ee, % (config.)
80a	80	82 (<i>R</i>)
80b	80	85 (<i>R</i>)
80c	98	78 (<i>R</i>)
83a	88	87 (<i>S</i>)
83b	90	70 (<i>S</i>)
83c	98	80 (<i>S</i>)

(+)-3-Carene, which was mentioned earlier as a precursor of *cis*- β -amino alcohol **25**, was used for the synthesis of *trans*- β -amino alcohol. The reaction was completed in two steps. First, 3-carene reacted with *m*-chloroperbenzoic acid (*m*CPBA) to form carane epoxide **84** and then MgBr_2 induced, diastereoselective, nucleophilic ring opening of epoxide with morpholine into *trans*- β -amino alcohol **85** (Scheme 26).⁶⁰

β -Amino alcohol **85** was used as a chiral auxiliary for the enantioselective addition of diethylzinc to aldehydes (Table 14).⁶⁰



Scheme 26.

Table 14. The addition of diethylzinc to aldehydes catalyzed by **85**.

Aldehyde	Yield, %	Ee, % (config.)
Benzaldehyde	68	81 (<i>R</i>)
<i>o</i> -Chlorobenzaldehyde	68	73 (<i>R</i>)
<i>p</i> -Chlorobenzaldehyde	66	33 (<i>R</i>)
<i>o</i> -Methoxybenzaldehyde	76	98 (<i>R</i>)
<i>p</i> -Methoxybenzaldehyde	77	73 (<i>R</i>)
<i>E</i> -Cinnamaldehyde	69	75 (<i>R</i>)

Asymmetric reduction of ketones with modified lithium aluminum hydride

A number of asymmetric inductions were realized in the reduction of prochiral ketones using chirally modified lithium aluminum hydride reagents to obtain optically active secondary alcohols. In these reactions, the chiral reducing agent is prepared in situ by mixing a solution of LiAlH_4 in diethyl ether with chiral derivative of amino alcohol **77a-d**.^{57, 61} First, reducing agents were tested in asymmetric reduction of acetophenone to find the best conditions (Table 15). Then chiral auxiliary **77b**, which gave the highest enantiomeric excess, was checked in asymmetric reduction of aryl-methyl ketones (Table 16).

Table 15. LiAlH_4 reduction of acetophenone using chiral modifiers **77a-d**.

Amino alcohol	Yield, %	Ee, %, config
77a	83	48 (<i>R</i>)
77b	85	62 (<i>R</i>)
77c	85	47 (<i>R</i>)
77d	86	46 (<i>R</i>)

All aryl-methyl ketones were reduced with modified lithium tetrahydridoaluminate producing 1-arylethanol with high yields and moderate to high enantiomeric excess (Table 16).⁵⁷ The highest enantiomeric excess (91 % ee) was achieved in reduction of 2-methoxyacetophenone.

Table 16. Reduction of methyl ketones with LiAlH₄ and chiral modifier **77b**.

Ketone, R=	Yield, %	Ee, % (config.)
Ph	85	62 (R)
<i>o</i> -Tolyl	86	79 (R)
2-Bromophenyl	86	78 (R)
2-Chlorophenyl	86	78 (R)
2-Methoxyphenyl	86	91 (R)
2-Nitrophenyl	85	72 (R)
1-Naphtyl	93	80 (R)
2-Naphtyl	96	50 (R)
1-Cyclohexenyl	89	74 (R)

Summary

Concluding, monoterpenes derived β -amino alcohols are synthesized in enantiomerically pure form by simple methods in good yields. All can be readily employed as catalysts in the asymmetric borane reduction of prochiral ketones. They can also be applied in asymmetric addition of dialkyl zinc reagents to aldehydes. In discussed reactions, either reductions or additions high asymmetric induction can be achieved modifying the structure of the monoterpenes.

Acknowledgement

Authors acknowledge financial support from the Ministry of Science and Higher Education, Warsaw, grant 2683/B/H03/2010/38 (N N204 268338).

References

1. Ojima, I., *Catalytic asymmetric synthesis*, 2nd Ed. John Wiley & Sons, Inc.: New York, 2000.
2. Brown, H. C.; Ramachandran, P. V., *Acc. Chem. Res.* **1992**, 25, 16-24.

3. Ramachandran, P. V.; Krzemiński, M. P.; Reddy, M. V. R.; Brown, H. C., *Tetrahedron: Asymmetry* **1999**, *10*, 11-15.
4. Matteson, D. S., *Chem. Rev.* **1989**, *89*, 1535-1551.
5. Malhotra, S. V., *Tetrahedron: Asymmetry* **2003**, *14*, 645-647.
6. Zaidlewicz, M.; Krzemiński, M., *Tetrahedron Lett.* **1996**, *37*, 7131-7134.
7. Ager, D. J.; Prakash, I.; Schaad, D. R., *Chem. Rev.* **1996**, *96*, 835-875.
8. (a) Cho, B. T., *Tetrahedron* **2006**, *62*, 7621-7643; (b) Corey, E. J.; Helal, C. J., *Angew. Chem. Int. Edit.* **1998**, *37*, 1987-2012.
9. Burak, K.; Chabudziński, Z., *Pol. J. Chem.* **1978**, *52*, 1721-1727.
10. Masui, M.; Shioiri, T., *Tetrahedron* **1995**, *51*, 8363-8370.
11. Carlson, R. G.; Pierce, J. K., *J. Org. Chem.* **1971**, *36*, 2319-2324.
12. Markowicz, S. W.; Pokrzepowicz, K.; Karolak-Wojciechowska, J.; Czyłkowski, R.; Omelańczuk, J.; Sobczak, A., *Tetrahedron: Asymmetry* **2002**, *13*, 1981-1991.
13. Masui, M.; Shioiri, T., *Synlett* **1996**, 49-50.
14. Hobuss, D.; Baro, A.; Laschat, S.; Frey, W., *Tetrahedron* **2008**, *64*, 1635-1640.
15. Jones, D. K.; Liotta, D. C.; Shinkai, I.; Mathre, D. J., *J. Org. Chem.* **1993**, *58*, 799-801.
16. Masui, M.; Shioiri, T., *Synlett* **1997**, 273-274.
17. Wei, D. H.; Tang, M. S.; Zhao, J.; Sun, L.; Zhang, W. J.; Zhao, C. F.; Zhang, S. R.; Wang, H. M., *Tetrahedron: Asymmetry* **2009**, *20*, 1020-1026.
18. Krzemiński, M. P.; Wojtczak, A., *Tetrahedron Lett.* **2005**, *46*, 8299-8302.
19. Łączkowski, K. Z.; Pakulski, M. M.; Krzemiński, M. P.; Jaisankar, P.; Zaidlewicz, M., *Tetrahedron: Asymmetry* **2008**, *19*, 788-795.
20. (a) Brown, H. C.; Jadhav, P. K., *J. Org. Chem.* **1984**, *49*, 4089-4091; (b) Brown, H. C.; Prasad, J. V. N. V.; Zaidlewicz, M., *J. Org. Chem.* **1988**, *53*, 2911-2916.
21. (a) Malkov, A. V.; Pernazza, D.; Bell, M.; Bella, M.; Massa, A.; Teply, F.; Meghani, P.; Kocovsky, P., *J. Org. Chem.* **2003**, *68*, 4727-4742; (b) Lu, T. J.; Lin, C. K., *J. Org. Chem.* **2011**, *76*, 1621-1633.
22. Krzemiński, M. P.; PL Pat. Appl. 383483, 10.04.2007.
23. Łączkowski, K. Z.; Kmiecik, A.; Kozakiewicz, A., *Tetrahedron: Asymmetry* **2009**, *20*, 1487-1492.
24. Krzemiński, M. P.; Karczmarzka-Wódzka, A., *Manuscript in preparation*.
25. Bosiak, M. J.; Krzemiński, M. P.; Jaisankar, P.; Zaidlewicz, M.,

- Tetrahedron: Asymmetry* **2008**, *19*, 956-963.
26. (a) Daniel, A.; Pavia, A. A., *Bull. Soc. Chim. Fr.* **1971**, 1060-1073; (b) Chittenden, R. A.; Cooper, G. H., *J. Chem. Soc. C* **1970**, 49-54.
 27. Santhi, V.; Rao, J. M., *Tetrahedron: Asymmetry* **2000**, *11*, 3553-3560.
 28. Santhi, V.; Rao, J. M., *Synthetic Commun.* **2000**, *30*, 4329-4341.
 29. Zou, H. H.; Hu, J.; Zhang, J.; You, J. S.; Ma, D.; Lu, D.; Xie, R. G., *J. Mol. Catal. A: Chem.* **2005**, *242*, 57-61.
 30. (a) Shan, Z. X.; Xiong, Y.; Zhao, D. J., *Tetrahedron* **1999**, *55*, 3893-3896; (b) Shan, Z. X.; Xiong, Y.; Li, W. Z.; Zhao, D. J., *Tetrahedron: Asymmetry* **1998**, *9*, 3985-3989.
 31. Liu, D. J.; Shan, Z. X.; Zhou, Y.; Wu, X. J.; Qin, J. G., *Helv. Chim. Acta.* **2004**, *87*, 2310-2317.
 32. Huang, X. G.; Ortiz-Marciales, M.; Huang, K.; Stepanenko, V.; Merced, F. G.; Ayala, A. M.; Correa, W.; De Jesus, M., *Org. Lett.* **2007**, *9*, 1793-1795.
 33. Stepanenko, V.; Ortiz-Marciales, M.; Correa, W.; De Jesus, M.; Espinosa, S.; Ortiz, L., *Tetrahedron: Asymmetry* **2006**, *17*, 112-115.
 34. Stepanenko, V.; De Jesus, M.; Correa, W.; Guzman, I.; Vazquez, C.; de la Cruz, W.; Ortiz-Marciales, M.; Barnes, C. L., *Tetrahedron Lett.* **2007**, *48*, 5799-5802.
 35. Stepanenko, V.; Ortiz-Marciales, M.; Barnes, C. L.; Garcia, C., *Tetrahedron Lett.* **2009**, *50*, 995-998.
 36. Krzemiński, M. P.; Ćwiklińska, M., *Tetrahedron Lett.* **2011**, *52*, 3919-3921.
 37. Stepanenko, V.; de Jesus, M.; Garcia, C.; Barnes, C. L.; Ortiz-Marciales, M., *Tetrahedron Lett.* **2012**, *53*, 910-913.
 38. Zhou, Y.; Shan, Z. X., *Tetrahedron* **2006**, *62*, 5692-5696.
 39. Chu, Y. B.; Shan, Z. X.; Liu, D. J.; Sun, N. N., *J. Org. Chem.* **2006**, *71*, 3998-4001.
 40. Zhou, Y.; Shan, Z. X.; Wang, B. S.; Xie, P., *Organometallics* **2006**, *25*, 4917-4919.
 41. Stepanenko, V.; De Jesus, M.; Correa, W.; Guzman, I.; Vazquez, C.; Ortiz, L.; Ortiz-Marciales, M., *Tetrahedron: Asymmetry* **2007**, *18*, 2738-2745.
 42. Stepanenko, V.; De Jesus, M.; Correa, W.; Bermudez, L.; Vazquez, C.; Guzman, I.; Ortiz-Marciales, M., *Tetrahedron: Asymmetry* **2009**, *20*, 2659-2665.
 43. Huang, K.; Ortiz-Marciales, M.; Correa, W.; Pomales, E.; Lopez, X. Y., *J. Org. Chem.* **2009**, *74*, 4195-4202.

44. Huang, K.; Wang, H. Y.; Stepanenko, V.; De Jesus, M.; Torruellas, C.; Correa, W.; Ortiz-Marciales, M., *J. Org. Chem.* **2011**, *76*, 1883-1886.
45. Huang, K.; Ortiz-Marciales, M.; Stepanenko, V.; De Jesus, M.; Correa, W., *J. Org. Chem.* **2008**, *73*, 6928-6931.
46. Huang, K.; Merced, F. G.; Ortiz-Marciales, M.; Melendez, H. J.; Correa, W.; De Jesus, M., *J. Org. Chem.* **2008**, *73*, 4017-4026.
47. Coleridge, B. M.; Angert, T. P.; Marks, L. R.; Hamilton, P. N.; Sutton, C. P.; Matos, K.; Burkhardt, E. R., *Tetrahedron Lett.* **2010**, *51*, 5973-5976.
48. Zhou, Y.; Shan, Z. X., *Tetrahedron Lett.* **2007**, *48*, 3531-3534.
49. Ray, R.; Matteson, D. S., *Tetrahedron Lett.* **1980**, *21*, 449-450.
50. (a) Lurain, A. E.; Carroll, P. J.; Walsh, P. J., *J. Org. Chem.* **2005**, *70*, 1262-1268; (b) Noyori, R., *Asymmetric Catalysis in Organic Chemistry*. Wiley: New York, 1994; (c) Nugent, W. A., *Org. Lett.* **2002**, *4*, 2133-2136.
51. (a) Oguni, N.; Omi, T., *Tetrahedron Lett.* **1984**, *25*, 2823-2824; (b) Oguni, N.; Omi, T.; Yamamoto, Y.; Nakamura, A., *Chem. Lett.* **1983**, 841-842.
52. Kitamura, M.; Suga, S.; Kawai, K.; Noyori, R., *J. Am. Chem. Soc.* **1986**, *108*, 6071-6072.
53. Goldfuss, B.; Houk, K. N., *J. Org. Chem.* **1998**, *63*, 8998-9006.
54. Nugent, W. A., *Chem. Commun.* **1999**, 1369-1370.
55. Goralski, C. T.; Chrisman, W.; Hasha, D. L.; Nicholson, L. W.; Rudolf, P. R.; Zakett, D.; Singaram, B., *Tetrahedron: Asymmetry* **1997**, *8*, 3863-3871.
56. Binder, C. M.; Bautista, A.; Zaidlewicz, M.; Krzemiński, M. P.; Oliver, A.; Singaram, B., *J. Org. Chem.* **2009**, *74*, 2337-2343.
57. Cherng, Y. J.; Fang, J. M.; Lu, T. J., *J. Org. Chem.* **1999**, *64*, 3207-3212.
58. (a) Chrisman, W.; Camara, J. N.; Marcellini, K.; Singaram, B.; Goralski, C. T.; Hasha, D. L.; Rudolf, P. R.; Nicholson, L. W.; Borodychuk, K. K., *Tetrahedron Lett.* **2001**, *42*, 5805-5807; (b) Steiner, D.; Sethofer, S. G.; Goralski, C. T.; Singaram, B., *Tetrahedron: Asymmetry* **2002**, *13*, 1477-1483.
59. Raban, M.; Burch, D. L.; Hortelano, E. R.; Durocher, D.; Kost, D., *J. Org. Chem.* **1994**, *59*, 1283-1287.
60. Joshi, S. N.; Deshmukh, A. R. A. S.; Bhawal, B. M., *Tetrahedron: Asymmetry* **2000**, *11*, 1477-1485.
61. Cherng, Y. J.; Fang, J. M.; Lu, T. J., *Tetrahedron: Asymmetry* **1995**, *6*, 89-92.

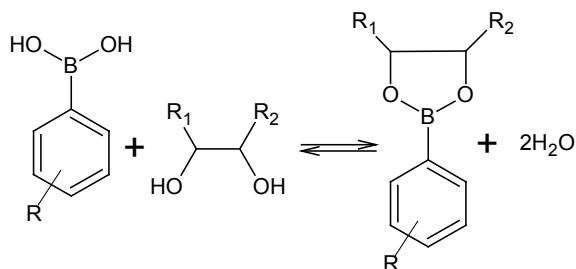
Chapter 9

Recent development in the chemistry of *ortho*-aminomethylphenylboronic acids

Alicja Pawełko, Agnieszka Adamczyk-Woźniak and Andrzej Sporzyński
*Warsaw University of Technology, Faculty of Chemistry,
Noakowskiego 3, 00-664 Warsaw, Poland*

Introduction

Arylboronic acids are systems that attract an increasing scientific interest due to their new applications in organic synthesis, catalysis, supramolecular chemistry, biology, medicine and material engineering ¹. Phenylboronic acids and their esters (Scheme 1) are widely used in many fields of science such as organic chemistry ², supramolecular chemistry ³, electrochemistry ⁴ and material science ⁵. Esterification reaction of phenylboronic acids is also investigated according to its usefulness in medicine ^{6,7} and industry ⁸.

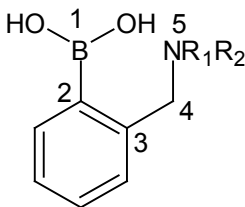


Scheme 1. Reversible formation of cyclic esters by phenylboronic acids.

Saccharides are fundamental to regulate metabolic pathways and are responsible for the cell-cell recognition and several biological responses. The interaction between cellular receptors and cell surface carbohydrates has been connected with metastatic diseases. Furthermore, the detection of blood sugar levels is one of the global challenges. D-glucose,

D-fructose, D-galactose are biologically important compounds. Especially significant is glucose due to the role in human metabolism. Improper level of this sugar can cause diabetes, hypoglycemia or syndrome x. It is said that 285 million people have diabetes and by 2030, this number is estimated to almost double. The most important factor in this disease is keeping the blood sugar range normal. Boronic acids are potential solution for fast and non-invasive determination of glucose. They are very important group of chemical receptors due to the strong covalent binding of sugar molecules, high stability and low toxicity. Binding constants (K) with monoboronic acids increases in the following order: D-glucose < D-galactose < D-fructose⁹. Hence, the majority of monoboronic acids have poor selectivity as well as sensitivity for glucose. Two receptors unit are required for selective glucose binding^{10,11}.

Phenylboronic acids with aminomethyl substituent at *ortho* position of the phenylboronic group (**I**, Fig. 1) play the special role due to their increased binding at neutral pH that influences the sugar sensitivity.



I

Fig. 1. *ortho*-Aminomethylphenylboronic acids.

This class of compounds was described as early as in 1982 by Wulff¹² and such compounds are often called “Wulff-type receptors” or “1–5 systems” according to atoms arrangement.

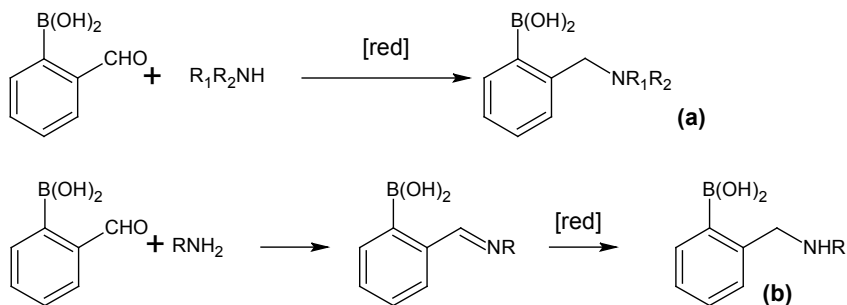
There is a huge number of papers dealing with synthesis, structure, and, first of all, applications of this class of compounds. In the present series of monographs three chapters on this subject have been already published. The first, general one, described all the classes of boronic receptors of sugars and mechanisms of the detection¹³. The second one concerned the synthetic methods, in which the compounds **I** were the most numerous group¹⁴. The third one was devoted to the structures of only one particular group: *ortho*-aminomethylphenylboronic acids¹⁵.

The aim of the present review is to discuss the newest papers published in the last 5 years, which have not been covered by the above-mentioned materials. It is divided to three parts: synthesis, structure and applications of *ortho*-aminomethylphenylboronic acids.

Synthesis

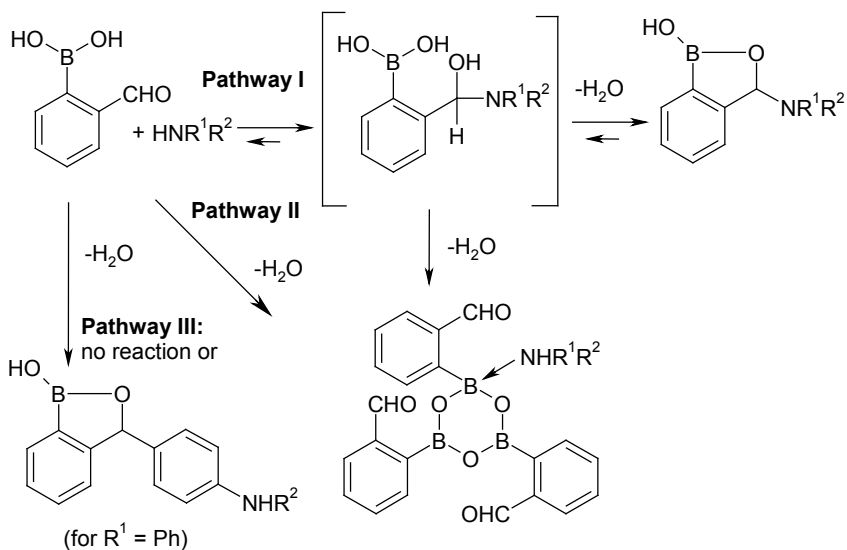
Amination-reduction reaction – simple and versatile, sometimes tricky.

The most common method of the synthesis of *ortho*-aminomethylphenylboronic acids is the amination-reduction reaction between *o*-formylphenylboronic acids and secondary amines. This reaction can be realized with the use of various reducing agents and leads to the products containing tertiary amino group (Scheme 2a). In the reaction with primary amines followed by reduction secondary amines are obtained as the product (Scheme 2b).



Scheme 2. Synthesis of *ortho*-aminomethylphenylboronic acids by amination-reduction reaction (a) or sequential Schiff base formation – reduction (b).

Although this method is well established, this reaction was recently further investigated. It was found, that in the reaction of 2-formylphenylboronic acid with secondary amines different products are formed depending on the structure of the amines. For aliphatic amines the reaction proceeds with the formation of 3-amino-substituted benzoxaboroles or with the formation of complexed boroxines (Scheme 3) ¹⁶.

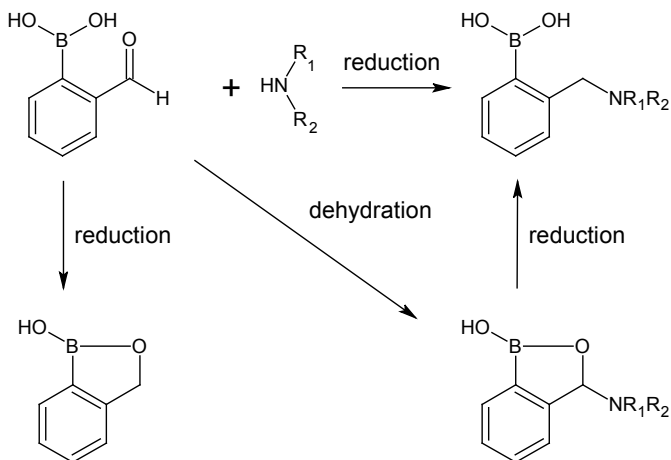


Scheme 3. Reactions of 2-formylphenylboronic acid with secondary amines.

Since 3-amino-substituted benzoxaboroles have been identified as intermediates in the synthesis of *o*-aminomethylphenylboronic acids, their formation is crucial in the amination-reduction reactions. The unsubstituted benzoxaborole has been identified as a by-product, resulting from fast reduction of 2-formylphenylboronic acid. To obtain the highest yields of the desired product, *o*-aminomethylphenylboronic acid, reaction conditions of amination-reduction have been optimized to diminish the formation of undesired product, unsubstituted benzoxaborole^{17,18} (Scheme 4).

The decrease of temperature from 65°C to -10°C resulted in 84% of isolated yield of the desired product (51% at 65°C)¹⁸. The following derivatives of aliphatic amines have been recently synthesized in the amination-reduction reaction of 2-formylphenylboronic acid^{19,20} (Fig. 2).

Adoption of the appropriate reaction conditions influences the reactivity of 2-formylphenylboronic acid with aromatic amines, enabling efficient synthesis of so far unobtainable 2-(arylaminoethyl)phenylboronic compounds. Satisfying results, with the yield more than 38%, were achieved after careful examination of reaction parameters such as solvent, reducing agent, temperature, catalyst, dehydrating agent, reaction temperature, and molar ratio of the reagents (Fig. 3)²¹.



Scheme 4. Products formed in the amination-reduction reaction.

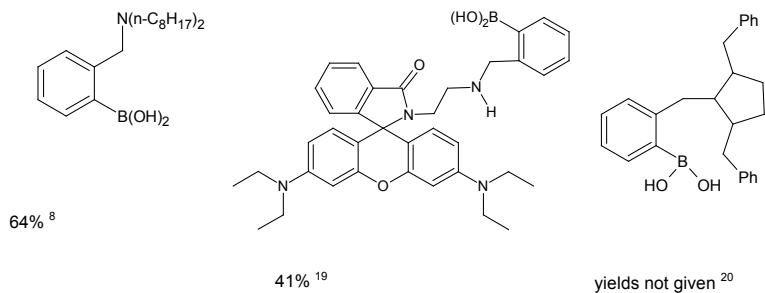


Fig. 2. Compounds obtained in the amination-reduction reaction.

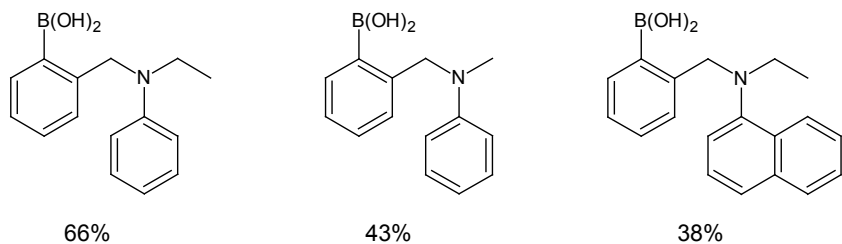
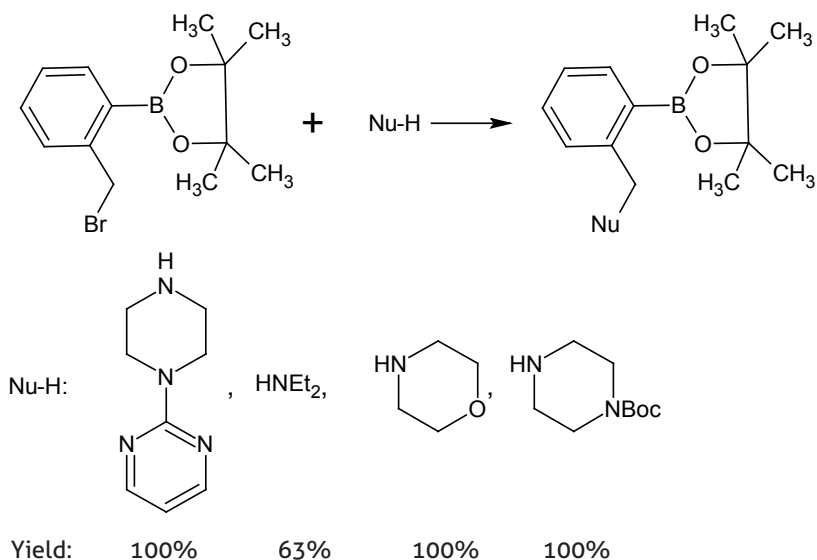


Fig. 3. Recently obtained aromatic amine derivatives²¹.

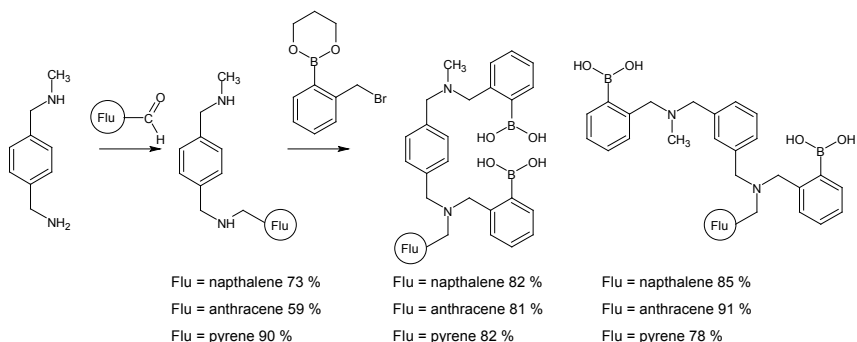
Nucleophilic substitution of benzyl bromides

Improvement of the synthesis of aminomethylphenylboronic acids has been recently achieved by the application of microwave irradiation instead of refluxing reaction mixture for several hours. The pinacol esters of aminomethylphenylboronic have been obtained in the reaction of the appropriate bromobenzyl bromide with secondary amines in high yields (63-100%) and short reaction time (15 min) (Scheme 5)²². It should be noted that authors do not mention any attempts of cleavage of the obtained pinacol esters resulting in the corresponding acids.



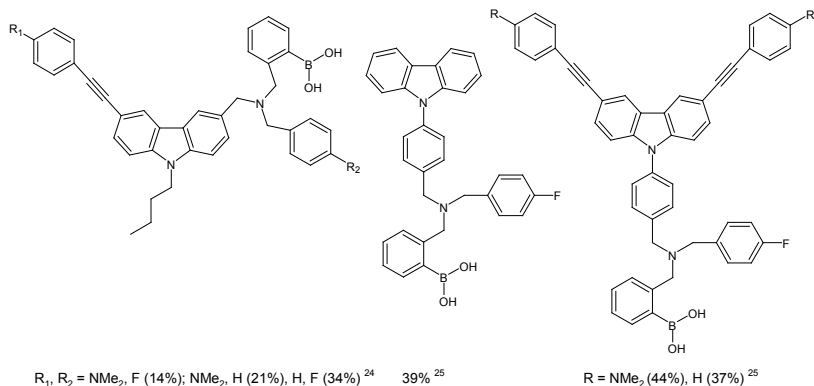
Scheme 5. Synthesis of *o*-aminomethylphenylboronic acids via MW-mediated reaction.

Boronic esters of benzyl bromides have been reacted with secondary benzylamines to give the corresponding *o*-aminomethylphenylboronic acids. Analogous transformations of *meta* benzyl amines resulted in the corresponding diboronic acids in high yields (Scheme 6)²³.



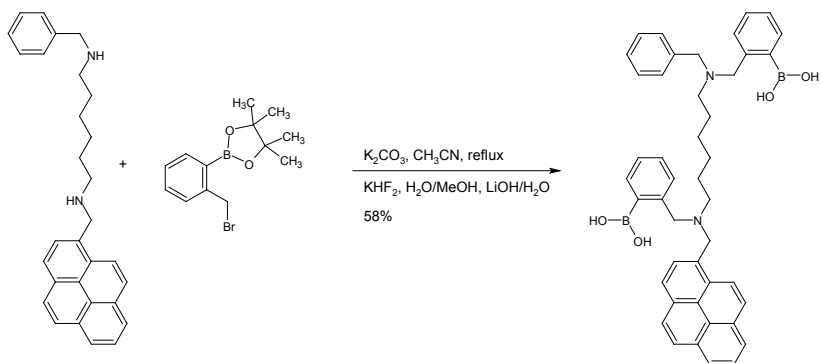
Scheme 6. Synthesis of fluorescent receptors by nucleophilic substitution of benzyl bromides.

The bromobenzyl boronic acid ester has been applied in the synthesis of several other *o*-aminomethylphenylboronic acids^{24,25} (Fig. 4).



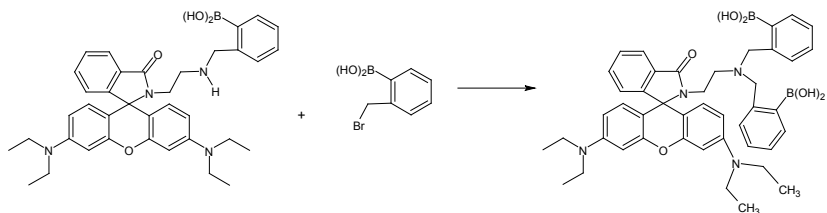
*Fig 4. Synthesized substituted *o*-aminomethylphenylboronic acids.*

Bromobenzyl pinacol phenylboronic ester has been applied in alkylation of secondary amine resulting in diboronic acid fluorescent sensor (Scheme 7)²⁶.



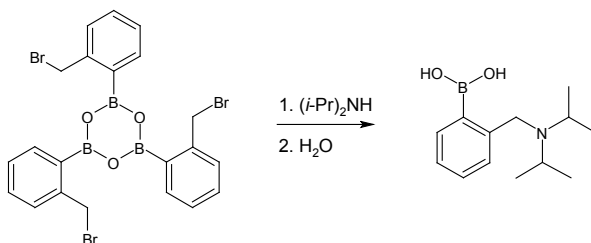
Scheme 7. Synthesis of the diboronic sensor, containing *o*-aminomethylphenylboronic moiety.

Alkylation of the secondary *o*-aminomethylphenylboronic acids with boronic benzyl bromide resulted in diboronic acid¹⁹ (Scheme 8).



Scheme 8. Alkylation of *o*-aminomethylphenylboronic acid.

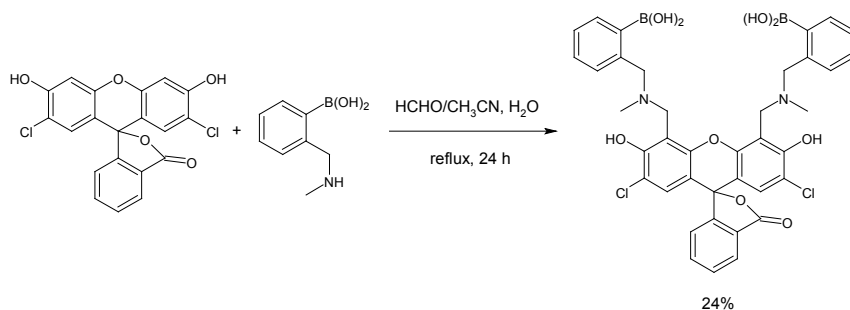
Boroxins have been also applied in the nucleophilic substitution with secondary amines resulting in the corresponding *o*-aminomethylphenylboronic acid (Scheme 9). Authors report no yield²⁷.



Scheme 9. Synthesis of *o*-aminomethylphenylboronic acid starting from boroxine bromide.

Other synthetic methods

2,7-Dichlorofluorescein derivative has been obtained by a Mannich reaction with 2-methylaminomethylphenylboronic acid in 24% yield (Scheme 10)²⁸.



Scheme 10. Synthesis of *o*-aminomethyl fluorescein derivative.

Several complex receptors containing *o*-aminomethyl moiety have been lately obtained in multistep processes with moderate yields^{7,29,30}. Some of them display chirality³¹ (Fig. 5).

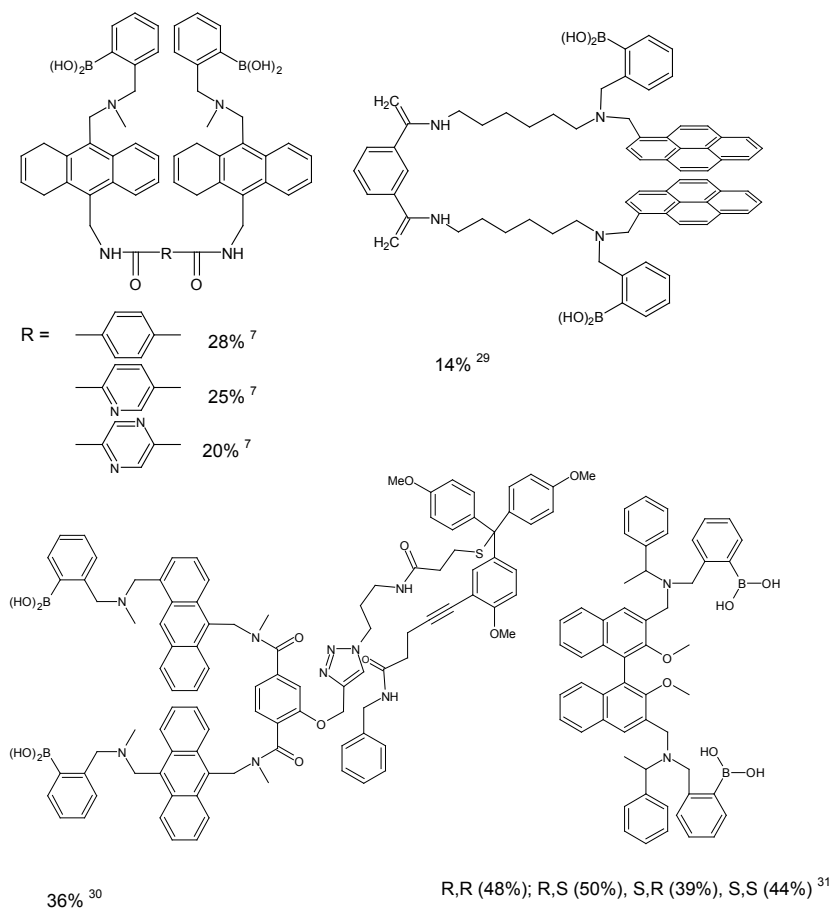


Fig. 5. Complex molecules containing *o*-aminomethylphenylboronic moiety.

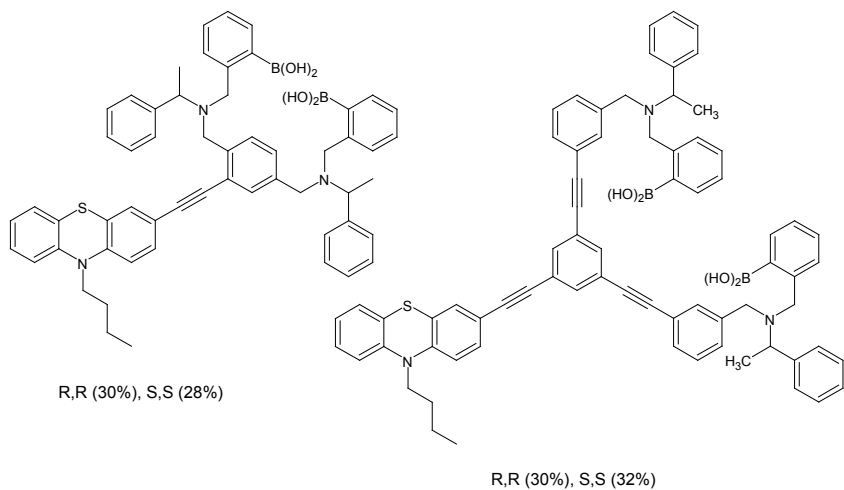
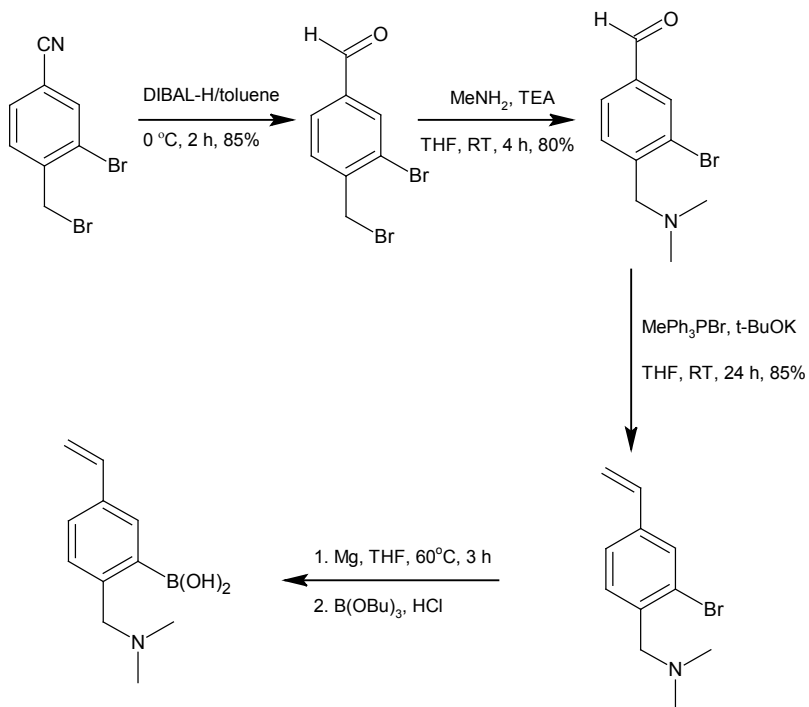


Fig. 6. Chiral *o*-aminomethylphenylboronic acids sensors.

Multistep synthesis resulted in a *para*-vinylic phenylboronic acid (Scheme 11), that was subjected to polymerization resulting in polymers containing the *o*-aminomethylphenylboronic acid moiety (Fig. 7)³³.



Scheme 11. Synthesis of *para*-vinylic phenylboronic acid.

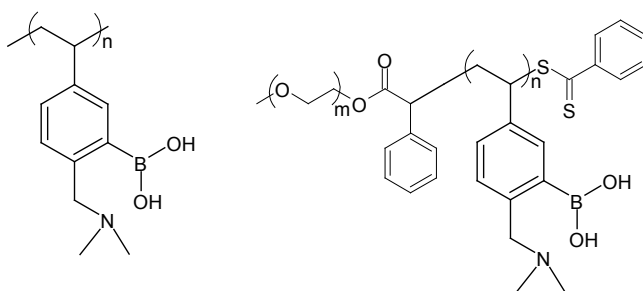


Fig. 7. Polymers containing *o*-aminomethylphenylboronic acid moiety.

Structures – not so simple as it appears...

In the review published in 2008¹⁵ structures of *ortho*-amino- and *ortho*-iminomethylphenylboronic acids, esters and boroxines have

been described and discussed. On the basis of the crystallographic data, it was found, that in the case of acids, formation of B-O-H...N bond is observed, whereas in the case of their esters the N→B bond is formed. For 9 structures of acids described in the literature, the average O-H...N distance is equal to 2.669 Å (range from 2.559 to 2.899 Å), which proves the formation of an intramolecular hydrogen bond. In this case, the N-B distance is much higher (more than 3 Å), which precludes formation of the dative N-B bond. For the 11 reported esters' structures, the average N-B distance is equal to 1.710 Å, which is characteristic for the dative bond. Dative bond is also present in the boroxines, with the examples of one, two or three such bonds formed in the boroxine molecule. There are however some exceptions:

1. In case of bulky substituents in aminomethyl group, steric hindrance disables the formation of intramolecular dative bond. Unfavorable arrangement of the donor atoms can also cause the lack of intramolecular coordination³⁴⁻³⁸.
2. For the compounds with amido group, the dative O→B bond is formed instead of the N→B one as it is energetically favorable (length *ca.* 1.5 Å)^{39,40}.

The comparison of the calculated energies of possible structures of *ortho*-iminomethylphenylboronic acids (A,B) and *ortho*-aminomethylphenylboronic acids (C, D, E) (Fig. 8) were recently carried out⁴¹.

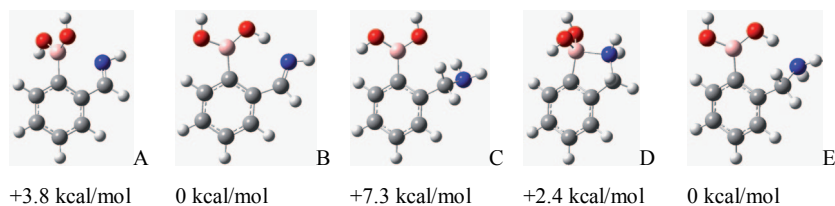


Fig. 8. Energy differences for the particular structures, related to the lowest energy forms.

The calculations on the MP2/6-31+G** level proved that both aminomethyl- and iminomethylphenylboronic acids are stabilized by intramolecular hydrogen bonds involving hydroxyl fragment at boronic group and nitrogen atom in β position of the substituent at *ortho* position. However, due to small difference in energy between possible forms, the structures with the N→B dative bond may exist in solution, gas phase, and although other polymorphs were not found, they possibly may also exist in the solid state. Notably, the substituents at the phenyl ring practically do not influence the preference of hydrogen bond or

dative bond formation. This statement is in accordance with the results published by Anslyn et al.^{42,27} The authors postulated, that the presence or absence of the dative N-B bond is a balance of many factors, of which crystal packing can have a significant effect. In the solid state only forms with intramolecular hydrogen bonds were obtained for the acids, but in the case of esters two types of intramolecularly complexed species were obtained depending on the solvent used during crystallization (Fig. 9).

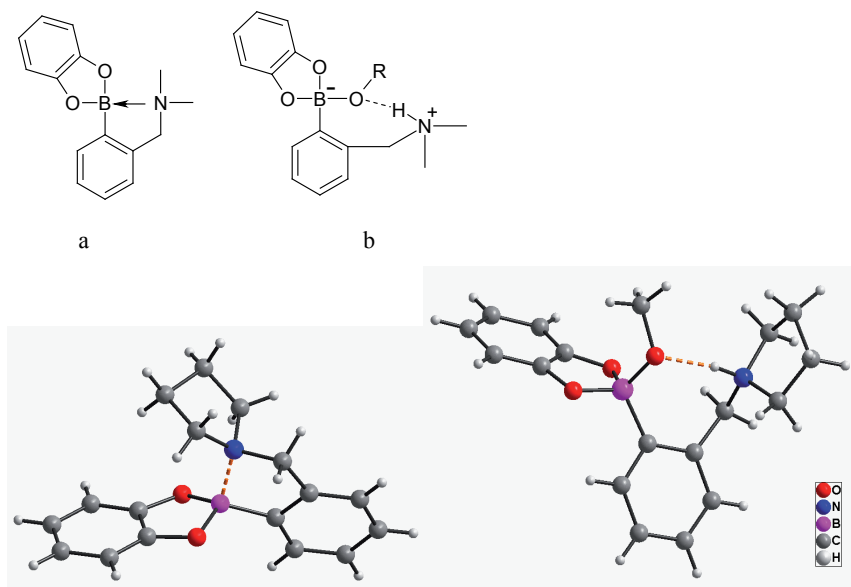


Fig. 9. Molecular structures of catechol ester of aminomethylphenylboronic acids: (a) with direct N→B bond, (b) with the solvent (methanol) molecule coordinating boron atom.

As it was mentioned above basing on the results of calculations¹⁵, discrepancies between the structure in the solid state and in solutions can be observed. The structures present in the solution can be deduced from the ¹¹B NMR spectra^{42,27}. On the basis of the results of titration of boronic acid with polyols in different solvents, chemical shifts were attributed to particular species (Fig. 10).

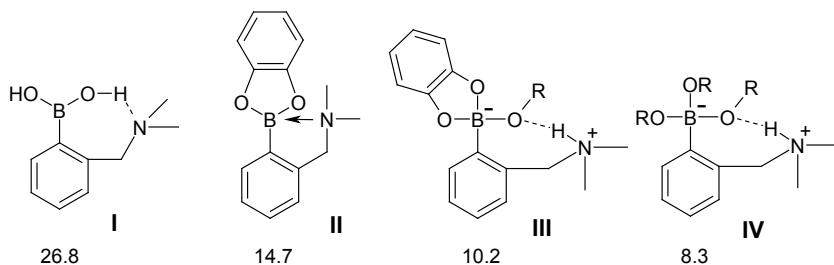


Fig. 10. Structures present in solutions and their ^{11}B chemical shifts (ppm).

The values of chemical shifts were assigned on the basis of thoroughly performed titration experiments. However, direct determination of the structure from the single value of ^{11}B chemical shift is rather doubtful. First of all, this value allows only to state the presence of the three- or tetra-coordinate boron atom (values ca. 30 and ca. 8-16 ppm, respectively). The situation is additionally complicated by the formation of boroxines in equilibrium with acids. For example, the signal at 26.8 ppm for the acid **I** (Fig. 10) is a minor one. The main signal observed in this case is that of 15.7 ppm, which can be attributed to the four-coordinate boron atoms in the corresponding boroxine⁴². Moreover, in case of dynamic processes an averaged signal are observed. For example, boroxines form 1:1 complexes with amines, and at room temperature only one signal for both types (three- and four-coordinate) boron atoms is observed. The coalescence of the signals depends not only on the exchange rate, but also on the frequency of the spectrometer. Anslyn *et al.* for example²⁷ observed for the boronic acid/catechol system only a single ^{11}B signal at 300 MHz, while two separated signal have been observed for the 500 MHz experiment.

Formation of the dative $\text{N}\rightarrow\text{B}$ bond can be affected by the steric hindrance on the nitrogen atom. As it was mentioned above, there are several examples of the compounds possessing bulky substituents on the nitrogen atom, in which such a bond is not formed. Anslyn *et al.*²⁷ compared the compounds with the primary, secondary and tertiary aminomethyl groups (*i.e.* $-\text{CH}_2\text{-NH}_2$, $-\text{CH}_2\text{-NHMe}$ and $-\text{CH}_2\text{-NMe}_2$) and they found, that there is only a very small increase in the extent of $\text{N}\rightarrow\text{B}$ bonding on going from a tertiary to a secondary or a primary amine.

In the last 5 years, several papers describing the structures of the *ortho*-aminomethyl-phenylboronic acids have been published^{18,21,41}. There are several new examples of the acids with a typical intramolecular hydrogen bond formation (Fig. 11).

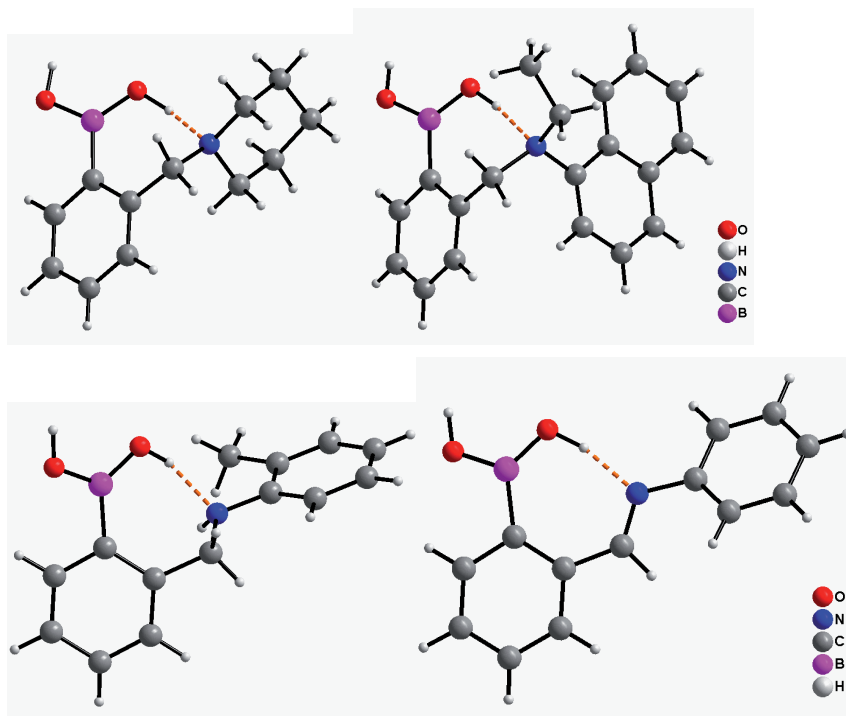
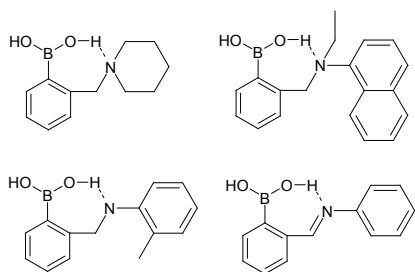


Fig. 11. Recently synthesized amino- and iminomethylphenylboronic acids and their molecular structures.

There is also an example of an ester with intramolecular N-B dative bond³³ (Fig. 12).

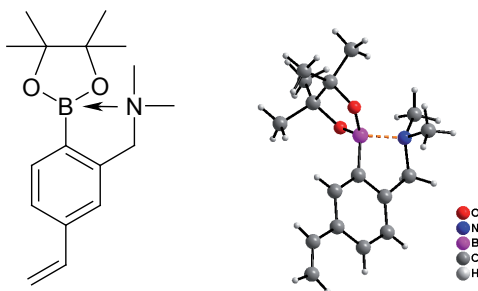


Fig. 12. Recently synthesized ester of aminomethylphenylboronic acid.

In addition to these well known structures, there is also one new unexpected structure ². It is the first example of the acid in which $N \rightarrow B$ dative bond is formed instead of intramolecular hydrogen bond. This molecule cocrystallizes with the molecule of boroxine (Fig. 13). However, in this paper only a figure of the structure was presented, and neither crystal data nor cif file are given.

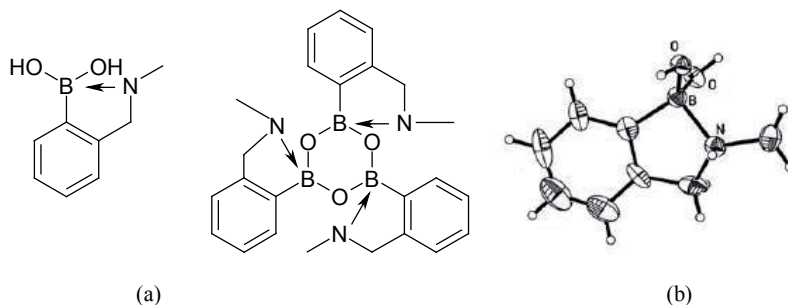
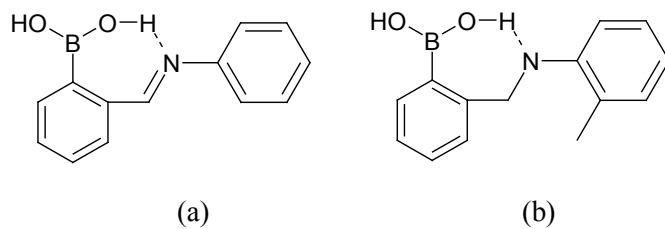
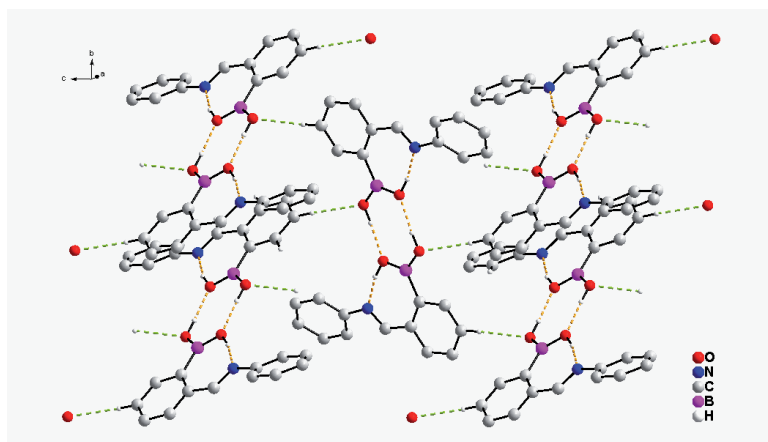


Fig. 13. First example of *ortho*-aminomethylphenylboronic acid with the dative $N-B$ bond: units present in co-crystal (a) and molecular structure of the acidic part (b).

As it was already mentioned, the factor which strongly influences the molecular structure and can determine the intramolecular interaction is the formation of weak interactions in crystal lattice. It is not the subject of the present review, but one example will be given. Fig. 14 shows the different crystal organization for the compounds of the similar molecular structures with intramolecular hydrogen bonds.



(a)



(b)

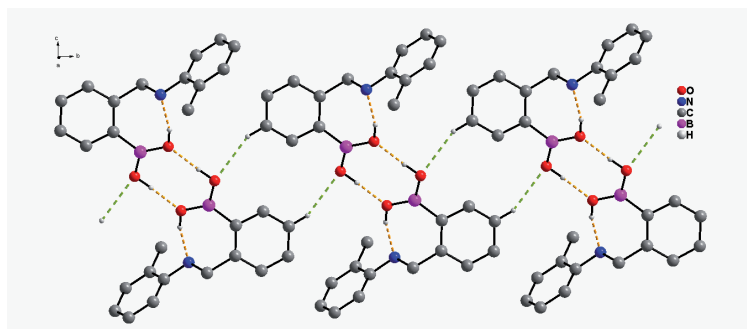


Fig. 14. Secondary supramolecular structure formed by C-H...O hydrogen bonds: (a) 2-D layer on (100) plane in crystals of **1a**; (b) 1-D ribbon motif along [100] direction in crystals of **2b**.

Very interesting structure was determined recently for the chiral ester of *R,R*-phenylboronic acid and *S,S*-hydrobenzoin (Fig. 15). In this case, presence of bulky substituents prevents the formation of the N→B bond²⁰.

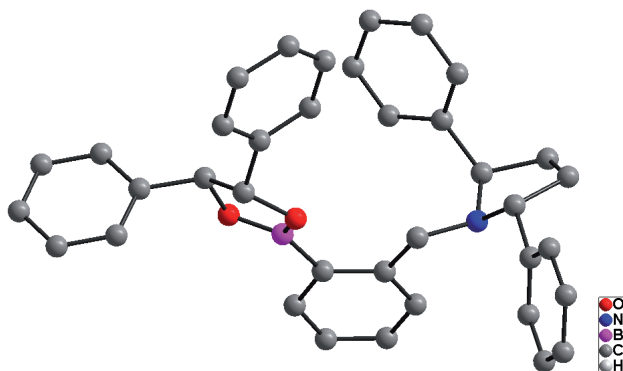


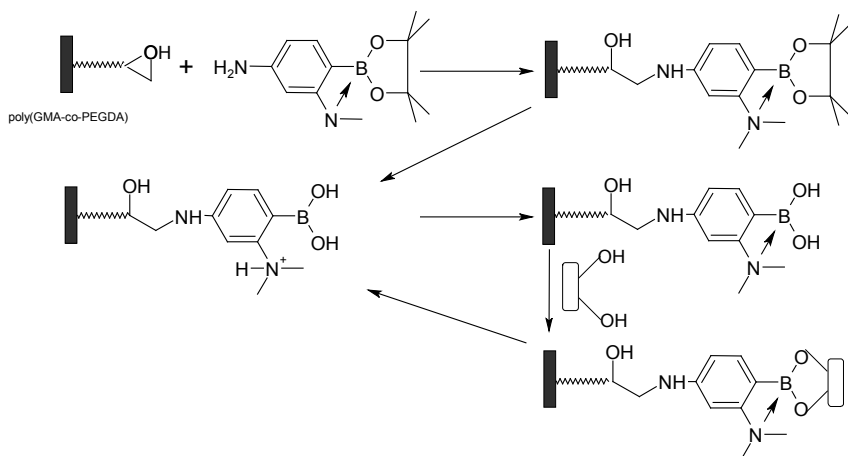
Fig. 15. Molecular structure of chiral boronic acid ester with *S,S*-hydrobenzoin. Hydrogen atoms omitted for clarity.

Applications – representative examples

Molecular receptors

The most important applications of *o*-aminomethylphenylboronic acids are connected with their unique binding ability of saccharides. Biologically important analytes are glycoproteins and glycopeptides in proteomics, nucleosides in metabolomics, and saccharides in glycomics. Most phenylboronic acids are generally weak acids (pK_a ca. 8-9), due to this fact a basic medium is required to form a stable ester. The presence of amine group enhances the stability of boronic acid esters and lowers the pK_a from 8.8 for phenylboronic acid to ca. 6.5, that results in forming tetrahedral species at neutral pH.

3-(Dimethylaminomethyl)aniline-4-pinacol boronate was immobilized on a polymer column (Scheme 12), which revealed affinity towards *cis*-diol under environmental pH or above 5.5⁴³.



Scheme 12. Immobilization of *o*-dimethylaminomethylphenylboronic acid.

A simple three step synthesis was developed to provide six novel modular sensors with naphthalene, anthracene and pyrene fluorophores. All the compounds displayed increasing fluorescence intensity upon the addition of D-glucose, D-galactose, D-fructose and D-mannose. All the sensors show enhanced selectivity for D-glucose, forming cyclic complexes. The most effective compound is shown in Fig. 16²³.

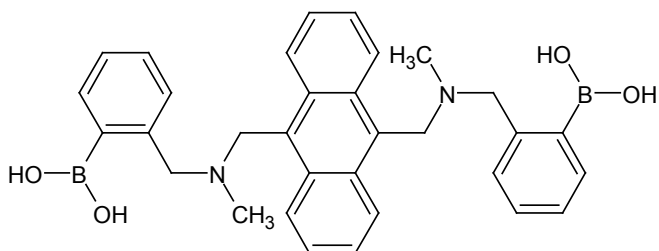
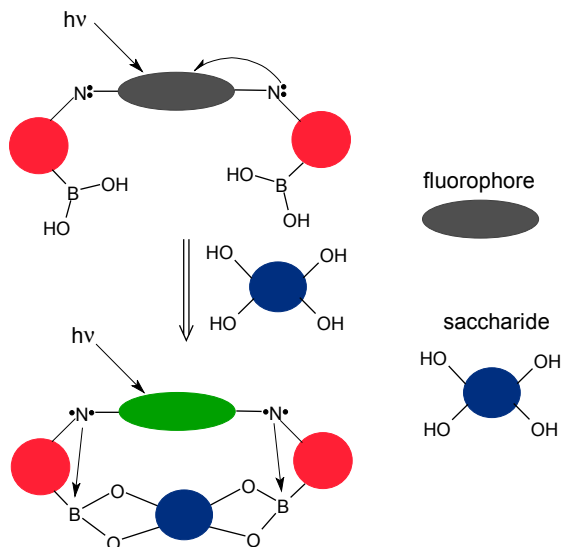


Fig. 16. Modular fluorescent photoinduced electron transfer (PET) sensor selective for glucose.

Photoinduced electron transfer mechanism is shown in Scheme 13.



Scheme 13. Photoinduced Electron Transfer (PET) mechanism ⁴⁴.

Click synthesized boronic acid-oligomer fluorophores (Fig. 17) showed excellent saccharide sensing function under physiological conditions in the mM range ⁴⁵.

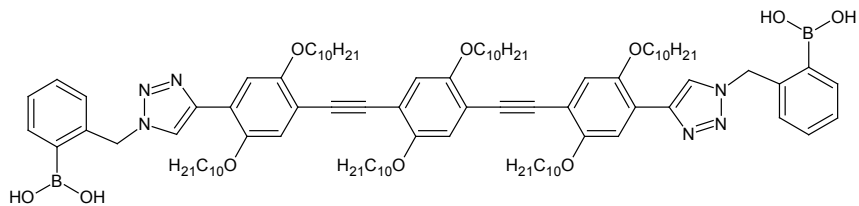


Fig. 17. Highly sensitive saccharide receptor.

A fluorescent bis(boronate) receptor (Fig. 18) with a unique response to a single monosaccharide, sialic acid, was obtained ⁴⁶. In presence of other common monosaccharides only sialic acid causes fluorescent quenching of the receptor to an extent that can be titrated. Such system may find application in design of other fluorophores to distinguish structurally similar molecules.

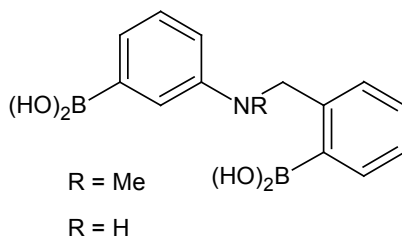


Fig. 18. Diboronic acid which binds selectively sialic acid.

There are several examples of chiral boronic acids receptors. Fig. 19 shows the compound used for the rapid determination of identity, concentration and enantiomeric excess of subtly different threo diols²⁰.

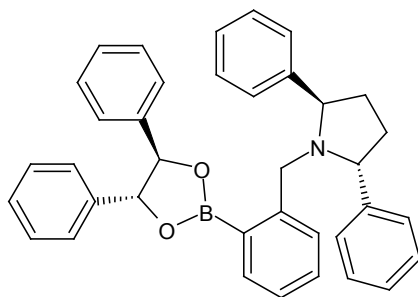


Fig. 19. Chiral receptor for threo diols.

Modular sensor based on chiral donor photoinduced-electron-transfer (Fig. 20) can be applied for the selective recognition of tartaric acids, disaccharides, and ginsenosides³².

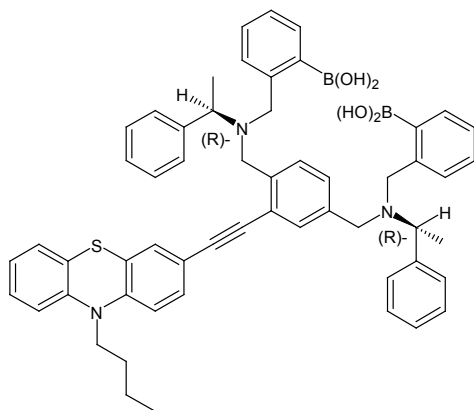
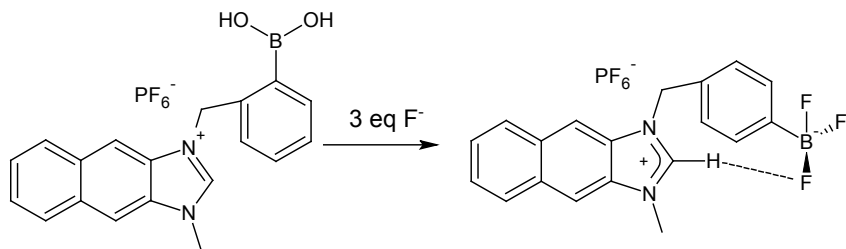


Fig. 20. Modular chiral receptor for ginsenosides.

Boronic acid with imidazolium group at *ortho* position (Scheme 14) revealed selective binding of fluoride over acetate and phosphate anions. *Meta* and *para* derivatives displayed no selectivity towards anions. ^{19}F NMR spectroscopy confirmed interaction and showed that one of the bound fluoride anions is involved in hydrogen bond ⁴⁷.



Scheme 14. Molecular receptor for fluorides.

Another example of various applications of phenylboronic acids are colorimetric chemosensors for copper ions with high selectivity (Fig. 20) ²⁸.

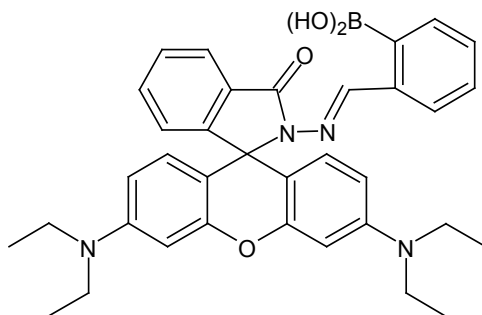


Fig. 20. Molecular receptor for Cu^{2+} ions.

Addition of Cu^{2+} to the solution of rhodamine B boronic acid in 20 mM HEPES (0.5% CH_3CN) at pH 7.4 caused change of the color from pink to orange. Detection of cations was also investigated in living organisms appearing in satisfying results.

Similar compound (Fig. 21) was found to display selective ‘Off–On’-type fluorescent enhancements and distinct color changes with Hg^{2+} ¹⁹.

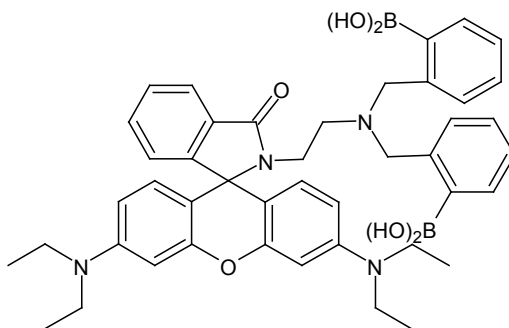


Fig. 21. Molecular receptor for Hg^{2+} ions.

Anthracene–boronic acid ester (Fig. 22) as a new class of fluorescence PET sensors for detection of a trace amount of water in organic solvents has been designed and developed ⁴⁸.

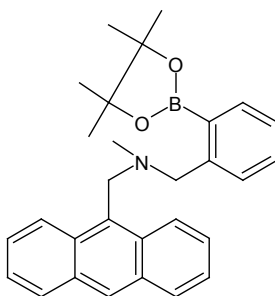


Fig. 22. Sensor for detection of trace amounts of water.

Biological applications

Much effort has been put in cell labeling with the use of boronic acid ⁴⁹. Among several investigated compounds one (Fig. 23) was shown to label the HepG2 selectively, liver carcinoma cell line in comparison to COS-7, a normal fibroblast cell line ⁷.

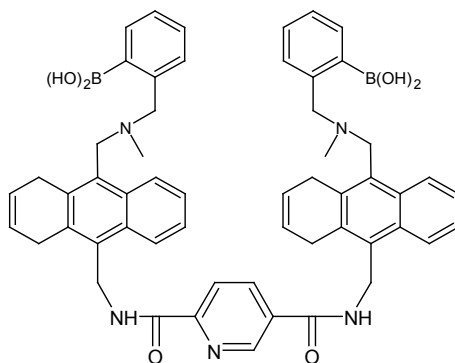


Fig. 23. Compounds used for selective labeling of HepG2.

Similar compound (Fig. 24) was used as a biomarker - the first boronolactin-MS tag conjugate, which allows for MALDI-based imaging of cancer based on its cell surface carbohydrate ³⁰.

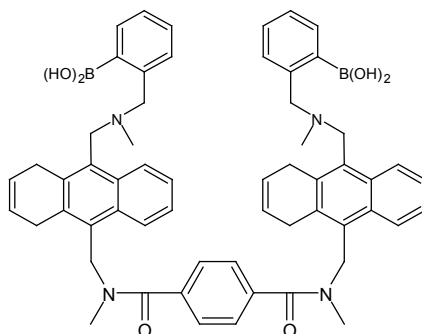


Fig. 24. Biomarker used for MALDI-based imaging of cancer.

Phenylboronic acids and their derivatives are known to have antimicrobial properties. Antibacterial and antifungal activity of several aminomethylphenylboronic acids (Fig. 25) were studied against *Escherichia coli*, *Staphylococcus aureus*, *Mycobacterium luteum*, *Aspergillus niger* and *Candida tenuis*⁵⁰.

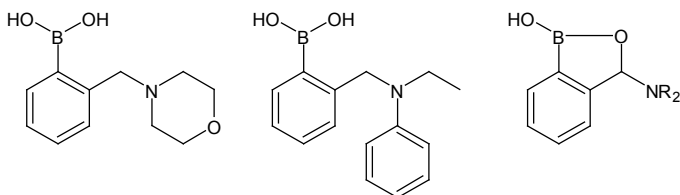
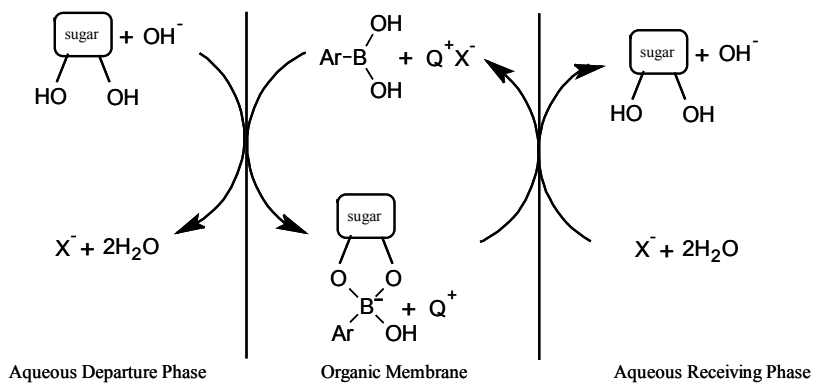


Fig. 25. Structures of investigated 2-aminomethylphenylboronic acids and corresponding benzoxaborole.

None of tested phenylboronic acids derivatives with aminomethyl group, ferrocene or fluorine substituent had significant effect. It is worth mentioning, that amino-substituted benzoxaboroles reveal very good antimicrobial properties contrary to the corresponding acids.

Transport across the membranes

Phenylboronic acids are potential sugar receptors for industry as well, they can be used to transport saccharides across a thin supported liquid membrane (Scheme 15).



Scheme 15. Transport mechanism ⁸.

This method may be used to isolate and purify sugars i.e. lactose, glucose, fructose and sucrose ⁸. Fig. 26 shows the compounds which reveals the highest recorded fructose flux promoted by a monoboronic acid under near-neutral conditions, and one of the highest fructose/glucose transport selectivities.

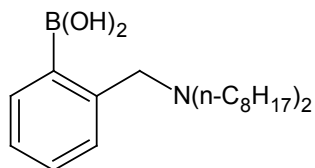


Fig. 26. Compound active in transport of sugar across membranes.

Catalysis

Arylboronic acid bearing bulky (*N,N*-dialkylamino)methyl groups at the 2,6-positions (Fig. 27) catalyze the intramolecular dehydrative condensation of di- and tetracarboxylic acids which is the first successful method for the catalytic dehydrative self-condensation of carboxylic acids ⁵¹.

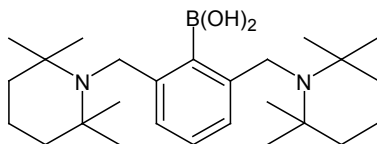
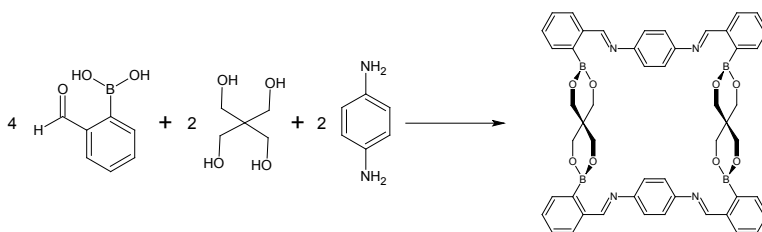


Fig. 27. Arylboronic acid bearing bulky (*N,N*-dialkylamino)methyl groups.

Supramolecular chemistry

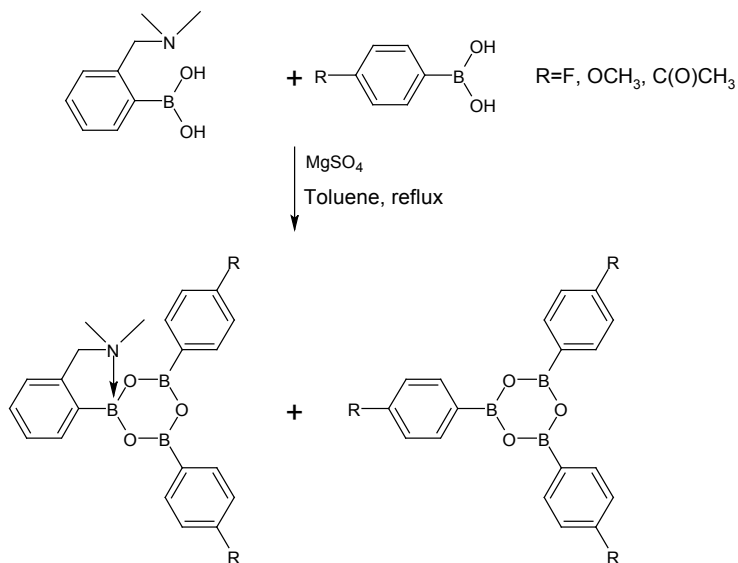
Boronic acids can be used as functional building blocks for the construction of multicomponent systems such as macrocycles, cages, dendritic structures, rotaxanes³, capsules⁵² and polymers. Self-assembled systems have become relevant to the field of material science⁵³.

Condensation reactions (Scheme 16) are used to form multicomponent systems i.e. macrocycles and molecular cages³⁶. The paper describes numerous examples of similar 3-component condensation reactions.



Scheme 16. Reaction of 2-formylphenylboronic acid, pentaerythritol and 1,4-diaminobenzene carried out to form macrocycle.

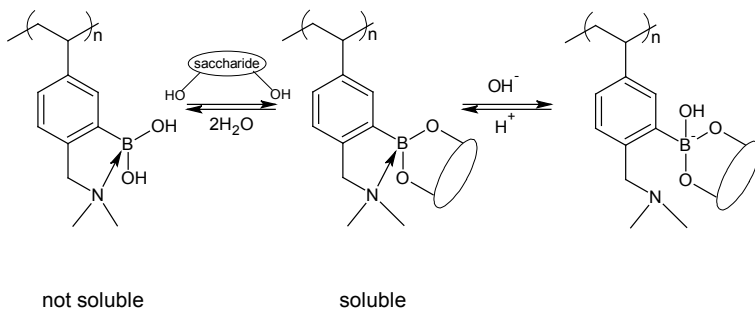
Interesting molecular systems were formed in dehydration reaction of two different substituted phenylboronic acids (Scheme 17)⁵⁴. Products of this reaction are the unique example of stable unsymmetrical boroxines.



Scheme 17. Formation of unsymmetrical boroxine.

Polymers

Esterification reaction can be used to increase solubility of phenylboronic acids containing polymers (Scheme 18) ³³.



Scheme 18. Esterification increasing solubility of polymers.

A phenylboronic acid-modified amphiphilic block polyether (Fig. 28) binds plasmid pGL3 effectively, forms sub-mm polymer/DNA complex particles, and greatly facilitates the cell uptake of the plasmid ⁵⁵.

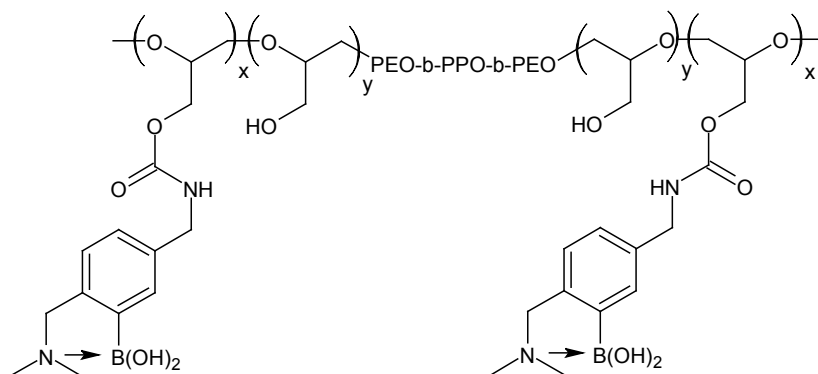
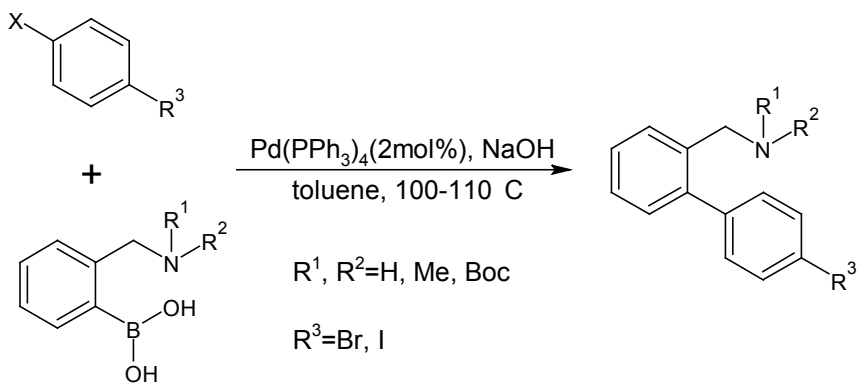


Fig. 28. Biologically active polymer.

Suzuki-Miyaura coupling

Phenylboronic acids are used in Suzuki-Miyaura coupling reaction, an useful and convenient tool for creating C-C bond in construction of biaryls, that are important parts in precursors of drugs⁵⁶⁻⁵⁹ polymers, liquid crystals and ligands for organometallic chemistry^{60,61}. Derivatives with 2-aminomethylbiphenyl moiety can be found in wide range of organic compounds and in several natural and bioactive products as well. Moieties of 2-aminomethylbiphenyls were prepared in reaction of *o*-(aminomethyl)arylboronic acids and aryl halides with electron-withdrawing and electron-donating groups at the *para* position (Scheme 19)².



Scheme 19. Suzuki coupling of *o*-aminomethylphenylboronic acids.

Reactivity of four *o*-(aminomethyl)arylboronic acids was studied, higher yields and shorter reaction times were obtained when amine group was protected by *tert*-butyloxycarbonyl (t-Boc) group (<1 h compared with up to 48 h for unprotected amine group)².

In addition to the cited above representative papers on the applications of the *o*-aminomethylphenylboronic acids, there are several papers recently published, not discussed in detail. Fossey *et al.*⁶² reviewed the development of boronic acids as separation tools. The review of Hansen *et al.*⁶³ deals with the non-invasive continuous glucose sensors. Further applications of *o*-aminomethylphenylboronic acids as saccharide sensors were mentioned in other papers^{24-26,29,31}. Synthesis and evaluation of boronic acids as inhibitors of penicillin binding proteins were described by Zervosen and co-workers⁶⁴. The construction of bisamphiphilic building blocks for artificial signal transduction across membranes has been studied by Maune *et al.*⁶⁵.

Acknowledgement

This work has been supported by the European Union in the framework of the European Social Fund through the Warsaw University of Technology Development Programme by the scholarship awarded by the Center of Advanced Studies for Alicja Pawelko.

References

1. Hall, D. G. In *Structure, Properties, and Preparation of Boronic Acid Derivatives*; Boronic Acids; Wiley-VCH Verlag GmbH & Co. KGaA: 2011; pp 1-133.
2. Boudreault, P. L.; Cardinal, S.; Voyer, N. Efficient Preparation of 2-Aminomethylbiphenyls Via Suzuki-Miyaura Reactions. *Synlett* **2010**, 2449-2452.
3. Severin, K. Boronic Acids as Building Blocks for Molecular Nanostructures and Polymeric Materials. *Dalton Trans.* **2009**, 5254-5264.
4. Żukowska, G.; Szczechura, M.; Marcinek, M.; Żubrowska, A.; Sporzyński, A.; Wiczorek, W. Investigation on the Anion Complexation Ability of Organoboron Additives in Lithium-Ion Battery Electrolytes - Spectroscopic Approach. *ECS Trans.* **2009**, *16*, 105.
5. Nishiyabu, R.; Kubo, Y.; James, T. D.; Fossey, J. S. Boronic Acid Building Blocks: Tools for Sensing and Separation. *Chem. Commun.* **2012**, *47*, 1106-1123.

6. Yang, W.; Gao, X.; Wang, B. *Med. Res. Rev.* **2003**, *23*, 346-368.
7. Craig, S. Synthesis and Evaluation of Aryl Boronic Acids as Fluorescent Artificial Receptors for Biological Carbohydrates. *Bioorg. Chem.* **2012**, *40*, 137-142.
8. Duggan, P. J.; Houston, T. A.; Kiefel, M. J.; Levonis, S. M.; Smith, B. D.; Szydzik, M. L. Enhanced Fructose, Glucose and Lactose Transport Promoted by a Lipophilic 2-(Aminomethyl)-Phenylboronic Acid. *Tetrahedron* **2008**, *64*, 7122-7126.
9. Lorand, J. P.; Edwards, J. O. Polyol Complexes and Structure of the Benzenboronate Ion. *J. Org. Chem.* **1959**, *24*, 769-774.
10. James, T. D.; Sandanayake, K. R. A. S.; Iguchi, R.; Shinkai, S. Novel Saccharide-Photoinduced Electron Transfer Sensors Based on the Interaction of Boronic Acid and Amine. *J. Am. Chem. Soc.* **1995**, *117*, 8982-8987.
11. Adamczyk-Woźniak, A.; Michałek, S.; Żukowski, K. Diboronowe Receptory Glukozy – Struktura a Selektywność. *Kosmetyki - chemia dla ciała*, Schroeder, G. (ed.), Kursiva, Poznań, **2011**, 143.
12. Wulff, G. *Pure Appl. Chem.* **1982**, *54*, 2093-2102.
13. Sporzyński, A.; Żubrowska, A. Kwasy Aryloboronowe jako Receptory Cukrów. *Syntetyczne receptory molekularne. Strategie syntezy. Metody badawcze*, Schroeder, G., (ed.), Betagraf, Poznań, **2007**, 119-138.
14. Sporzyński, A.; Żubrowska, A.; Adamczyk-Woźniak, A. Synthesis of Boronic Acids – Molecular Receptors for Sugars. *Synthetic receptors in molecular recognition*, Rybachenko, V. I. (ed.), Schidnyj Wydawnyczyj Dim, Donetsk, Ukraine, **2007**, 51-88.
15. Sporzyński, A.; Adamczyk-Woźniak, A.; Żubrowska, A. Intramolecular Interactions in *Ortho*-(Aminomethyl)Phenylboronic Acids – Potent Saccharide Receptors. *From concept to molecular receptor*, Rybachenko V. I. (ed.), Schidnyj Wydawnyczyj Dim, Donetsk, Ukraine, **2008**, 77-92.
16. Adamczyk-Woźniak, A.; Madura, I.; Velders, A. H.; Sporzyński, A. Diverse Reactivity of 2-Formylphenylboronic Acid with Secondary Amines: Synthesis of 3-Amino-Substituted Benzoxaboroles. *Tetrahedron Lett.* **2010**, *51*, 6181-6185.
17. Adamczyk-Woźniak, A.; Brzózka, Z.; Cyrański, M. K.; Filipowicz-Szymańska, A.; Klimentowska, P.; Żubrowska, A.; Żukowski, K.; Sporzyński, A. *Ortho*-(Aminomethyl)phenylboronic Acids - Synthesis, Structure and Sugar Receptor Activity. *Appl. Organometal. Chem.* **2008**, *22*, 427-432.

18. Adamczyk-Woźniak, A.; Madura, I.; Pawełko, A.; Sporzyński, A.; Żubrowska, A.; Żyła, J. Amination-Reduction Reaction as Simple Protocol for Potential Boronic Molecular Receptors. Insight in Supramolecular Structure Directed by Weak Interactions. *Cent. Eur. J. Chem.* **2011**, *9*, 199-205.
19. Kim, S. K.; Swamy, K. M. K.; Chung, S.; Kim, H. N.; Kim, M. J.; Jeong, Y.; Yoon, J. New Fluorescent and Colorimetric Chemosensors Based on the Rhodamine and Boronic Acid Groups for the Detection of Hg²⁺. *Tetrahedron Lett.* **2010**, *51*, 3286-3289.
20. Shabbir, S. H.; Joyce, L. A.; da Cruz, G. M.; Lynch, V. M.; Sorey, S.; Anslyn, E. V. Pattern-Based Recognition for the Rapid Determination of Identity, Concentration, and Enantiomeric Excess of Subtly Different Threo Diols. *J. Am. Chem. Soc.* **2009**, *131*, 13125-13131.
21. Adamczyk-Woźniak, A.; Madura, I. D.; Pawełko, A.; Sporzyński, A.; Tumanowicz, M.; Żyła, J.; Fratila, R. M.; Velders, A. H. Reactivity of 2-Formylphenylboronic Acid Toward Secondary Aromatic Amines in Amination-Reduction Reactions. *Tetrahedron Lett.* **2011**, *52*, 6639.
22. Spencer, J.; Baltus, C. B.; Patel, H.; Press, N. J.; Callear, S. K.; Male, L.; Coles, S. J. Microwave-Mediated Synthesis of an Arylboronate Library. *ACS Comb. Sci.* **2011**, *13*, 24-31.
23. Larkin, J. D.; Frimat, K. A.; Fyles, T. M.; Flower, S. E.; James, T. D. Boronic Acid Based Photoinduced Electron Transfer (PET) Fluorescence Sensors for Saccharides. *New J. Chem.* **2010**, *34*, 2922-2931.
24. Zhang, X.; Chi, L.; Ji, S.; Wu, Y.; Song, P.; Han, K.; Guo, H.; James, T. D.; Zhao, J. Rational Design of d-PeT Phenylethynylated-Carbazole Monoboronic Acid Fluorescent Sensors for the Selective Detection of α -Hydroxyl Carboxylic Acids and Monosaccharides. *J. Am. Chem. Soc.* **2009**, *131*, 17452-17463.
25. Zhang, X.; Wu, Y.; Ji, S.; Guo, H.; Song, P.; Han, K.; Wu, W.; Wu, W.; James, T. D.; Zhao, J. Effect of the Electron Donor/Acceptor Orientation on the Fluorescence Transduction Efficiency of the d-PET Effect of Carbazole-Based Fluorescent Boronic Acid Sensors. *J. Org. Chem.* **2010**, *75*, 2578-2588.
26. Xing, Z.; Wang, H.; Cheng, Y.; Zhu, C.; James, T. D.; Zhao, J. Selective Saccharide Recognition using Modular Diboronic Acid Fluorescent Sensors. *Eur. J. Org. Chem.* **2012**, *2012*, 1223-1229.
27. Collins, B.; Sorey, S.; Hargrove, A.; Shabbir, S.; Lynch, V.; Anslyn, E. Probing Intramolecular B-N Interactions in ortho-Aminomethyl

- Arylboronic Acids. *J. Org. Chem.* **2009**, *74*, 4055-4060.
28. Swamy, K. M. K.; Ko, S.; Kwon, S. K.; Lee, H. N.; Mao, C.; Kim, J.; Lee, K.; Kim, J.; Shin, I.; Yoon, J. Boronic Acid-Linked Fluorescent and Colorimetric Probes for Copper Ions. *Chem. Commun.* **2008**, 5915-5917.
 29. Phillips, M. D.; Fyles, T. M.; Barwell, N. P.; James, T. D. Carbohydrate Sensing using a Fluorescent Molecular Tweezer. *Chem. Commun.* **2009**, 6557-6559.
 30. Dai, C.; Cazares, L. H.; Wang, L.; Chu, Y.; Wang, S. L.; Troyer, D. A.; Semmes, O. J.; Drake, R. R.; Wang, B. Using Boronolactin in MALDI-MS Imaging for the Histological Analysis of Cancer Tissue Expressing the Sialyl Lewis X Antigen. *Chem. Commun.* **2011**, *47*, 10338-10340.
 31. Li, Q.; Guo, H.; Wu, Y.; Zhang, X.; Liu, Y.; Zhao, J. Enhanced Enantioselective Recognition with Diastereoisomeric BINOL Based Chiral Fluorescent Boronic Acid Sensors. *J. Fluoresc.* **2011**, *21*, 2077-2084.
 32. Wu, Y.; Guo, H.; Zhang, X.; James, T. D.; Zhao, J. Chiral Donor Photoinduced-Electron-Transfer (d-PET) Boronic Acid Chemosensors for the Selective Recognition of Tartaric Acids, Disaccharides, and Ginsenosides. *Chem. Eur. J.* **2011**, *17*, 7632-7644.
 33. Kim, K. T.; Cornelissen, J. J. L. M.; Nolte, R. J. M.; Hest, J. C. M. v. Polymeric Monosaccharide Receptors Responsive at Neutral pH. *J. Am. Chem. Soc.* **2009**, *131*, 13908-13909.
 34. Spencer, J.; Burd, A. P.; Goodwin, C. A.; Merette, S. A. M.; Scully, M. F.; Adatia, T.; Deadman, J. J. Synthesis of Ortho-Modified Mercapto- and Piperazino-Methyl-Phenylboronic Acid Derivatives. *Tetrahedron* **2002**, *58*, 1551-1556.
 35. Barkhuizen, D. A.; Howie, R. A.; Maguire, G. E. M.; Rademeyer, M. N-(10-Bromoanthracen-9-ylmethyl)-N-[2-(5,5-dimethyl-1,3,2-Dioxaborinan-2-Yl)benzyl]methylamine at 240 K. *Acta Cryst. E* **2004**, *60*, o571-o573.
 36. Hutin, M.; Bernardinelli, G.; Nitschke, J. An Iminoboronate Construction Set for Subcomponent Self-Assembly. *Chem. Eur. J.* **2008**, *14*, 4585-4593.
 37. Scrafton, D. K.; Taylor, J. E.; Mahon, M. F.; Fossey, J. S.; James, T. D. "Click-Fluors": Modular Fluorescent Saccharide Sensors Based on a 1,2,3-Triazole Ring. *J. Org. Chem.* **2008**, *73*, 2871-2874.
 38. Appoh, F.; Manning, M.; Gullon, T.; Hansen, M.; Bevans, E.; Hogan, K.; Turner, C.; Vogels, C.; Decken, A.; Westcott, S. Ugi Products

- Containing Boronate Esters. *Cent. Eur. J. Chem.* **2008**, *6*, 359-364.
39. Coghlan, S. W.; Giles, R. L.; Howard, J. A.; Patrick, L. G.; Probert, M. R.; Smith, G. E.; Whiting, A. Synthesis and Structure of Potential Lewis Acid - Lewis Base Bifunctional Catalysts: 2-N,N-Diisopropylaminophenylboronate Derivatives. *J. Organomet. Chem.* **2005**, *690*, 4784-4793.
 40. Liu, X.; Hubbard, J. L.; Scouten, W. H. Synthesis and Structural Investigation of Two Potential Boronate Affinity Chromatography Ligands Catechol 2-(diisopropylamino)carbonyl]phenylboronate and Catechol 2-(diethylamino)carbonyl, 4-methyl]phenylboronate. *J. Organomet. Chem.* **1995**, *493*, 91-94.
 41. Adamczyk-Woźniak, A.; Cyrański, M. K.; Frączak, B. T.; Lewandowska, A.; Madura, I. D.; Sporzyński, A. Imino- and Aminomethylphenylboronic Acids: Stabilizing Effect of Hydrogen Bonds. *Tetrahedron* **2012**, *68*, 3761-3767.
 42. Zhu, L.; Shabbir, S. H.; Gray, M.; Lynch, V. M.; Sorey, S.; Anslyn, E. V. A Structural Investigation of the N-B Interaction in an o-(N,N-Dialkylaminomethyl)Arylboronate System. *J. Am. Chem. Soc.* **2006**, *128*, 1222-1232.
 43. Li, H.; Liu, Y.; Liu, J.; Liu, Z. A Wulff-Type Boronate for Boronate Affinity Capture of Cis-Diol Compounds at Medium Acidic pH Condition. *Chem. Commun.* **2011**, *47*, 8169-8171.
 44. James, T. D.; Sandanayake, K. R. A. S.; Shinkai, S. Novel Photoinduced Electron-Transfer Sensor for Saccharides Based on the Interaction of Boronic Acid and Amine. *J. Chem. Soc., Chem. Commun.* **1994**, 477-478.
 45. Mulla, K.; Dongare, P.; Zhou, N.; Chen, G.; Thompson, D. W.; Zhao, Y. Highly Sensitive Detection of Saccharides Under Physiological Conditions with Click Synthesized Boronic Acid-Oligomer Fluorophores. *Org. Biomol. Chem.* **2011**, *9*, 1332-1336.
 46. Levonis, S. M.; Kiefel, M. J.; Houston, T. A. Boronlectin with Divergent Fluorescent Response Specific for Free Sialic Acid. *Chem. Commun.* **2009**, 2278-2280.
 47. Xu, Z.; Kim, S. K.; Han, S. J.; Lee, C.; Kociok-Kohn, G.; James, T. D.; Yoon, J. Ratiometric Fluorescence Sensing of Fluoride Ions by an Asymmetric Bidentate Receptor Containing a Boronic Acid and Imidazolium Group. *Eur. J. Org. Chem.* **2009**, *2009*, 3058-3065.
 48. Ooyama, Y.; Matsugasako, A.; Oka, K.; Nagano, T.; Sumomogi, M.; Komaguchi, K.; Imae, I.; Harima, Y. Fluorescence PET (Photo-Induced

- Electron Transfer) Sensors for Water Based on Anthracene-Boronic Acid Ester. *Chem. Commun.* **2011**, 47, 4448-4450.
49. Yang, W.; Fan, H.; Gao, X.; Gao, S.; Karnati, V.; Ni, W.; Hooks, W.; Carson, J.; Weston, B.; Wang, B. The First Fluorescent Diboronic Acid Sensor Specific for Hepatocellular Carcinoma Cells Expressing Sialyl Lewis X. *Chem. Biol.* **2004**, 11, 439-448.
 50. Adamczyk-Woźniak, A.; Komarowska-Porokhnyavets, O.; Misterkiewicz, B.; Novikov, V. P.; Sporzyński, A. Biological Activity of Selected Boronic Acids and their Derivatives. *Appl. Organometal. Chem.* **2012**, 26, 390-393.
 51. Sakakura, A.; Ohkubo, T.; Yamashita, R.; Akakura, M.; Ishihara, K. Brønsted Base-Assisted Boronic Acid Catalysis for the Dehydrative Intramolecular Condensation of Dicarboxylic Acids. *Org. Lett.* **2011**, 13, 892-895.
 52. Nishiyabu, R.; Kubo, Y.; James, T. D.; Fossey, J. S. Boronic Acid Building Blocks: Tools for Self Assembly. *Chem. Commun.* **2011**, 47, 1124-1150.
 53. Adamczyk-Woźniak, A. Phenylboronic Compounds as Molecular Recognition and Self-Assembling Agents. *Application of molecular receptors*, Rybachenko, V. I. (ed.), Schidnyj Wydawnyczyj Dim, **2009**, 9-24.
 54. Iovine, P. M.; Gyselbrecht, C. R.; Perttu, E. K.; Klick, C.; Neuwelt, A.; Loera, J.; DiPasquale, A. G.; Rheingold, A. L.; Kua, J. Hetero-Arylboroxines: The First Rational Synthesis, X-Ray Crystallographic and Computational Analysis. *Dalton Trans.* **2008**, 3791-3794.
 55. Chen, F.; Zhang, Z.; Cai, M.; Zhang, X.; Zhong, Z.; Zhuo, R. Phenylboronic-Acid-Modified Amphiphilic Polyether as a Neutral Gene Vector. *Macromol. Biosci.* **2012**, 12, 962-969.
 56. Bauer, U.; Giordanetto, F.; Bauer, M.; O'Mahony, G.; Johansson, K. E.; Knecht, W.; Hartleib-Geschwindner, J.; Carlsson, E. T.; Enroth, C. Discovery of 4-Hydroxy-1,6-Naphthyridine-3-Carbonitrile Derivatives as Novel PDE10A Inhibitors. *Bioorg. Med. Chem. Lett.* **2012**, 22, 1944-1948.
 57. Boschelli, D. H.; Wu, B.; Barrios Sosa, A. C.; Chen, J.; Asselin, M.; Cole, D. C.; Lee, J.; Yang, X.; Chaudhary, D. Synthesis and PKC θ Inhibitory Activity of a Series of 4-(Indol-5-Ylamino)thieno[2,3-b]Pyridine-5-Carbonitriles. *Bioorg. Med. Chem. Lett.* **2008**, 18, 2850-2853.
 58. Wu, B.; Boschelli, D. H.; Lee, J.; Yang, X.; Chaudhary, D. Second

- Generation 4-(4-Methyl-1H-Indol-5-Ylamino)-2-phenylthieno[2,3-b] Pyridine-5-Carbonitrile PKC θ , Inhibitors. *Bioorg. Med. Chem. Lett.* **2009**, *19*, 766-769.
59. Subrath, J.; Wang, D.; Wu, B.; Niu, C.; Boschelli, D. H.; Lee, J.; Yang, X.; Brennan, A.; Chaudhary, D. C-5 Substituted Heteroaryl 3-Pyridinecarbonitriles as PKC θ , Inhibitors: Part I. *Bioorg. Med. Chem. Lett.* **2009**, *19*, 5423-5425.
60. Chaumeil, H.; Signorella, S.; Le Drian, C. Suzuki Cross-Coupling Reaction of Sterically Hindered Aryl Boronates with 3-Iodo-4-Methoxybenzoic Acid Methyl ester. *Tetrahedron* **2000**, *56*, 9655-9662.
61. Kitamura, Y.; Sakurai, A.; Udzu, T.; Maegawa, T.; Monguchi, Y.; Sajiki, H. Heterogeneous Pd/C-Catalyzed Ligand-Free Suzuki-Miyaura Coupling Reaction using Aryl Boronic Esters. *Tetrahedron* **2007**, *63*, 10596-10602.
62. Fossey, J. F.; D'Hooge, F.; VanDenElsen, J. M.; Morais, M. P.; Pascu, S. I.; Bull, S. D.; Marken, F.; Jenkins, A. T.; Jiang, Y.; James, T. D. The Development of Boronic Acids as Sensors and Separation Tools. *Chem. Rec.* **2012**, *12*, 464-478.
63. Hansen J.S.; Christensen J.B.; Petersen J.F.; Norrild J.C. Arylboronic Acids: A Diabetic Eye on Glucose Sensing. *Sens. Actuators B Chem.* **2012**, *161*, 35-35.
64. Zervosen, A.; Bouillez, A.; Herman, A.; Amoroso, A.; Joris, B.; Sauvage, E.; Charlier, P.; Luxen, A. Synthesis and Evaluation of Boronic Acids as Inhibitors of Penicillin Binding Proteins of Classes A, B and C. *Bioorg. Med. Chem.* **2012**, *20*, 3915-3924.
65. Maune, M.; Bernitzki, K.; Ellermann, M.; Schrader, T. Bifunctional Bisamphiphilic Transmembrane Building Blocks for Artificial Signal Transduction. *Synthesis* **2008**, *14*, 2247-2256.

Chapter 10

Synthesis of pyrazole-based bidentate and tridentate supramolecular ligands

Michał Cegłowski and Grzegorz Schroeder
*Adam Mickiewicz University in Poznań, Department of Chemistry,
Umultowska 89b, 61-614 Poznań*

1. Introduction

Self-assembly is one of the most interesting process in modern supramolecular chemistry. Although its nature and complexity have been known from biochemical research, the ability to fully control it and construct “supermolecules” has stemmed from the developments made in supramolecular chemistry. It is now possible to design and construct molecules whose complexity and size can match those observed in biological assemblies. The self-assembly process of metal complexes formation is determined by two factors: the type, geometry and number of ligand active sites and the geometric preferences of the metal cation. While the second factor is usually known or easy to predict (for example Pt(II) is usually square planar) the first factor can be altered by synthesis of appropriate ligand. That is why of key importance for a successful self-assembly process leading to target supermolecules with metal complexes is to design and synthesise the right type of ligand.

The most extensively used ligands in metal coordination chemistry are π -electron deficient heterocyclic compounds such as 2,2'-bipyridine, 2,2':6',2''-terpyridine and 1,10-phenanthroline. Because they are π -electron deficient they act as a π -acceptors and are considered to be soft sites. Pyrazole is an aromatic compound which is classified as a π -excessive compound [1] and therefore acts as a hard donor site [2]. That is why it is possible to directly attach pyrazole to common π -electron deficient heterocycles (for example pyridine) in order to obtain ligands with interesting electronic properties. Moreover, it is possible to attach pyrazole to a desired heterocycle with incorporation of an appropriate linker that will provide additional space and therefore flexibility to the ligand obtained (for example alkyl chain). Such a linker can also be another

binding site (for example amine, ether or thioether group) that will improve coordination properties of the final ligand.

Pyrazoles act as a monodentate ligands if they coordinate metal with nitrogen lone pair in the sp^2 orbital or as bidentate ligands after deprotonation of the N-H group. Moreover, after deprotonation the corresponding anion can be an *endo* (η^2) or *exo*-bidentate ($\eta^1-\eta^1$) bridging ligand (Figure 1) [3]. Substituents at positions 3-, 4-, 5- and on N atom (instead of the N-H group) can modify the steric properties and change the electronic properties of a pyrazole-based ligand.

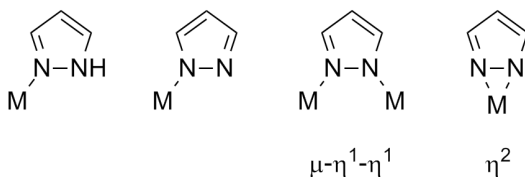


Figure 1. Coordination modes of pyrazole ligand and the corresponding anion [3].

2. Bidentate ligands

Ligands described in this section have two binding sites, which are pyrazole ring and another donor atom or two pyrazole rings linked through a spacer.

Synthesis of ligand **1**, obtained by attaching pyrazole ring to pyridine, has been reported. The highest yield of the reaction was observed when it was carried out in DMF with the use of pyrazole and 2-bromopyridine as reagents, copper(I) chloride with 6-(1*H*-pyrazol-yl) nicotinic acid as a catalyst and K_3PO_4 as a base (Figure 2) [4]. A simple method for the synthesis of ligand **1** with a similar yield and requires refluxing a mixture of 2-hydroxypyridine and pyrazole in trichlorophosphate without any metal catalyst has been reported recently [5]. Complexes of ruthenium of the stoichiometry of $RuCl_2(cod)$ (**1**) (*cod* – 1,5-cyclooctadien) have been prepared and characterized by NMR and IR spectroscopy [6]. It has been concluded that three isomers are possible depending on the relative disposition of the ligands (Figure 3). The *cis*-chloro isomers had C_1 symmetry, whereas the *trans*-chloro isomers had C_s symmetry. Ligand **1** was also used to prepare $[Ru(bipy)_2\mathbf{1}]^{2+}$ (*bipy* – 2,2'-bipyridyl) complex [7]. Electrochemical data indicated that ligand **1** is weaker π -acceptor than *bipy* but the complex obtained has similar excited-state properties to $[Ru(bipy)_3]^{2+}$.

Ligand **2**, which has a methylene group between pyrazole and pyridine ring in comparison to ligand **1**, has been synthesized from pyrazole and 2-(chloromethyl)pyridine hydrochloride in the presence of sodium hydroxide and tetrabutylammonium hydroxide with benzene as a solvent (Figure 4) [8].

It has been used to prepare complexes with cobalt(II) ($[\text{Co}(\mathbf{2})_2\text{Cl}_2]\cdot 4\text{H}_2\text{O}$) [9], nickel(II) ($[\text{Ni}(\mathbf{2})_2\text{Cl}_2]\cdot 4\text{H}_2\text{O}$) [9], palladium(II) ($[\text{Pd}(\text{Ime}(\mathbf{2}))]$) [10] and ruthenium(II) ($[\text{Ru}(\eta^6\text{C}_6\text{H}_6)(\mathbf{2})\text{Cl}][\text{PF}_6]$) [11]. The crystallographic data of complex $[\text{Co}(\mathbf{2})_2\text{Cl}_2]\cdot 4\text{H}_2\text{O}$ reveal that the coordination of cobalt(II) is *trans* octahedral. An interesting feature to note is that the Co-N (pyridine) bond is longer than the Co-N (pyrazole) bond by about 0.1 Å. What is more, the four positions around cobalt(II) occupied by nitrogen atoms of pyrazole and pyridine rings have coordination angles ranging from 85.7° to 94.3°. Because the theoretical value is exactly 90°, this results indicates that the structure is distorted [9].

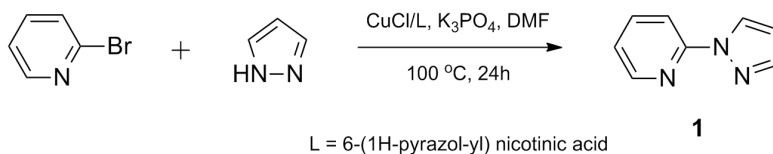


Figure 2. Synthetic route to *N*-arylated pyrazole ligand **1**.

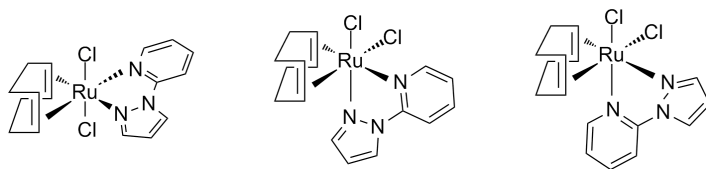


Figure 3. Isomers of $\text{RuCl}_2(\text{cod})(\mathbf{1})$ depending on the relative disposition of the ligands [6].

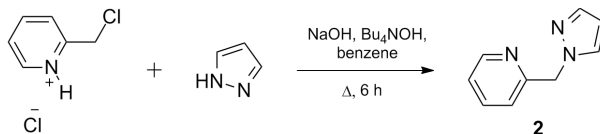


Figure 4. Synthetic route to ligand **2**.

Ligand **3** has been synthesized by the same method as that used for the synthesis of ligand **2**. Pyrazole and 2(chloromethyl)thiophene were heated in benzene in the presence of sodium hydroxide and tetrabutylammonium hydroxide (Figure 5) [12]. What is interesting, ligand **3** appeared to be monodentate when

coordinating to palladium (it gave $\text{Pd}(\mathbf{3})_2\text{Cl}_2$ as a resulting complex). It has been suggested that the nitrogen of pyrazole is the donor atom and sulphur from the thiophene ring is not coordinated [12].

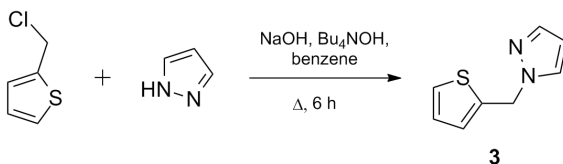


Figure 5. Synthetic route to ligand **3**.

Many interesting properties can be observed if the heterocycle-like pyridine or thiophene is replaced by another pyrazole ring to give a bis(pyrazolyl) ligand. Such a synthesis involves the reaction of pyrazole with methylene chloride (as a reagent and solvent) with the use of tetrabutylammonium hydrogensulfate and water solution of sodium hydroxide (Figure 6) [13]. Crystal structure of thus obtained ligand **4** (Figure 7 **A**) reveals that the crystal is additionally stabilized by weak N-H intermolecular hydrogen bonds [13]. Moreover, the bond lengths in both pyrazole rings are in excellent agreement. The greatest difference in their lengths is visible on C(1) atom that binds two pyrazole rings, because the length of C(1)-N(11) bond is 1.446(2) Å, while that of C(1)-N(21) bond is 1.436(2) Å.

Ligand **4** forms complexes with rhenium(V) [$\text{ReCl}_2(\text{NNPh})(\mathbf{4})(\text{PPh}_3)$] and [$\text{ReOCl}_3(\mathbf{4})$]. The latter slowly creates dimeric species and forms [$\text{Re}_2\text{O}_3\text{Cl}_4(\mathbf{4})_2$] (Figure 7 **B**) that were isolable by evaporation of acetonitrile from the solution of [$\text{ReOCl}_3(\mathbf{4})$][14]. The first of the above complexes was characterized by NMR and IR spectroscopy, whereas the next two complexes (mono- and dimeric) were characterized by X-ray diffractometry. [$\text{ReOCl}_3(\mathbf{4})$] could be hydrogenated to polyhydride $\text{Re}(\mathbf{4})\text{H}_7$ with the use of LiAlH_4 and further hydrolysis [15]. Ligand **4** was also used to prepare complexes with molybdenum(II) ($\text{Mo}(\text{CO})_2(\mathbf{4})\text{Br}_2$) [16], tungsten(II) ($\text{W}(\mathbf{4})(\text{CO})_3\text{Br}_2$) [16] and rhodium(III) ($[(\eta^5\text{C}_5\text{Me}_5)\text{Rh}(\mathbf{4})\text{Cl}][\text{CF}_3\text{SO}_3]$) [17].

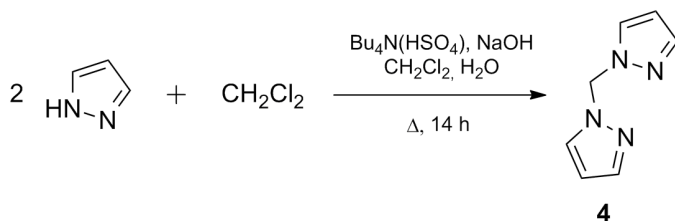


Figure 6. Synthetic route to ligand 4.

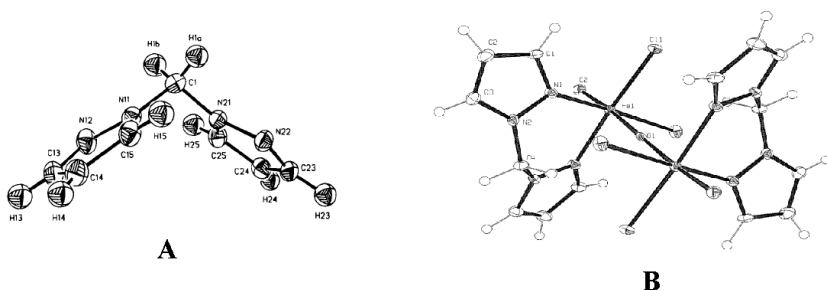


Figure 7. (A) Structure and labelling of atoms in the ligand 4; [13] (B) Structure of the complex $[\text{Re}_2\text{O}_3\text{Cl}_4(\mathbf{4})_2]$ [14].

Besides binding pyrazole ring to other heterocyclic compounds it can be attached to aliphatic amine that could also be a donor binding site in the ligand obtained. A simple procedure involving condensation of 6-aminohexan-1-ol with benzaldehyde (or other aldehydes) was used to produce imine intermediate. After reduction with NaBH_4 the compound obtained was condensed with 1-hydroxymethylpyrazole at 70°C without a solvent to form ligand **5** (Figure 8) [18]. Complex of ligand **5** with copper(II) was used toward catalytic oxidation of 3,5-di-*tert*-butylcatechol. It appeared that the complex formed with **5** had a higher catalytic rate for this reaction than its analogues bearing pyridine or pyrazine residues instead of phenyl group. The authors explained this results by a lower stability of the copper(II) complex with **5** due to poor electronic density and higher accessibility of 3,5-di-*tert*-butylcatechol to the metallic centre thanks to the absence of the coordination arm [18].

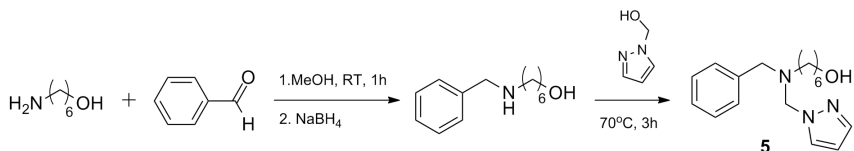


Figure 8. Synthetic route to ligand **5** [18].

3. Tridentate ligands

Tridentate pyrazole ligands make a wide group of ligands including tris(pyrazolyl)borate (first introduced by Trofimenko [19]) and substituted tris(pyrazolyl)borate. Coordination chemistry of this class of ligands has been extensively developed because of abundant possibilities to modify steric and electronic environment around the metal centre by different substitutions of pyrazole ring. The research work of Trofimenko and his followers has been extended over tris(pyrazolyl)alkanes that are isoelectronic and isosteric with poly(pyrazolyl)borates [20].

Tris(pyrazolyl)borate can be synthesized by the reaction of alkali metal borohydride with pyrazole. The number of attached pyrazole rings strongly depends on the reaction temperature (Figure 9) [21]. The products are stable compounds isolable after acidification, and can be converted into organic-soluble quaternary ammonium salts after neutralization with NR_4OH . B-substituted ligands are accessible by starting with $(\text{BR}_n\text{H}_{4-n})^-$ and C-substituted ligands are prepared by using appropriate pyrazole derivatives.

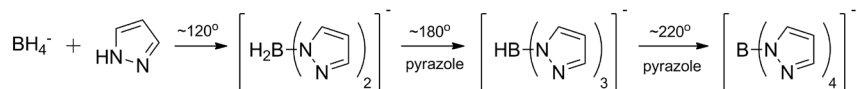


Figure 9. Synthesis of poly(pyrazolyl)borates [21].

Structure of octahedral coordination compounds formed by $\text{RB}(\text{pyrazole})_3^-$ with divalent transition metals is presented in Figure 10. If the R group is another 1-pyrazolyl group the whole ligand still remains tridentate. $[\text{HB}(\text{pyrazole})_3]_2\text{M}$ compounds are stable to light, air, water, dilute bases and acids, they can be sublimated *in vacuo* and can be dissolved in organic solvents [21].

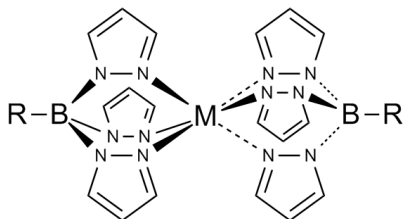


Figure 10. Structure of coordination compounds formed by $RB(\text{pyrazole})_3^-$ with divalent transition metals.

Reaction of 3-(2-pyridyl)pyrazole with KBH_4 in melt gives tris(3-(2-pyridyl)pyrazole)borate (ligand **6**). Combination of ligand **6** with $[\text{Cu}(\text{MeCN})_4][\text{PF}_6]$ affords $[\text{Cu}_3(\mathbf{6})_2][\text{PF}_6]$ (structure presented in Figure 11) [22]. In $[\text{Cu}_3(\mathbf{6})_2]^+$ each bidentate arm of each ligands is bonded to a different metal ion. Pseudo-tetrahedral coordination environment around Cu(I) ion is therefore formed by two bidentate arms that belong to different ligand molecules. The distances between Cu(I) ions are not equivalent, because there is one short Cu-Cu separation (2.915 Å) and two longer ones (3.500 Å and 3.614 Å). The length of the shortest Cu-Cu separation is the result of π -stacking interactions between ligands attached to the two metal ions.

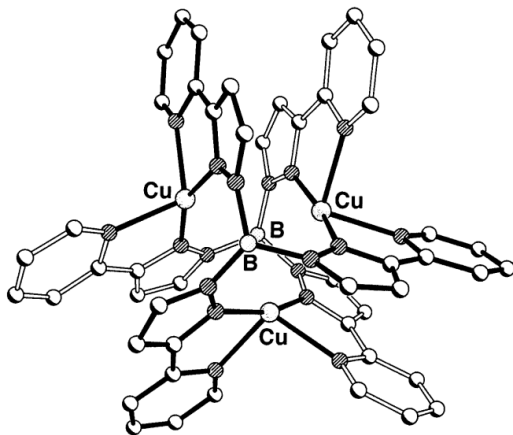


Figure 11. Structure of $[\text{Cu}_3(\mathbf{6})_2]^+$ [22].

Tris(pyrazolyl)alkanes are ligands isoelectronic and isosteric with poly(pyrazolyl)borates that can be easily prepared with many different substituents that will modify the electronic and steric effects up to desired values. Theazole rings are usually very chemically resistant against both oxidizing and reducing reagents or other chemical attacks. The simplest member of this class of ligands, tris(pyrazolyl)methane (ligand **7**), can be prepared by the phase transfer procedure involving heating at reflux of a mixture of pyrazole, potassium carbonate, chloroform and tetrabutylammonium hydrogensulfate (Figure 12) [23]. Complexes of tris(pyrazolyl)alkanes with titanium(III) ([Ti(**7**)Cl₃]) have been reported as catalysts for polymerization of olefins. Other compounds of the formula RE(pyrazolyl)₃MX₃ (R = H, alkyl, aryl, halide, amino group; E = C, Si, Ge, Pb, Sn; M = Ti, Zr, Hf) have been reported as catalysts of this process [24]. What is more, compounds of the formula RC(pyrazolyl)₃Cr(R)_n (R = halide, chain or branched alkyl, n = 1-3) have been used as catalysts to produce 1-hexene by ethylene trimerization [25].

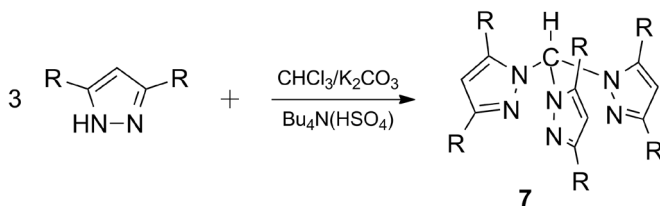


Figure 12. Synthesis of tris(pyrazolyl)methane.

Tridentate pyrazole ligands can be also prepared by attaching pyrazole ring to already existing donor sites. Ligand **8** was prepared by a simple mixing of *N*-hydroxymethylpyrazole with ethylamine in acetonitrile (Figure 13) [26]. With the use of ligand **8** compounds of the formula $[\text{M}(\mathbf{8})_2]\text{X}_2$ (M = Mn, Fe, Co, Ni, Cu, Zn, Cd, X = BF₄ or M = Ni, Cu; X = NO₃) were prepared [26]. The X-ray structure of a similar complex compound $[\text{Cu}(\mathbf{8})_2][\text{CF}_3\text{SO}_3]$ has revealed that the copper cation is surrounded by four nitrogen atoms from pyrazole rings of two ligand molecules. The geometry of the copper atom coordination is slightly distorted tetrahedral. The tertiary amine group is 3.91 Å away from the copper atom so it is too far away to create even medium strength bond [27].

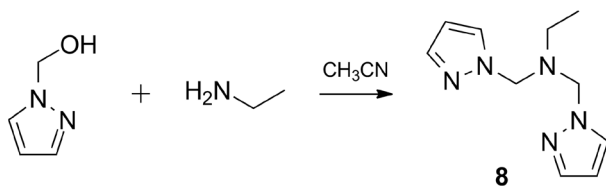


Figure 13. Synthetic route to ligand **8**.

Ligand **9**, which has a hydrogen atom instead of an ethyl group on the nitrogen atom and one methylene group more between the tertiary amine and pyrazole ring than ligand **8**, has very different coordination chemistry than ligand **8**. It was synthesized in the reaction of sodium 3,5-dimethylpyrazolate with bis(2-chloroethyl)amine hydrochloride in DMF (Figure 14) [28]. X-ray structure of copper(II) complexes of Cu(**9**)·2NO₃ and Cu(**9**)·NO₃·H₂O showed that two symmetrically independent complexes were formed: [Cu(**9**)(NO₃)₂] and [Cu(**9**)(NO₃)(H₂O)][NO₃]. The coordination of copper(II) is an intermediate between distorted trigonal bipyramid and an octahedron. Nitrogen atoms of the two pyrazole rings and amino nitrogen form T-shaped arrangement around the copper(II) ion. In both complexes there is a nitrate group that is involved in coordination through one short and one long bond. The second nitrate group (or a water molecule in the second complex) coordinates monodentately [28].

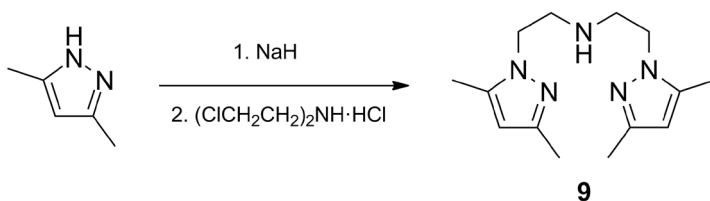


Figure 14. Synthetic route to ligand **9**.

Instead of a simple amine group, a pyridine ring was introduced into the ligand system. Ligand **10** was obtained in the reaction between sodium 3,5-dimethylpyrazolate with 2,6-bis(chloromethyl)pyridine in DMF (Figure 15) [29]. Copper(I) complexes with ligand **10** were prepared: [Cu(**10**)OCIO₃]₂·CH₂Cl₂ and [Cu(**10**)(PPh₃)]. In the first complex, copper is coordinated with pyridine, two pyrazole nitrogen and oxygen from the perchlorate group. The coordination around copper(I) is distorted tetrahedron with weakly coordinated perchlorate group that makes the coordination of the whole ligand to be similar to distorted

trigonal-planar. In $[\text{Cu}(\mathbf{10})(\text{PPh}_3)]$ copper is coordinated with pyridine, two pyrazole nitrogen and phosphorus from triphenylphosphine group and the chelation ring has a boat-like structure [29].

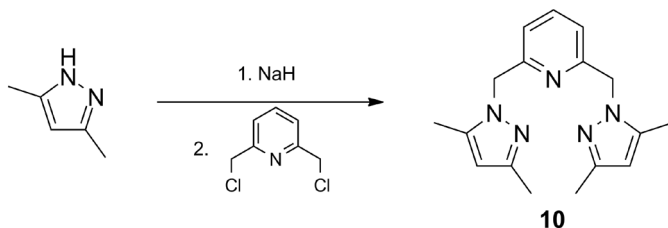


Figure 15. Synthetic route to ligand **10**.

Unsymmetrical ligand **11**, which also consists of two pyrazole rings and a pyridine ring, was prepared by mixing pyrazole and sodium hydride in freshly distilled THF. After that thionyl chloride and subsequently 2-pyridinecarboxaldehyde with a catalytic amount of cobalt(II) chloride were added (Figure 16) [30]. Ligand **11** was used to prepare metal(II) complexes $[\text{M}(\mathbf{11})_2][\text{NO}_3]$ ($\text{M} = \text{Fe}, \text{Co}, \text{Ni}, \text{Cu}, \text{Zn}$). X-ray crystallography studies revealed that metal(II) complexes have octahedral geometry with a small trigonal distortion. Moreover, the ligand-metal bonds are significantly shorter than those in monodentate complexes of pyridine or pyrazole ligands with metals. The high energies of the ‘d-d’ transitions indicated that ligand **11** produces a relatively strong ligand field, stronger than monodentate pyridine or pyrazole groups [31].

Ligand **12** which is a combination of pyrazole ring and 1,10-phenanthroline has been prepared in a multistep reaction. 2,9-Dimethyl-1,10-phenanthroline was oxidized with selenium dioxide to produce aldehyde groups that were subsequently reduced with sodium borohydride. Further bromination with HBr and reaction with 3,5-dimethylpyrazole in the presence of NaOH solution and tetrabutylammonium hydroxide (TBAH) solution results in a desired product (Figure 17) [32].

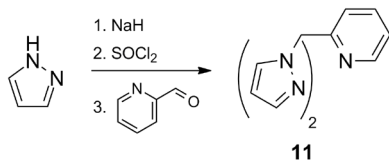


Figure 16. Synthetic route to ligand **11**.

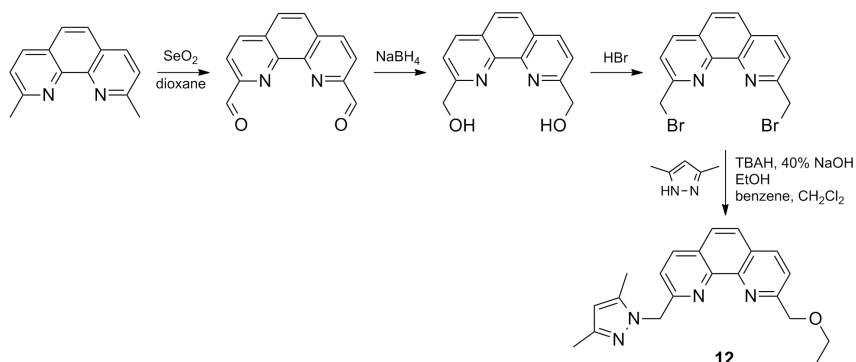


Figure 17. Synthetic route to ligand **12**.

Ligand **12** was used to prepare nickel(II) complex $[\text{Ni}(\mathbf{12})\text{Cl}_2] \cdot \text{CH}_3\text{CN}$. This complex has a five-coordinate geometry provided by two 1,10-phenanthroline nitrogen atoms, the nitrogen atom from pyrazolyl ring and two chloride atoms (structure presented in Figure 18). The geometry of the complex is described as distorted trigonal bipyramid with one of 1,10-phenanthroline nitrogen atoms being equatorial, while the chloride atoms and the second 1,10-phenanthroline nitrogen and nitrogen from pyrazolyl ring being axial. In this type of complex, nickel and three equatorial ligands should be coplanar, while the axial ligands should be disposed above and below the plane. The mean deviation from this four-atoms least-square plane through nickel and axial ligand atoms is only 0.039 Å so they can be considered as coplanar [32].

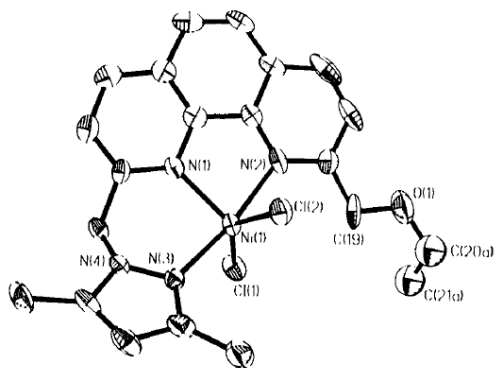


Figure 18. View of the structure of the neutral complex $[\text{Ni}(\mathbf{12})\text{Cl}_2]$ [32].

Sulphur-containing ligand **13** was prepared in a sequence of chemical reactions. 2-Hydroxyethylhydrazine was condensed with acetylacetone to yield *N*-(2-hydroxyethyl)-3,5-dimethylpyrazole that was further tosylated with *p*-toluenesulfonyl chloride in water/acetone mixture and NaOH as a base [33]. The tosylated *N*-(2-hydroxyethyl)-3,5-dimethylpyrazole was reacted with $\text{Na}_2\text{S}\cdot 7\text{H}_2\text{O}$ and NaOH in water to yield ligand **13** (Figure 19) [34]. It was used to prepare complexes $[\text{M}(\mathbf{13})(\text{NCS})_2]$ ($\text{M} = \text{Co}$ or Zn), $\text{Cu}(\mathbf{13})(\text{F})(\text{BF}_4)$, $[\text{Ni}(\mathbf{13})(\text{NCS})_2(\text{H}_2\text{O})]$, $\text{M}(\mathbf{13})\text{Cl}_2$ ($\text{M} = \text{Co}$ or Cu), $\text{Zn}(\mathbf{13})\text{Cl}_2\cdot 0.5\text{EtOH}$, $\text{M}(\mathbf{13})(\text{NO}_3)_2$ ($\text{M} = \text{Co}$ or Cu), $\text{Cu}(\mathbf{13})\text{X}$ ($\text{X} = \text{Br}$ or Cl), $[\text{Cu}(\mathbf{13})\text{BF}_4\cdot \text{H}_2\text{O}]$ and $\text{Ag}(\mathbf{13})(\text{NO}_3)$. The coordination geometry in $[\text{Co}(\mathbf{13})(\text{NO}_3)_2]$ is distorted octahedral and cobalt ion is coordinated by two pyrazole nitrogen atoms, thioether sulphur and two nitrate anions of which one is bidentate. In $\text{Cu}(\mathbf{13})\text{Br}$ copper(I) atom is coordinated by two pyrazole nitrogens, one thioether and one bromide. The two nitrogen donors are not part of one ligand molecule, which results in a polymeric nature of $\text{Cu}(\mathbf{13})\text{Br}$ [34].

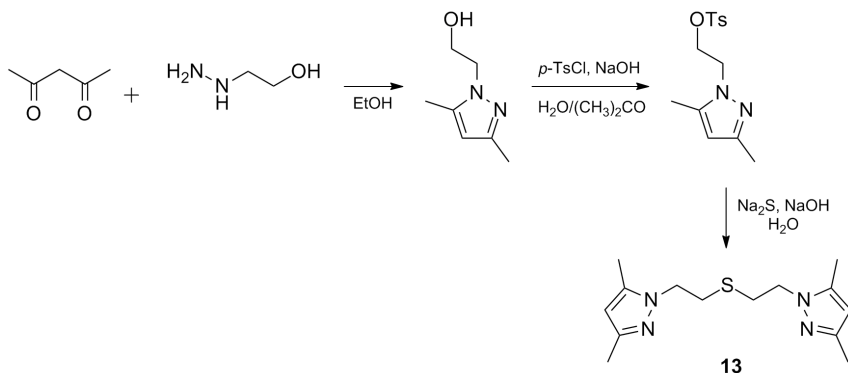


Figure 19. Synthetic route to ligand **13**.

4. Conclusions

Synthesis and coordination properties of various pyrazole based bidentate and tridentate ligands have been presented. It is worth noting that in all cases synthesis of appropriate ligand is limited to only few steps and a target product can be isolated with satisfying yields. It has been demonstrated that geometries and binding properties of chelating ligands can be varied by changing substituent groups near the donor site of the ligand. In future the design of new pyrazole-based ligands will depend on the creativity of researcher and requirements imposed by a particular scientific problem. What is more, the ligands of this

type can be used as building blocks that construct complex supramolecular architectures, such as supramolecular polymers or other sophisticated products.

Acknowledgements

This work was partially supported from the funds of National Science Centre (grant no. 2012/05/N/ST5/01274).

References

1. Albert, A., *Heterocyclic Chemistry*. London, 1968; ISBN: 048511092X
2. Mukherjee, R., Coordination chemistry with pyrazole-based chelating ligands: molecular structural aspects. *Coord. Chem. Rev.* **2000**, *203* (1), 151-218.
3. Viciano-Chumillas, M.; Tanase, S.; de Jongh, L. J.; Reedijk, J., Coordination Versatility of Pyrazole-Based Ligands towards High-Nuclearity Transition-Metal and Rare-Earth Clusters. *Eur. J. Inorg. Chem.* **2010**, *2010* (22), 3403-3418.
4. Liu, H.-Y.; Yu, Z.-T.; Yuan, Y.-J.; Yu, T.; Zou, Z.-G., Efficient N-arylation catalyzed by a copper(I) pyrazolyl-nicotinic acid system. *Tetrahedron* **2010**, *66* (47), 9141-9144.
5. Deng, X.; Roessler, A.; Brdar, I.; Faessler, R.; Wu, J.; Sales, Z. S.; Mani, N. S., Direct, Metal-Free Amination of Heterocyclic Amides/Ureas with NH-Heterocycles and N-Substituted Anilines in POCl₃. *J. Org. Chem.* **2011**, *76* (20), 8262-8269.
6. Elguero, J.; Guerrero, A.; de la Torre, F. G.; de la Hoz, A.; Jalon, F. A.; Manzano, B. R.; Rodriguez, A., New complexes with pyrazole-containing ligands and different metallic centres. Comparative study of their fluxional behaviour involving M-N bond rupture. *New J. Chem.* **2001**, *25* (8), 1050-1060.
7. Hage, R.; Prins, R.; Haasnoot, J. G.; Reedijk, J.; Vos, J. G., Synthesis, spectroscopic, and electrochemical properties of bis(2,2[prime or minute]-bipyridyl)-ruthenium compounds of some pyridyl-1,2,4-triazoles. *J. Chem. Soc., Dalton Trans.* **1987**, (6), 1389-1395.
8. House, D.; Steel, P.; Watson, A., Chiral Heterocyclic Ligands. II. Synthesis and Palladium(II) Complexes of Chiral Pyrazolylmethyl-Pyridines and Pyrazolylmethyl-Pyrazoles. *Aust. J. Chem.* **1986**, *39* (10), 1525-1536.
9. Kumar Lal, T.; Mukherjee, R., New cobalt(II) and nickel(II) complexes with 2-(pyrazol-1-ylmethyl)pyridine. Stereochemical variations in

- cobalt(II) complexes and X-ray crystal structure of bis[2-(pyrazol-1-ylmethyl) pyridine]dichlorocobalt(II) tetrahydrate. *Polyhedron* **1997**, *16* (20), 3577-3583.
10. Byers, P. K.; Cauty, A. J., Synthetic routes to methylpalladium(II) and dimethylpalladium(II) chemistry and the synthesis of new nitrogen donor ligand systems. *Organometallics* **1990**, *9* (1), 210-220.
 11. Shirin, Z.; Mukherjee, R.; Richardson, J. F.; Buchanan, R. M., New piano-stool ruthenium(II) complexes of benzene and bidentate/tridentate nitrogen-donor ligands: synthesis and characterization. *J. Chem. Soc., Dalton Trans.* **1994**, (4), 465-469.
 12. Watson, A.; House, D.; Steel, P., Chiral Heterocyclic Ligands. VIII. Syntheses and Complexes of New Chelating Ligands Derived From Camphor. *Aust. J. Chem.* **1995**, *48* (9), 1549-1572.
 13. Churchill, M.; Churchill, D.; Huynh, M.; Takeuchi, K.; Castellano, R.; Jameson, D., Crystal and molecular structure of di(1-pyrazolyl) methane, $\text{CH}_2(\text{C}_3\text{N}_2\text{H}_3)_2$. *J. Chem. Crystallogr.* **1996**, *26* (2), 93-97.
 14. Cowley, A. R.; Dilworth, J. R.; Salichou, M., Syntheses and structures of pyrazolylmethane complexes of rhenium(III), (IV) and (V). *Dalton Trans.* **2007**, (16), 1621-1629.
 15. Hamilton, D. G.; Luo, X. L.; Crabtree, R. H., The first polyhydrides stabilized only by N-donor ligands, hexahydro[hydrotris(pyrazolyl) borato]rhenium and heptahydro[dipyrazolylmethane]rhenium. *Inorg. Chem.* **1989**, *28* (16), 3198-3203.
 16. Shiu, K. B.; Liou, K. S.; Wang, S. L.; Wei, S. C., Organotransition-metal complexes of multidentate ligands. 10. Steric vs. electronic control on formation of six- and seven-coordinate carbonyl halides of molybdenum(II) and tungsten(II). *Organometallics* **1990**, *9* (3), 669-675.
 17. Pettinari, C.; Pettinari, R.; Marchetti, F.; Macchioni, A.; Zuccaccia, D.; Skelton, B. W.; White, A. H., Synthesis, Reactivity, Spectroscopic Characterization, X-ray Structures, PGSE, and NOE NMR Studies of $(\eta^5\text{-C}_5\text{Me}_5\text{-Rhodium and -Iridium Derivatives Containing Bis(pyrazolyl)alkane Ligands. *Inorg. Chem.* **2007**, *46* (3), 896-906.$
 18. Marion, R.; Saleh, N. M.; Le Poul, N.; Floner, D.; Lavastre, O.; Geneste, F., Rate enhancement of the catechol oxidase activity of a series of biomimetic monocopper(ii) complexes by introduction of non-coordinating groups in N-tripodal ligands. *New J. Chem.* **2012**, *36* (9), 1828-1835.
 19. Trofimenko, S., Boron-pyrazole chemistry. II. Poly(1-pyrazolyl)-

- borates. *J. Am. Chem. Soc.* **1967**, *89* (13), 3170-3177.
20. Pettinari, C.; Pettinari, R., Metal derivatives of poly(pyrazolyl)alkanes: I. Tris(pyrazolyl)alkanes and related systems. *Coord. Chem. Rev.* **2005**, *249* (5–6), 525-543.
 21. Trofimenko, S., Coordination chemistry of pyrazole-derived ligands. *Chem. Rev. (Washington, DC, U. S.)* **1972**, *72* (5), 497-509.
 22. Jones, P. L.; Jeffery, J. C.; Maher, J. P.; McCleverty, J. A.; Rieger, P. H.; Ward, M. D., A Triangular Copper(I) Complex Displaying Allosteric Cooperativity in Its Electrochemical Behavior and a Mixed-Valence Cu(I)–Cu(I)–Cu(II) State with Unusual Temperature-Dependent Behavior. *Inorg. Chem.* **1997**, *36* (14), 3088-3095.
 23. Juliá, S.; del Mazo, J. M.; Avila, L.; Elguero, J., Improved synthesis of polyazolylmethanes under solid-liquid phase-transfer catalysis. *Org. Prep. Proced. Int.* **1984**, *16* (5), 299-307.
 24. Nakazawa, H.; Igai, S.; Kai, Y. JP 10338698, 1998.
 25. Yoshida, O.; Okada, H.; Yamamoto, T.; Murakita, H. JP 2002205960, 2002.
 26. Veldhuis, J. B. J.; Driessen, W. L.; Reedijk, J., A pyrazole derivative of aminoethane as a tridentate chelating ligand towards transition metals. The X-ray structure of [N,N-bis(pyrazol-1-ylmethyl)aminoethane] dibromocopper(II). *J. Chem. Soc., Dalton Trans.* **1986**, (3), 537-541.
 27. Pennings, Y. C. M.; Driessen, W. L.; Reedijk, J., Copper(I) coordination compounds with two bidentate chelating pyrazole ligands. X-ray crystal structures of DI- μ -chloro-bis[[N,N-bis(1-pyrazolylmethyl)aminoethane]copper(I)] and [bis(N,N-bis(1-pyrazolylmethyl)aminoethane)copper(I) triflate]. *Polyhedron* **1988**, *7* (24), 2583-2589.
 28. Martens, C. F.; Schenning, A. P. H. J.; Feiters, M. C.; Berens, H. W.; van der Linden, J. G. M.; Admiraal, G.; Beurskens, P. T.; Kooijman, H.; Spek, A. L.; Nolte, R. J. M., X-ray Structures and Redox Properties of Copper(II) Bis(pyrazole) Complexes. *Inorg. Chem.* **1995**, *34* (19), 4735-4744.
 29. Manikandan, P.; Varghese, B.; Manoharan, P. T., Structure, characterisation and dynamics of copper(I) complexes of 2,6-bis(3,5-dimethylpyrazol-1-ylmethyl)pyridine. *J. Chem. Soc., Dalton Trans.* **1996**, (3), 371-376.
 30. Hoffmann, A.; Flörke, U.; Schürmann, M.; Herres-Pawlis, S., Novel Synthetic Strategy towards the Efficient Synthesis of Substituted Bis(pyrazolyl)(2-pyridyl)methane Ligands. *Eur. J. Org. Chem.* **2010**, *2010* (21), 4136-4144.

31. Astley, T.; Canty, A. J.; Hitchman, M. A.; Rowbottom, G. L.; Skelton, B. W.; White, A. H., Structural, spectroscopic and angular-overlap studies of the nature of metal-ligand bonding for tripod ligands. *J. Chem. Soc., Dalton Trans.* **1991**, (8), 1981-1990.
32. Masood, M. A.; Hodgson, D. J., Five- and Six-Coordinate Nickel(II) Complexes of New Multidentate Ligands Containing 2,9-Disubstituted-1,10-Phenanthroline and Pyrazolyl Units. *Inorg. Chem.* **1994**, 33 (14), 3038-3042.
33. Haanstra, W. G.; Driessen, W. L.; Reedijk, J.; Turpeinen, U.; Hamalainen, R., Unusual chelating properties of the ligand 1,8-bis(3,5-dimethyl-1-pyrazolyl)-3,6-dithiaoctane (bddo). Crystal structures of Ni(bddo)(NCS)₂, Zn(bddo)(NCS)₂ and Cd₂(bddo)(NCS)₄. *J. Chem. Soc., Dalton Trans.* **1989**, (11), 2309-2314.
34. Haanstra, W. G.; Driessen, W. L.; van Roon, M.; Stoffels, A. L. E.; Reedijk, J., Co-ordination compounds with the N2S-donor ligand 1,5-bis(3,5-dimethylpyrazol-1-yl)-3-thiapentane. *J. Chem. Soc., Dalton Trans.* **1992**, (3), 481-486.

Chapter 11

Mesoporous silicas as carriers in controlled release systems in biomedicine and cosmetics industry

Dawid Lewandowski and Grzegorz Schroeder
*Adam Mickiewicz University in Poznań, Department of Chemistry,
Umultowska 89b, 61-614 Poznań*

1. Introduction

Porous materials have attracted more attention since the 1960s because of their numerous scientific and technological applications. Generally, the term ‘pore’ means any tiny hole (unoccupied space) admitting passage of a liquid (fluid or gas) and according to the International Union of Pure and Applied Chemistry, three main pores categories may be distinguished: micropores (<2 nm), mesopores (2-50 nm), and macropores (>50 nm). In view of a wide variety of materials that can be classified as porous an additional classifications are required^[1], i.e. between regular and irregular porous materials (distribution of the pores in silica particles), uniformly-sized and non-uniformly-sized materials (when speaking of pores or particles size distribution), highly ordered and amorphous (internal structure), spherical, fibrous and irregular (particles shape).

The breakthrough in porous materials chemistry occurred in 1992, when researchers from Mobil Oil Corporation discovered a group of mesoporous silica oxides known as M41S family^[2] with MCM-41 as the most important from among them. However, some sources mention that the discovery of such materials had taken place over 20 years earlier, when as described ‘low-bulk density silica’ had been obtained^[3].

Until now many new silica families have been discovered - as mentioned in the literature:

- MCM-41 (space group $p6mm$), MCM-50 (space group $p2$), MCM-48 (space group $Ia\bar{3}d$) and other from M41S silicas family (**M**obil **C**omposition of **M**atter) – ordered mesoporous silicas templated by cationic surfactants with pore diameter of about 2-10 nm^[2]
- SBA-1, SBA-12, SBA-15 (University of California at **S**anta **B**arbara) –

ordered mesoporous silicas templated by neutral copolymers (triblock copolymers), usually larger pores

- KIT-1 (**K**orea **A**dvanced **I**nstitute of **S**cience and **T**echnology 1) or MSU-X (**M**ichigan **S**tate **U**niversity) - disordered mesoporous silicas^[4]
- IBN (**I**nstitute of **B**ioengineering and **N**anotechnology)^[5]
- FDU-n (**F**udan **U**niversity)^[6]
- KSW silicas - orthorhombic structure with rectangular arrangements of semi-squared one-dimensional channels^[7,8]
- FSM (**F**olded **S**heet **M**aterial) - hexagonal array of uniform channels^[9]
- HMS (**H**exagonal **M**esoporous **S**ilica)^[10]

Amongst numerous advantages of mesoporous silicas some most important may be distinguished: good thermal stability, high surface area (650 – >1000m²/g) and surface/volume relationship^[1], narrow pores size distribution^[11], tunable pores size and volume^[12].

Another advantage of mesoporous silicas is that their channels, which serve as cargo reservoirs, can be opened or closed by different systems, i. e. nanocrystals^[13], polymers^[14], photosensitive derivatives^[15] and other organic or inorganic moieties. Triggers such as pH^[16], chemicals (dithiothreitol^[13], carboxylates^[16], pseudorotaxanes^[17], cucurbit[6]uril^[18], cucurbit[7]uril^[19], α -cyclodextrins^[20]), light^[4,5], ultrasound^[14], heat^[21,22], redox reactions^[23], enzymes^[24], magnetism^[12,25] or a combination of two or more of them^[12] can be applied to control the cargo delivery.

Each of these families have been used in different applications including supports for catalysis, adsorption, enzyme adsorption and immobilization^[26], separation, filtration^[11], low-k-materials^[27], detection and sensing^[28-30].

Mesoporous silicas have also been studied in the context of biomedical use – drug delivery^[14,16,31-33] and protein delivery^[34] with complete cargo release in the matter of minutes, hours or days^[31,35], drug targeting^[36,37], tissue engineering^[38,39], gene transfection^[40] and cell tracking^[41].

However, there are several hurdles to make mesoporous silica particles competitive with other drug formulations (microcapsules, micelles, vesicles, dendrimers, polymeric matrices^[42], nanocrystals or cyclodextrins^[43]): first of them is to develop nanocarriers that can encapsulate enough therapeutic agents with activated release. Second one is to deliver these nanoparticles through all the *in vivo* barriers to targeted location. Third is the toxicity, which is still an important issue, and the fourth are costs of fabrication that are still too high for industrial application^[44].

2. Preparation and properties

2.1. General mechanism

There are two different mechanisms involved: first, so called true liquid-crystal template mechanism, mentions about the formation of lyotropic liquid-crystalline phase under high surfactant concentration and prevailing conditions, even without a presence of silica source. Second one concerns lower surfactant concentrations, when silica source is needed for directed (hexagonal, cubic or laminar) self-assembly of structure directing agent. This process is known as cooperative crystal template mechanism^[45].

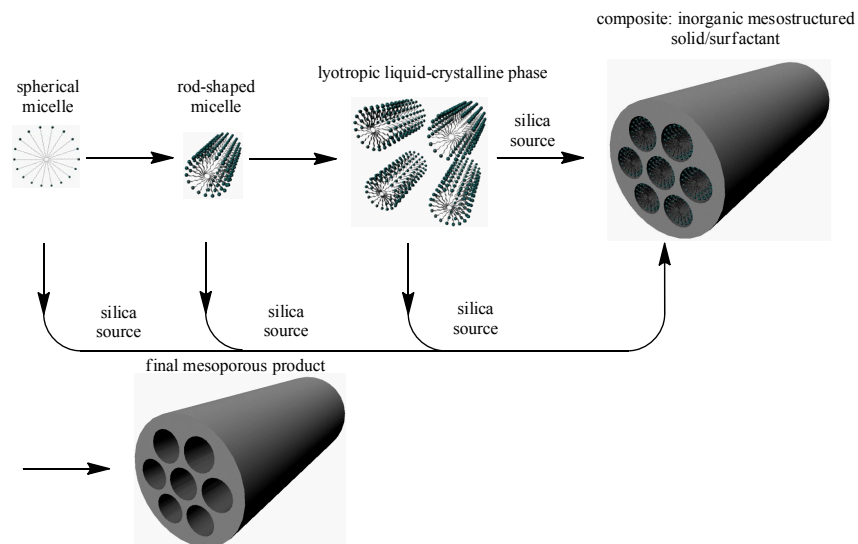


Figure 1. General mechanism of mesoporous silica formation.

2.2. Simple (unmodified) silica particles

Generally, the easiest way of obtaining mesoporous silicas is a solution synthesis, similar to Stöber method for preparation of silica particles^[46], which is carried out under basic conditions, but there are many other methods in both, acidic and basic, conditions; with use of anionic, cationic or neutral surfactants, and sometimes mediator ions are required to enhance interactions between silica source and structure directing agent^[45].

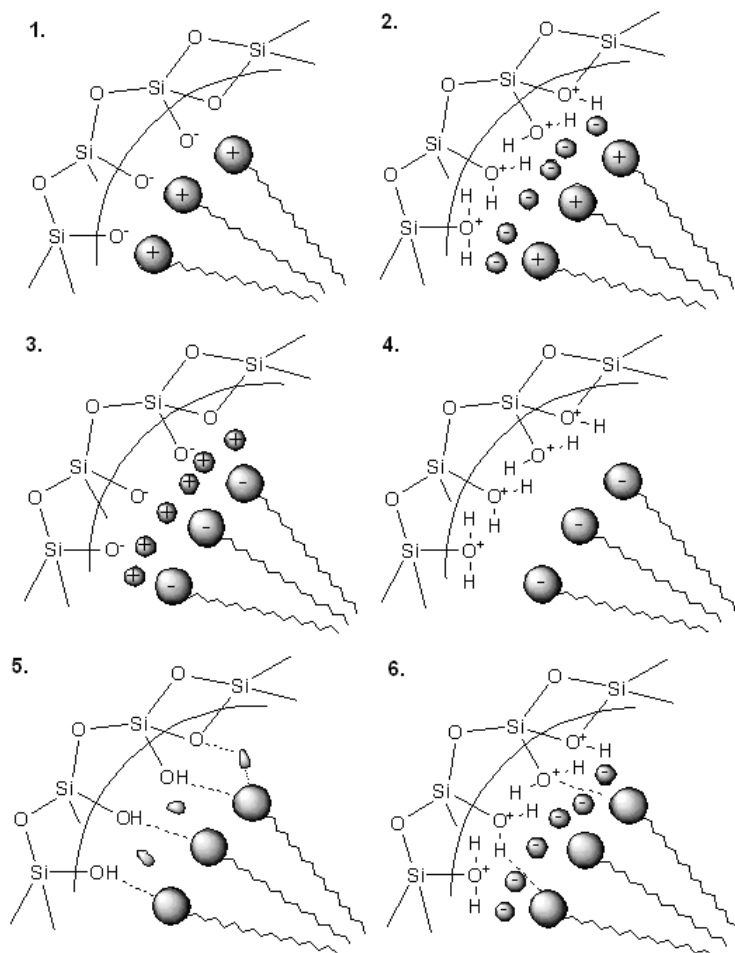


Figure 2. Interactions between the particles during silica matrix formation.

Following Vallet-Regi's *et al.* procedure a water solution of surfactant is mixed with a solution of silica source in a basic solvent (i. e. tetramethylammonium hydroxide - TMAOH, where hydrolysis of silica source takes place) by slow addition of silica source to avoid its condensation, and stirred until silica source hydrolysis is completed^[31].

Obtained gel is dried and the surfactant is removed by extraction with a

mixture of concentrated hydrochloric acid and ethanol (1:10 ratio) and kept at reflux for 24 hours. Final material is filtered, washed with water and ethanol, and dried^[31]. Other possibility to remove surfactant is to calcinate condensed gel at 500°C for a few hours, while all organic content is burned out.

Under basic conditions most of existing silanol groups is deprotonated and to match this negative charge, cationic surfactants are normally used. Moreover, the hydrolysis and condensation rates of the silica source (tetramethoxysilane – TMOS, tetraethoxysilane – TEOS and others) is highly dependent on several factors such as pH, type of silica source, additives and temperature^[47].

The influence of pH value is vital. Hydrolysis rate of silica source generally increases with the pH increase and reaches its maximum at 8,4 for TEOS. Still, there is no evidence, that pH value has a direct influence on size of the obtained particles^[48,49]. However, condensation rate, rather than the hydrolysis rate, is the most important factor affecting the particles size. Chiang *et al.* demonstrated that pH is more significant than the amount of silica source used and the reaction time^[50].

Only very few trials have been made to prepare mesoporous silicas under acidic conditions. Amongst the advantages of applying these conditions is the capability to use other structure directing agents (SDAs), i. e. block copolymers, allowing to achieve larger pores diameter, but at the cost of uniformity of particles size and shape^[51].

There have been also reports indicating that silica source has an influence on particles size. For example, using TMOS as silica source and hexadecyltrimethylammonium bromide (C₁₆TMABr) as a SDA gave particles smaller than 20 nm in size, while TEOS gave *ca.* 30 nm particles. Differences were explained as a result of different hydrolysis rates for both silica sources^[52].

The particles size can also be modified by addition of organic (e. g. co-solvents) organosilane compounds, which disturb the interactions between silica source and surfactant^[53].

In a suspension of synthesized mesoporous silica, nanoparticles collide and aggregate, attaching to each other *via* van der Waals forces. Aggregation usually occurs during the removal of surfactant and reduces the quality of obtained product^[47]. However, when applying different removal procedures^[52] or external surface functionalization^[54], uniform dispersity may be achieved.

Particles morphology can also be determined by the catalyst (base) type used: TMAOH and NaOH form sphere-shaped particles of MCM-41, NH₄OH may also be used and it leads to rod-like particles^[55].

Moreover, for other silica families: Nazar *et al.* presented a synthesis of SBA-15 rods with smaller, than normal, length (300-600 nm) and large pores

(~6 nm) using very dilute solution of P123^[56] and Kim *et al.* prepared SBA-15-type nanospheres with pluronic P104 as a template and TMOS as a silica source^[57]. More difficult than the production of spherical-shaped particles is the preparation of fibers. Under specific conditions, the formation of hollow tubules^[58] or fibers consisting of agglomerated particles has already been reported^[59-61].

Han *et al.* obtained IBN-type mesoporous cubic-structured silica by using cationic fluorocarbon surfactants with a higher surface activity and lipophobic nature and pore sizes up to 20 nm^[5].

Pore size depends mainly on the surfactant used in the synthesis but also on other parameters of the synthesis^[2,62] such as addition of auxiliary organic molecules solubilized in the hydrophobic part of the micelles, increasing their size^[62], or *via* hydrothermal treatment of product to restructure it^[63]. Functionalization and silica precursor type^[44] can also modify the pores size.

However, pore size doesn't affect wall thickness, which is mainly connected with the head group of the surfactant^[4]. Walls thickness can be modulated by pH value - it increases when pH decreases^[4].

External walls surface of the pores consist mainly of silanol groups and siloxane bridges that could be used to attach many chemical species and serve as a matrix, even without functionalization^[31]. Siloxane bridges may be irreversibly hydrolyzed, which is well documented^[64].

Pores order may be influenced by the surfactant used - the longer alkyl chain used the higher is the order degree. This is explained by higher hydrophobicity of those longer chains, which create well-defined cylindrical micelles. Moreover, magnetic field may also be used to alter the orientation of silica-surfactant liquid crystal before the final product is formed^[65,66]. Heat is another factor influencing on pore structure, i. e. poorly condensed MCM-41, formed in less than 2 hours undergoes phase transformation upon thermal treatment and, depending on experimental conditions, it can be transformed either into a lamellar phase or into cubic MCM-48^[67]

The nature and concentration of inorganic or organic anions existing in reaction mixture influences many properties of the final product, such as wall thickness, overall stability and its long range order^[65]. This can be associated with changing the total amount of dissociated silanol groups required to balance the surfactant electrical charge and amount of water stabilized in organic-inorganic interface^[4].

Methods described in this section are classified as endotemplate methods ("soft-matter templating"). In exotemplate methods ordered mesoporous silicas are used as templates in place of the surfactant and, after whole synthesis process,

cured, leaving “negative image” of mesoporous structure^[68,69]. However, this strategy is complex, time-consuming and labor-intensive.

2.3. Modified mesoporous silica particles

2.3.1 Hollow sphere silica particles

Hollow sphere mesoporous particles have already been synthesized by using different techniques: gas bubbles^[70], silica or latex beads^[71], emulsions^[72] and vesicles^[73]. Making small (<200 nm) and uniformly sized particles was developed using two co-templates – polyvinylpyrrolidone (PVP-10) and dodecylamine (DDA)^[74].

Until now, many different synthesis methods have been developed for the preparation of hollow silica spheres: soft templating, hard templating, layer-by-layer method^[75], Kirkendall effect^[76], Ostwald ripening^[77] and galvanic replacement^[78].

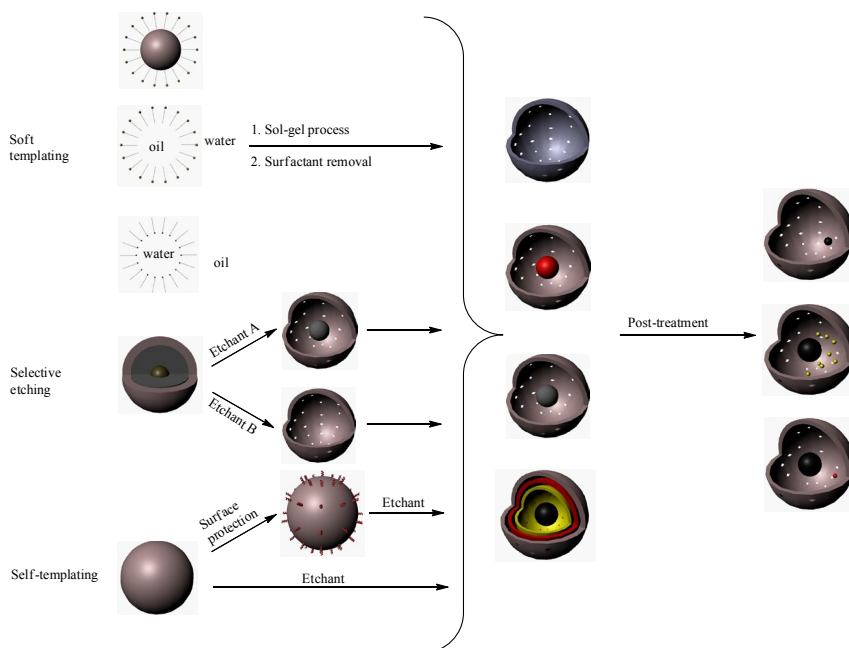


Figure 3. Routes of hollow mesoporous silica particles preparation.

Soft-templating method allows to synthesize different types of hollow

sphere silica, i. e. yolk-shell particles prepared by Xu *et al.* by dispersing SiO₂ or Au nanoparticles into aqueous mixtures of a zwitterionic surfactant, lauryl sulfonate betaine (LSB) and an anionic surfactant, sodium dodecyl benzenosulfonate (SDBS), to induce formation of vesicles with movable, solid nanoparticle cores. Then they attached 3-aminopropyltriethoxysilane on both surfaces of the vesicles, which served as an additional SDA. After removing the surfactant final product may be obtained^[79]. This method can also be used for the synthesis of multilayered shells and hollow spheres with tunable wall thickness^[80]. Mesoporous silica shells with hollow interior may also be prepared by other soft-template methods with addition of co-template^[73], oil-in-water^[81] or water-in-oil^[82] microemulsions, water/oil/water emulsion^[83] and micelle polymer aggregate^[84]. Advantages of soft-template methods are simplicity and effectiveness for the synthesis of hollow- and rattle-type nanomaterials. Unfortunately, there are some disadvantages too. i. e. it is difficult to obtain good dispersity of particles, their size and shell thickness over a broad range. Another one is that large amounts of surfactants are needed, which greatly increases the total cost of industrial synthesis, also complete removal of surfactants is very difficult, and surfactant residues may cause undesirable consequences in biomedical applications^[44].

Selective etching method uses structure and composition differences between pure silica framework and hybrid organic-inorganic networks and their behavior against different etching agents or under exceptional temperature or pH conditions. It allows to easily prepare multilayer core/shell nanoparticles and nanoreactors^[44].

So called self-template method, that doesn't require any additional template was firstly reported in 2005, when the alkaline treatment of cationic polyelectrolyte (poly-(dimethyldiallylammonium chloride) (PDDA)) pre-coated mesoporous silica spheres could transfer the nanoparticles to hollow structure^[85]. It was found that hydroxyl groups permeate through PDDA layer to generate dissolved negatively charged silicate oligomers, which then immigrate and deposit onto the positively charged PDDA layer and cross-link forming the final silica-PDDA complex shell.

2.3.2. Mesostructured silica thin films

Mesostructured silica thin films can be prepared from a solution at room temperature by a process named "evaporation-induced self-assembly", in which one-pot sol, comprising of a silica source and a templating surfactant in aqueous ethanol, is needed^[86]. A substrate (glass or silicon) is dipped into the solution and a thin film of liquid is pulled along with the substrate as it is

retracted. Preferential evaporation of the ethanol during the film deposition leads to the formation of surfactant micelles, that further assemble into crystalline mesophase. Condensation of the silica source around the formed micelles finally produces desired mesostructured silica films^[87].

Mesostructured silica films may be used as a matrix for quantum dots^[88].

2.3.3. Mesoporous silica particles with incorporated metals

Mesoporous silica spheres can be formed around the metal nanocrystals by mixing the silica precursor with an aqueous solution of surfactant-coated nanocrystal^[89]. The electrostatic interactions between the surfactant-coated nanocrystals, free surfactant molecules and hydrolyzed silicate molecules lead to base-catalyzed silica condensation and form the mesostructure. This procedure has been used to embed iron oxide, gold and silver nanocrystals. Such functionalized mesoporous nanoparticles may be used for imaging, as well as for the delivery of biologically active molecules^[90].

Also simple impregnation of mesoporous silica can be useful – Pt/MCM-41 is far more active catalyst than amorphous silica^[91]. Basic catalysts using MCM-41 as the matrix can also be prepared by impregnating it with caesium and lanthanum^[92].

2.3.4. Surface-functionalized mesoporous materials

Surface functionalization for mesoporous silica can be applied by different methods, i. e. co-condensation, by preparing periodically mesoporous organosilicas (PMOs) or by post-synthetic modification called “grafting”.

Co-condensation is an example of direct synthesis route for surface-modified mesoporous materials. In this method SDA is stirred together with a silica source, which is a mixture of standard tetraalkoxysilanes (TMOS and TEOS) and organotrialkoxysilica compounds of the type $(R'O)_3SiR$. The reaction leads to materials with organic residues anchored covalently to pore walls. This synthetic route has some advantages in compare with other ways: organic groups introduced into silica matrix don't block pore opening as it happens in post-synthetic modification and are more homogenously distributed over material's surface. However, co-condensation has also some disadvantages. Increasing concentration of organic residues within the mesostructure influences negatively its order, which can lead to totally disordered products. Maximal reasonable content of organic groups incorporated by co-condensation method cannot exceed 40 mol %. Also, the amount of organic functionalities inside the matrix is generally lower than it corresponds to the starting mixture. This is

caused by the differences in hydrolysis and condensation rates, which leads to favorable homocondensation of organotrialkoxysilanes rather than cross-linking. Moreover, increased content of loading of the incorporated groups causes reduction of pore diameter, pore volume and specific surface areas^[45]. Another inconvenience of this method is that only extraction, as for removing of residual surfactant, may be used, calcination is not suitable.

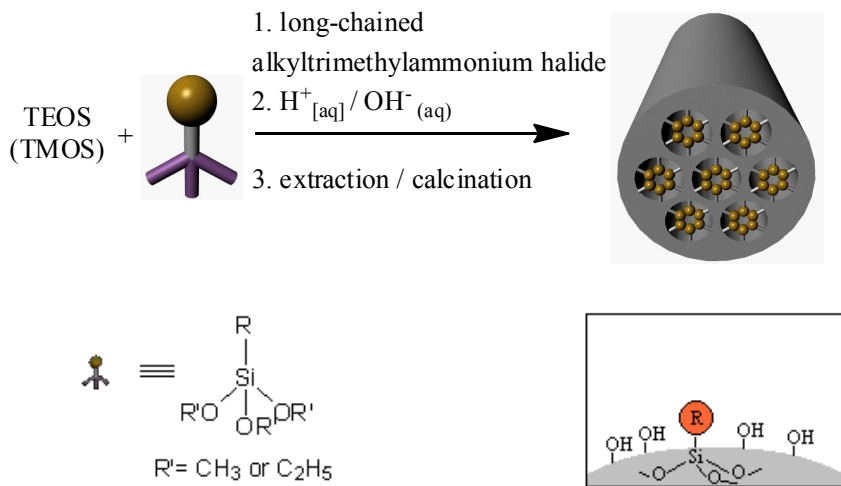


Figure 4. Functionalization through direct synthesis – general scheme for co-condensation method.

The chemical nature of condensing reagents influences the final shape of particles – hydrophilic agents lead to preparation of small, round particles while hydrophobic ones give rod shaped particles^[26].

Also mutual orientation of 2D hexagonal channels in mesoporous silicas may be altered by an addition of chemicals, i. e. some urea-organosilane in different amounts changes alignment of mesoporous channels from straight, helical to radial^[93].

After pioneering articles of the groups of Mann^[94], MacQuarrie^[95] and Stein^[96] many other organically modified mesoporous silicas have been prepared by co-condensation, including alkyl, thiol, vinyl/allyl^[97], amino, cyano/isocyano^[98], alkoxy^[99], organophosphine and aromatic groups^[100]. Mesoporous materials, obtained by following direct synthesis route exhibit interesting catalytic and adsorption properties^[101-107]. It is possible to modify mesoporous silica with even

more complex groups, such as cyclam molecules^[108], large chelate ligands^[109], cyclodextrins^[110], calyx[8]arenes^[111] and pH-sensitive dyes^[112].

Some different mesoporous materials prepared by co-condensation method have been reported. Corriu *et al.* synthesized in 1998 a new hybrid xerogels with pores diameter less than 3,5 to 4 nm^[113]. For the preparation they used dendrimer-like organosilanes.

Preparation of periodic mesoporous organosilicas (PMOs) is another method of obtaining hybrid organic-inorganic materials.

It has been known for a long time in sol-gel chemistry as hydrolysis and condensation of bridged organosilica compounds of the type (R'O)₃Si-R-Si(OR')₃. In this case organic units are incorporated into three-dimensional silica network through two covalent bonds and thus distributed homogenously in the pore walls. Materials prepared in this way as aero- and xerogels can have up to 1800 m² g⁻¹ of surface area but with completely disordered pore systems and wide pore size distribution^[45]. PMOs differ from these amorphous materials with periodically organized pore system and narrow pore size distribution. They were synthesized in 1999 by three groups working independently^[114-116] (Inagaki's group – ethane-bridged, Ozin's and Stein's groups – ethene-bridged PMOs). PMO materials are considered as promising candidates for a series of technical applications, i. e. catalysis, chromatography, adsorption, nanoelectronics or cargo releasing systems^[45].

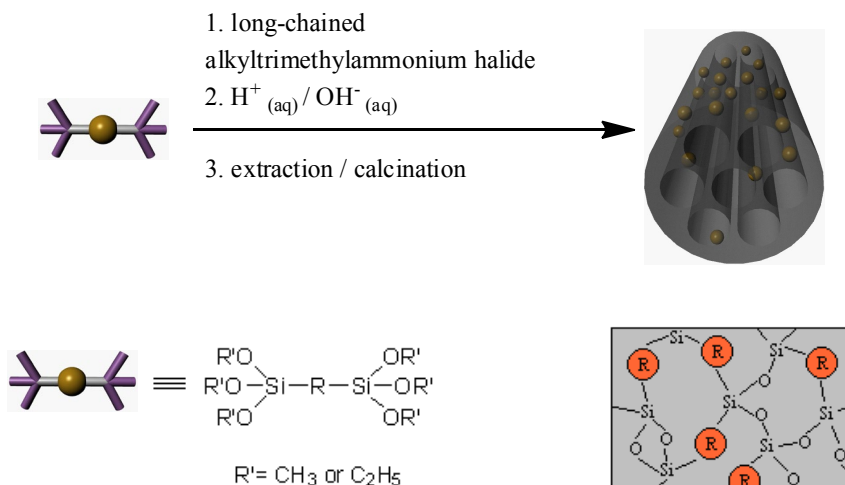


Figure 5. Functionalization through direct synthesis – general scheme for preparation of PMOs.

In a general review of already prepared PMOs, some more interesting may be distinguished:

- aromatic PMOs – benzene^[117], 2,5-dimethylbenzene and 2,5-dimethoxybenzene^[118] bridged with high degree of structural order and pore diameters of about 2 nm
- crystal-like benzene-, bisphenyl-bridged PMOs with long range ordered walls^[119,120]
- ethane-bridged PMOs with use of gemini surfactants and some swelling agents to obtain products with 11 nm pores and without long range order^[121]
- PMOs made with the use of nonionic polymers, with large pores of a diameter up to 20 nm^[122,123], further researches increased their walls order by an addition of inorganic salts^[124] or, without them, by changing the silica precursor and surfactant ratios^[125]; aromatic and unsaturated PMOs with large pores have also been prepared^[126,127]; PMOs based on nonionic surfactants but with smaller pores have also been presented^[128]
- PMOs from tri- and multisilylated precursors^[129,130]
- PMAs (periodic mesoporous aminosilicas) with amino groups anchored in the matrix^[131]
- carbon/silica nanoparticles prepared from benzene-bridged PMOs^[132]
- PMOs from different mixtures of silica precursors.

There have been some studies to adapt PMOs, their morphology, pore size and wall order to different applications: chromatography – monodispersed, spherical, with a particle size of about a few μm ^[133], adsorbents – with large surface area^[134], low-k materials – PMO films^[135], nanowires and catalysis – defined pore geometry, large inner surface area^[136].

Grafting method refers to subsequent modification of the inner surfaces of mesoporous silica phases with organic groups. It's usually carried out by reaction of organosilanes of the type $(\text{R}'\text{O})_3\text{SiR}$ or chlorosilanes ClSiR_3 or silazanes $\text{HN}(\text{SiR}_3)_3$ with the free silanol groups on the pore surfaces.

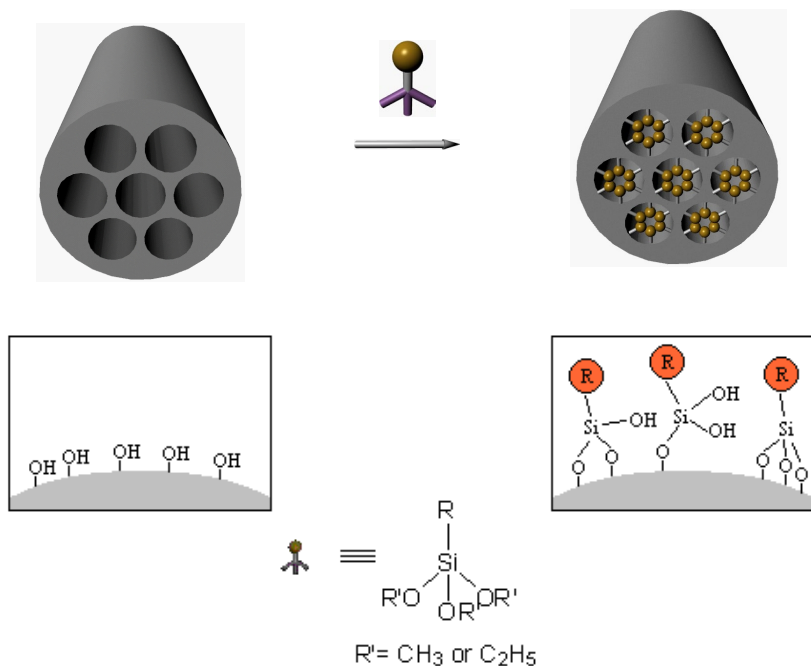


Figure 6. Post-synthetic functionalization – general scheme for grafting.

It is considered, that the reaction of anchoring silanes in presence of water consists of four steps, which can go simultaneously after the first hydrolysis step

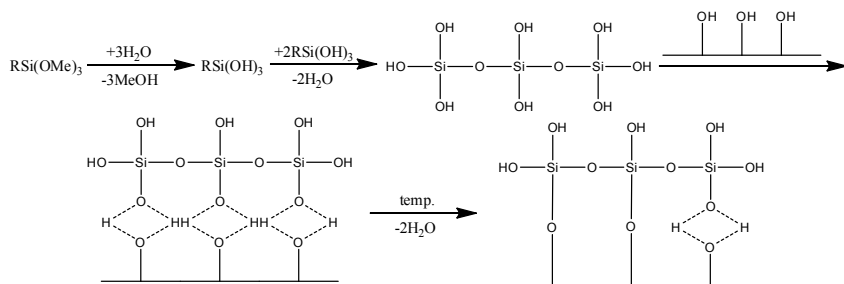


Figure 7. Mechanism of post-synthetic modification through the grafting process in presence of water.

Presence of water in the reacting mixture and its influence on grafting reaction has also been studied. Modifying with 3-aminopropyltrimethoxysilane (APTMS) in presence of water leads to clustering of APTMS and preferential grafting at the pore entrances, reducing uniformity of distribution^[137]. However, for the preparing of the monolayer comprised with 3-mercaptopropyltrimethoxysilane, water is crucial for the formation of respecting hydroxysilane^[138] so there is no one certain answer to the water presence in the reaction mixture.

Anhydrous conditions leads to one-step reaction

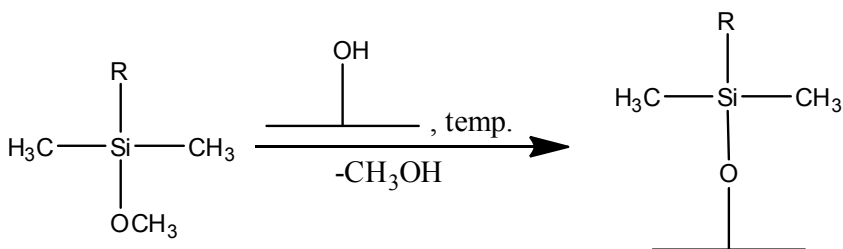


Figure 8. Mechanism of post-synthetic modification through the grafting process in absence of water.

Usually, only one bond between the surface and silane is formed, other two substituents undergo condensation or remain free^[139].

This method has an advantage that the mesostructure of the starting silica phase is usually retained. If the organosilanes react with silanol groups at the pore entrances, the diffusion of other molecules can be impaired or even stopped (pore blockade)^[45,140]. Also solvents used affect the distribution of functional groups on the surface, i. e. toluene is not a proper choice, because it leads to anchoring organosilanes near pore entrances, while alcohols or THF produce higher degree of site isolation and more homogenous distribution^[141,142].

Obtaining of site-isolated functionalization of silica's surface has also been performed. McKittrick and Jones used tritylimine patterning agent to control the minimum distance between the amino- groups anchored to the surface, and after grafting the tritylimine to the surface and capping remaining silanol groups with hexamethyldisilazane, they hydrolyzed patterning agent to get the final product^[143]. The use of smaller protecting group leads to higher grafting density. Also imprinting method can be used to get site-isolated functionalization of the surface. Circle molecules can be grafted onto internal surface, leaving some part of the surface free. Then, another functionality can be introduced, but only on

the unoccupied part of the surface. In the last step, circle molecules are removed, leaving site-isolated modified surface.

Selective grafting of the external surface can be done, while SDA is still inside the pores of as-synthesized silica^[144].

It is also possible to graft thin silica films for an additional functionality – Tanaka *et al.* prepared such films modified by a new vapor-infiltration technique, where the samples were exposed to the vapor of organosilica functionalization reagents at high temperature for several hours in an autoclave^[145].

Grafting can also be done for larger organic groups like dendrimers^[146], chlorophyll^[147] and fullerenes^[148], for making acid^[149], base^[150], oxidative^[151] and chiral^[152] catalysts. Thiol functionalized MCM-41 has been used as an adsorptive for heavy metals from solution^[153].

3. Application of mesoporous silicas in biomedicine and cosmetics industry

3.1. Biocompatibility and toxicity

An ideal delivery system used in biomedicine should be able to deliver cargo to a targeted site in a controlled manner and be characterized by:

- biocompatibility and biodegradability
- controlled release of cargo
- controlled loading and targeted release of therapeutics
- zero premature release
- stimuli responsiveness^[26].

Mesoporous silica MCM-41 compared to solid silica spheres was found to be less toxic^[154]. Surface functionalization has drastic effect on the toxicity of mesoporous silicas^[155].

Positively charged silicas induces more immune response and cytotoxicity than neutral or negatively charged ones but they are better for transvascular transport in tumor^[156]. Silanol groups can react with biological molecules such as lipids and proteins destroying their structures^[157]. Unmodified silica with negative zeta potential is rapidly associated with serum opsonin in blood and cleared from circulating system. The most effective coating, increasing biocompatibility and half-time of mesoporous silica particles is PEGylation, approved by FDA, which creates a protective, hydrophilic layer around them^[158]. PEGylation also improves silica's properties in the hemolytic activity and cytotoxicity, and decreases the endocytosis of modified silica particles^[155]. *In vitro* studies have shown how mesoporous silica interacts with different cell lines, i. e. 3T3 endothelial cells^[159], human colon carcinoma (Caco-2)^[160], glioma cells^[161], human mesenchymal stem cells^[162] and HeLa cells^[163]. *In vivo* biodistribution and excretion can be regulated by adding the functional groups like amino, carboxyl,

phenyl and methyl phosphonate with different zeta potentials, i. e. nitrogen-modified (different functional groups) manipulates the particle endocytosis of HeLa cells^[164]. Coating silica with lipid layer improves its biocompatibility and performance, gives better suspensibility and much lower nonspecific binding *in vitro* in compare to unmodified silica^[165]. Cellular uptake studies may be performed and visualized by attaching a fluorescent dye to the silica surface by co-condensation method^[41].

Influence of particles shape on the endocytosis rate is also significant – there is a model with a concept of “wrapping time” which explains, why the spherical particles undergo faster endocytosis than the cylindrical ones^[166] for both *in vitro* and *in vivo* (human fibroblast cells^[167]) studies.

Size of the mesoporous silica particles has an uncertain status of being important for their toxicity – although some sources mention that the smaller particles used the less cytotoxic they are^[168]. Particles with a diameter less than 500 nm are easily taken up by the cell through endocytosis and can be localised in lysosomes of the cell.

Structure and high surface area of mesoporous silica particles may also be an important factor influencing the total toxicity – large amount of free silanol groups generate reactive oxygen species that are the cause of nanomaterial-caused injuries^[169]. It is also a cause of cellular and mitochondrial respiration inhibition^[170] and oxidative stress^[171].

He *et al.* found that the synthesis method plays also some role in the overall toxicity – different MCM-41 particles using Triton, CTAB and SDBS as surfactants were prepared and their toxicity was tested. CTAB-based MCM-41 was more toxic than SDBS one and the least was Triton-based MCM-41^[172].

Also the influence of size, porosity, particles coating and dosage of mesoporous materials on the activity of hemolytic cells was tested and the results were that the smaller particles the higher is their hemolytic activity^[173]. However, *in vivo* studies have shown that mesoporous silica nanoparticles reveal size-independent toxicity but highly dependent on the administration route^[174].

Mesoporous particles are eliminated from the human body by hepatobiliary excretion, which was proved by Souris *et al*^[175]. Elimination rate is size and surface modification dependent as well as the way of synthesis – mesoporous silicas prepared by extraction are much faster eliminated than calcinated and amorphous ones^[176].

3.2. Adsorption and release studies

Until now, a wide variety of drugs (or dyes) have been loaded and released in a controlled manner using unmodified or modified mesoporous silicas^[26]:

- MCM-41 – ibuprofen, vancomycin, gentamycin, aspirin, alendronate, camptothecin, atenolol, BSA, cytochrome C, paclitaxel, DNA, vitamine B₂, calcein, safranin O,
- SBA-15 – gentamycin, amoxicillin, erythromycin, alendronate, L-tryptophan, BSA,
- hollow mesoporous silicas – fluorescein isothiocyanate,
- MSN – Orange II, rhodamine-B, DNA, ibuprofen, alendronate,
- MSN II – DNA into plant cells,
- MCM-48 – erythromycin,
- FSM – Taxol,

There are many physicochemical parameters, that can affect adsorption and release of cargo from mesoporous silicas:

- particle size and morphology – Monzano *et al.* studied the release of ibuprofen from spherical MCM-41 particles with a size between 490-770 nm and they concluded that better release control was achieved with smaller particles. However, it was much slower than while using irregularly shaped particles. They summarized, that spherical particles are better in controlled delivery of ibuprofen^[177]. Qu *et al.* showed that adsorption of captopril was higher in rod shaped particles than in spherical ones^[178]; hollow structured mesoporous silicas show higher loading capacities than typical ones, except of pore blocking molecules (effective pore volume decreases rapidly for hollow particles^[179]),
- pore size – Hata *et al.* first reported the effect of pore size and influence of solvent on the loading and release of Taxol^[180] and Vallet-Regi *et al.* – release rate of ibuprofen^[31]. Large pores are required for adsorption and separation of proteins^[181,182] and adsorption of DNA or RNA^[183]; pore size affects also loading kinetics, which has been proved for captopril^[178],
- pore structure – it is demonstrated that pore connectivity, geometry and matrix degradation have an influence on adsorption and release properties of mesoporous silica, i. e. Linden *et al.*^[184] showed that SBA-1 mesoporous silica with interconnected pores system revealed similar loading capacity and slightly faster release rate of ibuprofen than SBA-3 mesoporous silica without internal interconnection,
- pore volume – it is considered as a critical factor for drug loading and release because of drug-drug interactions which may be even more important than drug-silica surface ones, it has been reported that consecutive loadings of drug in ordered mesoporous materials leads to larger filling of the mesopores^[185],

- surface area – increased number of active adsorption sites increases amount of cargo adsorbed, which has been verified for alendronate^[186],
- surface functionalization – carried out by co-condensation, grafting and PMO synthesis methods, i. e. creating different coatings made of PEI (polyethyleneimine) increases amount of DNA and siRNA adsorbed or improves the delivery of paclitaxel^[187]; Tourne-Peteilh *et al.* prepared transport system for ibuprofen by simple anchoring it to the surface through ester bond, where release was achieved after its cleavage^[188],
- pH at which the adsorption is carried out – for proteins the highest amount of cargo loaded was observed near the isoelectric point^[189],
- molecule's polarity – since silica surface is polar (silanol groups) or negatively charged ($pK_a \sim 2,5$) at higher pH values, polarity is an important factor affecting the amount and distribution of molecules adsorbed – Okazaki and Toriyama have studied the diffusion of isopropanol and cyclohexane in contact with MCM-41 and they have found that alcohol preferred to occupy the regions at and near the external surface while the cyclohexane deposited deeper within the nanochannels^[190],
- surface polarity – silica may be functionalized with hydrophobic species, in this case cargo-surface interactions don't play any significant role, but the cargo transport out of the matrix is seriously impeded as the polar solvents don't easily penetrate it^[186]; hydrophobization of silica surface makes it more resistant to hydrolysis^[191].

Amount of drug needed is a very important issue, because even with achieving high loading capacities, large amounts of mesoporous matrix is needed to create a drug formulation, which can be digested by i. e. oral route (tablets usually). As an examples of daily drug dose/matrix needed: gentamicin:SBA-15 150-300mg:2g, erythromycin:SBA-15 1,5-3g:3,4g, ibuprofen:MCM-41 0,9-1,2g:7g^[186].

Liu *et al.* synthesized multi-shelled hollow spheres, which can be utilized to load different chemicals in each shell and release them controllably by changing the walls thickness^[192].

Release of the cargo can be activated by different stimuli such as:

- pH – it is one of the most important factor triggering release of trapped molecules, because of the facility to control it and that in human's body there are regions, organs, cells differing in the pH value, which can be used in targeted delivery; the most often pH sensitive systems use amine functionalization because of their ability to protonate/deprotonate at certain pH values^[20]; some of the more interesting systems using pH triggering are: coating made of cyclodextrin and

- PEI complexes releasing cargo upon breaking the polypseudorotaxane protection^[17], molecular machines made of cucurbituril complexes with the silica, opening at lower pH values and closing at higher ones (so called molecular clock)^[193] or the use of surface modifying individuals with bonds breaking at certain pH values (hydrazone^[194], acetal^[195] or orthoester^[196]),
- enzymes – systems based on enzymes contain coatings sensitive to the treatment of specific enzymes, i. e. capping mesoporous silica with biotin-avidin complex makes it sensitive to proteases^[24], β -CD coating is responsive to the α -amylase and lipase enzymes^[197],
 - chemicals – CdS capped nanoparticles sensitive to the reaction of amidation was reported by Lai *et al.*^[13]; gold nanoparticles associated with the surface by photocleavable linker, thioundecyltetraethyleneglycoester-*o*-nitrobenzylethyl dimethyl ammonium bromide (TUNA) sensitive to UV irradiation reported by Lin *et al.*^[198] and Amoros *et al.*^[199]; also some magnetic nanoparticles coated with supraparamagnetic iron oxide with anti-oxidants as triggering factor were prepared; glucose responsive delivery of insulin with a gluconic acid modified insulin proteins immobilized on mesoporous silica is another example of chemical trigger for cargo release^[163] and anion-driven gate-like system based on polyamines (sensitive to different organic and inorganic anions like chloride, acetate or ATP)^[200],
 - thermal responsive systems are based on sensitive polymers like poly-N-isopropylacrylamide (PNIPAm)^[201]; moreover, it is possible to create a system based on PNIPAm, in which conformational changes of polymer induce structural changes in silica – it can give a possibility to release cargo at certain temperature^[202],
 - light – irradiation at certain wavelength can induce breaking bonds of pore blocking individuals, as presented by Mal *et al.* who grafted coumarin onto the outer surface of MCM-41 mesoporous silica and irradiated them with UV light at 310 nm. Coumarin dimerization then and closes pore openings, making cargo release impossible. Subsequent irradiation at 250 nm breaks the coumarin dimer and allows to release the cargo^[15]; Sierocki *et al.* reported similar light responsiveness for azobenzene derivatives, that change their *cis-trans* geometry upon light irradiation^[203].

There are also some sophisticated systems based on catenanes and rotaxanes (mechanically interlocked molecules) which use different interactions such as donor-acceptor^[204], hydrogen bonding^[205], metal-ligand^[206] and hydrophobic^[207]

interactions to release cargo in a controllable way.

Release profiles differ from each other, depending on the adsorption and functionalization methods: nonfunctionalized matrices (a) shows burst release at start and then slow release, diffusion or dissolution processes (b) presents first-order kinetics with respect to drug concentration, zero-order release kinetics (c) for some functionalized systems, profile (d) corresponds sophisticated stimulus-responsive system with release rate controlled by external changes^[186].

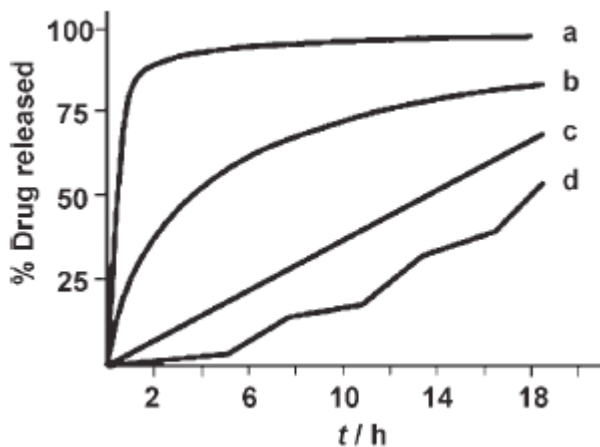


Figure 9. Release profiles from different mesoporous systems – adapted from^[186].

3.3. Sensors and some other applications

Functionalized mesoporous silicas may also have an important meaning as sensors.

Radu *et al.* synthesized by co-condensation method thiol-functionalized MCM-41 silica and attached epoxyhexyl groups to the outer surface before removal of the surfactant. Inner thiol groups were modified by *o*-phthalaldehyde and a layer of poly-L-lactic acid was polymerized onto the outer surface to eventually obtain a neurotransmitter sensor, which could differentiate between three different neurotransmitters: dopamine, tyrosine and glutamic acid. The outer, polymeric coating has different permeability for each of them and that caused the selectivity^[208].

Descalzo *et al.* prepared an ATP sensor based on N-propylanthracene-10-amino functionalized MCM-41 silica. Presence of ATP was detected by the reduction of fluorescence signal^[209].

Mesoporous silica-based may also be used in analytic chemistry, i. e. to quantitative determination of copper ions^[210], binding mercury(II)^[211], palladium(II) and platinum(II)^[212] or borate^[213] ions.

Iron oxide may be used in cancer treatment as superparamagnetic nanoparticles embedded in mesoporous silica, delivering heat under alternating magnetic fields, as a result of Brownian rotation and Neel relaxation^[214].

Acknowledgements

This work was partially supported from the funds of National Science Centre (grant no. 2011/03/B/ST5/01573).

References

1. Hasanzadeh, M.; Shadjou, N.; Eskandani, M.; de la Guardia, M. Mesoporous silica-based materials for use in electrochemical enzyme nanobiosensors. *Trends in Analytical Chemistry* **40**, 106-118 (2012).
2. Kresge, C. T.; Leonowicz, M. E.; Roth, W. J.; Vartuli, J. C.; Beck J. S. Ordered mesoporous sieves synthesized by a liquid crystal templating mechanism. *Nature* **359**, 710-712 (1992).
3. Di Renzo, F.; Cambon, H.; Dutarte R. A 28-year-old synthesis of micelle-templated mesoporous silica. *Micropor. Mater.* **10**, 283-286 (1997).
4. Davidson, A. Modyfying the walls of mesoporous silicas prepared by supramolecular-templating. *Colloid & Interface Science* **7**, 92-106 (2002).
5. Han, Y.; Ying, J. Y. Generalized Fluorocarbon-Surfactant-Mediated Synthesis of Nanoparticles with Various Mesoporous Structures. *Angew. Chem. Int. Ed.* **44**, 288-292 (2004).
6. Huo, Q.; Margolese, D. I.; Ciesla, U.; Feng, P.; Gier, T. E.; Sieger, P.; Leon, R.; Petroff, P. M.; Schuth, F.; Stucky, G. D. Generalized synthesis of periodic surfactant/inorganic composite materials. *Nature* **368**, 317-321 (1994).
7. Shigeno, T.; Nagao, M.; Kimura, T.; Kuroda, K. Direct Silylation of a Mesostructured Precursor for Novel Mesoporous Silica KSW-2. *Langmuir* **18**, 8102-8107 (2002).
8. Kimura, T.; Itoh, D.; Okazaki, N.; Kaneda, M.; Sakamoto, Y.; Terasaki, O.; Sugahara, Y.; Kuroda, K. Lamellar hexadecyltrimethylammonium silicates derived from kanemite. *Langmuir* **16**, 7624-7628 (2000).
9. Inagaki, S.; Fukushima, Y.; Kuroda, K. Synthesis of Highly Ordered

- Mesoporous Materials from a Layered Polysilicates. *J. Chem. Soc., Chem. Commun.*, 680-682 (1993).
- Zhang, W.; Pauly, T. R.; Pinnavaia, T. J. Tailoring the Framework and Textural Mesopores of HMS Sieves through an Electrically Neutral (S⁰) Assembly Pathway. *Chem. Mater.* **9**, 2491-2498 (1997).
 - Kadib, A. E.; Katir, N.; Bousmina, M.; Majoral, J. P. Dendrimer-silica hybrid mesoporous materials. *New J. Chem.* **36**, 241-255 (2012).
 - Ruiz-Hernandez, E.; Baeza, A.; Vallet-Regi, M. Smart Drug Delivery through DNA/Magnetic Nanoparticle Gates. *ACS Nano* **5**, 1259-1266 (2011).
 - Lai, C. Y.; Trewyn, B. G.; Jeftinija, D. M.; Jeftinija, K.; Xu, S.; Jeftinija, S. et al. A mesoporous silica nanosphere-based carrier system with chemically removable CdS nanoparticle caps for stimuli-responsive controlled release of neurotransmitters and drug molecules. *J. Am. Chem. Soc.* **125**, 4451-4459 (2003).
 - Kim, H. J.; Matsuda, H.; Zhou, H. S.; Honma, I. Ultrasound-triggered smart drug release from a poly(dimethylsiloxane)-mesoporous silica composite. *Adv. Mater.* **18**, 3083 (2006).
 - Mal, N. K.; Fujiwara, M.; Tanaka, Y. Photocontrolled reversible release of guest molecules from coumarin-modified mesoporous silica. *Nature* **421**, 350-353 (2003).
 - Yang, Q.; Wang, S. H.; Fan, P. W.; Wang, L. F.; Di, Y.; Lin, K. F. et al. pH-Responsive carrier system based on carboxylic acid modified mesoporous silica and polyelectrolyte for drug delivery. *Chem. Mater.* **17**, 5999-6003 (2005).
 - Park, C.; Oh, K.; Lee, S. C.; Kim, C. Controlled Release of Guest Molecules from Mesoporous Silica Particles Based on a pH-Responsive Polypseudorotaxane Motif. *Angew. Chem. Int. Ed.* **46**, 1455-1457 (2007).
 - Khashab, N. M.; Belowich, M. E.; Trabolsi, A.; Friedman, D. C.; Valente, C.; Lau, Y.; Khatib, H. A.; Zink, J. I.; Stoddart, J. F. pH-Responsive mechanized nanoparticles gated by semirotaxanes. *Chem. Commun.*, 5371-5373 (2009).
 - Khashab, N. M.; Trabolsi, A.; Lau, Y. A.; Ambrogio, M. W.; Friedman, D. C.; Khatib, H. A.; Zink, J. L.; Stoddart, J. F. Redox- and pH-controlled mechanized nanoparticles. *Eur. J. Org. Chem.*, 1669-1673 (2009).
 - Du, L.; Liao, S.; Khatib, H. A.; Stoddart, J. F.; Zink, J. I. Controlled-Access Hollow Mechanized Silica Nanocontainers. *J. Am. Chem. Soc.* **131**, 15136-15142 (2009).

21. Fu, Q.; Rao, G. V. R.; Ista, L. K.; Wu, Y.; Andrzejewski, B. P.; Sklar, L. A. et al. Control of molecular transport through stimuli-responsive ordered mesoporous materials. *Adv. Mater.* **15**, 1262-1266 (2003).
22. Aznar, E.; Mondragon, L.; Ros-Lis, J. V.; Sancenon, F.; Marcos, D.; Martinez-Manez, R.; Soto, J.; Perez-Paya E.; Amoros, P. Finely Tuned Temperature-Controlled Cargo Release Using Paraffin-Capped Mesoporous Silica Nanoparticles. *Angew. Chem. Int. Ed.* **50**, 11172-11175 (2011).
23. Hernandez, R.; Tseng, H.-R.; Wong, J. W.; Stoddart, J. F.; Zink, J. I. An Operational Supramolecular Nanovalve. *J. Am. Chem. Soc.* **126**, 3370-3371 (2004).
24. Patel, K.; Angelos, S.; Dichtel, W. R.; Coskun, A.; Yang, Y.-W.; Zink, J. I.; Stoddart, J. F. Enzyme-Responsive Snap-Top Covered Silica Nanocontainers. *J. Am. Chem. Soc.* **130**, 2382-2383 (2008).
25. Arruebo, M.; Galan, M.; Navascues, N.; Tellez, C.; Marquina, C.; Ibarra, M. R. et al. Development of magnetic nanostructured silica-based materials as potential vectors for drug-delivery applications. *Chem. Mater.* **18**, 1911-1919 (2006).
26. Papat, A.; Hartono, S. B.; Stahr, F.; Liu, J.; Qiao, S. Z.; Lu, G. Q. Mesoporous silica nanoparticles for bioadsorption, enzyme immobilisation, and delivery carriers. *Nanoscale* **3**, 2801-2818 (2011).
27. Theije, F. K. de; Balkenende, A. R.; Verheijen, M. A.; Baklanov, M. R.; Mogilnikov, K. P.; Furukawa, Y. Structural Characterization of Mesoporous Organosilica Films for Ultralow- k Dielectrics. *J. Phys. Chem.* **107**, 4280-4289 (2003).
28. Tao, S.; Li, G. Porphyrin-doped mesoporous silica films for rapid TNT detection. *Colloid Polym. Sci.* **285**, 721-728 (2007).
29. Hasanzadeh, M.; Shadjou, N.; Eskandani, M.; de la Guardia, M.; Sheikhzadeh, P. Mesoporous silica-based materials for use in biosensors. *Trends in Analytical Chemistry* **33**, 117-129 (2012).
30. Trewyn, B. G.; Giri, S.; Slowing, I. I.; Lin, V. S.-Y. Mesoporous silica nanoparticles based controlled release, drug delivery, and biosensor systems. *Chem. Commun.*, 3236-3245 (2007).
31. Vallet-Regi, M.; Ramila, A.; del Real, R. P.; Perez-Pariente, J. A New Property of MCM-41: Drug Delivery System. *Chem. Mater.* **13**, 308-311 (2001).
32. Barbe, C.; Bartlett, J.; Kong, L. G.; Finnie, K.; Lin, H. Q.; Larkin, M. et al. Silica particles: a novel drug-delivery system. *Adv. Mater.* **16**, 1959-1966 (2004).

33. Ambrogi, V.; Perioli, L.; Marmottini, F.; Giovagnoli, S.; Esposito, M.; Rossi, C. Improvement of dissolution rate of piroxicam by inclusion into MCM-41 mesoporous silicate. *Eur. J. Pharm. Sci.* **137**, 30-37 (2007).
34. Song, S.-W.; Hidajat, K.; Kawi, S. Functionalized SBA-15 Materials as Carriers for Controlled Drug Delivery: Influence of Surface Properties on Matrix-Drug Interactions. *Langmuir* **21**, 9568-9575 (2005).
35. Lopez, T.; Basaldella, E. I.; Ojeda, M. L.; Manjarrez, J.; Alexander-Katz, R. Encapsulation of valproic acid and sodic phenytoin in ordered mesoporous SiO₂ solids for the treatment of temporal lobe epilepsy. *Opt. Mater.* **29**, 75-81 (2006).
36. Pasqua, L.; Testa, F.; Aiello, R.; Cundari, S.; Nagy, J. B. Preparation of bifunctional hybrid mesoporous silica potentially useful for drug targeting. *Microporous and Mesoporous Materials* **103**, 166-173 (2007).
37. Gu, J.; Fan, W.; Shimojima, A.; Okubo, T. Organic-inorganic mesoporous nanocarriers, integrated with biogenic ligands. *Small* **3**, 1740-1744 (2007).
38. Izquierdo-Barba, I.; Ruiz-Gonzalez, L.; Doadrio, J. C.; Gonzalez-Calbet, J. M.; Vallet-Regi, M. Tissue regeneration: a new property of mesoporous materials. *Solid State Sci.* **7**, 983-989 (2005).
39. Li, X.; Shi, J. L.; Zhu, Y. F.; Shen, W. H.; Li, H.; Liang, J. et al. A template route to the preparation of mesoporous amorphous calcium silicate with high in vitro bone-forming bioactivity. *J. Biomed. Mater. Res. B.* **83B**, 431-439 (2007).
40. Radu, D. R.; Lai, C. Y.; Jeftinija, K.; Rowe, E. W., Jeftinija, S.; Lin, V. S. Y. A polyamidoamine dendrimer-capped mesoporous silica nanosphere-based gene transfection reagent. *J. Am. Chem. Soc.* **126**, 13216-13217 (2004).
41. Lin, Y. S.; Tsai, C. P.; Huang, H. Y.; Kuo, C. T.; Hung, Y.; Huang, D. M. et al. Well-ordered mesoporous silica nanoparticles as cell markers. *Chem. Mater.* **17**, 4570-4573 (2005).
42. Aznar, E.; Sancenon, F.; Marcos, M. D.; Martinez-Manez, R.; Stroeve, P.; Cano, J.; Amoros, P. Delivery Modulation in Silica Mesoporous Supports via Alkyl Chain Pore Outlet Decoration. *Langmuir* **28**, 2986-2996 (2011).
43. Marcato, P. D.; Duran, N. New Aspects of Nanopharmaceutical Delivery Systems. *J. Nanosci. Nanotechnol.* **8**, 1-14 (2008).
44. Tang, F.; Li, L.; Chen, D. Mesoporous Silica Nanoparticles: Synthesis,

- Biocompatibility and Drug Delivery. *Adv. Mater.* **24**, 1504-1534 (2012).
45. Hoffmann, F.; Cornelius, M.; Morell, J.; Froba, M. Silica-Based Mesoporous Organic-Inorganic Hybrid Materials. *Angew. Chem. Int. Ed.* **45**, 3216-3251 (2006).
 46. Stober, W.; Fink, A.; Bohn, E. Controlled growth of monodisperse silica spheres in the micron size range. *J. Colloid Interface Sci.* **26**, 62-69 (1968).
 47. Wu, K. C.-W.; Yamauchi, Y. Controlling physical features of mesoporous silica nanoparticles (MSNs) for emerging applications. *Journal of Materials Chemistry* **22**, 1251-1256 (2012).
 48. Lu, F.; Wu, S. H.; Hung, Y.; Mou, Y. N. Size effect on Cell Uptake in Well-Suspended, Uniform Mesoporous Silica Nanoparticles. *Small* **5**, 1408 (2009).
 49. Qiao, Z. A.; Zhang, L.; Guo, M.; Liu, Y.; Huo, Q. Synthesis of Mesoporous Silica Nanoparticles via Controlled Hydrolysis and Condensation of Silicon Alkoxide. *Chem. Mater.* **21**, 3823-3829 (2009).
 50. Chiang, Y.-D.; Lian, H.-Y.; Leo, S.-Y.; Wang, S.-G.; Yamauchi, Y.; Wu, K.C.-W. Controlling particle size and structural properties of mesoporous silica nanoparticles using the taguchi method. *J. Phys. Chem. C* **115**, 13158-13165 (2011).
 51. Berggren, A.; Palmqvist, A.E.C. Particle size control of colloidal suspensions of mesostructured silica. *J. Phys. Chem. C* **112**, 732-737 (2008).
 52. Urata, C.; Aoyama, Y.; Tonegawa, A.; Yamauchi, Y.; Kuroda, K. Dialysis process for the removal of surfactants to form colloidal mesoporous silica nanoparticles. *Chem. Commun.*, 5094-5096 (2009).
 53. Anderson, M. T.; Martin, J. E.; Odinek, J. G.; Newcomer, P. P. Surfactant-Templated Silica Mesophases Formed in Water:Cosolvent Mixtures. *Chem. Mater.* **10**, 311-321 (1998).
 54. Rosenholm, J. M.; Sahlgren, C.; Linden, M. Towards multifunctional, targeted drug delivery systems using mesoporous silica nanoparticles - Opportunities & challenges. *Nanoscale* **2**, 1870-1883 (2010).
 55. Cai, Q.; Luo, Z.-S.; Pang, W.-Q.; Fan, Y.-W.; Chen, X.-H.; Cui, F.-Z. Dilute solution routes to various controllable morphologies of MCM-41 silica with a basic medium. *Chem. Mater.* **13**, 258-263 (2001).
 56. Ji, X.; Lee, K. T.; Monjauze, M.; Nazar, L. F. Strategic synthesis of SBA-15 nanorods. *Chem. Commun.*, 4288-4290 (2008).
 57. Kim, T.-W.; Slowing, I. I.; Chung, P.-W.; Lin, V.S.-Y. Ordered mesoporous polymer-silica hybrid nanoparticles as vehicles for the

- intracellular controlled release of macromolecules. *ACS Nano* **5**, 360-366 (2011).
58. Lin, H.-P.; Mou, C.-Y. 'Tubules-within-a-tubule' hierarchical order of mesoporous molecular sieves in MCM-41. *Science* **273**, 765-768 (1996).
 59. Schacht, S.; Huo, Q.; Voigt-Martin, I. G.; Stucky, G. D.; Schuth, F. Oil-water interface templating of mesoporous macroscale structures. *Science* **273**, 768-771 (1996).
 60. Huo, Q.; Zhao, D.; Feng, J.; Weston, K.; Buratto, S. K.; Stucky, G. D.; Schacht, S.; Schuth, F. Room temperature growth of mesoporous silica fibers: A new high-surface-area optical waveguide. *Adv. Mater.* **9**, 974-978 (1997).
 61. Bruinsma, P. J.; Kim, A. Y.; Liu, J.; Baskaran, S. Mesoporous Silica Synthesized by Solvent Evaporation: Spun Fibers and Spray-Dried Hollow Spheres. *Chem. Mater.* **9**, 2507-2512 (1997).
 62. Beck, J. S.; Vartuli, J. C.; Roth, W. J.; Leonowicz, M. E.; Kresge, C. T.; Schmitt, K. D.; Chu, C. T.-W.; Olson, D. H.; Sheppard, E. W.; McCullen, S. B.; Higgins, J. B.; Schlenker, J. L. A new family of mesoporous molecular sieves prepared with liquid crystal templates. *J. Am. Chem. Soc.* **114**, 10834-10843 (1992).
 63. Khushalani, D.; Kuperman, A.; Ozin, G.A.; Tanaka, K.; Garces, J.; Olken, M. M.; Coombs, N. Metamorphic materials: Restructuring siliceous mesoporous materials. *Adv. Mater.* **7**, 842-846 (1995).
 64. Zhao, X. S.; Audsley, F.; Lu, G. Q. Irreversible change of pore structure of MCM-41 upon hydration at room temperature. *J. Phys. Chem. B* **102**, 4143-4146 (1998).
 65. Schulz-Ekloff, G.; Rathousky, J.; Zukal, A. Controlling of morphology and characterization of pore structure of ordered mesoporous silicas. *Microporous and Mesoporous Materials* **27**, 273-285 (1999).
 66. Sierra, L.; Guth, J.-L. Synthesis of mesoporous silica with tunable pore size from sodium silicate solutions and a polyethylene oxide surfactant. *Microporous and Mesoporous Materials* **27**, 243-253 (1999).
 67. Landry, C. C.; Tolbert, S. H.; Gallis, K. W.; Monnier, A.; Stucky, G. D.; Norby, P.; Hanson, J. C. Phase transformations in mesostructured silica/surfactant composites. Mechanisms for change and applications to materials synthesis. *Chem. Mater.* **13**, 1600-1608 (2001).
 68. Ryoo, R.; Joo, S. H.; Jun, S. Synthesis of highly ordered carbon molecular sieves via template-mediated structural transformation. *J. Phys. Chem. B* **103**, 7745-7746 (1999).

69. Lee, J.; Yoon, S.; Hyeon, T.; Oh, S. M.; Kim, K. B. Synthesis of a new mesoporous carbon and its application to electrochemical double-layer capacitors. *Chem. Commun.*, 2177-2178 (1999).
70. Rana, R. K.; Mastai, Y.; Gedanken, A. Acoustic cavitation leading to the morphosynthesis of mesoporous silica vesicles. *Adv. Mater.* **14**, 1414-1418 (2002).
71. Blas, H.; Save, M.; Pasetto, P.; Boissiere, C.; Sanchez, C.; Charleux, B. Elaboration of monodisperse spherical particles with ordered mesoporous silica shells via dual latex/surfactant templating: Radial orientation of mesopore channels. *Langmuir* **24**, 13132-13137 (2008).
72. Sun, Q.; Kooyman, P. J.; Grossmann, J. G.; Bomans, P. H. H.; Frederik, P. M.; Magusin, P. C. M. M.; Beelen, T. P. M.; Van Santen, R. A.; Sommerdijk, N. A. J. M. The formation of well-defined hollow silica spheres with multilamellar shell structure. *Adv. Mater.* **15**, 1097-1100 (2003).
73. Yeh, Y.-Q.; Chen, B.-C.; Lin, H.-P.; Tang, C.-Y. Synthesis of hollow silica spheres with mesostructured shell using cationic-anionic-neutral block copolymer ternary surfactants. *Langmuir* **22**, 6-9 (2006).
74. Du, L. Song, H.; Liao, S. Tuning the morphology of mesoporous silica by using various template combinations. *Applied Surface Science* **255**, 9365-9370 (2009).
75. Javier, A. M.; Kreft, O.; Semmling, M.; Kempter, S.; Skirtach, A. G.; Bruns, O. T.; Del Pino, P.; Bedard, M. F.; Raedler, J.; Kas, J.; Plank, C.; Sukhorukov, G. B.; Parak, W. J. Uptake of colloidal polyelectrolyte-coated particles and polyelectrolyte multilayer capsules by living cells. *Adv. Mater.* **20**, 4281-4287 (2008).
76. Yin, Y.; Rioux, R. M.; Erdonmez, C. K.; Hughes, S.; Somorjal, G. A.; Alivisatos, A. P. Formation of Hollow Nanocrystals Through the Nanoscale Kirkendall Effect. *Science* **304**, 711-714 (2004).
77. Low, X. W.; Yuan, C.; Rhoades, E.; Zhang, Q.; Archer, L. A. Encapsulation and Ostwald ripening of Au and Au-Cl complex nanostructures in silica shells. *Adv. Funct. Mater.* **16**, 1679-1684 (2006).
78. Chen, J.; McLellan, J. M.; Siekkinen, A.; Xiong, Y.; Li, Z.-Y.; Xia, Y. Facile synthesis of gold-silver nanocages with controllable pores on the surface. *J. Am. Chem. Soc.* **128**, 14776-14777 (2006).
79. Wu, X.-J.; Xu, D. Formation of Yolk/SiO₂ shell structures using surfactant mixtures as template. *J. Am. Chem. Soc.* **131**, 2774-2775 (2009).
80. Djojoputr, H.; Zhou, X. F.; Qiao, S. Z.; Wang, L. Z.; Yu, C. Z.; Lu, G.

- Q. Periodic mesoporous organosilica hollow spheres with tunable wall thickness. *J. Am. Chem. Soc.* **128**, 6320-6321 (2006).
81. Li, J.; Liu, J.; Wang, D.; Guo, R.; Li, X.; Qi, W. Intefacially controlled synthesis of hollow mesoporous silica spheres with radially oriented pore structures. *Langmuir* **26**, 12267-12272 (2010).
 82. Lin, Y.S.; Wu, S.-H.; Tseng, C.-T.; Hung, Y.; Chang, C.; Mou, C.-Y. Synthesis of hollow silica nanospheres with a microemulsion as the template. *Chem. Commun.*, 3542-3544 (2009).
 83. Fujiwara, M.; Shiokawa, K.; Sakakura, I.; Nakahara, Y. Silica hollow spheres with nano-macroholes like diatomaceous earth. *Nano Lett.* **6**, 2925-2928 (2006).
 84. Khanal, A.; Inoue, Y.; Yada, M.; Nakashima, K. Synthesis of silica hollow nanoparticles templated by polymeric micelle with core-shell-corona structure. *J. Am. Chem. Soc.* **129**, 1534-1535 (2007).
 85. Ren, N.; Wang, B.; Yang, Y.-H.; Zhang, Y.-H.; Yang, W.-L.; Yue, Y.-H.; Gao, Z.; Tang, Y. General method for the fabrication of hollow microcapsules with adjustable shell compositions. *Chem. Mater.* **17**, 2582-2587 (2005).
 86. Brinker, C. J.; Lu, Y.; Sellinger, A.; Fan, H. Evaporation-induced self-assembly: Nanostructures made easy. *Adv. Mater.* **11**, 579-585 (1999).
 87. Coti, K. K.; Belowich, M. E.; Liong, M.; Ambrogio, M. W.; Lau, Y. A.; Khatib, H. A.; Zink, J. I.; Khashab, N. M.; Stoddart, J. F. Mechanised nanoparticles for drug delivery. *Nanoscale* **1**, 16-39 (2009).
 88. Tang, Y. S.; Cai, S.; Jin, G.; Duan, J.; Wang, K. L.; Soyez, H. M.; Dunn, B. S. SiGe quantum dots prepared on an ordered mesoporous silica coated Si substrate. *Appl. Phys. Lett.* **71**, 2448-2450 (1997).
 89. Fan, H.; Yang, K.; Boye, D. M.; Sigmon, T.; Malloy, K. J.; Xu, H.; Lopez, G. P.; Brinker, C. J. Self-Assembly of Ordered, Robust, Three-Dimensional Gold Nanocrystal/Silica Arrays. *Science* **304**, 567-571 (2004).
 90. Liong, M.; France, B.; Bradley, K. A.; Zink, J. I. Antimicrobial activity of silver nanocrystals encapsulated in mesoporous silica nanoparticles. *Adv. Mater.* **21**, 1684-1689 (2009).
 91. Corma, A.; Martinez, A.; Martinez-Soria, V. Hydrogenation of aromatics in diesel fuels on Pt/MCM-41 catalysts. *J. Catal.* **169**, 4880-4891 (1997).
 92. Kloestra, K. R.; van Laren, M.; van Bekkum, H. Binary caseium-lanthanum ocide supported on MCM-41: a new stable heterogenous basic catalyst. *J. Chem. Soc. - Faraday Trans.* **93**, 1211-1220 (1997).

93. Wang, S.-G.; Wu, C.-W.; Chen, K.; Lin, V. S.-Y. Fine-tuning mesochannel of organically functionalized mesoporous silica nanoparticles. *Chem.-Asian J.* **4**, 658-661 (2009).
94. Burkett, S. L.; Sims, S. D.; Mann, S. Synthesis of hybrid inorganic-organic mesoporous silica by co-condensation of siloxane and organosiloxane precursors. *Chem. Commun.*, 1367-1368 (1996).
95. Macquarrie, D. J. Direct preparation of organically modified MCM-type materials. Preparation and characterisation of aminopropyl-MCM and 2-cyanoethyl-MCM. *Chem. Commun.*, 1961-1962 (1996).
96. Lim, M. H.; Blanford, C. F.; Stein, A. Synthesis and characterization of a reactive vinyl-functionalized MCM-41: Probing the internal pore structure by a bromination reaction. *J. Am. Chem. Soc.* **119**, 4090-4091 (1997).
97. Mercier, L.; Pinnavaia, T. J. Direct synthesis of hybrid organic-inorganic nanoporous silica by a neutral amine assembly route: Structure-function control by stoichiometric incorporation of organosiloxane molecules. *Chem. Mater.* **12**, 188-196 (2000).
98. Huh, S.; Wiench, J. W.; Yoo, J.-C.; Pruski, M.; Lin, V.S.-Y. Organic Functionalization and Morphology Control of Mesoporous Silicas via a Co-Condensation Synthesis Method. *Chem. Mater.* **15**, 4247-4256 (2003).
99. Fowler, C. E.; Burkett, S. L.; Mann, S. Synthesis and characterization of ordered organo-silica-surfactant mesophases with functionalized MCM-41-type architecture. *Chem. Mater.*, 1769-1770 (1997).
100. Cagnol, F.; Grosso, D.; Sanchez, C. A general one-pot process leading to highly functionalised ordered mesoporous silica films. *Chem. Commun.* **10**, 1742-1743 (2004).
101. Macquarrie, D. J., Jackson, D. B. Aminopropylated MCMs as base catalysts: A comparison with aminopropylated silica. *Chem. Commun.*, 1781-1782 (1997).
102. Lim, M. H.; Blanford, C. F.; Stein, A. Synthesis of Ordered Microporous Silicates with Organosulfur Surface Groups and Their Applications as Solid Acid Catalysts. *Chem. Mater.* **10**, 467-470 (1998).
103. Margolese, D.; Melero, J. A.; Christiansen, S. C.; Chmelka, B. F.; Stucky, G. D. Direct syntheses of ordered SBA-15 mesoporous silica containing sulfonic acid groups. *Chem. Mater.* **12**, 2448-2459 (2000).
104. Yang, C.-M.; Zibrowius, B.; Schuth, F. A novel synthetic route for negatively charged ordered mesoporous silica SBA-15. *Chem. Commun.* **9**, 1772-1773 (2003).

105. Corriu, R. J. P.; Datas, L.; Guari, Y.; Mehdi, A.; Reye, C.; Thieuleux, C. Ordered SBA-15 mesoporous silica containing phosphonic acid groups prepared by a direct synthetic approach. *Chem. Commun.*, 763-764 (2001).
106. Nooney, R. I.; Kalyanaraman, M.; Kennedy, G.; Maginn, E. J. Heavy metal remediation using functionalized mesoporous silicas with controlled macrostructure. *Langmuir* **17**, 528-533 (2001).
107. Guari, Y.; Thieuleux, C.; Mehdi, A.; Reye, C.; Corriu, R. J. P.; Gomez-Gallardo, S.; Philippot, K.; Chaudret, R.; Dutartre, R. In situ formation of gold nanoparticles within functionalised ordered mesoporous silica via an organometallic "chimie douce" approach. *Chem. Commun.*, 1374-1375 (2001).
108. Corriu, R. J. P.; Mehdi, A.; Reye, C.; Thieuleux, C. Direct Synthesis of Functionalized Mesoporous Silica by Non-Ionic Assembly Routes, Quantitative Chemical Transformations within the Materials Leading to Strongly Chelated Transition Metal Ions. *Chem. Mater.* **16**, 159-166 (2004).
109. Jia, M.; Seifert, A.; Berger, M.; Giegengack, H.; Schulze, S.; Thiel, W. R. Hybrid Mesoporous Materials with a Uniform Ligand Distribution: Synthesis, Characterization, and Application in Epoxidation Catalysis. *Chem. Mater.* **16**, 877-882 (2004).
110. Huq, R.; Mercier, L.; Kooyman, P. J. Incorporation of cyclodextrin into mesostructured silica. *Chem. Mater.* **13**, 4512-4519 (2001).
111. Liu, C.; Naismith, N. Fu, L.; Economy, J. Ordered mesoporous organic-inorganic hybrid materials containing microporous functional calix[8]arene amides. *Chem. Commun.* **9**, 2472-2473 (2003).
112. Wirnsberger, G.; Scott, B. J.; Stucky, G. D. pH sensing with mesoporous thin films. *Chem. Commun.*, 119-120 (2001).
113. Boury, B.; Corriu, R. J. P.; Nunez, R. Hybrid Xerogels from Dendrimers and Arborols. *Chem. Mater.* **10**, 1795-1804 (1998).
114. Inagaki, S.; Guan, S.; Fukushima, Y.; Ohsuna, T.; Terasaki, O. Novel mesoporous materials with a uniform distribution of organic groups and inorganic oxide in their frameworks. *J. Am. Chem. Soc.* **121**, 9611-9614 (1999).
115. Melde, B. J.; Holland, B. T.; Blanford, C. F.; Stein, A. Mesoporous sieves with unified hybrid inorganic/organic frameworks. *Chem. Mater.* **11**, 3302-3308 (1999).
116. Asefa, T.; MacLachlan, M. J.; Coombs, N.; Ozin, G. A. Periodic mesoporous organosilicas with organic groups inside the channel walls.

- Nature* **402**, 867-871 (1999).
117. Yoshina-Ishii, C.; Asefa, T.; Coombs, N.; MacLachlan, M. J.; Ozin, G. A. Periodic mesoporous organosilicas, PMOs: Fusion of organic and inorganic chemistry 'inside' the channel walls of hexagonal mesoporous silica. *Chem. Commun.*, 2539-2540 (1999).
 118. Temtsin, G.; Asefa, T.; Bittner, S.; Ozin, G. A. Aromatic PMOs: Tollyl, xylyl and dimethoxyphenyl groups integrated within the channel walls of hexagonal mesoporous silicas. *J. Mater. Chem.* **11**, 3202-3206 (2001).
 119. Inagaki, S.; Guan, S.; Ohsuna, T.; Terasaki, O. An ordered mesoporous organosilica hybrid material with a crystal-like wall structure. *Nature* **416**, 304-307 (2002).
 120. Kapoor, M. P.; Yang, Q.; Inagaki, S. Self-assembly of biphenylene-bridged hybrid mesoporous solid with molecular-scale periodicity in the pore walls. *J. Am. Chem. Soc.* **124**, 15176-15177 (2002).
 121. Liang, Y.; Anwender, R. Synthesis of pore-enlarged mesoporous organosilicas under basic conditions. *Microporous and Mesoporous Materials* **72**, 153-165 (2004).
 122. Muth, O.; Schellbach, C.; Froba, M. Triblock copolymer assisted synthesis of periodic mesoporous organosilicas (PMOs) with large pores. *Chem. Commun.*, 2032-2033 (2001).
 123. Burleigh, M. C.; Markowitz, M. A.; Wong, E. M.; Lin, J.-S.; Gaber, B. P. Synthesis of periodic mesoporous organosilicas with block copolymer templates. *Chem. Mater.* **13**, 4411-4412 (2001).
 124. Guo, W.; Park, J.-Y.; Oh, M.-O.; Jeong, H.-W.; Cho, W.-J.; Kim, I.; Ha, C.-S. Triblock copolymer synthesis of highly ordered large-pore periodic mesoporous organosilicas with the aid of inorganic salts. *Chem. Mater.* **15**, 2295-2298 (2003).
 125. Bao, X.Y.; Zhao, X.S.; Li, X.; Chia, P. A.; Li, J. . A Novel Route toward the Synthesis of High-Quality Large-Pore Periodic Mesoporous Organosilicas. *J. Phys. Chem. B* **108**, 4684-4689 (2004).
 126. Goto, Y.; Inagaki, S. Synthesis of large-pore phenylene-bridged mesoporous organosilica using triblock copolymer surfactant. *Chem. Commun.*, 2410-2411 (2002).
 127. Wang, W.; Xie, S.; Zhou, W.; Sayari, A. Synthesis of Periodic Mesoporous Ethylenesilica under Acidic Conditions. *Chem. Mater.* **16**, 1756-1762 (2004).
 128. Burleigh, M. C.; Markowitz, M. A.; Spector, M. S.; Gaber, B. P. Nanoporous organosilicas: Periodic materials synthesized with surfactant templates in acidic media. *J. Phys. Chem. B* **106**, 9712-9716 (2002).

129. Kuroki, M.; Asefa, T.; Whitnal, W.; Kruk, M.; Yoshina-Ishii, C.; Jaroniec, M.; Ozin, G. A. Synthesis and properties of 1,3,5-benzene periodic mesoporous organosilica (PMO): Novel aromatic PMO with three point attachments and unique thermal transformations. *J. Am. Chem. Soc.* **124**, 13886-13895 (2002).
130. Landskron, K.; Hatton, B. D.; Perovic, D. D.; Ozin, G. A. Periodic mesoporous organosilicas containing interconnected [Si(CH₂)₃]₃ rings. *Science* **302**, 266-269 (2003).
131. Asefa, T.; Kruk, M.; Coombs, N.; Grondey, H.; MacLachlan, M. J.; Jaroniec, M.; Ozin, G. A. Novel route to periodic mesoporous aminosilicas, PMAs: Ammonolysis of periodic mesoporous organosilicas. *J. Am. Chem. Soc.* **125**, 11662-11673 (2003).
132. Pang, J.; John, V. T.; Loy, D. A.; Yang, Z.; Lu, Y. Hierarchical mesoporous carbon/silica nanocomposites from phenyl-bridged organosilane. *Adv. Mater.* **17**, 704-707 (2005).
133. Kim, D.-J.; Chung, J.-S.; Ahn, W.-S.; Kang, G.-W.; Cheong, W.-J. Morphology control of organic-inorganic hybrid mesoporous silica by microwave heating. *Chem. Lett.* **33**, 422-423 (2004).
134. Zhang, L.; Zhang, W.; Shi, J.; Hua, Z.; Li, Y.; Yan, J.; A new thioether functionalized organic-inorganic mesoporous composite as a highly selective and capacious Hg₂⁺ adsorbent. *Chem. Commun.* **9**, 210-211 (2003).
135. Lu, Y.; Fan, H.; Doke, N.; Loy, D. A.; Assink, R. A.; LaVan, D. A.; Brinker, C. J. Evaporation-induced self-assembly of hybrid bridged silsesquioxane film and particulate mesophases with integral organic functionality. *J. Am. Chem. Soc.* **122**, 5258-5261 (2000).
136. Fukuoka, A.; Sakamoto, Y.; Guan, S.; Inagaki, S.; Sugimoto, N.; Fukushima, Y.; Hirahara, K.; Iijima, S.; Ichikawa, M. Novel templating synthesis of necklace-shaped mono- and bimetallic nanowires in hybrid organic-inorganic mesoporous material [1]. *J. Am. Chem. Soc.* **123**, 3373-3374 (2001).
137. Gartmann, N.; Schutze, C.; Ritter, H.; Bruhwiler, D. The effect of water on the functionalization of mesoporous silica with 3-aminopropyltriethoxysilane. *J. Phys. Chem. Lett.* **1**, 379-382 (2010).
138. Liu, J.; Feng, X.; Fryxell, G. E.; Wang, L.-Q.; Kim, A. Y.; Gong, M. Hybrid mesoporous materials with functionalized monolayers. *Adv. Mater.* **10**, 161-165 (1998).
139. Gelest, Inc. Silane Coupling Agents: Connecting Across Boundaries. 2-20 (2006).

140. Lim, M. H.; Stein, A. Comparative studies of grafting and direct syntheses of inorganic-organic hybrid mesoporous materials. *Chem. Mater.* **11**, 3285-3295 (1999).
141. Sharma, K. K.; Anan, A.; Buckley, R. P.; Ouellette, W.; Asefa, T. Toward efficient nanoporous catalysts: Controlling site-isolation and concentration of grafted catalytic sites on nanoporous materials with solvents and colorimetric elucidation of their site-isolation. *J. Am. Chem. Soc.* **130**, 218-228 (2008).
142. Salmio, H.; Bruhwiler, D. Distribution of amino groups on a mesoporous silica surface after submonolayer deposition of aminopropylsilanes from an anhydrous liquid phase. *J. Phys. Chem. C* **111**, 923-929 (2007).
143. McKittrick, M. W.; Jones, C. W. Toward single-site functional materials - Preparation of amine-functionalized surfaces exhibiting site-isolated behavior. *Chem. Mater.* **15**, 1132-1139 (2003).
144. Gartmann, N.; Bruhwiler, D. Controlling and Imaging the Functional-Group Distribution on Mesoporous Silica. *Angew. Chem. Int. Ed.* **48**, 6354-6356 (2009).
145. Tanaka, S.; Kaihara, J.; Nishiyama, N.; Oku, Y.; Egashira, Y.; Ueyama, K. Incorporation of organic groups within the channel wall of spin-on mesostructured silica films by a vapor infiltration technique. *Langmuir* **20**, 3780-3784 (2004).
146. Acosta, E. J.; Carr, C. S.; Simanek, E. E.; Shantz, D. F. Engineering nanospaces: Iterative synthesis of melamine-based dendrimers on amine-functionalized SBA-15 leading to complex hybrids with controllable chemistry and porosity. *Adv. Mater.* **16**, 985-989 (2004).
147. Murata, S.; Kata, H.; Kimura, T.; Sugahara, Y.; Kuroda, K. Effective adsorption of chlorophyll a by FSM-type mesoporous silica modified with 1,4-butanediol. *Langmuir* **16**, 7106-7108 (2000).
148. Fukuoka, A.; Fujishima, K.; Chiba, M.; Yamagishi, A.; Inagaki, S.; Fukushima, Y.; Ichikawa, M. Photooxidation of cyclohexene and benzene with oxygen by fullerenes grafted on mesoporous FSM-16. *Catal. Lett.* **68**, 241-244 (2000).
149. Dufaud, V.; Davis, M. E.; Design of heterogeneous catalysts via multiple active site positioning in organic-inorganic hybrid materials. *J. Am. Chem. Soc.* **125**, 9403-9413 (2003).
150. Corma, A.; Iborra, S.; Rodriguez, I.; Sanchez, F. Immobilized proton sponge on inorganic carriers: The synergic effect of the support on catalytic activity. *J. Catal.* **211**, 208-215 (2002).
151. Brunel, D.; Fajula, F.; Nagy, J. B.; Deroide, B.; Verhoef, M. J.; Veum,

- L.; Peters, J. A.; Van Bekkum, H. Comparison of two MCM-41 grafted TEMPO catalysts in selective alcohol oxidation. *Appl. Catal. A* **213**, 73-82 (2001).
152. Motorina, I.; Crudden, C. M. Asymmetric dihydroxylation of olefins using cinchona alkaloids on highly ordered inorganic supports. *Org. Lett.* **3**, 2325-2328 (2001).
153. Mercier, L.; Pinnavaia, T. J. Access in mesoporous materials: Advantages of a uniform pore structure in the design of a heavy metal ion adsorbent for environmental remediation. *Adv. Mater.* **9**, 500-503 (1997).
154. Di Pasqua, A. J.; Sharma, K. K.; Shi, Y.-L.; Toms, B. B.; Ouellette, W.; Dabrowiak, J. C.; Asefa, T. Cytotoxicity of mesoporous silica nanomaterials. *Journal of Inorganic Biochemistry* **102**, 1416-1423 (2008).
155. Tao, Z.; Toms, B. B.; Goodisman, J.; Asefa, T. Mesoporosity and functional group dependent endocytosis and cytotoxicity. *Chem. Res. Toxicol.* **22**, 1869-1880 (2009).
156. Verma, A.; Stellacci, F. Effect of surface properties on nanoparticle-cell interactions. *Small* **6**, 12-21 (2010).
157. Slowing, I. I.; Wu, C.-W.; Vivero-Escoto, J. L.; Lin, V.S.-Y. Mesoporous silica nanoparticles for reducing hemolytic activity towards mammalian red blood cells. *Small* **5**, 57-62 (2009).
158. Veronese, F. M.; Pasut, G. PEGylation, successful approach to drug delivery. *Drug Discovery Today* **10**, 1451-1458 (2005).
159. Thomas, M. J. K.; Slipper, I.; Walunj, A.; Jain, A.; Favretto, M. E.; Kallinteri, P.; Douroumis, D. Inclusion of poorly soluble drugs in highly ordered mesoporous silica nanoparticles. *International Journal of Pharmaceutics* **387**, 272-277 (2010).
160. Heikkila, T.; Santos, H. A.; Kumar, N.; Murzin, D. Yu; Salonen, J.; Laaksonen, T.; Peltonen, L.; Hirvonen, J.; Lehto, V.-P. Cytotoxicity study of ordered mesoporous silica MCM-41 and SBA-15 microparticles on Caco-2 cells. *European Journal of Pharmaceutics and Biopharmaceutics* **74**, 483-494 (2010).
161. Yu, J.; Zhao, H.; Ye, L.; Yang, H.; Ku, S.; Yang, N.; Xiao, N. Effect of surface functionality of magnetic silica nanoparticles on the cellular uptake by glioma cells in vitro. *J. Mater. Chem.* **19**, 1265-1270 (2009).
162. Huang, D.-M.; Chung, T.-H.; Hung, Y.; Lu, F.; Wu, S.-H.; Mou, C.-Y.; Yao, M.; Chen, Y.-C. Internalization of mesoporous silica nanoparticles induces transient but not sufficient osteogenic signals in human mesenchymal stem cells. *Toxicol. Appl. Pharmacol.* **231**, 208-215

- (2008).
163. Zhao, Y.; Trewyn, B. G.; Slowing, I. I.; Lin, V.S.-Y. Mesoporous silica nanoparticle-based double drug delivery system for glucose-responsive controlled release of insulin and cyclic AMP. *J. Am. Chem. Soc.* **131**, 8398-8400 (2009).
 164. Slowing, I.; Trewyn, B. G.; Lin, V. S.-Y. Effect of surface functionalization of MCM-41-type mesoporous silica nanoparticles on the endocytosis by human cancer cells. *J. Am. Chem. Soc.* **128**, 14792-14793 (2006).
 165. Wang, L.-S.; Wu, L.-C.; Lu, S.-Y.; Chang, L.-L.; Teng, I.-T.; Yang, C.-M.; Ho, J.-A. A. Biofunctionalized phospholipid-capped mesoporous silica nanoshuttles for targeted drug delivery: Improved water suspensibility and decreased nonspecific protein binding. *ACS Nano* **4**, 4371-4379 (2010).
 166. Gao, H.; Shi, W.; Freund, L. B. Mechanics of receptor-mediated endocytosis. *PNAS* **102**, 9469-9474 (2005).
 167. Trewyn, B. G.; Nieweg, J. A.; Zhao, Y.; Lin, V. S.-Y. Biocompatible mesoporous silica nanoparticles with different morphologies for animal cell membrane penetration. *Chemical Engineering Journal* **137**, 23-29 (2008).
 168. Napierska, D.; Thomassen, L. C. J.; Rabolli, V.; Lison, D.; Gonzalez, L.; Kirsch-Volders, M.; Martens, J. A.; Hoet, P. H. Size-dependent cytotoxicity of monodisperse silica nanoparticles in human endothelial cells. *Small* **5**, 846-853 (2009).
 169. Nel, A.; Xia, T.; Madler, L.; Li, N. Toxic potential of materials at the nanolevel. *Science* **311**, 622-627 (2006).
 170. Tao, Z.; Morrow, M. P.; Asefa, T.; Sharma, K. K.; Duncan, C.; Anan, A.; Penefsky, H. S.; Goodisman, J.; Souid, A.-K. Mesoporous silica nanoparticles inhibit cellular respiration. *Nano Lett.* **8**, 1517-1526 (2008).
 171. Eom, H.-J.; Choi, J. Oxidative stress of silica nanoparticles in human bronchial epithelial cell, Beas-2B. *Toxicology In Vitro* **23**, 1326-1332 (2009).
 172. He, Q.; Shi, J.; Chen, F.; Zhu, M.; Zhang, L. An anticancer drug delivery system based on surfactant-templated mesoporous silica nanoparticles. *Biomaterials* **31**, 3335-3346 (2010).
 173. Lin, Y.-S.; Haynes, C. L. Impacts of mesoporous silica nanoparticle size, pore ordering, and pore integrity on hemolytic activity. *J. Am. Chem. Soc.* **132**, 4834-4842 (2010).

174. Hudson, S. P.; Padera, R. F.; Langer, R.; Kohane, D. S. The biocompatibility of mesoporous silicates. *Biomaterials* **29**, 4045-4055 (2008).
175. Souris, J. S.; Lee, C.-H.; Cheng, S.-H.; Chen, C.-T.; Yang, C.-S.; Ho, J. A. A.; Mou, C.-Y.; Lo, L.-W. Surface charge-mediated rapid hepatobiliary excretion of mesoporous silica nanoparticles. *Biomaterials* **31**, 5564-5574 (2010).
176. He, Q.; Shi, J.; Zhu, M.; Chen, Y.; Chen, F. The three-stage in vitro degradation behavior of mesoporous silica in simulated body fluid. *Microporous and Mesoporous Materials* **131**, 314-320 (2010).
177. Manzano, M.; Aina, V.; Arean, C. O.; Balas, F.; Cauda, V.; Colilla, M.; Delgado, M. R.; Vallet-Regi, M. Studies on MCM-41 mesoporous silica for drug delivery: Effect of particle morphology and amine functionalization. *Chemical Engineering Journal* **137**, 30-37 (2008).
178. Qu, F.; Zhu, G.; Huang, S.; Li, S.; Sun, J.; Zhang, D.; Qiu, S. Controlled release of Captopril by regulating the pore size and morphology of ordered mesoporous silica. *Microporous and Mesoporous Materials* **92**, 1-9 (2006).
179. Yang, P.; Gai, S.; Lin, J. Functionalized mesoporous silica materials for controlled drug delivery. *Chem. Soc. Rev.* **41**, 3679-3698 (2012).
180. Hata, H.; Saeki, S.; Kimura, T.; Sugahara, Y.; Kuroda, K. Adsorption of taxol into ordered mesoporous silicas with various pore diameters. *Chem. Mater.* **11**, 1110-1119 (1999).
181. Chen, L.; Zhu, G.; Zhang, D.; Zhao, H.; Guo, M.; Shi, W.; Qiu, S. Novel mesoporous silica spheres with ultra-large pore sizes and their application in protein separation. *J. Mater. Chem.* **19**, 2013-2017 (2009).
182. Katiyar, A.; Pinto, N. G. Visualization of size-selective protein separations on spherical mesoporous silicates. *Small* **2**, 644-648 (2006).
183. Gao, F.; Botella, P.; Corma, A.; Blesa, J.; Dong, L. Monodispersed mesoporous silica nanoparticles with very large pores for enhanced adsorption and release of DNA. *J. Phys. Chem. B* **113**, 1796-1804 (2009).
184. Andersson, J.; Rosenholm, J.; Areva, S.; Linden, M. Influences of material characteristics on ibuprofen drug loading and release profiles from ordered micro- and mesoporous silica matrices. *Chem. Mater.* **16**, 4160-4167 (2004).
185. Azais, T.; Tourne-Peteilh, C.; Aussenac, F.; Baccile, N.; Coelho, C.; Devoisselle, J.-M.; Babonneau, F. Solid-state NMR study of ibuprofen confined in MCM-41 material. *Chem. Mater.* **18**, 6382-6390 (2006).

186. Vallet-Regi, M.; Balas, F.; Arcos, D. Mesoporous Materials for Drug Delivery. *Angew. Chem. Int. Ed.* **46**, 7548-7558 (2007).
187. Xia, T.; Kovoichich, M.; Liang, M.; Meng, H.; Kabehie, S.; George, S.; Zink, J. I.; Nel, A. E. Polyethyleneimine coating enhances the cellular uptake of mesoporous silica nanoparticles and allows safe delivery of siRNA and DNA constructs. *ACS Nano* **3**, 3273-3286 (2009).
188. Tourne-Peteilh, C.; Brunel, D.; Begu, S.; Chiche, B.; Fajula, F.; Lerner, D. A.; Devoisselle, J.-M. Synthesis and characterisation of ibuprofen-anchored MCM-41 silica and silica gel. *New J. Chem.* **27**, 1415-1418 (2003).
189. Katiyar, A.; Ji, L.; Smirniotis, P.; Pinto, N. G. Protein adsorption on the mesoporous molecular sieve silicate SBA-15: Effects of pH and pore size. *J. Chromatogr. A* **1069**, 119-126 (2005).
190. Okazaki, M.; Toriyama, K. Inhomogenous distribution and collective diffusion of solution molecules in the nanochannel of mesoporous silica. *J. Phys. Chem. B* **107**, 7654-7658 (2003).
191. Matsumoto, A.; Tsutsumi, K.; Schumacher, K.; Unger, K. K. Surface functionalization and stabilization of mesoporous silica spheres by silanization and their adsorption characteristics. *Langmuir* **18**, 4014-4019 (2002).
192. Liu, J.; Hartono, S. B.; Jin, Y. G.; Li, Z.; Lu, G. Q.; Qiao, S. Z. A facile vesicle template route to multi-shelled mesoporous silica hollow nanospheres. *J. Mater. Chem.* **20**, 4595-4601 (2010).
193. Angelos, S.; Khashab, N. M.; Yang, Y.-W.; Trabolsi, A.; Khatib, H. A.; Stoddart, J. F.; Zink, J. I. pH clock-operated mechanized nanoparticles. *J. Am. Chem. Soc.* **131**, 12912-12914 (2009).
194. Bae, Y.; Fukushima, S.; Harada, A.; Kataoka, K. Design of environment-sensitive supramolecular assemblies for intracellular drug delivery: Polymeric micelles that are responsive to intracellular pH change. *Angew. Chem. Int. Ed.* **42**, 4640-4643 (2003).
195. Kaihara, S.; Fisher, J. P.; Matsumura, S. Chemo-enzymatic synthesis of degradable PTMC-b-PECA-b-PTMC triblock copolymers and their micelle formation for pH-dependent controlled release. *Macromol. Biosci.* **9**, 613-621 (2009).
196. Tang, R.; Ji, W.; Panus, D.; Palumbo, R. N.; Wang, C. Block copolymer micelles with acid-labile ortho ester side-chains: Synthesis, characterization, and enhanced drug delivery to human glioma cells. *J. Controlled Release* **151**, 18-27 (2011).
197. Park, C.; Kim, H.; Kim, S.; Kim, C. Enzyme responsive nanocontainers

- with cyclodextrin gatekeepers and synergistic effects in release of guests. *J. Am. Chem. Soc.* **131**, 16614-16615 (2009).
198. Vivero-Escoto, J. L.; Slowing, I. I.; Wu, C.-W.; Lin, V. S.-Y. Photoinduced intracellular controlled release drug delivery in human cells by gold-capped mesoporous silica nanosphere. *J. Am. Chem. Soc.* **131**, 3462-3463 (2009).
199. Aznar, E.; Marcos, Ma. D.; Martinez-Manez, R.; Sancenon, F.; Soto, J.; Amoros, P.; Guillem, C. pH- and photo-switched release of guest molecules from mesoporous silica supports. *J. Am. Chem. Soc.* **131**, 6833-6843 (2009).
200. Casaus, R.; Marcos, M. D.; Martinez-Manez, R.; Ros-Lis, J. V.; Soto, J.; Villaescusa, L. A.; Amoros, P.; Beltran, D.; Guillem, C.; Latorre, J. Toward the development of ionically controlled nanoscopic molecular gates. *J. Am. Chem. Soc.* **126**, 8612-8613 (2004).
201. Park, J.-H.; Lee, Y.-H.; Oh, S.-G. Preparation of thermosensitive PNIPAm-grafted mesoporous silica particles. *Macromol. Chem. Phys.* **208**, 2419-2427 (2007).
202. Chung, P.-W.; Kumar, R.; Pruski, M.; Lin, V. S.-Y. Temperature responsive solution partition of organic-inorganic hybrid poly(N-isopropylacrylamide)-coated mesoporous silica nanospheres. *Adv. Funct. Mater.* **18**, 1390-1398 (2008).
203. Sierocki, P.; Maas, H.; Dragut, P.; Richardt, G.; Vogtle, F.; De Cola, L.; Brouwer, F.; Zink, J. I. Photoisomerization of azobenzene derivatives in nanostructured silica. *J. Phys. Chem. B* **110**, 24390-24398 (2006).
204. Collier, C. P.; Mattersteig, G.; Wong, E. W.; Luo, Y.; Beverly, K.; Sampaio, J.; Raymo, F. M.; Stoddart, J. F.; Heath, J. R. A [2]catenane-based solid state electronically reconfigurable switch. *Science* **289**, 1172-1175 (2000).
205. Perez, E. M.; Dryden, D. T. F.; Leigh, D. A.; Teobaldi, G.; Zerbetto, F. A generic basis for some simple light-operated mechanical molecular machines. *J. Am. Chem. Soc.* **126**, 12210-12211 (2004).
206. Collin, J.-P.; Laemmel, A.-C.; Sauvage, J.-P. Photochemical expulsion of a Ru(phen)₂ unit from a macrocyclic receptor and its thermal recoordination. *New J. Chem.* **25**, 22-24 (2001).
207. Murakami, H.; Kawabuchi, A.; Matsumoto, R. Ido, T.; Nakashima, N. A multi-mode-driven molecular shuttle: Photochemically and thermally reactive azobenzene rotaxanes. *J. Am. Chem. Soc.* **127**, 15891-15899 (2005).
208. Radu, D. R.; Lai, C.-Y.; Wiench, J. W.; Pruski, M.; Lin, V. S.-Y.

- Gatekeeping Layer Effect: A Poly(lactic acid)-coated Mesoporous Silica Nanosphere-Based Fluorescence Probe for Detection of Amino-Containing Neurotransmitters. *J. Am. Chem. Soc.* **126**, 1640-1641 (2004).
209. Descalzo, A. B.; Jimenez, D.; Marcos, M. D.; Martinez-Manez, R.; Soto, J.; El Haskouri, J.; Guillem, C.; Beltran, D.; Amoros, P.; Borrachero, M. V. A new approach to chemosensors for anions using MCM-41 grafted with amino groups. *Adv. Mater.* **14**, 966-969 (2002).
210. Rodman, D. L.; Pan, H.; Clavier, C. W.; Feng, X.; Xue, Z.-L. Optical metal ion sensor based on diffusion followed by an immobilizing reaction. Quantitative analysis by a mesoporous monolith containing functional groups. *Anal. Chem.* **77**, 3231-3237 (2005).
211. Mercier, L.; Pinnavaia, T. J. Heavy metal ion adsorbents formed by the grafting of a thiol functionality to mesoporous silica molecular sieves: Factors affecting Hg(II) uptake. *Environ. Sci. Technol.* **32**, 2749-2754 (1998).
212. Kang, T.; Park, Y.; Choi, K.; Lee, J. S.; Yi, J. Ordered mesoporous silica (SBA-15) derivatized with imidazole-containing functionalities as a selective adsorbent of precious metal ions. *J. Mater. Chem.* **14**, 1043-1049 (2004).
213. Rodriguez-Lopez, G.; Marcos, M. D.; Martinez-Manez, R.; Sancenon, F.; Soto, J.; Villaescusa, L. A.; Beltran, D.; Amoros, P. Efficient boron removal by using mesoporous matrices grafted with saccharides. *Chem. Commun.* **10**, 2198-2199 (2004).
214. Mornet, S.; Vasseur, S.; Grasset, F.; Duguet, E. Magnetic nanoparticle design for medical diagnosis and therapy. *J. Mater. Chem.* **14**, 2161-2175 (2004).
215. d their micelle formation for pH-dependent controlled release. *Macromol. Biosci.* **9**, 613-621 (2009).

Chapter 12

Application of transition metals NMR in supramolecular chemistry

Błażej Gierczyk

*Adam Mickiewicz University in Poznań, Faculty of Chemistry,
Umultowska 89b, 61-614 Poznań, Poland*

1. Introduction

The phenomenon of the self-organization and formation of stable chemical individua *via* non-bonding interactions is the area of interest of supramolecular chemistry. This interdisciplinary science is located at the intersection of various branches of chemistry (inorganic, physical, organic, analytical etc.), physics, biology, material science, mathematics, geology and biochemistry. As the other disciplines of science, supramolecular chemistry requires the analytical methods for studying of the processes and objects of its interest. Some of these techniques are the same as used in other areas of chemistry, physics or biology, while the others are unique for this discipline. Among many instrumental methods, nuclear magnetic resonance plays very important role in studying of supramolecular complexes in solution and solid state. This method is used not only for the determination of the structures of supermolecules, but also for the determination of association constants, kinetics of their formation or ligand exchanges, the dynamics of supramolecular individua, their shape and interactions with solvent and in many other aspects of their physicochemistry. Apart from the application of the NMR spectroscopy of so called “common nuclei”, as ^1H , ^{13}C and, less frequent, ^{15}N , ^{19}F or ^{29}Si , the nuclear magnetic resonance of some “exotic” elements is also used in supramolecular chemistry. As some of them are only occasionally studied by this technique (e.g. ^{27}Al or ^{35}Cl), the others are widely used for studying of supermolecules. Among the published examples of application of ^7Li , ^{23}Na , ^{133}Cs or ^{129}Xe NMR in chemistry, most of them are the papers on various aspects of supramolecular chemistry.

The nuclear magnetic resonance spectroscopy of transition metal (*d* and *f* blocks) nuclei takes a special place in NMR spectroscopy, because the

measurements of their resonance signals are not routine and easy to made. This is the effect of various limitations and experimental difficulties. Two elements (Ce, Th) have not natural isotopes active in NMR. Only few of the elements of *d* and *f* blocks have natural isotopes of $\frac{1}{2}$ nuclear spin (^{87}Fe , ^{89}Y , ^{103}Rh , $^{107/109}\text{Ag}$, $^{111/113}\text{Cd}$, ^{169}Tm , ^{171}Yb , ^{183}W , ^{187}Os , ^{195}Pt , $^{197/199}\text{Hg}$), while the other transition element natural isotopes are only the quadrupolar nuclei. This limits the application of NMR for studying of their compounds, because of the widening of the spectral line due to quadrupolar relaxation, e.g. for ^{197}Au or ^{235}U the signals were not recorded in liquid or are observed only for the species of high symmetry (UF_6). In conclusion, among 44 naturally occurring transition metals, only 11 have isotopes which nuclei have not a quadrupolar moment, 31 have only quadrupolar isotopes. Most of them have also paramagnetic states (e.g. Cu^{2+} or most on the Ln^{3+}), therefore they could not be observed by NMR method, due to fast relaxation. Additionally, the paramagnetic impurities in the sample (e.g. presence of the Cu^{2+} ions in Cu^+ containing complex) disturb the measurement. Other problem is a low natural abundance of some NMR active isotopes and/or their low γ values. This causes the low sensitivity of NMR measurements of these elements and elongates the acquisition time. The resonance frequencies of low γ nuclei are often over the range of the commercial spectrometer, so their observation by this technique requests the expensive NMR machine hardware modification. Moreover, the spectra recorded at low frequencies are often disturbed by so called accusing ringing, the mechanical resonances of the NMR probehead elements. Some elements (Co, Cu) have a huge range of chemical shifts, broader than the frequency range possible to acquire in one experiment. This causes the need of the measuring of a few spectra for one sample, with different resonance frequency values (transmitter offset). Therefore, the nuclear magnetic resonance spectroscopy of transition metal is not very popular and widely used.

This paper presents examples of application of NMR of transition metal nuclei in supramolecular chemistry. Only these studies, where the transition metal atom (as a inorganic ion or metalorganic species) plays the role of a guest, were chosen for this review. The solid state NMR data have not been included. The application of *p* block elements NMR spectroscopy in zeolite, mesoporous material or heteropolyacids chemistry, traditionally included in supramolecular chemistry, has not been either presented here.

2. Transition metal NMR in supramolecular chemistry

2.1 Group 3 & lanthanides

2.1.1 Scandium

The only stable natural scandium isotope, ^{45}Sc is active in NMR spectroscopy, but has a spin $+7/2$, so its nucleus has a quadrupolar moment ($-0.22 \times 10^{-28} \text{ m}^2$), but it is not enough large to limit seriously a possibility of ^{45}Sc NMR measurements. Scandium has a high receptivity (0.3 of that of proton). The resonance frequency ($\mathcal{E} = 24.292 \text{ MHz}$) is sufficiently high to avoid the experimental difficulties. Scandium forms the Sc^{3+} ions, which are diamagnetic. The IUPAC recommends reference is 0.1 M solution of $\text{Sc}(\text{ClO}_4)_3$ in water at low pH, which corresponds to $\text{Sc}(\text{H}_2\text{O})_6^{3+}$ species. The chemical shift range is small (-100 $+250$ ppm).

In 1999 Meehan and Willey have reported the ^{45}Sc NMR studies of Sc^{3+} complexes with crown ethers in solutions.¹ They have used six different ligands: 12-crown-4 (12C4), 15-crown-5 (15C5), dibenzo-24-crown-8 (DB24C8), dibenzo-30-crown-10 (DB30C10), 1-aza-15-crown-5 (N15C5) and 1-aza-18-crown-6 (N18C6); Fig. 1. The authors have reported the chemical shifts for the complexes of above mentioned coronands with ScCl_2^+ in acetonitrile and toluene (Table 1). The counter ion in these studies was SbCl_6^- . For 15C5 and N15C5, which fit to the ScCl_2^+ ion, to form a complex of pentagonal bipyramidal geometry, they have observed the sharp signals. For the systems with larger crowns (DB24C8 and DB30C10) one signal occurs in spectra at room (or elevated) temperature, which splits into two broad ones with decreasing of the sample temperature. The chemical shifts of these two peaks are smaller than that after coalescence. This indicates complicated, dynamical process, involving different modes of scandium complexation and different crown conformation. The authors have postulated the existence of Sc^{3+} -crown ether complex at lower temperature and have assigned the upfield shifted signals to these species. The system with N18C6 shows one signal at 298K, which splits into three with decreasing of the temperature (183.2, 170.0 and 144.2 ppm at 243K). They have been assigned to different modes of ScCl_2^+ complexation. Two downfield shifted signals come from two separated O_4N environment, while this at 144.2 ppm is from the O_5 complex. The mixture containing ScCl_2^+ and 12C4 ligand shows two signals, one assigned to 1:1 complex, second to L_2Sc^{3+} species. The first one is distinctly wider than the second, which indicates the highly asymmetric structure (sandwich-like complex). The same system, in the presence of the excess of SbCl_5 , which stoichiometry induces the formation of Sc^{3+} ions in the place of ScCl_2^+ cations shows the more complex spectrum and complicated temperature-spectrum dependence. The authors have not assigned the defined structures to the signals observed.

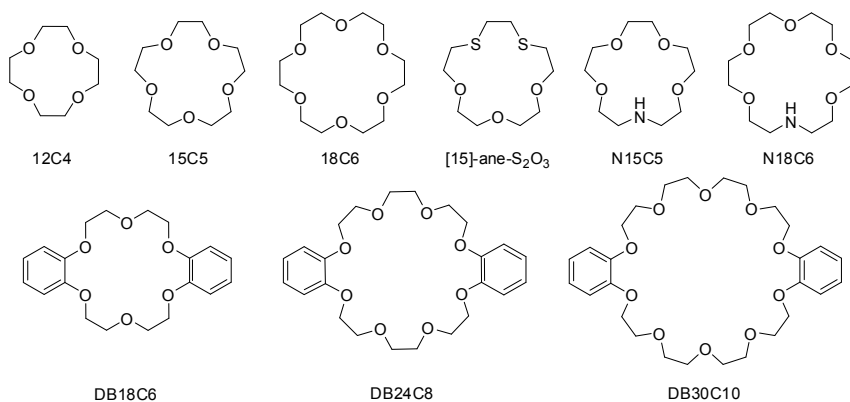


Fig. 1. Structures of macrocyclic ligands studied as scandium receptors

The paper of Brown et al.² presents the series of scandium containing crown ether complexes. The authors have prepared the compounds containing ScCl_2^{2+} and ScCl_2^+ , complexed by 15C5, 18-crown-6 (18C6) and 1,4-dithia-7,10,13-trioxacyclopentadecane ([15]aneS₂O₃; Fig. 1). They have been characterized by ⁴⁵Sc NMR spectra (Table 1) and X-ray crystallography. The acetonitrile solution containing $[\text{ScCl}_2(18\text{C6})]^+$ (δ 132 ppm) has been reacted with Lewis acid (FeCl_3), with producing new species (δ 101 and -2 ppm, respectively), assigned to $[\text{ScCl}(\text{MeCN})(18\text{C6})]^{2+}$ and $[\text{Sc}(\text{MeCN})_2(18\text{C6})]^{3+}$. In the presence of SbCl_5 instead of FeCl_3 the signal at -19 ppm is observed, not detected in solutions containing FeCl_3 . This has been assigned to the species containing SbCl_5 coordinated to the oxygen atom of 18C6 ligand, which is not bonded to Sc center: $[\text{Sc}(18\text{C6}\times\text{SbCl}_5)(\text{MeCN})_2]^{3+}$. The authors have studied also the system with 12C4. They have confirmed the assignment of the signal at 25 ppm to $[\text{Sc}(12\text{C4})_2]^{3+}$, but the signal at 153 ppm was recognized as the product of hydrolysis: $[\text{ScCl}_3(\text{H}_2\text{O})_3]$. In addition some data for hydrogen bonded scandium containing complexes with crown ethers have been published in this paper. In these compounds crown macrocycle is bonded *via* O \cdots HO bond to water molecules coordinated to scandium ion (e.g. $[\text{Sc}(\text{H}_2\text{O})_3(\text{NO}_3)_3]\cdot 18\text{-crown-6}$ or $[\text{Sc}(\text{H}_2\text{O})_3\text{Cl}_3]\cdot 15\text{-crown-5}$). In solutions they dissociate to form free $[\text{Sc}(\text{H}_2\text{O})_6]^{3+}$ (*ca.* +2 ppm) or $[\text{Sc}(\text{H}_2\text{O})_3\text{Cl}_3]$ (+153 ppm).

Table 1. ^{45}Sc NMR chemical shifts of scandium(III) complexes with macrocyclic ligands

Complex	$\delta^{45}\text{Sc}$ [ppm]	Complex	$\delta^{45}\text{Sc}$ [ppm]
$[\text{Sc}(\text{12C4})_2]^{3+}$	25.6	$[\text{ScCl}_2(\text{N15C5})]^+$	148.9
$[\text{ScCl}_2(\text{12C4})]^+$	152.5 ^a	$[\text{ScCl}_2(\text{N18C6})]^+$	182.5
$[\text{ScCl}_2(\text{15C5})]^+$	127.6	$[\text{ScCl}_2(\text{N18C6})]^+$ (at 243 K)	183.2 & 170.0 [O_4N] 144.2 [O_5]
$[\text{ScCl}_2(\text{18C6})]^+$	132	$[\text{ScCl}(\text{CH}_3\text{CN})(\text{18C6})]^{2+}$	101
$[\text{ScCl}_2(\text{DB24C8})]^+$	127.8	$[\text{ScCl}(\text{CH}_3\text{CN})_2(\text{18C6})]^{2+}$	-2
$[\text{ScCl}_2(\text{DB30C10})]^+$	142.3	$[\text{ScCl}(\text{CH}_3\text{CN})_2(\text{18C6}\cdot\text{SbCl}_5)]^{2+}$	-19

^a according to Brown *et al.*² this signal comes from the hydrolysis product

The ScCl_3 complexes with podand ligands have been studied by Gierczyk *et al.*³ The polyoxaethylene phosphates, phosphites, pyrophosphates, sulfites, arsenates(III) and borates have been used as supramolecular ligands. Besides of a large number of non-supramolecular adducts, formed when the ligands act as monodentate ones, the signal of the Sc^{3+} ion, complexed inside a channel surrounded by podand side arms, has been detected. Such complexes are formed only for three ligands (Fig. 2). The chemical shift of the scandium nucleus in these structures, is 230-233 ppm. The ligands containing $\text{O}=\text{X}$ group ($\text{X} = \text{P}, \text{S}$) prefer to coordinate *via* the sp^2 oxygen, *i.e.* forming a $\text{Sc}\cdots\text{O}=\text{X}$ bonds.

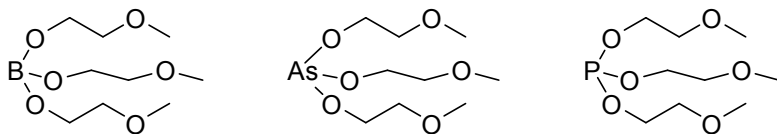


Fig. 2. Structures of the polypodand ligands used as a scandium ion hosts

The ^{45}Sc NMR spectroscopy is also used for studying of fullerenes, containing encapsulated scandium atoms. The first example has been published by Bethune *et al.*⁴ The authors have observed broad signal at 200 ppm for the solution of a mixture containing $\text{Sc}_2@C_n$ species. Miyake and coworkers have obtained the pure samples of two isomers (I and III) of $\text{Sc}_2@C_{84}$ and have recorded ^{45}Sc NMR spectra in CS_2 and 1,2-dichlorobenzene in wide range of temperature (238-404K).⁵ Contrary to IUPAC directives, the spectra were referred to 2 M solution of ScCl_3 in $\text{HCl}/\text{H}_2\text{O}$. The spectra of isomer I show two signals (*ca.* 190 and 250

ppm), indicating on the existence of two magnetically nonequivalent sites inside fullerene ball. The signals coalesced at 383K. The temperature dependence of the line shape has permitted to estimate the rate constants (1-100 s⁻¹ at room temperature) of the exchange of Sc ions between these two sites and energetic barrier for this motion (80 kJ mol⁻¹). The isomer III shows only one signal in ⁴⁵Sc NMR spectrum (*ca.* 225 ppm). As the spectrum has the same shape at different magnetic fields, the authors have deduced, that both scandium ions are located in the sites of the same magnetic environment (they are equivalent). The measurements of T_1 and T_2 relaxation times of ⁴⁵Sc nuclei in solvent of different viscosity permit to establish that the ions are rigidly attached to fullerene cage and its correlation time is determined by the reorientation of whole molecule. Further investigation of this material caused the redetermination of the structure.⁶ They are the carbides of the formula Sc₂C₂@C₈₂.

Krause et al.⁷ have synthesized endohedral C₈₀ fullerenes, containing Sc₃CH and Sc₃N clusters. These compounds have been characterized by ⁴⁵Sc NMR technique (spectra have been referred to 0.2 M solution of Sc(NO₃)₃ in concentrated HNO₃). For the second one signal at *ca.* 220 ppm has been observed. The spectrum of (Sc₃CH)@C₈₀ is more complicated, because two broad lines of the same intensity, at *ca.* +400 and -300 ppm occur. The authors have rationalized it as an effect of Sc-H scalar coupling, so the signal has a doublet structure. They have not calculated a coupling constant, but on the basis of the experimental data it could be estimated on ${}^2J_{ScH} = 85\,000$ Hz, which value is completely improbable. The literature data gives ${}^2J_{ScH} = 30$ Hz for Sc(BH₄)₃. The effect of the splitting of the ⁴⁵Sc NMR line of (Sc₃CH)@C₈₀ must have a different origin.

Scandium carbide containing endohedral fullerenes have been studied by Okimoto and coworkers.⁸ They have isolated two isomers (II and III) of (Sc₂C₂)@C₈₂ by preparative HPLC. The prepared materials have been studied by ⁴⁵Sc NMR in solid state at various temperatures to determine the activation energy of the rotation of Sc₂C₂ in a fullerene cage. The spectra were referred to 1M solution of Sc(NO₃)₃. The spectra of both isomers show one broad line at 214 ppm. On the basis of temperature dependence of linewidth the E_a values have been determined to be 6.4 and 6.6 kJ mol⁻¹ for isomers II and III, respectively. The Sc₂C₂@C₈₀ (C_{2v}) has also been studied.⁹ Also two signals, coalescent at 373 K, have been observed.

Mixed metal nitrides, containing Sc atom, encapsulated in C₈₀ fullerene, have been studied by Yang et al., Zang et al. and Wang et al.¹⁰⁻¹³ The authors have prepared a series of compounds containing Ln_xSc_(3-x)N, where Ln is Ho or Lu. The CeSc₂N@C₈₀ has been also obtained. For each clusterfullerene two isomers (I and

II) have been isolated, although minor cerium containing isomer have not been isolated. The authors have not given the information on used reference solution. The chemical shifts of these compounds are collected in Table 2. The difference between the shifts of Ce and Lu containing clusters have been rationalized by the presence of unpaired f electron of the cerium atom, which strongly influences the chemical shift. Holmium containing compounds show a large paramagnetic shift (800-1200 ppm), and their spectra shape and chemical shifts are very depending on the temperature. The ^{45}Sc NMR signals of these compounds are distinctly broader due to paramagnetic relaxation than those containing scandium nitride or mixed scandium-lutetium nitride clusters. The temperature dependence of chemical shift of $\text{HoSc}_2\text{N}@C_{80}$ permits to determine the contribution of Fermi contact and pseudo-contact shifts. The prevalence of pseudo-contact effects have been stated, although the contact term could not be also negligible. Also for $\text{CeSc}_2\text{N}@C_{80}$ the pseudo-contact mechanism dominates. The authors have discussed the temperature dependence of the chemical shift of both isomers and have compared them with that observed for $\text{CeSc}_2\text{N}@C_{80}$ fullerene. The ten-fold higher sensitivity of δ ^{45}Sc value of holmium analogues on temperature variation than that of Ce one is caused by higher magnetic moment of Ho^{3+} ion than that of Ce^{3+} one. The differences between two Ho-containing isomers are not clear.

Dunsch et al.¹⁴ have studied the clusterfullerenes containing metal sulfide. The obtained $\text{Sc}_2\text{S}@C_{82}$ ($8:C_{3v}$) have been characterized by ^{45}Sc NMR spectroscopy. It has been found that both scandium atoms are equivalent, or the cluster rotates inside the fullerene cavity with a rate causing averaging of the signals. Similar results have been obtained by Chen for $\text{Sc}_2\text{S}@C_{72}$ (C_s).¹⁵ Other studied cluster has been $\text{Sc}_3\text{NC}@C_{80}$ ($7:I_h$),¹⁰ which shows two signals of 1:2 intensity ratio at room temperature, which stays in accordance with a C_{2v} symmetry of the Sc_3NC unit.

Table 2. ^{45}Sc NMR data of endohedral fullerene compounds

Compound	^{45}Sc NMR data [ppm]	Condition	Reference used	Reference
$\text{Sc}_2@C_n$ (probably $\text{Sc}_2\text{C}_2@C_{n-2}$)	35, very broad	CS_2	n.r.	4
$\text{Lu}_2\text{ScN}@C_{80}$ ($7:I_h$)	199.5	room temperature; CS_2	n.r.	12
$\text{LuSc}_2\text{N}@C_{80}$ ($7:I_h$)	194.7	room temperature; CS_2	n.r.	12
$\text{Sc}_3\text{N}@C_{80}$ ($7:I_h$)	199.5	room temperature; CS_2	n.r.	12
$\text{Lu}_2\text{ScN}@C_{80}$ ($6:D_{5h}$)	194.7	room temperature; CS_2	n.r.	12

$\text{LuSc}_2\text{N@C}_{80}$ (6: D_{5h})	194.7	room temperature; CS_2	n.r.	12
$\text{Sc}_3\text{N@C}_{80}$ (6: D_{5h})	211.7	room temperature; CS_2	n.r.	12
$\text{CeSc}_2\text{N@C}_{80}$ (7: I_h)	257.3	313 K; o-dichlorobenzene	n.r.	11
$\text{HoSc}_2\text{N@C}_{80}$ (7: I_h)	$\sim 1\ 000^a$	298 K; CS_2	n.r.	13
$\text{LuSc}_2\text{N@C}_{80}$ (6: D_{5h})	$\sim 800^a$	298 K; CS_2	n.r.	13
$\text{Sc}_3\text{N@C}_{80}$	$\sim 220^a$	room temperature; CS_2	0.2 M $\text{Sc}(\text{NO}_3)_3$ in conc. HNO_3	7
$\text{Sc}_3\text{CH@C}_{80}$	~ -400 & $+300^{a,b}$	room temperature; CS_2	0.2 M $\text{Sc}(\text{NO}_3)_3$ in conc. HNO_3	7
$\text{Sc}_2\text{C}_2@\text{C}_{82}$	127 & 164 ^a	293; solvent not given	n.r.	9
$\text{Sc}_2\text{C}_2@\text{C}_{82}$ (C_3) ^c	~ 190 & 250 ^a	298 K; CS_2	2 M ScCl_3 in $\text{H}_2\text{O}/\text{HCl}$	5
$\text{Sc}_2\text{C}_2@\text{C}_{82}$ (C_3) ^c	~ 190 & 250 ^a	293 K; o-dichlorobenzene	2 M ScCl_3 in $\text{D}_2\text{O}/\text{HCl}$	16
$\text{Sc}_2\text{C}_2@\text{C}_{82}$ (C_{3v}) ^c	~ 225	293 K; CS_2	2 M ScCl_3 in $\text{H}_2\text{O}/\text{HCl}$	5
$\text{Sc}_2\text{C}_2@\text{C}_{82}$ (C_{2v})	214	300 K; solid-state	1 M $\text{Sc}(\text{NO}_3)_3$	8
$\text{Sc}_2\text{C}_2@\text{C}_{82}$ (C_{3v})	214	300 K; solid-state	1 M $\text{Sc}(\text{NO}_3)_3$	8
$\text{Sc}_2\text{S@C}_{82}$ (C_{3v})	290	room temperature; CS_2	0.2 M $\text{Sc}(\text{NO}_3)_3$ in conc. HNO_3	14
$\text{Sc}_2\text{S@C}_{72}$ (C_3)	183.3	room temperature; $\text{CS}_2/\text{toluene-}d_8$	0.2 M $\text{Sc}(\text{NO}_3)_3$ in conc. HNO_3	15
$\text{Sc}_3\text{NC@C}_{80}$ (7: I_h)	365 & 275 ^a	CS_2	not given	10

^a no chemical shift given, the δ values readed from the spectrum published; ^b signals reported as a doublet due to scalar Sc-H coupling; ^c previously reported as $\text{Sc}_2@\text{C}_{84}$ isomers

2.1.2 Yttrium

The natural yttrium contains 100% of NMR active nuclei – ^{89}Y , which has a spin $\frac{1}{2}$. Unfortunately, it has a low gyromagnetic factor (γ), therefore its resonance frequencies are low ($\bar{\nu} = 4.998$ MHz). This causes some experimental difficulties. First, its resonance frequencies are unavailable on most commercial spectrometer. Additionally, its spectra are often disturbed by acoustic ringing. The low γ value causes also relatively low receptivity in ^{89}Y NMR measurements (its receptivity is 1.18×10^{-4} that of proton). Another problem is a long relaxation

time of the yttrium nuclei. In consequence the NMR experiments need long relaxation delays (10 s and more), so the acquisition is time consuming. IUPAC recommends reference is $\text{Y}(\text{NO}_3)_2$ solution in water. The chemical shifts range is not very broad, *ca.* 1300 ppm.

The first examples of the application of ^{89}Y NMR to investigate of supramolecular systems is the report of Hall et al.^{17,18}, who have studied the complexation of Y^{3+} by cryptands, derived from 1,6-diaza-15-crown-5 and 1,10-diaza-18-crown-6 (K21, K22; Fig. 3). The K21 ligand has been used as a receptor for Y^{3+} cations.¹⁷ The ^{89}Y NMR chemical shifts of this complex is -6.0 ppm. The authors have made the NMR titration of yttrium perchlorate with DMF to establish the chemical shift of yttrium complexes with amide ligands and maximum number of the DMF molecules, coordinated to Y center. The formation of DMF- Y^{3+} adducts causes the opposite (i.e. upfield) shifts in comparison with Y^{3+} K21 formation. The spectra have been referred to 1 M solution of $\text{Y}(\text{ClO}_4)_3$ in acetonitrile/acetonitrile- d_3 . The complexes have been measured as acetonitrile solutions (no temperature given). For the complex of K22 (1:1 mixture of ligand and $\text{Y}(\text{ClO}_4)_3 \times 4.7 \text{ H}_2\text{O}$ in acetonitrile) two signals have been observed, at 11.6 (sharp) and -6.7 ppm (very broad), respectively.¹⁸ The first one has been assigned to uncomplexed hydrate ($\text{Y}(\text{ClO}_4)_3 \times 7.6 \text{ H}_2\text{O}$), while the second one to two complexes (LY^{3+} and L_2Y^{3+}), detected by ^1H and ^{13}C NMR spectroscopy. The authors have reported also the $^2J_{\text{C-Y}}$ coupling constant, observed in ^{13}C NMR spectrum of the C=O group (3 Hz). The $\text{Y}(\text{ClO}_4)_3 \times 4.7 \text{ H}_2\text{O}$ in acetonitrile has been used as reference.

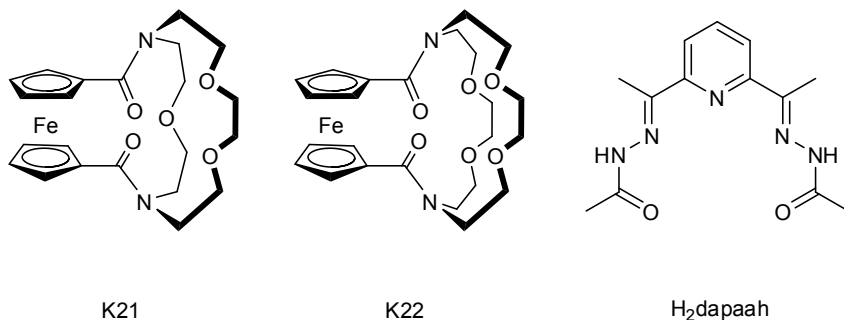


Fig. 3. Ligands used as a yttrium ion hosts

Summers et al.¹⁹ have characterized the yttrium complex of pentadentate hydrazone ligand ($\text{H}_2\text{dap-R}$; Fig. 3) by ^{89}Y NMR in D_2O . They have observed a

small shift (1.53 ppm vs. YCl_3), but they have not reported any details about the reference solution (solvent, concentration) and the measurements temperature.

Bradley and coworkers have prepared a series of ether complexes of tris(1,1,1,3,3,3-hexafluoro-2-methylpropan-2-oxy)yttrium with alkyl ethers, ammonia and alcohols.²⁰ Among them one linear analogue of crown ethers – monopodand 2,5,8-trioxanonan (diglyme; Fig. 4) has been isolated in crystal form and characterized by X-ray crystallography and NMR technique. The ^{89}Y NMR chemical shift of this complex is 78.6 ppm (in toluene- d_8 /diglyme 2:3 v/v mixture; referred to YCl_3 ; no temperature and solvent of the reference given).

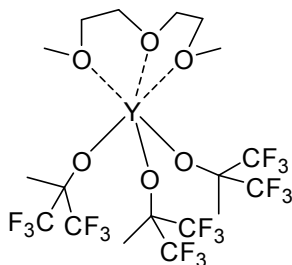


Fig. 4. Diglyme complex of yttrium fluoroalkoxide

The complexes of Y^{3+} with EDTA-like ligand (EDTA- PA_2 ; Fig. 4a) have been studied by Plates-Iglesias and coworkers. The authors have applied also other methods (1H , ^{13}C , ^{17}O NMR, relaxation time measurements, luminescence measurements, nuclear magnetic relaxation dispersion, UV-Vis spectroscopy and potentiometry) to determine the structure, stability and dynamics of the complexes of ligand studied with various lanthanide ions. The presence of two signals of complexed yttrium ion at 100.6 and 102.3 ppm and a signal of free one (0 ppm) in the spectrum measured for L: Y^{3+} stoichiometry 1:2 has been detected. This indicates the presence of two isomeric form of the complex in solution. The increasing of the L/Y ratio to 1:1 causes the coalescence of the downfield shifted signals into one at 101.4 ppm and disappearing of that at 0 ppm. The increasing of the ligand concentration to stoichiometry 2:1 causes the shift of the signal upfield to 90.5 ppm. The authors have not assigned a definite structures to the signals observed. The spectra have been recorded in D_2O (0.15 M solution of YCl_3 , pD = 6.0) and referred to 2 M solution of YCl_3 (solvent used in the reference sample and temperature during the measurements have not been given).

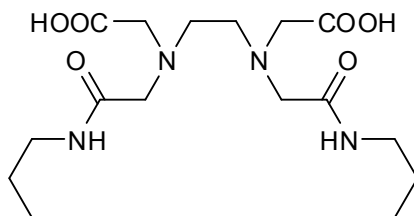
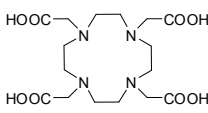
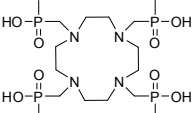
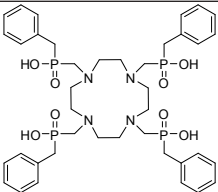
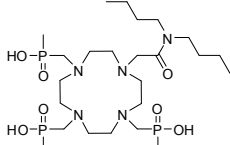
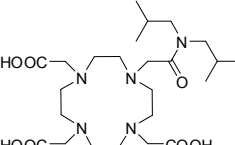
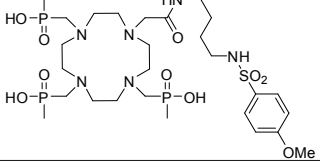


Fig. 4a. Structure of EDTA-like ligand (EDTA-PA₂)

In 2010 y. Merritt et al.²¹ have used a hyperpolarized ⁸⁹Y NMR to study yttrium complexes and its application as a pH sensitive probes. The authors have reported the pH dependence of the ⁸⁹Y chemical shift of yttrium-DOTP and yttrium-DO3A-NTs (Fig. 5) complexes. The spectra have been taken in H₂O/D₂O (85:15; v/v) and have been referenced to YCl₃ (no solvent and concentration given) at 298 K. The hyperpolarization has been obtained by DNP method. In whole studied pH range (4-9) one resonance signal has been observed, which indicated fast exchange between protonated and unprotonated species. The chemical shifts of Y-DOTP system vary from 150 to 140 ppm in the above mentioned pH values, while Y-DO3A-NTs show opposite tendencies, i.e. changing from 132 to 158 ppm. The Y-DOTP chemical shift is strongly affected only by the protonation of the first uncoordinated oxygen. The further proton bonding steps have much less effects. For Y-DO3A-NTs in a range of pH between 5 and 7 no ⁸⁹Y NMR signal has been detected, even in thermally polarized samples, which have been rationalized by existence of two different species in solution. The fast exchange between them causes the huge line broadening and absence of the measurable signal. The T₁ relaxation times of ⁸⁹Y nuclei in Y-DOTP complex at various pH have been also reported. They are between 57 s (pH = 9) to 202 s (pH = 4).

The complexes of various cyclam derivatives with Y³⁺ ion have been studied by Pullukody et al.²² They have reported some ⁸⁹Y NMR data for these adducts (Table 3). They pointed out the higher chemical shifts of complexes of -PO₃H containing ligands vs. that of -COOH analogues. No isotope effect of H₂O/D₂O used as solvents has been observed. The spectra were recorded for solutions in water (pH = 6.5) at 295 K and referred to 1 M YCl₃ (no solvent given).

Table 3. Structures of cyclam derivatives and the ^{89}Y NMR data of their complexes with Y^{3+} ion

		
111.8	156.8 ($J_{yp} = 5$ Hz)	152.8 ($J_{yp} = 5$ Hz)
		
168.3	111.3	151.9 ($J_{yp} = 5.1$ Hz)

The hyperpolarized DOTAM complexes (Fig. 5) of yttrium have been studied by Miéville et al.²³ They have studied the kinetics of complexation of Y^{3+} by the ligand in D_2O /glycerol system at pH 5.01. The authors have observed separated signals of free (0 ppm) and complexed (123 ppm) yttrium ions. The complexation kinetics were determined from the changing of the intensities of both signals in time. The hyperpolarization has been obtained by microwave irradiation at 1.15 K.

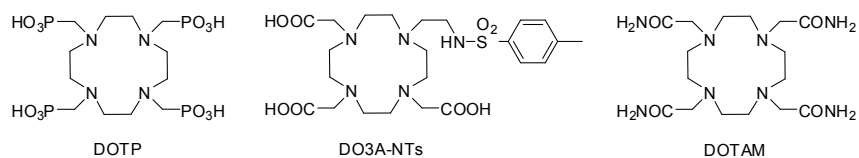
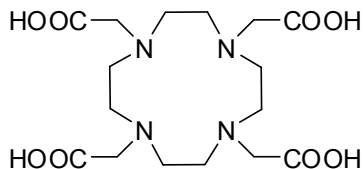


Fig. 5. Structures of cyclam-derived ligands

Lumata et al.²⁴ have shown that the oxygen, nitrogen and carbon nuclei of ^{13}C -enriched DOTA- Y^{3+} complex may be co-polarized during yttrium DNP-hyperpolarization (Fig. 6). The hypopolarization process has been optimized to obtain the strongest ^{13}C and ^{89}Y signals. Also the T_1 relaxation times have been determined. The authors have reported the ^{89}Y NMR chemical shift of this complex as 109.88 ppm. The spectra have been recorded in water, at 298 K and referred to external 3 M YCl_3 in water. The non-labeled DOTA- Y^{3+} has been

studied by the same authors as a model compound for optimizing of the DNP enhancement method on using of various free radicals, a presence of Gd(III) species in the sample and microwave frequency.²⁵ The kinetic of decay of hyperpolarized ^{89}Y at various concentration of Gd^{3+} has been studied as well as a phenomenon of co-polarization of ^{13}C nuclei of $[1\text{-}^{13}\text{C}]\text{pyruvate}$.



DOTA

Fig. 6. DOTA structure

The two-center homo- and heteronuclear complexes of cyclam dimer (Fig. 7), have been studied by ^{89}Y NMR.²⁶ The molecules containing two Y^{3+} ions bonded as well as one Y^{3+} and one Gd^{3+} have been synthesized. Although the authors have mentioned the studies of homonuclear $(\text{Y}^{3+})_2$ complex, their NMR characterization data have not been presented. The ^{89}Y NMR spectrum heteronuclear Y,Gd L complex shows two signals, one at 126.3 ppm and second at 175.4 ppm. The relative intensities of these two species are 4:5. The signal at higher field has been assigned to *TSAP* isomer (mono-capped twisted square antiprismatic geometry), while the second to *SAP* isomer (mono-capped square antiprismatic geometry). The T_1 relaxation times of ^{89}Y nucleus have been determined and used to calculation of Gd-Y distance. The spectra have been measured for aqueous solutions at pH 7, at 298 K, referred to 1 M $\text{Y}(\text{NO}_3)_3$ in water, containing 1 mol% of $\text{Gd}(\text{NO}_3)_3$.

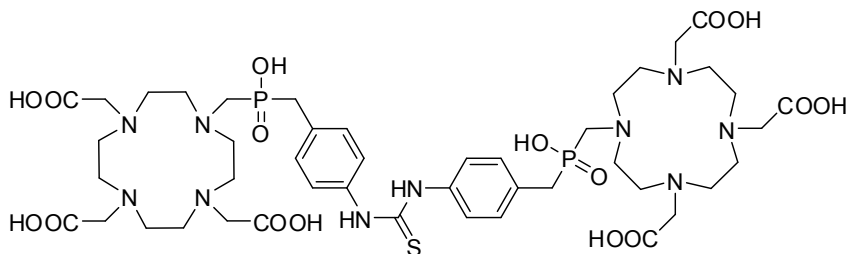


Fig. 7. Structure of cyclam dimer

Popovici and coworkers²⁷ have investigated the complexation of yttrium ions by P=O moieties containing tridentate ligand, P11 (Fig. 8). To overcome the problems with long relaxation times of yttrium nuclei, they have applied the inverse ^{31}P detection with a ^{31}P , $^{89}\text{Y}\{^1\text{H}\}$ HMQC sequence. The chemical shifts of the obtained complexes: $[\text{Y}(\text{P11})(\text{NO}_3)_3]$ and $[\text{Y}(\text{P11})_2(\text{NO}_3)](\text{NO}_3)_2$ (Fig. 4) are -1.5 and -23.7 ppm, respectively (room temperature). For $[\text{Y}(\text{P11})(\text{NO}_3)_3]$ at room temperature only the correlation with one phosphorus atom ($\text{Ar}_2\text{P}=\text{O}$) is observed. The other signals could be recorded at decreased temperatures. The ^{89}Y signal of this complex shows a small temperature dependence (only *ca.* 0.2 ppm/60 K). The $^2J_{\text{Y,P}}$ coupling constants are 7.7 Hz. The second compound, $[\text{Y}(\text{P11})_2(\text{NO}_3)](\text{NO}_3)_2$, shows the ^{89}Y signal splitted into seven lines (^{89}Y , $^{31}\text{P}\{^1\text{H}\}$ DEPT experiments) which observation provides the coordination of six P=O group into yttrium cation. The $^2J_{\text{Y,P}}$ coupling constants are 5.6 & 8.4 Hz. The spectra have been referred to $\text{Y}(\text{NO}_3)_3$ (no solvent and concentration given) and have been recorded in CD_3CN .

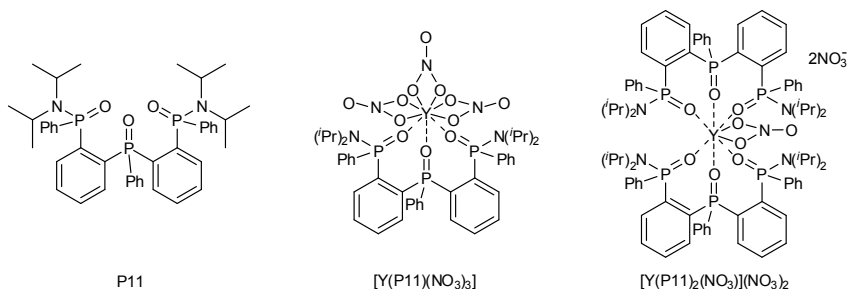


Fig. 8. Structures of tridentate phosphor-containing ligand and its yttrium complexes

The supramolecular ligands L2 i L3 have been used for preparation of yttrium complex (Fig. 9).²⁸ The complexation modes were elucidated on the basis of ^1H , ^{89}Y HMQC experiments. The observed chemical shifts are -4.9 and 0.4 ppm, respectively. The coupling with $\text{CH}=\text{N}$ protons has been detected. The spectra have been recorded in CD_3CN , and referred to $\text{Y}(\text{NO}_3)_3$ solution (no temperature of the measurements as well as reference concentration and solvent have been given).

Zimmermann and coworkers have studied the mechanism of C-H bond activation in rare-earth metal complexes.²⁹ The authors have confirmed the structure of the backbone metalated ligand on the basis of ^{89}Y - ^1H 2D HMQC experiments. In the presence of AlMe_3 , complex **10B** undergoes decomposition due to metalation of *iso*-propyl group and methane elimination. The complex

formed (**10C**) shows the ^{89}Y NMR signal at 426 ppm. The yttrium nucleus is coupled with methine ArC-H proton and one of the Y-CH₂-Al hydrogen atoms ($J_{\text{YH}} = 14.0$ and 15.5 Hz, respectively). Moreover, the coupling with one AlCH₃ group is observed ($J_{\text{YH}} = 1.2$ Hz). On the basis of X-ray crystallography and NMR spectra, the authors postulated the presence of two three-center bonds: Y-H-C_{CH₂Al} and Y-H-C_{CH₂Ar}.

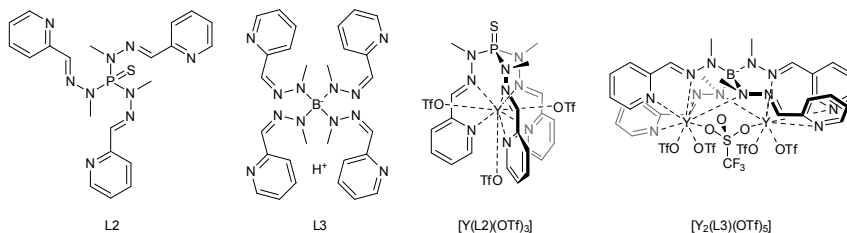


Fig. 9. Pyridine containing ligands and their complexes

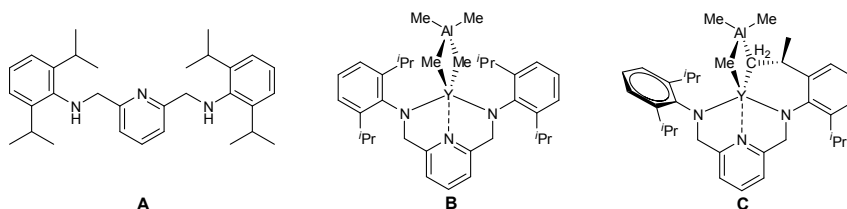


Fig. 10. Tridentate nitrogen ligand (A) and its yttrium complexes (B,C)

Fu et al.³⁰ have prepared family of $\text{Y}_3\text{N}@C_{2n}$ where $n = 40-43$ fullerene clusters and have characterized them by ^{89}Y NMR spectra. The chemical shift values were as follows: $\text{Y}_3\text{N}@C_{80}$ (I_h), 191.63 ppm; $\text{Y}_3\text{N}@C_{86}$ (D_3), 62.65 ppm; $\text{Y}_3\text{N}@C_{84}$ (C_s), 104.32, 65.33 & -19.53 ppm. The $\text{Y}_3\text{N}@C_{84}$ (C_s) cluster shows three signals due to coordination of one yttrium ion to pentalene motif of the cage, resulting in the three different magnetic environment inside the fullerene ball for the Y_3N^{6+} clusters yttrium atoms. The spectra were recorded in *o*-dichlorobenzene at 298 K and referred to YCl_3 in D_2O (no concentration given).

2.1.3 Lanthanum

Two natural isotopes of lanthanum are available for NMR experiments: ^{138}La and ^{139}La . First one has a spin +5 and a huge quadrupolar moment (0.47

$\times 10^{-28} \text{ m}^2$). Additionally, it has a very low natural abundance (0.09 %) which, together with relatively low γ value ($\mathcal{E} = 13.193 \text{ MHz}$) causes extremely low receptivity (7.35×10^{-5} that of ^1H). The second NMR active isotope, ^{139}La , has smaller quadrupolar moment ($I = 7/2$; $Q = 0.21 \times 10^{-28} \text{ m}^2$) and a slightly higher resonance frequency ($\mathcal{E} = 14.126 \text{ MHz}$). The high natural abundance (99.91 %) causes an easy observation of it in NMR experiments (receptivity: 5.92×10^{-2} that of ^1H), although its resonance signals are usually broad. It is the only isotope of lanthanum used in NMR studies. The IUPAC recommends reference is 0.01 M solution of LaCl_3 in D_2O . The chemical shift range is *ca.* 1900 ppm.

Chen et al.³¹ have studied the interaction of $\text{La}^{3+}/18\text{-crown-6}$ interactions, using ^{139}La NMR method (Fig. 1). The spectrum of lanthanum chloride heptahydrate consists of one signal at 165 ppm (0.2 M in methanol; $\Delta\nu_{1/2} = 1900 \text{ Hz}$). An addition of crown ether causes the formation of new chemical species, giving a broader, upfield shifted resonance line. This indicates slow exchange between free and complexed La^{3+} ion in NMR timescale. The authors have performed the NMR titration at constant ion concentration. The obtained spectra have been deconvoluted, using Gold and Zdunek model, to calculate transverse relaxation time and chemical shifts of both lanthanum species. The spectra measured at various salt concentration (0.2, 0.1 & 0.05 M in MeOH) show that the T_2 parameter of solvated ion is concentration dependent, which indicates the ion association in solution. Also the chemical shift of free (solvated) ion changes (increases) with the decreasing of the concentration of the salt (from 165 to 230 ppm). The changes observed for complexed lanthanum ion are less pronounced (from 130 to 167 ppm), however it indicates the participation of chloride ion in La^{3+} coordination. The transverse relaxation rates of complexed La^{3+} are very large and have been estimated to be $1.5\text{-}3.5 \times 10^{-5} \text{ s}^{-1}$. It is the effect of the high electronic field anisotropy around lanthanum centre in the complex, causing fast quadrupolar relaxation. The spectra were referred to external $\text{La}(\text{NO}_3)_3 \times 6\text{H}_2\text{O}$ in $\text{D}_2\text{O}/\text{H}_2\text{O}$ mixture (2:8, v/v) at 300 K (the spectra at other temperatures have been also recorded).

The substituted azacrown (SK22) has been studied as La^{3+} receptor by ^{139}La NMR.³² The authors have measured the lanthanum spectra of $\text{La}(\text{NO}_3)_3$ solution in acetonitrile (8 ppm) in the presence of K22 ligand (15 ppm) and model compound – 1,10-diaza-18-crown-6 ($\text{N}_2\text{18C6}$; see Fig. 11 for structures). The signal of SK22- La^{3+} complex is sharper than that of $\text{N}_2\text{18C6}$, due to the higher symmetry of lanthanum coordination sphere. This effect is a result of acting of phenolate oxygen of SK22 as a donor atom, bonded to lanthanum ion in axial positions.

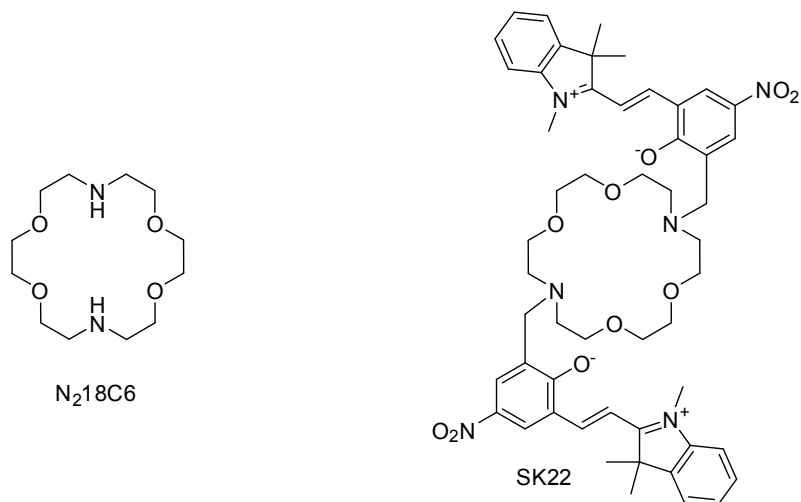


Fig. 11. Structures of diaza-18-crown-6 and its derivative, used as a lanthanum hosts

Israëli et al.³³ have studied binding of the La^{3+} by *p*-sulfonatocalix[4]arene (c[4]AS; Fig. 12). The spectra have been recorded at 300 K in 0.01 M HCl in H_2O/D_2O (95:5; w/w) and referred to 0.001 M solution of $LaCl_3$ in 0.01 M HCl (-0.22 ppm) and 0.0071 M solution of $LaCl_3$ in D_2O (0.00 ppm). The ^{139}La NMR titration with constant concentration of La^{3+} salt have been made to establish a stability constant of La^{3+} -c[4]AS complexes. The experiments have been repeated at various temperatures (290 to 340 K) to determine thermodynamic parameters of the complexation. Two parameters, ^{139}La chemical shift and linewidth have been measured. The complex formed has a 1:1 stoichiometry. At 300 K the stability constant of the complex is 4900, while the chemical shift of the complexed ion -7.3 ppm. The authors have stated the good agreement between the $\log K$, ΔH and ΔS of complexation obtained from NMR measurements and microcalorimetry. The half linewidth measurements permit to determine transverse relaxation time, T_2 . On the basis of the quadrupolar relaxation theory, the authors determine the effective radius of the complex. The calculated value (6 Å) permits to exclude the possibility of formation of complexes of higher stoichiometry, observed in solid state.

The complex formation between La^{3+} and pentadentate Schiff base (Fig. 13) in $DMSO-d_6$ has been checked by ^{139}La NMR.³⁴ The signal at -265 ppm ($\Delta\nu_{1/2} = 6540$ Hz) with respect to dilute $La(ClO_4)_3$ in water has been detected for this system.

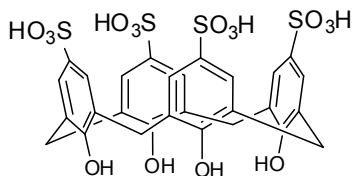


Fig. 12. Structure of *p*-sulfonatocalix[4]arene

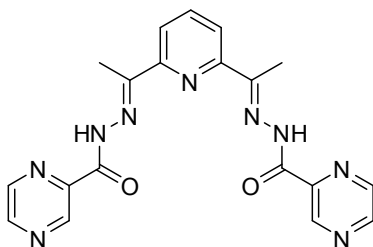


Fig. 13. Structure of pentadentate Schiff base

Akasaka et al.³⁵ have prepared the $\text{La}_2@C_{80}$ complex and have studied them by NMR methods. They have observed single line in ^{139}La NMR spectrum (-402.6 ppm), which suggest that lanthanum atoms are equivalent. On the basis of ^{13}C NMR measurements the authors assign to the obtained compound cage structure of the symmetry I_h . The linewidth of ^{139}La signal depends on temperature (258 to 363 K). The authors have postulated fast circulation of both La^{3+} ions inside the fullerene ball. The spectra have been recorded in *o*-dichlorobenzene and referred to 0.6 M LaCl_3 in D_2O . The $\text{La}@C_{82}$ monoanion has been studied by Akasaka et al.³⁶ It shows the signal at -470 ppm ($\Delta\nu_{1/2} = 2\ 600$ Hz; in *o*-dichlorobenzene- d_2 ; against 0.6 M LaCl_3 in D_2O).

Kato et al.³⁷ have studied lanthanum containing C_{72} fullerene (so called “missing fullerene” due to it has not been isolated in pure form). The La_2 cluster, encapsulated inside the fullerene cage gives one, broad signal in ^{139}La NMR spectrum at -575.6 ppm (in *o*-dichlorobenzene, at 333.6 K; referred to $\text{La}_2@C_{80}$ complex, -402.6 ppm). This indicates, that both are equivalent. The lower symmetry of $\text{La}_2@C_{72}$ causes the signal broadening in comparison with $\text{La}_2@C_{80}$. The D_2 non-IPR (isolated pentagon rule) structure of the C_{72} cage has been proposed. Wakahara and coworkers have obtained the silylated derivatives of $\text{La}_2@C_{80}$ (Fig. 14A,B) and have characterized them by ^{139}La NMR spectra, recorded in various temperatures.³⁸ The strong broadening of the signal of 14a and 14b with elevation of the temperature from 183 to 303 K has been observed,

which indicates the hopping of the La atoms inside the fullerene cage. The X-ray structures suggest, that there is not a three dimensional motion, but the lanthanum ions exchange between two sites along the equatorial plane of the C_{80} ball. The ^{129}La NMR chemical shifts at 295 K are -400.0 and -362.1 ppm for **14A** and **14B**, respectively. The spectra were recorded in $\text{CS}_2/\text{CD}_2\text{Cl}_2$ mixture (no composition given). The authors have not reported the reference used in ^{139}La NMR measurements. The same fullerene cluster has been modified by Yamada et al.,³⁹ by Prato reaction (two isomers, due to [5,6] and [6,6] cycloaddition). One ([5,6] isomer) has been studied by ^{139}La NMR. The chemical shifts of adducts obtained are -464 (two overlapping La signals). The signal chemical shift is temperature independent, the linewidth changes from 570 Hz (278 K) to 627 Hz (313 K). The spectra have been recorded in *o*-dichlorobenzene vs. LaCl_3 as reference (no solvent and concentration given). The temperature dependence of the lanthanum chemical shift of two isomeric [5,6] silirane adducts of $\text{La}_2@C_{80}$ indicate on the both La atoms are not still but dynamically move inside the cage.⁴⁰ The chemical shifts are -397.78 and -392.48 ppm, for **14E** and **14F**, respectively (in $\text{CS}_2/\text{CD}_2\text{Cl}_2$, 1:1 v/v; 278 K).

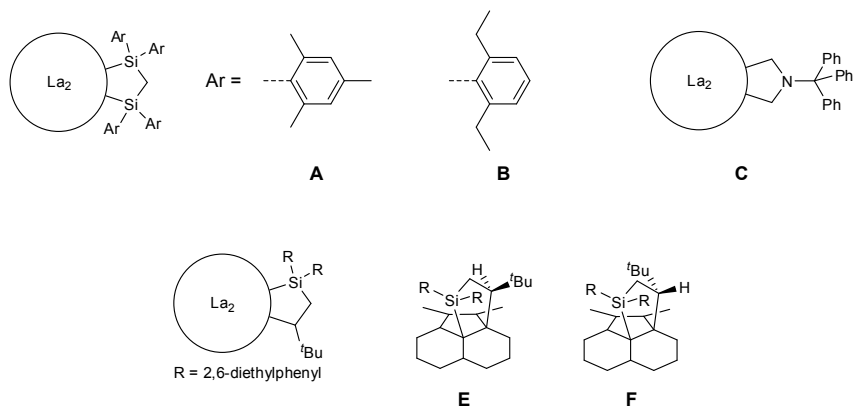


Fig. 14. Schematic structures of the $\text{La}_2@C_{80}$ adducts

2.1.4 Ytterbium

Among seven natural isotopes of ytterbium, two of them are active in NMR spectroscopy. Among them one (^{173}Yb) is a quadrupolar nucleus. Its quadrupolar moment ($3.9 \times 10^{-28} \text{ m}^2$) and low resonance frequency ($\mathcal{E} = 4.852 \text{ MHz}$) make it useless for NMR experiments. The second one (^{171}Yb) has a $\frac{1}{2}$ nuclear spin and sufficient natural abundance (14.3 %). Its γ factor ($\mathcal{E} = 17.613 \text{ MHz}$) makes it

easy to be observed by NMR method (receptivity 7.81×10^{-4} relatively to ^1H). Unfortunately, ytterbium(III) compounds are paramagnetic, so only the Yb^{2+} ones are available for ^{171}Yb NMR. IUPAC recommends a $\text{Yb}(\text{Me}_5\text{C}_5)_2$ in THF as a reference. The chemical shift range is over 1 200 ppm.

The only one example of the application of ^{171}Yb NMR spectroscopy in supramolecular chemistry is the paper of Dietel et al.,^{41,42} who have studied bimetallic complexes of Yb with a N3 ligand (D1; Fig. 15). The authors have obtained three ytterbium complexes, studied by NMR method: $\text{Yb}_2\text{I}(\text{D1})_3\text{THF}$, $\text{Yb}_2(\text{D1})_4(\text{THF})_2$ and $[\text{Yb}_2(\text{D1})_2\{\text{N}(\text{SiMe}_2)_2\}]$. The spectra were recorded in THF and benzene at room temperature. They are referenced to $\text{Yb}(\text{Me}_5\text{C}_5)_2$ in THF. The ^{171}Yb spectrum of $\text{Yb}_2\text{I}(\text{D1})_3\text{THF}$ shows two signals, at 585.6 (broad) and 646.6 ppm. The second one has two satellites line, due to Yb-Yb coupling ($^1J_{\text{Yb-Yb}} = 76.1$ Hz). In THF complex $\text{Yb}_2\text{I}(\text{D1})_3\text{THF}$ decomposes to form binuclear compound $\text{Yb}_2(\text{D1})_4(\text{THF})_2$, which ^{171}Yb spectrum composes of one signal at 681.9 ppm. The complex $\text{Yb}_2(\text{D1})_4(\text{THF})_2$ also contains two equivalent ytterbium centers; $\delta^{171}\text{Yb} = 503.4$ ppm.

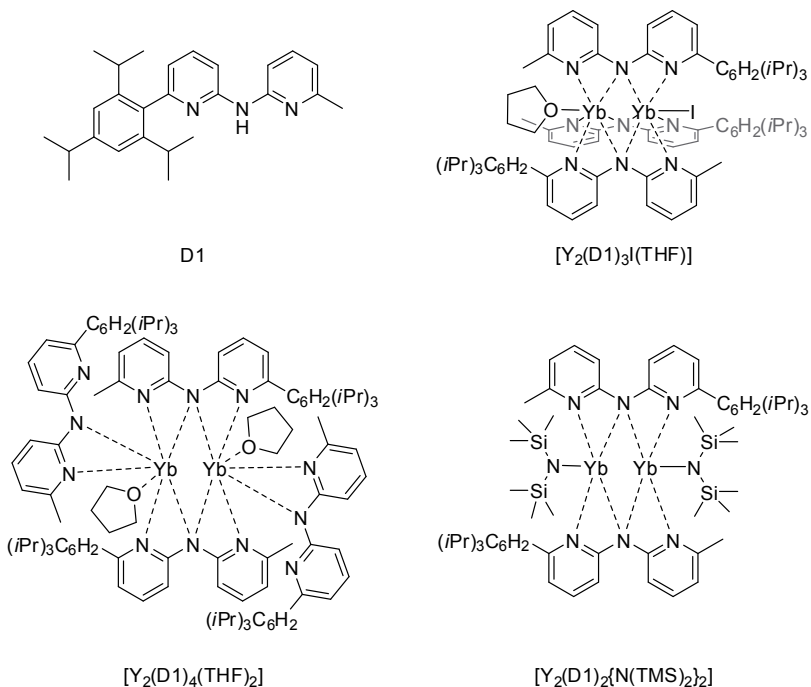


Fig. 15. Structure of D1 ligand and its complexes with ytterbium

2.2 Group 5

2.2.1 Vanadium

Both naturally occurring vanadium isotopes (^{50}V and ^{51}V) are NMR active, however the first one was never studied by this technique in solution, due to low natural abundance (0.25 %), low resonance frequency ($\mathcal{E} = 9.970$ MHz) and moderate quadrupole moment ($0.21 \times 10^{-28} \text{ m}^2$; $I = 6$); receptivity of this isotope is 1.33×10^{-4} vs. that of ^1H . The ^{51}V isotope is much more proper for NMR measurements. Its natural abundance is high (99.75%). Together with high γ value ($\mathcal{E} = 26.289$ MHz) it makes this isotope easy to detect by NMR method (receptivity 0.381 that of ^1H). It has a low quadrupolar moment ($-0.052 \times 10^{-28} \text{ m}^2$; $I = 7/2$), so the resonance lines are often not very broad. Vanadium chemical shifts range is over 4 500 ppm. IUPAC recommends neat VOCl_3 as a standard.

As the supramolecular chemistry of vanadium compounds is rather limited, except the studies of inorganic systems, as zeolites and heteropolyacids, the literature on the application of ^{51}V NMR to study supermolecules is scarce. Zhang et al.⁴³ have used this method for studying the bonding of HVO_4^{2-} by synthetic orthovanadate receptor (Z1; Fig. 16). They made titration experiments at constant pH (10.2) to determine a stability constant of the complex formed ($K = 1\ 100 \text{ M}^{-1}$). The authors have not reported the ^{51}V NMR chemical shift of complexed vanadate ion, calculated from the fitting the experimental points to the model. At the [Z1] to $[\text{HVO}_4^{2-}]$ ratio equal to 8, the $\delta^{51}\text{V}$ is -544 ppm. The authors have not given any experimental conditions (reference, temperature, solvent etc.).

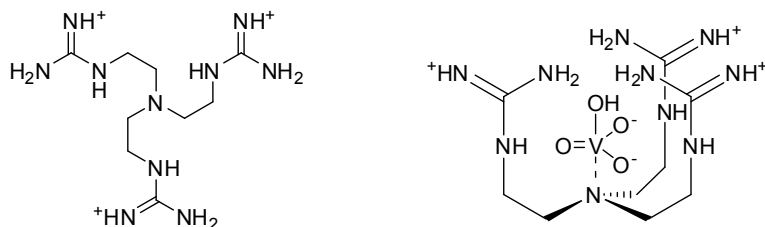


Fig. 16. Triguanidine ligand and its complex with vanadate ion

Nielsen et al.⁴⁴ have compared the ^{51}V NMR parameters of some *bpg* complexes (Fig. 17) measured in liquid and solid samples. Both hydrated and anhydrous complexes have been studied. The peroxo complex $[\text{VO}(\text{O}_2)(\text{bpg})]$ gives the signal at -550 ppm, while the $[\text{VO}_2(\text{bpg})]$ molecule – at -494 ppm. The spectra have been measured in CD_3CN vs. neat VOCl_3 . For $[\text{VO}(\text{O}_2)(\text{bpg})]$ Colpas et al. have reported slightly smaller shift, -543 ppm (in CH_3CN ; vs. neat

VOCl_3).⁴⁵ The authors have compared these results with spectra measured for solid samples by MAS technique. They have shown that the vanadium chemical shift is highly sensitive on the second coordination sphere – the δ values of hydrates differ distinctly from anhydrous complexes.

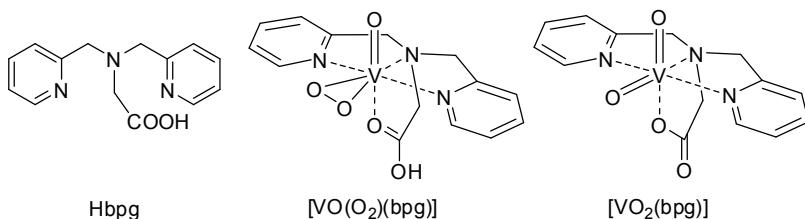


Fig. 17. *Hbpg* and its oxovanadium complexes

Časný and Rehder have synthesized the oxovanadium complexes with some nitrogen ligands.⁴⁶ Among them one (*bpa*, Fig. 18) may be considered as supramolecular ligand. The authors have obtained two complexes of *bpa* with oxovanadyl ion ($[\text{VO}(\text{O}_2)]^+$). One ($[\text{VO}(\text{O}_2)(\text{Hbpa})](\text{ClO}_4)$) has been characterized by ^{51}V NMR. The compound shows a signal at -624 ppm ($\text{H}_2\text{O}/\text{D}_2\text{O}$ mixture) or -610 ($\text{D}_2\text{O}/\text{EtOH}$ mixture). The authors report also the value for neutral complex of *bpa* with VO_2^+ (-533 ppm). The spectra have been referred to VOCl_3 ; temperature of measurements has not been given.

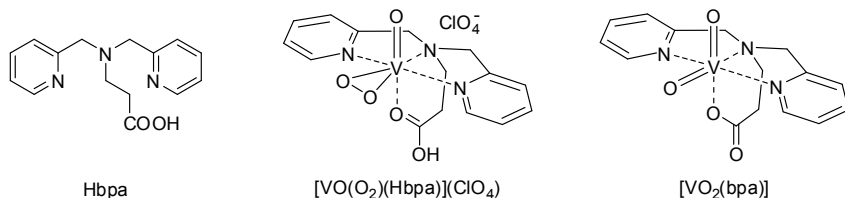


Fig. 18. *Hbpa* and its oxovanadium complexes

Martinez et al.⁴⁷ have studied the formation of hemicyptophane-oxodovanadium(V) complexes. Two diastereomeric hemicyptophanes have been investigated (Fig. 19A & C) and their complexes with VO_4^{3-} have been obtained (Fig. 10c&d). For 19B two signals have been observed in the ^{51}V NMR spectrum (-382.5 & -397.1 ppm), which suggests the presence of two isomeric form of the adduct (Fig. 20) in equilibrium. The similar result has been obtained for 19D, but the signals are poorer resolved (-380.6 & -387.5 ppm). The authors

have studied these equilibria by ^1H NMR. The spectra have been recorded in CDCl_3 vs. VOCl_3 as reference. Temperature of the measurements has not been given.

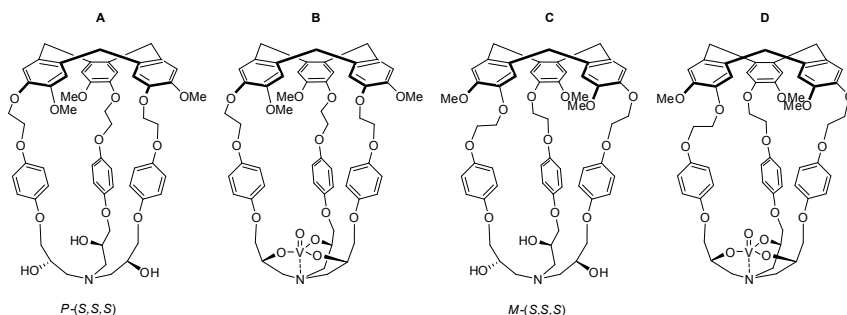


Fig. 19. Hemicryptophane **19A** & **C** and their vanadium complexes

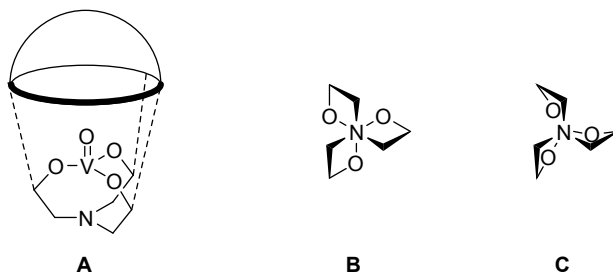


Fig. 20. Isomeric forms of **19B** & **D**

Browne et al. have studied the vanadium complexes with N_2O ligands (Fig. 21).⁴⁸ In $\text{DMF-}d_7$, the ^{51}V NMR spectrum of **21A** shows one signal at -450 ppm. The acid addition, causing the protonation of 1,2,4-triazole ligands, results in an appearing of new signal (triplet) at a -507 ppm (the value of J_{V-14N} is not given). In methanol- d_4 , the ^{51}V NMR spectrum of this compound show more complicated changes upon acidification due to the formation of at least two protonated complexes and products of their partial decomposition. The **21C** in $\text{DMF-}d_7$, gives a signal at -515 ppm. The addition of acid to the solution shifts the signal to -565 ppm (doublet), which has been explained by solvent coordination and ligand exchange. The oxidation of **21A** with hydrogen peroxide causes the formation of peroxovanadate complex (-567 ppm). The spectra were referred to neat VOCl_3 . Two other similar complexes **21B** and **21D** have been characterized

by ^{51}V NMR spectra, with signals at -543 and -540 ppm, respectively (in $\text{DMSO-}d_6$, no reference and temperature given).⁴⁹

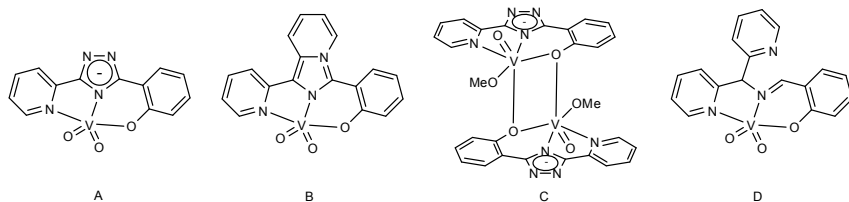


Fig. 21. Oxovanadium complexes of tridentate N_2O ligands

The spectra of the complex of oxovanadium ion with tris(pyridine) podand (Fig. 22) have been studied by Colpas et al.⁴⁵ It shows the resonance signal at -574 ppm (in $\text{DMSO-}d_6$, vs. VOCl_3).

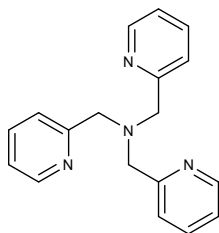


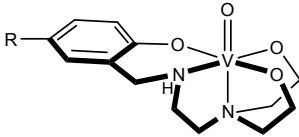
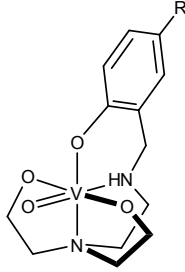
Fig. 22. Structure of tris(pyridine) vanadium host

Baerd et al.⁵⁰ have reported the chemical shifts of the VOCl_3 adducts with 18-crown-6 ($[(\text{VOCl}_3)_2(18\text{-crown-6})]$) and 15-crown-5 ($[(\text{VOCl}_3)(15\text{-crown-5})]$); see Fig. 1 for ligand structures. The structure of the complexes formed is not known, however the authors postulate that the cyclic ethers act as O_2 donor ligands. The $\delta^{51}\text{V}$ values are -6 ppm ($\Delta\nu_{1/2} = 2\,000$ Hz) for 18-crown-6 derivative and -21 ppm ($\Delta\nu_{1/2} = 350$ Hz) for 15-crown-5 one. The temperature dependence ^1H and ^{51}V NMR spectra indicates very fast ligand exchange, even at 183 K.

Plas has studied the vanadium(V) with amine alcohols.⁵¹ For each ligand two isomers, *fac* and *mer* have been detected in solution. These systems are dynamic, as at 410 K the coalescence of the signals of both isomers is observed. Plas has reported a chemical shifts and line half-width in various solvents. The equilibrium constants of isomerization have been determined on the basis of NMR measurements. In methanol solution additional signals due to methanolysis have

been detected, one has been assigned to $\text{OV}(\text{OMe})_3$ (-554 ppm) while the second to partially methanolysed complexes, containing $\text{VO}(\text{OMe})_2$ unit, bonded to both nitrogen and phenolate oxygen atoms ($\delta^{51}\text{V}$ -486 to -496 ppm, depending on the *R* substituent). NMR spectra have been recorded in various solvents (DMSO, DMF, DMF/ H_2O , MeOH, CHCl_3) in a wide range of temperatures and have been referred to neat VOCl_3 . In Table 4 the data for CHCl_3 solutions at room temperature are presented.

Table 4. Structures and ^{51}V NMR data of amine alcohol complexes of vanadium

		
R = H	$\delta^{51}\text{V} = -437$ ppm; $\Delta\nu_{1/2} = 150$ Hz	$\delta^{51}\text{V} = -449$ ppm; $\Delta\nu_{1/2} = 310$ Hz
R = OMe	$\delta^{51}\text{V} = -431$ ppm; $\Delta\nu_{1/2} = 160$ Hz	$\delta^{51}\text{V} = -446$ ppm; $\Delta\nu_{1/2} = 390$ Hz
R = Br	$\delta^{51}\text{V} = -437$ ppm; $\Delta\nu_{1/2} = 160$ Hz	$\delta^{51}\text{V} = -450$ ppm; $\Delta\nu_{1/2} = 310$ Hz
R = NO_2	$\delta^{51}\text{V} = -432$ ppm	$\delta^{51}\text{V} = -446$ ppm; $\Delta\nu_{1/2} = 350$ Hz

2.3 Group 6

2.3.1 Molybdenum

Two natural isotopes of molybdenum may be studied by NMR technique, ^{95}Mo and ^{97}Mo . Both have a nuclear spin of 5/2. Their quadrupolar moments are 0.12×10^{-28} and 1.1×10^{-28} respectively. Their natural abundances are 15.92 and 9.55 %, while the resonance frequencies, $\mathcal{E} = 6.514$ MHz and 6.652 MHz for ^{95}Mo and ^{97}Mo , respectively. Therefore their receptivities are rather similar, i.e. 5.07×10^{-4} (^{95}Mo) and 3.25×10^{-4} (^{97}Mo) that of ^1H . As it comes from comparison, more suitable for NMR detection is ^{95}Mo , because of higher receptivity and smaller quadrupolar moment. The chemical shift range of molybdenum nuclei is large, *ca.* 7500 ppm. Similar values of \mathcal{E} cause the possibility of observation of signals of both isotopes on one spectrum. IUPAC recommends 2 M solution of Na_2MoO_4 in D_2O (pH = 11) as reference.

Although ^{95}Mo NMR is widely used in studies of Mo complexes, most structures may be not recognized as supramolecular complexes. The acyclic Sb_2N ligand (Fig. 23) forms a complex with $\text{Mo}(\text{CO})_4$, but acts as a bidentate Sb_2 ligand, therefore its supramolecular character is controversial.⁵² The chemical shift observed is -1729 ppm (CDCl_3 , $1 \text{ M Na}_2\text{MoO}_4$ in water as reference; temperature not given).

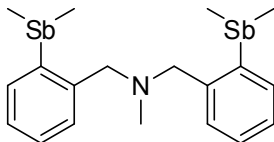
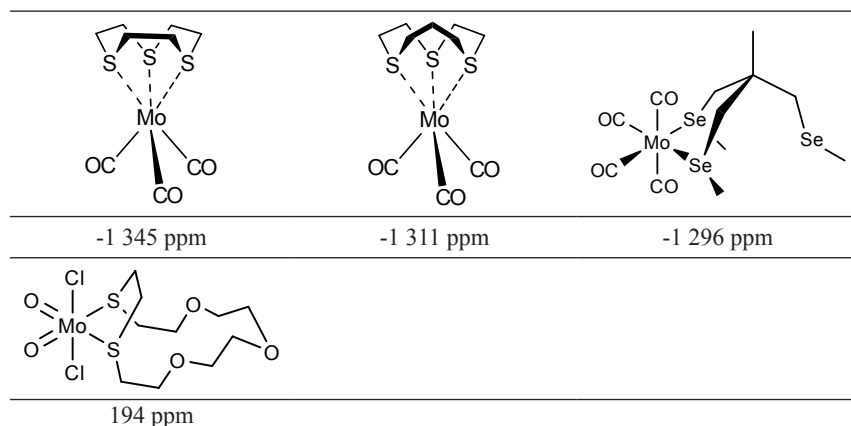


Fig. 23. Structure of Sb_2N ligand

Barton et al. have studied the $\text{Mo}(\text{CO})_3$ with tripodal thia-, seleno- and telluraethers and cyclic thiacrovnns.⁵³ The spectra have been recorded at 240 K in dichloromethane- d_2 against aqueous solution of MoO_4^{2-} as reference (authors have not precised the counter ion and the concentration). The obtained results are presented in Table 5. The complexes of MoO_2Cl_2 with macrocyclic mixed thia/oxa ligand, $[\text{15}] \text{aneS}_2\text{O}_3$, bonded *via* sulfur atoms, to result in $\text{O}_2\text{Cl}_2\text{S}_2$ coordination mode have been studied by ^{95}Mo NMR spectroscopy (dichloromethane/chloroform- d , vs. $1 \text{ M Na}_2\text{MoO}_4$; 300 K).⁵⁴

Table 5. Structures and ^{95}Mo NMR data of molybdenum compounds with S, Se and Te supramolecular ligands

-1 138 ppm	-1 216 ppm	-1 336 ppm



2.4 Group 7

2.4.1 Manganese

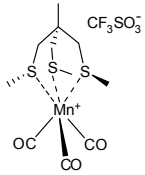
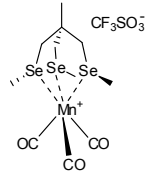
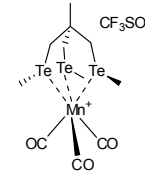
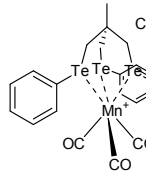
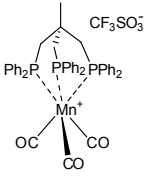
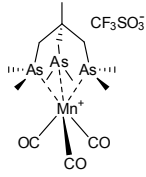
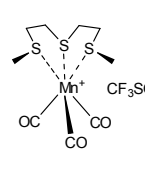
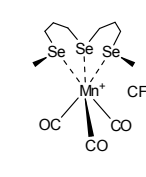
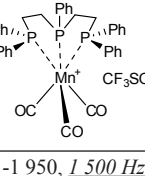
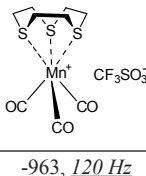
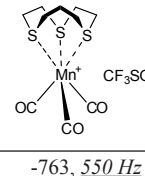
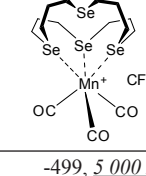
Although the NMR active manganese isotope, ^{55}Mn has a 100% natural abundance, and has a high receptivity (0.175 that of ^1H) it is very useless in NMR studies. ^{55}Mn nucleus has a large quadrupole moment ($0.55 \times 10^{-28} \text{ m}^2$; $I = 5/2$), which reduces the observability of manganese spectra. Moreover, compounds containing manganese on only few oxidation states (-1, 0, +1) are diamagnetic (the except among the other oxidation states is MnO_4^- ion), which does not cover the major part of manganese chemistry. The γ factor is high ($\mathcal{E} = 24.664 \text{ MHz}$). IUPAC recommends aqueous solution of KMnO_4 as a reference.

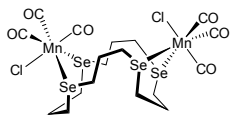
One of few examples of ^{55}Mn NMR application in supramolecular chemistry is a characterization of $\text{Mn}(\text{CO})_5(\text{CF}_3\text{SO}_3)$ complex with a Sb_2N tridentate ligand (Fig. 23).⁵² The obtained compound $[\text{Mn}(\text{CO})_5\text{L}](\text{CF}_3\text{SO}_3)$ shows the signal in ^{55}Mn NMR spectrum at -850 ppm (CDCl_3 ; referred to aqueous KMnO_4 ; no concentration of reference substance and measurements temperature given). The authors have not obtained X-ray structure but, on the basis of conductivity measurements, mass spectrometry and IR spectra postulated a tridentate Sb_2N coordination.

Levason et al.⁴⁹⁻⁵¹ have obtained a complexes of $\text{Mn}(\text{CO})_3^+$ ion with phospho-, thia- seleno- and telluratripodands. They are characterized by ^{55}Mn NMR spectroscopy. The chemical shifts of *fac* isomers obtained, are collected on Table 6. As the methyl group may occupy different position, conformer exists in solution. Since the selenium or tellurium centers inversion is slow in NMR timescale, the separated sets of signals are expected. The *syn* isomer, with three $\text{Se}(\text{Te})\text{Me}$ groups pointed in the same direction is more stable, dominant

structure. The *anti* one has been found in minor amounts (*ca.* 3-5 %). The authors have emphasized, that the signals of the complexes with cyclic molecule [9]-andS₃ are very sharp, if compared with the mono-, di- or tridentate acyclic ligands. This indicates high electronic field symmetry around manganese nucleus. Similarly, the complex with symmetric tripodal phosphine ligand shows the well resolved quartet, due to ⁵⁵Mn-³¹P coupling, while the signal of linear triphosphine complex is broadened in effect of fast quadrupolar relaxation of manganese nucleus. Also the complexes with larger selenacrown ([16]aneSe₄) have been obtained and their ⁵⁵Mn NMR spectra have been recorded. The spectra have been measured in CH₂Cl₂/CDCl₃ (9:1 v/v) mixtures, using KMnO₄ in water as reference. Temperature and concentration of reference solution have not been given.

Table 6. Chemical shifts and signal half-widths of Mn(CO)₃⁺ complexes with tripodal and monopodal ligands [Ref. 49-51]

			
-477, <u>5 000</u>	-721, <u>3 610 Hz (anti)</u> -672 (<i>syn</i>)	-1509, <u>1 200 Hz (anti)</u> -672 (<i>syn</i>)	-1320, <u>2 100</u>
			
-1 798, <i>J</i> _{MnP} = 190 Hz	-1 857, <u>600 Hz</u>	-696, <u>3 500 Hz</u> - 712, <u>sharp</u>	-560, <u>2 540 Hz</u>
			
-1 950, <u>1 500 Hz</u>	-963, <u>120 Hz</u>	-763, <u>550 Hz</u>	-499, <u>5 000 Hz</u>



-210, 2 100 Hz

2.4.2 Technetium

Although technetium does not occur naturally and all of its isotopes are radioactive, easy accessibility to ^{99}Tc and their relatively long decaying time make a ^{99}Tc NMR quite common technique. Technetium-99 is obtained in pure isotopic form which together with a high γ value ($\mathcal{E} = 22.508$ MHz) causes, it is fifth most sensitive nuclei (0.275 of the sensitivity of ^1H). ^{99}Tc is quadrupolar nucleus (-0.13×10^{-28} m 2 ; $I = 9/2$), which causes some difficulties due to line broadening. The compounds containing technetium on some oxidation states (Tc(II), Tc(IV) and Tc(VI)) are paramagnetic. IUPAC recommends the solution of NH_4TcO_4 in D_2O as a reference.

Katayev et al.⁵⁵ have used ^{99}Tc NMR titration for determination of stability constant between N_7 receptor (K1; Fig. 24) and pertechnetate in CDCl_3 . The authors have compared the NMR result with a UV-Vis titration. Due to small shift of ^{99}Tc signal (from 21.24 to 20.88 ppm) upon addition of three equivalents of ligand, the NMR method has given an underestimated $\log K$ value (2.75 vs. 3.88 from UV-VIS spectra). The authors have not calculated the ^{99}Tc NMR shift of the TcO_4^- complex. The same authors have studied a similar receptor (K2; Fig. 24) and observed similar shifts (from 21.30 to 20.54 ppm; $\log K = 1.96$; in CDCl_3).⁵⁶ In both papers the authors have not given the information about the reference used and temperature during measurements.

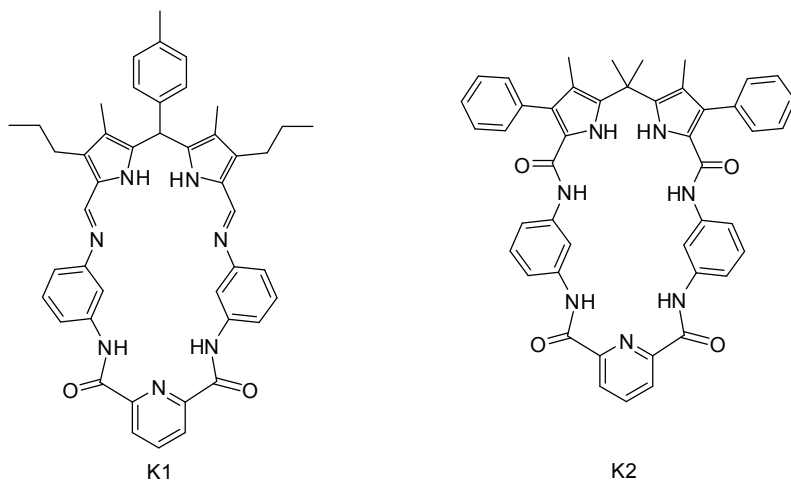


Fig. 24. Technetium selective ligands studied by ^{99}Tc NMR

2.5 Group 8

2.5.1 Iron

Natural iron contains one isotope suitable for NMR measurements – ^{57}Fe . It has a nuclear spin $\frac{1}{2}$, so ^{57}Fe NMR spectra are not broadened due to quadrupolar effects. Unfortunately, the natural abundance of this isotope is low, because only 2.1 %. Moreover, its low γ factor ($\mathcal{E} = 3.231$ MHz) causes the ^{57}Fe NMR spectra extremely difficult to recording. The receptivity of this nucleus is small (only 7.39×10^{-7} that of ^1H) and the spectra are disturbed by acoustic ringing effects. Additionally, the long relaxation times elongate the acquisition. The resonance frequencies of this isotope is not available on the NMR spectrometers of standard configuration. IUPAC recommends neat $\text{Fe}(\text{CO})_5$ as reference.

The application of ^{57}Fe in supramolecular chemistry is limited to studying of porphyrin complexes. The importance of iron-porphyrin systems in biochemistry induces the intensive study on the model systems. In Table 7 available ^{55}Fe NMR data of porphyrin complexes are presented.

La Mar and coworkers have studied the carbonyl myoglobin and model compounds.⁵⁷ They have reported the chemical shifts of protoporphyrin IX (FeCO)²⁺ complexes, containing imidazole ligands bonded in apical positions. They have used the inverse detection method. The chemical shift of ^{57}Fe nucleus has been determined by shifting of decoupler frequency (tuned at the iron resonance values range) with simultaneous observation of the half-width of the carbon signal of ^{13}C O ligand.

Baltzer and Landergren⁵⁸ have studied the protoporphyrin XI Fe(CO) complexes, containing various heterocyclic aromatic amines (imidazoles and pyridines) as a ligand in axial position. They have shown the correlation between ⁵⁷Fe NMR chemical shift and the logarithm of association constant between Fe(PPIX)(CO) and corresponding amine (determined spectrophotometrically). They shown also a high sensitivity of the δ value on solvent character. In the next paper they have studied some hindered iron containing porphyrins.⁵⁹ The ruffling of porphyrin macrocycle has been proposed as a factor causing the *d*-orbital energy levels inversion. The studies of model “basket-handle” porphyrins complexes of Fe(II) have been continued and presented in the next papers.⁶⁰ The authors have studied these molecules by multinuclear magnetic resonance and IR spectroscopy to determine their structure and ligand exchange dynamics. They mentioned the large difference between the loose BH12 complexes and the analogues with more hindered structure (BH9¹). They have explained this effect by electronic changes around Fe centre, caused by porphyrin plane. For these crowded molecules (BH9 & BH10) the authors have observed opposite changes upon the increasing of electron donating properties of nitrogen ligand (*py*, *buim* etc.), when comparing with the previously studied complexes. They have also reported the chemical shift of the pyridine complex of protoporphyrin-iron-CO complex, measured in pyridine.⁶¹

Gerothanassis et al.^{59,60} have studied the similar complexes. The spectrum of FePocPiv(Me2im) complex shows two signals, attributed to two atropoisomers. They have been assigned on the basis of ¹H-¹H nOe spectra. These studies have been continued with larger set of compounds. The authors have shown that more crowded “basket-handle” porphyrin, BH6, forms a mixture of two atropoisomers, which give separated signals in ⁵⁷Fe NMR spectrum. Since complex with 1,2,4,5-tetrasubstituted benzene cap (FeCap) is solid state exists as a conformer mixture, in solution only one signal is observed in NMR spectrum, which indicates fast interconversion between these conformers. The ⁵⁷Fe NMR spectrum of FeBB complex consists of two signals, due to presence of two conformers is solution, stabilized by stopped rotation of imidazole unit along Fe-N^{lm} bond. The authors have shown a good correlation between ⁵⁷Fe chemical shift with an average displacement of the *meso* carbon atoms relative to the porphyrin core mean plain, determined from X-ray experiments. They have confirmed the hypothesis of the high influence of porphyrin ring ruffling on iron chemical shift. The good correlation between δ ⁵⁷Fe and chemical shift of *meso* carbon atom have been also found. The same set of complexes have

¹ the further papers have cited this compound as a eight carbon long chain containing ones (BH8)

been discussed in next paper Gerothanassis et al.⁶² The new ¹³C and ¹⁷O NMR data have been presented, but not new ⁵⁷Fe NMR ones. Also the effects observed in ⁵⁷Fe NMR spectra discussed in this paper are the revision of the previously published one. The same authors have shown the correlation between previously published NMR data and IR parameters and X-ray structural data.⁶³

Mink and coworkers^{63,64} have investigated model heme compounds – iron complexes of *meso*-tetraphenylporphyrin (TPP) and their analogues as well as octaethylporphyrine (OEP), containing phosphines as an axial ligand, bonded to Fe centre. To reduce acquisition times, they used ⁵⁷Fe enriched samples. The authors have observed doublet in ³¹P NMR spectrum during slowly shifting of ⁵⁷Fe decoupling frequency. The frequency at which a doublet collapse, has been used to calculate of ⁵⁷Fe chemical shift. The ¹J_{P-Fe} coupling constants in the studied compounds are between 36 (TPPFe(PMe)(CO)) and 59 Hz (TPPFe(PMe)(meim) & TPPFe(PMe)(py)). The excellent correlation between ⁵⁷Fe and ³¹P NMR chemical shifts has been found as well as the δ ⁵⁷Fe of two series of complexes: TPP and OEP. The authors have discussed the effect of the substituent in phenyl rings of TPP and have compared the observed trends with that for other, previously reported porphyrins and heme proteins. For few complexes the temperature dependence of the ⁵⁷Fe chemical shift have been studied. The linear effects of +2.11 to +2.34 ppm/K have been observed. The authors have also compared the chemical shifts in five different solvents (benzene, toluene, THF, dichloromethane, chloroform) but have not found significant solvent effects (Δδ < 16 ppm). Unfortunately, they have not indicated the complex(es) used in these studies. Further comparison with cobalt analogues suggests, that the solvent dependence has been studied for TPPFe(PMe)₂. The authors have discussed also the conception of the use of cobalt(III) containing analogues of Fe-porphyrin complexes as models in NMR studies. As ⁵⁹Co NMR spectra are much more easily recorded, this is very promising approach, although Mink et al.⁶⁴ have shown many disadvantages of such approach. First, a ⁵⁹Co signals are broader, so the small shifts may be overlooked. Additionally, the sensitivity of cobalt resonance on solvent or temperature changes are more pronounced than those observed for ⁵⁷Fe, since their substituent induced shifts are smaller than those of Fe complexes.

Polam et al.⁶⁵ have correlated the literature ⁵⁷Fe NMR data of porphyrin complexes with Mössbauer quadrupole splitting. The good correlation has been found, except two points, TPPFe(py)₂ and TPPFe(pyrr)₂. Re-measurement of the chemical shift of the TPPFe(py)₂ (with deuterated pyridine as a ligand) has given a correct values. The authors determine a temperature effect on ⁵⁷Fe chemical shift of these complex. It is 2.9 ppm/K. The reasons for existence of Mössbauer-NMR

correlation have been discussed. Godbout and coworkers have studied the ^{57}Fe NMR shieldings and Mössbauer quadrupole splitting using DFT calculations, but have used only previously published experimental data. They have obtained excellent correlation between calculated shieldings and experimental chemical shifts of various naturally occurring porphyrins as well as model complexes.

Godbout et al.⁶⁶ have calculated the ^{57}Fe NMR chemical shifts and Mössbauer quadrupole splitting on the basis of DFT theory. They have compared the results with published and unpublished experimental data. The chemical shifts of two Fe^{II} complexes with unsubstituted porphyrin have been given.

The short review of application on NMR method (including ^{57}Fe NMR) has been published by Sanders et al.⁶⁷

Iron complexes with phthalocyanine ligand have been studied.⁶⁸ The ^{57}Fe chemical shifts of only two compounds, containing phosphite ligands in axial position, have been published. Their values have been determined from 2D $^{31}\text{P}, ^{57}\text{Fe}\{^1\text{H}\}$ HMQC spectra, measured in $\text{THF-}d_8$ and referred to external neat $\text{Fe}(\text{CO})_5$.

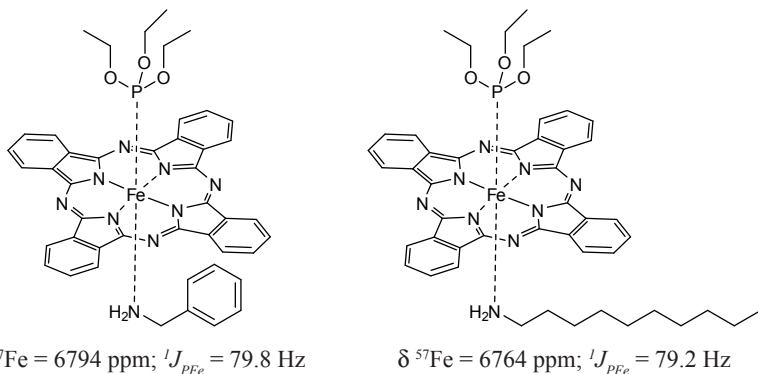
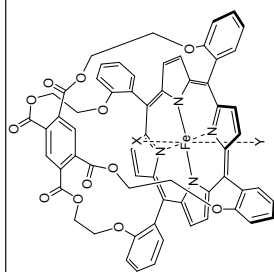


Fig. 25. Phthalocyanine Fe^{2+} complexes and their ^{57}Fe NMR data

Table 7. ^{57}Fe NMR data for iron porphyrin complexes

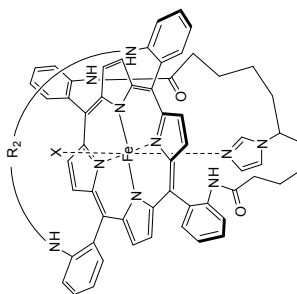
Symbol	Structure	$\delta^{57}\text{Fe}$	Conditions	Standard	Ref.
FeBH6(CO)py A	$R_1 = \text{NHCOCMe}_3$; $R_2 = \text{CO}(\text{CH}_2)_6\text{CO}$; $R_3 = \text{H}$; $X = \text{CO}$; $Y = 1\text{-methylimidazole}$	7 735	CD_2Cl_2 ; 298 K	$\text{Fe}(\text{CO})_5$	69
FeBH6(CO)py B	$R_1 = \text{H}$; $R_2 = \text{CO}(\text{CH}_2)_6\text{CO}$; $R_3 = \text{NHCOCMe}_3$; $X = \text{CO}$; $Y = 1\text{-methylimidazole}$	7 911	CD_2Cl_2 ; 298 K	$\text{Fe}(\text{CO})_5$	69
FeBH9(CO)py	$R_1 = \text{NHCOCMe}_3$; $R_2 = \text{CO}(\text{CH}_2)_6\text{CO}$; $R_3 = \text{H}$; $X = \text{CO}$; $Y = \text{pyridine}$	7 488	toluene- d_6 ; 298 K	$\text{Fe}(\text{CO})_5$	59, 60
FeBH9(CO)buim	$R_1 = \text{NHCOCMe}_3$; $R_2 = \text{CO}(\text{CH}_2)_6\text{CO}$; $R_3 = \text{H}$; $X = \text{CO}$; $Y = 1\text{-butylimidazole}$	7 500	toluene- d_6 ; 298 K	$\text{Fe}(\text{CO})_5$	59, 60
FeBH9(CO)s-buam	$R_1 = \text{NHCOCMe}_3$; $R_2 = \text{CO}(\text{CH}_2)_6\text{CO}$; $R_3 = \text{H}$; $X = \text{CO}$; $Y = 2\text{-butylamine}$	7 502	toluene- d_6 ; 298 K	$\text{Fe}(\text{CO})_5$	60
FeBH10(CO)py	$R_1 = \text{NHCOCMe}_3$; $R_2 = \text{CO}(\text{CH}_2)_{10}\text{CO}$; $R_3 = \text{H}$; $X = \text{CO}$; $Y = \text{pyridine}$	7 717	toluene- d_6 ; 298 K	$\text{Fe}(\text{CO})_5$	59, 60
FeBH10(CO)buim	$R_1 = \text{NHCOCMe}_3$; $R_2 = \text{CO}(\text{CH}_2)_{10}\text{CO}$; $R_3 = \text{H}$; $X = \text{CO}$; $Y = 1\text{-butylimidazole}$	7 728	toluene- d_6 ; 298 K	$\text{Fe}(\text{CO})_5$	59, 60
FeBH12(CO)py	$R_1 = \text{NHCOCMe}_3$; $R_2 = \text{CO}(\text{CH}_2)_{12}\text{CO}$; $R_3 = \text{H}$; $X = \text{CO}$; $Y = \text{pyridine}$	8 055	toluene- d_6 ; 298 K	$\text{Fe}(\text{CO})_5$	59, 60
FeBH12(CO)buim	$R_1 = \text{NHCOCMe}_3$; $R_2 = \text{CO}(\text{CH}_2)_{12}\text{CO}$; $R_3 = \text{H}$; $X = \text{CO}$; $Y = 1\text{-butylimidazole}$	8 036	toluene- d_6 ; 298 K	$\text{Fe}(\text{CO})_5$	59, 60
FePocPiv(Me2Im) A	$R_1 = \text{NHCOCMe}_3$; $R_2 = \text{H}$; $X = \text{CO}$; $Y = 1,2\text{-dimethylimidazole}$	7 402.0 (7 400)	CD_2Cl_2 ; 298 K	$\text{Fe}(\text{CO})_5$	70 (69)
FePocPiv(Me2Im) B	$R_1 = \text{H}$; $R_2 = \text{NHCOCMe}_3$; $X = \text{CO}$; $Y = 1,2\text{-dimethylimidazole}$	7 559.9	CD_2Cl_2 ; 298 K	$\text{Fe}(\text{CO})_5$	70

Fe(CO)₅CD₂Cl₂; 298 K

8 282

X = CO; Y = 1-methylimidazol

FeCap(Melm)

Fe(CO)₅CD₂Cl₂; 298 K

8 207

X = CO

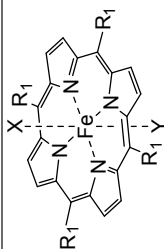
FeBB conformer A

Fe(CO)₅CD₂Cl₂; 298 K

8 199

X = CO

FeBB conformer B



FePicket(Me2Im)	R ₁ = 2-(Me ₂ CCONH)C ₆ H ₄ ; X = CO; Y = 1,2-dimethylimidazol	8 099	CD ₂ Cl ₂ ; 298 K	Fe(CO) ₂	69
FeP(Melm)	R ₁ = Ph; X = CO; Y = 1-methylimidazol	8 195	CD ₂ Cl ₂ ; 298 K	Fe(CO) ₂	69
T(PCl)PF ₂ e(PMe) ₂	R ₁ = 4-ClC ₆ H ₄ ; X, Y = PMe ₃	7 623	C ₆ D ₆ ; 296 K	Fe(CO) ₂	64
TPPF ₂ e(PMe) ₂	R ₁ = Ph; X, Y = PMe ₃	7 652	C ₆ D ₆ ; 296 K	Fe(CO) ₂	64
T(POMe)PF ₂ e(PMe) ₂	R ₁ = 4-MeOC ₆ H ₄ ; X, Y = PMe ₃	7 670	C ₆ D ₆ ; 296 K	Fe(CO) ₂	64
TPPF ₂ e(PMe)(CO)	R ₁ = Ph; X = CO; Y = PMe ₃	7 627	C ₆ D ₆ ; 296 K	Fe(CO) ₂	64
TPPF ₂ e(PMe)(BuNC)	R ₁ = Ph; X = n-BuNC; Y = PMe ₃	8 091	C ₆ D ₆ ; 296 K	Fe(CO) ₂	64
TPPF ₂ e(PMe)(BuNH ₂)	R ₁ = Ph; X = n-BuNH ₂ ; Y = PMe ₃	8 797	C ₆ D ₆ ; 296 K	Fe(CO) ₂	64
TPPF ₂ e(PMe)(BnSMe)	R ₁ = Ph; X = PhCH ₂ SMe; Y = PMe ₃	8 813	C ₆ D ₆ ; 296 K	Fe(CO) ₂	64
TPPF ₂ e(PMe)(meim)	R ₁ = Ph; X = 1-methylimidazole; Y = PMe ₃	8 864	C ₆ D ₆ ; 296 K	Fe(CO) ₂	64
TPPF ₂ e(PMe)(DMAP)	R ₁ = Ph; X = 4-Me ₂ NPY; Y = PMe ₃	8 883	C ₆ D ₆ ; 296 K	Fe(CO) ₂	64
TPPF ₂ e(PMe)(py)	R ₁ = Ph; X = pyridine; Y = PMe ₃	8 973	C ₆ D ₆ ; 296 K	Fe(CO) ₂	64
TPPF ₂ e(PMe)(CNPy)	R ₁ = Ph; X = 4-CNPy; Y = PMe ₃	9 033	C ₆ D ₆ ; 296 K	Fe(CO) ₂	64
TPPF ₂ e(PMe) ₂	R ₁ = 2,4,6-Me ₃ Ph; X, Y = PMe ₃	7 743	C ₆ D ₆ ; 296 K	Fe(CO) ₂	64
TPPF ₂ e(PMe)(BuNC)	R ₁ = 2,4,6-Me ₃ Ph; X = n-BuNC; Y = PMe ₃	8 001	C ₆ D ₆ ; 296 K	Fe(CO) ₂	64
TPPF ₂ e(PMe)(BnSMe)	R ₁ = 2,4,6-Me ₃ Ph; X = PhCH ₂ SMe; Y = PMe ₃	8 837	C ₆ D ₆ ; 296 K	Fe(CO) ₂	64
TPPF ₂ e(PMe)(meim)	R ₁ = 2,4,6-Me ₃ Ph; X = 1-methylimidazole; Y = PMe ₃	8 827	C ₆ D ₆ ; 296 K	Fe(CO) ₂	64
TPPF ₂ e(PMe)(DMAP)	R ₁ = 2,4,6-Me ₃ Ph; X = 4-Me ₂ NPY; Y = PMe ₃	8 871	C ₆ D ₆ ; 296 K	Fe(CO) ₂	64
TPPF ₂ e(PMe)(py)	R ₁ = 2,4,6-Me ₃ Ph; X = pyridine; Y = PMe ₃	8 896	C ₆ D ₆ ; 296 K	Fe(CO) ₂	64
T(POMe)PF ₂ e(PMe) ₂	R ₁ = 4-MeOC ₆ H ₄ ; X, Y = PMe ₃	7 676	C ₆ D ₆ ; 296 K	Fe(CO) ₂	64
T(POMe)PF ₂ e(PMe)(meim)	R ₁ = 4-MeOC ₆ H ₄ ; X = PMe ₃ ; Y = 1-methylimidazole	8 890	C ₆ D ₆ ; 296 K	Fe(CO) ₂	64
TPPF ₂ e(PMe) ₂	R ₁ = 2,4,6-Me ₃ Ph; X, Y = PMe ₃	7 741	C ₆ D ₆ ; 296 K	Fe(CO) ₂	64
TPPF ₂ e(PMe)(meim)	R ₁ = 2,4,6-Me ₃ Ph; X = 1-methylimidazole; Y = PMe ₃	8 824	C ₆ D ₆ ; 296 K	Fe(CO) ₂	64
TPPF ₂ e(PMe)(2meim)	R ₁ = 2,4,6-Me ₃ Ph; X = 2-methylimidazole; Y = PMe ₃	8 893	C ₆ D ₆ ; 296 K	Fe(CO) ₂	64
TPPF ₂ e(pyd5) ₂	R ₁ = Ph; X, Y = pyridine- <i>d</i> ₅	11 715	C ₆ D ₆ ; 296 K	Fe(CO) ₂	65
T(PMe)PF ₂ e(pyrr) ₂	R ₁ = 4-MeC ₆ H ₄ ; X, Y = pyrrolidine	7 341	CDCl ₃ /pyrrolidine (1:1 v/v) 302 K	Fe(CO) ₂	69, 70
TPPF ₂ e(py) ₂	R ₁ = Ph; X, Y = pyridine	7 258	CDCl ₃ /pyrrolidine (1:1 v/v) 302 K	Fe(CO) ₂	69, 70

T(Pniv)PFe(CO)(buim)	R ₁ = 4-(tBuCO)C ₆ H ₄ ; X = CO; Y = 1-butylimidazole	8 11 ¹	toluene-d ₆ ; 298 K	not given	59
T(Pniv)PFe(CO)(buim)	R ₁ = 4-(tBuCO)C ₆ H ₄ ; X = CO; Y = 1-butylimidazole	8 131	DMF/H ₂ O, 9:1 (v/v); 298 K	not given	59
T(Pniv)PFe(CO)(py)	R ₁ = 4-(tBuCO)C ₆ H ₄ ; X = CO; Y = pyridine	8 124	toluene-d ₆ ; 298 K	not given	59

PF ₂ (PMe) ₂	R ₁₋₃ = H; X, Y = PMe ₃	7 873	not given	Fe(CO) ₅	66
PF ₂ (pyr) ₂	R ₁₋₃ = H; X, Y = pyridine	11 723	not given	Fe(CO) ₅	66
OEPF ₂ (PMe) ₂	R ₁₋₃ = Et; X, Y = PMe ₃	7 873	C ₆ D ₆ ; 296 K	Fe(CO) ₅	64
OEPF ₂ (PMe)(CO)	R ₁₋₃ = Et; X = CO; Y = PMe ₃	7 877	C ₆ D ₆ ; 296 K	Fe(CO) ₅	64
OEPF ₂ (PMe)(BuNC)	R ₁₋₃ = Et; X = n-BuNC; Y = PMe ₃	8 231	C ₆ D ₆ ; 296 K	Fe(CO) ₅	64
OEPF ₂ (PMe)(BnNH ₂)	R ₁₋₃ = Et; X = n-BuNH ₂ ; Y = PMe ₃	9 120	C ₆ D ₆ ; 296 K	Fe(CO) ₅	64
OEPF ₂ (PMe)(BnSMe)	R ₁₋₃ = Et; X = PhCH ₂ SMe; Y = PMe ₃	9 064	C ₆ D ₆ ; 296 K	Fe(CO) ₅	64
OEPF ₂ (PMe)(meim)	R ₁₋₃ = Et; X = 1-methylimidazole; Y = PMe ₃	9 075	C ₆ D ₆ ; 296 K	Fe(CO) ₅	64
OEPF ₂ (PMe)(DMAP)	R ₁₋₃ = Et; X = 4-Me ₂ NPy; Y = PMe ₃	9 128	C ₆ D ₆ ; 296 K	Fe(CO) ₅	64
OEPF ₂ (PMe)(py)	R ₁₋₃ = Et; X = pyridine; Y = PMe ₃	9 224	C ₆ D ₆ ; 296 K	Fe(CO) ₅	64
OEPF ₂ (PMe)(CNPy)	R ₁₋₃ = Et; X = 4-CNPy; Y = PMe ₃	9 275	C ₆ D ₆ ; 296 K	Fe(CO) ₅	64
Fe(<i>meso</i> -PIX)(py45)(CO)	R ₁ = Me; R ₂ = Et; R ₃ = (CH ₂) ₂ COOH; X = pyridine-d ₅ ; Y = CO	8 188	toluene-d ₆ ; 298 K	not given	59
Fe(PPIX)(py45)(CO)	R ₁ = Me; R ₂ = CH=CH ₂ ; R ₃ = (CH ₂) ₂ COOH; X = pyridine-d ₅ ; Y = CO	8 205	toluene-d ₆ ; 298 K	not given	59
Fe(PPIX)(py)(CO)	R ₁ = Me; R ₂ = CH=CH ₂ ; R ₃ = (CH ₂) ₂ COOH; X = pyridine; Y = CO	8 185 ^{2,3}	DMF/H ₂ O, 9:1 (v/v); 298 K	Fe(CO) ₅	58
Fe(PPIX)(4acpy)(CO)	R ₁ = Me; R ₂ = CH=CH ₂ ; R ₃ = (CH ₂) ₂ COOH; X = 4-acetylpyridine; Y = CO	8 208 ²	DMF/H ₂ O, 9:1 (v/v); 298 K	Fe(CO) ₅	58

Fe(PPIX)(4cnpy)(CO)	$R_1 = \text{Me}; R_2 = \text{CH}=\text{CH}_2; R_3 = (\text{CH}_2)_2\text{COOH}; X = 4\text{-cyanopyridine}; Y = \text{CO}$	8 218 ²	DMF/H ₂ O, 9:1 (v/v); 298 K	Fe(CO) ₅	58
Fe(PPIX)(4mepy)(CO)	$R_1 = \text{Me}; R_2 = \text{CH}=\text{CH}_2; R_3 = (\text{CH}_2)_2\text{COOH}; X = 4\text{-methylpyridine}; Y = \text{CO}$	8 138 ²	DMF/H ₂ O, 9:1 (v/v); 298 K	Fe(CO) ₅	58
Fe(PPIX)(4dmapy)(CO)	$R_1 = \text{Me}; R_2 = \text{CH}=\text{CH}_2; R_3 = (\text{CH}_2)_2\text{COOH}; X = 4\text{-}(dimethylamino)pyridine; Y = \text{CO}$	8 185 ²	DMF/H ₂ O, 9:1 (v/v); 298 K	Fe(CO) ₅	58
Fe(PPIX)(2meim)(CO) ⁴	$R_1 = \text{Me}; R_2 = \text{CH}=\text{CH}_2; R_3 = (\text{CH}_2)_2\text{COOH}; X = 2\text{-methylimidazole}; Y = \text{CO}$	8 151 ²	DMF/H ₂ O, 9:1 (v/v); 298 K	Fe(CO) ₅	58
Fe(PPIX)(im)(CO)	$R_1 = \text{Me}; R_2 = \text{CH}=\text{CH}_2; R_3 = (\text{CH}_2)_2\text{COOH}; X = \text{imidazole}; Y = \text{CO}$	8 150 ²	DMF/H ₂ O, 9:1 (v/v); 298 K	Fe(CO) ₅	58
Fe(PPIX)(imH)(CO)	$R_1 = \text{Me}; R_2 = \text{CH}=\text{CH}_2; R_3 = (\text{CH}_2)_2\text{COOH}; X = \text{imidazole}; Y = \text{CO}$	8 151	DMSO- <i>d</i> ₆	Fe(CO) ₅	57
Fe(PPIX)(im)(CO)	$R_1 = \text{Me}; R_2 = \text{CH}=\text{CH}_2; R_3 = (\text{CH}_2)_2\text{COOH}; X = \text{imidazate ion}; Y = \text{CO}$	8 041	DMSO- <i>d</i> ₆	Fe(CO) ₅	57
Fe(PPIX)(py)(CO)	$R_1 = \text{Me}; R_2 = \text{CH}=\text{CH}_2; R_3 = (\text{CH}_2)_2\text{COOH}; X = \text{pyridine}; Y = \text{CO}$	8 211	pyridine; 295 K	Fe(CO) ₅	61

¹ by Polam et al.⁶⁵ have cited as 1-methylimidazole complex

² ¹he numerical value not given; the δ values read from the graph published

³ Polam et al.⁶⁵ have cited this value as 8 211 ppm (sic!)

⁴ Polam et al.⁶⁵ have cited this compound as imidazole complex, while Baltzers and Landevgren⁵⁹ as a 1-methylimidazole derivative

2.6 Group 9

2.6.1 Cobalt

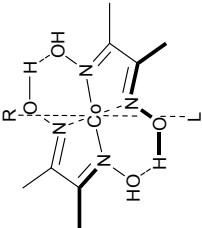
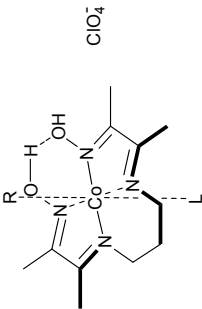
The ^{59}Co isotope, the only naturally occurring one nuclide of cobalt, has a nuclear spin $7/2$. Therefore it is available for NMR measurements, however its resonance signals are broadened due to quadrupole moment ($0.4 \times 10^{-28} \text{ m}^2$). It has a high receptivity (0.277 of that of ^1H). The resonance frequency at 2.3488 T is $\nu = 23.614 \text{ MHz}$. The only one difficulty in the observation of ^{59}Co NMR signal is its large chemical shift range (over 18 000 ppm), which could not be observed in one experiment. Therefore, many spectra must be recorded for one sample, with stepwise shifting of the transmitter frequency to check all possible chemical shift regions. Moreover, the arduous effect of signal folding is difficult to be avoided. Not all cobalt species may be observed by NMR technique, due to the paramagnetism of cobalt ion in many compounds (containing cobalt at oxidation +2 and some at +3). IUPAC recommends a solution of $\text{K}_3[\text{Co}(\text{CN})_6]$ in D_2O as a reference (0.00 ppm), however some other substances are also used, e.g. $\text{Co}(\text{acac})_3$ (ca. 12 500 ppm). Cobalt chemical shift is highly sensitive to temperature, solvent and concentration.

Two major aspects of supramolecular chemistry of cobalt have been studied by ^{59}Co NMR. First one is a structure and dynamics of cobalt containing complexes with polyaza and polythia macrocyclic ligands, second, the chemistry of cobalt-porphyrin (or phthalocyanin) complexes, which are widely studied as models of vitamin B_{12} .

Lawrance et al.⁷¹ have studied the complexes of Co^{3+} with macrobicyclic polyamines. Unfortunately, the authors have not published the ^{59}Co NMR data, but have included them as Supplementary Material, which are not available.

Tavagnacco et al.⁷² have studied some systems to understand vitamin B_{12} chemistry. They have chosen cobaloxime derivatives as model compounds. The complexes with dimethylglyoxime and their bridged analogues have been investigated by ^{59}Co NMR spectroscopy. The ^{59}Co NMR data were collected in Table 8. The spectra have been recorded in acetone at 298 K, a referred to 1 M solution of $\text{K}_3[\text{Co}(\text{CN})_6]$ in water. The linewidths of the studied systems are 1.7-12.5 kHz. The authors have found similar character of the relationship between $\delta^{59}\text{Co}$ and the Taft σ^* constants of the alkyl substituent observed for all four series of compounds as well as parallel trends of the R and L substituents influence on both ^{59}Co NMR chemical shift and half wave potential of $\text{Co}(\text{III})$ to $\text{Co}(\text{II})$ reduction.

Table 8. ^{59}Co NMR chemical shifts of Co^{III} dimethylglyoximate derivatives

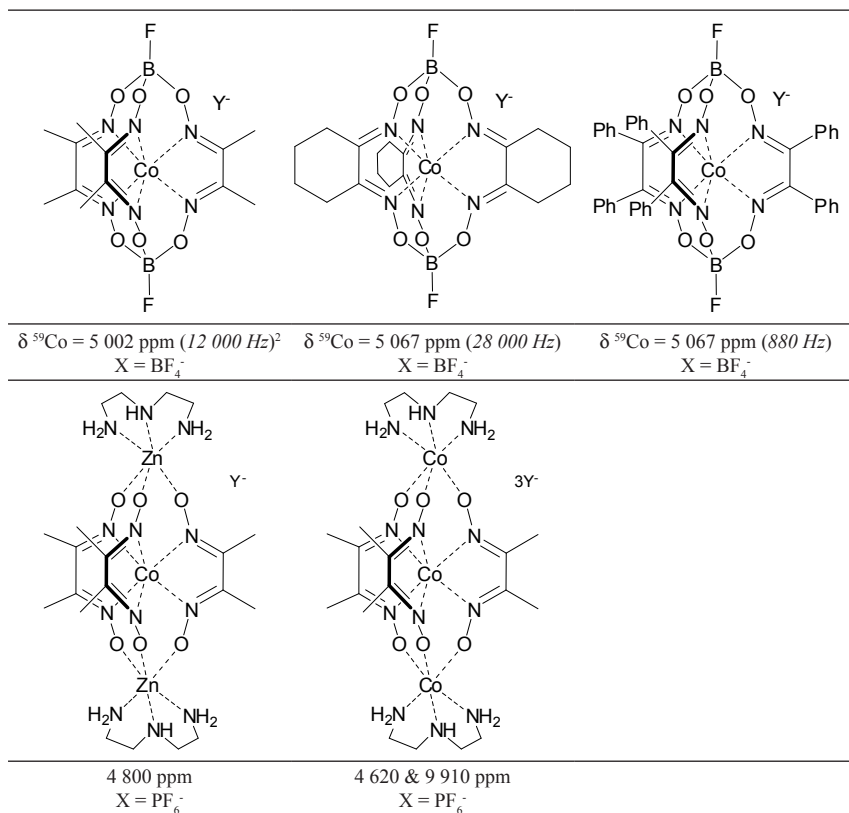
^{59}Co NMR chemical shift											
											
R-Co(dmg)L											
L	Me	Et	Pr	Bu	<i>i</i> -Pr	<i>c</i> -C ₄	<i>c</i> -C ₅	<i>c</i> -C ₆	<i>i</i> -Bu	<i>neo</i> -C ₅	Bn
H ₂ O	4 156	4 180	4 185	4 195	4 410	-	-	-	-	-	4 565
pyridine	3 640	3 654	3 673	3 679	3 819	3 700	3 746	3 842	3 887	3 948	-
											
R-Co(DOH)L											
L	Me	Et	Pr	R							
H ₂ O	4 630	4 660	4 670	4 670	Pr	<i>i</i> -Pr	Bn				
benzimidazole	-	4 270	-	-	-	-	-				
5,6-dimethyl-benzimidazole	-	4 250	-	-	-	-	-				
imidazole	-	4 140	-	-	-	-	-				
1-methylimidazole	-	4 130	-	-	-	-	-				
pyridine	-	4 140	-	-	-	-	-				

<p style="text-align: center;">R-Co(DBF)L</p>						
R						
L	Me	Et	Pr	Bu	<i>i</i> -Pr	Bn
H ₂ O	3 888	3 898	3 912	3 915	4 094	4 264
<p style="text-align: center;">R-Co(DOBFL)</p>						
R						
L	Me	Et	Pr	Pr	Pr	Bn
H ₂ O	4 588	4 612	4 678	4 678	5 021	5 021

Voloshin et al.⁷³ have studied the macrocyclic tris-dioximates of cobalt(III), crosslinked with tin tetrachloride and boron trifluoride (Table 9). The complexes obtained have been characterized by ⁵⁹Co NMR spectroscopy and other analytical methods. The significant difference between line half-widths of boron and tin containing clathrochelates has been explained on the basis of the different symmetry of these two class of compounds. As a tin-stabilized molecules have a trigonal antiprism coordination around cobalt atom, the boron containing ones are distorted towards trigonal prismatic coordination. This decreases the symmetry of the electronic field around cobalt atom and increases the rate of quadrupolar relaxation. In consequence, the signals of the boron analogues are distinctly broader. The spectra have been recorded in acetone-*d*₆ or acetonitrile-*d*₃ (the authors have not specified which solvent has been used for each compound) and referred to K₃[Co(CN)₆] (no solvent of reference sample, its concentration and temperature of measurements given). Similar structures, containing other metal centers as clathrochelate stabilizing ones, have been studied by Drago and Elias.⁷⁴

Table 9. ⁵⁹Co NMR data for cobalt(III) clathrochelates

$\delta^{59}\text{Co} = 4\ 603\ \text{ppm}\ (519\ \text{Hz})$ $X = \text{Et}_2\text{NH}_2^+$	$\delta^{59}\text{Co} = 4\ 687\ \text{ppm}\ (700\ \text{Hz})$ $X = \text{Et}_2\text{NH}_2^+$	$\delta^{59}\text{Co} = 4\ 662\ \text{ppm}\ (1\ 000\ \text{Hz})$ $X = \text{Et}_2\text{NH}_2^+$
$\delta^{59}\text{Co} = 4\ 684\ \text{ppm}\ (370\ \text{Hz})$ $X = \text{H}^+$	$\delta^{59}\text{Co} = 4\ 741\ \text{ppm}\ (950\ \text{Hz})$ $X = \text{H}^+$	$\delta^{59}\text{Co} = 4\ 658\ \text{ppm}\ (370\ \text{Hz})\ (?)^1$ $X = \text{Et}_2\text{NH}_2^+$

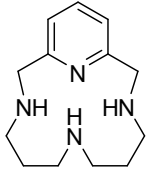
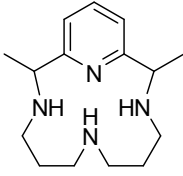
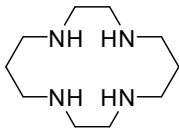


¹ authors have not presented the data for this complex, however in the same table presents the ⁵⁹Co NMR chemical shift for Fe complex; it is probably printing error

¹ 4 970 ppm in Ref. (74) Drago, R. S.; Elias, J. H. *J. Am. Chem. Soc.* 1977, 99, 6570. in acetonitrile (3 130 ppm vs. [Co(NH₃)₆]Cl₃)

The other N-donor macrocyclic ligands studied as hosts for Co(III) species are macrocyclic polyamines (L₁-L₃; Table 10).⁷⁵ Their aquacomplexes with alkylcobalt derivatives have been studied by ⁵⁹Co NMR (see Table 10 for chemical shifts). The water molecule and alkyl substituent are in axial positions while to nitrogen atoms coordinate to Co centre in equatorial plane. The cobalt NMR spectra show the existence of more than one Co containing species. This has been explained by the presence of various isomers in solution, however the authors have not proposed their structures. The spectra were recorded in nitromethane-*d*₃ and acetone-*d*₆ at 298 K and referred to external Co(acac)₃ (0.00 ppm; no solvent & concentration given).

Table 10. ^{59}Co NMR data for *N*-donor macrocyclic ligands

			
	L ₁	L ₂	L ₃
Complex	^{59}Co NMR chemical shift & peaks intensities		Solvent
[MeCoL ₁ (OH ₂)] [ClO ₄] ₂	6 977 (3%); 6 835 (96%); 6 421 (2%)		CD ₃ CN
[EtCoL ₁ (OH ₂)] [ClO ₄] ₂	6 919 (84%); 6 561 (15%); 6 477 (1%)		(CD ₃) ₂ CO
[PrCoL ₁ (OH ₂)] [ClO ₄] ₂	6 950 (84%); 6 531 (12%); 6 322 (4%)		CD ₃ CN
[BuCoL ₁ (OH ₂)] [ClO ₄] ₂	6 964 (94%); 6 542 (4%); 6 327 (2%)		(CD ₃) ₂ CO
[PrCoL ₂ (OH ₂)] [ClO ₄] ₂	6 996 (76%); 6 620 (7%); 6 572 (14%); 6 353 (3%)		CD ₃ CN
[BuCoL ₃ (OH ₂)] [ClO ₄] ₂	6 918 (81%); 6 350 (15%); 5 983 (4%)		CD ₃ CN

The linear (diethylenetriamine, triethylenetetramine, tetraethylenepentamine) and cyclic (cyclam) polyamine ligands containing Co^{III} complexes have been studied by Kapanadze et al.⁷⁶ The authors have identified the series of isomeric complexes, containing additional NH₃, OH⁻ and NO₂⁻ monodentate ligands in coordination sphere (the authors have not indicated, if NO₂⁻ ligand is bonded by N or O atom in complexes studied). All individuals formed have been characterized by ^{59}Co NMR spectroscopy (Table 11). The spectra have been recorded in water and referred to [Co(NH₃)₆]Cl₃. Although the chemical shifts of many species have been reported, since the authors have not rationalized the signals assignments, some results presented are highly speculative. The *trans* complexes of cyclam with Co(OH)(NH₃)₂²⁺ ion and Co(OH)₂⁺ ion show some additional peaks, assigned to conformational isomers. The signal of *cis*-[Co(cyclam)(OH)₂]⁺ complex has been identified in experiment with addition of *d*-tartaric acid. The signals, which split due to the formation of two diastereoisomeric species have been assigned to this molecule. Also the formation of dimeric (μ-OH) molecules has been detected. For complex with triethylenetetramine two signals have been assigned to such species ([Co₂(trien)₂(NH₃)₂OH]⁺), while for tetraethylenepentamine, four signals ([Co(tetraen)]₂OH]⁺). Their detailed structures have not been elucidated.

Table 11. ^{59}Co NMR data of cobalt(III) ion polyamine complexes

-1 430 ppm 280 Hz		A = N ¹ ; E = N ² ; D = N ³ ; B, F = NO ₂ ; C = NH ₃
-1 480 ppm 310 Hz		A = N ¹ ; E = N ² ; D = N ³ ; C, F = NO ₂ ; B = NH ₃
-1 530 ppm 420 Hz		E = N ¹ ; D = N ² ; C = N ³ ; A, B = NO ₂ ; F = NH ₃
-1 550 ppm 420 Hz		E = N ¹ ; D = N ² ; C = N ³ ; A, F = NO ₂ ; B = NH ₃
-1 800 ppm 685 Hz		B = N ¹ ; C = N ² ; D = N ³ ; E = N ⁴ A, F = NO ₂
-1 680 ppm 510 Hz		A = N ¹ ; E = N ² ; D = N ³ ; F = N ⁴ B, C = NO ₂
-1760 ppm 560 Hz		A = N ¹ ; E = N ² ; D = N ³ ; C = N ⁴ B, F = NO ₂
-880 ppm 250 Hz		B = N ¹ ; C = R-N ² ; D = R-N ³ ; E = N ⁴ A, F = NH ₃
-665 ppm 260 Hz		B = N ¹ ; C = R-N ² ; D = S-N ³ ; E = N ⁴ A, F = NH ₃
-850 ppm 350 Hz		A = N ¹ ; E = N ² ; D = N ³ ; F = N ⁴ B, C = NH ₃
-955 ppm 325 Hz		A = N ¹ ; E = R-N ² ; D = R-N ³ ; C = N ⁴ B, F = NH ₃
-973 ppm 310 Hz		A = N ¹ ; E = R-N ² ; D = S-N ³ ; C = N ⁴ B, F = NH ₃
-122 ppm 165 Hz		B = N ¹ ; C = N ² ; D = N ³ ; E = N ⁴ A = NH ₃ , F = OH
30 ppm 205 Hz		A = N ¹ ; E = N ² ; D = N ³ ; F = N ⁴ B = NH ₃ , C = OH

-47 ppm 280 Hz		A = N ¹ ; E = N ² ; D = N ³ ; C = N ⁴ F = NH ₃ , B = OH
3 ppm 185 Hz		A = N ¹ ; E = N ² ; D = N ³ ; C = N ⁴ B = NH ₃ , F = OH
1 095 ppm 130 Hz		B = N ¹ ; C = R-N ² ; D = R-N ³ ; E = N ⁴ A, F = OH
985 ppm 150 Hz		B = N ¹ ; C = R-N ² ; D = S-N ³ ; E = N ⁴ A, F = OH
-620 ppm 1 800 Hz		B = N ¹ ; C = N ² ; D = N ³ ; E = N ⁴ A, B = NH ₃
-590 ppm 1 005 Hz		A = N ¹ ; D = N ² ; E = N ³ ; F = N ⁴ B, C = NH ₃
140 & 100 ppm 290 & 310 Hz		B = N ¹ ; C = N ² ; D = N ³ ; E = N ⁴ A = OH; B = NH ₃
-3 ppm 250 Hz		A = N ¹ ; D = N ² ; E = N ³ ; F = N ⁴ B = OH; C = NH ₃
1 092, 1 185, 1 153, 1 086 & 1 145 ppm		B = N ¹ ; C = N ² ; D = N ³ ; E = N ⁴ A, B = OH
993 ppm		A = N ¹ ; D = N ² ; E = N ³ ; F = N ⁴ B, C = OH
225 ppm 950 Hz		A = N ¹ , E = N ² , D = N ³ , F = N ⁴ , C = N ⁵ B = OH

310 ppm 470 Hz		B = N ¹ , E = N ² , D = N ³ , F = N ⁴ , C = N ⁵ A = OH
490 ppm 210 Hz		A = N ¹ , E = N ² , D = N ³ , C = N ⁴ , F = N ⁵ B = OH
545 ppm 290 Hz		B = N ¹ , E = N ² , D = N ³ , C = N ⁴ , F = N ⁵ A = OH
-885 ppm 1 350 Hz		A = N ¹ , E = N ² , D = N ³ , F = N ⁴ , C = N ⁵ B = NH ₃
-1 040 ppm 1 220 Hz		B = N ¹ , E = N ² , D = N ³ , F = N ⁴ , C = N ⁵ A = NH ₃
-1 100 ppm 420 Hz		A = N ¹ , E = N ² , D = N ³ , C = N ⁴ , F = N ⁵ B = NH ₃
-1 170 ppm 485 Hz		B = N ¹ , E = N ² , D = N ³ , C = N ⁴ , F = N ⁵ A = NH ₃

Grohmann et al.⁷⁷ have synthesized a complex of methylcobalt(III) with pentadentate amine ligand, derived from pyridine (Fig. 26). The complex has been characterized by ⁵⁹Co NMR spectrum. A single line at 6070 ppm has been observed, $\Delta\nu_{1/2} = 30.7$ kHz (in DMSO-d₆, vs. K₃[Co(CN)₆] in D₂O; no standard concentration and temperature given).

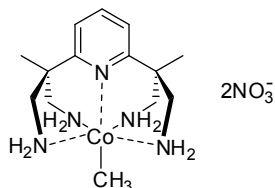


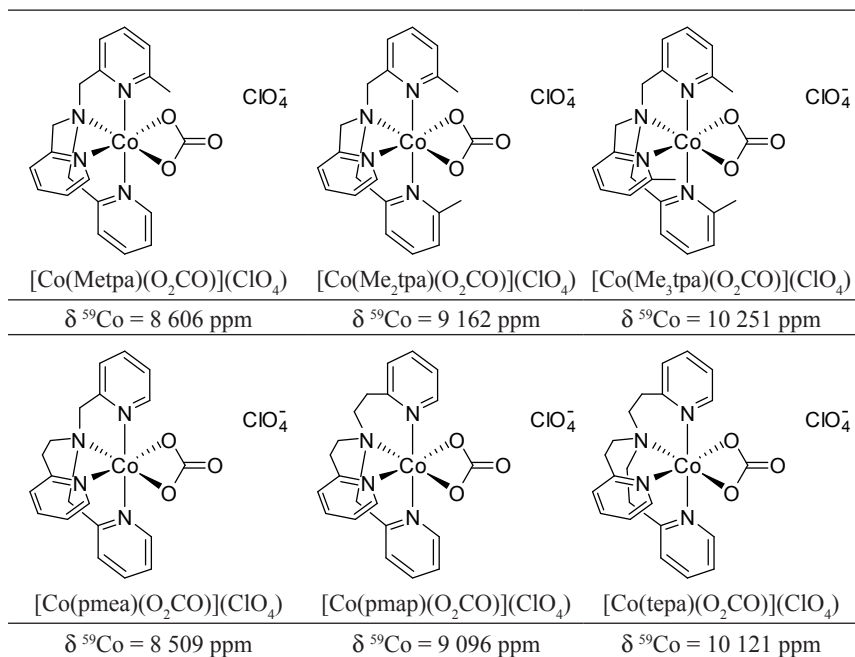
Fig. 25. Structure of Co(III) complex with pentadentate ligand

McClintock et al.⁷⁷⁻⁷⁹ have studied various carbonatecobalt(III) complexes with tripodal tetraamines (Table 12). Twelve obtained compounds have been

characterized by ^{59}Co NMR method (see Table 12 for details). The structures of the complexes have been determined by X-ray diffractometry. Cobalt NMR spectra were measured in D_2O vs. $\text{K}_3[\text{Co}(\text{CN})_6]$. The experimental NMR results have been correlated with UV-Vis parameters (magnetogyric ratio, γ vs. wavelength of the lowest $d-d$ transition, λ_{max} ; chemical shift, δ vs. wavenumber of the lowest $d-d$ transition, Δ) with very good R^2 coefficients. The authors have also calculated the chemical shift by DFT method. The computed values are smaller of about 900-1400 ppm from experimental ones, but reproduces well the experimental trends. The DFT calculations of the experimental parameters, among others, ^{59}Co NMR chemical shifts of these set of compounds have been also published.⁷⁸ The good agreement between the computed and measured value has been found (calculations reproduce trend, although in the individual cases the significant deviation is observed).

Table 12. Polypodal carbonatecobalt complexes – structures and ^{59}Co NMR data

<p>Chemical structure of [Co(baep)(O₂CO)](ClO₄), where baep is a bicyclic polyamine ligand with two secondary amine groups and two tertiary amine groups.</p>	<p>Chemical structure of [Co(abap)(O₂CO)](ClO₄), where abap is a bicyclic polyamine ligand with two secondary amine groups and two tertiary amine groups, in a different conformation than baep.</p>	<p>Chemical structure of [Co(trpn)(O₂CO)](ClO₄), where trpn is a bicyclic polyamine ligand with two secondary amine groups and two tertiary amine groups, in a different conformation.</p>
[Co(baep)(O ₂ CO)](ClO ₄)	[Co(abap)(O ₂ CO)](ClO ₄)	[Co(trpn)(O ₂ CO)](ClO ₄)
$\delta^{59}\text{Co} = 8\ 728\ \text{ppm}$	$\delta^{59}\text{Co} = 9\ 117\ \text{ppm}$	$\delta^{59}\text{Co} = 9\ 574\ \text{ppm}$
<p>Chemical structure of [Co(uns-penp)(O₂CO)](ClO₄), where uns-penp is a complex ligand containing a piperidine ring and a pyridine ring.</p>	<p>Chemical structure of [Co(dppa)(O₂CO)](ClO₄), where dppa is a complex ligand containing a piperidine ring and a pyridine ring.</p>	<p>Chemical structure of [Co(tpa)(O₂CO)](ClO₄), where tpa is a complex ligand containing a piperidine ring and a pyridine ring.</p>
[Co(uns-penp)(O ₂ CO)](ClO ₄)	[Co(dppa)(O ₂ CO)](ClO ₄)	[Co(tpa)(O ₂ CO)](ClO ₄)
$\delta^{59}\text{Co} = 8\ 132\ \text{ppm}$	$\delta^{59}\text{Co} = 8\ 365\ \text{ppm}$	$\delta^{59}\text{Co} = 8\ 890\ \text{ppm}$



The cobalt(III) complexes with macrocyclic polythioethers (Fig. 26) have been studied by ^{59}Co NMR spectroscopy by Chandrasekhar and McAuley.⁷⁹ They have obtained two adducts: $\text{Co}([9\text{-aneS}_3)_2(\text{ClO}_4)_3$ and $\text{Co}([10\text{-aneS}_3)_2(\text{ClO}_4)_3$ and have recorded the cobalt-59 NMR spectra in CD_3CN for the first compound and in D_2O for the second. The spectra were measured at 298 K and referred to $\text{K}_3[\text{Co}(\text{CN})_6]$ (no solvent and concentration given). For $\text{Co}([10\text{-aneS}_3)_2(\text{ClO}_4)_3$ two signals have been observed, at 2336 and 2268 ppm, respectively, due to the presence of *cis* and *trans* isomers in the solution. As the electrostatic field gradient in a *cis* isomer is smaller, the signal attributed to this species is narrower (624 Hz) than that of *trans* one (1220 Hz). The symmetrical [9]-aneS₃ ligand forms only one isomer with Co^{3+} ion, therefore single signal occurs in ^{59}Co NMR spectrum (1511 ppm). By addition of a paramagnetic $\text{Co}([10\text{-aneS}_3)_2(\text{ClO}_4)_2$ complex to the solution containing $\text{Co}([10\text{-aneS}_3)_2(\text{ClO}_4)_3$ and plotting the relation of the ^{59}Co NMR linewidth of diamagnetic Co^{3+} complex against an amount of added paramagnetic Co^{2+} compounds, the rate of electron transfer between these species has been determined. Similar experiment has been performed for [9]-aneS₃ derivatives.

The crown thioethers of larger cavity (Fig. 26) have been studied as ligands

for Co^{3+} complexation by Grant et al.⁸⁰ They have obtained the values 2464 ppm for $\text{Co}([\text{20}]\text{-aneS}_6)(\text{BF}_4)_3$ and 1646 ppm for $\text{Co}([\text{18}]\text{-aneS}_6)_2(\text{ClO}_4)_3$. Both spectra have been recorded in nitromethane- d_3 and referred to $[\text{Co}(\text{CN})_6]^{3-}$ (no solvent and temperature given).

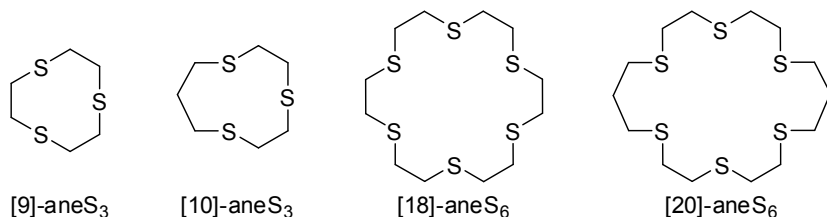


Fig. 26. Macrocyclic thioethers used as a cobalt(III) complexes

Cyclic ($[\text{14}]and\text{S}_4$) and acyclic ($2,5,8,11\text{-S}_4[\text{12}]$, $2,6,9,13\text{-S}_4[\text{14}]$) tetradentate thioethers have been also used as ligands for complexation of CoX_2^+ ions (where X is the halide anion).⁸¹ The structures of the complexes formed are presented on Fig 27. The $[\text{14}]and\text{S}_4$ forms only *trans* isomers with a dihalidecobalt(III) ions. The chemical shifts are 7 384 ppm $[\text{Co}([\text{14}]and\text{S}_4)\text{Cl}_2](\text{BF}_4)$, 7 062 ppm $[\text{Co}([\text{14}]and\text{S}_4)\text{Br}_2](\text{BF}_4)$ and 7 342 ppm $[\text{Co}([\text{14}]and\text{S}_4)\text{Cl}_2](\text{BPh}_4)$. Also $[\text{Co}(2,5,8,11\text{-S}_4[\text{12}])\text{I}_2](\text{BPh}_4)$ exists only as a *trans* isomer (7 472 ppm). The other complexes studied show the *cis/trans* isomerism. For $[\text{Co}(2,5,8,11\text{-S}_4[\text{12}])\text{Cl}_2](\text{BPh}_4)$ and $[\text{Co}(2,6,9,13\text{-S}_4[\text{14}])\text{Br}_2](\text{BPh}_4)$ two signals (at 7 584 & 7 433 ppm for the first and 8 130 & 7 921 ppm for the second compounds, respectively) have been detected. This indicates the presence of two isomers in solution. Three geometric isomers have been found to be formed in the reaction leads to $[\text{Co}(2,5,8,11\text{-S}_4[\text{12}])\text{Br}_2](\text{BPh}_4)$ ($\delta^{59}\text{Co}$ NMR: 7 210, 7 030 and 6 856 ppm). The authors have not assigned definite structures to the signal observed. The spectra have been recorded for the solutions of the complexes in nitromethane, although the solvent effects have been checked by measuring of cobalt-59 chemical shifts of selected compounds in acetonitrile. Small shifts, of 1-26 ppm are observed. The authors have isolated also the complex of S_6 coordination mode, $[\text{Co}([\text{14}]and\text{S}_4)(2,5\text{-S}_2[6])](\text{BF}_4)$, showing the signal at 6 830 ppm (CH_3NO_2). All chemical shifts were measured vs. 1 M solution of $\text{K}_3[\text{Co}(\text{CN})_6]$ in water. As it could be seen, the data for S_6 complexes of Co(III) published by Grant et al. are not coherent with that of Jenkinson group.

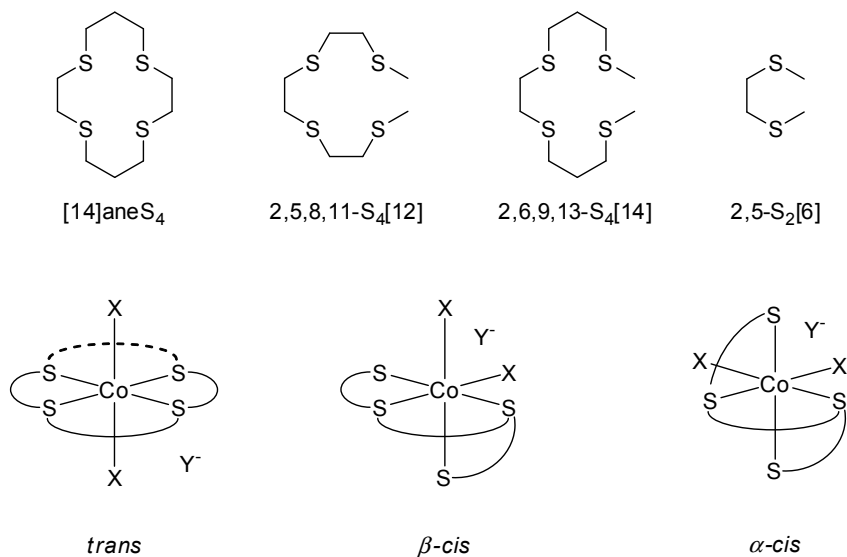


Fig. 27. Macrocyclic and acyclic polythioethers and geometry of their complexes with cobalt(III) ion

The selenamacrocycles have been studied as Co³⁺ ligands by Levason et al.⁸² They have prepared the series of complexes of general formula presented on Fig. 28, containing various halide anion coordinated to Co centre. For Br derivative two salts, differ in a counter ion, have been obtained. For [Co([16]aneSe₄)Cl₂](PF₆) and [Co([16]aneSe₄)Br₂](PF₆) single, broad resonance has been observed in ⁵⁹Co NMR spectrum, indicating on the presence of only one isomer (*trans*) in solution (chemical shifts 9 590 and 9 125 ppm, respectively). This observation has been confirmed by ⁷⁷Se NMR spectroscopy. Its structure has been determined by X-ray diffractometry and verified by IR and UV-Vis spectroscopy in solution. The changing of the counter ion from PF₆⁻ to BPh₃⁻ does not result in any shift in cobalt NMR spectrum. For [Co([16]aneSe₄)I₂](PF₆) complex two signals have been detected in NMR spectrum, one at 8 436 and the second at 8 465 ppm. Also in selenium-77 spectrum two sets of signals occur. They have been assigned to two isomers, *cis* and *trans* one. The major, *trans* isomer gives the signal at 8 436 ppm. The spectra have been recorded in CH₃NO₂ and referred to aqueous [Co(CN)₆]³⁻. The measurements temperature and concentration of reference have not been given.

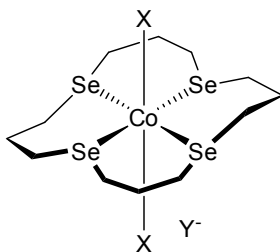


Fig. 28. Structure of [16]aneSe₄ ligand Co³⁺ complex

Open chain P₂S₂ podands (Fig. 29) have been used as ligands in a series of complex of general formula [CoX₂(P₂S₂)]PF₆, synthesized by Connolly et al.⁸³ The obtained chemical shifts are collected in Table 13.

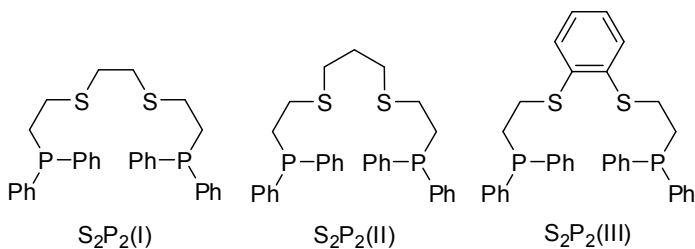


Fig. 29. Structures of P₂S₂ ligands

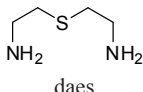
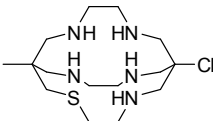
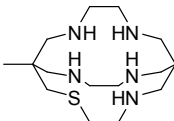
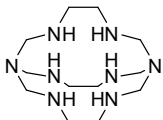
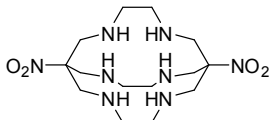
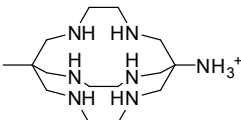
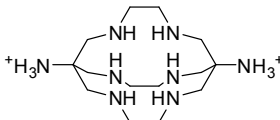
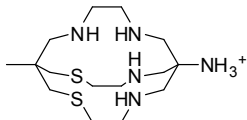
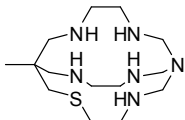
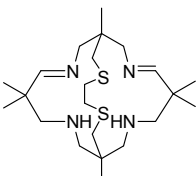
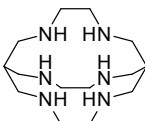
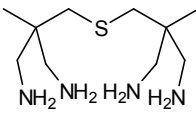
Table 13. ⁵⁹Co NMR chemical shifts of Co^{III} ion complexes with P₂S₂ ligands

Complex	L		
	S ₂ P ₂ (I)	S ₂ P ₂ (II)	S ₂ P ₂ (III)
[CoCl ₂ (L)](PF ₆)	3 410	3 390	3 210
[CoBr ₂ (L)](PF ₆)	3 420	3 290	3 180

Mixed nitrogen/sulfur containing ligands have been studied by Sharrad et al. (Table 14).⁸⁶⁻⁸⁸ They have compared them with many other Co(III) complexes, with mono-, di- and polydentate N or S/N ligands. All spectra have been recorded in water and referred against 0.1 M K₃[Co(CN)₆] at 301 K. The authors have correlated the chemical shifts with energy of ¹A_{1g} → ¹T_{1g} transient, determined from UV-Vis spectra. The relation between linewidth and complexes symmetry has been also included.

Table 14. Structures and ^{59}Co NMR data of polydentate mixed N,S ligands

<i>meso</i> -1,2-Me ₂ EtN ₄ S ₂ amp	<i>rac</i> -1,2-Me ₂ EtN ₄ S ₂ amp	EtN ₄ S ₂ amp
5 661 ppm (370 Hz) as Co(L)Cl ₂ (ClO ₄) ₄	5 579 ppm (630 Hz) as Co(L)Cl ₂ (ClO ₄) ₄	5 638 ppm (740 Hz) as Co(L)Cl(ClO ₄) ₂
PrN ₄ S ₂ amp	BuN ₄ S ₂ amp	XyN ₄ S ₂ amp
6 125 ppm (1 700 Hz) as Co(L)Cl(ClO ₄) ₂	6 223 ppm (2 700 ppm) as Co(L)Cl ₂ (ClO ₄) ₄	6 476 ppm (12 000 Hz) as Co(L)Br ₃
N ₃ S ₃	ClN ₃ S ₃ sar	AMN ₃ S ₃ sarH ⁺
4 455 ppm (510 Hz) as Co(L)(ClO ₄) ₃	4 413 ppm (2 100 Hz) as Co(L)(ClO ₄) ₃	4 448 ppm (2 700 Hz) as Co(L)Cl ₄
N ₄ S ₂	sen	N ₅ S
5 390 ppm (900 Hz) as Co(L)(ClO ₄) ₃	6 920 ppm (250 Hz) ¹ as Co(L)(ClO ₄) ₃	6 229 ppm (900 Hz) as Co(L)(ClO ₄) ₃

 daes	 ClN ₅ Ssar	 HN ₅ Ssar
5 553 ppm (230 Hz) as Co(L ₂)Br ₃	6 250 ppm (1 400 Hz) as Co(L)(ClO ₄) ₃	6 224 ppm (1 800 Hz) as Co(L)(ClO ₄) ₃
 sep	 diNOsar	 AMN ₆ sarH ⁺
6 941 ppm (260 Hz) ² as Co(L)Cl ₃	6 875 ppm (1 200 Hz) ³ as Co(L)Cl ₃	6 839 ppm (840 Hz) as Co(L)Cl ₄
 diAMN ₆ sarH ₂ ²⁺	 AMN ₄ S ₂ sarH ⁺	 AZAN ₅ Ssar
6 877 ppm (1 400 Hz) ⁴ as Co(L)C ₅	5 416 ppm (4 000 Hz) as Co(L)(ClO ₄) ₃	6 229 ppm (1 000 Hz) as Co(L)(ClO ₄) ₃
 Me ₆ docosadieneN ₄ S ₂	 sar	 N ₄ Samp
6 501 ppm as [Co(L)](ClO ₄) ₃	6 800 ppm (280 Hz) no counter ion and experimental details given	7 077 ppm (5 350 Hz) as [Co(L)Cl](ZnCl ₄) 7 296 ppm as [Co(L) (H ₂ O)](ZnCl ₄)

¹ 6 800 ppm (360 Hz) according to Hendry and Ludi³⁴ (no experimental details and counter ion given)² 952 ppm (260 Hz) according to Voloshin et al.⁷³ (no solvent given; the high difference between the values suggest a typographic error or the effect of the signal folding)³ 6 887 ppm (1 100 Hz) according to Voloshin et al.⁷³ (no solvent given) and 6 870 (270 Hz) according to Hendry and Ludi³⁴ (no experimental details and counter ion given)⁴ 7 324 ppm (3 000 Hz) according to Voloshin et al. (no solvent given) and 6 790 ppm (780 Hz) according to Hendry and Ludi³⁴ (no experimental details and counter ion given)

Iida et al.⁸⁵ have studied the formation of micelles build of substituted polyamine complexes of Co^{3+} . The studies have been performed for two complexes, differ in a length of alkyl chain (Fig. 30; $n = 1$ or 4 ; $X = \text{Cl}^-$ or ClO_4^-). The aggregation process has been studied in D_2O . The authors have monitored the ^{59}Co linewidths and relaxation times (both transverse and longitudinal) measured at various concentration of complex. Simultaneously the ^2H and ^{35}Cl NMR parameters have been determined. The authors give the chemical shifts of both derivatives (no counter ion mentioned) to be -573 (C_8) and -571 ppm (C_{12}) vs. 5 mmol kg^{-1} solution of $[\text{Co}(\text{NH}_3)_6]^{3+}$ (0.00 ppm; no solvent and temperature given).

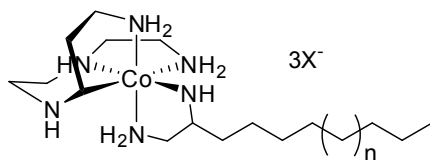


Fig. 30. Cobalt containing micelles precursor

Hagen et al.⁸⁶ have presented the first examples of ^{59}Co NMR spectra of Co^{3+} ion complexes with porphyrins. The data presented are summarized in Table 15. The authors have measured the chemical shifts and line half widths for two Co-porphyrin systems (with tetraphenyl- and octaethylporphyrin; TPP and OEP) with different nitrogen heterocycle ligands coordinated to Co centre and different counter ions. The authors have observed small anion (counter ion) effect, *ca.* 2 ppm in MeOH and slightly higher one (10 ppm) in other solvents. Two complexes ($[\text{TPPCo}(\text{Im})_2](\text{ClO}_4)$ and $[\text{TPPCo}(\text{MeIm})_2](\text{ClO}_4)$) have been also studied in various solvents (methanol, acetone, acetonitrile, dichloromethane, tetrahydrofuran, dichloroethane) to estimate the sensitivity of cobalt chemical shift on solvent character. The solvent effects are 92 and 98 ppm, respectively. The authors have also estimated the solvent effect in THF/ CH_2Cl_2 mixtures at various temperatures and have found, that the changes at 296.9 and 304.5 K are different. The results for studied porphyrin as well as other Co^{III} complexes have been correlated with δ ^{57}Fe NMR data obtained for analogous (or similar) compounds. The next paper of these authors presents the influence of the substitution of phenyl ring of TPP ligand on ^{59}Co NMR chemical shift of $[\text{T}(4\text{-R}_1\text{C}_6\text{H}_4)\text{PCo}(\text{R}_2\text{Im})_2](\text{BF}_4)$ in different solvents (see Table 15; data reported for MeOH solutions are only cited for $\text{T}(4\text{-XC}_6\text{H}_4)\text{PCo}(\text{Im})_2](\text{BF}_4)$).⁸⁷ Six different R_1 substituents (CN, CF_3 , Cl, H, Me, OMe), four R_2 group (H, Me, Et, Bu) and 28 solvents have been used. The authors have shown the linear relationship

between $\delta^{59}\text{Co}$ value and Hammett σ_p constant. The tendency was observed (i.e. the deshielding of cobalt nucleus with increasing of electronegativity of R_1 substituent) for both imidazole and 1-methylimidazole complexes, in all solvents studied. The influence of R_2 group is also clearly seen. The shielding is increased in the following order $\text{Me} > \text{Et} > \text{Bu}$. The observed changes of ^{59}Co chemical shift of $[\text{TPPCo}(\text{Im})](\text{BF}_4)$ on the addition of free imidazole indicate the high sensitivity of this parameter on the formation of hydrogen bonds by the complex molecule with the other species present in the solution. The line half widths have been measured at various field strengths ($B = 2.114, 5.872 \text{ \& } 9.395 \text{ T}$) to estimate the shielding anisotropy (SA). As the differences observed are small and random in sign, the authors have concluded, that the effects due to SA are below the experimental error limits. The nature of R_1 and R_2 influences chemical shift and linewidth have been discussed. The analysis of the results has shown, that the substituent effects are transmitted to the metal *via* porphyrin π electrons system, not σ ones. The variation of $\Delta v_{1/2}$ has been explained on the basis of the changes of the field gradient, caused by the substituent. The correlation between $\Delta v_{1/2}$ and substituent Hammett constants has been found. These studies have been continued and published in 1989. Eighteen porphyrine- Co^{3+} complexes, containing octaethyl-, *meso*-tetraphenyl-, *meso*-tetrakis(4-pyridyl)-, *meso*-tetramesityl- and *meso*-tetrakis(2,4-dichlorophenyl)porphyrine as a macrocyclic ligand and imidazole, 1-methylimidazole, 1-ethylimidazole, 1-butyylimidazole, phenylimidazole and pyridine as ligands in axial positions have been studied in 28 different solvents. The ^{59}Co NMR chemical shifts and line half widths have been measured. The data reported for the solutions in CH_2Cl_2 are presented in Table 15 (except porphine complex, which has not been measured in this solvent). The authors have discussed the influence of axial ligand character of linewidth, which increases with the increasing of the imidazole N-substituent size. The Kamlet-Taft (KAT) approach has been chosen to analyze the solvent effects. It has been pointed, that chemical shifts of some compounds (e.g. TPPCoMeIm^+ and TPyPCoMeIm^+) measured in different solvents correlate well, while the correlation between the other pairs of complexes (e.g. TPPCoMeIm^+ and OEPCoMeIm^+) has not been observed. The KAT equation have been applied to five complexes (OEPCoIm^+ , OEPCoMeIm^+ , TPPCoIm^+ , TPPCoMeIm^+ and TPyPCoMeIm^+).

Cassidei et al.⁸⁸ have studied some of previously reported compounds by ^{13}C NMR relaxometry. They have cited some ^{59}Co NMR chemical shifts and linewidth and have discussed the reasons for a huge difference in $\Delta v_{1/2}$ values between the compounds with imidazole and pyridine ligands in axial positions. This is assigned to lower effective value of quadruple coupling constant in

imidazole derivatives.

Bang and coworkers continued their studies on cobalt-porphyrin complexes and have published the paper on the effects of *ortho* substituents in phenyl rings of TPP on chemical shifts and linewidths of cobalt complexes.⁸⁹ They have based on the data published previously^{92,95} but also have given the new experimental data, measured for known compounds, but in solvents, which had not been used previously. They have shown the X-ray structures of hindered complexes and have presented the absence of the correlation between NMR parameters of hindered vs. unhindered compounds, measured in wide range of solvents. Again the KAT approach has been used to evaluate the influence of various solvent characters of NMR parameters.

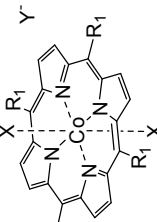
Solid state ⁵⁹Co NMR spectra of some porphyrin complexes have been also recorded and compared with those obtained in solution.⁹⁰ The authors have studied eight compounds, among which six ones have been previously studied by Bang and Hagen groups (TPPCoIm⁺; TPPCoMeIm⁺; OEPCoIm⁺; OEPCoMeIm⁺; T(OMeP)PCoIm⁺; TPPCopy⁺), although the solution spectra have been remeasured (in acetone; referred to 1M K₃[Co(CN)₆] in water; temperature not given). The values obtained stay in agreement with that published previously, within the error of 5-15 ppm (probably due to different measurements temperature and reference concentration). The authors have reported also the results for two new complexes (Table 15). Fast MAS and static measurements have afforded the isotropic and anisotropic chemical shift values and quadrupolar coupling constants. The unexpectedly high shielding anisotropies of Co sites have been found.

Munro et al. have studied the complexes of amines with *meso*-tetraphenyl porphyrinecobalt(III). The structures of compounds studied and NMR data are collected in Table 15. The spectra have been recorded in 1:1 (v/v) mixture of chloroform-*d* and corresponding amine (K₃[Co(CN)₆] in D₂O has been used as reference; the concentration of the reference solution is not given). Among studied amines, two of them form complexes which are silent in NMR experiments, probably due to fast ligand exchange and resulted line broadening. The ⁵⁹Co chemical shifts of studied compounds are strongly temperature-depended. The temperature coefficients are between 2.88 (TPPCoEt₂N/cl) and 3.72 ppm/K (TPPBzN/cl). The broadest signals have been observed for derivative of 2-phenethylamine, while the narrowest one for the diethylamine complex. For complexes with benzylamine, diethyl- and dibutylamine, the splitting of ⁵⁹Co signal, caused by coupling with two ¹⁴N nuclei, has been observed ($^1J_{Co-14N} = 600$ Hz for all compounds). The coupling with nitrogen atoms of porphyrin ring is not observed. In the spectra measured for hindered amine derivatives

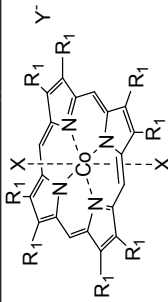
(diethyl- and dibutylamine), the signals assigned to molecules containing one amine and one Cl⁻ ligand in axial positions have been detected (the chemical shift values have not been reported). Moreover, the spectrum of [Co(TPP)(Et₂NH)₂]Cl shows additional set of signals near the major peak. It has been assigned to *S*₄-ruf conformer of this complex (the conformer with non-planar geometry of porphyrin ring). This signal is about 20-30 ppm upfield shifted vs. the signal of planar isomer. The authors have interpreted the shielding according to Ramsey's theory and have found the linear correlation between chemical shifts and DFT calculated 3*d* orbital's radius expectation values $\langle r^{-3} \rangle_{3d}$. The linewidths have been correlated with squares of DFT calculated electronic field gradients, q_{val}^2 . The authors have measured also the chemical shifts of model compound, [Co(TPP)Cl].

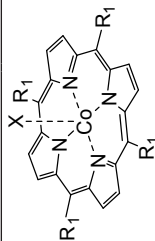
The short review of application on NMR method (including ⁵⁹Co NMR) has been published by Sanders et al.⁶⁷

Table 15. ^{59}Co NMR data of cobalt(III) porphyrin complexes

Complex	Structure	$\delta^{59}\text{Co}$; $\Delta\nu_{1/2}$	Conditions	Standard	Ref.
TPPCoIm/pc		$8\ 300$; 500	MeOH; 297 K	$\text{K}_3[\text{Co}(\text{CN})_6]/\text{D}_2\text{O}$; $0.1\ \text{M}$	86
TPPCoMeIm/pc		$8\ 355$; 860	MeOH; 297 K	$\text{K}_3[\text{Co}(\text{CN})_6]/\text{D}_2\text{O}$; $0.1\ \text{M}$	86
TPPCoIm/bp		$8\ 302$; 700	MeOH; 297 K	$\text{K}_3[\text{Co}(\text{CN})_6]/\text{D}_2\text{O}$; $0.1\ \text{M}$	86
TPPCoMeIm/bp		$8\ 354$; $1\ 000$	MeOH; 297 K	$\text{K}_3[\text{Co}(\text{CN})_6]/\text{D}_2\text{O}$; $0.1\ \text{M}$	86
TPPCoIm/bf		$8\ 300$; 430	MeOH; 297 K	$\text{K}_3[\text{Co}(\text{CN})_6]/\text{D}_2\text{O}$; $0.1\ \text{M}$	86
TPPCoMeIm/bf		$8\ 355$; 920	MeOH; 297 K	$\text{K}_3[\text{Co}(\text{CN})_6]/\text{D}_2\text{O}$; $0.1\ \text{M}$	86
TPPCoIm/bf		$8\ 302$; 474	MeOH; 297.7 K	$\text{K}_3[\text{Co}(\text{CN})_6]/\text{D}_2\text{O}$; $0.1\ \text{M}$	87
T(MeOP)PCoIm/bf		$8\ 316$; 770	MeOH; 297.7 K	$\text{K}_3[\text{Co}(\text{CN})_6]/\text{D}_2\text{O}$; $0.1\ \text{M}$	87
T(MeOP)PCoMeIm/bf		$8\ 415$; $1\ 050$	acetone	$\text{K}_3[\text{Co}(\text{CN})_6]/\text{H}_2\text{O}$; $1\ \text{M}$	90
T(MeP)PCoIm/bf		$8\ 310$; 474	MeOH; 297.7 K	$\text{K}_3[\text{Co}(\text{CN})_6]/\text{D}_2\text{O}$; $0.1\ \text{M}$	87
T(CFP)PCoIm/bf		$8\ 302$; 300	MeOH; 297.7 K	$\text{K}_3[\text{Co}(\text{CN})_6]/\text{D}_2\text{O}$; $0.1\ \text{M}$	87
T(CIP)PCoIm/bf		$8\ 297$; 491	MeOH; 297.7 K	$\text{K}_3[\text{Co}(\text{CN})_6]/\text{D}_2\text{O}$; $0.1\ \text{M}$	87
T(CNP)PCoIm/bf		$8\ 283$; 257	MeOH; 297.7 K	$\text{K}_3[\text{Co}(\text{CN})_6]/\text{D}_2\text{O}$; $0.1\ \text{M}$	87
TPPCoIm/bf		$8\ 390$; $1\ 000$	CH_2Cl_2 ; 298.5 K	$\text{K}_3[\text{Co}(\text{CN})_6]/\text{D}_2\text{O}$; $0.1\ \text{M}$	87
TPPCoIm/bf		$8\ 389$; 946	CH_2Cl_2 ; 298 K	$\text{K}_3[\text{Co}(\text{CN})_6]/\text{D}_2\text{O}$; $0.1\ \text{M}$	91
TPPCoMeIm/bf		$8\ 446$; $1\ 000$	CH_2Cl_2 ; 296.3 K	$\text{K}_3[\text{Co}(\text{CN})_6]/\text{D}_2\text{O}$; $0.1\ \text{M}$	87
TPPCoMeIm/bf		$8\ 450$; 947	CH_2Cl_2 ; 297 K	$\text{K}_3[\text{Co}(\text{CN})_6]/\text{D}_2\text{O}$; $0.1\ \text{M}$	91

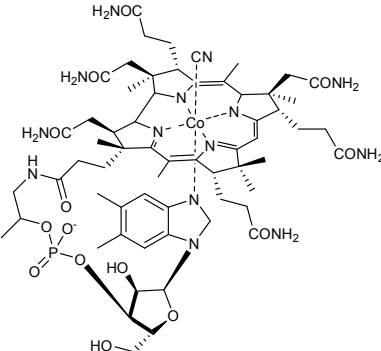
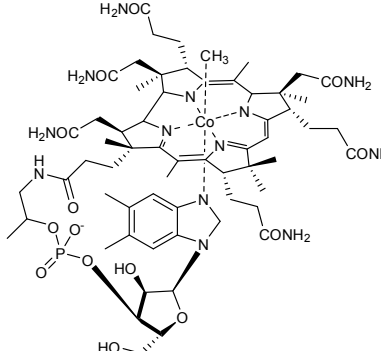
TPPCoEtIm/bf	R ₁ = Ph; Y = BF ₄ ⁻ ; X = 1-ethylimidazole	8 364; 1 060	CH ₂ Cl ₂ ; 297.5 K	K ₃ [Co(CN) ₆]/D ₂ O; 0.1 M	87
TPPCoEtIm/bf	R ₁ = Ph; Y = BF ₄ ⁻ ; X = 1-ethylimidazole	8 364; 1 055	CH ₂ Cl ₂ ; 297 K	K ₃ [Co(CN) ₆]/D ₂ O; 0.1 M	91
TPPCoBuIm/bf	R ₁ = Ph; Y = BF ₄ ⁻ ; X = 1-butylimidazole	8 322; 840	CH ₂ Cl ₂ ; 300.3 K	K ₃ [Co(CN) ₆]/D ₂ O; 0.1 M	87
TPPCoBuIm/bf	R ₁ = Ph; Y = BF ₄ ⁻ ; X = 1-butylimidazole	8 321; 850	CH ₂ Cl ₂ ; 300 K	K ₃ [Co(CN) ₆]/D ₂ O; 0.1 M	91
TPPCoPhIm/bf	R ₁ = Ph; Y = BF ₄ ⁻ ; X = 1-phenylimidazole	8 425; 2 414	CH ₂ Cl ₂ ; 298 K	K ₃ [Co(CN) ₆]/D ₂ O; 0.1 M	91
TPPCopy/pc	R ₁ = Ph; Y = ClO ₄ ⁻ ; X = pyridine	8 097; 16 433; 16	CH ₂ Cl ₂ ; 298 K	K ₃ [Co(CN) ₆]/D ₂ O; 0.1 M	91
TPPCoiqi/bf	R ₁ = Ph; Y = BF ₄ ⁻ ; X = isoquinoline	8 143; 16 600	acetone	K ₃ [Co(CN) ₆]/H ₂ O; 1 M	90
PPyPCoMeIm/bf	R ₁ = 4-Py; Y = BF ₄ ⁻ ; X = 1-methylimidazole	8 420; 400	CH ₂ Cl ₂ ; 297 K	K ₃ [Co(CN) ₆]/D ₂ O; 0.1 M	91
T(Cl2P)PCoIm/bf	R ₁ = 2,4-Cl ₂ C ₆ H ₃ ; Y = BF ₄ ⁻ ; X = imidazole	8 091; 520	CH ₂ Cl ₂ ; 298 K	K ₃ [Co(CN) ₆]/D ₂ O; 0.1 M	91
T(Cl2P)PCoMeIm/bf	R ₁ = 2,4-Cl ₂ C ₆ H ₃ ; Y = BF ₄ ⁻ ; X = 1-methylimidazole	8 190; 454	CH ₂ Cl ₂ ; 297 K	K ₃ [Co(CN) ₆]/D ₂ O; 0.1 M	91
TMPCoIm/bf	R ₁ = 2,4,6-Me ₃ C ₆ H ₂ ; Y = BF ₄ ⁻ ; X = imidazole	8 012; 3 400	CH ₂ Cl ₂ ; 299 K	K ₃ [Co(CN) ₆]/D ₂ O; 0.1 M	91
TMPCoMeIm/bf	R ₁ = 2,4,6-Me ₃ C ₆ H ₂ ; Y = BF ₄ ⁻ ; X = 1-methylimidazole	8 066; 3 300	CH ₂ Cl ₂ ; 299 K	K ₃ [Co(CN) ₆]/D ₂ O; 0.1 M	91
PCoIm/bf	R ₁ = H; Y = BF ₄ ⁻ ; X = imidazole	8 733; 266	acetone; 302 K	K ₃ [Co(CN) ₆]/D ₂ O; 0.1 M	91
TPPCoBzN/cl	R ₁ = Ph; Y = Cl ⁻ ; X = PhCH ₂ NH ₂	8 222; 640	CDCl ₃ /ligand X; 297 K	K ₃ [Co(CN) ₆]/D ₂ O	97
TPPCoBuN/cl	R ₁ = Ph; Y = Cl ⁻ ; X = BuNH ₂	8 386; 270	CDCl ₃ /ligand X; 297 K	K ₃ [Co(CN) ₆]/D ₂ O	92
TPPCoPhEtN/cl	R ₁ = Ph; Y = Cl ⁻ ; X = PhCH ₂ CH ₂ NH ₂	8 460; 4 300	CDCl ₃ /ligand X; 297 K	K ₃ [Co(CN) ₆]/D ₂ O	92
TPPCoEt ₂ N/cl	R ₁ = Ph; Y = Cl ⁻ ; X = Et ₂ NH	8 675; 560	CDCl ₃ /ligand X; 290.5 K	K ₃ [Co(CN) ₆]/D ₂ O	92
TPPCoBu ₂ N/cl	R ₁ = Ph; Y = Cl ⁻ ; X = Bu ₂ NH	8 661; 2 400	CDCl ₃ /ligand X; 297 K	K ₃ [Co(CN) ₆]/D ₂ O	92

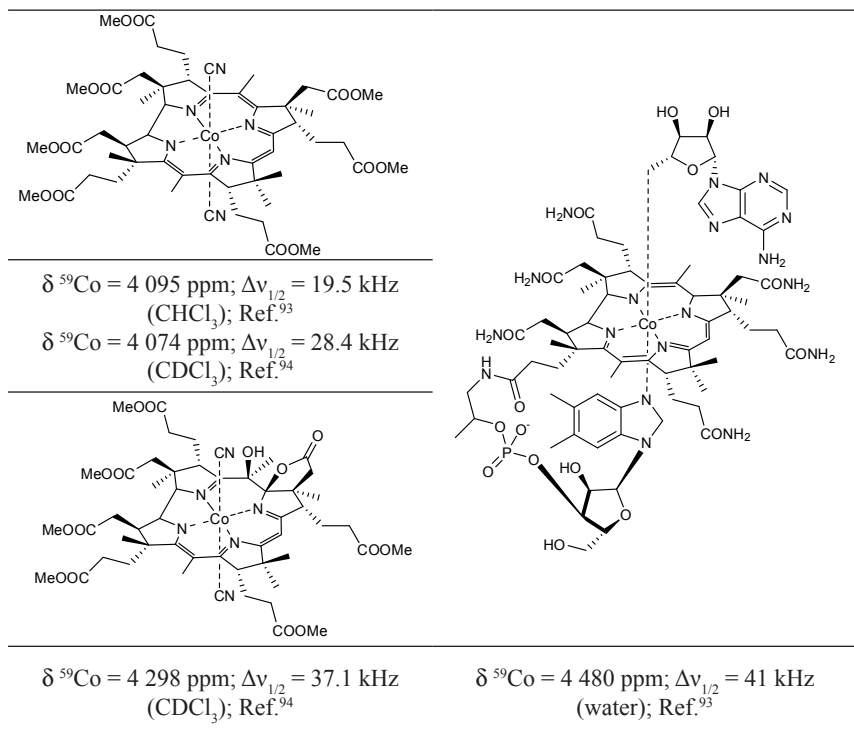
							
OEPCoIm/bf	R ₁ = Et; Y = BF ₄ ⁻ ; X = imidazole	8 753; 130	MeOH; 297 K	K ₃ [Co(CN) ₆]/D ₂ O; 0.1 M	86		
OEPCoIm/bf	R ₁ = Et; Y = BF ₄ ⁻ ; X = imidazole	8 813; 309	CH ₂ Cl ₂ ; 298 K	K ₃ [Co(CN) ₆]/D ₂ O; 0.1 M	91		
OEPCoMeIm/bf	R ₁ = Et; Y = BF ₄ ⁻ ; X = 1-methylimidazole	8 810; 230	MeOH; 297 K	K ₃ [Co(CN) ₆]/D ₂ O; 0.1 M	86		
OEPCoMeIm/bf	R ₁ = Et; Y = BF ₄ ⁻ ; X = 1-methylimidazole	8 871; 320	CH ₂ Cl ₂ ; 297 K	K ₃ [Co(CN) ₆]/D ₂ O; 0.1 M	91		
OEPCoEtIm/bf	R ₁ = Et; Y = BF ₄ ⁻ ; X = 1-ethylimidazole	8 842; 280	CH ₂ Cl ₂ ; 298 K	K ₃ [Co(CN) ₆]/D ₂ O; 0.1 M	91		
OEPCoBuIm/bf	R ₁ = Et; Y = BF ₄ ⁻ ; X = 1-butylimidazole	8 787; 235	CH ₂ Cl ₂ ; 299 K	K ₃ [Co(CN) ₆]/D ₂ O; 0.1 M	91		
OEPCoPhIm/bf	R ₁ = Et; Y = BF ₄ ⁻ ; X = 1-phenylimidazole	8 831; 1 015	CH ₂ Cl ₂ ; 299 K	K ₃ [Co(CN) ₆]/D ₂ O; 0.1 M	91		
OEPCoPy/bf	R ₁ = Et; Y = BF ₄ ⁻ ; X = pyridine	8 557; 1 2950	CH ₂ Cl ₂ ; 297 K	K ₃ [Co(CN) ₆]/D ₂ O; 0.1 M	91		
TPPCoCl	R ₁ = Ph; X = Cl	8 247; 410	CDCl ₃ ; 297 K	K ₃ [Co(CN) ₆]/D ₂ O	92		



The NMR studies of natural corrinoids have been presented by Medek et al.⁹³ The authors have applied both solution and solid-state ^{59}Co NMR spectroscopy to investigate the structures of vitamin B₁₂ derivatives. The studied compounds and chemical shifts are presented on Table 16. The spectra have been recorded in water and chloroform at room temperature, and have been referred to 1 M solution of $\text{K}_3[\text{Co}(\text{CN})_6]$ in water. The further studies of the Co^{III} ion in corrins have been made by Chemaly et al.⁹⁴ They have studied six model compounds, three derivatives of cobyrinic acid heptamethyl ester (CbsMe₇) and three of 5,6-dihydro-5-hydroxy-hexamethylcob(III)yrinate-*c*,6-lactone (CSYCbsMe₆). Two complexes, dicyano- CbsMe₇ and dicyano- CSYCbsMe₆ have been studied by ^{59}Co NMR spectroscopy. The authors have noted a significant difference in chemical shifts (4074 vs. 4298 ppm, respectively). As this effect could not be caused by differences in Co-C bond length and geometry, which are the same for both compounds (as comes from X-ray crystallography and DFT calculations), the authors have explained it by the interaction of Co^{III} ion with the corrine macrocycle. The more delocalized π -electron system of CbsMe₇ favors the formation of more covalent bond between the Co center and macrocyclic ligand, causing a stronger shielding. The spectra have been recorded at 300 K and referred to external saturated solution of $\text{K}_3[\text{Co}(\text{CN})_6]$ in D₂O.

Table 16. ^{59}Co NMR data for vitamin B₁₂ and their derivatives

	
$\delta^{59}\text{Co} = 4\ 650\ \text{ppm}; \Delta\nu_{1/2} = 28\ \text{kHz}$ (water); Ref. ⁹³	$\delta^{59}\text{Co} = 4\ 215\ \text{ppm}; \Delta\nu_{1/2} = 14.5\ \text{kHz}$ (water); Ref. ⁹³



2.6.2 Rhodium

Despite the only natural rhodium isotope, ^{103}Rh , is NMR active and does not have a quadrupolar moment ($I = 1/2$), it is one of the most difficult to observe nucleus. Its low γ coefficient causes its low resonance frequencies ($\mathcal{E} = 3.172$ MHz). In consequence, its receptivity is low (3.12×10^{-5} that of ^1H). The large chemical shifts range (over 10 000 ppm) results in such experimental problems as signals folding or necessity of the recording of many spectra to cover all range of the $\delta^{103}\text{Rh}$ values. Moreover, the low resonance frequencies cause such problems as acoustic ringing provoked baseline distortions. The ^{103}Rh nucleus has long relaxation times (in a range of minutes), which increases the time needed to spectrum acquisition. If it is possible, the indirect detection experiments are always recommended. IUPAC does not indicate the reference, most often the $\text{Rh}(\text{acac})_3$ or spectral reference is used.

The only two examples of supramolecular complex of Rh, studied by ^{103}Rh NMR are presented in literature. One is a cycloheptatriene grafted tripodand,

obtained by Herberhold et al. It forms a 1:1 complex with RhCl (Fig. 31). The rhodium signal has been detected by indirect $^{31}\text{P}\{^{103}\text{Rh}, ^1\text{H}\}$ experiment, performed for CDCl_3 solution at 298 K, and referred to spectral reference ($\Xi(^{103}\text{Rh}) = 3.16$ MHz). The chemical shift of this complex is -355 ppm ($^1J_{\text{RhP}} = 189.5$ Hz).

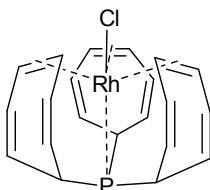


Fig. 31. Structure of cycloheptatriene ligand Rh complex

The second supramolecular complex of Rh, studied by ^{103}Rh NMR is a bis(ethyldiphenylphosphine) adduct with *meso*-tetramethylporphyrin Rh-derivative (Fig. 32).⁹⁵ The ^{103}Rh NMR spectra have been recorded by 2D $^{31}\text{P}, ^{103}\text{Rh}\{^1\text{H}\}$ inverse method. Two compounds have been detected, the major product, containing two ethyldiphenylphosphine ligands and a minor one, with one ethyldiphenylphosphine and one ethylphenylphosphine addends. This two compounds give separated ^{103}Rh signals, first at 2 558, second at 2 711 ppm (300K, in chloroform-*d*; referred to spectral reference, $\Xi(^{103}\text{Rh}) = 3.16$ MHz). The $^1J_{\text{RhP}}$ coupling constants are 82.1 and 82.4 Hz for major and minor components, respectively. The authors have shown the linear temperature dependences of both rhodium and phosphorus chemical shifts (which are *ca.* 0.91 and 0.0013 ppm/K, respectively) and explained them on the basis of Ramsey's nuclear shielding theory as well as Jameson model, based on the changes of M-L bond length changes.

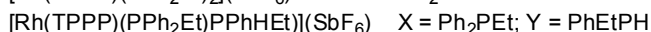
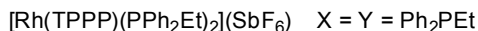
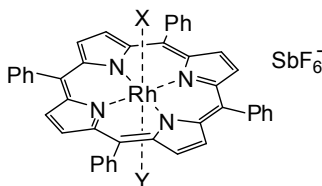


Fig. 32. Structure of rhodium-porphyrin complexes

2.7 Group 10

2.7.1 Platinum

The ^{195}Pt isotope of natural abundance 33.8% is widely studied by NMR technique, because of its excellent NMR properties: $\frac{1}{2}$ nuclear spin (no quadrupolar moment), high receptivity (3.36×10^{-3} that of ^1H) and high magnetogiric ratio ($\mathcal{E} = 21.499$ MHz). Other natural platinum isotopes are not active in NMR technique. Platinum has a huge chemical shift range (over 15 000 ppm) so if the recording of the spectrum in whole range is needed, it must be measured in several parts, covering narrower chemical shifts domains. The special caution must be paid to avoid peak folding. IUPAC recommends $\text{K}_2[\text{PtCl}_6]$ as a reference sample although many other compounds are used. As a platinum chemical shift is strongly temperature, concentration and solvent depended, the special care must be taken to obtain a valuable and reliably data.

The first example of supramolecular Pt complex studies by ^{195}Pt NMR has been published by Balch et al.⁹⁶ They have prepared a lariat crown ether, containing PPh_2 groups in side arms (Fig. 33A). This has been converted into 1:1 complex with $\text{Pt}(\text{CN})_2$, but the authors have not presented the ^{195}Pt data. The second complex synthesized is a derivative containing Tl^+ ion inside the crown ring and a $\text{Pt}(\text{CN})_2$ unit, complexed *via* phosphine moieties (Fig. 33B). The small Pt-Tl distance (2.911 and 2.958 Å for two independent species in the asymmetric unit) causes the ^{195}Pt - $^{203/205}\text{Tl}$ coupling. The ^{195}Pt signal occurs at -4 684 ppm as a doublet of triplets ($^1J_{\text{Pt-Pt}} = 2\,293$ Hz; $^1J_{\text{Pt-}^{203}\text{Tl}} = ^1J_{\text{Pt-}^{205}\text{Tl}} = 3\,825$ Hz). The authors have not given the solvent used for spectra recording, measurements temperature and reference.

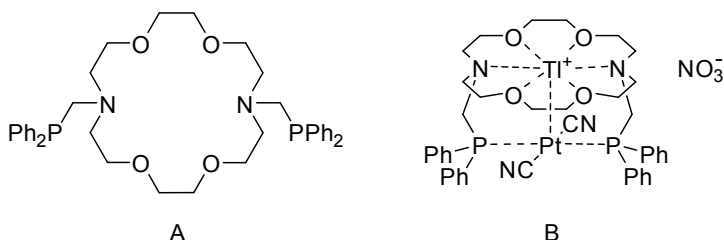


Fig. 33. Structure of lariat crown ether (A) and its complex with Tl^+ and $\text{Pt}(\text{CN})_2$

The further studies of supramolecular platinum complexes are concerned on the application of polythioether (or mixed S,O ethers) macrocycles as ligands. Grant et al.⁹⁷ have obtained two mixed oxa-/thia- macrocycles (Fig. 34) and their complexes with $\text{Pt}(\text{II})$ (as PF_6^- salts). Both compounds have been characterized

by ^{195}Pt NMR spectroscopy and X-ray crystallography. The [9]-aneS₂O ligands form 2:1 complex $[\text{Pt}([\text{9}]\text{-aneS}_2\text{O})_2](\text{PF}_6)_2$. The ligand molecules coordinate to Pt centre only *via* sulphur atoms. In NMR spectrum one signal at -4 739 ppm ($\Delta\nu_{1/2} = 557$ Hz) occurs. The second macrocycle complexes Pt ion in 1:1 mode: $[\text{Pt}([\text{18}]\text{-aneS}_4\text{O}_2)](\text{PF}_6)_2$, but also only S atoms participate in coordination. The signal in ^{195}Pt spectrum occurs at -4 571 ppm and is distinctly narrower (only 84 Hz) than that of the first complex. The authors have not discussed this difference. The spectra have been recorded in nitromethane-*d*₃ vs. $[\text{PtCl}_6]^{2-}$ in water (no temperature and reference concentration given).

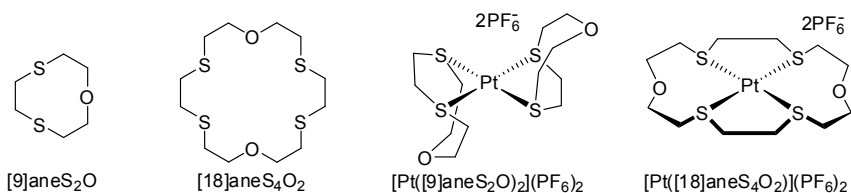


Fig. 34. Structures of mixed S/O cyclic ligands and their complexes with Pt^{II}

Maleonitrile-dithiacrown complexes of Pt(II) have been also obtained. This ligand molecules have limited conformational flexibility, due to a presence of double C=C bond. Crowns with various number of oxygen atoms have been synthesized (from S₂O₂ to S₂O₃). The complex of the first ligand from this series (*mn*-12S₂O₂) with Pt(II) has been characterized by ^{195}Pt NMR spectra. The single signal at -3779 ppm has been observed (vs. 0.1 M Na₂[PtCl₆] in D₂O).

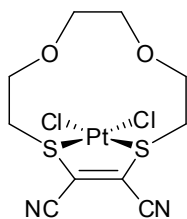


Fig. 35. Structure of maleonitrile-derived thiacycrown complex with Pt^{II}

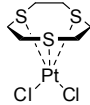
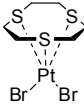
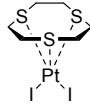
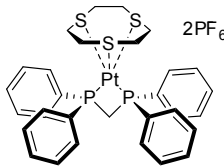
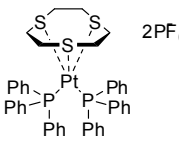
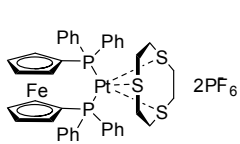
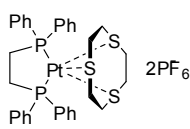
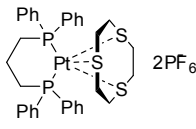
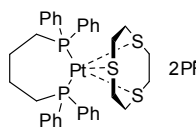
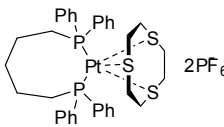
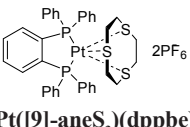
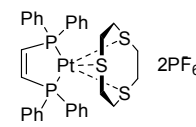
The series of heteroleptic Pt complexes with [9]-aneS₃ ligand (see Fig. 26) have been studied by several authors. The chemical shifts are presented in Table 17. In all studied cases the [9]-aneS₃ ligand molecule is coordinated asymmetrically. Two sulphur atoms are in equatorial positions (Pt-S distance

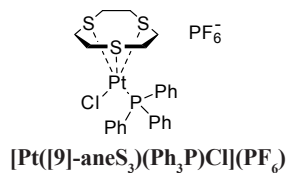
2.20-2.50 Å), *trans* to phosphor or halide ligands while the third one coordinates at axial position (Pt-S distance 2.65-3.00 Å). The Grant et al.⁹⁸ studies on halogen complexes of ([9]-aneS₃)Pt core show the significant influence of halide anion of ¹⁹⁵Pt chemical shifts. The chemical shift correlates with Pt-S_{axial} distance (deshielding occurs upon elongation of Pt-S bond). The further studies on phosphine complexes do not include any extended discussion of structure-NMR parameters relationships.¹⁰⁴⁻¹⁰⁸ For the mixed complex [Pt([9]-aneS₃)(Ph₃P)Cl](PF₆) the authors state that the value “lies intermediate between the ones reported for [Pt([9]-aneS₃)(Ph₃P)Cl₂] (...) and for [Pt([9]-aneS₃)(Ph₃P)₂](PF₆)₂”.⁹⁹ The same authors have published the papers on the complexes on ([9]-aneS₃)Pt unit with heterocyclic diimine ligands but have not discussed the ¹⁹⁵Pt NMR results.^{109,110} The complexes of [Pt([9]aneS₃)]²⁺ with arsines and stibines have been also prepared.¹⁰⁰ The ¹⁹⁵Pt NMR spectra of the systems of S₃X₂ (where X = As or Sb) coordination sphere have been recorded. The signals are quite narrow and easy to detect. The molecules containing only one As(Sb) ligand and halide anion, bonded to Pt center are NMR silent. The reasons of the absence of the signal are not clear.

The formation of stable complexes between *N*-heterocyclic ligands and [Pt([9]aneS₃)]²⁺ core has been utilized for a synthesis of molecular squares.¹⁰¹ The reaction of [Pt([9]aneS₃)](OTf)₂ with 4,4'-bipyridine leads to the formation of 4+4 complex, [Pt₄([9]aneS₃)₄(4bpy)₄](OTf)₈. This has been characterized by X-ray method and NMR spectroscopy. The ¹⁹⁵Pt NMR spectrum shows only one signal, at -3134 ppm, indicating on the S₂N₂+S coordination mode (Fig. 36). The spectrum has been recorded from solution in CD₃NO₂ at 298 K; water solution of [PtCl₆]²⁻ has been used as reference. The by-product, [(Pt([9]aneS₃)Cl)₂(4bpy)](PF₆)₂ has been also isolated.¹⁰² In the same paper diaqua complex, [Pt([9]aneS₃)(H₂O)₂](TfO)₂ has been characterized, however the authors have given a wrong formula for this compound and wrong theoretical elemental analysis data, consistent with experimental ones (sic!) (see Table 17 for structures).

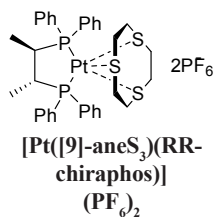
The excellent review on the synthesis, structure and spectral properties of thiacycrown complexes of platinum has been published by Grant.¹⁰³

Table 17. Structures and ^{195}Pt NMR data of [9]aneS₃ ligand with platinum species

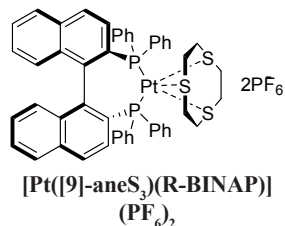
 <p>[Pt([9]-aneS₃)Cl₂]</p>	 <p>[Pt([9]-aneS₃)Br₂]</p>	 <p>[Pt([9]-aneS₃)I₂]</p>
<p>-3605 ppm; $\Delta\nu = 130$ Hz (CD₃)₂SO; vs. [PtCl₆]²⁻ aq; Ref. ⁹⁸</p>	<p>-3779 ppm; $\Delta\nu = 132$ Hz (CD₃)₂SO; vs. [PtCl₆]²⁻ aq; Ref. ⁹⁸</p>	<p>-4147 ppm; $\Delta\nu = 135$ Hz (CD₃)₂SO; vs. [PtCl₆]²⁻ aq; Ref. ⁹⁸</p>
 <p>[Pt([9]-aneS₃)(dppm)](PF₆)₂</p>	 <p>[Pt([9]-aneS₃)(Ph₃P)₂] (PF₆)₂</p>	 <p>[Pt([9]-aneS₃)(dppf)](PF₆)₂</p>
<p>-4601 ppm; $^1J_{PPt} = 3188$ Hz CD₃NO₂; vs. [PtCl₆]²⁻ aq; Ref. ¹⁰⁴</p>	<p>-4399 ppm; $^1J_{PPt} = 3365$ Hz CD₃NO₂; vs. [PtCl₆]²⁻ aq; Ref. ¹⁰⁴</p>	<p>-4353 ppm; $^1J_{PPt} = 3511$ Hz CD₃NO₂; vs. [PtCl₆]²⁻ aq; Ref. ¹⁰⁵</p>
 <p>[Pt([9]-aneS₃)(dppe)](PF₆)₂</p>	 <p>[Pt([9]-aneS₃)(dppp)] (PF₆)₂</p>	 <p>[Pt([9]-aneS₃)(dppb)](PF₆)₂</p>
<p>-4069 ppm; $^1J_{PPt} = 2740$ Hz CD₃NO₂; vs. [PtCl₆]²⁻ aq; Ref. ¹⁰⁶</p>	<p>-4478 ppm; $^1J_{PPt} = 3069$ Hz CD₃NO₂; vs. [PtCl₆]²⁻ aq; Ref. ¹⁰⁶</p>	<p>-4497 ppm; $^1J_{PPt} = 3211$ Hz CD₃NO₂; vs. [PtCl₆]²⁻ aq; Ref. ¹⁰⁶</p>
 <p>[Pt([9]-aneS₃)(dpppe)](PF₆)₂</p>	 <p>[Pt([9]-aneS₃)(dppbe)] (PF₆)₂</p>	 <p>[Pt([9]-aneS₃)(dppv)](PF₆)₂</p>
<p>-4426 ppm; $^1J_{PPt} = 3239$ Hz CD₃NO₂; vs. [PtCl₆]²⁻ aq; Ref. ¹⁰⁶</p>	<p>-4568 ppm; $^1J_{PPt} = 3202$ Hz CD₃NO₂; vs. [PtCl₆]²⁻ aq; Ref. ¹⁰⁶</p>	<p>-4681 ppm; $^1J_{PPt} = 3219$ Hz CD₃NO₂; vs. [PtCl₆]²⁻ aq; Ref. ¹⁰⁶</p>



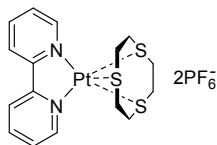
-4080 ppm; $^1J_{Pt} = 3399$ Hz
 CD₃NO₂; vs. [PtCl₆]²⁻ aq;
 Ref. ⁹⁹



-4452 ppm; $^1J_{Pt} = 3144$ Hz
 CD₃NO₂; vs. [PtCl₆]²⁻ aq;
 Ref. ¹⁰⁷

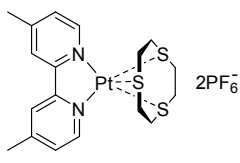


-4167 ppm; $^1J_{Pt} = 3296$ Hz
 CD₃NO₂; vs. [PtCl₆]²⁻ aq;
 Ref. ¹⁰⁷



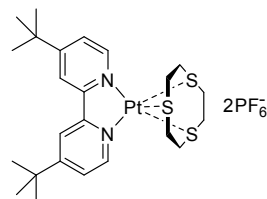
[Pt([9]-aneS₃)(bpy)](PF₆)₂

-3261 ppm; $\Delta\nu = 726$ Hz
 CD₃NO₂; vs. [PtCl₆]²⁻ aq;
 Ref. ¹⁰⁸



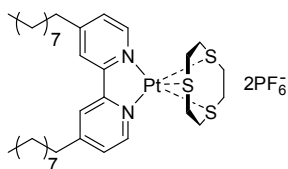
**[Pt([9]-aneS₃)(Me₂bpy)]
(PF₆)₂**

-3279 ppm; $\Delta\nu = 678$ Hz
 CD₃NO₂; vs. [PtCl₆]²⁻ aq;
 Ref. ¹⁰⁸



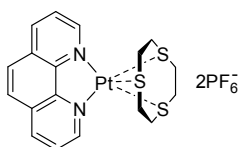
**[Pt([9]-aneS₃)(Bu₂bpy)]
(PF₆)₂**

-3289 ppm; $\Delta\nu = 539$ Hz
 CD₃NO₂; vs. [PtCl₆]²⁻ aq;
 Ref. ¹⁰⁸



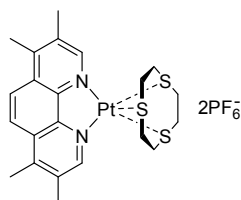
**[Pt([9]-aneS₃)(non₂bpy)]
(PF₆)₂**

-3284 ppm; $\Delta\nu = 353$ Hz
 CD₃NO₂; vs. [PtCl₆]²⁻ aq;
 Ref. ¹⁰⁸



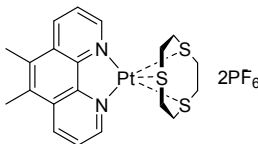
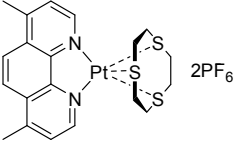
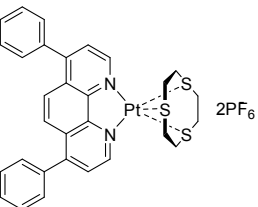
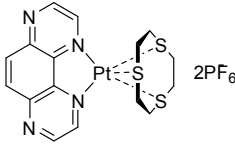
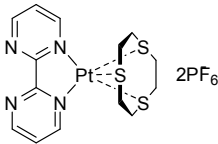
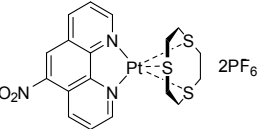
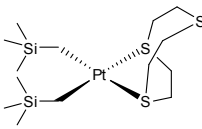
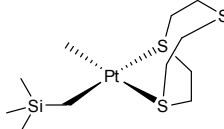
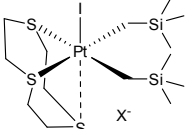
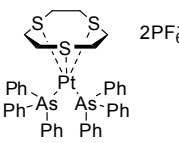
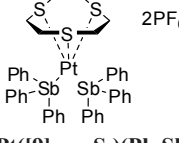
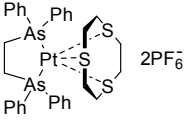
**[Pt([9]-aneS₃)(phen)]
(PF₆)₂**

-3292 ppm; $\Delta\nu = 754$ Hz
 CD₃NO₂; vs. [PtCl₆]²⁻ aq;
 Ref. ¹⁰⁸



**[Pt([9]-aneS₃)(Me₄phen)]
(PF₆)₂**

-3312 ppm; $\Delta\nu = 822$ Hz
 CD₃NO₂; vs. [PtCl₆]²⁻ aq;
 Ref. ¹⁰⁸

 <p>[Pt([9]-aneS₃)(5,6-Me₂phen)] (PF₆)₂</p>	 <p>[Pt([9]-aneS₃)(4,7-Me₂phen)] (PF₆)₂</p>	 <p>[Pt([9]-aneS₃)(Ph₂phen)] (PF₆)₂</p>
<p>-3286 ppm; $\Delta\nu = 641$ Hz CD₃NO₂; vs. [PtCl₆]²⁻ aq; Ref. ¹⁰⁹</p>	<p>-3298 ppm; $\Delta\nu = 657$ Hz CD₃NO₂; vs. [PtCl₆]²⁻ aq; Ref. ¹⁰⁹</p>	<p>-3288 ppm; $\Delta\nu = 501$ Hz CD₃NO₂; vs. [PtCl₆]²⁻ aq; Ref. ¹⁰⁹</p>
 <p>[Pt([9]-aneS₃)(tap)](PF₆)₂</p>	 <p>[Pt([9]-aneS₃)(bpm)] (PF₆)₂</p>	 <p>[Pt([9]-aneS₃)(NO₂phen)] (PF₆)₂</p>
<p>-3198 ppm; $\Delta\nu_{1/2} = 446$ Hz CD₃NO₂; vs. [PtCl₆]²⁻ aq; Ref. ¹⁰⁹</p>	<p>-3277 ppm; $\Delta\nu = 567$ Hz CD₃NO₂; vs. [PtCl₆]²⁻ aq; Ref. ¹⁰⁹</p>	<p>-3255 ppm; $\Delta\nu = 552$ Hz CD₃NO₂; vs. [PtCl₆]²⁻ aq; Ref. ¹⁰⁹</p>
 <p>-4246 ppm C₆D₆; vs. Na₂[PtCl₆] aq. Ref. ¹¹⁰</p>	 <p>-4249 ppm CDCl₃; vs. Na₂[PtCl₆] aq. Ref. ¹¹⁰</p>	 <p>X = I, TfO⁻; -3976 ppm CD₂Cl₂; vs. Na₂[PtCl₆] aq. Ref. ¹¹⁰</p>
 <p>[Pt([9]-aneS₃)(Ph₃As)](PF₆)₂</p>	 <p>[Pt([9]-aneS₃)(Ph₃Sb)] (PF₆)₂</p>	 <p>[Pt([9]-aneS₃)(dpae)](PF₆)₂</p>
<p>-4489 ppm; $\Delta\nu_{1/2} = 120$ Hz CD₃NO₂; vs. [PtCl₆]²⁻ aq. Ref. ¹⁰⁰</p>	<p>-4822 ppm; $\Delta\nu_{1/2} = 640$ Hz CD₃NO₂; vs. [PtCl₆]²⁻ aq. Ref. ¹⁰⁰</p>	<p>-4772 ppm; $\Delta\nu_{1/2} = 140$ Hz CD₃NO₂; vs. [PtCl₆]²⁻ aq. Ref. ¹⁰⁰</p>

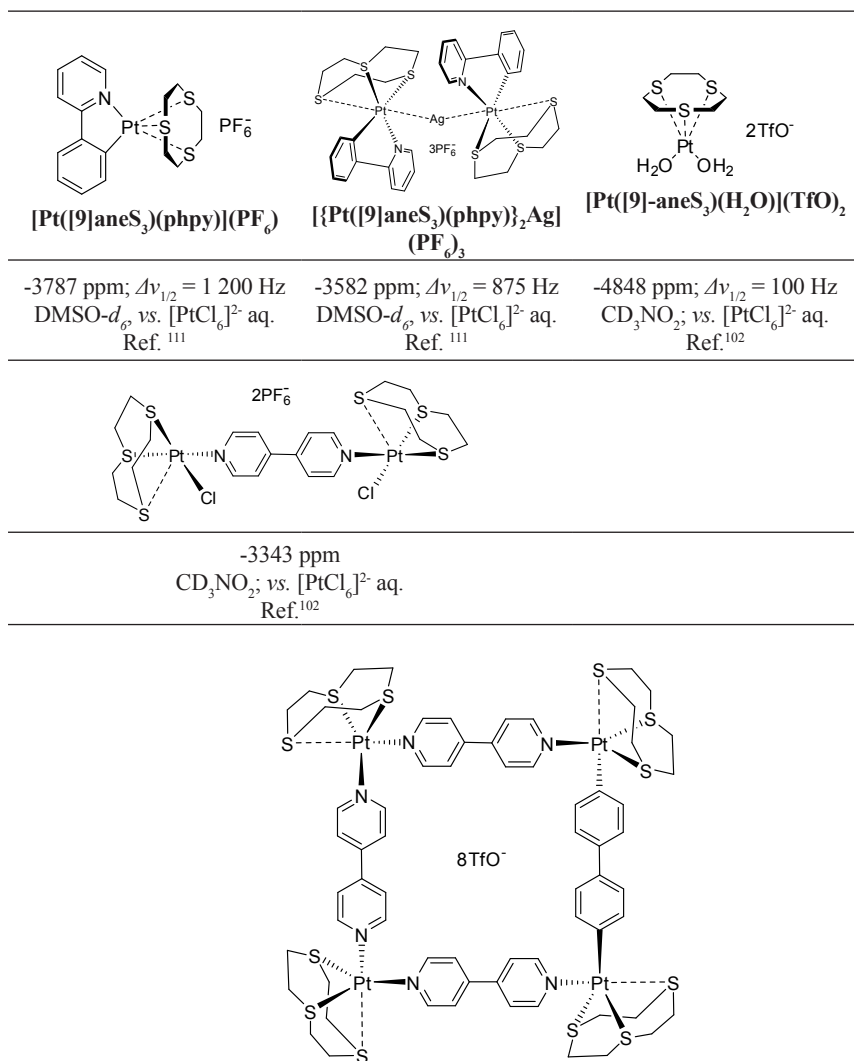


Fig. 36. The 4+4 platinum-containing square, $[\text{Pt}_2([9]\text{aneS}_3)_2(4\text{bpy})](\text{OTf})_8$

Homo- and heteroleptic derivatives of larger thia-crowns have been also studied. Grant et al. have obtained a series of $\text{L}_2\text{Pt}(\text{PF}_6)_2$ and $\text{LPt}(\text{PF}_6)_2$ complexes and have measured the ^{195}Pt spectra.^{103,117} The structures and NMR data are

collected in Table 18. The authors have shown, that the platinum signal undergoes shielding with an increasing of the number of sulphur donor ligands. Moreover, within the set of the complexes of the same number of coordinated S atoms, the chemical shifts depend on the orientation of lone pairs of sulphur atom. Also scattered data for heteroleptic complexes containing larger sulphur macrocycles (Table 18) have been published. Blake et al.¹¹² have reported the ^{195}Pt NMR data of above mentioned compounds. The chemical shifts are slightly different from that reported by Grant and co-workers. It is probably the effect of other solvent used for measurements. They also obtained the platinum NMR spectra of PtX_2^{2+} complexes with selected macrocyclic thiaethers. The authors have discussed the influence of ring diameter and flexibility and platinum oxidation state on chemical shift. They have compared the experimental results with those published for bidentate thiaethers and cyclic selenoethers.

Champness et al. have described the formation of Pt(II) complex with macrocyclic mixed phosphatid ligand, $[\text{Pt}(\text{Ph}_2[14]\text{aneS}_2\text{P}_2)](\text{PF}_6)$. The ^{195}Pt NMR spectrum of this molecule has been recorded.¹¹³

Bennett et al. have reported the ^{195}Pt chemical shifts of some Pt(II) and Pt(IV) organoplatinum derivatives, bonded to [9]aneS₃ ligand but have not discussed these results (Table 17).¹¹⁰ The interesting example of cyclometalated Pt supramolecular complex interactions with Ag^+ ions has been studied by Janzen et al.¹¹¹ with application of ^{195}Pt NMR spectroscopy (Table 17). The orthometalated complex $[\text{Pt}([9]\text{aneS}_3)(\text{phpy})](\text{PF}_6)$ gives the signal at -3 787 ppm. The AgPF_6 addition caused the significant shift of 205 ppm (to -3 582 ppm) and narrowing of the resonance line. The solid complex, stabilized by Pt→Ag dative bonds, containing acetonitrile molecules coordinated to Ag atom,*- has been isolated and characterized by X-ray crystallography.

Hesfold et al.¹¹⁴ have studied hexadentate macrocyclic tellurium and selenium containing ligands (crown ethers derivatives containing two Se or Te atoms) as receptors for various metals, among them platinum has been studied. They have characterized obtained complexes with ^{195}Pt NMR (see Table 18). Other example of this type of complexes has been reported by Levason et al.¹¹⁵ The ^{195}Pt and ^{77}Se NMR spectra have permitted to determine the coordination environment of both Pt atoms in complex $[(\text{PtCl}_2)_2(\text{DB2+2})]$ as a planar Se_2Cl_2 coordination.

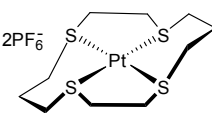
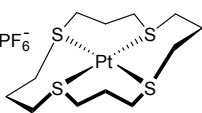
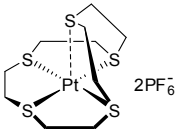
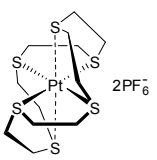
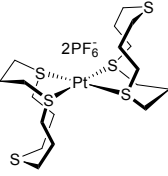
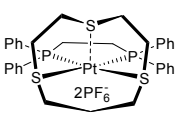
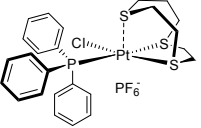
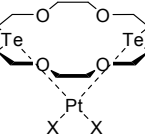
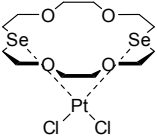
Also the compounds containing only Se atoms in macrocyclic ring have been studied as ligands for obtaining a platinum complexes (see Table 18 for details). These compounds have been investigated by Levason and co-workers. The first published examples are the complexes of [16]aneSe₄ ligand with PtX_2^{2+} ion (X = Cl, Br). The obtained complexes have been characterized by NMR and X-ray crystallography.¹¹⁶ The analogical complex with Pt(II) has been obtained

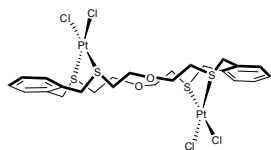
(Pt[16]aneSe₄)(PF₆)₂.¹¹⁷ The ¹⁹⁵Pt NMR spectrum, recorded in acetone-*d*₆ at 300 K, shows three signals, at -4568, -4587 and -4676 ppm. The cooling of the sample causes changes, at 210 K only one signal (-4750 ppm) occurs. This behaviour has been explained by the existence of invertomers in solution. A few Pt(II) complexes with tripodal Se containing ligand have been obtained, but only for one, [Pt(tseme)₂](PF₆)₂ the ¹⁹⁵Pt NMR data have been reported.¹¹⁸ The X-ray crystallography has shown, that this ligand acts as a bidentate one and the structure of the complex reveals planar square Se₄ coordination. Due to equilibriums between invertomers, two signals have been detected.

The alkylplatinum complexes, containing thiacoronands and thiapodands have been studied (Table 18).¹¹⁹ The ¹⁹⁵Pt NMR spectrum of [Me₃Pt([16]-aneSe₄)](PF₆) at room temperature shows a very broad signal, which has sharpened with temperature decreasing. This indicates the dynamic process (probably so called “ring-whizzing”), resulting in fast interchange of free and complexed Se atoms. Similarly, the signal of [Me₃Pt(tseme)I] is broad at RT. It splits into three peaks with cooling. This is the effect of the presence of three isomers of the complex, two *meso* forms and one *DL* isomer. The signals have not been assigned to definite isomers. Other studied systems are the methylplatinum complexes with small-ring Se₃ ligands.¹²⁰ Two compounds: [Me₃Pt([12]aneSe₃)I], [Me₃Pt(B[11]aneSe₃)I] and [Me₃Pt(P[8]aneSe₂N)I] are dynamic at 298 K, therefore the ¹⁹⁵Pt NMR spectra have been also recorded at 233 K. The observed Se-Pt scalar couplings prove the κ³-coordination mode. The authors report also the chemical shift of [Pt(B[13]aneSe₃Cl₂)] in DMF (-3644 ppm), but have not discussed the structure of this compound.

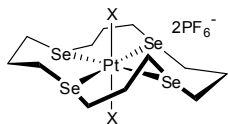
Table 18. Structures and ¹⁹⁵Pt NMR data for Pt complexes with S, Se and Te donor ligands

<p>[Pt([9]aneS₃)₂](PF₆)₂</p>	<p>[Pt([10]aneS₃)₂](PF₆)₂</p>	<p>[Pt([12]aneS₄)](PF₆)₂</p>
<p>-4117 ppm; Δν = 541 Hz CD₃NO₂; vs. [PtCl₆]²⁻ aq; Ref. ⁹⁸</p>	<p>-4029 ppm; Δν = 441 Hz CD₃NO₂; vs. [PtCl₆]²⁻ aq; Ref. ⁹⁸</p>	<p>-4708 ppm; Δν = 99 Hz CD₃NO₂; vs. [PtCl₆]²⁻ aq; Ref. ⁹⁸ -4690 ppm CH₃CN/CD₃CN; 300 K vs. Na₂[PtCl₆] aq, 1M; Ref.</p>

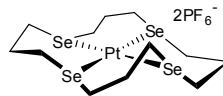
 <p>[Pt([14]aneS₄)](PF₆)₂</p>	 <p>[Pt([16]aneS₄)](PF₆)₂</p>	 <p>[Pt([15]aneS₅)](PF₆)₂</p>
<p>-4683 ppm; $\Delta\nu = 78$ Hz CD_3NO_2; vs. $[\text{PtCl}_6]^{2-}$ aq; Ref. ⁹⁸ -4645 ppm $\text{CH}_3\text{CN}/\text{CD}_3\text{CN}$; 300 K vs. $\text{Na}_2[\text{PtCl}_6]$ aq, 1M; Ref.</p>	<p>-4205 ppm; $\Delta\nu = 89$ Hz CD_3NO_2; vs. $[\text{PtCl}_6]^{2-}$ aq; Ref. 103,127 -4177 ppm $\text{CH}_3\text{CN}/\text{CD}_3\text{CN}$; 300 K vs. $\text{Na}_2[\text{PtCl}_6]$ aq, 1M; Ref.</p>	<p>-3831 ppm; $\Delta\nu = 162$ Hz CD_3NO_2; vs. $[\text{PtCl}_6]^{2-}$ aq; Ref. ⁹⁸</p>
 <p>[Pt([18]aneS₆)](PF₆)₂</p>	 <p>[Pt([12]aneS₃)](PF₆)₂</p>	 <p>[Pt([10]aneS₃(dppe)] (PF₆)₂</p>
<p>-4152 ppm; $\Delta\nu = 192$ Hz CD_3NO_2; vs. $[\text{PtCl}_6]^{2-}$ aq; Ref. 103,127</p>	<p>-4201 ppm; $\Delta\nu = 75$ Hz CD_3NO_2; vs. $[\text{PtCl}_6]^{2-}$ aq; Ref.¹²¹</p>	<p>-4602 ppm; $^1J_{\text{PPt}} = 3224$ Hz CD_3NO_2; vs. $[\text{PtCl}_6]^{2-}$ aq; Ref. ¹⁰⁶</p>
 <p>[Pt([10]aneS₃)(PPh₃)Cl]</p>	 <p>[Pt([18]aneTe₂O₄)X₂]</p>	 <p>[Pt([18]aneSe₂O₄)Cl₂]</p>
<p>-4154 ppm; $^1J_{\text{PPt}} = 3442$ Hz CD_3NO_2; vs. $[\text{PtCl}_6]^{2-}$ aq; Ref. ⁹⁹</p>	<p>X = Cl: -4257 ppm; $^1J_{\text{TePt}} = 862$ Hz X = Br: -4756 ppm; $^1J_{\text{TePt}} = 690$ Hz CD_2Cl_2, 223 K; $\text{Na}_2[\text{PtCl}_6]$ aq, 1 M Ref. ¹¹⁴</p>	<p>X = Cl: -3861 ppm; $^1J_{\text{SePt}} = 550$ Hz CD_2Cl_2; $\text{Na}_2[\text{PtCl}_6]$ aq, 1 M Ref. ¹¹⁴</p>


 $[\text{PtCl}_2(\text{DB2+2})]$

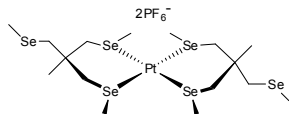
-3681 ppm; $^1J_{\text{SePt}} = 383$ Hz
 $\text{CH}_3\text{CN}/\text{CDCl}_3$; vs. $\text{Na}_2[\text{PtCl}_6]$ aq,
 1 M
 Ref.¹¹⁵


 $[\text{Pt}(\text{[16]aneSe}_4)\text{Cl}_2](\text{PF}_6)_2$

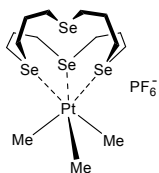
X = Cl: -3079 ppm; $\Delta\nu_{1/2} = 200$ Hz
 X = Br: -3785 ppm
 CD_3CN ; vs. $\text{Na}_2[\text{PtCl}_6]^{2-}$ in
 H_2O
 Ref.¹¹⁶


 $[\text{Pt}(\text{[16]aneSe}_4)](\text{PF}_6)_2$

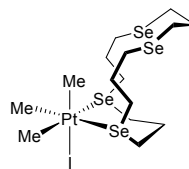
-4568, -4587 & -4676 ppm
 $\text{acetone-}d_6$; vs. $\text{Na}_2[\text{PtCl}_6]^{2-}$
 in H_2O
 300 K
 Ref.¹¹⁷


 $[\text{Pt}(\text{tseme})_2](\text{PF}_6)_2$

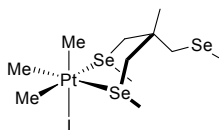
-4630 & -4888 ppm
 $\text{acetone}/\text{CDCl}_3$; 220 K;
 vs. $[\text{PtCl}_6]^{2-}$ aq; Ref.¹¹⁸


 $[\text{Me}_3\text{Pt}(\text{[16]aneSe}_2)](\text{PF}_6)$

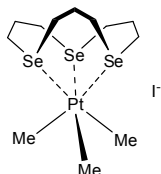
-3648 ppm; $^1J_{\text{SePt}} = 249$ Hz
 CDCl_3 ; 298 K
 vs. $\text{Na}_2[\text{PtCl}_6]$ aq, 1 M; Ref.¹¹⁹


 $[\text{Me}_3\text{Pt}(\text{[16]aneSe}_4)]$

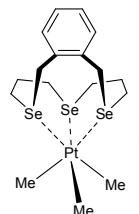
-3616 ppm; $^1J_{\text{SePt}} = 266$ Hz
 CDCl_3 ; 243 K
 vs. $\text{Na}_2[\text{PtCl}_6]$ aq, 1 M;
 Ref.¹¹⁹


 $[\text{Me}_3\text{Pt}(\text{tseme})]$

-3447, -3543 & -3550 ppm
 CDCl_3 ; 223 K
 vs. $\text{Na}_2[\text{PtCl}_6]$ aq, 1 M; Ref.¹¹⁹


 $[\text{Me}_3\text{Pt}(\text{[12]aneSe}_3)]\text{I}$

-3866 ppm; $^1J_{\text{SePt}} = 286$ Hz
 CDCl_3 ; 298 K
 vs. $\text{Na}_2[\text{PtCl}_6]$ aq, 1 M; Ref.¹²⁰


 $[\text{Me}_3\text{Pt}(\text{B[13]aneSe}_3)]\text{I}$

-3769 ppm
 acetonitrile ; 298 K
 vs. $\text{Na}_2[\text{PtCl}_6]$ aq, 1 M;
 Ref.¹²⁰

$[Me_3Pt(B[11]aneSe_3)I]$	$[Me_3Pt(BP[11]aneSe_2N)I]$	$[Me_3Pt(P[8]aneSe_2N)I]$
<p>-3674 ppm; $^1J_{SePt} = 293$ & 318 Hz $CDCl_3$; 223 K vs. $Na_2[PtCl_6]$ aq, 1 M; Ref. ¹²⁰</p>	<p>-3082 ppm; $^1J_{SePt} = 279$ Hz $CDCl_3$; 298 K vs. $Na_2[PtCl_6]$ aq, 1 M; Ref. ¹²⁰</p>	<p>-3227 ppm (broad) acetonitrile; 298 K vs. $Na_2[PtCl_6]$ aq, 1 M; Ref. ¹²⁰</p>
$trans-[PtX_2([16]aneS_4)](PF_6)_2$	$cis-[PtX_2([14]aneS_4)](PF_6)_2$	$cis-[PtX_2([12]aneS_4)](PF_6)_2$
<p>X = Cl: -2587 ppm X = Br: -3245 ppm CH_3CN/CD_3CN; 300 K vs. $Na_2[PtCl_6]$ aq, 1M; Ref. ¹¹²</p>	<p>X = Cl: -3313 ppm X = Br: -3990 ppm CH_3CN/CD_3CN; 300 K vs. $Na_2[PtCl_6]$ aq, 1M; Ref. ¹¹²</p>	<p>X = Cl: -3417 ppm X = Br: -3975 ppm CH_3CN/CD_3CN; 300 K vs. $Na_2[PtCl_6]$ aq, 1M; Ref. ¹¹²</p>
$[Pt(Ph_2[14]aneS_2P_2)](PF_6)_2$		
<p>-5174 ppm; $^1J_{PPt} = 2718$ Hz CH_3CN; vs. $Na_2[PtCl_6]$ aq. Ref. ¹¹³</p>		

An interesting Pt complex has been obtained by Hyrberhold et al. They have prepared the C=C bonds containing tripodand and its complexes with platinum(II) (Fig. 37). The signal has been observed at -462.6 ppm ($^1J_{PtP} = 4048$ Hz) (spectrum recorded in acetone- d_6 at 298 K; referred to spectral reference $\Xi(^{195}Pt) = 21.4$ MHz).

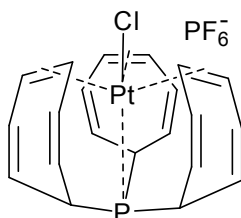
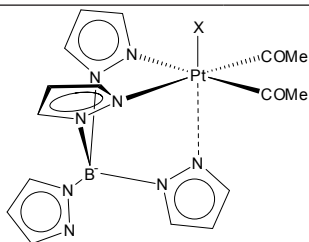


Fig. 37. Platinum complex with unsaturated tripodand

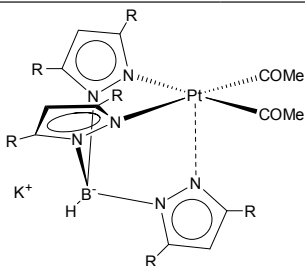
The chemistry of pyrazole ligands and their complexes is widely studied. Special attention is given to scorpionate ligands, derivatives of tris(pyrazolyl) borane. Some data of their complexes with platinum have been published, but ^{195}Pt NMR characteristic of these compounds has been reported only by Bette and co-workers.¹²² Their NMR results are presented in Table 19.

Table 19. Structures and NMR properties of platinum-pyrazole complexes

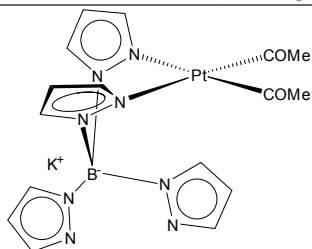
Structure	δ ^{195}Pt [ppm]	Conditions & standards	Ref.
R = H; X = H	-1618.1 ($^1J_{\text{HPt}} = 1506.9$ Hz)	acetone- d_6 ; $\text{Na}_2[\text{PtCl}_6]$ aq	Ref. ¹²²
R = H; X = Cl	-762.9	CDCl_3 ; $\text{Na}_2[\text{PtCl}_6]$ aq	Ref. ¹²²
R = Me; X = H	-1740.0 ($^1J_{\text{HPt}} = 1500$ Hz)	THF- d_8 ; $\text{Na}_2[\text{PtCl}_6]$ aq	Ref. ¹²²
R = Me; X = Cl	-763.0	CDCl_3 ; $\text{Na}_2[\text{PtCl}_6]$ aq	Ref. ¹²²
R = H; X = Me	-1461.5	acetone- d_6 ; $\text{Na}_2[\text{PtCl}_6]$ aq	Ref. ¹²²
R = H; X = Et	-1396.5	acetone- d_6 ; $\text{Na}_2[\text{PtCl}_6]$ aq	Ref. ¹²²
R = H; X = PhCH_2	-1281.5	acetone- d_6 ; $\text{Na}_2[\text{PtCl}_6]$ aq	Ref. ¹²²



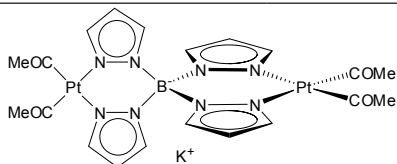
X = Me	-1489.2	acetone- d_6 ; Na ₂ [PtCl ₆] aq	Ref. ¹²²
X = Et	-1436.4	acetone- d_6 ; Na ₂ [PtCl ₆] aq	Ref. ¹²²
X = PhCH ₂	-1314.8	acetone- d_6 ; Na ₂ [PtCl ₆] aq	Ref. ¹²²



R = H	-3351.4	THF- d_8 ; Na ₂ [PtCl ₆] aq	Ref. ¹²²
R = Me	-3372.7	THF- d_8 ; Na ₂ [PtCl ₆] aq	Ref. ¹²²

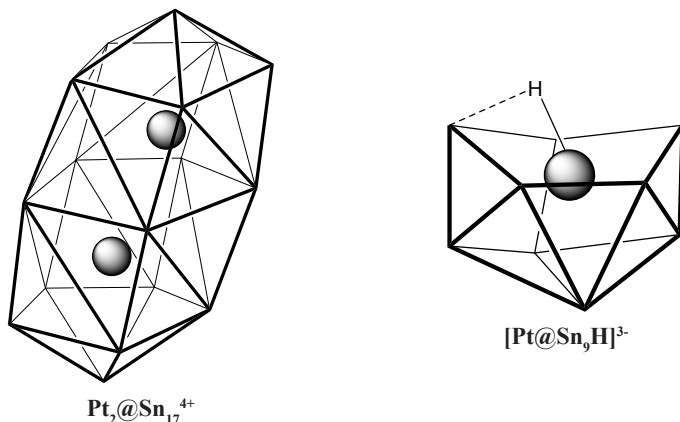


-3371.4	THF- d_8 ; Na ₂ [PtCl ₆] aq	Ref. ¹²²
---------	--	---------------------



-3339.8	DMSO- d_6 ; Na ₂ [PtCl ₆] aq	Ref. ¹²⁸
---------	---	---------------------

An interesting example of supramolecular complexes of platinum is represented by the so called “Rudolph’s complexes”, containing Pt atoms encapsulated inside cages formed by tin atoms. An example of such structure may be cluster $[\text{Pt}_2@_{\text{Sn}}]^{4+}$ (Fig. 38).¹²³ Its ^{195}Pt NMR spectrum shows a single resonance at -5713 ppm, splitted due to coupling with seventeen tin nucleus, $^1J_{\text{Pt-}^{195}\text{Sn}} = ^1J_{\text{Pt-}^{117}\text{Sn}} = 780$ Hz. The spectrum has been recorded in $\text{DMF-}d_8$, at 298 K (referred to aqueous $[\text{PtCl}_6]^{2-}$). The other, similar cluster $[\text{Pt}@_{\text{Sn}_9}\text{H}]^{3-}$ has been obtained. It has a fluxional nature sine all nine tin atoms are equivalent and are coupled with the hydrogen atom. The ^{195}Pt spectrum consists from one signal at -5303 ppm, which shows the coupling with both ^{117}Sn and ^{119}Sn isotopes ($^1J_{\text{Pt-}^{117}\text{Sn}} = 1472$ Hz; $^1J_{\text{Pt-}^{117}\text{Sn}} = 1540$ Hz) and hydrogen atom ($^1J_{\text{PtH}} = 32$ Hz). Its spectra have been recorded in 1,2-diaminoethane/toluene- d_8 mixture at 298 K. The Sn_9^{4-} may also bond two platinum atoms. The well known example of such structure is $[\text{Sn}_9\text{Pt}_2(\text{PPh}_3)]^{2-}$ cluster.¹²⁴ The two complexed Pt atoms do not interchange in NMR time scale, but they show two well resolved, sharp signals, at -5 270 and -6 010 ppm, respectively. The first one has been assigned to interstitial, while the second one to vertex Pt atom. The more deshielded signal is splitted by a coupling second platinum atom ($^1J_{\text{PtPt}} = 2 472$ Hz), phosphorus ($^2J_{\text{PtPt}} = 305$ Hz) and tin ($^1J_{\text{Pt-}^{191}\text{Sn}} = ^1J_{\text{Pt-}^{117}\text{Sn}} = 1 690$ Hz). The peak becoming from the vertex Pt nucleus is coupled with P ($^1J_{\text{PtP}} = 4 800$ Hz) and Pt ($^1J_{\text{PtPt}} = 2 472$ Hz). The spectra have been obtained at 263 K in $\text{DMF-}d_8$ (referred to aqueous $[\text{PtCl}_6]^{2-}$). Similar structures have been obtained for lead (instead of tin). The first example is the $[\text{Pt}@_{\text{Pb}}]^{2-}$ cluster.^{131,132} The platinum atom, enclosed into icosahedral lead cage gives the NMR signal at -4 527 ppm. The signal is splitted due to Pt-Pb couplings, $^1J_{\text{PtPb}} = 3 440$ Hz (in DMF, at 284 K; referred to H_2PtCl_6).



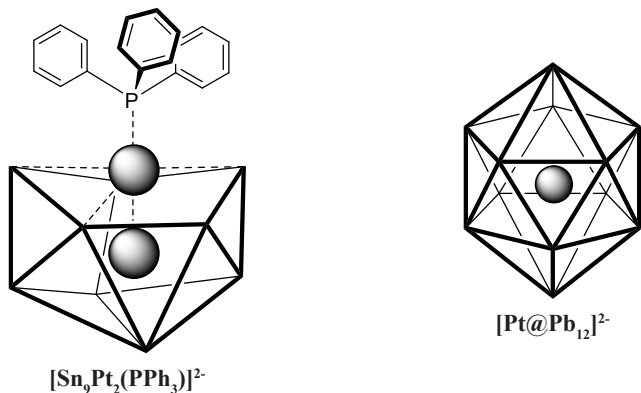


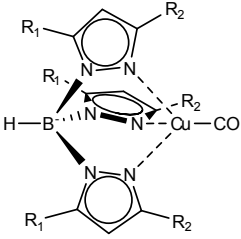
Fig. 38. Structures of Pt containing Rudolph's complexes

2.8 Group 11

2.8.1 Copper

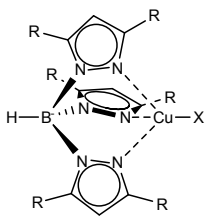
Both naturally occurring copper isotopes (^{63}Cu , ^{65}Cu) are suitable for NMR experiments, however the heavier one is much more frequently used. It has a spin $3/2$ and a rather small quadrupole moment $-0.195 \times 10^{-28} \text{ m}^2$ (for ^{63}Cu these parameters are $I = 3/2$; $Q = -0.211 \times 10^{-28} \text{ m}^2$). Due to high content in natural copper (69.17 % vs. 30.83 for lighter isotope), it characterizes a good receptivity, 0.11 that of ^1H (for ^{63}Cu it is 0.0931). Copper isotopes have similar resonance frequencies, i.e. $\mathcal{E} = 26.505$ for ^{63}Cu and 28.394 MHz for ^{65}Cu . The chemical shifts range is about 3000 ppm. The only experimental problem is a presence of broad signal, coming from the resonance of metallic copper present in a probehead, in a spectra. Unfortunately, many copper compounds (e.g. Cu^{2+} salts) are paramagnetic, so unavailable for ^{65}Cu NMR studies. IUPAC recommends $[\text{Cu}(\text{CH}_3\text{CN})_6](\text{ClO}_4)$ in acetonitrile as a standard.

The copper NMR has been sparsely used in supramolecular chemistry. Imai et al.¹²⁵ have measured the ^{63}Cu NMR spectra for series of complexes of $\text{Cu}(\text{CO})^+$ with scorpionate pyrazoylborate ligands (Table 20). The spectra have been recorded in toluene- d_8 and referred to $[\text{Cu}(\text{CH}_3\text{CN})_6](\text{PF}_6)$ (no solvent of reference and temperature given). The signals observed are quite sharp, due to high electronic field symmetry around tetrahedral copper centre. The complexes with phenyl substituents show the broader line due to lower field symmetry, caused by π acceptor properties of aromatic rings. The ^{63}Cu chemical shifts have been correlated with a wavelength of $\text{C}\equiv\text{O}$ stretching vibration, determined from IR spectra.

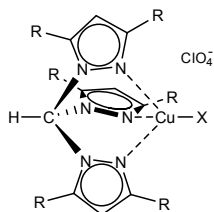
Table 20. NMR data of $[Cu(CO)]^+$ scorpionate pyrazoylborate complexes


R_1	R_2	$\delta^{63}\text{Cu}$ [ppm]	$\Delta v_{1/2}$ [Hz]	R_1	R_2	$\delta^{63}\text{Cu}$ [ppm]	$\Delta v_{1/2}$ [Hz]
Me	Me	716	110	$i\text{Pr}$	$t\text{Bu}$	703	75
$i\text{Pr}$	$i\text{Pr}$	730	205	$i\text{Pr}$	Ph	603	2 900
Me	$t\text{Bu}$	700	70	Ph	Ph	583	4 200

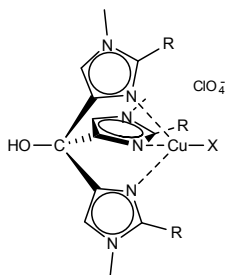
These studies have been continued with a more diverse ligands group. The tris(pyrazoyl), tris(imidazolyl) and tris(2-pyridyl)methane derivatives as well as cyclic polyamines have been chosen for these studies.¹²⁶ Also the other monodentate ligands have been used in place of CO molecule. The structures and spectral data published are collected in Table 21. The spectra were measured in dichloromethane- d_2 , except the CH_3CN complexes, which have been measured in acetonitrile. The signals of the compounds with PPh_3 or AN molecule, bonded to copper atom have distinctly higher line half widths (for some compounds peaks are too broad to measure the chemical shift).

Table 21. NMR data of $[CuX]^+$ scorpionate complexes


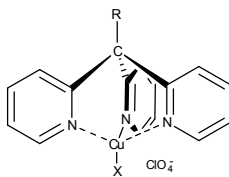
R	X	$\delta^{63}\text{Cu}$ [ppm]	$\Delta v_{1/2}$ [Hz]	R	X	$\delta^{63}\text{Cu}$ [ppm]	$\Delta v_{1/2}$ [Hz]
$i\text{Pr}$	CH_3CN	166	12 000	$i\text{Pr}$	PPh_3	118	11 000



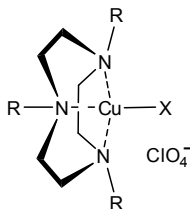
R	X	$\delta^{63}\text{Cu}$ [ppm]	$\Delta\nu_{1/2}$ [Hz]	R	X	$\delta^{63}\text{Cu}$ [ppm]	$\Delta\nu_{1/2}$ [Hz]
Me	CO	419	4 700	ⁱ Pr	CO	449	8 200
Ph	CO	440	12 000	ⁱ Pr	CH ₃ CN	113	9 700



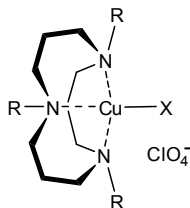
R	X	$\delta^{63}\text{Cu}$ [ppm]	$\Delta\nu_{1/2}$ [Hz]	R	X	$\delta^{63}\text{Cu}$ [ppm]	$\Delta\nu_{1/2}$ [Hz]
Et	CO	609	1 300	ⁱ Pr	CO	621	1 800
Ph	CO	543	4 500	ⁱ Pr	CH ₃ CN	to broad	-



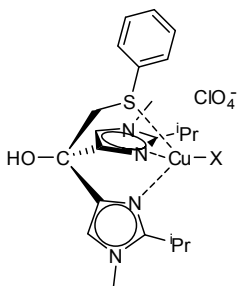
R	X	$\delta^{63}\text{Cu}$ [ppm]	$\Delta\nu_{1/2}$ [Hz]	R	X	$\delta^{63}\text{Cu}$ [ppm]	$\Delta\nu_{1/2}$ [Hz]
OH	CO	504	6 600	MeO	CO	524	8 700
OH	CH ₃ CN	to broad	-	H	CO	489	6 500



R	X	$\delta^{63}\text{Cu}$ [ppm]	$\Delta\nu_{1/2}$ [Hz]	R	X	$\delta^{63}\text{Cu}$ [ppm]	$\Delta\nu_{1/2}$ [Hz]
ⁱ Pr	CO	461	5 500	Me	CO	419	4 100
ⁱ Pr	CH ₃ CN	-62	14 000	PhCH ₃	CO	394	14 000



R	X	$\delta^{63}\text{Cu}$ [ppm]	$\Delta\nu_{1/2}$ [Hz]	R	X	$\delta^{63}\text{Cu}$ [ppm]	$\Delta\nu_{1/2}$ [Hz]
Me	CO	585	410	Me	CH ₃ CN	-83	6 600



$$\delta^{63}\text{Cu} = 451 \text{ ppm}; \Delta\nu_{1/2} = 10\,000 \text{ Hz}$$

Hesford et al.¹¹⁴ have prepared the complex of Cu(I) with mixed telluro/oxa crown (Fig. 39), $[\text{Cu}([\text{18}] \text{aneTe}_2\text{O}_4)_2](\text{BF}_4)$ and have recorded the ^{63}Cu NMR spectrum (no solvent given, with excess of the ligand added). The very broad signal at -59 ppm has been observed ($\Delta\nu_{1/2} = 11\,000$ Hz), attributed to tetrahedral copper centre of Te_2 coordination. The experiment details have not been given.

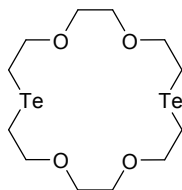


Fig. 39. Structure of $[\text{18}] \text{aneTe}_2\text{O}_4$ ligand

2.8.2 Silver

Natural silver composes from two isotopes of almost equal content (51.84 % of ^{107}Ag and 48.16 % of ^{109}Ag). Both of them are NMR active, and are not a quadrupolar nuclei ($I = 1/2$), since ^{107}Ag has a smaller gyromagnetic ratio, which leads in lower resonance frequency ($\bar{\nu} = 4.046 \text{ MHz vs. } 4.652 \text{ MHz}$ for ^{109}Ag) and poorer receptivity (3.44×10^{-5} for ^{107}Ag and 4.86×10^{-5} for ^{109}Ag that of ^1H). Therefore, ^{109}Ag is preferred by NMR spectroscopists. The low γ causes other serious experimental problem, i.e. the distortion of base line caused by acoustic ringing. The other experimental difficulty is a long relaxation time of silver nucleus (even over 10 min.). This causes the increasing of the experiment time. The negative γ value causes the negative Overhauser effect, so using of the broadband decoupling may decrease the signal intensity. IUPAC recommends 1 M aqueous solution of AgNO_3 as a reference.

The examples of the application of ^{109}Ag NMR in supramolecular chemistry are very scarce. Doel et al.¹²⁷ have obtained the complex of P_2S_2 ligand with Ag^+ ions (Fig. 40). The spectrum, recorded at 220 K in $\text{CH}_2\text{Cl}_2/\text{CDCl}_3$ shows triplet at 1 117 ppm ($^1J_{\text{AgP}} = 510 \text{ Hz}$). At 300 K no ^{109}Ag signal has been observed, probably due to fast ligand exchange. The spectra have been referred to external 9.1 M solution of Ag^+ in water (-47 ppm), TEMPO has been added to the sample as a relaxation agent.

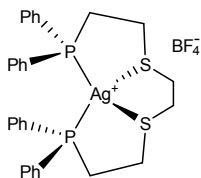
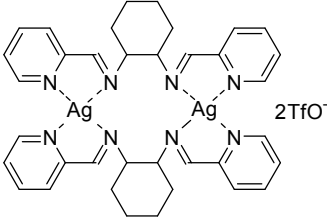
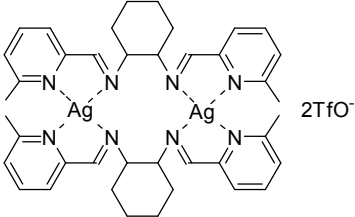
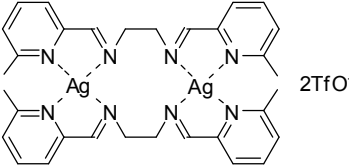
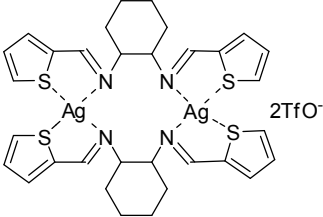
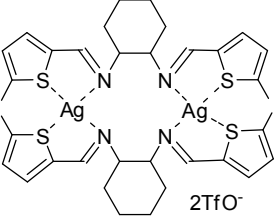
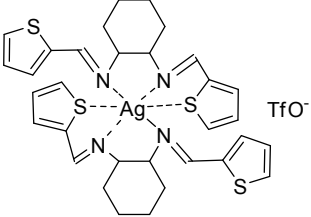


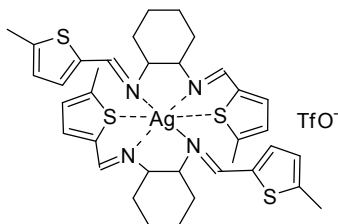
Fig. 40. Structure of silver(I)/ P_2S_2 ligand complex

Brevard et al.¹²⁸ have worked on application of the INEPT inverse detection method to observe the NMR signal of low γ nuclei in imine complexes. The first published example is a dinucleate complex $[\text{L}_2\text{Ag}_2](\text{TfO})_2$, containing *trans*-1,2-bis(pyridine-2-carbaldehydeimine)cyclohexane as a ligand (Table 22). The ^{109}Ag NMR chemical shift of this compound is 580 ppm (in CD_3OD). The INEPT experiment is based on $^3J_{^{109}\text{Ag-H}}$ coupling with imine hydrogen atoms (for anisochronous imine protons $^3J_{^{109}\text{Ag-H}}$ values are 9.3 & 6.3 Hz). For the 6-methylpyridyl analogue, the shift is 612 ppm.¹²⁹ The changing of the cyclohexane unit onto ethane one causes only small shift (to 618 ppm).¹³⁰ The presence of one signal in the ^{109}Ag NMR spectrum proves the formation of only

one diastereoisomer of the complex. The thiophene and 5-methylthiophene analogues of the parent complex has been also studied by this technique.^{131,132} Surprisingly small difference of the chemical shift between the silver atom in N_4 and N_2S_2 kernels has been stated. All spectra have been measured against 2 M $AgNO_3$.

Table 22. Structures and ^{109}Ag NMR data of silver complexes with Schiff base ligands

	
580 ppm (in CD_3OD)	612 ppm (in CD_3OD)
	
618 ppm (in CD_3OD ; 294 K)	678 ppm (in CD_2Cl_2)
	
659 ppm (in CD_2Cl_2)	582 ppm (in CD_2Cl_2 ; 190 K)



583 ppm (in CD_2Cl_2 ; 190 K)

Drew and coworkers prepared a disilver complexes of imine cryptates.¹³³ Two of them have been characterized by ^{109}Ag NMR spectroscopy (Fig. 41). The INEPT sequence has been used for detection of silver NMR signal. The chemical shifts are 610.0 ppm for thiophene derivative and 609.7 ppm for furan one. The three bond coupling with a hydrogen nuclei has been observed ($^3J_{\text{AgH}}$ is ca. 8 Hz). The spectra have been recorded in CD_3CN at 294 and 228 K. The reference has not been specified, however the comparison with the other complexes, measured vs. 2 M AgNO_3 in water has been discussed.

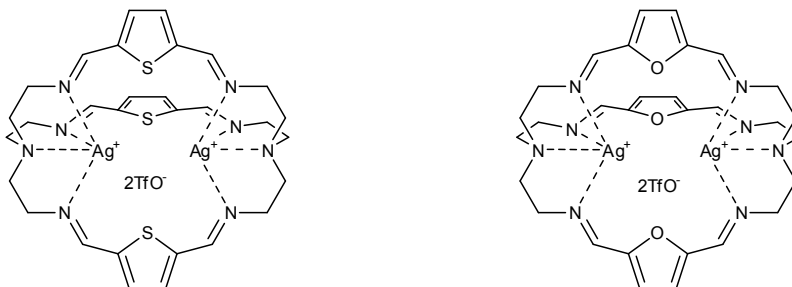


Fig. 41. Structures of Ag^+ cryptates

2.9 Group 12

2.9.1 Cadmium

Among eight natural stable cadmium isotopes two are suitable for NMR measurements, ^{111}Cd and ^{113}Cd . Both of them have a nuclear spin $\frac{1}{2}$, therefore their signals are not broadened due to quadrupolar interactions. However the heavier isotope is slightly less abundant (12.22 % vs. 12.81 %) it has a higher γ coefficient, resulting in higher resonance frequency ($\mathcal{E} = 22.182$ MHz vs. 21.205 MHz) and higher receptivity – 1.34×10^{-3} that of ^1H (for ^{111}Cd this value is 1.22×10^{-3}). Therefore, the ^{113}Cd NMR is preferred to study cadmium

compounds. The chemical shifts range is *ca.* 1 200 ppm. IUPAC recommends neat dimethylcadmium as a reference. Since its high toxicity and volatility, aqueous solution of $\text{Cd}(\text{NO}_3)_2$ or $\text{Cd}(\text{ClO}_4)_2$ are frequently used.

Cadmium NMR is widely used in supramolecular chemistry. The complexes of Cd^{2+} ions with crown ethers, 15-crown-5 and benzo-15-crown-5 (Fig. 42), have been investigated by Talebpour et al.¹³⁴ The authors have used the NMR titration technique to determine the association constants. Both changes of ^1H and ^{113}Cd chemical shifts have been monitored. In all cases the signals of free and complexed ions are averaged. The experiments in acetonitrile and acetonitrile-nitromethane mixtures have been performed. In both studied host-guest systems, in all solvents used, only formation of 1:1 complexes has been detected. Unfortunately, the authors have not reported the chemical shifts of bounded cadmium ion, obtained from the fitting of the experimental curves. The chemical shifts, read from the graphs presented are -115 ppm for Cd-B15C5 system (3.5 excess of ligand; in acetonitrile) and -123 ppm (3.8 excess of ligand; in acetonitrile). The spectra have been referred to 0.5 M $\text{Cd}(\text{NO}_3)_2$ in D_2O and have been measured at 298 K.

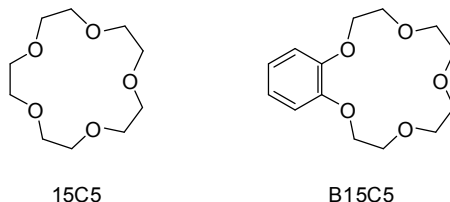


Fig. 42. Structures of the crown ethers used as a ligands for Cd^{2+} ions

Kennedy et al.¹³⁵ have published the results of single crystal and CP-MAS NMR study of $\text{CdX}_2 \cdot 18\text{-crown-6}$ compounds (see Fig. 1 for ligand structure). The isotropic chemical shift of 33 ppm for chloride, -25 ppm for bromide and -172 ppm for iodide salt (*vs.* 0.1 M $\text{Cd}(\text{NO}_3)_2$ in water) have been calculated from the CP-MAS solid state measurements.

The macrocyclic thiaethers have been also used as ligand for a constructing of cadmium containing supramolecular systems. Helm and coworkers¹³⁶ report the synthesis of $[\text{Cd}(\text{[10]aneS}_3)_2](\text{ClO}_4)_2$ complex and its characterization by ^{113}Cd NMR method. In nitromethane- d_3 solution one, sharp signal at 612 ppm ($\Delta\nu_{1/2} = 38.66$ Hz) has been observed. For analogous octahedral complex, $[\text{Cd}(\text{[9]aneS}_3)_2](\text{ClO}_4)_2$, signal at 731 ppm has been found. The authors have not defined the reference used. The further studies of these researchers bring

^{113}Cd NMR results for larger set of sulfur, nitrogen and mixed sulfur/nitrogen ligands.^{144,145} The NMR data are collected in Table 23. All spectra have been recorded in CD_3NO_2 at 298 K, and referred 0.1 M of $\text{Cd}(\text{ClO}_4)_2$ in D_2O . It has been shown that non-coordinating anion does not influence the chemical shift. The increasing of sulfur donor atoms in coordination sphere cause the increasing of the chemical shift. The corresponding nitrogen ligands causes smaller deshielding. The signal of $[\text{Cd}([\text{18}] \text{aneS}_6)](\text{ClO}_4)_2$ has not been detected. For complex with $[\text{18}] \text{aneS}_4\text{N}_2$ ligand two diastereoisomers have been observed in NMR spectra. Similar troubles have occurred for $[\text{Cd}([\text{9}] \text{aneS}_2\text{O}_2)](\text{ClO}_4)_2$. These complexes differ in orientation of NH protons. The authors have not assigned the signals in ^{113}Cd NMR spectrum to definite structures. Some complexes have been prepared as mixtures of 1:1 and 1:2 ones (e.g. $[\text{Cd}([\text{12}] \text{aneS}_3)](\text{ClO}_4)_2$). Pentaazacyclopentadecane ($[\text{15}] \text{aneN}_5$) complexes with cadmium ion have been studied by Franklin et al.¹³⁷ The authors have discussed the difference in chemical shifts of the studied compounds in chloroform-*d* and heavy water. The shifts observed in CDCl_3 correspond to the individuals detected in solid state. In water the complexes dissociate. The $[\text{Cd}([\text{15}] \text{aneN}_5)\text{Cl}_2]$ forms $[\text{Cd}([\text{15}] \text{aneN}_5)\text{Cl}]^+$ cation. The loss of one chloride ligand and changing of the coordination geometry causes the downfield shift of 16 ppm. The second complex, $[\text{Cd}([\text{15}] \text{aneN}_5)(\text{NO}_3)](\text{NO}_3)$ undergoes the ligand exchange. The NO_3^- groups from inner coordination sphere are substituted by water molecule. This causes the deshielding of 98 ppm. The spectra have been referred vs. CdSO_4 in D_2O (δ ^{113}Cd = -3.0 ppm) and have been recorded at 298 K.

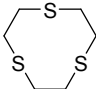
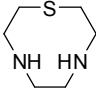
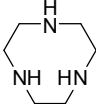
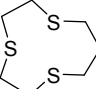
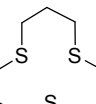
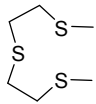
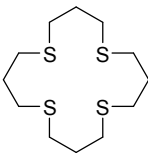
Roy et al.¹³⁸ have studied the series of Cd^{2+} complexes with an octamethyl[14]ane N_4 . One complex, *trans*- $[\text{Cd}(\text{Me}_8[\text{14}] \text{aneN}_4(\text{NCS})_2)]$ has been characterized by ^{113}Cd NMR method, to determine the mode of SCN ligand coordination. The chemical shifts indicate the bonding through S atom. The spectrum has been recorded in CDCl_3 (no experimental conditions and reference used have been given).

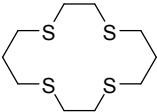
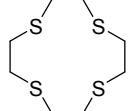
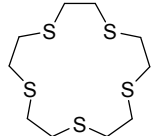
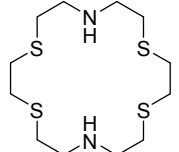
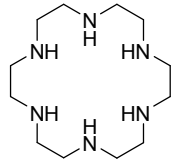
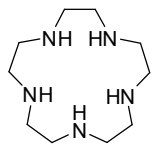
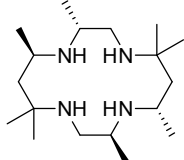
Niu and coworkers have synthesized the cross-bridged cyclam and cyclen ligands.¹³⁹ The structures of their complexes with cadmium have been investigated by X-ray crystallography and NMR spectroscopy. Three cadmium-containing derivatives of cyclam have been characterized by ^{113}Cd NMR spectra. The spectra have been recorded in D_2O and referred to 3 M CdSO_4 in the same solvent (δ ^{113}Cd = -3.0 ppm). The distinct difference between the complex obtained from CdCl_2 and these prepared with using of cadmium nitrate or perchlorate has been explained by the chloride ion coordination to Cd atom, even in water solution.

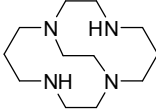
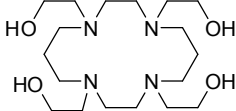
Clarke et al.¹⁴⁰ have shown the slow chemical exchange between the

free and complexed cadmium ion in solution containing $\text{Cd}(\text{ClO}_4)_2$ and tetrakis(hydroksyethyl)cyclam ligand in methanol- d_4 solution. The well resolved, narrow signals of the $[\text{Cd}(\text{L})]^{2+}$ and solvated Cd^{2+} ions have been observed. The spectra have been referred to 0.1 M solution of $\text{Cd}(\text{ClO}_4)_2$ in D_2O and measured at 300.6 K.

Table 23. ^{113}Cd NMR data of cadmium macrocyclic complexes

Ligand	Complex	^{113}Cd NMR chemical shifts [ppm]	Half linewidths [Hz]
	$[\text{Cd}([\text{9}]\text{aneS}_3)_2](\text{ClO}_4)_2$	731 (in CD_3NO_2)	20
	$[\text{Cd}([\text{9}]\text{aneS}_3)_2](\text{PF}_6)_2$	730 (in CD_3NO_2)	28
	$[\text{Cd}([\text{9}]\text{aneN}_2\text{S}_2)](\text{ClO}_4)_2$	521 (in CD_3NO_2)	34
	$[\text{Cd}([\text{9}]\text{aneN}_3)_2](\text{ClO}_4)_2$	409 (in CD_3NO_2)	22
	$[\text{Cd}([\text{10}]\text{aneS}_3)_2](\text{ClO}_4)_2$	612 (in CD_3NO_2)	38
	$[\text{Cd}([\text{12}]\text{aneS}_4)](\text{ClO}_4)_2$	225 (in CD_3NO_2)	100
	$[\text{Cd}(\text{ttn})_2](\text{ClO}_4)_2$	454 (in CD_3NO_2)	558
	$[\text{Cd}([\text{16}]\text{aneS}_4)](\text{ClO}_4)_2$	280 (in CD_3NO_2)	400

	$[\text{Cd}([\text{14}] \text{aneS}_4)](\text{ClO}_4)_2$	322 (in CD_3NO_2)	250
	$[\text{Cd}([\text{12}] \text{aneS}_4)](\text{ClO}_4)_2$	289 (in CD_3NO_2)	33
	$[\text{Cd}([\text{15}] \text{aneS}_5)](\text{ClO}_4)_2$	368 (in CD_3NO_2)	700
	$[\text{Cd}([\text{18}] \text{aneS}_4\text{N}_2)](\text{PF}_6)_2$	527 (in CD_3NO_2)	78
		560 (in CD_3NO_2)	87
	$[\text{Cd}([\text{18}] \text{aneN}_6)](\text{BF}_4)_2$	277 (in D_2O)	57
	$[\text{Cd}([\text{15}] \text{aneN}_5)\text{Cl}_2]$	293 (in D_2O) 277 (in CDCl_3)	n.r.
	$[\text{Cd}([\text{15}] \text{aneN}_5)\text{NO}_3](\text{NO}_3)$	267 (in D_2O) 169 (in CDCl_3)	n.r.
	<i>trans</i> - $[\text{Cd}(\text{Me}_8[\text{14}] \text{aneN}_4)(\text{SCN})_2]$	420.54 (in CDCl_3)	n.r.

	$[\text{Cd}(\text{cross}[14]\text{aneN}_4)\text{Cl}_2]$	326 (in D_2O)	n.r.
	$[\text{Cd}(\text{cross}[14]\text{aneN}_4)(\text{NO}_3)_2]$	262 (in D_2O)	n.r.
	$[\text{Cd}(\text{cross}[14]\text{aneN}_4)(\text{ClO}_4)_2]$	267 (in D_2O)	n.r.
	$[\text{Cd}(\text{HE}[14]\text{aneN}_4)(\text{ClO}_4)_2]$	68 (in CD_3OD)	70

Jäntti et al.¹⁴¹ have prepared two cadmium complexes of Schiff-base podates. Both compounds have been characterized by ^{113}Cd NMR, however the results obtained have not been discussed in details. For **42A** (as $[\text{CdL}_A](\text{ClO}_4)_2$) the chemical shift is 84.4 ppm (in $\text{DMSO}-d_6$; 348 K), while for **42B** (as $[\text{CdL}_B](\text{NO}_3)_2$), 188.1 ppm (in $\text{CDCl}_3/\text{DMSO}-d_6$, 10:1 v/v; 303 K). The spectra have been referred to 0.1 M $\text{Cd}(\text{ClO}_4)_2$ in water. Similar compounds have been reported by Salehzadeh et al.¹⁴² They have measured the ^{113}Cd NMR chemical shift of one complex (Fig. **42C**; as perchlorate salt): 140.5 ppm ($^3J_{113\text{Cd}-\text{H}} = 41.9$ Hz; in CD_3CN ; referred to 0.1 M $\text{Cd}(\text{ClO}_4)_2$ in water).

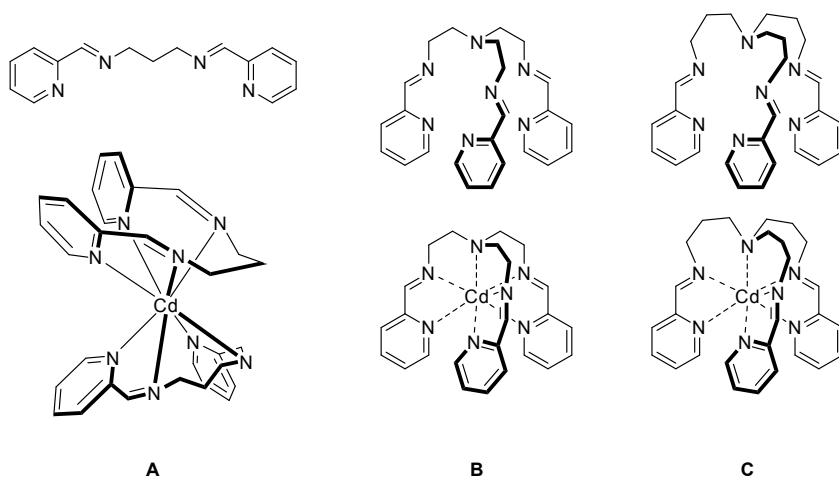


Fig. 42. Structures of pyridine ligands and their complexes with cadmium ion

The macrocyclic imine crown ether (Fig. 43) has been used as receptor for Cd^{2+} ions.¹⁴³ They show the signal at -75.0 ppm (in $\text{DMSO}-d_6$ at 295 K; vs.

0.1 M $\text{Cd}(\text{ClO}_4)_2$ in water). The coupling with hydrogen atoms is clearly seen, $^3J_{^{113}\text{Cd}-\text{H}} = 22$ Hz). The sample has been titrated by pyridine- d_5 with inspection by ^{113}Cd NMR. The progressive downfield shift has been observed, the calculated infinite value is 8.3 ppm. This is caused by the exchange of two oxygen ligands (water or DMSO molecules) in apical positions onto the N-coordinating ones (pyridine). The complex shows the slow exchange in NMR timescale. The addition of $\text{Cd}(\text{ClO}_4)_2$ to the solution of complex causes no line broadening and only insignificant shift of *ca.* 0.4 ppm. The signal of solvated Cd^{2+} ions is also well developed.

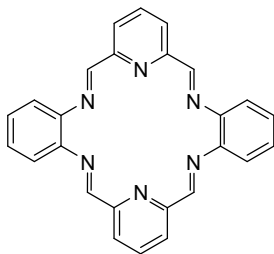
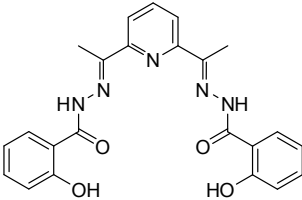
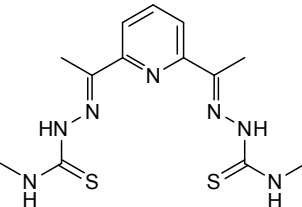
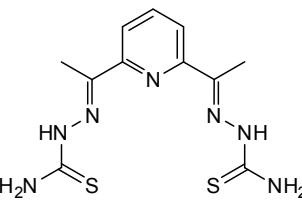


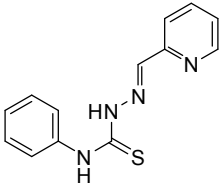
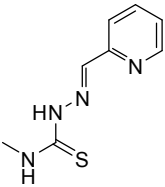
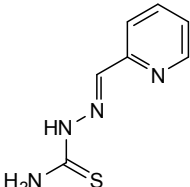
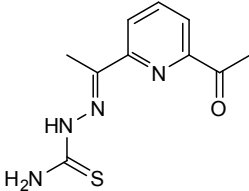
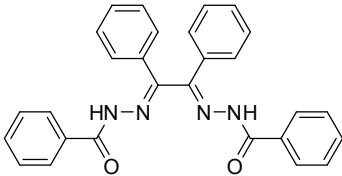
Fig. 43. Structure of tetraimine ligand, used as a Cd^{2+} host

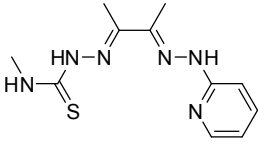
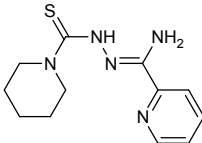
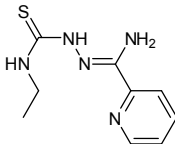
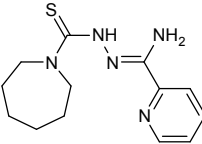
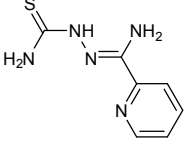
The widely studied ligands, used as cadmium hosts, are hydrazones and their derivatives. Pedrido et al.¹⁵³⁻¹⁵⁵ have synthesized a various ligand and its complexes with several metal cations, among them, with cadmium. The obtained complexes have been characterized by ^{113}Cd NMR. The chemical shifts have been used for a deduction of the character of the coordination sphere. The interesting example has been shown by López-Torres and Mendiola.¹⁴⁴ They have prepared the Cd^{2+} complex with a ligand derived from bis(benzylhydrazone). The compound has a stoichiometry $[\text{Cd}_2\text{L}_2]$ but in the NMR spectrum two different metal ions have been detected ($\delta^{113}\text{Cd} = 26.4$ & 2.9 ppm in $\text{DMSO}-d_6$; vs. Me_2Cd). This has been confirmed by CP-MAS spectra, which show the signals at 111.8 & 91.7 ppm (vs. $\text{Cd}(\text{NO}_3)_2 \times 4\text{H}_2\text{O}$; -100 ppm). The crystal structure has not been determined for this complex. They have also reported a series of complexes of pyridylhydrazone ligand.¹⁴⁵ The obtained cadmium complexes have been characterized by CP-MAS ^{113}Cd NMR spectra. Two different complexes of the stoichiometry $[\text{Cd}(\text{NO}_3)_2\text{LH}_2]$ have been obtained, one with a NO_3 ligands acting as O_2 bidentate ones, second with a NO_3 groups bonding only *via* one oxygen to Cd centre. Similar type of complexes has been prepared by Casas et al.^{146 147} They also have used the ^{113}Cd NMR spectra for a characterization of the prepared compounds and determination of complexation modes. For aquadichlorocomplex

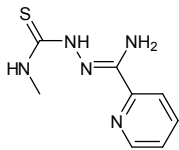
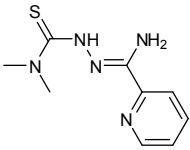
with 2,6-diacetylpyridine monthiosemicarbazone ($[\text{Cd}(\text{HL})\text{Cl}_2(\text{H}_2\text{O})]$) the very broad signal has been observed, due to the unspecified equilibria in solution. For the thiosemicarbazone complexes with $\text{Cd}(\text{OAc})_2$ two signals have been detected in ^{113}Cd NMR spectrum, at *ca.* 250 and 450 ppm.¹⁴⁸ According to the authors, this indicates the equilibrium between five-coordinate $\text{N}_2\text{O}_2\text{S}$ and N_4S_2 complexes. For complexes with CdX_2 ($\text{X} = \text{Cl}, \text{Br}$ or I), only signal at *ca.* 400 ppm occurs.¹⁶¹⁻¹⁶³

Table 24. ^{113}Cd NMR data for hydrazone complexes of cadmium ion

Ligand	Complex	Chemical shift	Solvent	Experimental conditions
 <p style="text-align: center;">H_4L</p>	$[\text{Cd}(\text{H}_2\text{L})(\text{H}_2\text{O})_2]$	38 ppm	$\text{DMSO-}d_6$	0.1 M $\text{Cd}(\text{ClO}_4)_2$
 <p style="text-align: center;">H_4L</p>	$[\text{Cd}(\text{H}_2\text{L})]$	305 ppm	$\text{DMSO-}d_6$	0.1 M $\text{Cd}(\text{ClO}_4)_2$
 <p style="text-align: center;">H_2L</p>	$[\text{Cd}(\text{H}_2\text{L})\text{Cl}_2]$	270 ppm	DMSO	0.1 M $\text{Cd}(\text{ClO}_4)_2$

	[CdL ₂]	405.8 ppm	DMSO- <i>d</i> ₆	0.1 M Cd(ClO ₄) ₂
HL				
	[CdL ₂]	410.2 ppm	DMSO- <i>d</i> ₆	0.1 M Cd(ClO ₄) ₂
HL				
	[Cd(HL)Cl ₂]	340.1 ppm	DMSO- <i>d</i> ₆	0.1 M Cd(ClO ₄) ₂
HL	[CdL ₂]	420.3 ppm	DMSO- <i>d</i> ₆	0.1 M Cd(ClO ₄) ₂
	[Cd(HL)Cl ₂ (H ₂ O)]	358 ppm	DMF- <i>d</i> ₇	0.1 M Cd(ClO ₄) ₂
HL				
	[Cd ₂ L ₂]	26.4 ppm 2.9 ppm	DMSO- <i>d</i> ₆	Me ₂ Cd
H₂L	[Cd ₂ L ₂]	111.8 ppm 91.7 ppm	solid state	Cd(NO ₃) ₂ × 4H ₂ O (-100 ppm)

 <p style="text-align: center;">HL</p>	$[\text{Cd}(\text{NO}_3)_2\text{LH}_2]$	198.7 ppm 175.3 ppm	solid state	$\text{Cd}(\text{NO}_3)_2 \times 4\text{H}_2\text{O}$ (-100 ppm) 298 K
	$[\text{Cd}(\text{NO}_3)_2\text{LH}_2]$	88.6 ppm		
	$[\text{CdL}_2]$	461.9 ppm		
	$[\text{Cd}(\text{NO}_3)_2\text{LH}_2]$	294.2 ppm		
 <p style="text-align: center;">HL</p>	$[\text{Cd}(\text{HL})\text{Cl}_2]$	411.5 ppm	DMSO- <i>d</i> ₆ 0.1 M Cd(ClO ₄) ₂	
	$[\text{Cd}(\text{HL})\text{Br}_2]$	378.2 ppm		
	$[\text{Cd}(\text{HL})\text{I}_2]$	301.5 ppm		
	$[\text{Cd}(\text{L})(\text{OAc})_2]$	450.1 ppm 251.4 ppm		
 <p style="text-align: center;">HL</p>	$[\text{Cd}(\text{HL})\text{Cl}_2]$	388.9 ppm	DMSO- <i>d</i> ₆ 0.1 M Cd(ClO ₄) ₂	
	$[\text{Cd}(\text{HL})\text{Br}_2]$	294.6 ppm		
	$[\text{Cd}(\text{HL})\text{I}_2]$	366.6 ppm		
	$[\text{Cd}(\text{L})(\text{OAc})_2]$	254.8 ppm 415.1 ppm		
 <p style="text-align: center;">HL</p>	$[\text{Cd}(\text{HL})\text{Cl}_2]$	408.8 ppm	DMSO- <i>d</i> ₆ 0.1 M Cd(ClO ₄) ₂	
	$[\text{Cd}(\text{HL})\text{Br}_2]$	378.7 ppm		
	$[\text{Cd}(\text{HL})\text{I}_2]$	300.9 ppm		
	$[\text{Cd}(\text{L})(\text{OAc})_2]$	251.6 ppm 449.3 ppm		
 <p style="text-align: center;">HL</p>	$[\text{Cd}(\text{L})(\text{OAc})_2]$	249 ppm 447 ppm	DMSO- <i>d</i> ₆ 0.1 M Cd(ClO ₄) ₂	

	[Cd(L)(OAc) ₂]	247 ppm 440 ppm	DMSO- <i>d</i> ₆ 0.1 M Cd(ClO ₄) ₂
HL			
	[Cd(L)(OAc) ₂]	251 ppm 451 ppm	DMSO- <i>d</i> ₆ 0.1 M Cd(ClO ₄) ₂
HL			

Grapperhaus et al.¹⁴⁹ have studied interesting models of zinc sulfur-methylation proteins. Three cadmium complexes have been prepared and studied by ¹¹³Cd NMR, since the zinc is often substituted by cadmium in zinc-containing proteins to obtain a molecule suitable for NMR measurements (the “spin-spy” approach). The chemical shifts of the obtained complexes are presented on Fig. 44. On the basis of the ¹¹³Cd NMR chemical shifts the coordination modes have been elucidated. The spectra have been referenced to Cd(ClO₄)₂ and measured in pyridine-*d*₃ at 373 K.

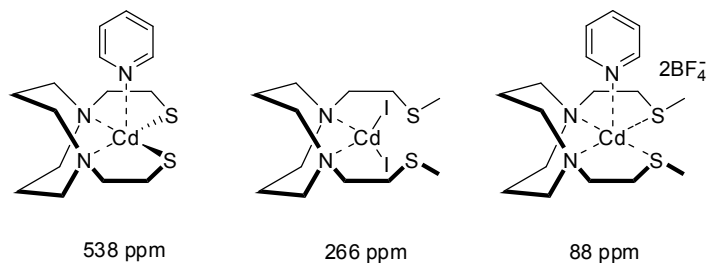


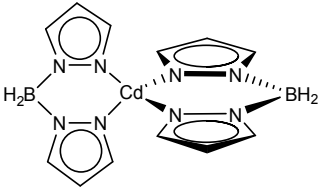
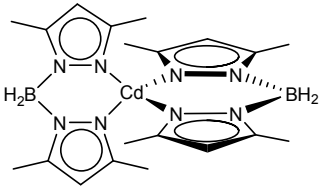
Fig. 44. Structures and ¹¹³Cd NMR chemical shifts of cadmium complexes with N₂S₂ ligands

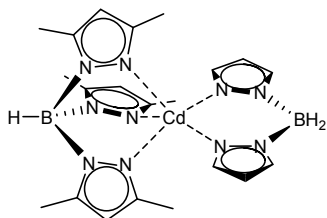
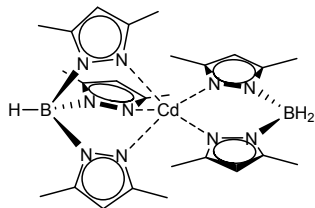
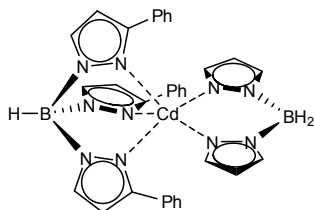
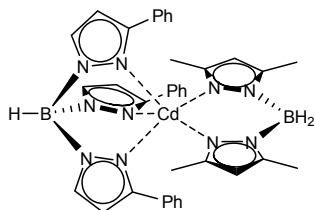
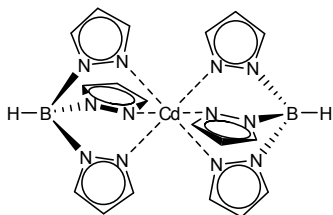
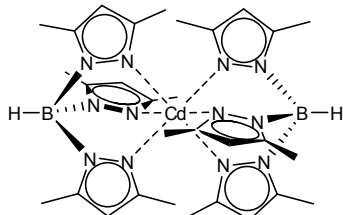
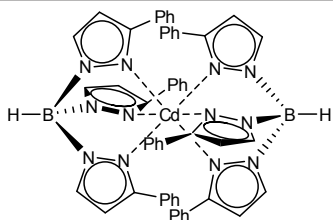
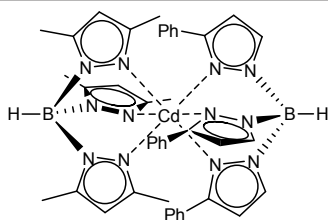
Various polydodal pyrazole containing ligands have been studied in a cadmium coordination chemistry. First results have been published by Reger et al.¹⁵⁰, who have investigated the pyrazolyl-borato molecules. The chemical shifts are collected in Table 25. The authors have pointed out the trends in the chemical shifts vs. the number of coordination nitrogen atoms. Also the series of similar complexes, containing carbon centre in the place of boron atom, have been studied

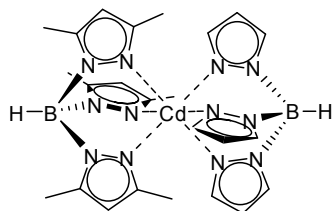
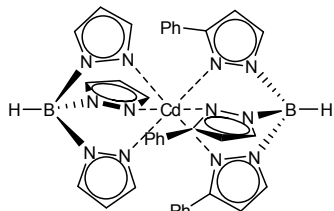
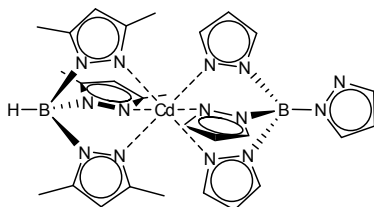
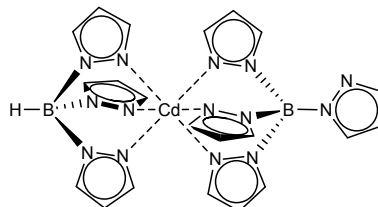
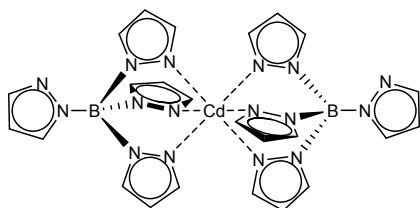
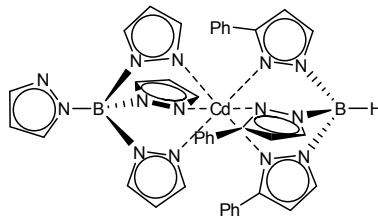
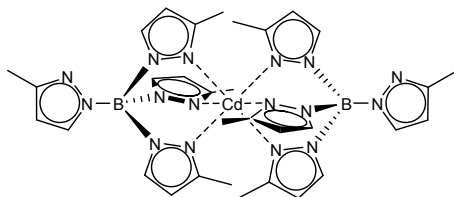
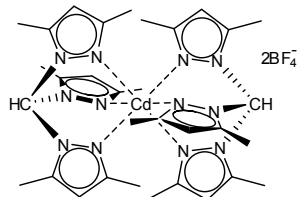
to estimate the effects of the charge on the anchoring atom.¹⁵¹ As the differences between these two series are small, it indicates that the charge in pyrazolyborato ligands is highly localized on boron atoms. The temperature and concentration dependence of the chemical shifts of some complexes has been also studied.¹⁵² Also other pyrazolyl-borato complexes, containing 2,4-pentanedionato or diethylaminodithiocarbamate ligands have been characterized by ¹¹³Cd NMR method.¹⁵³ The authors have discussed the effect of the number of donor atom and their character on chemical shift, as well as an influence of the side groups on this parameter. Sulfur-containing ligands have been shown to produce large deshielding. The spectra have been recorded at 298 K in CDCl₃ or CD₂Cl₂ and referenced to 0.1 M Cd(ClO₄)₂.

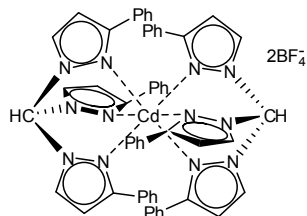
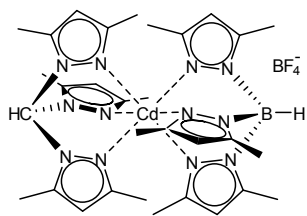
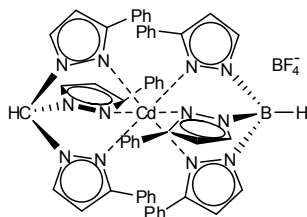
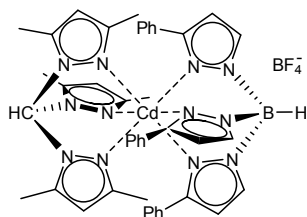
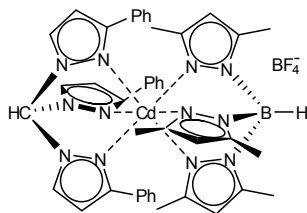
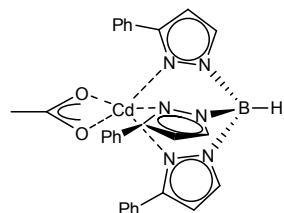
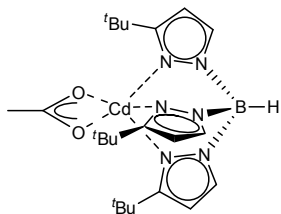
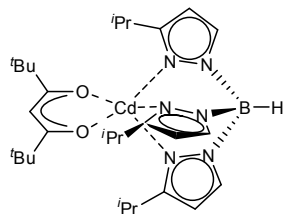
Darensbourg et al.¹⁵⁴ have studied the intermediates in the homopolymerization of oxiranes and related processes. They have studied the model compounds, the complexes of cadmium acetate with hydrotris(3-phenylpyrazolyl)borate ([TP^{Ph}Cd(OAc)₂]) and their adducts with various ethers and thiaethers. The parent compound shows the ¹¹³Cd NMR signal at *ca.* 156 ppm (N₃O₂ coordination). An addition of ether or thiaether (1:1 stoichiometry) does not influence this value significantly at room temperature, however the addition of the high excess of ligand or cooling the sample causes the shift of the equilibrium and the adducts with a Lewis bases are formed. The signals of adducts with ethers ([TP^{Ph}Cd(OAc)₂L], where L = THF, dioxane, propylene oxide, cyclohexane oxide) occur at 82-83 ppm (N₃O₃ coordination sphere), since for the complex with propylene sulfide at 113 ppm (N₃O₂S coordination). As the addition of 2,3-dimethylbutene oxide or toluene does not shift the signal, even at low temperatures, the authors have stated, that these compounds do not coordinate to Cd centre. Similarly, a hydrotris(3-*tert*-butylpyrazolyl)borate ([TP^{tBu}Cd(OAc)₂]) chemical shift is insensitive on the addition of ether (THF) or thiirane, therefore the complex formation is forbidden, probably due to steric factors. The spectra have been referenced to 0.1 M Cd(ClO₄)₂.

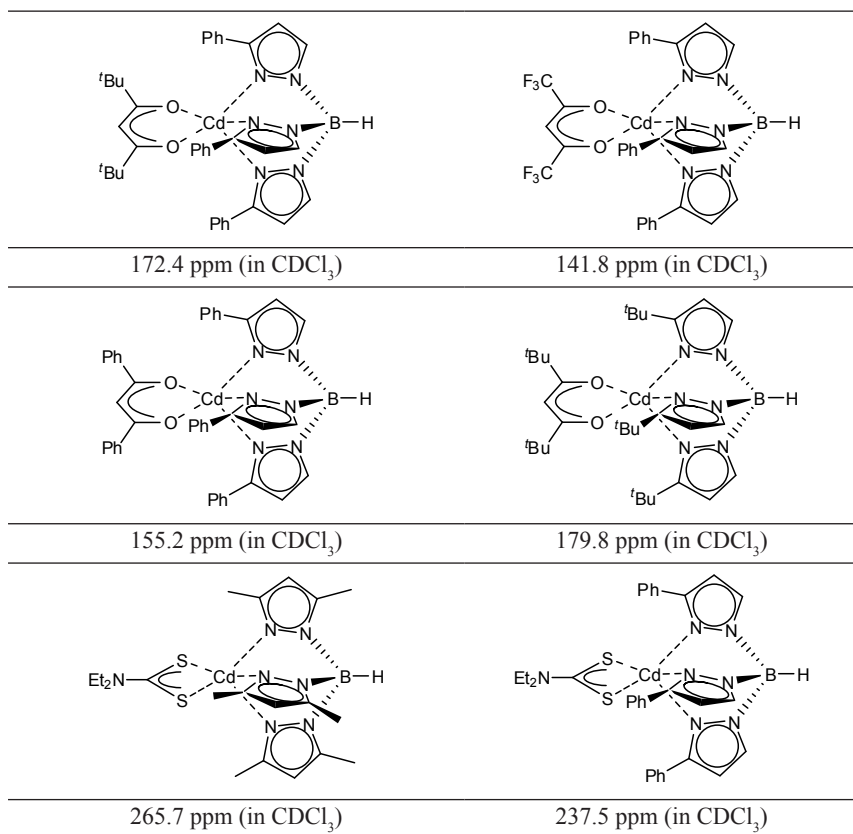
Table 24. ¹¹³Cd NMR data of cadmium-pyrazole ligands

	
298.7 ppm (in CDCl ₃)	303.3 ppm (in CDCl ₃)

225.1 ppm (in CDCl₃)224.3 ppm (in CDCl₃)205.7 ppm (in CDCl₃)193.6 ppm (in CDCl₃)198.3 ppm (in CDCl₃)201.9 ppm (in CDCl₃)
201.5 ppm (in CD₂Cl₂)94.0 ppm (in CDCl₃)148.0 ppm (in CDCl₃; Ref. ¹⁵¹).
147.5 (in CDCl₃; Ref. ¹⁵²)

201.2 ppm (in CDCl_3)138.8 ppm (in CDCl_3)209.0 ppm (in CDCl_3)198.2 ppm (in CDCl_3)221.1 ppm (in CDCl_3)146.2 ppm (in CDCl_3)202.5 ppm (in CDCl_3)207 ppm (in CD_2Cl_2)

116 ppm (in CD_2Cl_2)211 ppm (in CD_2Cl_2)110 ppm (in CDCl_3)140 ppm (in CDCl_3)168 ppm (in CDCl_3)156 ppm (in CD_2Cl_2)146 ppm (in CD_2Cl_2)
148.1 ppm (in CDCl_3)168.1 ppm (in CDCl_3)



Pons and coworkers have studied the Cd(II) complexes with bi- and tridentate nitrogen donor, open chain ligands, pyrazole derivatives.¹⁵⁵ The obtained complexes have been characterized by ¹¹³Cd NMR spectroscopy. First of them, [Cd(bdmae)Cl₂] shows one broad signal at 180 ppm, not changing significantly in temperature range 233-298 K (in CD₃CN). The signal broadening has been explained on the basis of the equilibrium between two modes of coordination of the ligand to Cd ion: $\kappa^2(\text{N}_{\text{pyr}}\text{N}_{\text{pyr}})$ and $\kappa^3(\text{N}_{\text{pyr}}\text{N}_{\text{amino}}\text{N}_{\text{pyr}})$ (Fig. 45).

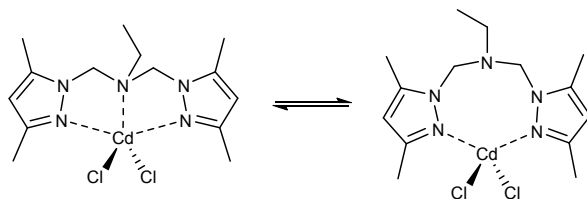


Fig. 45. Equilibrium between two modes of coordination of CdCl_2 by *bdmae*

The spectrum of the second complex (with *bdeae* ligand), consists of two very broad signals, at 200 and 500 ppm (CD_3CN). This is the effect of the equilibrium between four different cadmium containing species (Fig. 46).

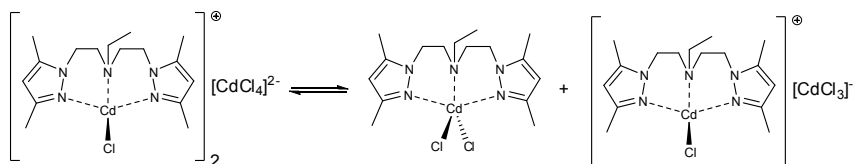


Fig. 46. Equilibrium between three cadmium containing complexes of CdCl_2 with *bdeae*

The oxygen and N-deethylated analogues of the above ligand, the *bdeo* and *bdea* molecules, have been also used as ligands for cadmium ions.¹⁵⁶ The complexes $[\text{Cd}(\text{bdea})(\text{NO}_3)_2]$ and $[\text{Cd}(\text{bdeo})(\text{NO}_3)_2]$ give the signals at -96.3 and -95.2 ppm, respectively (in MeOH/MeOD mixture; vs. 0.1 M $\text{Cd}(\text{ClO}_4)_2$ in D_2O). As this value is very similar to that, obtained for methanol solution of cadmium nitrate (-94.3 ppm), the solid-state CS-MAS spectra have been made. The isotropic chemical shifts of both complexes are *ca.* 106 ppm, therefore it is quite plausible, that the compounds do not dissociate in methanol solution, but that the chemical shift of the complexes are very close to that of the $\text{Cd}(\text{NO}_3)_2$.

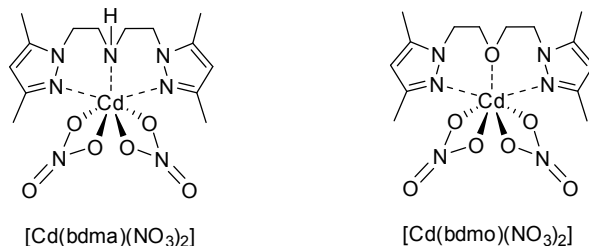


Fig. 47. Cadmium complexes with *bdea* and *bdeo*

For a similar ligand, containing two oxygen atoms in the bridge connecting pyrazol units, chemical shift is 80.1 ppm ($[\text{CdLCl}_2]$ in D_2O , vs. 0.1 M $\text{Cd}(\text{ClO}_4)_2$).¹⁵⁷ The κ^4 NOON coordination mode has been detected for this ligand (Fig. 48).

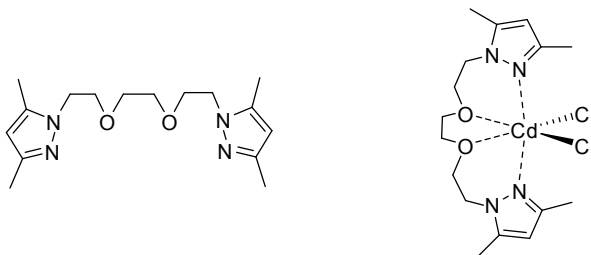


Fig. 48. Dioxatriethylene bridged pyrazole ligand and its CdCl_2 complex

Unique cyclotriphosphazene based pyrazolyl ligand has been obtained by Byun et al.¹⁵⁸ The complexes of these molecules have been obtained, among them one with CdCl_2 , ($[\text{Cd}_2\text{LCl}_2]$). Cadmium centers are equivalent, the ligand acts as a bis(tridentate) one. In solid state at both coordination sites the formation of complex involves two pyrazol N^2 atoms and one phosphazene ring nitrogen atom. In solution the complicate equilibria occurs. At 298 K in a ^{113}Cd NMR spectrum one signal is observed (at *ca.* 328 ppm) and two broad peaks in ^{31}P spectrum. Temperature decreasing causes the signals narrowing and splitting. In ^{31}P NMR spectrum above 253 K two AB_2 spin systems are clearly visible. Between 253 K and 233 K three species of AB_2 spin system in ^{31}P NMR spectrum are observed. At 233 K the ^{113}Cd NMR spectrum shows two signals, at 330 and 275 ppm. The existence of three Cd complexes has been postulated in solution (Fig. 49). The spectra have been measured in CD_2Cl_2 and referenced to 0.1 M $\text{Cd}(\text{ClO}_4)_2$ in D_2O .

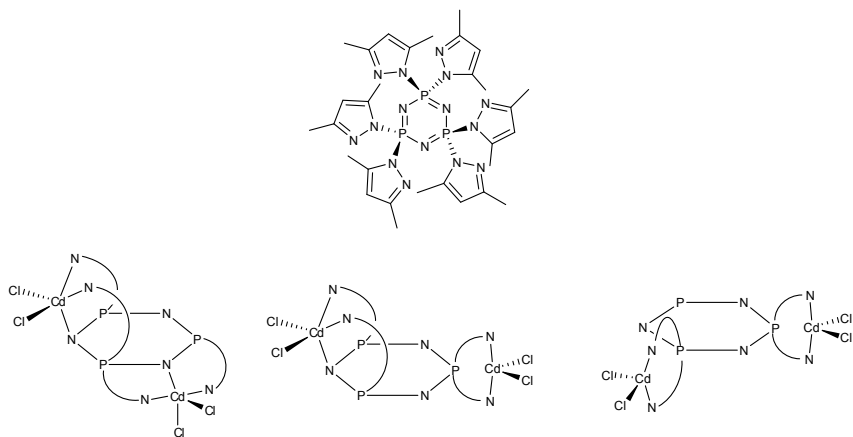


Fig. 49. Cyclotriphosphazene derived pyrazole ligand and its three isomeric complexes with cadmium chloride

Al-Rasi et al.¹⁵⁹ have prepared the dodecanuclear, cubooctaedral cages using two ligands (one complexing two, one – three metal ions) and Cd²⁺ cations. The complex formed: [Cd₁₂(μ³-L¹)₄(μ-L²)₁₂](ClO₄)₂₄ contains three inequivalent metal centers, since nonsymmetrical coordination to L¹ ligand (Fig. 50). Each cadmium ion stays in N₆ coordination environment. The ¹¹³Cd NMR spectrum (in CD₃NO₂) shows three signals in chemical shift range -440 to -450 ppm (no reference given).

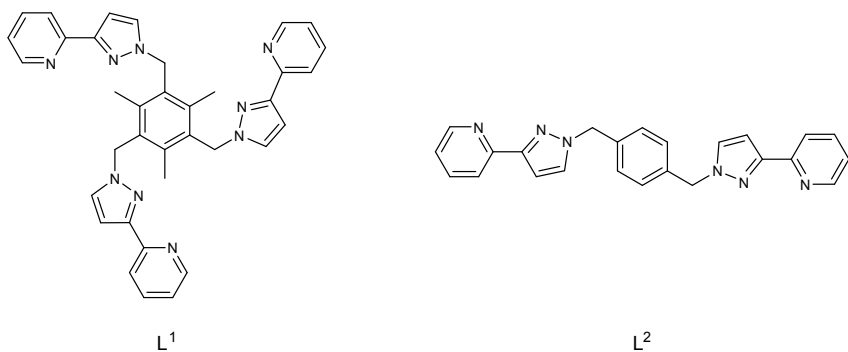


Fig. 50. Structures of N₆ ligands, used for the construction of cubooctaedral Cd₁₂ cage

Some porphyrin and porphyrin-like ligands have been also studied, in a form of cadmium complexes, by ^{113}Cd NMR spectroscopy. Kennedy et al.¹⁶⁰ have measured the solid and liquid state spectra of some texaphyrin complexes with Cd^{2+} ion. The parent compound ($[\text{CdTXP}]\text{Cl}$) shows the signal at 163 ppm (298 K, in CHCl_3 ; relative to 0.1 M $\text{Cd}(\text{ClO}_4)_2$ in water). An addition of benzimidazole causes the formation of $[\text{CdTXP}(\text{BzIm})]\text{Cl}$ complex, with a BzIm molecule in one of the apical position. The signal of Cd nucleus is shifted upfield, to 158 ppm (298 K). If pyridine is used as Lewis base, the effects are not observed, due to the low equilibrium constant of pyridine- $[\text{CdTXP}]\text{Cl}$ adducts formation. At 233 K the exchange is so slow, that the separated signals of free $[\text{CdTXP}]\text{Cl}$ as well as its adducts with pyridine, $[\text{CdTXP}(\text{py})]\text{Cl}$ and $[\text{CdTXP}(\text{py})_2]\text{Cl}$ are well resolved. Pyridine molecule(s) occupies the axial (apical) position(s). The six coordinate complex $[\text{CdTXP}(\text{py})]\text{Cl}$ gives the signal at 148 ppm, while the seven coordinate one, at 210 ppm.

Rodesiler et al.¹⁶¹ have studied the *meso*-tetraphenylporphinatocadmium(II) and its complex with dioxan. The shift of ^{113}Cd signal (in MeOH/DMF mixture) is highly concentration-dependent and varies from 454 to 419 ppm in concentrations range between 2.7 to 16.2 mM. This has been explained by a stacking of the CdTPP molecules in solution. It is very plausible, that the solvent molecules coordinate to Cd atom. Upon addition of dioxan (16.1:1 excess of ether) the cadmium nucleus is deshielded of *ca.* 16 ppm. The stoichiometry of $[\text{Cd}(\text{TPP})(\text{dioxan})_x]$ complex in solution has not been investigated. In crystals dioxan coordinate to Cd atom in both apical positions. The shifts have been measured against 0.1 M $\text{Cd}(\text{ClO}_4)_2$. The pyridine complexes of CdTPP have been studied.¹⁶² The spectra have been recorded in CDCl_3 at 303 K. The $[\text{Cd}(\text{TPP})(\text{pyridine})]$ molecule gives the signal at 426.8 ppm (*vs.* 0.1 M $\text{Cd}(\text{ClO}_4)_2$ in D_2O). While the ^{15}N -labeled porphyrin, the splitting due to interactions with four nitrogen-15 nuclei has been observed ($^1J_{^{113}\text{Cd}-^{15}\text{N}} = 150.1$ Hz). Also the $^4J_{^{113}\text{Cd}-^1\text{H}}$ coupling has been clearly seen (5.0 Hz). The pyridine molecule coordinates in a apical position). The systematic studies of the influence of the Lewis base used on the ^{113}Cd NMR chemical shift of CdTPP have been published in 1985 by the same authors.¹⁶³ The results are collected in Table 26. The complexes of stoichiometry $[\text{Cd}(\text{TPP})(\text{L})]$ and $[\text{Cd}(\text{TPP})\text{L}_2]$ have been obtained. The spectra have been recorded in CDCl_3 at 300 K and referenced to the reference used previously. The cadmium derivatives of protoporphyrin IX ($[\text{CdPPIX}]$) and its dimethyl ester ($[\text{CdPPIXMe}_2]$) have been studied by ^{113}Cd NMR spectroscopy.¹⁶⁴ The $[\text{CdPPIXMe}_2]$ complex shows the huge changes of the NMR spectrum upon temperature variation. In CDCl_3 at 293 K one signal, narrow (411.5 ppm) is observed. The decreasing of the temperature causes the progressive broadening

and finally splitting into two peaks (405.8 & 374.0 ppm at 213 K). This has been explained by a formation of polymeric species, stabilized by apical, intermolecular coordination of carboxylic groups to cadmium atom. In DMF the signal of $[\text{CdPPIXMe}_2]$ is shifted to 390.4 ppm (298 K), due to the interaction with solvent molecules. This sample has been titrated with pyridine. During this reaction upfield shift of ^{113}Cd signal has been observed. The association constant of the formation of $[\text{Cd}(\text{PPIXMe}_2)(\text{pyridine})]$ has been estimated on 0.22 M. The extrapolated value of the chemical shift of cadmium ion in $[\text{Cd}(\text{PPIXMe}_2)(\text{pyridine})]$ molecule has been calculated to be *ca.* 435.5 ppm. Also the $[\text{CdPPIX}]$ complex shows a temperature dependence of the chemical shift. Due to the limited solubility, it has been measured in a pyridine/water (7:3; v/v) in the presence of KOH (2.2 eq. vs. a $[\text{CdPPIX}]$ concentration); at 293 K the chemical shift is 432.3 ppm. The temperature dependence of the chemical shift is caused by a equilibrium between four coordinated Cd atom in $[\text{CdPPIX}]$ and five coordinated in $[\text{Cd}(\text{PPIX})(\text{pyridine})]$. The $[\text{CdPPIX}]$, measured in 0.1 M bicarbonate buffer gives the signal at 345 ppm. The chemical shifts have been measured against 0.1 M $\text{Cd}(\text{ClO}_4)_2$.

Table 25. Structures of cadmium-porphyrin complexes

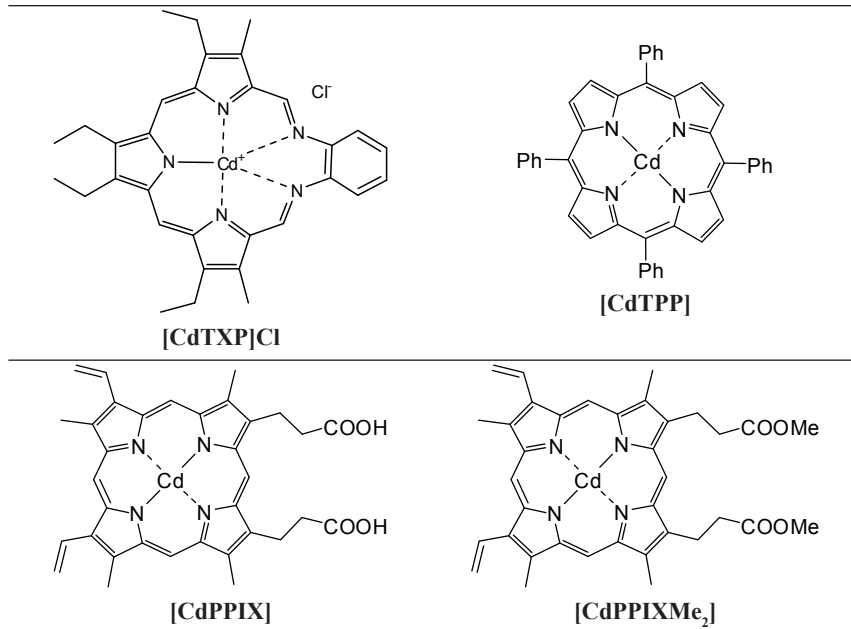


Table 26. Chemical shifts of [CdTPP] complexes with various Lewis bases

Complex	¹¹³ Cd chemical shift	Complex	¹¹³ Cd chemical shift
[Cd(TPP)(pyridine)]	425	[Cd(TPP)(1,2-dimethylimidazole)]	421
[Cd(TPP)(4-methylpyridine)]	423	[Cd(TPP)(tetrahydrofuran)]	434
[Cd(TPP)(4-acetylpyridine)]	432	[Cd(TPP)(tetrahydrofuran) ₂]	425
[Cd(TPP)(3-chloropyridine)]	418	[Cd(TPP)(triphenylphosphine)]	498
[Cd(TPP)(piperidine)]	438	[Cd(TPP)(dioxane)]	425
[Cd(TPP)(1-methylimidazole)]	421	[Cd(TPP)] ¹¹	476

The complexes of the cadmium ion with various piperazine-pyridine ligands have been studied.¹⁶⁵ The spectra have been measured in ethanol/water mixtures (water content depends on a sample solubility) at 223 K against 0.1 M Cd(ClO)₄ in ethanol (Fig. 51). In water, in the temperature range 273-303 K one, averaged signal in ¹³³Cd NMR spectra has been observed. At reduced temperatures, in mixed solvent, the signals of the cadmium ions, complexed in different bonding sites of the ligand, are clearly separated.

Gomblér et al.¹⁶⁶ have reported the ¹¹³Cd NMR data for five diglyme adducts of bis(perfluoroalkyl)cadmium or bis(perfluoroaryl)cadmium, (R_f)₂Cd·diglyme (where R_f are CF₃, C₂F₅, *n*-C₃F₇, *i*-C₃F₇ and C₆F₅). Unfortunately, they have not presented the structures and stoichiometry of the complexes formed. As the free bis(perfluoroalkyl)cadmium compounds are unstable and, therefore, unavailable for comparisons, the trends observed for the above series have been likened to non-fluorinated cadmium compounds, R₂Cd (in free form, not as a complex with diglyme). The chemical shifts of the (R_f)₂Cd·diglyme adducts are: -489.7 (CF₃), -432.4 (C₂F₅), -439.1 (*n*-C₃F₇), -288.3 (*i*-C₃F₇) and -290.0 ppm (C₆F₅). This data are obtained for solutions in CD₃CN at 295 K, referenced against 50 vol% of Me₂Cd in CDCl₃. The predominant contribution into a nuclear shielding of cadmium nuclei originates from the ligand, not from R_f groups. The difference between two perfluoropropyl isomers comes from the electronegativity differences and spatial effects. The bulky *i*-C₃F₇ group decreases the complex stability. The chemical shifts of (R_f)₂Cd·diglyme adducts are highly solvent-dependent, e.g. the signal of bis(pentafluoroethylcadmium)-diglyme adduct in CDCl₃ is of about 34 ppm shielded vs. the compound in CD₃CN. This is the effect of the equilibrium between the (R_f)₂Cd·diglyme and (R_f)₂Cd·CD₃CN complexes.

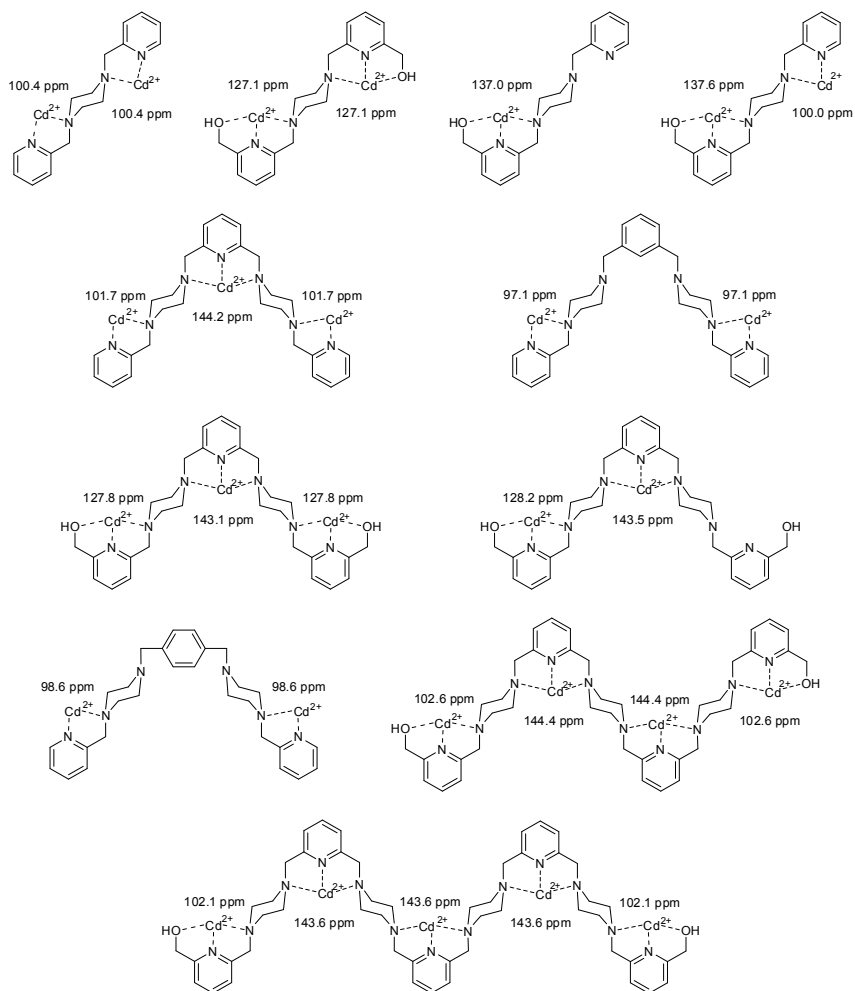


Fig. 51. Structures and chemical shifts of complexes of cadmium ion with a various piperazine-pyridine

2.9.1 Mercury

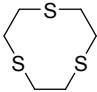
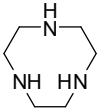
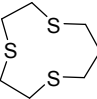
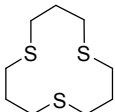
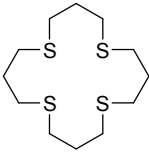
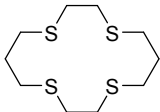
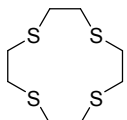
Seven stable isotopes composes a natural mercury. Two of them are NMR active nuclei, however one of them is a quadrupolar nuclei (^{201}Hg ; $I = 3/2$; $Q = 0.5 \times 10^{-28} \text{ m}^2$), while the second (^{199}Hg) has a nuclear spin $I = 1/2$. In consequence, the lighter isotope is preferred in NMR experiments. It has a natural abundance

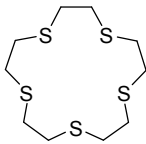
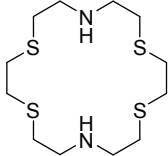
17.0% and a resonance frequency $\nu = 17.827$ MHz (for ^{201}Hg : 13.2 % and 6.599 MHz, respectively). The receptivity in ^{199}Hg NMR experiments is 9.54×10^{-4} that of ^1H (for $^{201}\text{Hg} - 1.90 \times 10^{-4}$). The chemical shift range is *ca.* 4000 ppm. IUPAC recommends a neat Me_2Hg as a reference, but since a deadly poisoning of NMR specialist during preparation of a reference for mercury measurements, other standards are used, e.g. aqueous $\text{Hg}(\text{ClO}_4)_2$.

The O-donor ligands have been only once studied by a ^{199}Hg NMR technique. The complexes formation between crown ethers: 15-crown-5, 18-crown-6 and dibenzo-24-crown-8 (see Fig. 1) and mercury(II) cyanide have been investigated by ^{199}Hg NMR titrations in various solvents (DMSO, DMF). On the basis of observed shifts the stability constants have been calculated. The smallest coronand does not form a complex with $\text{Hg}(\text{CN})_2$ – the shift of the ^{199}Hg signal is not observed upon addition of the ligand. For both larger macrocycles the complex formation has been observed. The authors have not reported the chemical shift of the complexed Hg^{2+} ion.

The interactions with thiamacrocycles have been much detailer studied. The results hitherto published are presented in Table 27. The first published result is a $[\text{Hg}([10]\text{aneS}_3)_2](\text{ClO}_4)_2$ complex and $[\text{Hg}([9]\text{aneS}_3)_2](\text{ClO}_4)_2$.¹³⁶ The first system shows the fast exchange between complexed and free ligand, even at 233 K, so their chemical shift has not been published. The well formed signal has been detected for $[\text{Hg}([10]\text{aneS}_3)_2](\text{PF}_6)_2$, but the authors have not explained the difference in the behavior of these two salts.¹⁶⁷ The further, systematic studies on these kinds of complexes have shown, that the anion effects are rather small (shift of 1-2 ppm).¹⁶⁸ The signal of the mercury ion bonded to $[18]\text{aneS}_6$ ligand has not been observed, both in perchlorate as in hexafluorophosphate salts. As the ^{13}C NMR spectra have been easy to obtain and the ^1H - ^{199}Hg couplings are observed, this is not a result of the fast exchange, that rather of the unusual mercury atom environment. The chemical shift ranges for the definite type of coordination kernels have been denoted. For the complex $[\text{Hg}([9]\text{aneN}_3)](\text{ClO}_4)_2$ two signals have been detected. It is due to the its partial dissociation and presence of both 1:1 and 1:2 complexes in the solution (the downfield shifted signal has been assigned to L_2M compound). Two observed signals for $[\text{Hg}([18]\text{aneS}_4\text{N}_2)]^{2+}$ ion correspond to two diastereoisomers present in a solution. The spectra have been measured at 298 K, and referenced against 0.1 M solution of $\text{Hg}(\text{ClO}_4)_2$ in D_2O (-2250 ppm)

Table 27. ^{199}Hg NMR chemical shifts of mercury ion complexes with macrocyclic ligands

Ligand	Complex	^{199}Hg NMR chemical shifts [ppm]	Half linewidths [Hz]
	$[\text{Hg}([\text{9}]\text{aneS}_3)_2](\text{ClO}_4)_2$	-275 (in CD_3NO_2)	17.19
	$[\text{Hg}([\text{9}]\text{aneS}_3)_2](\text{PF}_6)_2$	-273 (in CD_3NO_2)	28
	$[\text{Hg}([\text{9}]\text{aneS}_3)_2](\text{BF}_4)_2$	-305 (in CD_3CN)	n.r.
	$[\text{Hg}([\text{9}]\text{aneN}_3)_2](\text{ClO}_4)_2$	-948 & -1313 (in CD_3NO_2)	141 & 167
	$[\text{Hg}([\text{10}]\text{aneS}_3)_2](\text{ClO}_4)_2$	-598 (in CD_3NO_2)	326
	$[\text{Hg}([\text{10}]\text{aneS}_3)_2](\text{PF}_6)_2$	-596 (in CD_3NO_2)	161
	$[\text{Hg}([\text{12}]\text{aneS}_3)](\text{ClO}_4)_2$	-795 (in CD_3NO_2)	136
	$[\text{Hg}([\text{16}]\text{aneS}_4)](\text{ClO}_4)_2$	-1120 (in CD_3NO_2)	322
	$[\text{Hg}([\text{14}]\text{aneS}_4)](\text{ClO}_4)_2$	-827 (in CD_3NO_2)	436
	$[\text{Hg}([\text{12}]\text{aneS}_4)](\text{PF}_6)_2$	-718 (in CD_3NO_2)	159

	$[\text{Hg}([\text{15}] \text{aneS}_3)](\text{ClO}_4)_2$	-484 (in CD_3NO_2)	335
	$[\text{Hg}([\text{18}] \text{aneS}_4\text{N}_2)](\text{PF}_6)_2$	-948 & -1313 (in CD_3NO_2)	124 & 211

The thioether complexes with organomercury compounds have been studied by Wiljhelm et al.¹⁶⁹ For two complexes, $[\text{MeHg}([\text{9}] \text{andS}_3)](\text{BF}_4)$ and $[\text{MeHg}([\text{12}] \text{andS}_3)](\text{BF}_4)$ the ^{199}Hg NMR spectra have been recorded. The first complex shows the signal at -194 ppm, while the second one at -886 ppm (both in acetonitrile-*d*₃). The NMR titration experiments of $[\text{MeHg}(\text{OH}_2)](\text{BF}_4)$ by a above ligands have shown that $[\text{MeHg}([\text{9}] \text{andS}_3)](\text{BF}_4)$ complex is stable against solvolysis in acetonitrile, but undergoes fast chemical exchange between free and complexated forms. The second complex, $[\text{MeHg}([\text{12}] \text{andS}_3)](\text{BF}_4)$, is markedly dissociated in acetonitrile. Moreover, the thiaether macrocycles tend to bind more than one methylmercury units in solution. In solid state the methylmercury ion is bonded to three sulfur atoms of one macrocyclic ring ($[\text{MeHg}([\text{9}] \text{andS}_3)](\text{BF}_4)$) or to three S-donor atoms of three different rings and a fluorine atom of BF_4^- anion ($[\text{MeHg}([\text{12}] \text{andS}_3)](\text{BF}_4)$). The authors have not explained the high difference in ^{199}Hg NMR chemical shifts of these complexes. The spectra have been measured against 0.1 M $\text{Hg}(\text{ClO}_4)_2$ in D_2O (-2250 ppm) at 290 K.

A scattered examples of the mercury complexes with polydentate phosphine ligands, studied by ^{199}Hg NMR have been published. The complex of methylmercury ion with a tris[2-(diphenylphosphino)ethyl]amine (*np*₃) has been characterized by this technique.¹⁷⁰ At 296 K the spectrum shows a quartet at 2 442 ppm ($^2J_{^{199}\text{Hg}-\text{1H}} = 172$ Hz), while at 205 K, a quartet-of-quartets at 2 515 ppm ($^2J_{^{199}\text{Hg}-\text{1H}} = 172$ Hz; $^1J_{^{199}\text{Hg}-\text{31P}} = 75$ Hz). The lost of Hg-P coupling occurs at *ca.* 230 K. The value of $^1J_{^{199}\text{Hg}-\text{31P}}$ coupling continuously increases with a temperature decreasing and a increasing of the concentration of the solution. This indicates the dissociation of the complex in a solution and the rapid interconversion between the isomers. The analogous complexes with ethylmercury ($[\text{EtHg}(\text{np}_3)](\text{TfO})$) and phenylmercury ($[\text{PhHg}(\text{np}_3)](\text{TfO})$) show similar chemical shifts (2 380 ppm at 243 K for the first one and 2 225 ppm at 292 K for the second compound) but distinctly higher Hg-P coupling constants, i.e. 443 and 318 Hz,

respectively.¹⁷¹ Analogous complexes with tris[2-(diphenylphosphino)ethyl]amine (pp_3) have been obtained: $[\text{PhHg}(pp_3)](\text{BF}_4)$ and $[\text{MeHg}(pp_3)](\text{BF}_4)$.¹⁷² These ones give the signals at 2 004 and 2 192 ppm, respectively (at 223 K). In solid state, as for complexes with np_3 ligand, Hg atom is bonded in P_3 kernel, however the $\text{P}(\text{CH}_2)_3$ phosphor atom participates in complex formation in the place of one $\text{P}(\text{Ph}_2)$ P-donor. In solution all phosphor atom are coupled with Hg. The signal appears as a doublet of quartets, while the coupling constants with $\text{P}(\text{CH}_2)_3$ are much higher (2 004 & 1 745 Hz for $[\text{PhHg}(pp_3)](\text{BF}_4)$ and $[\text{MeHg}(pp_3)](\text{BF}_4)$, respectively) than with a $\text{P}(\text{Ph}_2)$ atom (598 & 584 Hz, respectively). The authors have postulated, that in solution these complexes retain the coordination observed in solid state, but undergo a rapid exchange of terminal $\text{P}(\text{Ph}_2)$ phosphorus. The spectra of all above discussed phosphine complexes have been recorded in dichloromethane- d_2 against 0.1 M $\text{Hg}(\text{ClO}_4)_2$ in 0.1 M HClO_4 .

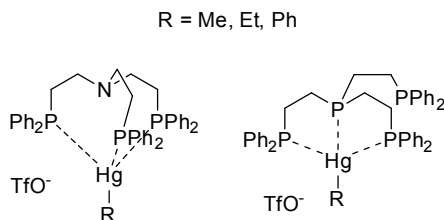
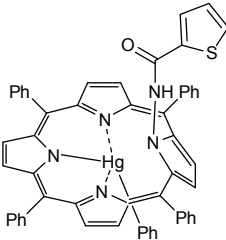
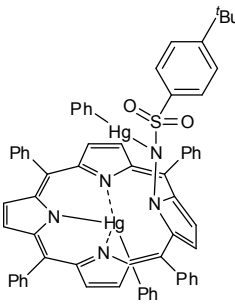
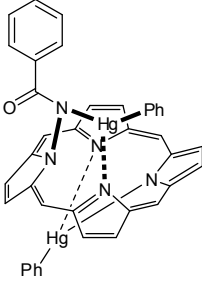
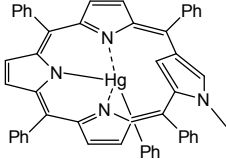


Fig. 52. Tripodal phosphine complexes with organomercury ions

The complexes of porphyrin and porphyrin-like ligands with (organo) mercury cations have been studied by Tung et al.¹⁸⁸⁻¹⁹⁰ The authors have reported the ¹⁹⁹Hg NMR chemical shifts of these compounds (Table 28). The N-substituted *meso*-tetraphenylporphyrin (TpCOTPP) forms a 1:1 complex with phenylmercury ion. The thiophene unit does not participate in mercury complexation. The ¹⁹⁹Hg NMR chemical shift of this compound is -1108 ppm (in CD₂Cl₂; at 293 K). The similar ligand, (BuBSOTPP) bonds two phenylmercury ions. One of them is coordinated by three pyrrole nitrogen atoms, while the second one bonds to sulfoamide N-atom. The spectrum of this compound shows two signal, at -1 074 & -1 191 ppm, respectively (in CDCl₃; at 293 K). The first one has been assigned to HgN₃ center, while the second one to HgN one. Other complex, containing two metal centers, has been obtained from N-benzamido derivative of TPP (BATPP). In the ¹⁹⁹Hg NMR spectrum two signals have been detected, at -1 088 ppm (³J_{199Hg-H} = 188 Hz) and -1 119 ppm (³J_{199Hg-H} = 177 Hz). The authors have assigned the downfield shifted signal to benzamide nitrogen

atom complexed one. Spectrum has been obtained for CDCl_3 at 293 K). In the complex of inverted porphyrin (MeITPP) the mercury nucleus gives the signal at -1037 ppm ($^3J_{199\text{Hg}-\text{H}} = 172$ Hz) (solution in CDCl_3 ; 293 K). All mercury-199 spectra of porphyrin-Hg complexes have been measured against 0.5 M solution of $\text{PhHg}(\text{OAc})$ in $\text{DMSO}-d_6$ (-1439.5 ppm).

Table 28. Structures of mercury-porphyrin complexes

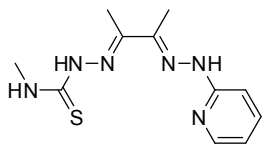
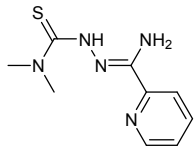
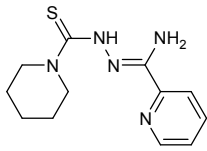
		
[PhHg(TpCOTPP)]	[(PhHg)₂(BuBSOTPP)]	[(PhHg)₂(BATPP)]
		
[PhHg(MeITPP)]		

Calatayud et al. have characterized some thiosemicarbazone complexes of Hg^{2+} and characterize them by ^{199}Hg spectra.^{157,191} Similar structures have been studied by Bermejo et al.¹⁴⁸

Interesting structures, containing mercurous dimer (Hg_2^{2+}) encapsulated inside the metallocryptand ($\text{M} = \text{Pt}(0)$ or $\text{Pd}(0)$) cavity have been studied by Catalano and coworkers (Fig. 53).¹⁷³ The obtained complexes have been characterized by NMR spectroscopy and X-ray crystallography. The signals have been observed at 770.8 ppm ($\text{M} = \text{Pt}$; $^1J_{199\text{Hg}-31\text{P}} = 620$ Hz; $^1J_{199\text{Hg}-195\text{Pt}} = 1602$ Hz) and 833 ppm ($\text{M} = \text{Pd}$; $^1J_{199\text{Hg}-31\text{P}} = 638$ Hz). The Hg_2^{2+} cluster undergoes fast motion inside the cage, therefore all phosphorus atoms are equivalent (the ^{199}Hg signal is splitted onto a triplet of septets). The spectra have been measured in CD_2Cl_2 at 298 K against $\text{Hg}(\text{OAc})_2$ in $\text{DMSO}-d_6$. Similar metallocryptand, based on $\text{Au}\cdots\text{P}$ interaction, complex one Hg atom.¹⁷⁴ The chemical shift of this

compound is -1199.8 ppm ($^1J_{199\text{Hg}-31\text{P}} = 48$ Hz) in CD_3CN , at 298 K (reference not given).

Table 29. ^{119}Hg NMR data of mercury-hydrazone complexes

Ligand	Complex	Chemical shift	Solvent	Experimental conditions
 H₂L	$[\text{Hg}(\text{H}_2\text{O})(\text{LH}_2)](\text{NO}_3)_2$	-1209.3	$\text{DMSO}-d_6$	Me_2Hg
	$[\text{Hg}(\text{NO}_3)(\text{LH})]$	-1232.1	$\text{DMSO}-d_6$	Me_2Hg
	$[\text{Hg}(\text{H}_2\text{O})(\text{L})]$	-1222.0	$\text{DMSO}-d_6$	Me_2Hg
 HL	$[\text{Hg}(\text{L})\text{Cl}]_2$	-1059	$\text{DMF}/\text{D}_2\text{O}$	0.1 M Me_2Hg
 HL	$[\text{Hg}(\text{HL})\text{Cl}_2]$	-1051	$\text{DMSO}-d_6$	n.r.

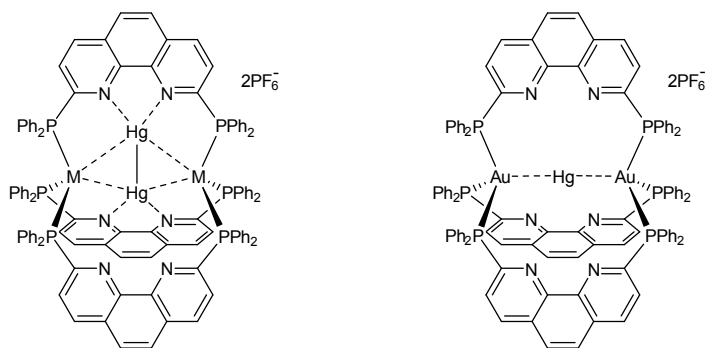


Fig. 53. Structures of metalocryptands containing mercury(0) species

3. Conclusions

As it has been shown, the NMR spectroscopy of transition metal nuclides offers an excellent tool for supramolecular chemistry. Unfortunately, the possibilities given by these methods are often underestimated. In consequence, many supramolecular systems, containing transition metal elements are not studied by less-common nuclei NMR. This decreases the number of information about the particular system, about the structure, interaction and dynamics of the supermolecule. Moreover, this reduces the set of the data, available for comparison. In the author opinion, more attention should be paid to the multinuclear magnetic resonance studies, even of the hardly observed nuclei, as ^{109}Ag or ^{103}Rh .

Acknowledgements

This work was supported by the Polish National Science Center (NCN; grant no. N N204 155840).

References

1. Meehan, P.R.; Willey, G.R. *Inorg. Chim. Acta* **1999**, 284, 71.
2. Brown, M.D.; Levason, W.; Murray, D.C.; Popham, M.C.; Reid, G.; Webster, M. *Dalton Trans.* **2003**, 857.
3. Gierczyk, B.; Schroeder, G. *Pol. J. Chem.* **2003**, 77, 1741.
4. Bethune, D.S.; Yannoni, C.S.; Hoinkis, M.; de Vries, M.; Salem, J.R.; Crowder, M.S.; Johnson, R.D. *Z. Phys. Chem.* **1993**, 153-158.
5. Miyake, Y.; Suzuki, S.; Kojima, Y.; Kikuchi, K.; Kobayashi, K.; Nagase, S.; Kainosho, M.; Achiba, Y.; Maniwa, Y.; Fisher, K. *J. Phys. Chem.* **1996**, 100, 9579.
6. Iiduka, Y.; Wakahara, T.; Nakajima, K.; Tsuchiya, T.; Nakahodo, T.; Maeda, Y.; Akasaka, T.; Mizorogi, N.; Nagase, S. *Chem. Comm.* **2006**, 2057.
7. Krause, M.; Ziegs, F.; Popov, A.A.; Dunsch, L. *ChemPhysChem* **2007**, 8, 537.
8. Okimoto, H.; Hemme, W.; Ito, Y.; Sugai, T.; Kitauro, R.; Eckert, H.; Shinohara, H. *Nano* **2008**, 3, 21.
9. Kurihara, H.; Lu, X.; Iiduka, Y.; Mizorogi, N.; Slanina, Z.; Tsuchiya, T.; Akasaka, T.; Nagase, S. *J. Am. Chem. Soc.* **2011**, 133, 2382.
10. Wang, T.-S.; Feng, L.; Wu, J.-Y.; Xu, W.; Xiang, J.-F.; Tan, K.; Ma, Y.-H.; Zheng, J.-P.; Jiang, L.; Lu, X.; Shu, C.-Y.; Wang, C.-R. *J. Am. Chem. Soc.* **2010**, 132, 16362.

11. Wang, X.; Zuo, T.; Olmstead, M.M.; Duchamp, J.C.; Glass, T.E.; Cromer, F.; Balch, A. L.; Dorn, H.C. *J. Am. Chem. Soc.* **2006**, 128, 8884.
12. Yang, S.; Popov, A.A.; Chen, C.; Dunsch, L. *J. Phys. Chem. C* **2009**, 113, 7616.
13. Zhang, Y.; Popov, A.A.; Schiemenz, S.; Dunsch, L. *Chem. Eur. J.* **2012**, 18, 9691.
14. Dunsch, L.; Yang, S.; Zhang, L.; Svitova, A.; Oswald, S.; Popov, A.A. *J. Am. Chem. Soc.* **2010**, 132, 5413.
15. Chen, N.; Beavers, C.M.; Mulet-Gas, M.; Rodríguez-Fortea, A.; Munoz, E.J.; Li, Y.Y.; Olmstead, M.M.; Balch, A.L.; Poblet, J.M.; Echegoyen, L. *J. Am. Chem. Soc.* **2012**, 134, 7851.
16. Lu, X.; Nakajima, K.; Iiduka, Y.; Nikawa, H.; Mizorogi, N.; Slanina, Z.; Tsuchiya, T.; Nagase, S.; Akasaka, T. *J. Am. Chem. Soc.* **2011**, 133, 19553.
17. Hall, C.D.; Tucker, J.H.R.; Sheridan, A.; Chu, S.Y.F.; Williams, D.J. *J. Chem. Soc. Dalton. Trans.* **1992**, 3133.
18. Hall, C.D.; Tucker, J.H.R.; Chu, S.Y.F. *J. Organomet. Chem.* **1993**, 448, 175.
19. Summers, S.P.; Abboud, K.A.; Brey, W.S.; Bechtel, B.; Palenik, R.C.; Palenik, G.J. *Polyhedron* **1996**, 15, 3101.
20. Bradley, D.C.; Chudzynska, H.; Hursthouse, M.B.; Motevalli, M. *Polyhedron* **1993**, 12, 1907.
21. Jindal, A.K.; Merritt, M.E.; Suh, E.H.; Malloy, C.R.; Sherry, A.D.; Kovács, Z. *J. Am. Chem. Soc.* **2010**, 132, 1784.
22. Pulkody, K.P.; Norman, T.J.; Parker, D.; Royle, L.; Broan, C.J. *J. Chem. Soc. Perkin. Trans. 2* **1993**, 605.
23. Miéville, P.; Jannin, S.; Helm, L.; Bodenhausen, G. *J. Am. Chem. Soc.* **2010**, 132, 5006.
24. Lumata, L.; Merritt, M.; Malloy, C.; Sherry, A.D.; Kovacs, Z. *Appl. Magn. Reson.* **2012**, 43, 69.
25. Lumata, L.; Jindal, A.K.; Merritt, M.E.; Malloy, C.R.; Sherry, A.D.; Kovacs, Z. *J. Am. Chem. Soc.* **2011**, 133, 8673.
26. Rudovský, J.; Botta, M.; Hermann, P.; Koridze, A.; Aime, S. *Dalton Trans.* **2006**, 2323.
27. Popovici, C.; Fernandez, I.; Oña-Burgos, P.; Rocés, L.; Garcia-Granda, S.; Ortiz, F.L. *Dalton Trans.* **2011**, 40, 6691.
28. Löble, M.W.; Casimiro, M.; Thielemann, D.T.; Oña-Burgos, P.; Fernández, I.; Roesky, P. W.; Breher, F. *Chem. Eur. J.* **2012**, 18, 5325.

29. Zimmermann, M.; Estler, F.; Herdtweck, E.; Törnroos, K.W.; Anwander, R. *Organometallics* **2007**, 26, 6029.
30. Fu, W.; Xu, L.; Azurmendi, H.; Ge, J.; Fuhrer, T.; Zuo, T.; Reid, J.; Shu, C.; Harich, K.; Dorn, H.C. *J. Am. Chem. Soc.* **2009**, 131, 11762.
31. Chen, Z.; Dettman, H.; Detellier, C. *Polyhedron* **1989**, 8, 2029.
32. Kimura, K.; Utsumi, T.; Teranishi, T.; Yokoyama, M.; Sakamoto, H.; Okamoto, M.; Arakawa, R.; Moriguchi, H.; Miyaji, Y. *Angew. Chem. Int. Ed.* **1997**, 36, 2452.
33. Israëli, Y.; Bonal, C.; Detellier, C.; Morel, J.P.; Morel-Desrosiers, N. *Can. J. Chem.* **2002**, 80, 163.
34. Kumar, P.A. *Ind. J. Chem.* **1998**, 37A, 460.
35. Akasaka, T.; Nagase, S.; Kobayashi, K.; Walchli, M.; Yamamoto, K.; Funasaka, H.; Kako, M.; Hoshino, T.; Erata, T. *Angew. Chem. Int. Ed.* **1997**, 36, 1643.
36. Akasaka, T.; Wakahara, T.; Nagase, S.; Kobayashi, K.; Waelchli, M.; Yamamoto, K.; Kondo, M.; Shirakura, S.; Okubo, S.; Maeda, Y.; Kato, T.; Kako, M.; Nakadaira, Y.; Nagahata, R.; Gao, X.; van Caemelbecke, E.; Kadish, K.M. *J. Am. Chem. Soc.* **2000**, 122, 9316.
37. Kato, H.; Taninaka, A.; Sugai, T.; Shinohara, H. *J. Am. Chem. Soc.* **2003**, 125, 7782.
38. Wakahara, T.; Yamada, M.; Takahashi, S.; Nakahodo, T.; Tsuchiya, T.; Maeda, Y.; Akasaka, T.; Kako, M.; Yoza, K.; Horn, E.; Mizorogi, N.; Nagase, S. *Chem. Commun.* **2007**, 2680.
39. Yamada, M.; Wakahara, T.; Nakahodo, T.; Tsuchiya, T.; Maeda, Y.; Akasaka, T.; Yoza, K.; Horn, E.; Mizorogi, N.; Nagase, S. *J. Am. Chem. Soc.* **2006**, 128, 1402.
40. Yamada, M.; Minowa, M.; Sato, S.; Kako, M.; Slanina, Z.; Mizorogi, N.; Tsuchiya, T.; Maeda, Y.; Nagase, S.; Akasaka, T. *J. Am. Chem. Soc.* **2010**, 132, 17953.
41. Dietel, A.M.; Döring, C.; Glatz, G.; Butovskii, M.V.; Tok, O.; Schappacher, F.M.; Pöttgen, R.; Kempe, R. *Eur. J. Inorg. Chem.* **2009**, 1051.
42. Dietel, A.M.; Tok, O.; Kempe, R. *Eur. J. Inorg. Chem.* **2007**, 4583.
43. Zhang, X.; Meuwly, M.; Woggon, W.-D. *J. Inorg. Biochem.* **2004**, 98, 1967.
44. Nielsen, U.G.; Hazell, A.; Skibsted, J.; Jakobsen, H.J.; McKenzie, C.J. *CrystEngComm* **2010**, 12, 2826.
45. Colpas, G.J.; Hamstra, B.J.; Kampf, J.W.; Pecoraro, V.L. *J. Am. Chem. Soc.* **1996**, 118, 3469.

46. Časný, M.; Rehder, D. *Dalton Trans.* **2004**, 839.
47. Martinez, A.; Robert, V.; Gornitzka, H.; Dutasta, J.-P. *Chem. Eur. J.* **2010**, 16, 529.
48. Browne, W.R.; Ligtenbarg, A. G.J.; De Boer, J.W.; Van Den Berg, T.A.; Lutz, M.; Spek, A.L.; Hartl, F.; Hage, R.; Feringa, B.L. *Inorg. Chem.* **2006**, 45, 2903.
49. Ligtenbarg, A.G.J.; Spek, A.L.; Hage, R.; Feringa, B.L. *J. Chem. Soc. Dalton Trans.* **1999**, 659.
50. Beard, C.D.; Barrie, R.J.; Evans, J.; Levason, W.; Reid, G.; Spicer, M.D. *Eur. J. Inorg. Chem.* **2006**, 4391.
51. Plass, W. *Z. anorg. allg. Chem.* **1997**, 623, 461.
52. Jura, M.; Levason, W.; Reid, G.; Webster, M. *Dalton Trans.* **2009**, 7811.
53. Barton, A.J.; Connolly, J.; Levason, W.; Mendia-Jalon, A.; Orchard, S.D.; Reid, G. *Polyhedron* **2000**, 19, 1373.
54. Davis, M.F.; Levason, W.; Light, M.E.; Ratnani, R.; Reid, G.; Saraswat, K.; Webster, M. *Eur. J. Inorg. Chem.* **2007**, 1903.
55. Katayev, E.A.; Kolensikov, G.V.; Khrustalev, V.N.; Antipin, M.Y.; Askerov, R.K.; Maharramov, A.M.; German, K.E.; Kirakosyan, G.A.; Tananaev, I.G.; Timoffea, T.V.J. *Radioanal. Nucl. Chem.* **2009**, 282, 385.
56. Kolensikov, G.V.; German, K.E.; Kirakosyan, G.A.; Tananaev, I.G.; Ustynyuk, Y.A.; Khrustalev, V.N.; Katayev, E.A. *Org. Biomol. Chem.* **2011**, 9, 7358.
57. La Mar, G.N.; Dellinger, C.M.; Sankar, S.S. *Biochem. Biophys. Res. Commun.* **1985**, 128, 628.
58. Baltzer, L.; Landergren, M. *J. Chem. Soc. Chem. Commun.* **1987**, 32.
59. Baltzer, L.; Landergren, M. *J. Am. Chem. Soc.* **1990**, 112, 2804.
60. Landergren, M.; Baltzer, L. *J. Chem. Soc. Perkin. Trans. 2* **1992**, 355.
61. Baltzer, L.; Becker, E.D.; Averill, B.A.; Hutchinson, J.M.; Gansow, O.A. *J. Am. Chem. Soc.* **1984**, 106, 2444.
62. Kalodimos, C.G.; Gerothanassis, I.P.; Pierattelli, R.; Troganis, A. *J. Inorg. Biochem.* **2000**, 79, 371.
63. Kalodimos, C.G.; Gerothanassis, I.P.; Hawkes, G.E. *Biospectroscopy* **1998**, 4, S57.
64. Mink, L.M.; Polam, J.R.; Christensen, K.A.; Bruck, M.A.; Walker, F.A. *J. Am. Chem. Soc.* **1995**, 117, 9329.
65. Polam, J.R.; Wright, J.L.; Christensen, K.A.; Walker, F.A.; Flint, H.; Winkler, H.; Grodzicki, M.; Trautwein, A.X. *J. Am. Chem. Soc.* **1996**, 118, 5272.

66. Godbout, N.; Havlin, R.; Salzmann, R.; Debrunner, P.G.; Oldfield, E. *J. Phys. Chem. A* **1998**, 102, 2342.
67. Sanders, L.K.; Arnold, W.D.; Oldfield, E. *J. Porphyrins Phtalocyanines* **2001**, 5, 323.
68. Oña-Burgos, P.; Casimiro, M.; Fernández, I.; Navarro, A.V.; Fernández Sánchez, J.F.; Carretero, A.S.; Fernández Gutiérrez, A. *Dalton Trans.* **2010**, 6231-6238.
69. Kalodimos, C.G.; Gerothanassis, I.P.; Rose, E.; Hawkes, G.E.; Pierattelli, R. *J. Am. Chem. Soc.* **1999**, 121, 2903.
70. Gerothanassis, I.P.; Kaladimos, C.G.; Hawkes, G.E.; Haycock, P. *J. Magn. Reson.* **1998**, 131, 163.
71. Lawrance, G.A.; Lay, P.A.; Sargeson, A.M. *Inorg. Chem.* **1990**, 29, 4808.
72. Tavagnacco, C.; Belducci, G.; Costa, G.; Täschler, K.; von Philipsborn, W. *Helv. Chim. Acta* **1990**, 73, 1469.
73. Voloshin, Y.Z.; Belsky, V.K.; Trachevskii, V.V. *Polyhedron* **1992**, 11, 1939.
74. Drago, R.S.; Elias, J.H. *J. Am. Chem. Soc.* **1977**, 99, 6570.
75. Omar, H.A.A.; Moore, P.; Alcock, N.W. *J. Chem. Soc. Dalton. Trans.* **1994**, 2631.
76. Kapanadze, T.S.; Kokunov, Y.V.; Buclaev, Y.A. *Polyhedron* **1990**, 2803.
77. Grohmann, A.; Heinemann, F.W.; Kofod, P. *Inorg. Chim. Acta* **1999**, 286, 98.
78. Cavigliasso, G.E.; Stranger, R.; McClintock, L.F.; Cheyne, S.E.; Jaffray, P.M.; Baxter, K.E.; Blackman, A.G. *Dalton Trans.* **2008**, 2433.
79. Chandrasekhar, S.; McAuley, A. *Inorg. Chem.* **1993**, 31, 480.
80. Grant, G.J.; Shoup, S.S.; Hadden, C.E.; VanDerveer, D.G. *Inorg. Chim. Acta* **1998**, 274, 192.
81. Jenkinson, J.J.; Levason, W.; Perry, R.J.; Spicer, M.D. *J. Chem. Soc. Dalton. Trans.* **1989**, 453.
82. Levason, W.; Quirk, J.J.; Reid, G. *J. Chem. Soc. Dalton Trans.* **1996**, 3713.
83. Connolly, J.; Forder, R.J.; Goodban, G.W.; Pope, S.J.A.; Predel, M.; Reid, G. *Polyhedron* **1999**, 18, 3553.
84. Hendry, P.; Ludi, A. *Adv. Inorg. Chem.* **1990**, 35, 117.
85. Iida, M.; Yamamodo, M.; Fujita, N. *Bull. Chem. Soc. Jpn.* **1996**, 69, 3217.
86. Hagen, K.I.; Schwab, C.M.; Edwards, J.O.; Sweigart, D.A. *Inorg. Chem.* **1986**, 25, 978.

87. Hagen, K.I.; Schwab, C.M.; Edwards, J.O.; Jones, J.G.; Lawler, R.G.; Sweigart, D.A. *J. Am. Chem. Soc.* **1988**, 110, 7024.
88. Cassidei, L.; Bang, H.; Edwards, J.O.; Lawler, R.G. *J. Phys. Chem.* **1991**, 95, 7186.
89. Bang, H.; Edwards, J.O.; Kim, J.; Lawler, R.G.; Reynolds, L.K.; Ryan, W.J.; Sweigart, D.A. *J. Am. Chem. Soc.* **1992**, 114, 2843.
90. Medek, A.; Frydman, V.; Frydman, L. *J. Phys. Chem. B* **1997**, 101, 8959.
91. Bang, H.; Cassidei, L.; Danford, H.; Edwards, J.O.; Hagen, K.I.; Krueger, C.; Lachowitz, J.; Schwab, C.M.; Sweigart, D.A.; Zhang, Z. *Magn. Reson. Chem.* **1989**, 27, 1117.
92. Munro, O.Q.; Shabalala, S.C.; Brown, N. *J. Inorg. Chem.* **2001**, 40, 3303.
93. Medek, A.; Frydman, V.; Frydman, L. *Proc. Nat. Acad. Sci. USA* **1997**, 94, 14237.
94. Chemaly, S.M.; Brown, K.L.; Fernandes, M.A.; Munro, O.Q.; Grimmer, C.; Marques, H.M. *Inorg. Chem.* **2011**, 50, 8700.
95. Munro, O.Q.; Camp, G.L.; Carlton, L. *Eur. J. Inorg. Chem.* **2009**, 2512.
96. Balch, A.L.; Fung, E.Y.; Nagle, J.K.; Olmstead, M.M.; Rowley, S.P. *Inorg. Chem.* **1993**, 32, 3295.
97. Grant, G.J.; Galas, D.F.; Jones, M.W.; Loveday, K.D.; Pennington, W.T.; Schimek, G.L.; Eagle, C.T.; Vanderveer, D.G. *Inorg. Chem.* **1998**, 37, 5299.
98. Grant, G.J.; Brandow, C.G.; Galas, D.F.; Davis, J.P.; Pennington, W.T.; Valente, E.J.; Zubkowski, J.D. *Polyhedron* **2001**, 20, 3333.
99. Grant, G.J.; Galas, D.F.; VanDerveer, D.G. *Polyhedron* **2002**, 23, 879.
100. Grant, G.J.; Benefield, D.A.; Vanderveer, D.G. *Dalton Trans.* **2009**, 8605.
101. Janzen, D.E.; Patel, K.N.; VanDerveer, D.G.; Grant, G.J. *Chem. Commun.* **2006**, 3540.
102. Grant, G.J.; Naik, R.D.; Janzen, D.E.; Benefield, D.A.; Vanderveer, D.G. *Supramol. Chem.* **2010**, 22, 109.
103. Grant, G.J. *Dalton Trans.* **2012**, 41, 8745.
104. Grant, G.J.; Poullaos, I.M.; Galas, D.F.; VanDerveer, D.G.; Zubkowski, J.D.; Valente, E.J. *Inorg. Chem.* **2001**, 40, 564.
105. Grant, G.J.; Carter, S.M.; Russell, A.L.; Poullaos, I.M.; VanDerveer, D.G. *J. Organomet. Chem.* **2001**, 637-639, 683.
106. Grant, G.J.; Galas, D.F.; Poullaos, I.M.; Carter, S.M.; VanDerveer, D.G. *J. Chem. Soc. Dalton Trans.* **2002**, 2973-2980.

107. Grant, G.J.; Pool, J.A.; VanDerveer, D.G. *Dalton Trans.* **2003**, 3981-3984.
108. Grant, G.J.; Patel, K.N.; Helm, M.L.; Mehne, L.F.; Klinger, D.W.; VanDerveer, D.G. *Polyhedron* **2004**, 23, 1361.
109. Grant, G.J.; Talbott, N.N.; Bajic, M.; Mehne, L.F.; Holcombe, T.J.; VanDerveer, D.G. *Polyhedron* **2012**, 31, 89.
110. Bennet, M.A.; Canty, A.J.; Felixberger, J.K.; Rendina, L.M.; Sunderland, C.; Willis, A.C. *Inorg. Chem.* **1993**, 32, 1951.
111. Janzen, D.E.; Mehne, L.F.; VanDerveer, D.G.; Grant, G.J. *Inorg. Chem.* **2005**, 44, 8182.
112. Blake, A.J.; Bywater, M.J.; Crofts, R.D.; Gibson, A.M.; Reid, G.; Schröder, M. *J. Chem. Soc. Dalton Trans.* **1996**, 2979.
113. Champness, N.R.; Frampton, C.S.; Reid, G.; Tocher, D.A. *J. Chem. Soc. Dalton Trans.* **1994**, 3031.
114. Hesford, M.J.; Levason, W.; Matthews, M.L.; Reid, G. *Dalton Trans.* **2003**, 2852.
115. Levason, W.; Manning, J.M.; Nirwan, M.; Ratnani, R.; Reid, G.; Smith, H.L.; Webster, M. *Dalton Trans.* **2008**, 3486.
116. Levason, W.; Quirk, J.J.; Reid, G.; Frampton, C.S. *Inorg. Chem.* **1994**, 33, 6120.
117. Champness, N.R.; Kelly, P.F.; Levason, W.; Reid, G.; Slawin, A.M.Z.; Williams, D.J. *Inorg. Chem.* **1995**, 34, 651.
118. Levason, W.; Orchard, S.D.; Reid, G. *Inorg. Chem.* **2000**, 39, 3853.
119. Levason, W.; Manning, J.M.; Pawelzyk, P.; Reid, G. *Eur. J. Inorg. Chem.* **2006**, 4380.
120. Levason, W.; Manning, J.M.; Reid, G.; Tuggey, M.; Webster, M. *Dalton Trans.* **2009**, 4569.
121. Grant, G.J.; Goforth, A.M.; VanDerveer, D.G.; Pennington, W.T. *Inorg. Chim. Acta* **2004**, 357, 2107.
122. Bette, M.; Rüffer, T.; Bruhn, C.; Schmidt, J.; Steinborn, D. *Organometallics* **2012**, 31, 3700.
123. Kesanli, B.; Halsig, J.E.; Zavalij, P.; Fettinger, J.C.; Lam, Y.F.; Eichhorn, B.W. *J. Am. Chem. Soc.* **2007**, 129, 4567.
124. Kesanli, B.; Fettinger, J.; Gardner, D.R.; Eichhorn, B. *J. Am. Chem. Soc.* **2002**, 124, 4779.
125. Imai, S.; Fujisawa, K.; Kobayashi, T.; Shirasawa, N.; Fujii, H.; Yoshimura, T.; Kitajima, N.; Moro-oka, Y. *Inorg. Chem.* **1998**, 37, 3066.
126. Kujime, M.; Kurahashi, T.; Tomura, M.; Fujii, H. *Inorg. Chem.* **2007**, 46, 541.

127. Doel, C.L.; Gibson, A.M.; Reid, G.; Frampton, C.S. *Polyhedron* **1995**, 14, 3139.
128. Brevard, C.; van Stein, G.C.; von Koten, G. *J. Am. Chem. Soc.* **1981**, 103, 6746.
129. van Stein, G.C.; van Koten, G.; Vrieze, K.; Brevard, C.; Spek, A.L. *Inorg. Chem.* **1984**, 106, 4486.
130. van Stein, G.C.; van Koten, G.; Vrieze, K.; Brevard, C. *Inorg. Chem.* **1984**, 23, 4269.
131. van Stein, G.C.; van Koten, G.; Vrieze, K.; Spek, A.L.; Klop, E.A.; Brevard, C. *Inorg. Chem.* **1985**, 24, 1367.
132. van Stein, G.C.; van Koten, G.; Blank, F.; Taylor, L.C.; Vrieze, K.; Spek, A.L.; Duisenberg, A.J.M.; Schreurs, A.M.M.; Kojić-Prodić, B.; Brevard, C. *Inorg. Chim. Acta* **1985**, 98, 107.
133. Drew, M.G.B.; Harding, C.J.; Howarth, O.W.; Lu, Q.; Marrs, D.B.; Morgan, G.G.; McKee, V.; Nelson, J. *J. Chem. Soc. Dalton Trans.* **1996**, 3021-3030.
134. Talebpour, Z.; Alizadeh, N.; Bijanzadeh, H.R.; Shamsipur, M. *J. Incl. Phenom. Macrocyclic Chem.* **2004**, 49, 101.
135. Kennedy, M.A.; Ellis, P.D.; Jakosen, H. *J. Inorg. Chem.* **1990**, 29, 550.
136. Helm, L.; Combs, C.M.; VanDerveer, D.G.; Grant, G.J. *Inorg. Chim. Acta* **2002**, 338, 182.
137. Franklin, G.W.; Riley, D.P.; Neumann, W.L. *Coord. Chem. Rev.* **1998**, 174, 133.
138. Roy, T.G.; Hazari, S.K.S.; Dey, B.K.; Meah, H.A.; Rahman, M.S.; Kim, D.I.; Park, Y.C. *J. Coord. Chem.* **2007**, 60, 1567.
139. Niu, W.; Wong, E.H.; Weisman, G.R.; Hill, D.C.; Tranchemontagne, D.J.; Lam, K.-C.; Sommer, R.D.; Zakharov, L.N.; Rheingold, A.L. *Dalton Trans.* **2004**, 3536.
140. Clarke, P.; Hounslow, A.M.; Keough, R.A.; Lincoln, S.F.; Wainwright, K.P. *Inorg. Chem.* **1990**, 29, 1793.
141. Jäntti, A.; Wagner, M.; Suontamo, R.; Kolehmainen, E.; Rissanen, K. *Eur. J. Inorg. Chem.* **1998**, 1555.
142. Salehzadeh, S.; Javarsineh, S.A.; Keypour, H. *J. Mol. Struct.* **2006**, 785, 54.
143. Marchetti, P.S.; Bank, S.; Bell, T.W.; Kennedy, M.A.; Ellis, P.D. *J. Am. Chem. Soc.* **1989**, 111, 2063.
144. López-Torres, E.; Mendiola, M.A. *Dalton Trans.* **2009**, 7639.
145. Calatayud, D.G.; López-Torres, E.; Dilworth, J.R.; Mendiola, M.A. *Inorg. Chim. Acta* **2012**, 381, 150.

146. Casas, J.S.; Castellano, E.E.; García-Tasende, M.S.; Sánchez, A.; Sordo, J.; Zukerman-Schpector, J. *Z. anorg. allg. Chem.* **1997**, 623, 825.
147. Casas, J.S.; Castaño, M.V.; García-Tasende, M.S.; Martínez-Santamarta, I.; Sordo, J.; Castellano, E.E.; Zukerman-Schpector, J. *J. Chem. Res. (M)* **1992**, 2626.
148. Bermejo, E.; Castiñeiras, A.; Garcia-Santos, I.; West, D.X. *Z. anorg. allg. Chem.* **2005**, 631, 2011.
149. Grapperhaus, C.A.; Tuntulani, T.; Reibenspies, J.H.; Darensbourg, M.Y. *Inorg. Chem.* **1998**, 37, 4052.
150. Reger, D.L.; Mason, S.S.; Rheingold, A.L.; Ostrander, R.L. *Inorg. Chem.* **1993**, 32, 5216.
151. Reger, D.L.; Collins, J.E.; Myers, S.M.; Rheingold, A.L.; Liable-Sands, L.M. *Inorg. Chem.* **1996**, 35, 4904.
152. Reger, D.L.; Myers, S.M.; Mason, S.S.; Darensbourg, D.J.; Holtcamp, M.W.; Reibenspies, J.H.; Lipton, A.S.; Ellis, P.D. *J. Am. Chem. Soc.* **1995**, 117, 10998.
153. Reger, D.L.; Myers, S.M.; Mason, S.S.; Rheingold, A.L.; Haggerty, B.S.; Ellis, P.D. *Inorg. Chem.* **1995**, 34, 4996.
154. Darensbourg, D.J.; Nizegoda, S.A.; Holtcamp, M.W.; Draper, J.D.; Reibenspies, J.H. *Inorg. Chem.* **1997**, 36, 2426.
155. Pons, J.; García-Antón, J.; Font-Bardia, M.; Calvet, T.; Ros, J. *Inorg. Chim. Acta* **2009**, 362, 2698.
156. Griffith, E.H.; Charles, N.G.; Lewinski, K.; Amma, E.L.; Rodesiler, P.F. *Inorg. Chem.* **1987**, 26, 3983.
157. Guerrero, M.; Pons, J.; Parella, T.; Font-Bardia, M.; Calvet, T.; Ros, J. *Inorg. Chem.* **2009**, 48, 8736.
158. Byun, Y.; Min, D.G.; Do, J.; Yun, H.; Do, Y. *Inorg. Chem.* **1996**, 35, 3981.
159. Al-Rasbi, N.K.; Tidmarsh, I.S.; Argent, S.P.; Adams, H.; Harding, L.P.; Ward, M.D. *J. Am. Chem. Soc.* **2008**, 130, 11641.
160. Kennedy, M.A.; Sessler, J.L.; Murai, T.; Ellis, P.D. *Inorg. Chem.* **1990**, 29, 1050.
161. Rodesiler, P.F.; Griffith, E.H.; Ellis, P.D.; Amma, E.L. *J. Chem. Soc. Chem. Commun.* **1980**, 492.
162. Jakobsen, H.J.; Ellis, P.D.; Inners, R.R.; Jensen, C.F. *J. Am. Chem. Soc.* **1982**, 104, 7442.
163. Rodesiler, P.F.; Griffith, E.H.; Charles, N.G.; Lebioda, L.; Amma, E.L. *Inorg. Chem.* **1985**, 24, 4595.
164. Kennedy, M.A.; Ellis, P.D. *J. Am. Chem. Soc.* **1989**, 111, 3195.

165. Ratilaincn, J.; Airola, K.; Kolehmaincn, E.; Rissanen, K. *Chem. Ber.* **1997**, 130, 1353.
166. Gombler, W.; Lange, H.; Naumann, D. *J. Magn. Reson.* **1990**, 89, 10.
167. Helm, M.L.; VanDerveer, D.G.; Grant, G.J. *J. Chem. Cryst.* **2003**, 33, 625.
168. Helm, M.L.; Helton, G.P.; VanDerveer, D.G.; Grant, G.J. *Inorg. Chem.* **2005**, 44, 5696.
169. Wilhelm, M.; Deeken, S.; Berssen, E.; Saak, W.; Lützen, A.; Koch, R.; Strasdeit, H. *Eur. J. Inorg. Chem.* **2004**, 2301.
170. Ghilardi, C.A.; Innocenti, P.; Midollini, S.; Orlandini, A.; Vacca, A. *J. Chem. Soc. Chem. Commun.* **1992**, 1691.
171. Barbaro, P.; Cecconi, F.; Ghilardi, C.A.; Midollini, S.; Orlandini, A.; Vacca, A. *Inorg. Chem.* **1994**, 33, 6163.
172. Cecconi, F.; Ghilardi, C.A.; Ienco, A.; Midollini, S.; Orlandini, A. *J. Organomet. Chem.* **1999**, 575, 119.
173. Catalano, V.J.; Malwitz, M.A.; Noll, B.C. *Inorg. Chem.* **2002**, 41, 6553.
174. Catalano, V.J.; Malwitz, M.A.; Noll, B.C. *Chem. Commun.* **2001**, 581.

Chapter 13

Cyclodextrins and calyx[n]arenes as inverse phase transfer catalysts

Viktor Anishchenko¹, Volodymyr Rybachenko¹, Grzegorz Schroeder²,
Konstantine Chotiy¹ and Andrey Redko¹

¹*L.M. Litvinenko Institute of physical-Organic and Coal Chemistry,
National Academy of Science of Ukraine, Department of Spectrochemical
Researches, R. Luxemburg 70; 81-134 Donetsk, Ukraine*

²*Adam Mickiewicz University in Poznań, Faculty of Chemistry,
Umultowska 89b, 61-614 Poznań, Poland*

The phase transfer catalysis is powerful technique in organic synthesis. It allows performing chemical transformation in the organic phase. In contrast to this, reactions can also be performed by transferring the organic reactants from the organic phase into the aqueous phase for reaction with a second reactant. Such a complementary methodology is named as “inverse phase transfer catalysis” (IPTC) by Mathias and Vaidya [1]. Recently, it was shown that the use of host compounds, such as cyclodextrins [2] and water-soluble calix[n]arenes [3], offers the opportunity to combine IPTC, molecular recognition, and transition metal catalysis, with additional economic and environmental advantages deriving from the use of water as a bulk solvent.

Cyclodextrins

Cyclodextrins are cyclic oligosaccharide/polyalcohols of α -D-glucose with six to eight monomeric units terms are commercially available under the names of α -, β -, and γ -cyclodextrin, respectively. These compounds are characterized by cylindrical-like structures in aqueous solution (Fig. 1). The inner cavity is essentially hydrophobic and can host organic guests via the various intermolecular forces between host and guest molecules [4], whereas hydrophilic-OH groups span from the upper and the lower rim, ensuring water solubility to the molecule.

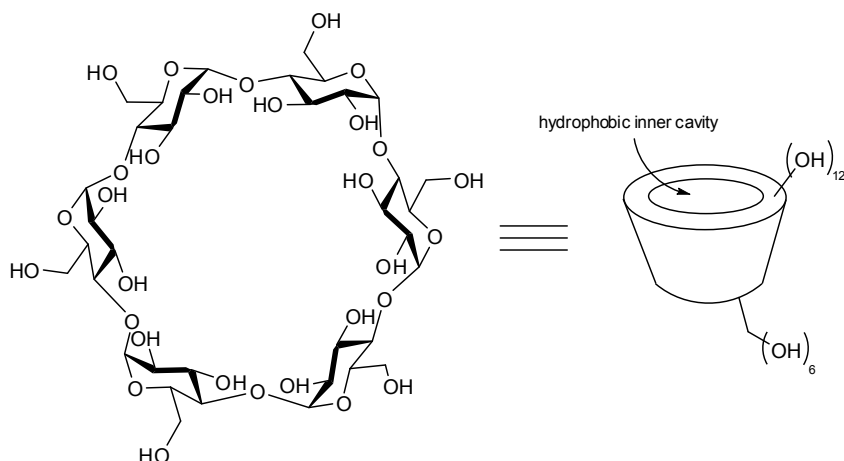


Figure 1. α -cyclodextrin structure.

Before the concept of IPTC was created, unmodified α - and β -cyclodextrins were used as carriers of organic molecules into water. For example, Trifonov and Nikiforov showed that β -cyclodextrin accelerate the reaction of the nucleophilic displacement of neat octyl bromide with aqueous cyanide, iodide, and thiocyanate anions [5]. Also, it was shown that α -cyclodextrin can catalyzed reaction too, but β -cyclodextrin are preferable.

After establishing of the IPTC concept, cyclodextrins found applications as IPTC catalysis in several important organic reactions catalyzed by transition metals. For instance, isomerization of 4-allylanisole catalyzed by IrCl_3 [6], oxidation CuCl_2 of olefins to ketones in water under aerobic condition and in presence of PdCl_2 and CuCl_2 (Wacker process) [7], the $\text{HCo}(\text{CN})_5^-$ catalyzed hydrogenation of conjugated dienes to monoolefins [8].

Further, the influence of chemically modification hydroxyls group of cyclodextrins on catalytic activity was studied. In 1994 by Mortreux and coworkers were found that the Wacker process of oxidation of 1-decene to 2-decanone with excellent yield (98%) in water, using $\text{O}_2/\text{PdSO}_4/\text{CuSO}_4/\text{H}_9\text{PV}_6\text{-Mo}_6\text{O}_{40}$ as the redox system. The lipophilic substrate was transferred into the aqueous phase by an amphiphilic β -cyclodextrin, in which about 60% of the free-OH groups were methylated [9]. Testing of other cyclodextrins (native α -, β -, γ -, fully acetylated β -cyclodextrin or 2-hydroxypropyl- β -cyclodextrins with different degrees of substitution) shows limited success. The optimal ratio of lipophilic and hydrophilic properties had a great importance, but

obtained results shows a significant role of molecular recognition based on reversible interactions between the cyclodextrins' host cavity and 1-decene. The methylated β -cyclodextrin was used as IPTC catalysts for the rhodium-catalyzed hydroformylation of water-insoluble olefins with high yield in an aqueous two-phase system free of organic solvent [10]. In contrast to terminal olefins, less-reactive internal olefins were found to be almost inert [11].

A general scheme obtained from these research studies: the amphiphilic cyclodextrin wraps the hydrophobic substrate (guest-molecule), acting as a host-molecule and transferring it into the aqueous phase, where the reaction occurs. The stability constant of the new host-guest complex is lower, and the product is then released into the organic phase (Fig. 5).

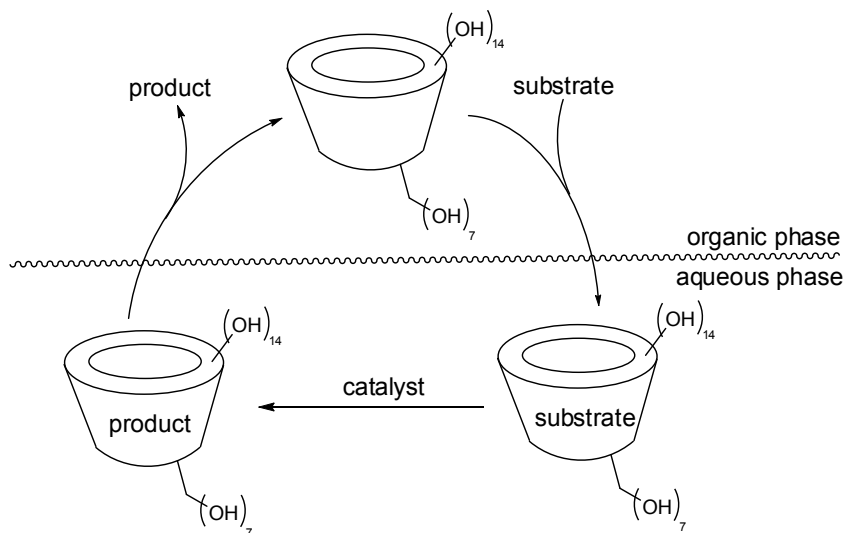


Figure 2. Catalytic cycle of cyclodextrin.

This scheme was confirmed by other catalytic organometallic reactions. Interesting results were obtained in the cleavage of allylic substrates in the presence of $\text{Pd}(\text{OAc})_2/\text{P}(\text{C}_6\text{H}_4\text{SO}_3\text{Na})_3$ [12-13], the hydrocarboxylation of olefins catalyzed by $\text{PdCl}_2/\text{P}(\text{C}_6\text{H}_4\text{SO}_3\text{Na})_3$ to give carboxylic acids [14], and the biphasic hydrogenation of water-insoluble aldehydes to alcohols catalyzed by $\text{RuCl}_3/\text{P}(\text{C}_6\text{H}_4\text{SO}_3\text{Na})_3$ [15].

The effect of partly methylated β -cyclodextrins on the other component of

the catalytic system was studied in the case of the hydroformylation of alkenes. Monflier and coworkers reviewed their previous model, considering formation of complexes between the cyclodextrin and some components of the catalytic system (e.g., $P(C_6H_4-SO_3Na)_3$) [16]. Independently, Kalck and coworkers proposed that the catalytically active rhodium complex include at least two cyclodextrin molecules [17]. From these results was concluded that chemically cyclodextrins influence the biphasic reaction not only as IPTC catalyst but also by modifying the equilibria between the components of the catalytic system [18].

More complicated catalytic systems based on β -cyclodextrin with combination of different functions in the same molecule were also conceived. Such complexes of modified β -cyclodextrin (Fig. 3) with rhodium were used as IPTC catalysts for the hydrogenation and the hydroformylation of alkenes in water-organic two-phase systems [19].

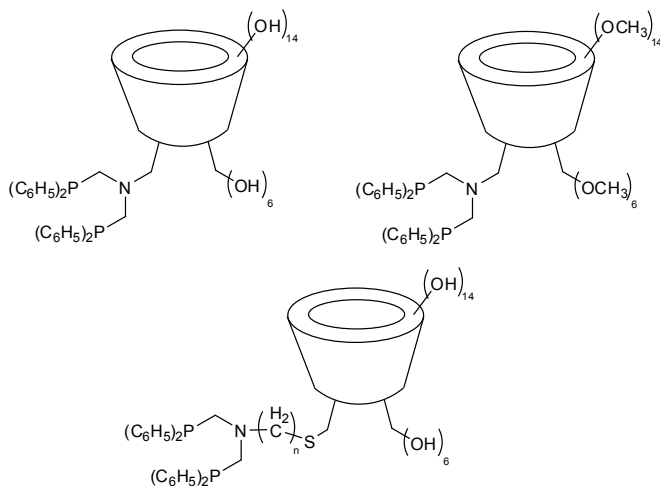


Figure 3. Multicomponent ligands for organometallic catalysis.

Such supramolecular catalysts showed high catalytic activity in the hydroformylation reactions and substrate selectivity in competition hydrogenation experiments. In contrast to the simple methylated β -cyclodextrin mentioned above, internal and cyclic olefins were oxidized into aldehydes. These improvements were explained with the formation of an inclusion complex at the phase boundary, with the cyclodextrin host fixing the substrate in the proximity of the catalytically active metal center (Fig. 4) [20].

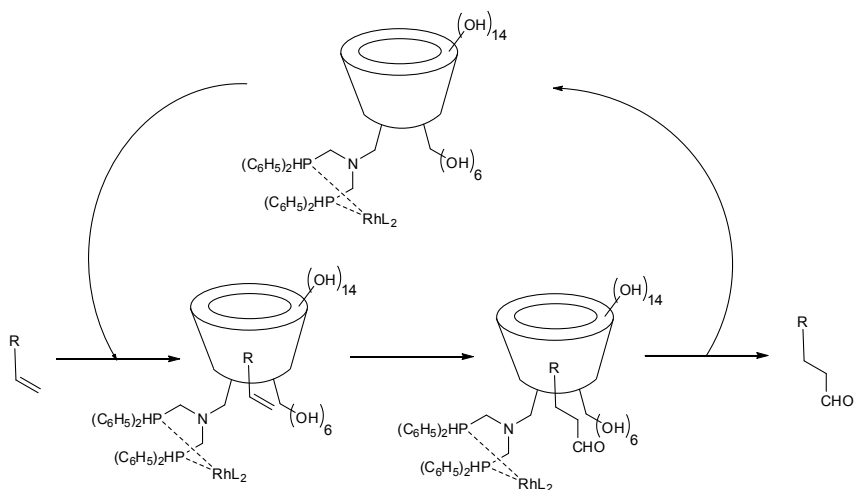


Figure 4. Proposed scheme of olefins oxidation by rhodium complexes of chelating phosphines tethered to β -cyclodextrins.

The effect of guest-molecule structure and type of cyclodextrin on binding constant was investigated using NMR and UV/VIS spectroscopy [21]. Chlorinated phenols were used as guest-molecules. α - and β -cyclodextrin form inclusion complexes with several chlorophenols with modest to low equilibrium constants. Results of studies are consistent with a simple 1 : 1 stoichiometry and the stability of the complexes is dependent on the structure of the chlorophenol and the cyclodextrin used. In general, the most stable complexes are formed between β -cyclodextrin and the 4-substituted chlorophenols. This suggests that the stability of the complexes is strongly influenced by the sizes and shapes of the guest and the cavity of the host. The polarity of the host chlorophenol plays an important role on the stability of the complex but is far less important than geometric fitting.

Recently, the Markovnikov enantioselective hydration of double bonds by an oxymercuration-demercuration reaction with cyclodextrins as catalysts was investigated [22]. Moderate ee (up to 32%) and yields (14–60%) were obtained for allylic amines and protected allylic alcohols as starting materials. It was found that an aromatic ring must be present in the substrate to achieve enantioselectivity. The best results are always obtained with α - or β -cyclodextrin. Modified cyclodextrins (2,6-di-O-methyl and random methyl cyclodextrins) neither improve yield nor enantioselectivity. N-allyl- N-benzylmethylamine

is an interesting example as the benzyl group may be removed by catalytic hydrogenation.

Kunishima and co-workers reported about a novel system for substrate-specific activation of carboxylic acids leading to the formation of carboxamides [23]. A combination of a water-soluble dehydrocondensing agent, 4-(4,6-dimethoxy-1,3,5-triazin-2-yl)-4-methylmorpholinium chloride (DMT-MM), and (hydroxypropyl)cyclodextrin (HP- β -CD), in a water/ether biphasic solvent system was found to be most effective. A lipophilic carboxylic acid with a strong affinity for the cavity of HP- β -CD can be selectively transferred to the aqueous phase and predominantly reacts with DMT-MM, dissolving in the aqueous phase. The substrate specificity was similar to that observed with a complex artificial enzyme based on CD. In result was found that substrate specificity similar to that obtained with a complex artificial enzyme can be achieved by using DMT-MM and a CD. This is the first example of a dehydrocondensation involving a step of carboxylic acid activation under IPTC conditions. It can be expected that this concept to be applicable to various solvent systems composed of fluoruous solvents or ionic liquids, and such applications are now under investigation.

A novel and efficient procedure has been developed by Li et al. for the preparation of Urapidil, from 6-[(3-chloropropyl)amino]-1,3-dimethyluracil and 1-(2-methoxyphenyl) piperazine hydrochloride under IPTC conditions [24]. To optimize the reaction conditions, the alkylation reaction was carried out with a range of IPTC catalysts, agitation speeds, reaction times, reaction temperatures, mole ratios and catalyst loadings. The experimental results demonstrate that the alkylation of 1-(2-methoxy-phenyl) piperazine hydrochloride with 6-[(3-chloropropyl)amino]-1,3-dimethyl-2,4(1H,3H)-pyrimidinedione is very rapid in the presence of cyclodextrins in aqueous media. β -cyclodextrin is the best catalyst owing to its excellent catalytic activity and eco-friendly nature. Urapidil was obtained as a white crystalline powder in 82.6% isolated yield with 99.6% purity after 2-3 h reaction in alkaline aqueous media at 95°C with an agitation rate of 1500 rpm. Compared to the N-alkylation under the same conditions without catalyst, the proposed method is suitable for the industrial scale synthesis of Urapidil.

Calix[n]arenes

Another class of supramolecules which was successfully used as IPTC catalysts are calix[n]arenes (Fig. 5). In contrast to mentioned above cyclodextrins, water-soluble calix[n]arenes (n - 4, 6, 8) were proposed as IPTC catalysts only a few years ago [25].

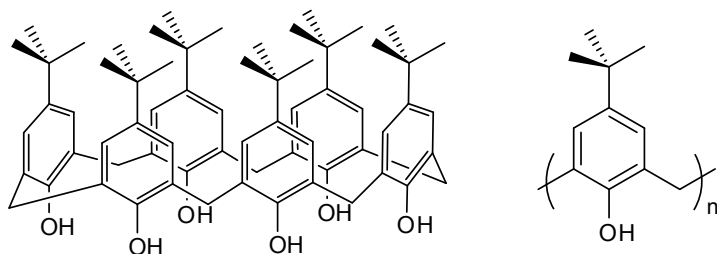


Figure 5. Calix[n]arenes.

Shimizu and coworkers found that nucleophilic displacement of arylalkyl and alkyl halides with NaCN, KI, KSCN in water can be catalyzed by substituted calix[n]arenes with trimethylammoniummethyl groups (Fig. 6). The catalytic activity of such compounds exceeded that of various cyclodextrin, whereas monomeric unit of the calix[n]arene (4-methoxybenzyltrimethylammonium chloride) did not catalyze reaction. It was also noted that the efficiency of the calix[n]arenes strongly depends on the geometry of the substrates, because of that it was proposed that they behave similarly to cyclodextrins.

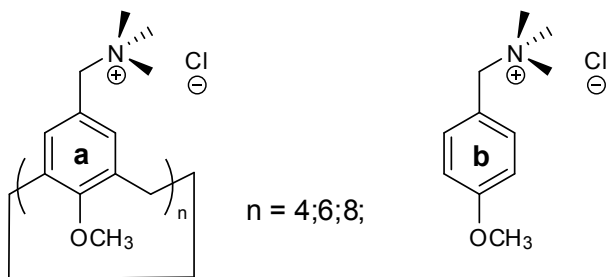


Figure 6. Water-soluble calix[n]arenes (a) and their monomeric unit (b).

Calix[n]arenes were used as IPTC catalysts in the aldol-type condensation and Michael addition reactions [26], and in alkylation of active methylene compounds with alkyl halides in aqueous NaOH solutions [27].

The aldol-type condensation of indene or acetophenone with benzaldehyde in aqueous NaOH under IPTC condition were compared with those conducted in aqueous micelles in the presence of cetyltrimethylammonium bromide as the surfactant. It was shown that in both cases selectivity's and yields were similar. On the other hand the IPTC procedure avoided the formation of emulsions,

thus facilitating product separation and catalyst recovery. The alkylation under IPTC of phenylacetone with octyl bromide allows intensifying alkylation versus hydrolysis and selectivities of reaction (C versus O alkylation) in comparison to the classical PTC reaction (with tetrabutylammonium bromide or hexadecyltributylammonium bromide as catalysis). Furthermore, the aqueous layer containing catalyst solution can be easily separated from the organic phase, where products contains, and no organic solvent was required.

Further, water-soluble calyx[n]arenes were integrated into catalytic systems, where organometallic catalysis are combined with calyx[n]arenes in a single molecule. Phosphacalix[4]arenes (Fig. 7) were synthesized and used as polydentate ligands in the rhodium-catalyzed hydroformylation of 1-octene and 1-decene [28].

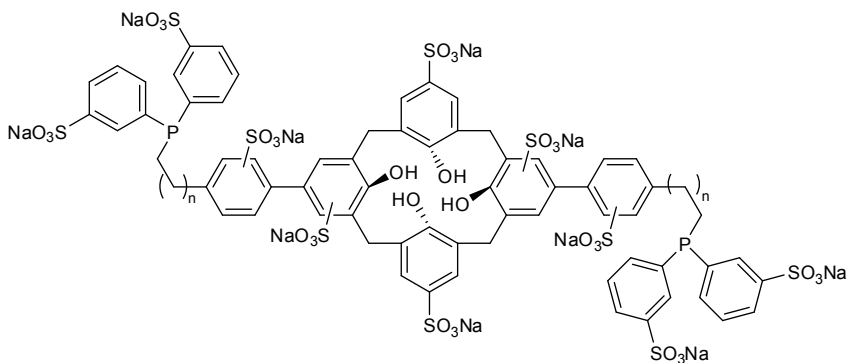
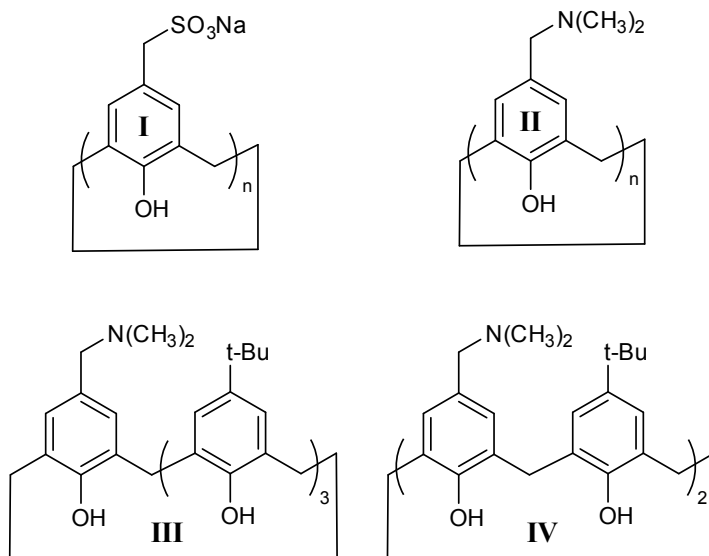


Figure 7. Water-soluble phosphacalix[4]arenes.

Recently, stability of the complexes formed in result of the inclusion of aromatic guests in the hydrophobic pocket of the water-soluble calixarenes **I-IV** was studied. For that reason ¹H-NMR titration experiments in aqueous buffered solutions were conducted. Additionally, molecular modeling studies in combination with ab initio NMR shift calculations were performed [29].



Association constants of various aromatic compounds with **I** were found to be close to those observed with β -cyclodextrin. But, it should be noted that iodobenzene, showed a higher affinity to β -cyclodextrin in contrast to the calixarenes. The association constants with the amino methyl-substituted calixarene **II** under acidic conditions were also higher than those measured with **I** at pH 7.4. Calix[n]arenes **I-IV** were used for catalyzing the Suzuki coupling of phenylboronic acid and iodobenzene in water under IPTC, yielding diphenyl as a product. In order to avoid the effect of inhibiting by product and to compare initial reaction rates the effect of **I-IV** was studied at low levels of conversions (10-15%). Better results were achieved with using amino-substituted calix[4]arenes **II-IV**.

Conclusion

In this chapter, a review of supramolecules (cyclodextrins and calyx[n]arenes) application as IPTC catalysts in different type of organic reactions is presented. The studies reviewed were directed on the development of new synthesis methods that meet the requirements of "green chemistry". Cyclodextrins and calyx[n]arenes have already established as valuable catalysts. And no doubt, variety of novel ways of using these catalysts wait for discovery and exploration.

References

1. Mathias LJ, Vaidya RA. *J. Am. Chem. Soc.* 1986; 108: 1093-1094.
2. D'Souza VT, Lipkowitz KB. *Chem. Rev.* 1998; 98: 1741-1742.
3. Gutsche CD. Royal Society of Chemistry: Letchworth, United Kingdom, 1998.
4. Bender ML, Komiyama M. Berlin: Springer. 1978.
5. Trifonov A, Nikiforov T. *J. Mol. Catal.* 1984; 24: 15-18.
6. Barak G, Sasson Y. *Bull. Soc. Chim. Fr.* 1988; 584.
7. Zahalka HA, Januszkievicz K, Alper H. *J. Mol. Catal.* 1986; 35: 249-253.
8. Lee JT, Alper H. *J. Org. Chem.* **1990**; 55: 1854-1856.
9. Monflier E, Blouet E, Barbaux Y, Mortreux A. *Angew. Chem., Int. Ed.* 1994; 33: 2100-2102.
10. Monflier E, Fremy G, Castanet Y, Mortreux A. *Angew. Chem., Int. Ed.* 1995; 34: 2269-2271.
11. Monflier E, Tilloy S, Fremy G, Castanet Y, Mortreux A. *Tetrahedron Lett.* 1995; 56: 9481-9484.
12. Lacroix T, Bricout H, Tilloy S, Monflier E. *Eur. J. Org. Chem.* 1999; 3127-3129.
13. Widehem R, Lacroix T, Bricout H, Monflier E. *Synlett.* 2000; 722-724.
14. Tilloy S, Bertoux F, Mortreux A, Monflier E. *Catal. Today.* 1999; 48: 245-253.
15. Monflier E, Tilloy S, Castanet Y, Mortreux A. *Tetrahedron Lett.* 1998; 39: 2959-2960.
16. Dessoudeix M, Urrutigoity M, Kalck P. *Eur. J. Inorg. Chem.* 2001; 1797-1800.
17. Tilloy S, Bertoux F, Mortreux A, Monflier E. *Catal. Today.* 1999; 48: 245-253.
18. Mathivet T, Meliet C, Castanet Y, Mortreux A, Caron L, Tilloy S, Monflier E. *J. Mol. Catal., A Chem.* 2001; 176: 105-116.
19. Reetz MT, Waldvogel SR. *Angew. Chem., Int. Ed.* 1997; 36: 865-867.
20. Reetz MT. *Catal. Today.* 1998; 42: 399-411.
21. Leyva E, Moctezuma E, Strouse J, Garcia-Garibay MA. *J. Incl. Phenom. Macrocyclic Chem.* 2001; 39: 41-46.
22. Abreu AR, Costa I, Rosa C, Ferreira LM, Lourenc A, Santos PP. *Tetrahedron.* 2005; 61: 11986-11990.
23. Kunishima M, Watanabe Y, Terao K, Tani S. *Eur. J. Org. Chem.* 2004; 4535-4540.
24. Wen L, Wenya Z, Xiaoqing M, Panpan W, Menghong D. *Appl. Catal.*

- A. 2012; 210-214.
25. Shimizu S, Kito K, Sasaki Y, Hirai C. *Chem. Commun.* 1997; 1629-1630.
 26. Shimizu S, Shirakawa S, Suzuki T, Sasaki Y. *Tetrahedron.* 2001; 57: 6169- 6173.
 27. Shimizu S, Suzuki T, Sasaki Y, Hirai C. *Synlett.* 2000; 1664-1666.
 28. Shimizu S, Shirakawa S, Sasaki Y, Hirai C. *Angew. Chem., Int. Ed.* 2000; 39: 1256-1259.
 29. Baur M, Frank M, Schatz J, Schildbach F. *Tetrahedron.* 2001; 57: 6985-6991.

Chapter 14

Role of electronic correlation in the calculations of supramolecular interactions in graphene-like aromatic systems

A.F. Dmitruk, O.M. Zarechnaya and I.A. Opeida

*Litvinenko Institute of Physical Organic Chemistry and Coal Chemistry,
National Academy of Sciences of Ukraine, Donetsk, 83114 Ukraine*

Coal beds almost always contain different gases, of which methane is of greatest interest as it is dangerous as a source of explosions in mines on one hand, and an environmentally friendly and efficient fuel on the other. It was found in [1] by means of X-ray structural analysis that many natural carbon-containing minerals over the lithogenetic diapason from peat to the graphitic stage contain structures consisting of two dimensional graphite-like networks 20–25 Å in diameter. Such flat networks are arranged into stacks of 4–7 parallel layers, forming domains. It is known that molecules of various elements and compounds can penetrate between graphite layers. Graphite crystallites are not destroyed in the process but are elongated along the direction perpendicular to the layers' plane [2, 3], forming so-called inclusion compounds in which the most important role is played by Van der Waals interactions. The molecular structures of polynuclear aromatic hydrocarbons (PAHs) are similar to the basic graphitic plane. So-called stacking interactions occur in the condensed state of these compounds, leading to the formation of molecular stacks. The Van der Waals forces between the PAH molecules predominate as in the case of graphitic planes. These common features allow us to use PAHs as model systems for investigating graphite-like layers in coals. This work is devoted to a quantum-chemical investigation of the possible intercalation of methane molecules between graphite-like planes. For most PAH dimers, the most energetically advantageous structure is one in which the planes are arranged in parallel with the layers shifted with respect to one another, the so-called AB type corresponding approximately to the stacking in graphite. Depending on the direction in which the molecules are shifted with respect to one another, several types of AB structures can exist. However, small

positional changes of the dimeric structure produce very small differences in energy, since the interaction potential is shallow with respect to these in-plane shifts and depends mainly on shifts in the vertical direction [4].

At the beginning it was studied the possibility of formation of stacings, consisting of 2 molecules of benzol, as a molecule of benzol is a fragment of structures of all of PAHs, which are more large fragments of graphene. It was assumed that the built clusters would serve as a starting model both for the choice of more exact method of calculation and for the construction of more complicated polyatomic fragments of graphene structures of coal.

On a Fig. 1 the results of quantum-chemical calculations of stacking-structure of benzol are presented. Calculations were made in the semi empiric approximation of PM3 (program MOPAC) and nonempiric (HF-6-31G, MP2, DFT) (program GAMESS).

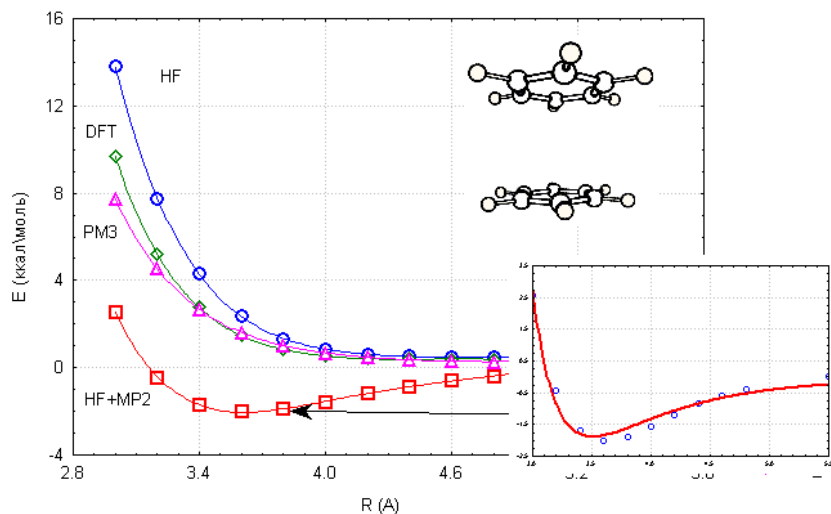


Fig. 1. Dependence of relative energy of interaction of molecules of benzol on distance in the different approximations (PM3, HF, HF+MP2, DFT).

The obtained results correlate with the known literature information on structures of liquid benzol, which show that in the liquid phase of benzol the parallel orientation of molecules prevails and the distances between them is $\sim 3 - 4$ Å. As we can see from Fig. 1 the minimum energy of intermolecular interaction is observed for distance $3,5$ Å (HF+MP2).

On Fig. 2 the results of analogical quantum-chemical calculations are presented (PM3, HF(6-31G), MP2, DFT) for the stacking-structure of fragments of graphene layers of coal, that are described more details further.

As we can see from Figs. 1 and 2, the minimum energy of intermolecular interaction is observed for distance 3,5 Å (HF+MP2). An analogical result is observed and for the polynuclear systems, that accords well with the known interplane distance in a graphite.

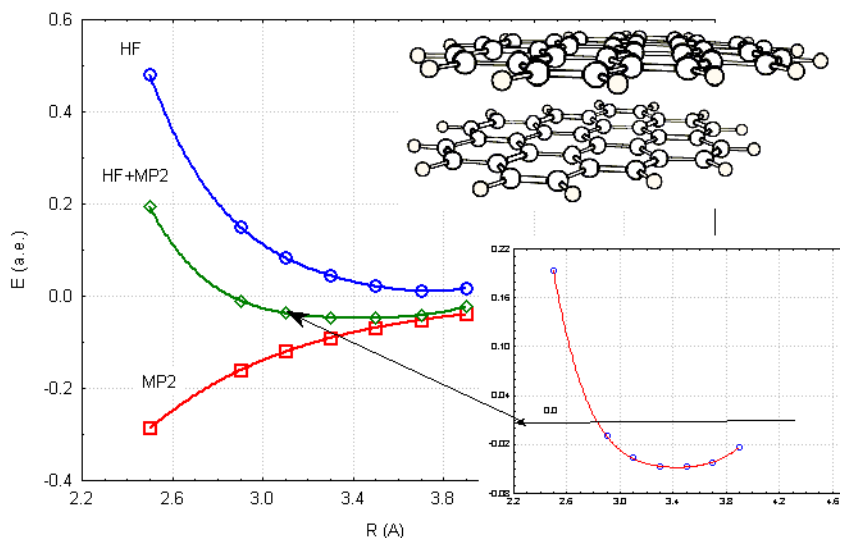


Fig. 2. Dependence of relative energy of interaction of two polynuclear aromatic molecules on distance in the different approximations (PM3, HF, HF+MP2, DFT).

Presented on Figs. 1 and 2 the nonlinear dependences of energy of intermolecular interaction on distance for both types of the systems are well described by the known Lennard-Jones potential, the obtained here constant of dispersion interaction is in a good agreement with known from literature estimations.

Thus, from the analysis of results, obtained with the different quantum-chemical approximations, we can see that description of intermolecular interaction in the structures of similar type in the single-electron approaching of Hartree–Fock approximation is not correct, it is necessary to take into account the multielectronic correlation energy.

Next in this work we studied the possibility of introduction of molecule of

methane between graphene planes.

An ovalene ($C_{32}H_{14}$) dimer with a parallel-shifted structure corresponding to the hexagonal form of graphite was, along with the clathrates (I, II, III, and IV) resulting from consecutive inclusion of methane (in amounts of one to four molecules) into the interplane space of the dimer ($(C_{32}H_{14})_2$), chosen as our model of interacting graphene layers (Fig. 3). *Ab initio* calculations were performed using the GAMESS [5] program complex and the 6-31G basisset with full optimization of the geometrical structures of ovalene and methane. Only the interplane distances were varied for structures I–IV and the ovalene dimer. As intermolecular interactions in the systems under study are determined by mostly dispersive forces whose nature is dictated by electron correlation effects, and the Hartree–Fock approximation is not sufficient for a correct estimation of noncovalent interactions, the electron correlation energy was considered within the second order Møller–Plesset perturbation theory (MP2), which lends itself well to such tasks [6].

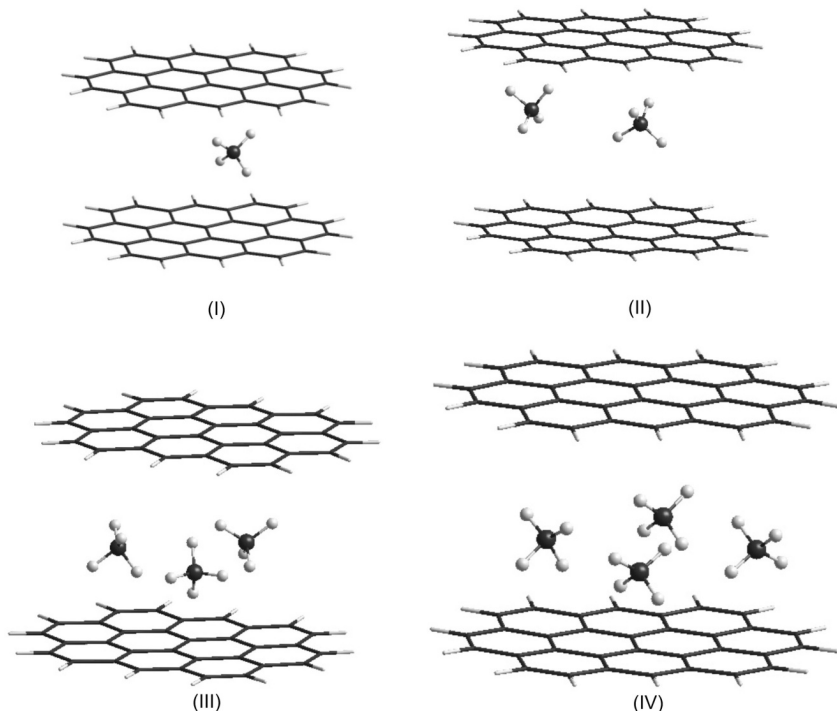


Fig. 3. Structures of clathrates of ovalene dimer with methane molecules.

The relative energy of intermolecular interaction was calculated as

$$\Delta E_n = E_{\text{tot}}^n - 2E_{\text{tot}}^{\text{OV}} - nE_{\text{tot}}^{\text{CH}_4}$$

where $2E_{\text{tot}}^{\text{OV}}$ is the total energy of two ovalene molecules, $E_{\text{tot}}^{\text{CH}_4}$ is the electronic energy of a methane molecule, E_{tot}^n is the total energy of the cluster $[n\text{CH}_4 + (\text{C}_{32}\text{H}_{14})_2]$, and n is the number of CH_4 molecules.

The binding energy of two ovalene molecules is thus.

$$\Delta E_0 = E_{\text{tot}}^0 - 2 E_{\text{tot}}^{\text{OV}}$$

The obtained dependence of the electronic energy of ovalene dimer on the interplane distance is presented in Fig. 4. It has the form of a classic Van der Waals curve. The energy minimum corresponds to a distance of 3.354 Å, which is close to the experimental value of the interplane distance in graphite (3.35 Å) [2]. The calculated energy of cohesion for the basic layers is 0.94 kcal/atom, fitting the known experimental range 0.8–1.2 kcal/atom for graphite [4, 7]. As clathrates II, III, and IV contain two and more methane molecules, the energetics of methane dimer formation was preliminarily investigated. For the level of theory used in this work, it was established that there is an energy minimum at a distance of 4.4 Å between the carbon atoms of methane molecules. The relative binding energy was –0.16 kcal/mol. This result is close to the data of other authors: intermolecular distance, 3.63–4.87 Å; intermolecular bond energy, 0.20–0.84 kcal/mol [8–10].

Due to the limited size of our model graphitic plane, the geometries of the trimer and tetramer of methane were set constant on the basis of the calculation results for the dimer of methane. The trimer of methane in structure III was represented by an equilateral triangle with a side length of 4.4 Å, with methane molecules in its corners. The tetramer of methane in structure IV was represented as a square with sides of 4.4 Å and methane molecules at its vertices. The results from calculating the relative electronic energy of clathrates I–IV in the interplane distance in the dimer of ovalene are presented in Fig. 3. It follows from our data that inclusion structures with one, two, and three methane molecules may exist. A structure with four methane molecules forms no bound supramolecular system. The equilibrium interplane distance rises with an increase in the amount of intercalated methane: 7.1 Å for I, 7.2 Å for II, and 7.5 Å for III. It should be noted that the relative intermolecular interaction energy of two grapheme layers is close to zero at a distance of 7.0 Å between the planes of ovalene molecules (Fig. 4), while in structures I, II, and III it lies in the range of the formation of bound systems. The stabilization energy of system I is 3.91 kcal/mol, which

is within the known interval of adsorption energies of methane on a surface of graphite (2.9 kcal/mol) [10] and a carbon nanotube (5.4 kcal/mol) [11]. It should be noted that the clathrate with methane in the dimeric form is the most stable of the studied systems. The binding energies for the studied clathrates are, respectively, -8.7 kcal/mol for system II, -3.9 kcal/mol for I, and -1.5 kcal/mol for III. Despite the modest basis set, our results within the Møller–Plesset perturbation theory are thus in satisfactory agreement with other investigations and can be used for the qualitative estimation of noncovalent interactions of methane and graphene layers.

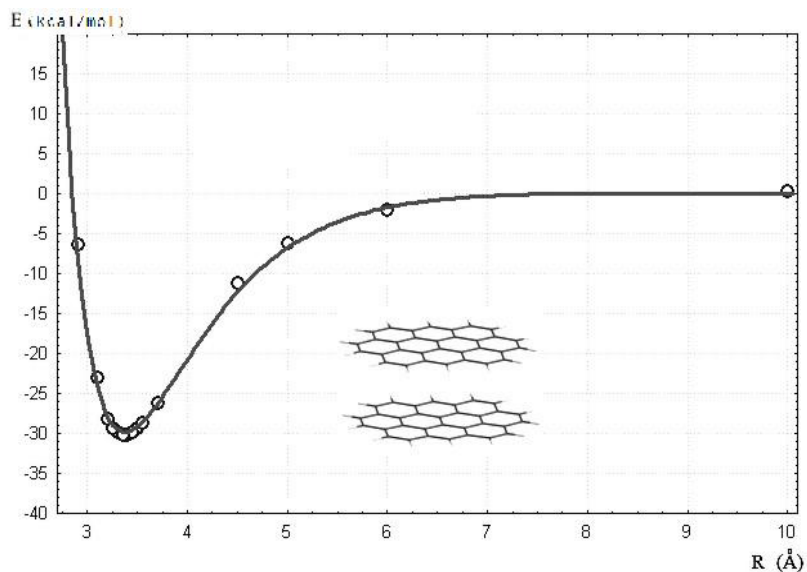


Fig. 4. Dependence of the relative electronic energy of graphene dimer on the interplane distance.

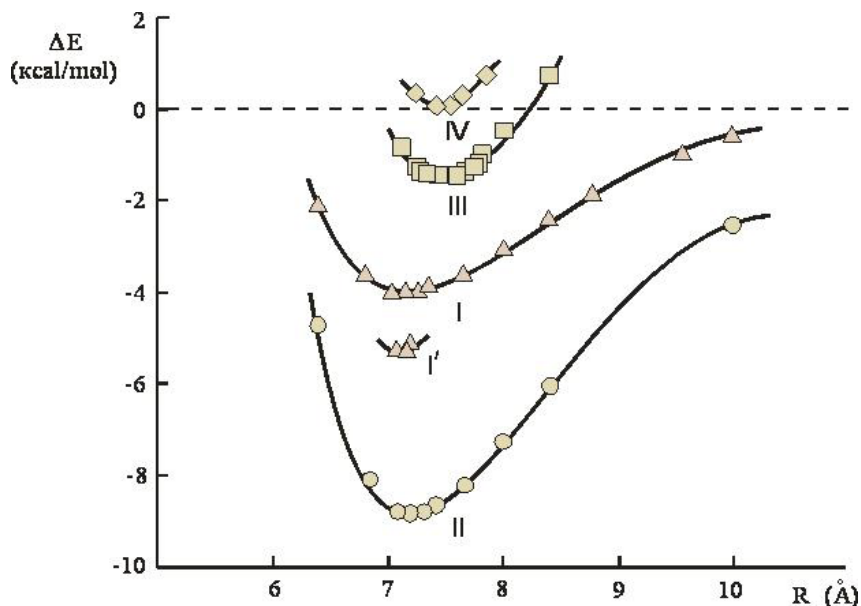


Fig. 5. Dependence of the relative electronic energy of clathrates I–IV on the interplane distance

It should be noted that the 6-31G basis used in this work is the minimal basis set possible in such investigations. Investigating dispersive interaction effects naturally requires the use of a more developed basis set that includes diffuse functions. However, such calculations for multiatomic systems are still tedious and time-consuming. We therefore performed calculations using polarization functions (the 6-31G(*d*) basis set) for the relative electronic energy dependence on the interatomic distance in a dimer of ovalene only for an inclusion structure with one methane molecule (clathrate I). The calculations were performed using the PC version of the GAMESS 7.1 (Firefly) program [12]. Several points were calculated in the range of the potential energy minimum (Fig. 5, curve I').

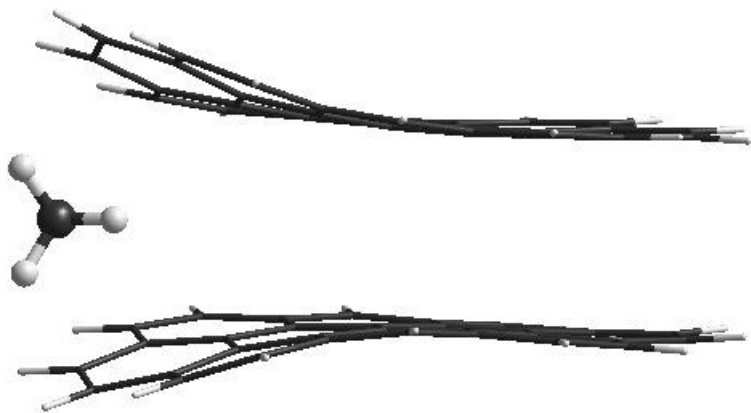


Fig. 6. Decomposition of clathrate I.

As follows from our results, extending the basis set raises the system's stabilization and binding energy to -5.52 kcal/mol, the interatomic distance remaining unchanged.

Conclusions

Our data demonstrate that the existence of inclusion compounds of methane in graphite-like systems is possible. However, such compounds are endothermic, i.e., unstable, as was observed in calculations with full geometry optimization (Fig. 6). Formally, graphene layers are separated in the process of intercalation, which requires the corresponding work be done. In natural coal substances, this work is performed by the surrounding medium under considerable external pressure. This could explain methane accumulation in deep-lying coal beds (1 km and lower) [13]. Upon a release of external pressure, spontaneous decomposition should occur, for which an increase in entropy and a large heat effect leading to an explosion is typical.

References

1. Yu. M. Korolev, *Khim. Tverd. Topl.*, No. 6, 11 (1989).
2. A. Wells, *Structural Inorganic Chemistry* (Clarendon, Oxford, 1984), Vol. 3.
3. V. S. Ostrovskii, Yu. S. Virgil'ev, V. I. Kostikov, and N. N. Shipkov, *Artificial Graphite* (Metallurgiya, Moscow, 1986) [in Russian].

4. S. D. Chakarova-Kack, A. Vojvodic, J. Kleis, et al., *New J. Phys.* **12**, 013017 (2010).
5. M. W. Schmidt, K. K. Baldrige, and J. A. Boatz, *J. Comput. Chem.* **14**, 1347 (1993).
6. B. Bezbaruah, P. Hazarika, A. Gogoi, et al., *J. Biophys.Chem.* **2**, 32 (2011).
7. S. D. Chakarova and E. Schroder, *J. Chem. Phys.* **122**,054102 (2005).
8. A. K. Rappe and E. R. Bernstein, *J. Phys. Chem. A***104**, 6117 (2000).
9. R. L. Rowley and T. Pakkanen, *J. Chem. Phys.* **110**,3368 (1999).
10. T. G. Metzger, W. A. Glauser, and D. M. Ferguson, *J. Comput. Chem.* **18**, 70 (1997).
11. A. V. Eletskii, *Phys. Usp.* **47**, 1119 (2004).
12. A. A. Granovsky, <http://classic.chem.msu.su/gran/gamess>.
13. I. L. Ettinger, *Outbursts of Coal and Gas and the Structure of Coal* (Nedra, Moscow, 1969) [in Russian].

Chapter 15

Design of polyfunctional nanosystems based on surfactants and polymers by noncovalent strategy

Lucia Zakharova, Elena Zhiltsova, Alla Mirgorodskaya
and Alexander Konovalov

*State Budgetary-Funded Institution of Science A.E. Arbuzov
Institute of Organic and Physical Chemistry of Kazan Scientific Center
of Russian Academy of Sciences, Arbuzova 8,
420088 Kazan, Russia*

Introduction

Supramolecular assemblies based on amphiphilic compounds are in the focus of modern physicochemical investigations including both fundamental and practical aspects. On the one hand, self-assembling systems are related to biomimetic object [1-3] and therefore information on their behavior makes it possible to model key factors controlling functions of biological systems. On the other, assemblies based on amphiphilic compounds (surfactants, block-copolymers, hydrophobized macrocycles and polymers) are widely used in high technologies [2-6]. Two main properties of amphiphiles are responsible for the growing interest to supramolecular systems, namely their capacity of aggregating in solutions beyond a certain concentration called for typical surfactants as critical micelle concentration (cmc), and the solubilization capacity of aggregates toward organic and bioorganic substrates [7-9]. The development of novel functional nanosystems assumes the elucidation of the correlation between chemical structure of amphiphiles, their aggregation behavior and functional activity as nanocontainers, catalysts, sensors, etc. Noteworthy that due to intensive growth of modern technologies, novel challenging tasks are appeared and therefore stronger criterions are nowadays advanced, such as biocompatibility, ecological safety, low cmcs, etc. In this connection it is evident that practical tasks dictate the necessity of systematic investigations of homological series of amphiphilic compounds, with the structure of hydrophobic and polar fragments varied [10-16].

1. Supramolecular systems based on dicationic gemini surfactants

Our works are focused on the development of polyfunctional systems based on the diversity of cationic surfactants. For this purpose, the correlation between their structure, aggregation capacity and functional characteristics, including solubilizing, catalytic, biological activity need to be studied. Taking into account current tendency in this field we pay special attention to the investigation of gemini surfactants. Geminis are composed of two head groups bearing hydrophobic alkyl tails, with heads bridged with each other by a spacer. Typical geminis have a polymethylene spacer and are abbreviated as m-s-m, here m is the number of carbon atoms in alkyl tail, while s is the number of methylene groups in the spacer. These surfactants demonstrate a number of advantages over their monocationic analogs. In particular, their cmcs are lower (by more than an order of magnitude) than those of conventional single-head surfactants [17]. Geminis stronger decrease the surface tension of water and show higher solubilization capacity [18]. Aggregation behavior of gemini surfactants are summarized in recent reviews [17-20] in which their quantitative characteristics are analyzed, i.e. cmcs, size and morphology of aggregates, counterion binding, numbers of aggregation, rheological behavior, surface properties, etc. The solubilization capacity of geminis and their catalytic activity are much less studied. In our works, the functional supramolecular systems are designed on the basis of alkylammonium geminis of general formula $[>(R)N(CH_2)_nN(R)<]^{2+}2Br^-$, with R varied from n-decyl to n-hexadecyl, and the number of methylene group in polymethylene spacer ranged from 4 to 12. Surfactant series with head groups of dialkylammonium, dimethylhydroxyethylammonium, and morpholinium types are involved in the study [21-31].

1.1. Aggregation behavior of dicationic gemini surfactants

In our works [21,23,26,31], aggregation behavior of homological series of dicationic surfactants has been studied by variety of methods and compared with that of monocationic analogs. Trends revealed are shown to be in line with literary data. Conductometry, tensiometry, potentiometry and others data indicate that a decrease in cmc by ca. two orders of magnitude occurs on transiting from monocationic to gemini surfactant with the same alkyl tail [21]. In the case of dicationic surfactants with hydroxyethyl fragment in the head group an additional 5-fold decrease in the cmc value is observed [31]. EPR-spectroscopy study with using spine probes demonstrated that dicationic surfactants with the shorter alkyl tails are characterized by less closer packing of surfactant molecules and their higher lability. In addition, these aggregates have lower polarity of their interior as compared to monocationic analogs [23]. NMR self-diffusion and

dynamic light scattering data prove a nanometer dimension of aggregate size, and determine the concentration ranges of existence of spherical and ellipsoid micelles [23].

1.2. Solubilizing capacity of micelles based on gemini surfactants

Dicationic surfactants above cmc show high solubilizing ability toward a variety of organic guests. The solubility of hydrophobic amines, fat acids and their esters in aqueous solutions of dicationic surfactants are quantitatively characterized by methods of potentiometry and spectrophotometry [24,31]. A marked 20-fold increase in the solubility of the above substrates is shown on transiting from water to micellar systems. This effect essentially depends on the alkyl chain length of surfactants, while the size of the spacer plays a minor role. The substitution of a methyl group in polar fragment by hydroxyalkyl moiety results in the enhanced solubilization capacity of micelles, which is exemplified by data on the solubility of *p*-nitrophenyl esters of carbonic acid in mono- and dicationic surfactant solutions as compared to water (Figure 1). Due to high solubilizing capacity of dicationic surfactants they may be considered as candidates for the design of nanocontainers for organic and bioorganic substrates.

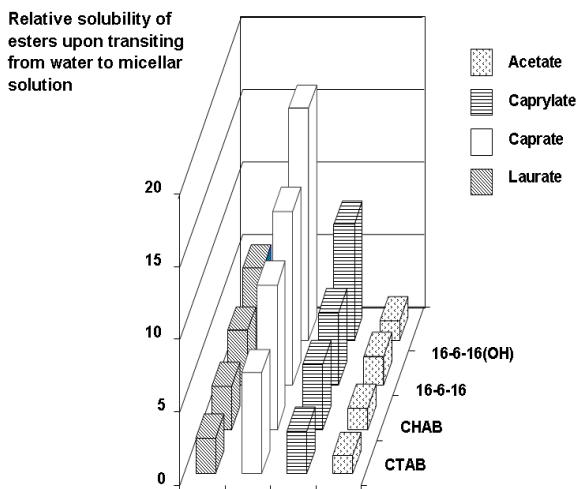
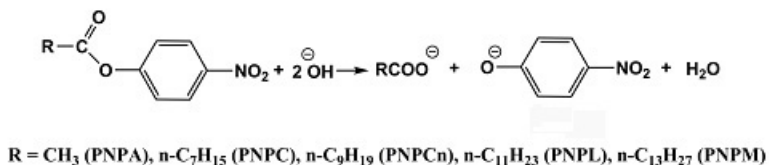


Figure 1. The solubility of *p*-nitrophenyl esters in micellar solutions of monocationic surfactants cetyltrimethylammonium bromide (CTAB) and cetylhydroxyethyltrimethylammonium bromide (CHAB) and geminis related to that of water.

Due to the solubilization of compounds in nanosized aggregates the concentration effect and changes in their microenvironment occur, which may modify their reactivity, acid-base properties, spectral characteristics, etc. As an example, marked decrease in pK_a value (of 1.0 to 1.5) for long-chain amines is shown as compared to water [22,24]. This is mainly due to the preferable binding of uncharged basic form of amines by cationic micelles relative to positively charged acid form, with the effect increasing with the surface potential of micelles. Based on this trend the surface potential of micelles may be estimated with the help of p-nitrophenol as a spectral probe capable of localizing in the interface and serve as an indicator of its properties. The value of the surface potential (Ψ) determined in such a way slightly depends on the structure of head group, while it is responsive to the transition from mono- to dicationic surfactants, e.g. $\Psi=130$ mV for CTAB, while it increases to $\Psi=155$ mV for 16-6-16 [27,31]. This difference is essential to distinguish between micellar rate effects of these surfactants, when they are used as reaction media especially for ion-molecular reactions.

1.3. Catalytic activity of gemini surfactants

Micellar rate effect of dicationic surfactants of m-s-m type is studied toward basic hydrolysis of carbonic acid esters p-nitrophenyl acetate (PNPA), caprylate (PNPC), caprinate (PNPCn), laurate (PNPL), and myristate (PNPM) (Scheme 1) [21,31] and phosphorus acid esters [26].



Scheme 1. Scheme of basic hydrolysis of carbonic acid esters.

Kinetic data obtained provide evidences on high catalytic effect of these surfactants, which realizes at lower concentrations as compared to monocationic analogs. High accelerations reaching in some cases three orders of magnitude are observed beyond cmc in the range of existence of spherical micelles. The micellar effect on the hydrolysis of substrates is mainly determined by factor of hydrophobicity, viz. catalytic effect increases with an increase in alkyl chain

length and the substrate hydrophobicity. In particular, micelles of 16-6-16 accelerate hydrolysis of PNPA by factor of 5, while hydrolysis of PNPCn is accelerated by factors of 115 (Figure 2).

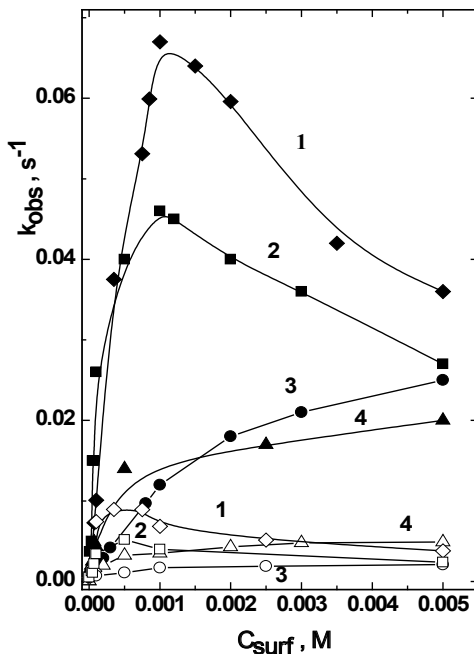


Figure 2. The observed rate constant of basic hydrolysis of PNPCn (1), PNPC (2), PNPA (3), PNPL (4) in micellar solutions of 16-6-16 (open symbols) and 16-6-16 (OH) (solid symbols) versus surfactant concentration; pH 9.2; 25 °C.

The substrate specificity is probably due to the substrate partition between micellar and bulk phases. For compounds with higher affinity toward micellar phase, their stronger binding by aggregates occurs, and therefore the larger concentration of reagents in micelles is observed, which is the main source of the acceleration.

Catalytic activity of dicationic surfactants can be controlled by both their directed functionalization (the covalent way) and by the addition of inert or reactive compounds capable of modifying structural and catalytic behavior (non-covalent way). Thus, the replacement of one of methyl substituents in head groups of the m-s-m molecule by hydroxyethyl moiety (hereinafter the abbreviation

m-s-m(OH) is used) makes it possible to involve specific intermolecular interactions along with hydrophobic effect and electrostatic forces. In this case, more effective self-assembling and additional contribution to the reagent binding may be expected. In addition, more polar substituent in head groups would increase the micropolarity in the reactive zone, thus favoring the chemical interaction due to stabilization of the transition state of reactions through the H-bonding. As a result, catalytic effect of hydroxyethylated surfactants is by 10-fold higher as compared to non-functionalized analogs (Figure 2). On the other hand, catalytic effect of dicationic surfactants can be modified by introducing of salt additives thereby affecting the value of the surface potential of aggregates [21,27]. For example, an addition of 0.01 M KCl to the micellar solution of 16-6-16 results in a decrease of the surface potential from 155 to 90 mV, which is followed by the change in cmc of the surfactant from 4.5×10^{-5} to 1.7×10^{-5} M [27]. Such a decrease in the surface potential reduces the concentration of the negatively charged nucleophiles in the surface layer and slows down the reaction in micellar phase up to the complete suppression of the catalytic effect (Figure 3).

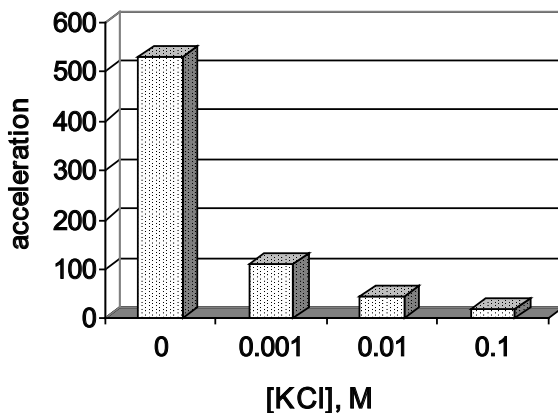


Figure 3. The influence of the additives of KCl on the catalytic effect of 16-6-16 toward basic hydrolysis of PNPCn; 0.001 M NaOH; 25 °C.

1.4. Mixed surfactant-polymer catalytic systems

One of the ways of modifying the functional activity of nanosystems based on surfactants is their admixture with polymers, which can play the role of matrix for surfactant molecules and their assemblies. Mixed polymer-colloid

aggregates possess properties differing from those of single systems, and combine advantages of both covalent and non-covalent assemblies. For the purpose of the design of nanocontainers and nanoreactors on the basis of dicationic surfactants and polymers, nonionic water-soluble polymers, polyethyleneglycol (PEG) with molecular mass of 20 KDa and block-copolymers polyethyleneoxide (PEO)/polypropyleneoxide (PPO) with different PEO/PPO ratio, viz. Pluronic 31R1, Pluronic F-127, and Synperonic L64 are used [28]. The formation of mixed surfactant systems is proved by methods of tensiometry, NMR self-diffusion and dynamic light scattering (DLS). Surface tension isotherms of mixed dicationic surfactant-polymer systems have two critical aggregation concentrations (cac), i.e. cac_1 and cac_2 , where first point indicates the onset of the formation of micelles immobilized on polymer matrix, while second critical point corresponds to the saturation of macromolecules by micelles and the formation of polymer-free aggregates. Typically, cac_1 value is lower than cmc of single surfactant solution, with the difference being larger for the higher polymer concentration. For block-copolymers, cac_1 decreases with their hydrophobicity (Table 1).

Table 1. Values of cac and surface potential of single and mixed systems based on cationic surfactants.

System	cac_1^a (cac_2) (mM)	Ψ (mV)
CTAB	0.9	129
CTAB + PEG (0.05 M)	0.9	128
16-6-16	0.045 (0.9)	155
16-6-16 + PEG (0.05 M)	0.010 (1.8)	145
16-6-16 + Pluronic F127 (0.05 M)	0.015 (2.3)	121

^a In single surfactant systems cac_1 corresponds to cmc.

The formation of mixed dicationic surfactant-polymer systems is followed by a decrease in the surface potential, with this effect being more marked for the less hydrophilic polymers. As shown with the use of spectral probes, the addition of PEG to the micellar 16-6-16 solution results in a decrease in the surface potential by 10 mV, while the more hydrophobic block-copolymer Pluronic F-127 reduce the Ψ value by 35 mV. This effect is responsible for the decrease in the catalytic activity of mixed systems toward ion-molecular reactions, in particular, basic hydrolysis of carbonic acid esters (Figure 4).

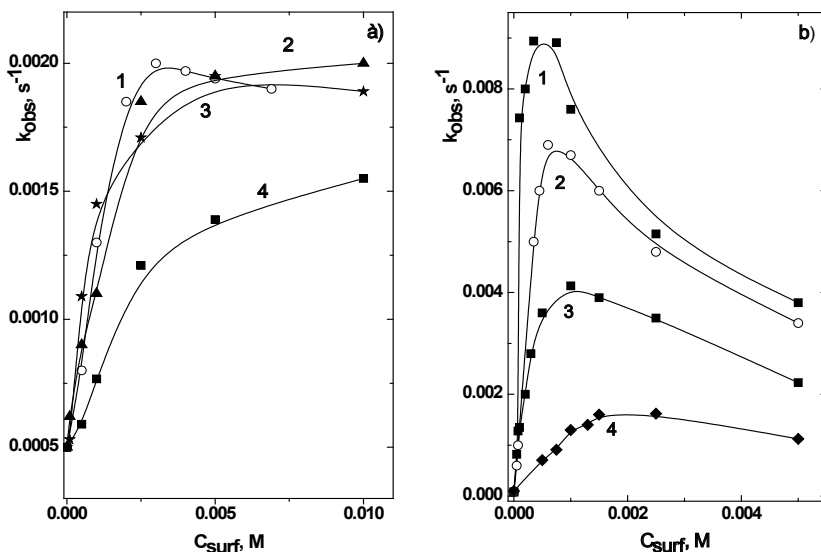


Figure 4. The observed rate constant of the cleavage of PNPA (a) and PNPC (b) in micellar 16-6-16 solutions without of additives (1) and in the presence of 0.02 M PEG (2), 0.05 M PEG (3), 0.05 M Pluronic F127 (4); pH 9.2; 25 °C.

Polymers bearing functional groups, such as polyethyleneimine (PEI) demonstrate specific behavior. On the one hand, similar to conventional hydrophilic polymers, PEI can mediate surfactant aggregation, thereby changing structural behavior of the system. On the other, primary and secondary aminogroups of PEI can contribute to chemical reactions, e.g. nucleophilic substitution at electrophilic phosphorus or carbon atoms [29,30] as both, reagents or catalysts. Mutual affinity of components in mixed surfactant-PEI systems may be enhanced by the hydrophobization of macromolecules, as it is exemplified in the comparative study of unsubstituted PEI (molecular mass of 25 KDa) and its analogs alkylated with dodecyl tails, APEI (the degree of alkylation of 0.1 to 0.4) [29,30]. The PEI-dicationic geminis systems demonstrate typical aggregation behavior, i.e. mixed aggregates are formed, which are characterized by two critical concentrations, with first critical point, cac_1 , lowering as the hydrophobicity of polymers increases. Catalytic activity of these systems is studied toward the cleavage of PNPA under basic conditions. In this case, parallel to the hydrolysis the aminolysis of the substrate occurs, that makes it possible to cleave the ester bond in mild conditions (pH 8-10, 25 °C) with a

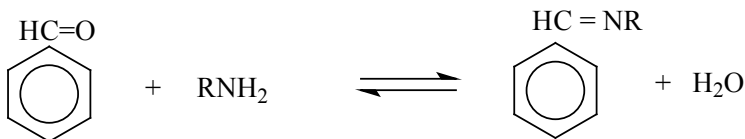
high rate. Under these conditions, unsubstituted PEI is less active as compared to APEI. Probably, hydrophobic effect contributed by alkyl groups of APEI and surfactants favors the formation of mixed aggregates, which in turn allows the solubilized substrate and reactive aminogroups of PEI to approach, thereby resulting in the acceleration of the cleavage of substrate.

To sum up, nanoreactors based on the PEI-dicationic surfactant systems demonstrate advanced characteristics; in particular, (i) they are stimuli responsive systems, since mutual affinity of components and contribution of hydrolysis and aminolysis of esters are strongly pH dependent, and therefore may be controlled by the variation of solution pH; (ii) geminis are characterized by higher micellar rate effect at the much lower surfactant concentrations as compared to single-head surfactants; (iii) far more accelerations and decrease of the concentration threshold may be achieved on transiting to mixed systems based on unsubstituted PEI and alkylated PEI. The summary augmentation of the catalytic effect (k_{cat}/k_0), toward the cleavage of PNPA in the series: aqueous molecular solution@CTAB@CTAB/PEI@CTAB/APEI is as follows: 1@4@22@120, while for 16-6-16 the order is: 1@4@56@200 (k_0 is the rate constant in alkali solution without additives, k_{cat} is the rate constant in the presence of catalyst).

1.5. Mixed systems dicationic surfactant – long-chain amine

The integration of low molecular mass long-chain amines into micelles based on geminis results in the formation of mixed aggregates, which is accompanied by the increase in micellar sizes, decrease in the mobility of alkyl chains, and changes in the counterion binding [24]. The properties of amines themselves change as well, i.e. a marked decrease in their basicity and the alteration of reactivity are observed. The pK_a of decylamine in micellar solution of 16-6-16 is lower by unity as compared to water [22,24]. This increases the fraction of neutral form of amine that possesses nucleophilic properties and therefore may take part in chemical reactions. Due to the increase in the concentration of a neutral form and the formation of mixed surfactant-amine aggregates the aminolysis of PNPA by decylamine accelerates by factor of 50 in the 16-6-16 solution.

In work [22], the application of aqueous gemini solutions as the reaction medium for the interaction of long-chain amines with benzaldehyde is demonstrated (Scheme 2).



Scheme 2. Scheme of the reaction of long-chain amines with benzaldehyde

This reaction yielding the azomethines (Schiff bases) is used for the analytic determination of benzaldehyde and primary amines in their mixtures with other amines. This analysis is not carried out in water, since the reaction is in equilibrium and the product formed can undergo fast hydrolysis. The solubilization of reagents and products in micelles based on dicationic surfactants shifts the equilibrium to the right. The reaction rate for the amine-benzaldehyde interaction is ca.10-fold higher in the micellar solution as compared to ethanol (Figure 5).

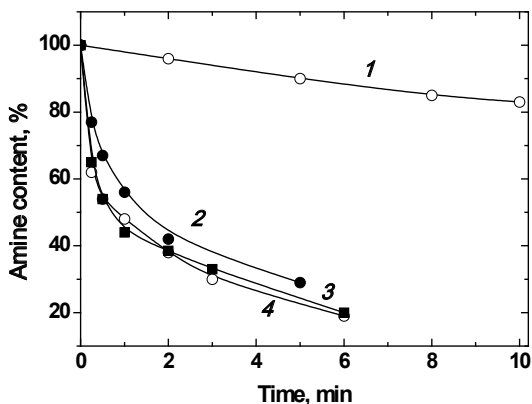
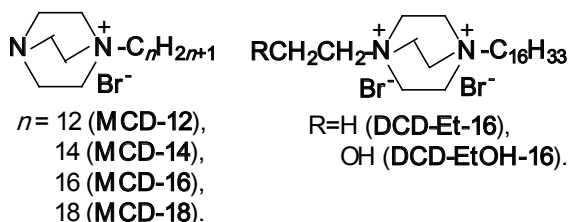


Figure 5. The conversion of amines due to its interaction with benzaldehyde in ethanol and aqueous micellar solutions: decylamine in ethanol (1), CTAB micelles (2), 16-6-16 micelles (3); octylamine in 16-6-16 micelles (4); 0.005 M surfactant; 25 °C.

It is noteworthy that in the case of hydrophilic amines the complete conversion cannot be achieved, since the parallel reaction in bulk phase can occur, hereupon the equilibrium shifts to the left. The high solubilization capacity of dicationic surfactants toward long-chained amines and benzaldehyde makes it possible to handle with high reagent concentrations and solve not only analytic tasks but also synthetic ones.

2. Supramolecular systems based on mono- and dicationic single-tailed derivatives of 1,4-diazabicyclo[2,2,2]octane

Due to wide applications of cationic surfactants as drug and gene carriers, antimicrobial preparations, and micellar catalysts design of novel amphiphiles with advanced property-activity relation is of current importance. The structure of the head group is shown to affect micellization and catalytic activity of cationic surfactant [32]. In particular, the introduction of bicyclic moiety in head group markedly enhances the effectiveness of the catalysis of cleavage of toxic phosphorus acid esters [33,34]. The use of cationic surfactants bearing bicyclic fragments in the head group as micellar catalysts is scarcely documented [35,36] and is exemplified by the acceleration of hydrolysis of p-nitrophenyl diphenyl phosphate in the micellar solution of alkylated 1,4-diazabicyclo[2,2,2]octane (DABCO) [36]. These surfactants are also attractive due to their potentiality as ionic liquids [37] and extraction agents for nucleotides [38]. Noteworthy that despite the key role of hydrophobicity of surfactants in their micellization and functional activity this aspect is poorly studied for alkylated DABCO excepting isolated publications [36,39]. Our works focus on the aggregation activity of mono- (MCD) and dicationic (DCD) derivatives of DABCO in water and chloroform [40-45,46,47], their catalytic and biological activity [42,44,47-49], adsorption on the air/water interface [40,47] in both single solution and in the presence of calixarenes [46-49], phosphorus substrates [44], and polymers [48]. As can be seen from the structural formulas below these surfactant series make it possible to compare the behavior of gemini surfactants bearing two charged fragments and two long-chain alkyl groups with dicationic surfactants bearing one long-chain alkyl fragment.



2.1. Aggregation behavior of alkylated 1,4-diazabicyclo[2,2,2]octane

Aggregation characteristics of surfactants studied (cmc, aggregation number, N_{agg} , hydrodynamic radius/diameter of aggregates, R_H/D_H , degree of counterion binding, β) are determined by methods of tensiometry, conductometry, potentiometry [40,46,47], dynamic light scattering [40,42], viscosimetry

[40], dye solubilization [46], fluorimetry [45], EPR-spectroscopy [40], NMR self-diffusion [41,43,44,46], and dielcometry [48]. Figures 6,7 exemplify tensiometry and conductometry data for MCD, from which the characteristic breakpoints are evident indicating the onset of the micellization in solution. Cmc values determined as breakpoints from concentration dependences of different parameters are summarized in Table 2. The data demonstrate that cmc values depend on both the hydrophobicity and number of charge fragments of surfactants. An increase in the number of carbon atoms in alkyl groups (n) results in a predictable decrease in cmc in accordance with a linear dependence: $-\log cmc = a + bn$. For homological series of monocationic bicyclic surfactants MCD, values of a and b are close to those for single-tailed cationic and anionic surfactants (Table 3). Noteworthy that dicationic single-tailed surfactants, DCD show higher cmcs as compared to monocationic analogs with head group of bicyclic (MCD), monocyclic (cetylpyridinium bromide, CPB) and acyclic (CTAB) type (Table 2). This behavior differs markedly from that of dicationic geminis and is probably due to a higher repulsion between two heads in Stern layer that is not compensated by a favorable contribution of second alkyl group as in the case of geminis.

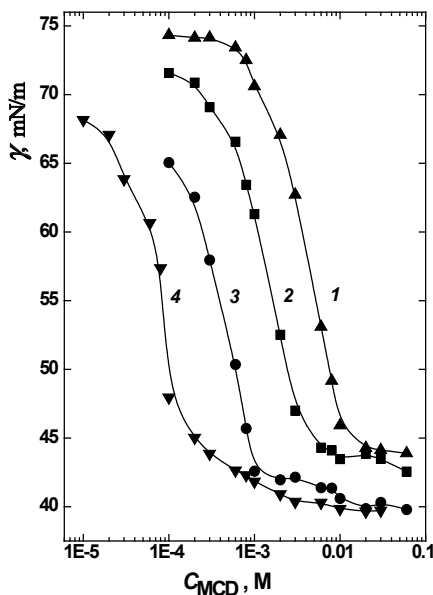


Figure 6. Surface tension isotherms of aqueous solutions of MCD-12 (1), MCD-14 (2), MCD-16 (3), MCD-18 (4); 25 °C.

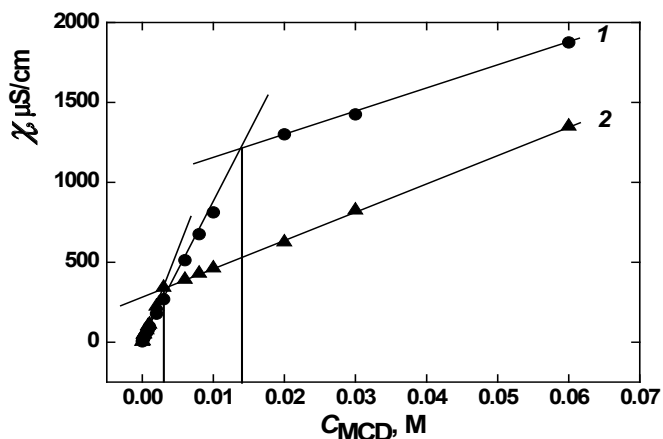


Figure 7. Specific conductivity versus surfactant concentration dependence for aqueous solutions of MCD-12 (1) and MCD-14 (2); 25 °C.

Table 2. Values of cmc of cationic surfactants in water; 25 °C.

Surfactant	cmc × 10 ³ (M)				
	Tensiometry	Conductometry	Potentiometry	NMR self-diffusion	EPR
MCD-12	11	14	16	15	-
MCD-14	4.0	3.0	3.7	3.4	-
MCD-16	1.0	1.0; 11 ^c	1.9	0.85	1.0 10 ^{c,d}
MCD-18	0.12	0.11; 0.91 ^c	0.22	0.11	-
DCD-Et-16	3.0	3.1; 10 ^b	2.0	-	-
DCD-EtOH-16	2.0	2.5; 10 ^b	3.0	-	-
CPB	0.68 ^a	0.68 ^a	-	-	-
CTAB	0.8 ^b	0.90 ^b	-	-	-
MCD-16 – NDEP ^e	-	-	-	0.9	-
MCD-16 – CR-1 ^f	0.4	0.1; 4.0 ^c	4.9 ^c	0.45	-
CR-1	9.0	13	-	5.0	-

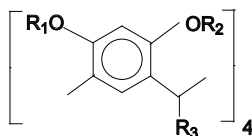
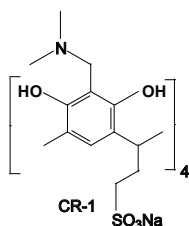
^a Data from [50]. ^b Data from [51]. ^c value of cmc₂. ^d 22 °C. ^e C_{NDEP} = 0.001 M. ^f C_{CR-1} = 0.001 M.

Table 3. Values a and b determined by different methods; (Eq.: $-\log \text{cmc} = a + bn$).

Method	MCD			Reference surfactant	-a	b
	-a	b	r^a			
Tensiometry	2.0	0.32	0.986	n-Alkyltrimethylammoniumbromides ^b	1.9	0.31
Conductometry	2.3	0.34	0.991	n-Alkylpyridinium bromides ^{b,c}	1.7	0.31
Potentiometry	1.7	0.29	0.980	n-Alkylsodium sulfates ^b	1.5	0.30
NMR self-diffusion	2.4	0.35	0.996	$C_n H_{2n+1} (OC_2 H_4)_6 OH$ ^{b,c}	1.8	0.49

^a r is a correlation coefficient. ^bData from [9]. ^c 30 °C.

Additives are shown to affect the cmc values. For aqueous MCD-16 solution the influence of the substrate, p-nitrophenyl diethyl phosphate (NDEP) [44] and water-soluble calix[4]arene (CR-1) [46,47] capable of self-assembling are used.



$R_1 = R_2 = C_2H_4OH$, $R_3 = n-C_7H_{15}$ (CR-2);
 $R_1 = C_2H_4OH$, $R_2 = C_2H_4OP(O)(OH)CH_2Cl$, $R_3 = n-C_9H_{19}$ (CR-3).

The presence of phosphate exerts a slight effect on the micellization of MCD, while the addition of CR-1 promotes the formation of mixed MCD-16/CR-1 aggregates and induces their further rearrangement at critical concentrations of cmc_1 and cmc_2 respectively (Table 2) [46,47]. It has been found that mixed aggregates enriched by CR-1 are formed beyond 0.4 mM due to electrostatic interactions, while above 5 mM aggregates based on MCD-16 occur contributed by hydrophobic effect, in which CR-1 is a minor component. In nonpolar media (chloroform), aggregation of MCD-16 is facilitated by the addition of PEI alkylated by tetradecyl moieties (APEI, the fraction of alkylation of 0.6) and calix[4]arene CR-2, as well as their mixture (Table 4) [48].

Table 4. Cmc and cac values of the systems based on cationic surfactants, APEI and CR-2 in chloroform; 25 °C.

surfactant	$\text{cmc}_1 \times 10^4 \text{ (M)}$	$\text{cmc}_2 \times 10^3 \text{ (M)}$	system *	$\text{cac}_1 \times 10^5 \text{ (M)}$	$\text{cac}_2 \times 10^3 \text{ (M)}$
MCD-12	1.9	5.9	MCD-16 - APEI	16	8.1
MCD-16	2.0	7.5	MCD-16 - CR-2	9.0	5.0
MCD-18	1.6	7.0	MCD-16 - APEI - CR-2	9.0	5.0

* $C_{\text{APEI}} = 5.0 \times 10^{-3} \text{ M}$, $C_{\text{CR-2}} = 8.0 \times 10^{-5} \text{ M}$.

Apart from cmcs the degree of counterion binding β , radiuses of MCD aggregates and number of aggregation are determined. For MCD-12, MCD-14 and MCD-18, β ranges from 0.67 to 0.84, while for MCD-16 it changes from 0.81 to 0.91 [40]. NMR diffusivity data reveal that around the cmc hydrodynamic radiuses equal 15.1, 20.3 and 22.8 Å, while aggregation numbers equal 24, 54, and 72 for MCD-12, MCD-14 and MCD-16 respectively [41,43], that is both parameters increase with the hydrophobicity of surfactants. For concentration range above cmc the radiuses and aggregation numbers are shown to depend on the MCD concentration (Table 5) [45]. At high MCD-14 concentrations the larger micelles are formed that are characterized by higher numbers of aggregation. This is confirmed by the fluorimetry data indicating that for the MCD-14 concentrations of 5×10^{-3} , 7.5×10^{-3} and $2.5 \times 10^{-2} \text{ M}$ aggregation numbers equal 40, 59 and 114 respectively.

Table 5. Hydrodynamic radiuses (R_H) and aggregation numbers (N_{agg}) at different MCD-14 concentrations in D_2O ; 25 °C.

$C_{\text{MCD-14}} \times 10^3 \text{ (M)}$	$R_H \times 10^{10} \text{ (m)}$	N_{agg}
5.0	20.3	54
7.5	22.7	75
8.75	23.4	83
10	23.6	86
25	26.3	118
37.5	26.2	116
50	27.3	132

Based on surface tension isotherms, the surface excess (Γ_{\max}), the surface area per molecule (A_{\min}), the standard free energy of micellization (ΔG_m) and the standard free energy of interfacial adsorption at the air/saturated monolayer interface (ΔG_{ad}) have been calculated (Table 6) [40]. An increase in the surfactant hydrophobicity slightly decreases Γ_{\max} and increases A_{\min} . These trends provide evidence on the less compact packing the molecules for more hydrophobic homologs, which is in line with their lower cmcs. At the same time, an increase in alkyl chain length results in a decrease of free energy of adsorption and micellization, i.e. favors these processes.

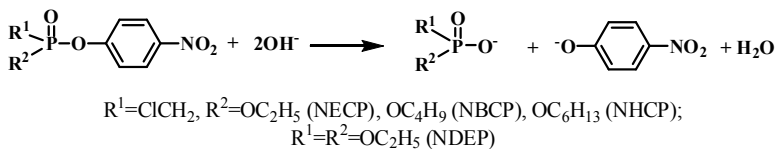
Table 6. Values of the surface excess, Γ_{\max} , the surface area, A_{\min} , the standard free energy of micellization, ΔG_m and the standard free energy of adsorption ΔG_{ad} for cationic surfactants; 25 °C.

surfactant	$\Gamma_{\max} \cdot 10^6$ (mol/m ²)	A_{\min} (nm ²)	$-\Delta G_{ad}$ (kJ/mol)	$-\Delta G_m$ (kJ/mol)
MCD-12	2.69	0.62	32.1	22.2
MCD-14	2.46	0.67	37.4	26.8
MCD-16	2.37	0.7	46.6	34.1
MCD-18	2.12	0.79	53.1	41.3

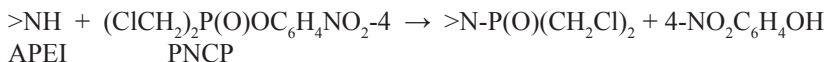
Along with the micellization, the liquid crystalline behavior of the systems based on MCD-16 is studied [41]. MCD-16 is shown to belong to amphotropic compounds capable of forming the mesophase of different types, i.e. thermotropic and lyotropic. It is found, that for lyotropic liquid crystals the wider temperature diapason is observed as compared to thermotropic phase. The existence of lyomesophase within the wide temperature range extends the application of these systems as matrix for the design of nanomaterials and models of membranes in biotechnological protocols.

2.2. Catalytic activity of surfactants with bicyclic head group

Catalytic activity of the systems based on MCD and DCD is exemplified by basic hydrolysis (in water) and aminolysis (in chloroform) of phosphorus acid esters (Schemes 3, 4) monitored by methods of spectrophotometry [42-44,47-49] and NMR spectroscopy [44].



Scheme 3. Scheme of basic hydrolysis of phosphorus acid esters.



Scheme 4. Scheme of aminolysis of phosphorus acid ester

Concentration dependences of observed rate constants of basic hydrolysis of NBCP in 0.001 M NaOH in the presence of MCD demonstrate extremal character (Figure 8) [43] and are treated in terms of pseudophase model of micellar catalysis (eq. 1) [52]:

$$k_{2,obs} = \frac{k_{2,0} + \left(\frac{k_{2,m}}{V} \right) K_S K_{Nu} C}{(1 + K_S C)(1 + K_{Nu} C)}, \quad (1)$$

here $k_{2,obs}$ ($\text{M}^{-1}\text{s}^{-1}$) is the observed second order rate constant obtained by division of k_{obs} by the nucleophile concentration; $k_{2,0}$ and $k_{2,m}$ ($\text{M}^{-1}\text{s}^{-1}$) are second order rate constants in bulk and micellar phases respectively; V (M^{-1}) is the molar volume of surfactant; K_S and K_{Nu} (M^{-1}) are binding constants of substrate and nucleophile respectively; C is the surfactant concentration minus cmc.

Results of quantitative treatment of kinetic data in terms of eq. 1 are summarized in Table 7.

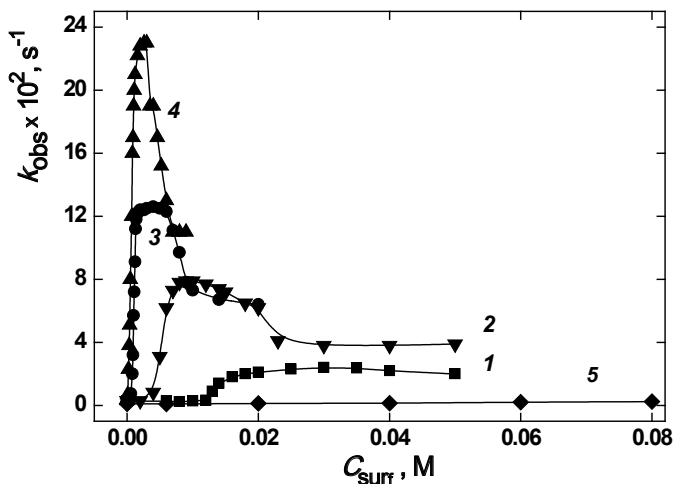


Figure 8. The observed rate constants of basic hydrolysis of NBCP in aqueous basic solutions of MCD-12 (1), MCD-14 (2), MCD-16 (3), MCD-18 (4), DABCO (5) as function of surfactant concentration; 0.001 M NaOH; 25 °C.

Table 7. Results of fitting the kinetic data on basic hydrolysis of NBCP in micellar solutions of MCD with the help of eq. 1.

surfactant	k_{2m} ($M^{-1}s^{-1}$)	K_S (M^{-1})	$K_{Nu}^>$ (M^{-1})	$(k_{obs}/k_0)_{max}$	F_m	F_c	$F_m \times F_c$	cmc (M)
MCD-12	0.91	330	10	7.7	0.29	24.7	7.2	0.012
MCD-14	0.43	2000	96	25	0.14	215	30	0.0046
MCD-16	0.48	4570	110	41	0.16	274	42	0.00075
MCD-18	0.56	2560	148	74	0.18	321	58	0.00008
DCD-Et-16	0.24	5440	80	15	0.068	210	14	0.0029
DCD-EtOH-16	0.33	5000	13	3.6	0.095	39	3.7	0.0019
MCD-16 ^a	0.0012	3800	70	23	0.125	180	23	0.0027

^a for basic hydrolysis of NDEP.

It is evident that k_{2m} slightly depend on the hydrophobicity of monocationic surfactants, with the exception of MCD-12. For the latter, second order rate constants in both phases are roughly similar, which is probably due to inconsiderable changes of micropolarity in the site of the location of reagents in micelles as compared to bulk phase. For all MCDs high binding constants of

substrate occur reaching one to two orders of magnitude, with the highest value being observed for cetyl homologs. Values of binding constants of OH ions and maximum acceleration of the reaction $(k_{obs}/k_0)_{max}$ increase with an increase in alkyl chain length of surfactants. Maximum acceleration can be expressed by eq. 2 that is obtained by the conversion of eq. 1.

$$\left(\frac{k_{obs}}{k_0} \right)_{max} = \frac{k_{2,m}}{k_{2,0}} \times \frac{K_S K_{Nu}}{V \left(K_S^{1/2} + K_{Nu}^{1/2} \right)^2}, \quad (2)$$

where the first term on the right is associated with the influence of the micellar microenvironment (F_m) and the second term reflects concentrating the reagents in micelles (F_c).

As can be seen from Table 7 in all cases F_m values are less than 1, while F_c exceeds two orders of magnitude. High F_c values compensate the negative effect of the factor of micellar microenvironment and resultant micellar effect equal to the multiplication of the two factors appears to be positive and increases with alkyl chain length of MCD by factor of 60. The key role of the hydrophobicity is evident from the comparison of the rate effect of long-chain MCDs with non-alkylated DABCO (Figure 8). Thus, catalytic effect of MCD on the basic hydrolysis of phosphonates is mainly contributed by the factor of concentration and increases with the surfactant hydrophobicity.

The micellar rate effect of the MCD series is compared with that of surfactants bearing head groups of monocyclic and acyclic structure exemplified by hexadecyl homologs. Kinetic curves of basic hydrolysis of NBCP for CPB and CTAB systems demonstrating the plateau are treated in terms of eq. 3 [53].

$$k_{obs} = \frac{k_m K_S (C - cmc) + k_0}{1 + K_S (C - cmc)}, \quad (3)$$

here k_0 and k_m (s^{-1}) are first order rate constants in bulk and micellar phases respectively; K_S (M^{-1}) is binding constants of substrate.

Results of quantitative treatment reveal that MCD-16 demonstrates higher binding constant with substrate and advanced micellar rate effect as compared to those of CPB and CTAB (Tables 7, 8).

Table 8. Results of the quantitative treatment of kinetic data of basic hydrolysis of NBCP catalyzed by cationic surfactants in terms of eq.3.

System	pH	k_m (s ⁻¹)	K_s (M ⁻¹)	cmc × 10 ⁴ (M)	k_m/k_0
CPB	11	0.13	2400	4.9	37
CTAB	11	0.099	1200	4.6	28
MCD-16 – CR-1 ^a	10	0.0019	14000	3.5	5.0 ^b
MCD-16 – CR-1 ^a	9.0	0.00051	6900	1.8	14 ^b

^a $C_{CR} = 0.001$ M. ^b Micellar rate effect compared to the reaction in the absence of surfactant and CR.

Transition from monocationic MCD-16 to dicationic surfactants DCD-16 and DCD-EtOH-16 results in a marked (more than tenfold) decrease in effectiveness of catalysis (Table 7) [42], which is contributed by a decrease in the concentration effect and a yet unfavorable microenvironmental factor.

The influence of macrocyclic additives on catalytic effect of DCD series is exemplified by the hydrolysis of phosphorus acid esters in the MCD-16-CR-1 system [47,49]. The addition of calixarene results in an increase of substrate binding constant and a decrease in catalytic activity (Tables 7,8). The effect of the macrocycle on catalysis becomes less negative upon decreasing the solution pH.

In nonaqueous media, viz. in the case of phosphorylation of PEI in chloroform MCD-16 solution (Scheme 4) the character and degree of the influence of macrocycle (CR-3) depend on the content of each component of the system (CR, surfactant, and PEI) [48]. In MCD chloroform solutions with no macrocycle added a ca.2.7-fold increase in k_{obs} occurs in the range of structural rearrangement of the system (0.015 to 0.03 M MCD) and then a ca.4.3-fold increase occurs again after the rearrangement (Figure 9, Table 9).

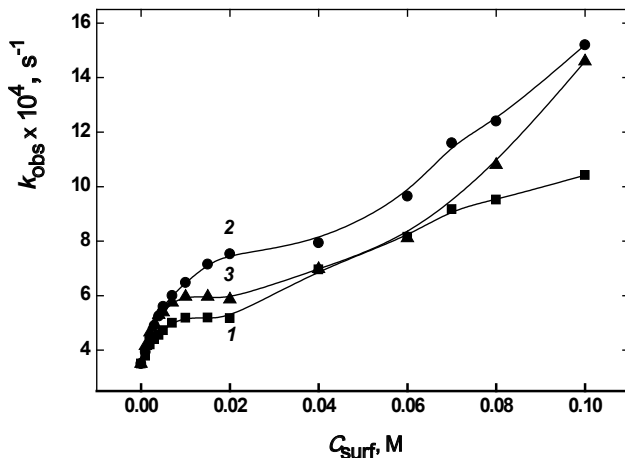


Figure 9. The observed rate constant of reaction of APEI with PNCP in the presence of MCD-12 (1), MCD-16 (2), MCD-18 (3) in chloroform as a function of surfactant concentration; $C_{APEI} = 0.01$ M, 25 °C.

Table 9. Results of the quantitative treatment of kinetic data of the reaction of APEI with PNCP in chloroform MCD solutions in terms of eq. 3.

surfactant	$k_m \times 10^4$ (s $^{-1}$)	K_s (M $^{-1}$)	cmc $\times 10^4$ (M)	k_m/k_{obs}
MCD-12	6.30	170	2.5	1.8
MCD-16	9.3	110	2.6	2.7
MCD-18	6.9	290	2.1	2.0

In the presence of phosphorus-bearing CR-3 a twofold increase in the catalytic effect of MCD-16 occurs within the low concentration range of the surfactant chloroform solutions. An increase in the calixarene concentration is accompanied by a decrease in the catalytic effect of the system up to the transition to a fourfold inhibition. Within the range of positive influence of calixarene a decrease in the concentration of surfactant and polymer in the APEI-MCD-16-CR-3 system increases the catalytic effect [48].

2.3. Antimicrobial activity of alkylated DABCO

In addition to the aggregation and catalytic properties, antimicrobial activity of alkylated DABCO is also studied, whereby the correlation of antimicrobial

and aggregation properties is analyzed [44]. The bacteriostatic, fungistatic, bactericidal, and fungicidal effects are tested for alkylated DABCO toward the collection of test-strains of microorganisms: *Staphylococcus aureus*-209 P (*St. aureus*); *Escherichia coli* F50 (*E. coli*); *Bacillus cereus* 8035 (*B. cereus*); *Pseudomonas aeruginosa* 9027 (*Ps. Aeruginosa*); *Trichophyton gipseum* (*Tr. Gipseum*); *Aspergillus niger* (*Asp. Niger*); and *Candida albicans* (*C. alb.*). As reference compounds, antibacterial commercial preparation ciprofloxacin, antifungal agent amphotericin B, and typical cationic surfactant CTAB are used. Data obtained reveal that surfactants studied exhibit antimicrobial activity that markedly depends on the alkyl chain length, with maximum effect occurring for octadecyl homolog. This trend is observed for almost the whole series of strains used and is most pronounced for static activity. The influence of head group is mostly evident in the case of *St. Aureus*, for which the transition from CTAB to MCD-16 provides a tenfold increase in bactericidal activity. Much higher antifungal activity exemplified by *Tr. gipseum* and *C. Alb* should also be noted for MCD-18 as compared to CTAB. Fungistatic activity of MCD-18 toward these strains is by 2-fold and 4-fold higher and fungicidal activity is by 16-fold and 10-fold higher than those for CTAB.

Second charge moiety exerts a negative influence on antifungal activity, e.g. the transition from MCD-16 to DCD-Et-16 results in fourfold decrease in antifungal activity toward *Tr. gipseum* and in tenfold decrease toward *C. alb.* At the same time antimicrobial activity toward *B. Cereus*, *E. coli* and *St. Aureus* remains practically the same. Data obtained demonstrate that the introduction of bicyclic polar fragment into surfactant platform may be of interest from the viewpoint of the design of antimicrobial preparations (in particular, antifungal ones) of little toxicity. The highest effect can be achieved by the increase of alkyl chain length and optimization of hydrophilic-lipophilic properties [44].

Thus, cationic surfactants based on alkylated DABCO are capable of forming micellar aggregates in water with high solubilization capacity toward the model organophosphorus toxicants, i.e. *p*-nitrophenyl esters of phosphorus acids and highly affect their basic hydrolysis. They demonstrate advanced antimicrobial activity as compared to analogs with acyclic head groups. All this nominates alkylated DABCO as promising candidates for application in modern technologies, which can be used for the development of polyfunctional nanosystems of complex activity.

3. Self-assembling systems based on cationic surfactants with phosphonium head group

Unlike typical cationic surfactants with ammonium head group amphiphilic

phosphonium salts are much less studied [54-56]. Meanwhile they find wide application in biotechnologies focused on the inhibition of aging the living systems, are used in antimicrobial and catalytic compositions, etc. [57,58]. Taking into account their high potential in the practice, we carried out systematic investigation of aggregation capacity of homological series of alkyl triphenylphosphonium bromides (TPPB-n, where n=8, 10, 12, 14, 16, 18) and compared their characteristics with other cationic surfactants. The estimation of micellization in aqueous solutions with the help of variety of methods (tensiometry, conductometry, potentiometry, dynamic light scattering, dye solubilization) demonstrates that cmc values and Krafft temperatures (T_K) of phosphonium salts are much lower as compared to corresponding trimethylammonium (TMA) analogs [59]. For homological series studied, the lg cmc vs. n dependences are described with linear equations with a very close slope coefficients.

- $\lg \text{ cmc} = 0.319 n - 1.055$ for TPPB series [59].
- $\lg \text{ cmc} = 0.308 n - 1.901$ for TMAB series [59].
- $\lg \text{ cmc} = 0.324 n - 2.05$ for DABCO series (Table 3).

Close slopes indicate that contributions of hydrophobic effect to the micellization of phosphonium and ammonium surfactants are similar, and therefore markedly lower cmcs of TPPB-n are contributed by interactions of charged moieties, i.e. head groups and counterions. Indeed the determination of counterion binding β with using the bromine-selective electrode revealed that for low homologs β does not exceed 0.5 to 0.6, while for TPPB-16 and TPPB-18 it reaches 0.80 to 0.97 [59]. Thus, high TPPB homologs are characterized by higher β values as compared to TMAB analogs. At the same time values of surface potential Ψ little differ for corresponding ammonium and phosphonium surfactants. Figure 10 shows that Ψ values almost linearly increase with the surfactant hydrophobicity in both series, with slopes being identical, i.e. of 7.1 and 7.0 for TPPB and TMAB homologs respectively.

High counterion binding for TPPB-16 and TPPB-18 are in apparent disagreement with the bulky phenyl groups located in the vicinity of charged atoms that can prevent their access for bromide-ions. RSA data obtained for close analog of TPPB-16, amphiphilic hexadecyl betaine with triphenylphosphonium head group, demonstrate [59] that for all the conformations, one of the phenyl fragments is spaced in such a manner that there is a channel towards the phosphorus cation.

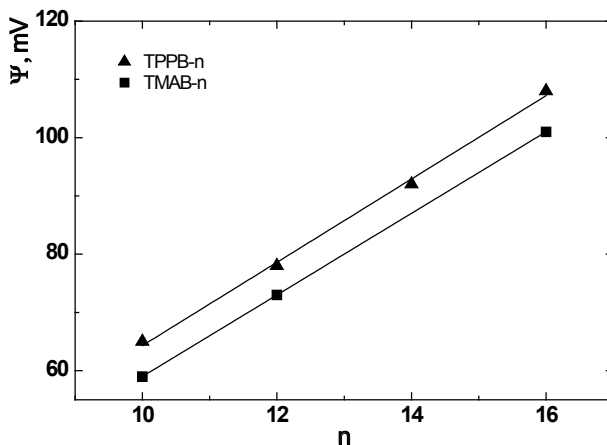


Figure 10. The surface potentials for homological series TPPB-n and TMAB-n.

Application of surfactants in biomedical protocols is due to the capacity of micellar systems to solubilize the water insoluble substrates. According to literary data [54] TPPB-n micelles have low numbers of aggregation, which would allow us to assume their low solubilizing capacity. Figure 11 presents data on the solubilization of hydrophobic probe Orange OT in TPPB micellar solutions.

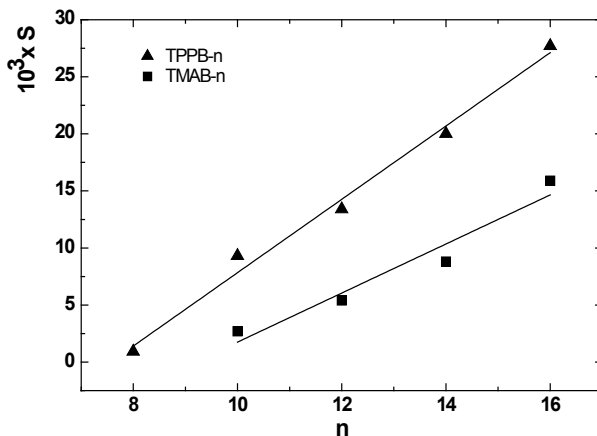


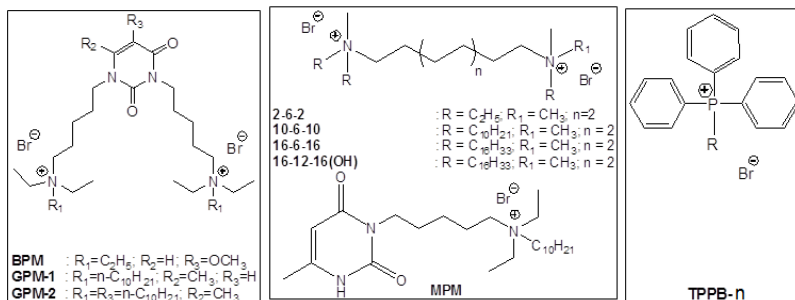
Figure 11. The solubilization capacity of TPPB and TMAB micelles toward the dye Orange OT.

The solubilization power S is calculated from the spectrophotometric measurements of the absorbency (A) of the probe at 500 nm using formula $S=b/\epsilon$, here b is a slope of the dependence A/l vs. C , l is an optical pathway, C is surfactant concentration, and ϵ is a molar extinction. The data indicate that the solubilization power of TPPB micelles is higher as compared to TMAB homologs, in particular, slopes of 3.22×10^{-3} and 2.15×10^{-3} are found for TPPB and TMAB series respectively. Noteworthy that alkylated DABCO, i.e. MCD-n series demonstrates still higher solubilization capacity [60].

The data obtained make it possible to consider novel monocationic surfactants with bicyclic and phosphonium head groups along with geminis as promising structural units for the design of nanocontainers for gene and drug delivery.

4. Cationic surfactants as gene delivery systems

In modern biotechnology, cationic surfactants approve themselves as a viable alternative for viral vectors [61,62], since the latter have such disadvantage as immune response, the impossibility of scale-up of protocols, etc. In our studies [60,62,63], mono- and dicationic surfactants are used for complexing the oligonucleotide (ONu) and DNA, with special focusing on those bearing pyrimidine fragment, i.e. structural analogs of uracil.



These structures make it possible to evaluate contributions of different interactions to the surfactant/DNA complexation. Bolaform surfactants 2-6-2 and BPM incapable of micellizing may provide information on stoichiometric electrostatic interactions with phosphate moieties of nucleotide bases. Micellizable surfactants may contribute to the nucleotide complexation through both electrostatic cooperative interactions of surface charge of micelles and solubilization mechanism. Monocationic pyrimidinic surfactant (MPM) with

mobile hydrogen is capable of complementary specific interactions through hydrogen bonds. The involvement of pyrimidinic geminis GPM-1 and GPM-2 as well as their conventional ammonium analogs of m-s-m type makes it possible to estimate the role of the hydrophobicity and micellizing capacity. Two main tasks upon the DNA complexation is the compaction of giant DNA molecules and the neutralization of anionic phosphate groups aimed at the facilitation of their transferring through cell membranes. Therefore the development of nonviral vectors assumes the control of the size of surfactant/ONu complexes (lipoplexes) and their charge.

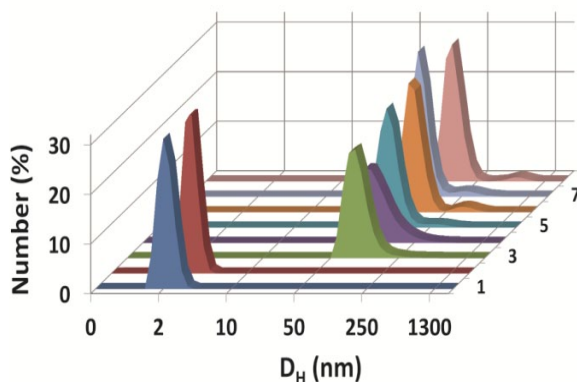


Figure 12. The DLS titration data in terms of number averaged size distribution for the ONu-16-6-16 pair; single ONu 2 mM (1), single 16-6-16 6 mM (2), N/P=0.01 (3), 0.05 (4), 0.05 (5), 0.5 (6), 1.0 (7), 2.50 (8); 25 °C.

Figure 12 exemplifies the DLS data for the lipoplex based on gemini 16-6-16 and ONu with the following base order: GCGTTAACGC. For all N/P ratio (here N is the number of charged ammonium groups and P is the number of phosphate anions) monomodal size distribution occurs, with prevail hydrodynamic diameter (D_H) being around 100-150 nm. This size answers geometric criterion of $D_H \leq 200$ nm that allows long circulation of complexes in the organism. Re-charging of the lipoplexes is controlled by the measuring of zeta-potential. Although charge compensation is observed for bolaform surfactants 2-6-2 and BPM, no re-charging occurs even at high N/P values of ~ 50 . For micellizable surfactants this value is close to unit, with higher concentrations in the point of recharging being observed for pyrimidinic surfactants as compared to m-s-m geminis. This may indicate that electrostatic mechanism is less involved in the case of GPMs.

Additional information on the surfactant/DNA complexation can be

obtained by method of fluorescent spectroscopy in the ethidium bromide (EB) exclusion study (Figure 13). Most effective complexing agent is revealed to be pyrimidinic surfactant GPM-2 and hydroxyalkylated gemini 16-12-16(OH). The latter is studied as transfectant along with other hydroxyalkylated geminis [63]. By method of flow cytometry, the effectiveness of plasmid DNA delivery into cells with the help of synthetic vectors is estimated. It has been shown that the fraction of cells incubated in the presence of 16-12-16(OH) inducing the eGFP expression reaches >50%, which is higher than for commercial transfectant Metafectene used as a reference sample.

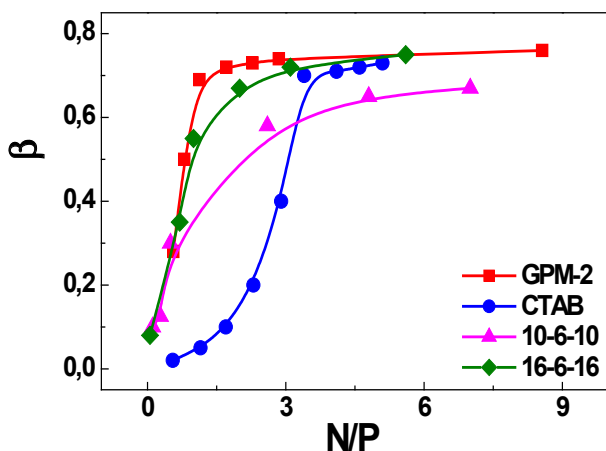


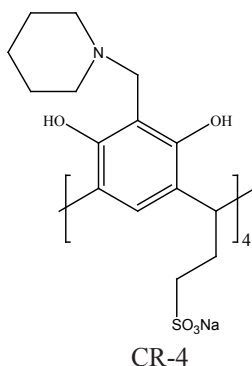
Figure 13. Fraction of the ONu bound by surfactants as a function of the surfactant/ONu molar ratio determined from the EB exclusion experiments.

5. Cationic surfactant-calixarene systems for controlled binding/release of hydrophobic guests

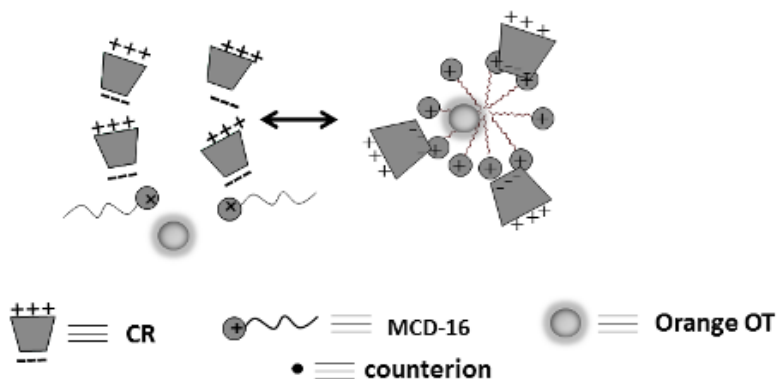
Supramolecular systems are widely used for the drug delivery due to their capacity of effectively binding of compounds with poor water solubility. Among such systems the priority belongs to the so-called lipid compositions [64,65], including micelles and microemulsions based on synthetic surfactants. The application of mixed surfactant-calixarene systems opens additional opportunities in this field, since the involvement of macrocyclic receptors may provide a high selectivity of the guest binding based on principles of the molecular recognition. A key point is that the self-assembling mechanism of surfactants and calixarenes may be strongly different that provides the possibility for the development of

nanocontainers with controlled binding/release properties by means of inducing the morphological re-arrangements.

As mention above (section 2.1) in the presence of CR-1 cationic surfactant MCD-16 starts to associate at the lower concentration and undergoes further morphological transitions with an increase in the concentration [46]. We carried out the design of nanocontainers based on mixed systems of MCD-16 with calix[4]resorcines CR-1 and CR-4, bearing amine groups at upper rim and sulfonate groups at lower rim.



In single aqueous solutions, CR-1 and CR-4 form “head-to-tail” associates due to electrostatic interaction of the negatively charged low rim and a partially protonated (depending on pH) upper rim of the calixarene cavity. Cationic surfactant MCD-16 is shown to form normal micelles in water due to contribution of hydrophobic effect. In mixed system, structural behavior is essentially governed by the ratio of components. In the case when the surfactant is a minor component, the “head-to-tail” association is preserved, while an increase in the surfactant/CR ratio induces structural transition resulting in the formation of micelle-like aggregates, and vice versa. By methods of conductometry, tensiometry, and NMR self-diffusion two critical concentrations (C_{cr}) are revealed for mixed system, viz. $C_{cr1}=0.4$ mM corresponding to the formation of the stack-like aggregates through electrostatic mechanism, and $C_{cr2}=5$ mM at which micelle-like aggregates are observed [46] (Scheme 5).



Scheme 5. Schematic representation of binding/release behavior of mixed surfactant-calix[4]resorcine mixtures controlled by morphological transitions.

Spectrophotometric control of the solubilization of hydrophobic dye Orange OT reveals that only mixed aggregates formed above C_{cr2} enriched by surfactant molecules are capable of binding the hydrophobic molecules, while increase in the CR concentration destructs micelles thereby triggering the substrate release. This approach may be put into the basis for the development of nanocontainers for controlled drug delivery.

6. The fabrication of polyelectrolyte capsules for small water insoluble guests via layer-by-layer strategy

The above design of supramolecular nanocontainer is based on non-covalent self-assembly of amphiphilic compounds. The obvious advantages of the latter are simple protocols, accessibility and low concentration of ingredients, high solubilization capacity of micelles and microemulsions, and nanoscale dimension of particles. Among few limitations of non-covalent strategy, dynamic character of the systems may be mentioned, whereupon the composition of aggregates changes at a time and depend on the bulk conditions. Alternative approach that is intensively developed at present is the strategy of layer-by-layer (LbL) deposition of the oppositely charged polyelectrolytes upon the sacrificial matrix or just upon the encapsulated substrate [66,67]. This method is nowadays widely used in different technologies including food industry, drug and gene delivery, sensor technologies, etc. [68,69]. In our work [70] novel simple protocol is developed for the encapsulation of water insoluble low molecular weight substrates (these include the majority of drugs and diagnostic probes). Unlike known procedures

this protocol need no sacrificial matrix for the capsule formation, and therefore exclude the stage of their removing, which markedly decrease the loss of the loads. The peculiarity of our method is the preliminary treatment of uncharged hydrophobic substrate with cationic surfactants, which imparts a positive charge to dispersed substrate particles and determines the order of alternation of polyelectrolyte layers. This protocol is used for the encapsulation of hydrophobic guests, namely p-nitrophenyl esters of carbonic acids laurate (PNPL), capriate (PNPCp), and myristate (PNPM) (Scheme 1). In addition, their basic hydrolysis is investigated, with conditions of the capsule fabrication being varied.

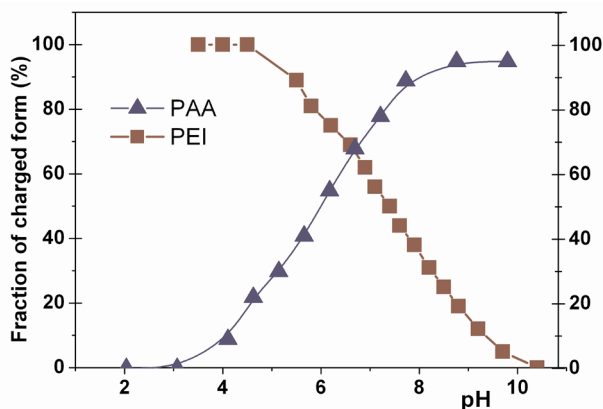


Figure 14. The pH-dependence of the fraction of charged forms in PAA and PEI macromolecules.

As polyelectrolytes, polyacrylic acid (PAA) and polyethyleneimine are used. These polyelectrolytes have carboxylic and amine groups in the molecules capable of pH dependent dissociating. Therefore, the fraction of charged fragments in both macromolecules can be controlled by the variation of solution pH. As evident from Figure 14, maximum charge density for both polyelectrolytes is achieved in the range of pH 6 to 8. Under these conditions, 50 to 90% of carboxylic groups of PAA and 40 to 80% of amine groups of PEI are in ionic form.

The key issue for the design of drug delivery carriers is their size. The majority of publications is devoted to the microcapsules with their size being in microscale range (up to $\geq 10 \mu\text{m}$) [71]. The proposed approach allows us to not only simplify procedure of loading the substrate, but also markedly decrease a capsule size. From the viewpoint of longtime circulation of drugs, the preferable

size is ≤ 200 nm. As can be seen in Figure 15, three- and five-layered capsules fabricated at pH 6.0 with the preliminary sonication correspond to this criterion.

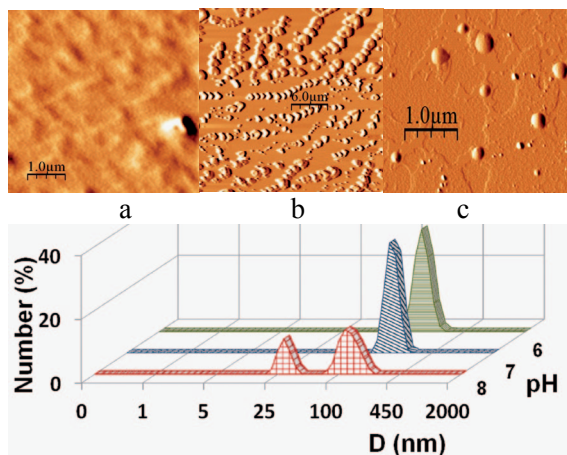


Figure 15. Size distribution analysis as function of pH adjusted at the LbL coating exemplified by three-layered PNPL-loaded capsules, 25 °C. Inset at the top shows AFM images of the PNPL@CTAB particles (a), PNPL loaded five-layered capsules fabricated under pH 7.0 without preliminary CTAB treatment (b) and PNPL@CTAB loaded three-layered capsules fabricated under pH 6.0 with ultrasonication (c).

In aqueous basic solutions the hydrolysis of esters is slow process, whereas it accelerates manifold in cationic micelles [8,31,32]. Thus, in 0.005 M CTAB and CHAB micellar solutions 275-fold and 500-fold accelerations of hydrolytic cleavage of PNPL occur [72], with the rate markedly depending on the nature of substrate: $\text{PNPM} < \text{PNPL} < \text{PNPCn}$. In the case of encapsulated esters their rate of hydrolysis is determined not only by chemical reaction that depends on the solution conditions (temperature, pH, the presence and concentration of admixtures), but also on the permeability of the capsule shells, with the latter factor becoming prevail. Indeed, as shown in work [70], the reactivity of encapsulated esters practically does not depend on the factors that play a key role in the molecular solution, i.e. pH, nature and concentration of surfactants, the structure of substrates. Therefore the rate of the release of loaded substrates and hence their reactivity toward reagents localized in bulk phase will be strongly controlled by the permeability of shells tuned by fabrication parameters. The advantages of the protocol developed are exemplified by data of half-life values (τ) for hydrolysis of encapsulated esters (Figure 16) demonstrating that τ can be

widely varied (from several minutes to hours) by alteration in the procedure of the capsule fabrication.

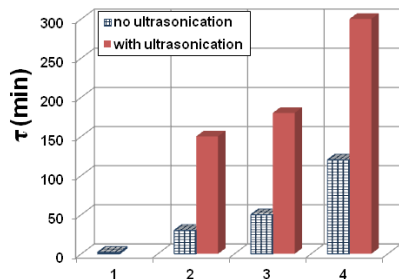


Figure 16. Half-life values for hydrolysis of free PNPL (1) and PNPL encapsulated in three-layered capsules fabricated in unbuffered conditions (2) under pH 6.0 (3), 7.0 (4); (bulk conditions: 0.0015 M CHAB; pH 9.2; 25 °C).

The information obtained is used for the working out the method of express monitoring of permeability of polyelectrolyte capsules and their integrity as well as for the control of the load and loss of substrates at all stages of encapsulation. The maximum loss of substrates is shown to occur on the stage of preparing of charged dispersed particles PNPL@CTAB (up to 20%), while stages of layer deposition is characterized by inconsiderable losses (within 1-2%).

We thank the Russian Foundation for Basic Researches (Grant 12-03-00668) for financial support.

List of abbreviations

DLS – dynamic light scattering
 cmc – critical micelle concentration
 cac – critical aggregation concentrations
 CTAB – cetyltrimethylammonium bromide
 CHAB – cetylhydroxyethyltrimethylammonium bromide
 CPB – cetylpyridinium bromide
 TPPB-n – alkyltriphenylphosphonium bromides
 TMAB-n – alkyltrimethylammonium bromides
 DABCO – 1,4-diazabicyclo[2,2,2]octane
 MCD – monocationic derivatives of DABCO
 DCD – dicationic derivatives of DABCO
 MPM – monocationic pyrimidinic surfactant

BPM – bolaform pyrimidinic surfactant
 GPM – gemini pyrimidinic surfactant
 PNPA – p-nitrophenyl acetate
 PNPC – p-nitrophenyl caprylate
 PNPCn – p-nitrophenyl caprinate
 PNPL – p-nitrophenyl laurate
 PNPM – p-nitrophenyl myristate
 NECP – p-nitrophenyl ethyl chloromethyl phosphonate
 NBCP – p-nitrophenyl n-buthyl chloromethyl phosphonate
 NHCP – p-nitrophenyl hexyl chloromethyl phosphonate
 NDEP – p-nitrophenyl diethyl phosphate
 BNMP – bis-p-nitrophenyl methyl phosphonate
 PEO – polyethyleneoxide
 PPO – polypropyleneoxide
 PEG – polyethyleneglycol
 PEI – polyethyleneimine
 APEI – alkylated polyethyleneimine
 CR – calix[4]resorcine
 ONu – oligonucleotide
 LbL – layer-by-layer
 PAA – polyacrylic acid
 EB – ethidium bromide

References

1. Fendler J. H. Atomic and molecular clusters in membrane mimetic chemistry. *Chem. Rev.* 1987. V. 87. № 5. P. 877-899.
2. Vriezema D., Aragone's M., Elemans J., Cornelissen J., Rowan A., Nolte R. Self-assembled nanoreactors. *Chem. Rev.* 2005. V. 105. N 4. P. 1445 - 1490.
3. Shi W. Y., He S., Wei M., Evans D. G., Duan X. Optical pH sensor with rapid response based on a fluorescein-intercalated layered double hydroxide. *Adv. Funct. Mater.* 2010. V. 20. N 22. P. 3856 - 3863.
4. Yadava P., Buethe D., Hughes J. A. Nonviral gene therapy with surfactants. *ACS Symp. Ser.* 2006. V. 923. № 14. P. 198 - 216.
5. Matile S., Jentzsch A.V., Montenegro J., Fin A. Recent synthetic transport systems. *Chem. Soc. Rev.* 2011. V. 40. N 5. P. 2453 - 2474.
6. Zhang X., Wang C. Supramolecular amphiphiles. *Chem. Soc. Rev.* 2011. V. 40. N 1. P. 94 - 101.
7. Rusanov A. I. *Micellization in Surfactant Solutions.* Gordon & Breach.

- New York. 1999.
8. Fendler E. J., Fendler J. H. Micellar catalysis in organic reactions: kinetic and mechanistic implications. *Adv. Phys. Org. Chem.* 1970. V. 8. P. 271 - 406.
 9. Holmberg K., Jonsson B., Kronberg B., Lindman B. Surfactants and polymers in aqueous solution. 2003. 2 ed. John Wiley&Sons Ltd. Chichester. England. 545p.
 10. Zakharova L. Ya., Mirgorodskaya A. B., Zhiltsova T. P., Kudryavtseva L. A., Konovalov A. I. Reactions in supramolecular systems. molecular encapsulation: organic reactions in constrained systems – Wiley. 2010. P. 397 - 420.
 11. Tzika E. D., Christoforou M., Pispas S., Zervou M., Papadimitriou V., Sotiroidis T. G., Leontidis E., Xenakis A. Influence of nanoreactor environment and substrate location on the activity of horseradish peroxidase in olive oil based water-in-oil microemulsions. *Langmuir*. **2011**. V. 27. N 6. P. 2692 – 2700.
 12. Mandal A. K., Thanigaivelan U., Pandey R. K., Asthana S., Khomane R. B., Kulkarni B. D. Preparation of spherical particles of 1,1-diamino-2,2-dinitroethene (fox-7) using a micellar nanoreactor. *Org. Process Res. Dev.* **2012**. V. 16. N 11. P. 1711 – 1716.
 13. Monteiro M. J. Nanoreactors for polymerizations and organic reactions. *Macromolecules*. **2010**. V. 43. N 3. P. 1159 – 1168.
 14. Marchetti L., Levine M. Biomimetic Catalysis. *ACS Catal.* **2011**. V. 1. N 9. P. 1090 – 1118.
 15. Pileni M. P. Reverse micelles as microreactors. *J. Phys. Chem.* 1993. V. 97. N 27. P. 6961 -6973.
 16. Dwars T., Paetzold E., Oehme G. Reactions in Micellar Systems. *Angew. Chem. Int. Ed.* 2005. V. 44. P. 7174 - 7199.
 17. Hait S. K., Moulik S. P. Gemini surfactants: a distinct class of self-assembling molecules. *Curr. Sci.* 2002. V. 82. N 9. P. 1101 - 1111.
 18. Shukla D., Tyagi V. K. Cationic gemini surfactants. *J. Oleo. Sci.* 2006. V. 55. N 8. P. 381 - 390.
 19. Menger F. M., Keiper J. S. Gemini surfactants. *Angew. Chem., Int. Ed. Engl.* 2000. V. 112. N 11. P. 1906 - 1920.
 20. Zana R. Dimeric (Gemini) surfactants: effect of the spacer group on the association behavior in aqueous solution. *J. Colloid Interface Sci.* 2002. V. 248. N 2. P. 203 - 220.
 21. Mirgorodskaya A. B., Kudryavtseva L. A., Pankratov V. A., Lukashenko S. S., Rizvanova L. Z., Konovalov A. I. Geminal alkylammonium

- surfactants: Aggregation properties and catalytic activity. *Russ. J. Gen. Chem.* 2006. V. 76. N 10. P. 1625 - 1631.
22. Mirgorodskaya A. B., Kudryavtseva L. A. Aqueous solutions of geminal alkylammonium surfactants as a medium for reactions of long-chain amines. *Russ. J. Gen. Chem.* 2009. V. 79. N 1. P. 42 - 48.
 23. Vylegzhanina N. N., Mirgorodskaya A. B., Pankratov V. A., Zuev Yu. F. Dynamic structure of the micelles of gemini alkylammonium surfactants. *Colloid J.* 2010. V. 72. N 2. P. 168 - 176.
 24. Mirgorodskaya A. B., Kudryavtseva L. A., Vylegzhanina N. N., Idiyatullin B. Z., Zuev Yu. F. Mixed micellar systems of geminal alkylammonium surfactants and long-chain amines. *Russ. Chem. Bull., Inter. Ed.* 2010. V. 59. N 4. P. 790 - 796.
 25. Mirgorodskaya A. B., Yackevich E. I., Lukashenko S. S., Voloshina A. D., Kulik N. V., Zobov V. V., Zakharova L. Ya. Aggregation behavior, micellar catalytic effect and antimicrobial action of gemini alkylammonium surfactants with varied length of hydrophobic radical. *Liquid Crystals and Their Application.* 2011. N 2. P. 75 - 82.
 26. Mirgorodskaya A. B., Valeeva F. G., Lukashenko S. S., Yatskevich E. I., Zakharova L. Ya., Konovalov A. I. Dicationic surfactant based catalytic systems for alkaline hydrolysis of phosphonic acid esters. *Kinetics and Catalysis.* 2012. V. 53. N 2. P. 206 – 213.
 27. Yackevich E. I., Mirgorodskaya A. B., Zakharova L. Ya., Konovalov A. I. Influence of the strong electrolyte on the aggregation behavior and catalytic properties of dicationic surfactants. *Russ. Chem. Bull., Inter. Ed.* 2011. V. 60. N 12. P. 2597 – 2601.
 28. Mirgorodskaya A. B., Yatskevich E. I., Zakharova L. Ya., Konovalov A. I. Gemini surfactant–nonionic polymer mixed micellar systems. *Colloid J.* 2012. V. 74. N 1. P. 91 – 98.
 29. Yurina A. V., Lukashenko S. S., Mirgorodskaya A. B., Zakharova L. Ya. Polyethyleneimine – gemini cationic surfactant polymer-colloid systems. *Physical chemistry of polymers. Synthesis, properties and application. Book of Articles.* Tver. 2010. N 16. P. 324 - 329 [in Russian].
 30. Mirgorodskaya A. B., Yackevich E. I., Zakharova L. Ya. Functional supramolecular systems based on amphiphilic and polymer compounds. *Liquid Crystals and Their Application.* 2011. N 4. P. 80 – 89 [in Russian].
 31. Mirgorodskaya A. B., Yackevich E. I., Lukashenko S. S., Zakharova L. Ya., Konovalov A. I. Solubilization and catalytic behavior of micellar system based on gemini surfactant with hydroxyalkylated head group. *J. Mol. Liq.* 2012. V. 169. P. 106 - 109.

32. Zakharova L. Ya., Mirgorodskaya A. B., Zhil'tsova E. P., Kudryavtseva L. A. Catalysis of nucleophilic substitution reactions in supramolecular systems. *Russ. Chem. Bull., Int. Ed.* 2004. V. 53. N 7. P. 1385 - 1401
33. Cristau H. J., Ginieys J. F., Torreilles E. Destruction d'esters organophosphores toxiques par le borate de sodium. Catalyse micellaire par de sels de phosphonium et d'ammonium. *Bull. Soc. Chim. Fr.* 1991. N 128. P. 712-716.
34. Zakharov A. V., Voronin M. A., Valeeva F. G., Gubanov E. F. Influence of the cationic surfactants structure on the surface properties, aggregation and catalysis of micelles and microemulsions. *Book of Articles on X All-Russian Conference Structure and Dynamics of Molecular Systems. Ioshkar-Ola.* 2003. V. 10, N 2. P. 89 – 92 [in Russian].
35. Bunton C. A., Kamego A. A., Minch M. J., Wright J. L. Effect of changes in surfactant structure on micellarly catalyzed spontaneous decarboxylations and phosphate ester hydrolysis. *J. Org. Chem.* 1975. V. 40. N 9. P. 1321 - 1327.
36. Menger F. M., Persichetti R. A. Two new amphiphilic catalysts for ester hydrolysis. *J. Org. Chem.* 1987. V. 52. N 15. P. 3451 - 3452.
37. Vecchi A., Melai B., Marra A., Chiappe C., Dondoni A. Microwave-enhanced ionothermal cuaac for the synthesis of glycoclusters on calix[4]arene platform. *J. Org. Chem.* 2008. V. 73. N 16. P. 6437 - 6440.
38. Tabushi I., Imuta J., Seko N., Kobuke Y. Highly discriminative binding of nucleoside phosphates by a lipophilic diammonium salt embedded in a bicyclic skeleton. *J. Am. Chem. Soc.* 1978. V. 100. N 19. P. 6287 - 6288.
39. Tamkovich N. V., Malyshev A. V., Konevets D. A., Sil'nikov V. N., Zenkova M. A., Vlassov V. V. Chemical ribonucleases. VII. Effect of positively charged RNA-binding domains and hydrophobic fragments of the conjugates based on 1,4-diazabicyclo[2.2.2]octane and imidazole on their ribonuclease activity. *Russ. J. Bioorg. Chem.* 2007. V. 33. N 2. P. 233 - 242.
40. Pashirova T. N., Zhil'tsova E. P., Kashapov R. R., Lukashenko S. S., Litvinov A. I., Kadirov M. K., Zakharova L. Ya., Konovalov A. I. Supramolecular systems based on 1-alkyl-4-aza-1-azoniabicyclo[2.2.2]octane bromides. *Russ. Chem. Bull., Inter. Ed.* 2010. V. 59. N. 9. P. 1745 - 1752.
41. Gaisin N. K., Gnezdilov O. I., Pashirova T. N., Zhil'tsova E. P., Lukashenko S. S., Zakharova L. Ya., Osipova V. V., Dzhabarov V. I., Galyametdinov Yu. G. Micellar and liquid-crystalline properties of

- bicyclic fragment-containing cationic surfactant. *Colloid J.* 2010. V. 72. N 6. P. 764 - 770.
42. Pashirova T. N., Zhil'tsova E. P., Lukashenko S. S., Zakharova L. Ya. Micelle formation and catalytic activity of hydrophobic mono- and biscationic derivatives of 1,4-diazabicyclo[2.2.2]octane. *Liquid Crystals and Their Application.* 2009. N 4 (30). P. 47 - 55.
 43. Zakharova L. Ya., Pashirova T. N., Kashapov R. R., Zil'tsova E. P., Gaisin N. K., Gnezdilov O. I., Konov A. B., Lukashenko S. S., Magdeev I.M. Catalytic properties of micellar systems based on 4-aza-1-alkyl-1-azoniabicyclo[2.2.2]octane bromides. *Kinetics and Catalysis.* 2011. V. 52. N 2. P. 179 - 185.
 44. Zhil'tsova E. P., Pashirova T. N., Kashapov R. R., Gaisin N. K., Gnezdilov O. I., Lukashenko S. S., Voloshina A. D., Kulik N. V., Zobov V. V., Zakharova L. Ya., Kononov A. I. Alkylated 1,4- diazabicyclo[2.2.2] octanes: self-association, catalytic properties, and biological activity. *Russ. Chem. Bull., Inter. Ed.* 2012. V. 61. N. 1. P. 113 - 120.
 45. Gaisin N. K., Gnezdilov O. I., Bashirov F. I., Kashapov R. R., Zhil'tsova E. P., Zakharova L. Ya., Pashirova T. N., Lukashenko S. S. Studying micellization of alkylated 1,4- diazabicyclo[2.2.2]octane by nuclear magnetic resonance technique using pulsed gradient of static magnetic field. *J. Mol. Liq.* 2012. V. 167. P. 89 - 93.
 46. Kashapov R. R., Pashirova T. N., Kharlamov S. V., Ziganshina A. Yu., Zhil'tsova E. P., Lukashenko S. S., Zakharova L. Ya., Latypov S. K., Kononov A. I. Novel self-assembling system based on resorcinarene and cationic surfactant. *Phys. Chem. Chem. Phys.* 2011. V. 13. Issue 35. P. 15891 - 15898.
 47. Kashapov R. R., Pashirova T. N., Zhil'tsova E. P., Zakharova L. Ya., Lukashenko S. S., Ziganshina A. Yu., Kononov A. I. Supramolecular systems based on aminomethylated calix[4]resorcinarene and a cationic surfactant. Self-association and catalytic activity. *Book of Articles on XVII All-Russian Conference Structure and Dynamics of Molecular Systems.* Ufa. 2010. V. 17. N 1. P. 329 – 332 [in Russian].
 48. Zhil'tsova E. P., Kashapov R. R., Zakharova L. Ya., Lukashenko S. S., Timosheva A. P., Kasymova E. M., Kayupov A. R., Burilov A. R. Alkylated polyethyleneimine – cationic surfactant – calix[4] resorcinarene – chloroform catalytic system. *Kinetics and Catalysis.* 2012. V. 53. N 2. P. 231 - 238.
 49. Kashapov R. R., Pashirova T. N., Zhil'tsova E. P., Lukashenko S. S., Ziganshina A. Yu., Zakharova L. Ya. Supramolecular systems based

- on aminomethylated calix[4]resorcinarene and a cationic surfactant catalysts of the hydrolysis of esters of phosphorus acids. *Russ. J. Phys. Chem. A.* 2012. V. 86. N 2. P. 200 - 204.
50. Callaghan A., Doyle R., Alexander E., Palepu R. Thermodynamic properties of micellization and adsorption and electrochemical studies of hexadecylpyridinium bromide in binary-mixtures of 1,2-ethanediol with water. *Langmuir.* 1993. V. 9. N 12. P. 3422 - 3426.
 51. Moulik S. P., Haque M. E., Jana P. K., Das A. R. Micellar properties of cationic surfactants in pure and mixed states. *J. Phys. Chem.* 1996. V. 100. N 2. P. 701 - 708.
 52. Berezin I. V., Martinek K., Yatsimirskii A. K. Physicochemical foundations of micellar catalysis. *Russ. Chem. Rev.* 1973. V. 42. N 10. P. 787 - 802.
 53. *Fendler E. J., Fendler J. H. Methods and advances in physical organic chemistry.* Mir. Moscow. 1973. 242p [in Russian].
 54. Prasad M., Moulik S. P., MacDonald A., Palepu R. Self-aggregation of alkyl (C10-, C12-, C14- and C16-) triphenyl phosphonium bromides and their 1: 1 Molar mixtures in aqueous medium: a thermodynamic study. *J. Phys. Chem. B.* 2004. V. 108. N 1. P. 355 - 362.
 55. Bakshi M. S., Singh J., Singh K., Kaur G. Mixed micelles of cationic gemini with tetraalkyl ammonium and phosphonium surfactants: the head group and hydrophobic tail contributions. *Colloid Surf. A.* 2004. V. 234. N 1. P. 77 - 84.
 56. Mohareb M. M., Ghosh K. K., Orlova G. and Palepu R. M. S(N)2 Reaction of sulfonate ester in the presence of alkyl triphenyl phosphonium bromides and mixed cationic systems. *J. Phys. Org. Chem.* 2006. V. 19. P. 281 - 290.
 57. Ross M. F., Kelso G. F., Blaikie F. H., James A. M., Cochemé H. M., Filipovska A., Da Ros T., Hurd T. R., Smith R. A. J., Murphy M. P. Lipophilic triphenylphosphonium cations as tools in mitochondrial bioenergetics and free radical biology. *Biochemistry.* 2005. V. 70. N 2. P. 222 - 230.
 58. Millard M., Pathania D., Shabaik Y., Taheri L., Deng J., Neamati N. Preclinical evaluation of novel triphenylphosphonium salts with broad-spectrum activity. *PLoS ONE.* 2010. V. 5. N 10: e13131. doi:10.1371.
 59. Gainanova G. A., Vagapova G. I., Ibragimova A. R., Valeeva F. G., Syakaev V. V., Tudriy E. V., Galkina I. V., Kataeva O. N., Zakharova L. Ya., Latypov Sh. K., Kononov A. I. Self-assembling systems based on amphiphilic alkyltriphenylphosphonium bromides. Elucidation of

- the role of head group. *J. Colloid Interface Sci.* 2012. V. 367. N 1. P. 327–336.
60. Zakharova L., Kashapov R., Vagapova G., Gabdrakhmanov D., Vasilieva E. Comparative study of aqueous solutions of cationic surfactants: structure/activity relation in their aggregation and solubilization behavior and complexation with oligonucleotide. *Chem. Lett.* 2012. V. 41. N 10. P. 1226 - 1228.
 61. Dasgupta A., Das P. K., Dias R. S., Miguel M. G., Lindman B., Jadhav V. M., Gnanamani M., Maiti S. Effect of headgroup on DNA-cationic surfactant interactions. *J. Phys. Chem. B.* 2007. V. 111. N 29. P. 8502 - 8508.
 62. Zakharova L., Voronin M., Gabdrakhmanov D., Semenov V., Giniyatullin R., Syakaev V., Latypov S., Reznik V., Kononov A., Zuev Y. Supramolecular systems based on mono- and dicationic pyrimidinic amphiphiles: self-organization and complexation with oligonucleotides. *ChemPhysChem*, 2012, V.13, P.788-796.
 63. Grigoriev I. V., Korobeinikov V. A., Cheresiz S. V., Pokrovsky A. G., Zakharova L. Ya., Voronin M. A., Lukashenko S. S., Kononov A. I., Zuev Yu. F. Cationic gemini surfactants as new agents for plasmid DNA delivery into cells. *Doklady Biochemistry and Biophysics.* 2012. V. 445. N 1. P. 197 – 199.
 64. Barenholz Y. Liposome application: problems and prospects. *Curr. Opin. Colloid Interface Sci.* 2001. V. 6. N 1. P. 66 – 77.
 65. Wissing S. A., Kayser O., Müller R. H. Solid lipid nanoparticles for parenteral drug delivery. *Adv. Drug Deliv. Rev.* 2004. V. 56. N 9. P. 1257 – 1272.
 66. Akiyama R., Kobayashi S. “Microencapsulated” and related catalysts for organic chemistry and organic synthesis. *Chem. Rev.* 2009. V. 109. N 2. P. 594 – 642.
 67. Antipov A. A., Sukhorukov G. B. Polyelectrolyte multilayer capsules as vehicles with tunable permeability. *Advan. Colloid Interface Sci.* 2004. V. 111. N 1-2. P. 49 – 61.
 68. De Geest B. G., De Koker S., Sukhorukov G. B., Kreft O., Parak W. J., Skirtach A. G., Demeester J., De Smedt S. C., Hennink W. E. Polyelectrolyte microcapsules for biomedical applications. *Soft Matter.* 2009. V. 5. N 2. P. 282 – 291.
 69. Sukhorukov G. B., Rogach A. L., Garstka M., Springer S., Parak W. J., Munoz-Javier A., Kreft O., Skirtach A. G., Susa A. S., Ramaye Y., Palankar R., Winterhalter M. Polymer microcapsules: novel tools for

- biological and pharmacological applications concept. *small*. 2007. V. 3. N 6. P. 944 – 955.
70. Zakharova L., Ibragimova A., Vasilieva E., Mirgorodskaya A., Yackevich E., Nizameev I., Kadirov M., Zuev Y., Konovalov A. Polyelectrolyte capsules with tunable shell behavior fabricated by the simple LBL technique for the control of the release and reactivity of small guests. *J. Phys. Chem. C*. **2012**. V. 116. N 35. P. 18865 – 18872.
 71. De Geest B. G., Sanders N. N., Sukhorukov G. B., Demeester J., De Smedt S. C. Release mechanisms for polyelectrolyte capsules. *Chem. Soc. Rev.* 2007. V. 36. N 4. P. 636 – 649.
 72. Mirgorodskaya A. B., Bogdanova L. R., Kudryavtseva L. A., Lukashenko S. S., Konovalov A. I., Role of surface potential in the catalytic action of micelles of cationic surfactants with a hydroxyalkyl fragment in the head group. *Russ. J. Gen. Chem.* 2008. V. 78. P. 163-170.

Chapter 16

Adsorption behavior, surface dilational rheology and foam stability of mixed sodium humates / cetyltrimethylammonium bromide solutions

Svetlana Khil'ko¹, Volodymyr Rybachenko¹ and Grzegorz Schroeder²

¹*L.M. Lytvynenko Institute of Physico-Organic and Coal Chemistry of Ukrainian National Academy of Sciences, 70 R. Luxemburg Street, Donetsk 83114, Ukraine*

²*Adam Mickiewicz University in Poznań, Faculty of Chemistry, Umultowska 89b, 61-614 Poznań, Poland*

Introduction

Mixtures of polyelectrolytes and oppositely charged surfactants are of increasing interest due to their importance in different branches of industry. Understanding interfacial rheology of adsorbed layers of such systems is very important for foam and emulsion stabilization. Indeed, destabilization of these systems can be due to several mechanisms such as drainage and thin-liquid film rupture both of which are known to be linked to the interfacial rheology of the dispersion interface [1].

Mixed polyelectrolyte / surfactant solutions show drastic changes of the surface properties with increasing surfactant concentration [2 – 4]. Even small additives of surfactant to polyelectrolyte solution lead to strong decrease of surface tension. This strong synergistic effect was known for many decades and explained by the formation of relatively hydrophobic polyelectrolyte / surfactant complexes.

Goddard proposed a simple model of the surface structure of dilute polyelectrolyte/surfactant solutions: the surfactant ions form a monolayer at the liquid surface and attract electrostatically the elongated charged macromolecules [5]. The charged groups of the polymer play the role of counterions. In [6] was shown that Goddard's model has some disadvantages: it does not take into account the chemical nature of the polyelectrolyte backbone chains, insufficient to explain the high surface elasticity at extremely dilute solutions. Authors [6]

proposed a modification of this classic model by taking into account hydrophobic interactions in the adsorption layer leading to the formation of almost two-dimensional nano- or micro-aggregates. These conclusions were corroborated by ellipsometry measurements [6]. Moreover application of the neutron reflectivity [7] has shown that the surface structure of polyelectrolyte/surfactant solutions can be divided into two main types. In the first case, as shown by neutron reflectivity, the adsorption layers are relatively thick and cannot be described in terms of a surfactant layer with some extended polymer (type 1). In the second case the adsorption layer thickness approaches the typical values of surfactant layers (type 2). The adsorption layers of these two kinds lead to different patterns of the surface tension dependency on surfactant concentration [7].

Humic acids (HA) are natural weak-acid polyelectrolytes. They contain hydrophilic functional groups (mainly carboxylic and hydroxyl) and hydrophobic aromatic and aliphatic moieties giving to the HA characteristics of an amphiphile [8, 9]. Thus, HA exhibit surface activity in aqueous solution [10 – 12] and the ability to associate with different molecules by electrostatic and/or hydrophobic interactions [13 – 18]. In [19] soluble and insoluble complexes, which are formed due to the interactions between the sodium humates and cetyltrimethylammonium bromide, were analyzed by small-angle X-ray scattering technics, and the possible structures of these complexes were proposed. In [15, 16, 18] for mixtures of humic acids with cationic dye and cationic surfactants (dodecyl- and cetylpyridinium chloride) was shown that the binding capacity of HA increases with pH (increasing degree of ionization of a polyelectrolyte) and the length of the surfactant hydrocarbon radical .

The effect of alkytrimethylammonium bromides additives on surface tension of sodium humates solutions was studied in [20]. It was shown that the effectiveness of reducing the surface tension increases with increasing surfactant chain length.

In this paper we aim to measure interfacial rheological properties of oppositely charged surfactant/polyelectrolyte layers at different pH values, composed of anionic polyelectrolyte, sodium humates, and a cationic surfactant, CTAB, with interfacial dilatational rheological measurement techniques. Furthermore, we attempt to correlate the surface rheology data to the foamability (e.g., the propensity of a system to generate foam) and the foam stability of the corresponding solutions.

Experimental

Humic acids and their sodium salts were received from brown coal of Alexandrian deposit (Ukraine). The procedure for producing HA samples and

the results of their elemental and functional analyses are presented in [21]. Sodium humates solutions to be examined were obtained by dissolving dry HA in a 0.1 N NaOH solution. The pH of the SH solutions was 11.5. The cationic surfactant, cetyltrimethylammonium bromide was from Sigma. The solutions were prepared in bidistilled water. All the measurements in this work were performed at two SH concentrations of $C_{SH} = 0.6$ g/l; 7.6 g/l and various CTAB concentrations and at three pH values: 4.0; 7.0; 11.5.

Regularities of the precipitation of humic substances from mixed with CTAB solutions were studied by photocolormetry. The sediment precipitated after 1 day was separated by centrifugation at 1500 revolutions per minute during 15 minutes, and the optical density of the supernatant liquid was measured with an KF-11 colorimeter at $\lambda = 430$ nm. The measurement results were presented in the form of relationship between the ratio of the optical density of the sodium humates solution at a given concentration of the added CTAB, D , to that of the initial sodium humates solution, D_0 .

The dynamic surface properties at the liquid/air interface of mixed solutions of sodium humates with CTAB were measured as a function of surface age, concentration of components, pH. The experiments were performed by the Du Noüy ring method (TE-1, Lauda, Germany) and drop profile analysis tensiometry (PAT-2P, SINTERFACE Technologies, Germany) at 25 °C. To study the dilational elasticity, the drop, after having reached the adsorption equilibrium, was subjected to harmonic oscillations with an amplitude of 7-8% and frequencies in the range between 0.005 and 0.2 Hz.

Dilatation modulus (E , mN/m) characterizes the viscoelastic properties of surfactant surface layers and takes into account all relaxation processes that affect surface tension γ . At a small amplitude ΔS of harmonic oscillations of a surface with an angular frequency of $\Omega = 2\pi\nu$, $\Delta S = \Delta \bar{S} \exp(i\Omega t)$ and the following expression can be derived for the dilatation viscoelastic modulus [22, 23]:

$$E = \frac{\Delta\gamma}{\Delta S / S_0} = \frac{d\gamma}{d \ln S}$$

The visco-elastic modulus E is a complex number, with a real part E_r (the storage modulus) equal to the elasticity and the imaginary part E_i (the loss modulus) given by the product of the viscosity, η_d , and the imposed angular frequency, Ω , of the area variations: $E = E_r + iE_i$

$$|E| = \sqrt{E_i^2 + E_r^2}$$

The foam was formed due to air barbotage at a rate of 50-60 mm³/s. Foam stability was evaluated as the ratio of the volume of foam remaining after 10 minutes, V_p , to the initial volume of foam, V_0 .

Results and discussion

1. Phase behavior

In this paper, the salts of humic acid (HA) were considered as promising natural compounds having properties of molecular receptors. It has been known that these are nano-sized (4-16 nm) polymeric aromatic polyoxipolycarboxylic acids, able to come into ionic and donor-acceptor interactions, form hydrogen bonds, and participate in redox and sorption processes. The presence of both hydrophobic and hydrophilic fragments in the structure of these macromolecules forms surface-active properties of the HA salts. The Diagram of elementary units of the macromolecules of HA has been shown in Figure 1.

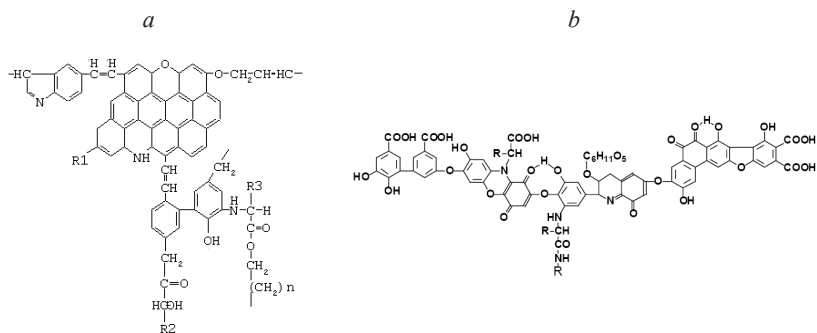


Figure 1. Diagram of elementary units of humic acids according to Orlov-Chukov (a) and Stevenson (b).

Before discussing the adsorption behavior of polyelectrolyte / surfactant mixtures, it is useful to give a brief description of the bulk phase behavior typical of these systems. Phase behavior of sodium humates solutions in the presence of CTAB additives is similar to that for other mixed oppositely charged polyelectrolyte / ionic surfactant solutions. When the concentration of CTAB is close to the concentration of oppositely charged groups of humic

substances macroscopic aggregates in solution are formed and phase separation or precipitation is observed [19, 24, 25]. With further increase in the CTAB concentration complexes may again become soluble due to their hydrophilization by interactions between the hydrophobic regions of HA chains and CTAB hydrocarbon radicals [19, 25].

Figure 2 is an illustration of the possible configurations of the SH-CTAB complexes as a function of CTAB concentration according to the data of [19].

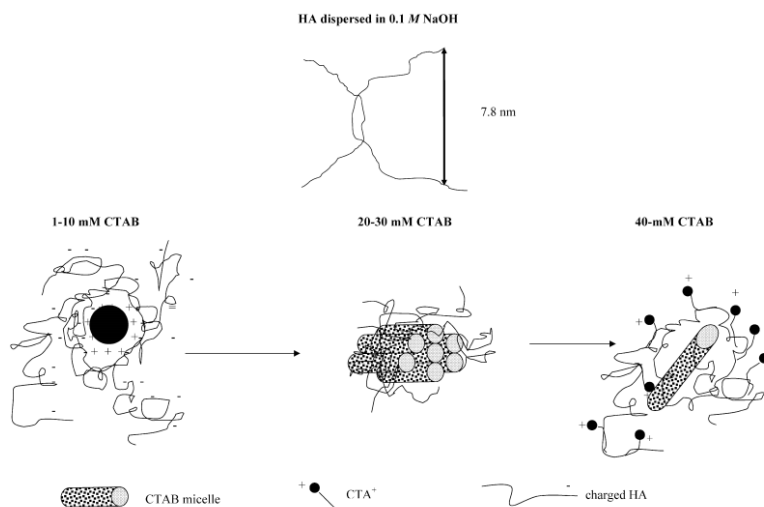


Figure 2. Illustration of possible configurations between humic acids (HA) and CTAB complexes under various experimental conditions.

The effects of CTAB additives on the solubility of humic substances according to the present work are shown in Fig. 3.

At very dilute CTAB concentrations, the mixtures are clear and transparent and it is assumed that any surfactant / polyelectrolyte complex is completely soluble. As the CTAB concentration is increased the optical density of solutions decreases, solutions tend to become increasingly turbid or cloudy, owing to the decrease in solubility of the complex. There is a minimum of solubility on the dependences of change in optical density of SH/CTAB solutions on CTAB concentration, after which further increase in the CTAB concentration leads to an increase in the optical density of the mixed solutions and the solutions become clear again. So the complexes can be resolubilized with the surfactant

concentration increase owing to the excess charge that accumulates on the complexes.

pH reduction shifts solubility minimum to lower CTAB concentrations, and the SH concentration increase – toward higher CTAB concentrations. This behavior is probably due to a change in the number of dissociated functional groups of HA macromolecules available for interactions with CTAB when pH and the SH concentration in the solution are changed.

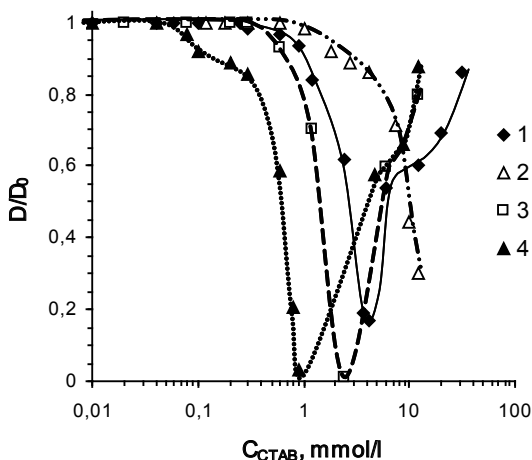


Figure 3. Dependences of the ratios of optical densities of mixed SH/CTAB solutions, D , to that of SH solution, D_0 , on CTAB concentration and pH:

1, 2 – pH = 11.5; 3 – pH = 7.0; 4 – pH = 4.0.

1, 3, 4 – $C_{SH} = 0.6$ g/l, 2 – $C_{SH} = 7.6$ g/l.

2. Adsorption behavior and surface dilational rheology

Figure 4 shows equilibrium surface tension isotherms for mixed sodium humates/CTAB solutions. There are two CTAB concentration ranges on the surface tension isotherms of SH/CTAB mixtures which are characterized by various slope angles of tangent line to these dependences. The surface tension of mixed SH / CTAB solutions is sharply reduced in the CTAB concentration range below C_1 and reaches a plateau. In this case the region of sharp change in the slope angle of the surface tension isotherm (C_1) can be associated with the beginning of ionic surfactant aggregates formation at some points of the polymer chains and is designated as a critical concentration of aggregation. The presence of a plateau in the surface tension isotherm in the range of $C_1 < C_{CTAB} < C_2$ may be

the result of aggregation in the bulk solution, leading to a nearly constant activity of the monomer. Further surface tension reducing of mixed solutions at CTAB concentrations above C_2 indicates the saturation of the polyelectrolyte molecules by ionic surfactant and the beginning of CTAB monomer concentration growth, which replace SH/CTAB complexes in the adsorption layer. The solubility of SH/CTAB complexes starts to decrease at CTAB concentrations above C_2 .

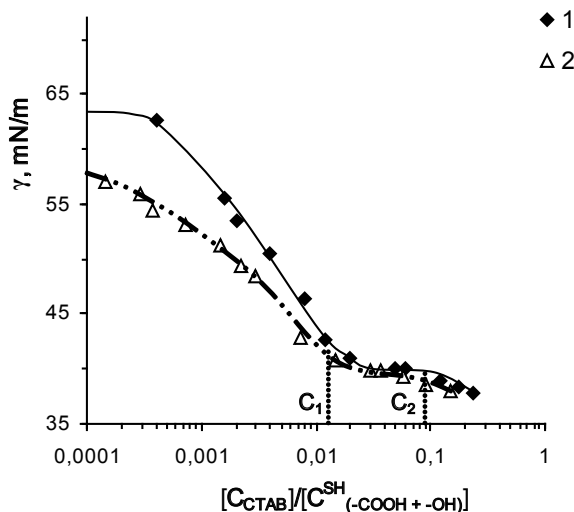


Figure 4. Dependences of equilibrium surface tension of SH/CTAB mixtures ($pH = 11.5$) on the ratio of CTAB concentration to the concentration of SH functional groups (1, 2), $[C_{CTAB}]/[C_{(-COOH + -OH)}^{SH}]$. Sodium humates concentration in the solution, g/l: 1 – 0.6; 2 – 7.6.

Surface viscoelasticity increases and reaches a maximum at CTAB concentrations below C_1 (Fig. 5), adsorption layers are elastic.

High elasticity modulus values of SH/CTAB solutions (up to ~ 97 mN/m and 65 mN/m for the $C_{SH} = 0.6$ and $C_{SH} = 7.6$ g/l, respectively) indicate that the rigid structure of the adsorption layer is formed, probably both through electrostatic and hydrophobic interactions between the hydrophobic parts of the SH chains or hydrocarbon radicals of CTAB and hydrophobic regions of the SH chains.

Further increase of the CTAB concentration leads to the beginning of viscoelastic modulus decrease and increase of the E_i/E_r ratio in the C_1 concentration range (Fig. 5). Adsorption layers become viscoelastic. Such

changes of surface rheological characteristics demonstrate the appearance of a new mechanism of surface stress relaxations, which may be related to exchange processes in consequence of the aggregates formation and disintegration in the adsorption layer.

Reduction of surface viscoelasticity is accompanied by a change of the E_r and E_i frequency dependences character (Fig. 6).

Thus, in the range of CTAB concentrations below values corresponding to the maximum E_r values slope angle of the elasticity modulus on the oscillation frequency dependence increases, and after reaching a maximum surface elasticity begins to decrease (Fig. 6 a).

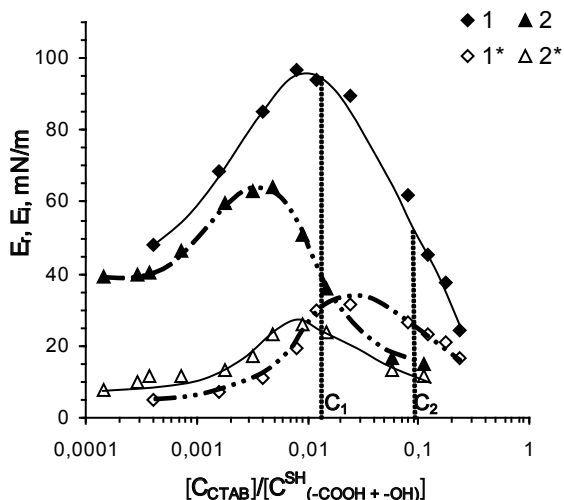


Figure 5. Dependences of surface elasticity E_r (1, 2) and viscosity E_i (1*, 2*) moduli of SH/CTAB mixtures ($pH = 11.5$) on the ratio of CTAB concentration to the concentration of SH functional groups (1, 2), $[C_{CTAB}]/[C^{SH}_{(-COOH + -OH)}]$. Sodium humates concentration in the solution, g/l: 1 – 0.6; 2 – 7.6. Oscillation frequency: 0.1 Hz.

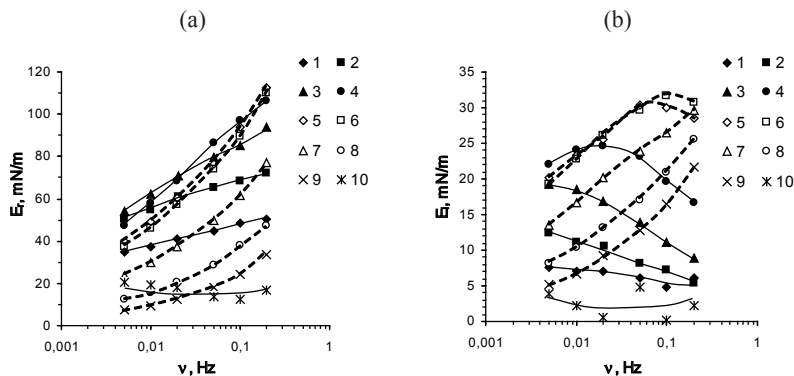


Figure 6. Dependences of surface elasticity E_s (a) and viscosity E_i (b) moduli of SH/CTAB mixtures ($\text{pH} = 11,5$) on the oscillation frequency. Ratios of CTAB concentration to the concentration of SH functional groups, $[C_{\text{CTAB}}]/[C_{\text{SH}}^{(-\text{COOH} + -\text{OH})}]$: 1 – 0.0004; 2 – 0.0016; 3 – 0.004; 4 – 0.008; 5 – 0.012; 6 – 0.024; 7 – 0.08; 8 – 0.18; 9 – 0.24; 10 – 0. Sodium humates concentration in the solution – 0.6 g/l.

Viscosity modulus decreases with increasing of oscillation frequency at CTAB concentrations below the values corresponding to a maximum E_i . At higher CTAB concentrations E_i increases with increasing of oscillation frequency (Fig. 6 b). At CTAB concentrations corresponding to the maximum values of the surface viscosity $E_i = f(\nu)$ dependences pass through a maximum.

The above results indicate a change in the structure of the adsorption layer of mixed SH/CTAB solutions in CTAB concentration range corresponding to the first kink in the surface tension isotherm, and may be due to the formation of aggregates.

In spite of different chemical nature and extent of hydrophobic molecules obtained in this study for the SH/CTAB mixtures concentration dependences of equilibrium surface tension, elasticity and viscosity moduli are qualitatively similar to those of a number of mixtures of synthetic polyelectrolytes with oppositely charged surfactants: polyethylenimine/sodium dodecylsulfate (PEI/SDS) [26], polyvinyl chloride/sodium dodecyl sulfate/NaCl (PVP chloride/SDS/NaCl) [27], polyacrylic acid/alkyltrimethylammonium bromide (PAA/CnTAB) [28], polystyrene sulfonate/dodecyltrimethylammonium bromide (PSS/DTAB) [6] and for mixtures of natural polyelectrolyte λ -carrageenan with DTAB [29].

All of the surface tension concentration dependencies for the systems described above are characterized by at least two concentration ranges with abrupt changes of the slope of the surface tension isotherm and the plateau region between them. At low surfactant concentrations adsorption layers are

elastic and characterized by high values of the elasticity modulus. At ionic surfactant concentrations corresponding to the first kink in the surface tension isotherm elasticity modulus sharply decreases and the contribution of the imaginary components to the surface viscoelasticity increases. Such changes in the surface properties of synthetic polyelectrolyte/ionic surfactant mixtures are connected with the formation of three-dimensional aggregates in the adsorption layer. Formation of the latter for PSS/DTAB solutions is confirmed by a strong increase in ellipsometric signal [6]. For the listed above synthetic polyelectrolyte/surfactant mixtures neutron reflection measurements indicate the formation of the multilayer structure of the adsorption layer [7] at surfactant concentrations higher than the first kink in the surface tension isotherm.

Adsorption and surface rheological properties of protein solutions mixed with ionic surfactant, as well as for other polyelectrolyte/ionic surfactant mixtures determined by complex formation between the components. Dependences of the equilibrium surface tension of protein/surfactant solutions on surfactant concentration are similar to the described above [2, 30]. The character of the concentration dependences of surface viscoelasticity for such systems is more complex and depends on the nature of the protein [3, 31, 32], the nature of surfactant – cationic or anionic [33]. As a result, with increasing surfactant concentration viscoelasticity modulus for such mixtures may go up, passing through a maximum [2, 3, 31], and may decrease from values which are character for individual protein solutions to the values which are character for surfactant [32].

The complexity of the studied in this work SH/CTAB systems does not permit to do a reliable conclusions about the behavior of the adsorption layer. The similarity between the concentration dependencies of the surface tension, dilational elasticity and viscosity moduli measured in this work (Figs. 4 and 5) and the results for synthetic polyelectrolyte/surfactant mixed solutions [6, 26 – 28] indicate that the same changes in the adsorption layers structure of these systems occur at increasing surfactant concentration. Considering the similarity in the adsorption and rheological characteristics of mixed SH/CTAB solutions with mixtures of synthetic polyelectrolyte/surfactant, and a high degree of hydrophobicity of humic acid macromolecules, we can assume that the structure of SH/CTAB adsorption layers could be close to a model for the absorption layer polyelectrolyte/surfactant mixtures [6], which takes into account the hydrophobic interactions in the surface layer, leading to the formation of two-dimensional nano- and micro-aggregates at low surfactant concentrations. The destruction of the rigid structure of the SH/CTAB adsorption layer with increasing CTAB concentration by analogy with mixtures of synthetic polyelectrolyte/surfactant

may occur due to the formation of three-dimensional aggregates in the surface layer.

The ionization degree of weak polyelectrolytes, which is a function of pH, affects the nature of their interactions with oppositely charged surfactant and on the adsorption behavior of such mixtures.

pH decrease leads to an increase in the values of equilibrium surface tension of mixed SH/CTAB solutions (Fig. 7). At low CTAB concentrations the surface tension value of mixture at pH 4.0 and 7.0 is slightly lower than at pH 11.5. This may be due to the higher surface activity of SH in the neutral and acidic pH. There is a maximum in the plateau region of surface tension isotherm of mixed SH/CTAB solutions at pH 4.0 (Fig. 7). The abrupt surface tension increase may be connected with the desorption of SH/CTAB complexes and their transition to the bulk phase due to the formation of macroscopic aggregates. So the optical density of SH/CTAB mixtures at pH 4.0 decreases in the same CTAB concentration range (0.1 – 0.4 mmol/l) in which the maximum on surface tension isotherm is observed.

Character of the elasticity and the viscosity moduli dependences of the SH/CTAB mixture on CTAB concentration in the neutral and acidic conditions is similar to those in the alkaline pH range (Fig. 8). pH reduction results in dilational elasticity increase and E_i/E_r decrease.

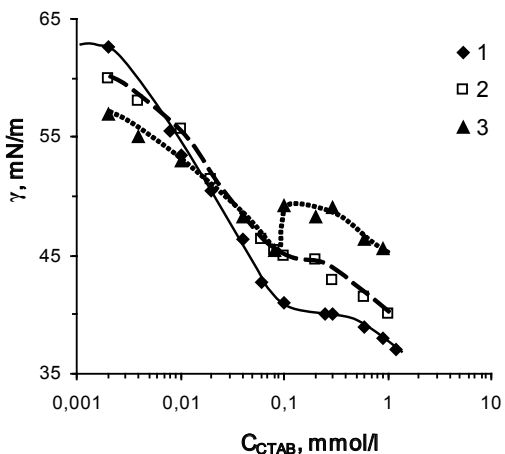


Figure 7. Dependences of equilibrium surface tension of SH/CTAB mixed solutions on CTAB concentration at different pH values: 1 – 11.5, 2 – 7.0, 3 – 4.0. $C_{SH} = 0.6$ g/l.

It is interesting to compare results obtained in this work with results for other weak polyelectrolytes. In [7] it was shown that controlling the degree of charge on weak polyelectrolytes by varying the pH of the system effects the adsorption behavior of mixed polyacrylic acid/dodecyltrimethylammonium bromide (PAA/DTAB) and branched polyethylenimine/sodium dodecylsulfate (PEI/SDS) solutions. PAA is anionic at high pH but neutral at low pH whereas PEI is cationic at low pH owing to protonation of the nitrogens but neutral at high pH.

For mixtures of PAA/DTAB were obtained similar to our results of the pH effect on the equilibrium surface tension value: the γ values in the range of ionic surfactant concentration below CMC in alkaline pH region is lower than in the acidic.

For mixtures of branched PEI with SDS the variation in adsorption behavior with pH is the opposite of what would be expected if the interactions in the system were predominantly electrostatic. There should be more pronounced adsorption behavior at low pH where the polymer is strongly cationic, whereas it appears that the strongest interactions in this system occur at pH 10 (γ values at pH 7 and 10 lower than at pH 3), when the polymer is essentially neutral. It seems likely, therefore, that the main driving force for interaction in this system is hydrophobic forces between the surfactant chains and the polymer backbones rather than electrostatic attractions between the oppositely charged headgroups and the protonated nitrogens on the polymer.

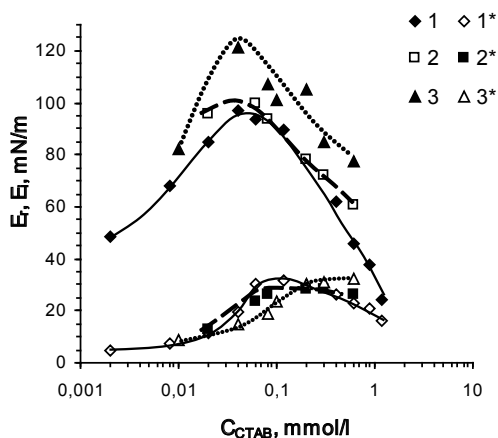


Figure 8. Dependences of surface elasticity E_s (1, 2, 3) and viscosity E_v (1*, 2*, 3*) moduli of SH/CTAB mixed solutions on CTAB concentration at different pH values: 1 – 11.5, 2 – 7.0, 3 – 4.0. $C_{SH} = 0.6$ g/l. Oscillation frequency: 0.1 Hz.

Probably the effect of pH on the adsorption behavior of SH/CTAB mixtures as well as PAA/DTAB, is associated with a strong interactions at high pH due to the greater degree of ionization of the polyanion and controlled mainly by electrostatic interactions between oppositely charged groups of ionic surfactant and polyelectrolyte, leading to the formation of surface-active complexes SH/CTAB. At low pH, when the number of ionized groups in the SH molecules lower, the interactions between polyelectrolyte and ionic surfactant have to be predominantly hydrophobic. This assumption is also consistent with an increase in the surface elasticity at lower pH. The contribution of the different types of interactions in the binding of HA with ionic surfactants depending on the pH, the length of the ionic surfactant hydrocarbon radical are shown in [13 – 19].

3. Foam stability of mixed SH/CTAB solutions

Figure 9 represents the dependences of foam stability for mixed SH/CTAB solutions at different pH and individual CTAB solutions as a function of CTAB concentration. For pure surfactant solutions, the foam volume increases monotonically from zero to 1 when the concentration of surfactant is raised from 0.01 to 10 mmol/l. For SH/CTAB mixtures there exist two CTAB concentration ranges where stable foam is formed.

There is a clear relationship between the dependences of foam stability (Fig. 9) and optical density (Fig. 3) of mixed SH/CTAB solutions on CTAB concentration at different pH values. The foam stability of mixtures increases with increasing of CTAB concentration and reaches a maximum at the limit of SH/CTAB complexes solubility. Reduction of the optical density of the mixed solutions is accompanied by a decrease of foam stability. At full deposition of precipitates from mixed solutions foam does not formed, while the foam stability for pure CTAB attain the maximum (Fig. 9). Further increase of CTAB concentration in the mixture leads to increase of the solubility and foam stability of SH/CTAB mixtures to values characteristic for the individual solutions of CTAB.

In [1] the foam formation and foam stability for mixtures of polystyrenesulfonate sodium salt (PSS) with dodecyltrimethylammonium bromide (DTAB) were studied. Dependences of foam stability of PSS/DTAB mixtures are similar to those obtained in the present work for SH/CTAB. Such dependences are characterized by two zones of surfactant concentrations where the foam stability measured with mixed solutions is higher than the foam stability for pure surfactant (or pure polyelectrolyte) solutions and a precipitation range between them, in which the foam is absent. It was shown that the first maximum of foam stability occurs when the polyelectrolyte/surfactant complexes are

on the limit of their solubility. The foam stability of PSS/DTAB mixtures is strongly correlated to shear surface moduli. The authors [1] believe that two phenomena are likely responsible for the absence of foam in a PSS/DTAB mixture in the precipitation region: (1) most of the surfactant is bound to the polymer complexes that have precipitated out of solution, leaving insufficient amounts for high foam stability, (2) the polymer-surfactant precipitates act as hydrophobic antifoam particles, which can provoke foam collapse. The foam absence at full deposition of precipitates from SH/CTAB mixture can probably be attributed to the same reasons.

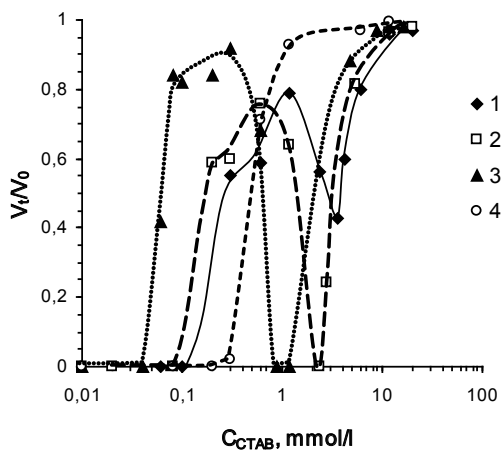


Figure 9. Dependences of ratios of foam volume remaining after 10 minutes, V_t to the initial foam volume V_0 of CTAB solutions (4) and SH/CTAB mixtures (1-3) on CTAB concentration at different pH: 1 – pH=11.5; 2 – pH=7.0; 3 – pH=4.0. $C_{SH} = 0.6$ g/l.

We also note that the protein solutions [34] and mixtures of polyelectrolyte/ionic surfactant [35] are capable to form stable foam at pH values close to the isoelectric point (IEP), with a minimum of foam films stability for polyelectrolyte/surfactant found in the IEP.

As can be seen from Fig. 8, foam stability of SH/CTAB mixtures increases with a pH decrease. This may be connected with increase in elasticity of mixed adsorbed layers on conversion from base to acid pH. The first maximum of foam stability shifts to lower CTAB concentrations with a pH decrease. Thus we can obtain more stable foams from mixed solutions than from pure surfactant (or pure polyelectrolyte) solutions by regulating the pH and proportion of components in the mixture.

Conclusions

1. The investigation of adsorption and surface rheological properties of mixed sodium humates/CTAB solutions at the liquid–gas interface is presented and the possible mechanism of mixed adsorption layers formation is proposed.
2. The main features of concentration dependences of surface tension, elasticity, viscosity moduli and of frequency dependences of rheological properties for mixed sodium humates/CTAB solutions give evidence on the change of adsorption layer structure and may be connected with the aggregate formation in the adsorption layers at appropriate CTAB concentrations.
3. The foam stability of mixed sodium humates/CTAB solutions is determined by the proportion of components in the mixture and increases with pH decrease, that leads to increase of elasticity modulus of SH/CTAB adsorption layers. The intervals of CTAB concentrations and pH values which characterized by formation of stable foams are determined.

References

1. Monteux C., Fuller G.G., Bergeron V. Shear and dilational surface rheology of oppositely charged polyelectrolyte/surfactant microgels adsorbed at the air-water interface. Influence on foam stability // *J. Phys. Chem. B.* – 2004. – V. 108. – P. 16473-16482.
2. Alahverdjieva V.S., Grigoriev D.O., Fainerman V.B. et al. Competitive adsorption from mixed hen egg-white lysozyme/surfactant solutions at the air-water interface studied by tensiometry, ellipsometry, and surface dilational rheology // *J. Phys. Chem. B.* – 2008. – V. 112. – P. 2136-2143.
3. Kotsmar Cs., Krägel J., Kovalchuk V.I. et al. Dilation and shear rheology of mixed β -casein/surfactant adsorption layers // *J. Phys. Chem. B.* – 2009. – V. 113. – P. 103–113.
4. Olea A.F., Gamboa C., Acevedo B., Martinez F. Synergistic effect of cationic surfactant on surface properties of anionic copolymers of maleic acid and styrene // *Langmuir.* – 2000. – V. 16. – P. 6884-6890.
5. Goddard E.D. Polymer/surfactant interaction—its relevance to detergent systems // *J. Am. Oil Chem. Soc.* – 1994. – V. 71. – P. 1-16.
6. Noskov B.A., Loglio G., Miller R. Dilational viscoelasticity of polyelectrolyte/surfactant adsorption films at the air/water interface: dodecyltrimethylammonium bromide and sodium poly(styrenesulfonate)

- // J. Phys. Chem. B. – 2004. – V. 108. – P. 18615-18622.
7. Taylor D.J.F., Thomas R.K., Penfold J. Polymer/surfactant interactions at the air/water interface // *Adv. in Colloid and Interface Science.* – 2007. – V. 132. – P. 69–110.
 8. Орлов Д.С. Гуминовые вещества в биосфере // *Соросовский образовательный журнал.* – 1997. – № 2. – С. 56–63. (in Russian)
 9. Stevenson F.J. Humus chemistry. Genesis, composition, reactions. – N.Y.: Wiley Interscience, 1982. — 443 p.
 10. Хилько С.Л., Ковтун А.И., Файнерман В.Б., Рыбаченко В.И. Адсорбционные и реологические характеристики солей гуминовых кислот на границе раздела жидкость-газ // *Коллоидный журнал.* – 2010. – Т. 72, № 6. – С. 1-9. (in Russian).
 11. Terashima M., Fukushima M., Tanaka S. Influence of pH on the surface activity of humic acid: micelle-like aggregate formation and interfacial adsorption // *Colloids and Surf. A: Physicochem. Eng. Aspects.* – 2004. – V. 247. – P. 77-83.
 12. Klavins M., Purmalis O. Humic substances as surfactants // *Environmental Chemistry Letters* – 2010. – V. 8, N4 – P. 349-354.
 13. Yee M.M., Miyajima T., Takisawa N. Evaluation of amphiphilic properties of fulvic acid and humic acid by alkylpyridinium binding study // *Colloids Surf. A.* – 2006. – V. 272. – P. 182-188.
 14. Ishiguro M., Tan W., Koopal L.K. Binding of cationic surfactants to humic substances // *Colloids Surf. A.* – 2007. – V. 306. – P. 29-39.
 15. Guo-Ping Sheng, Meng-Lin Zhang, Han-Qing Yu Quantification of the interactions between a cationic dye and humic substances in aqueous solutions // *J. Colloid Interface Sci.* – 2009. – V. 331. – P. 15-20.
 16. Yee M.M., Miyajima T., Takisawa N. Thermodynamic studies of dodecylpyridinium ion binding to humic acid and effect of solution parameters on their binding // *Colloids Surf. A.* – 2007. – V. 295. – P. 61-66.
 17. Yee M.M., Miyajima T., Takisawa N. Study of ionic surfactants binding to humic acid and fulvic acid by potentiometric titration and dynamic light scattering // *Colloids Surf. A.* – 2009. – V. 347. – P. 128-132.
 18. Koopal L.K., Goloub T.P., Davis T.A. Binding of ionic surfactants to purified humic acid // *J. Colloid Interface Sci.* – 2004. – V. 275. – P. 360-367.
 19. Shang Ch., Rice J.A. Investigation of humate-cetyltrimethylammonium complexes by small-angle X-ray scattering // *J. Colloid Interface Sci.* – 2007. – V. 305. – P. 57-61.

20. Gamboa C., Olea A.F. Association of cationic surfactants to humic acid Effect on the surface activity // *Colloids Surf. A.* – 2006. – V. 278. – P. 241-245.
21. Khil'ko S.L., Kovtun A.I., Rybachenko V.I. Potentiometric titration of humic acids // *Solid Fuel Chemistry.* – 2011. – V. 45, N. 5. – P. 337–348.
22. Ravera F., Liggieri L., Loglio G. Dilational rheology of adsorbed layers by oscillating drops and bubbles // *Progress in Colloid and Interface Science, Interfacial Rheology*: ed. by R. Miller and L. Liggieri. – Leiden: Brill, 2009. – V. 1. – P. 137-177.
23. Zholob S.A., Kovalchuk V.I., Makievski A.V. et al. Determination of the dilational elasticity and viscosity from the surface tension response to harmonic area // *Progress in Colloid and Interface Science, Interfacial Rheology*: ed. by R. Miller and L. Liggieri. – Leiden: Brill, 2009. – V. 1. – P. 77-102.
24. Adou A.F.Y., Muhandiki V.S., Shimizu Y., Matsui S. A new economical method to remove humic substances in water: adsorption onto a recycled polymeric material with surfactant addition // *Water Sci. Technol.* – 2001. – V. 43 (11). – P. 1-7.
25. De Nobili M., Contin M., Leita L. Alternative method for carboxyl group determination in humic substances // *Can. J. Soil Sci.* – 1990. – V. 70. – P. 531-536.
26. Bykov A.G., Lin S.-Y., Loglio G. et al Dynamic surface properties of polyethylenimine and sodium dodecylsulfate complex solutions // *Colloids Surf. A.* – 2010. – V. 367. – P. 129-132.
27. Noskov B.A., Bykov A.G. , Grigoriev D.O. et al Dilational viscoelasticity of polyelectrolyte/surfactant adsorption layers at the air/water interface: poly(vinyl pyridinium chloride) and sodium dodecylsulfate // *Colloids Surf. A.* – 2008. – V. 322. – P. 71-78.
28. Bykov A.G., Lin S.-Y., Loglio G. et al Impact of surfactant chain length on dynamic surface properties of alkyltrimethylammonium bromide/polyacrylic acid solutions // *Colloids Surf. A.* – 2010. – V. 354. – P. 382-389.
29. Nobre T.M., Wong K., Zanicuelli M.E.D. Equilibrium and dynamic aspects of dodecyltrimethylammonium bromide adsorption at the air/water interface in the presence of λ -carrageenan // *J Colloid Interface Sci.* – 2007. – V. 305. – P. 142-149.
30. Santos S.F., Zanette D., Fischer H., Itri R. A systematic study of bovine serum albumin (BSA) and sodium dodecyl sulfate (SDS) interactions by surface tension and small angle X-ray scattering // *J. Colloid Interface*

- Sci. – 2003. – V. 262. – P. 400–408.
31. Alahverdijeva V.S., Fainerman V.B., Aksenenko E.V. et al. Adsorption of hen egg-white lysozyme at the air–water interface in presence of sodium dodecyl sulphate // *Colloids Surf. A.* – 2008. – V. 317. – P. 610-617.
 32. Pradines V., Krägel J., Fainerman V.B., Miller R. Interfacial properties of mixed β -lactoglobulin–SDS layers at the water/air and water/oil interface // *J. Phys. Chem. B.* – 2009. – V. 113. – P. 745-75
 33. Latnikova A.V., Lin S.-Y., Loglio G. et al. Impact of surfactant additions on dynamic properties of β -casein adsorption layers // *J. Phys. Chem. C.* – 2008. – V. 112. – P. 6126-6131.
 34. Alahverdijeva V.S., Khristov Khr., Exerowa D., Miller R. Correlation between adsorption isotherms, thin liquid films and foam properties of protein/surfactant mixtures: lysozyme/C10DMPO and lysozyme/SDS // *Colloids Surf. A.* – 2008. – V. 323. – P. 132-138.
 35. Kristen N., Vüllings A., Laschewsky A. et al. Foam films from oppositely charged polyelectrolyte/surfactant mixtures: effect of polyelectrolyte and surfactant hydrophobicity on film stability // *Langmuir* – 2010. – V. 26. – P. 9321-9327.

Chapter 17

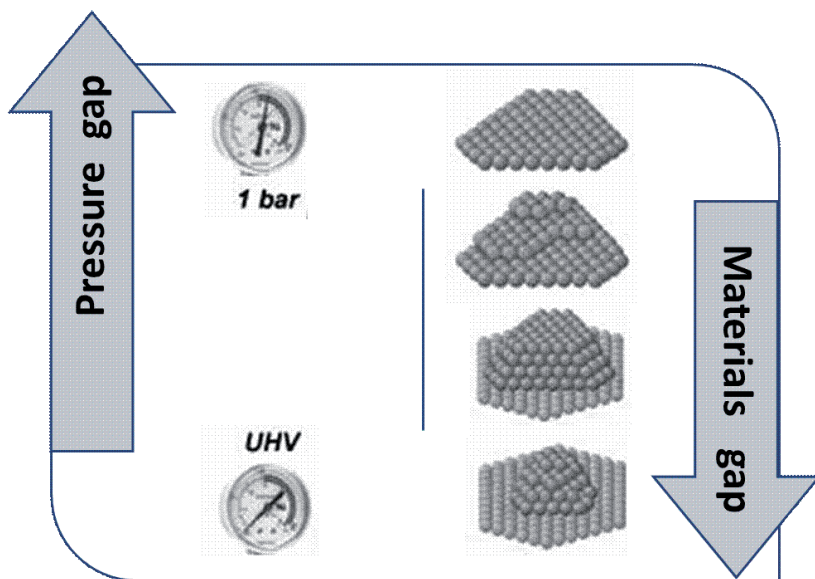
Nanoporous films – model catalysts in the materials gap

Izabela Nowak

*Adam Mickiewicz University in Poznań, Faculty of Chemistry,
Umultowska 89b, 61-614 Poznań, Poland*

Catalysis is the single most important interdisciplinary technology in the chemical industry. More than 85% of all today's chemical products are produced using catalytic processes. As a phenomenon, catalysis started to be known in the first decades of the nineteenth century, i.e. when Berzelius defined catalysis as a spectacle that changes the composition of a reaction mixture but leaves the catalyst unaltered [1]. Generally, a catalyst is a 'object' that accelerates a chemical reaction without being consumed itself in the process. Without catalysts, some chemical reactions would not take place or proceed so slowly at a certain temperature that they could not be detected because of high activation barriers.

Surface science (spectroscopic analyses at UHV) and heterogeneous catalysis (industrial reactions carried out at higher pressures) have a lot in common but they are still separated by 'materials' as well as 'pressure' gaps (scheme 1) [2]. Accordingly, in the last two decades increasing efforts to bridge the gaps between reaction conditions, often known as the 'pressure gap', and between materials (the 'materials gap') were undertaken [3-7]. There is a long history of studies in surface science of the uncomplicated steps in catalytic reactions with idealized model systems. In order to bridge the 'materials gap' between the high-area-surface real catalysts and single crystal metal surfaces (or even single species), one should design a kind of material that is not porous or a powder, which have too complicated surface structures to be analysed easily by spectroscopy. The material should not be as ideal as a single crystal surface, it has to be a solid material. Bearing in mind the materials applied in real catalysts, people thought naturally of metals supported on oxides. Furthermore, because the metal nanoparticles supported on oxides have large exposed surface and interface area, this led to the synthesis of supported metal nanoparticles, e.g. films on oxide supports.

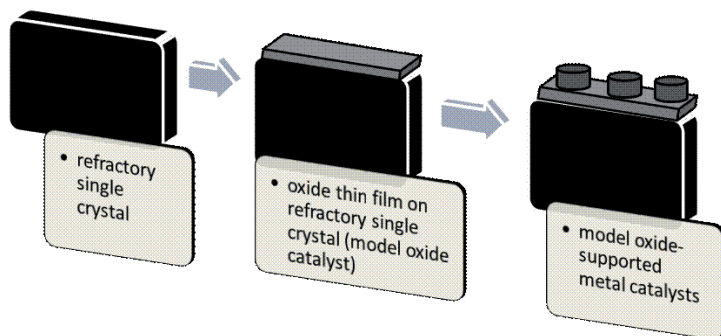


Scheme 1. Illustration of the 'pressure and materials gap' between surface science and heterogeneous catalysis. The largest gap exists between UHV investigations of single crystals and atmospheric-pressure processes on supported metal nanoparticles (adapted from [2]).

The model catalysts can be prepared in different ways falling into one of three broad categories: wet chemical deposition; physical vapour deposition and chemical vapour deposition. Among others the most popular is deposition of the respective active metal phase by evaporation, deposition of preformed metal nanoparticles or chemical impregnation. While structurally and chemically still reasonably well defined, these systems are also more realistic than pure metal substrates in that they include, e.g., particle size effects or effects resulting from the interface between the support and the active material. These model systems differ from realistic catalysts, however, in one important aspect with respect to their (internal) transport properties, as given, e.g., by the absence/presence of pore diffusion. Therefore, recently scientists started to develop a new type of model system, consisting of a nanoscale catalyst layer of a hundred to a few hundred nanometers thickness on a planar support. It has been recognized that the thickness of the oxide films, as they are grown on metal substrates, may be used as a design parameter to create materials of potential in catalysis. A concept to control the catalytic activity of a dispersed metal by the thickness of

an insulating oxide layer was introduced 25 years ago by Maier and co-workers using silica layers covering Pt[8,9] (in this case, the catalytic performance for dehydrogenation of cycloalkenes depended significantly on the thickness of the silica films, which was explained by the decreasing transport of hydrogen atoms produced at the Pt surface through the silica film). However, there are lots of opportunities to explore various combinations of metals with varying electronegativities in combination with metal/oxide thin film systems [10].

The preparation of a model catalyst, illustrated schematically in scheme 2, begins with a cleaning a surface (typically a metal one) by of high-temperature annealing and/or O₂ treatment. The next step is to deposit a thin metal oxide film, typically 1–10 nm thick. The final step in model catalyst preparation is to vapour deposit the metal of choice onto the thin oxide film. By controlling the metal exposure and flux, tight control can be exercised over both cluster sizes and densities. Various supported metal systems have been studied and applied in the catalysis field, however in this paper some representative examples will be presented.



Scheme 2. Schematic illustration of model oxide-supported metal catalysts preparation. Please bear in mind the following sizes: oxide thin films (e.g. SiO₂, MgO, TiO₂, etc.) – 1-10 nm; supported metal clusters (e.g. Ni, Pt, Pd, Au, Ag, etc.) – 1-50 nm.

Hydrogen production

Amorphous molybdenum sulphide films are efficient hydrogen evolution catalysts in water. The films were prepared via simple electro-polymerization procedures and were characterized by XPS, electron microscopy and electronic absorption spectroscopy. The catalysis was compatible with a wide range of pHs (e.g., 0 to 13). The amorphous molybdenum sulphide films are among the most active non-precious hydrogen evolution catalyst [11].

Reduction/oxidation/decomposition reactions

Au nanoparticle (NP)-gelatine mesoporous composite thin films were successfully prepared by the formation of Au NPs in the mesoporous gelatine films through in situ reduction of HAuCl_4 at room temperature. The mesoporous gelatine films were prepared by using copper hydroxide nanostrands as both the assembling frames and the pore generators. It was found that both the trace aldehyde groups of the glutaraldehyde cross-linker and the reduction groups of gelatine contributed to the formation of Au NPs. The Au NPs were homogeneously formed and dispersed in the gelatine films. These Au NP-gelatine mesoporous composite films demonstrated superior catalytic properties for the reduction of o-nitroaniline to 1,2-benzenediamine, and several to tens times higher activity than those reported of the Au NP-polymer (or oxide) composites [12].

Three CoS_2 -, NiS_2 - and $(\text{Co,Ni})\text{S}_2$ -based thin films were prepared by magnetron sputtering and studied as catalysts for the oxygen reduction reaction (ORR). Electrochemical assessments indicate that all three films have significant ORR catalytic activities, with that of $(\text{Co,Ni})\text{S}_2$ -type showing the best performance with regard to both open circuit potential (OCP) and current density. The ternary film has an OCP value of 0.89 V vs. the reversible hydrogen electrode, and shows a closer approach to values for Pt than have been obtained to date for other transition metal chalcogenides [13].

A new method of sol-gel polymer template synthesis of mesoporous catalytic titania thin films has been proposed which allows controlling the chemical nature of the film, the porosity, thickness and loading with an active species. The mesoporous films with a long-order structure can be obtained in a narrow range of surfactant-to-metal precursor molar ratios from 0.006 to 0.009. The catalytic film thickness was varied from 300 to 1000 nm while providing a uniform catalyst distribution with a desired catalyst loading (1 wt. % Au nanoparticles) throughout the film. The calcination of the as-synthesized films at 573 K reduced Ti^{4+} sites to Ti^{3+} . A 300 nm thick Au-containing film showed an initial TOF of 1.4 s^{-1} and a selectivity towards unsaturated alcohols as high as 90% in the hydrogenation of citral. Thicker films demonstrated a high selectivity towards the saturated aldehyde (above 55%) and a lower intrinsic catalytic activity (initial TOF of $0.7\text{--}0.9 \text{ s}^{-1}$) in the absence of internal diffusion limitations [14].

The stability ranges of potassium promoted iron oxide model catalyst films in dependence on the annealing temperature and oxygen partial pressure was investigated at Fritz-Haber-Institute of the MPG in Berlin. At conditions which simulate the technical ethylbenzenedehydrogenation reaction, $\text{K}_x\text{Fe}_{22}\text{O}_{34}$ (0001) is partially covered by KFeO_2 . Both phases are exposed at the surface. As the

same KFeO_2 -shell around a $\text{K}_2\text{Fe}_{22}\text{O}_{34}$ -core was identified for the active state in technical catalyst samples [15].

CO oxidation with oxygen over model Au catalysts was also studied [16,17] in an attempt to shed light on the well-known structure sensitivity. It was evidenced that a maximum in reactivity is observed for clusters with a diameter of 3.2 nm. This result is identical to that obtained over high-surface area Au/ TiO_2 catalyst. These results suggest that the onset of CO oxidation activity may be related to the unique electronic structure of 2D clusters. On the other hand the activity over supported Pd clusters for CO oxidation with NO follow the same trend as that of the single-crystal data: smaller clusters are more like open surfaces and larger clusters are more like close-packed surfaces [18].

In order to solve the problems of fuel combustion in internal-combustion engines and exhaust gas purification, one may use catalytic coatings deposited either on cylinders and pistons or on the surfaces of bulk supports in the systems of catalytic afterburning of exhaust gas. Both problems can be solved by using the manufacturable method of depositing the coatings with catalytic properties – plasma electrolytic oxidation [19].

The decomposition and (partial) oxidation of methanol were studied on Pd model catalysts based on ordered Al_2O_3 and Fe_3O_4 thin films, i.e. either on well-defined particles supported on powders or on Pd single crystals. The interaction of Pd nanoparticles and Pd(111) with CH_3OH and $\text{CH}_3\text{OH}/\text{O}_2$ mixtures was examined from ultrahigh vacuum conditions up to ambient pressures, utilizing a broad range of surface specific vibrational spectroscopies. Detailed kinetic studies in the low pressure region were performed by molecular beam methods, providing comprehensive insights into the microkinetics of the reaction system. The results showed that, by combining suitable experimental and theoretical approaches, a detailed picture of a complex catalytic reactions system can be developed, which provides a microscopic-level understanding of structure, size and support dependent effects in heterogeneous catalysis, ranging from ideal ultra-high vacuum to real ambient pressure conditions [20].

The next reaction – overall reaction of NO, leading to decomposition, is almost identical in the two systems, i.e. on Cu(110) and on Cu nanoclusters deposited on a 0.5 nm thick Al_2O_3 film. Both types of Cu surfaces promotes the formation of NO dimers, which are precursors to the dissociation products N_2O , N_2 and O. Although the overall reaction is independent of surface structure, the IR spectra clearly showed differences in the adsorption sites occupied on the single crystal and the clusters, a disparity that was also shown by CO adsorption experiments (Fig. 1 left). In contrast, the reaction pathway of dichloroethene did show differences on the two types of Cu surfaces. On both surfaces, the

initial reaction step is insensitive to structure and efficient dechlorination leads to the production of adsorbed acetylene (Fig. 1 right). However, the fate of this intermediate depends critically on the underlying surface. On Cu(110), the acetylene trimerises readily into benzene at 350 K. However, this reaction shows a significant size dependent behaviour on the supported nanocluster systems, with the probability for trimerisation diminishing with decreasing cluster size [21].

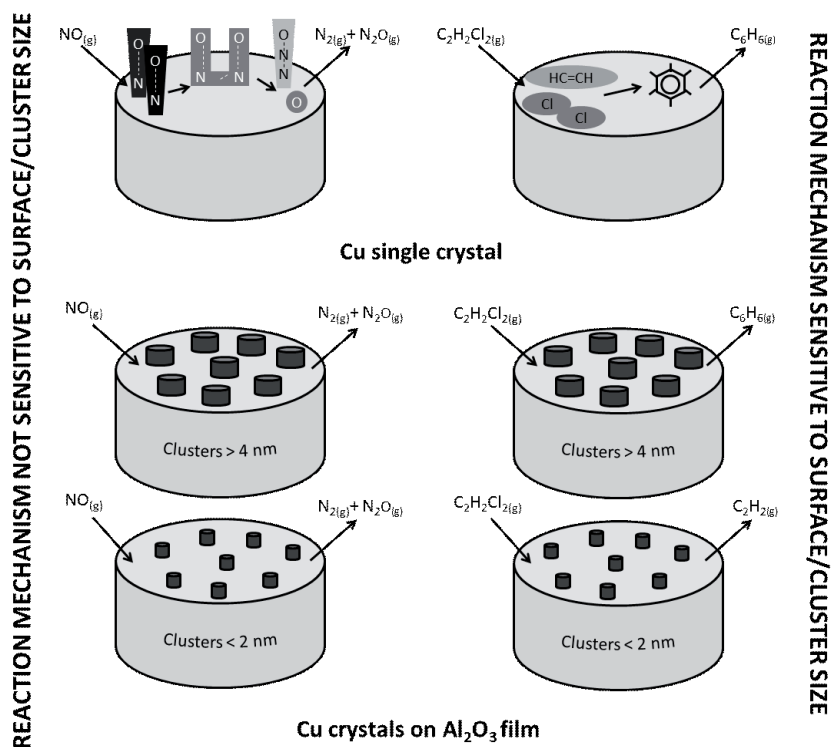


Figure 1. Schematic diagrams of NO and dichloroethene reactivity on Cu single crystal (top) and supported Cu nanoparticles (bottom) (adapted from [21])

Photocatalysis

Photo-oxidation by using TiO₂ photocatalyst is being widely studied as a relatively new technique of pollution abatement. Coating of mesoporous TiO₂ nanocrystalline films on stainless steel (Grade 304) was conducted using

an evaporation-induced self-assembly (EISA) process in the presence of a Pluronic F127 triblock copolymer. The photocatalytic properties of mesoporous TiO_2 films were evaluated using orange II in aqueous solution under ultraviolet irradiation. The photocatalytic activities of the subsequently deposited mesoporous TiO_2 films were significantly improved, which can be attributed to the enhanced charge carrier separation and excellent optical reflection properties of the interlayer [22].

On the other hand thin films of iron (Fe) doped titanium dioxide (Fe– TiO_2) were prepared on a variety of substrates by using Ti-peroxy sol–gel dip coating method. The surface structure of the film was modified by adding different concentrations of polyethylene glycol (PEG) into the TiO_2 sol. Most of the metal ion doped entered TiO_2 lattice resulting the shift in optical absorption edge towards visible side. The adsorbed hydroxyl content of such porous films is found to increase with amount of PEG added. Photocatalytic properties of the surface modified and Fe ion doped TiO_2 catalyst was investigated by degradation of methyl orange in sunlight. The photocatalytic activity of the PEG added Fe– TiO_2 catalyst was enhanced by 2–2.5 times than undoped TiO_2 [23].

A novel approach that adds reactant selectivity to existing, non-porous oxide catalysts by first grafting the catalyst particles with single-molecule sacrificial templates, then partially overcoating the catalyst with a second oxide through atomic layer deposition was recently presented [24]. This technique is used to create sieving layers of Al_2O_3 (thickness, 0.4–0.7 nm) with ‘nanocavities’ (<2 nm in diameter) on a TiO_2 photocatalyst. The additional layers result in selectivity (up to 9:1) towards less hindered reactants in otherwise unselective, competitive photocatalytic oxidations and transfer hydrogenations.

Conclusions

The use of thin films as supports enables complete characterization using surface science techniques. In this short review a number film oxide-supported catalysts were presented to investigate reaction kinetics in an attempt to address such issues as structure sensitive/insensitive reactions and size-dependent catalytic properties. Activity comparisons between model catalysts and traditional supported catalysts provide convincing evidence that the ‘materials gap’ has indeed been bridged.

Acknowledgement

This paper was written with partial support from National Science Centre (grant no. N204 538839; 2010–2013).

References

1. R.A. van Santen, J.W. Niemantsverdriet, *Chemical Kinetics and Catalysis* (A Division of Plenum Publishing Corporation, New York and London, 1995).
2. G. Rupprechter, Sum Frequency Generation and Polarization-Modulation Infrared Reflection Absorption Spectroscopy of Functioning Model Catalysts from Ultrahigh Vacuum to Ambient Pressure, *Adv. Catal.* 51 (2007) 133.
3. P. Stoltze, J.K. Nørskov, Bridging the “Pressure Gap” between Ultrahigh-Vacuum Surface Physics and High-Pressure, *Phys. Catalysis. Rev. Lett.*, 55 (1985) 2502.
4. J. Aßmann, E. Löffler, A. Birkner, M. Muhler, Ruthenium as oxidation catalyst: bridging the pressure and material gaps between ideal and real systems in heterogeneous catalysis by applying DRIFT spectroscopy and the TAP reactor, *Catal. Today*, 85 (2003) 235.
5. H. Over, M. Muhler, Catalytic CO oxidation over ruthenium—bridging the pressure gap, *Prog. Surf. Sci.*, 72 (2003) 3.
6. R. Imbihl, R.J. Behm, R. Schloegl, Bridging the pressure and material gap in heterogeneous catalysis, *Phys. Chem. Chem. Phys.*, 9 (2007) 3459.
7. R.T. Vang, L.E. Egsgaard, F. Besenbacher, Bridging the pressure gap in model systems for heterogeneous catalysis with high-pressure scanning tunneling microscopy, *Phys. Chem. Chem. Phys.*, 9 (2007) 3460.
8. A.B. McEwen, W.F. Maier, R.H. Fleming, S.M. Baumann, Thin film porous membranes for catalytic sensors, *Nature*, 329 (1987) 531.
9. J.M. Cogen, K. Ezaz-Nikpay, R.H. Fleming, S.M. Baumann, W.F. Maier, *Angew. Chem. Int. Ed.*, 26 (1987) 1182.
10. H.J. Freund, Metal-supported ultrathin oxide film systems as designable catalysts and catalyst supports, *Surf. Sci.*, 601 (2007) 1438.
11. D. Merki, S. Fierro, H. Vrubel, X. Hu, Amorphous molybdenum sulfide films as catalysts for electrochemical hydrogen production in water, *Chem. Sci.*, 2 (2011) 1262.
12. L. Shi, Q. Yu, Y. Mao, H. Huang, H. Huang, Z. Ye, X. Peng, High catalytic performance of gold nanoparticle–gelatin mesoporous composite thin films, *J. Mater. Chem.*, 22 (2012) 21117.
13. L. Zhu, D. Susac, M. Teo, K.C. Wong, P.C. Wong, R.R. Parsons, D. Bizzotto, K.A.R. Mitchell, S.A. Campbell, Investigation of CoS₂-based thin films as model catalysts for the oxygen reduction reaction, *J. Catal.*, 258 (2008) 235.

14. L.N. Protasova, E. Rebrov, T.S. Glazneva, A. Berenguer-Murcia, Z.R. Ismagilov, J.C. Schouten, Control of the thickness of mesoporous titania films for application in multiphase catalytic microreactors, *J. Catal.*, 271(2010) 161.
15. G. Ketteler, W. Ranke, R. Schlögl, Potassium promoted iron oxide model catalyst films for the dehydrogenation of ethylbenzene: An example for complex model systems, *J. Catal.*, 212 (2002) 104.
16. M. Valden, X. Lai and D.W. Goodman, Onset of Catalytic Activity of Gold Clusters on Titania with the Appearance of Nonmetallic Properties, *Science*, 281 (1998) 1647.
17. T.V. Choudhary, D.W. Goodman, Catalytically active gold: The role of cluster morphology, *Appl. Catal. A: General*, 291 (2005) 32.
18. D.R. Rainer, S.M. Vesecky, M. Koranne, W.S. Oh, D.W. Goodman, The CO+NO reaction over Pd: a combined study using single-crystal, planar-model-supported, and high-surface-area Pd/Al₂O₃ catalysts, *J. Catal.*, 167 (1997) 234.
19. N.B. Kondrikov, V.S. Rudnev, M.S. Vasilyeva, L.M. Tyrna, T.P. Yarovaya, A.Y. Rozhkov, Outlooks for the automobile application of oxide film catalysts formed by means of plasma electrolytic oxidation, *Chem. Sus. Develop.*, 13 (2005) 847.
20. M. Baumer, J. Libuda, K.M. Neyman, N. Rosch, G. Rupprechter, H.-J. Freund, Adsorption and reaction of methanol on supported palladium catalysts: microscopic-level studies from ultrahigh vacuum to ambient pressure conditions *Phys. Chem. Chem. Phys.*, 9 (2007) 3541.
21. S. Haq, R. Raval, NO and dichloroethene reactivity on single crystal and supported Cu nanoparticles: just how big is the materials gap?, *Phys. Chem. Chem. Phys.*, 9 (2007) 3641.
22. J.H. Pan, Z. Lei, W.I. Lee, Z. Xiong, Q. Wang, X.S. Zhao, Mesoporous TiO₂ photocatalytic films on stainless steel for water decontamination, *Catal. Sci. Technol.*, 2(2012) 147.
23. R.S. Sonawane, B.B. Kale, M.K. Dongare, Preparation and photocatalytic activity of Fe–TiO₂ thin films prepared by sol–gel dip coating, *Mater. Chem. Phys.*, 85 (2004) 52.
24. Ch.P. Canlas, J. Lu, N.A. Ray, N.A. Grosso-Giordano, S. Lee, J.W. Elam, R.E. Winans, R.P. Van Duyne, P.C. Stair, J. M. Notestein, Shape-selective sieving layers on an oxide catalyst surface, *Nature Chem.*, 4 (2012) 1030.

Chapter 18

Silica surface functionalized by supramolecular systems as effective agent for cesium ions removal

Joanna Kurczewska

*Adam Mickiewicz University in Poznań, Faculty of Chemistry
Umultowska 89b, 61-614 Poznań, Poland*

Nuclear technologies are responsible for the production of cesium isotopes (Cs-135 and Cs-137) through uranium fission in nuclear reactors. Their presence in the environment results from several sources like nuclear accidents, nuclear weapon testing or radioactive wastes. Cs-137 is characterized by relatively long half-life (about 30 years) and gamma energy of 661 keV, therefore it is considered as potential source of radiation and heat (heat emitting nuclide) in medicine and industry [1-7].

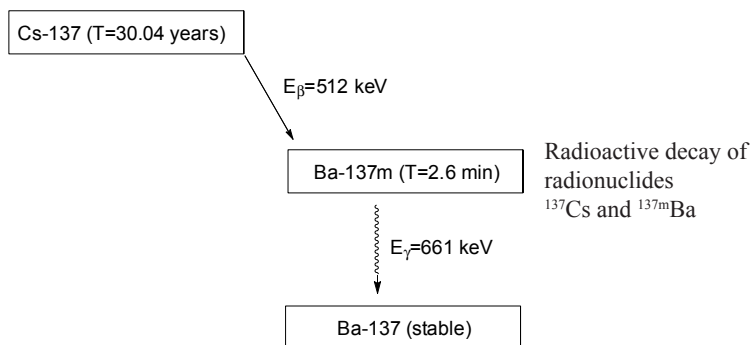


Figure 1. Decay of cesium-137.

However, before it can be applied anywhere, it has to be separated from highly active liquid waste (HLW). The unlimited solubility of the nuclide takes in effect in its migration to the underground water. In the consequence of its presence in the food chain and water supply, radiocesium is taken up by living

organisms instead of potassium. Therefore safer storage of HLW is possible after separation of cesium, which should reduce radiation risk to health and environment. Selective separation of Cs-137 is very difficult and challenging problem for chemical engineering. For example concentration of nanomolar level of cesium in sea and river waters is not only difficult to be removed but also to be detected because of concurrent presence of other cations (sodium, potassium...) in much higher concentration. The concentration of cesium-137 in HLW can be monitored by Ge detectors of high purity but these measurements are disturbed by the presence of other fission products.

The most common methods of cesium separation are ion exchange, adsorption or liquid-liquid solvent extraction. Zeolites are often applied as selective ion exchangers of metal ions from radioactive wastes. Very good sorption of ^{137}Cs properties are demonstrated by hexacyanoferrate and potassium nickel or cobalt ferrocyanides (FCN) of different composition have been used for treatment of active nuclear waste solutions. Ferrocyanides of transient metals, commonly used in nuclear technology, are characterized by low solubility and high selectivity for cesium in the presence of other alkali as well as alkaline metals. They are also stable in the wide range of pH. Generally, the sorbents are prepared by the precipitation method. After that it is usually filtrated, dried and crushed to small particles. There are two methods of practical application of FCN. If the product is stable enough, it can be used itself in a column. However, it is difficult to achieve therefore a composite sorbent is effective alternative. Silica gel provides very good mechanical stability for the matrix. On the other hand it does not influence negatively the sorption capacity of FCN compared to pure FCN. However, before detailed analysis of composite sorbents, it is worth to mention about the adsorption behaviour of Cs on unmodified silica gel [8]. The adsorption process takes place in the pores and it is commonly applied for wastewater treatment. Dependently on, particle size, cation concentration and temperature, the cesium adsorption could differ. The experiments described by Bascetin et al. were carried out for the concentration between 1×10^{-6} and 1×10^{-3} mol/dm³. It was observed that the adsorption capability was low but increased with increasing particle size and the exchange process was responsible for the ion adsorption on silica gel. The calculation of thermodynamic parameters supplied additional information. In case of particles 15-40 μm , the reaction was favorable in higher temperatures and the process was spontaneous. For particles 40-63 and 63-200 μm , the spontaneity of the reaction was even enhanced. Generally, the differences caused by changing temperature were insignificant.

Orechowska et al. [9, 10] focused on composite sorbents based on silica gel and ferrocyanide in order to combine the properties of FCN for Cs removal

and incorporate additional stable matrix. Firstly, they prepared several sorbents with different amount of the active components ($K_{1.48}Ni_{1.26}Fe(CN)_6 \cdot 1.01 KNO_3$; $K_{1.62}Ni_{1.19}Fe(CN)_6$; $Ni_2Fe(CN)_6 \cdot 2.93 KNO_3$; $K_{1.38}Ni_{1.31}Fe(CN)_6 \cdot 0.95 KNO_3$). The sorption studies were carried out in the concentration range 1×10^{-1} – 10^{-5} mol/dm³. It was observed that the distribution coefficient decreased below and above the concentration 1×10^{-4} mol/dm³. In higher concentration it can be explained by the decrease of sorption capacity due to occupied sorption sites of the sorbents by cesium. In case of low concentration, colloids formation should be seen as a cause of the distribution coefficient decreasing. This problem can be easily avoided by ultrafiltration that removes colloids. The other studied parameter, the influence of competitive ions (K, Na, Ca cations), confirmed the assumption about potassium competing influence because of its similar ionic radius, hydration energy, dimension and charge density. Moreover the presence of calcium ions can take effect in coagulation of colloidal particles. Nevertheless, such sorbents can be used for removal of radiocesium in the presence of competitive ions.

The same research group developed other composite sorbents named "NIFSIL". Again sorbents, based on potassium nickel ferrocyanide and silica gel, were used as matrix. This time they were prepared as spherical beads by a sol-gel method. Generally, the sorbent capacity depends on the FCN amount in the sorbent. Again it was proved that the silica matrix was neutral for cesium sorption. It was also demonstrated that sorption of other radionuclides (strontium and plutonium) was rather low. If such systems could be used in column operations, there is higher possibility of their practical application.

Independently on commonly applied FCN, it would be interesting to consider other compounds as selective separator of radio-cesium. A combination of supramolecular systems: calixarene and crown-ethers gives new class of compounds: calix-crown molecules that are characterized by a complementary cavity for cesium ion. Moreover, an application of bis-crown ligands generates even higher uptake of cesium when compared to monocrowns. Mohapatra et al. [11] discussed the properties of three calix-crowns (Figure 2) as potential agents for cesium removal from highly active liquid waste.

The abilities of calix -mono and biscrowns for cesium removal can be applied for the formation of chromatographic resin. Hao et al. [12] immobilized calix[4]-bis-crown-6 on polymeric material (polystyrene -divinylbenzene) that demonstrated high absorption ability of cesium(I) in the presence of other radioactive elements.

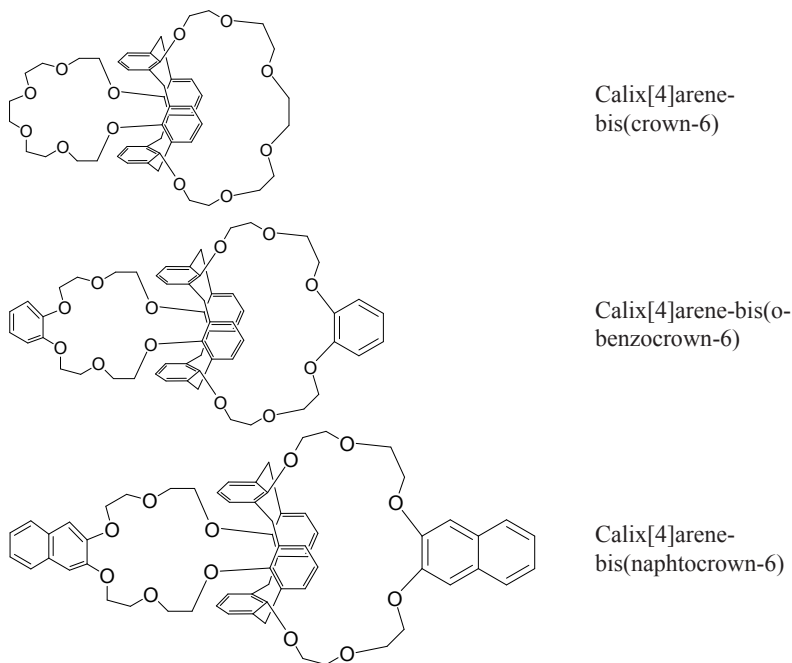


Figure 2. The calix-biscrown ligands' structures.

Another step of discussed subject is the usage of silica core surrounded by organic surface bearing layer with receptor molecules. Such selective receptors were prepared by Nechifor et al. [13]. Firstly they obtained suitable calixarene derivative (Figure 3) by adding undecyl chains with terminal OH groups. It is well known that surface silanol groups are easily esterified with octadecyl alcohol giving colloids. Then they focused on the control of colloidal stability in different conditions by choosing a proper solvent. A solvent should be common for "bare" silica particles, organic molecules and final grafted particles. 2-nitrophenyl octyl ether and triethyl phosphate were chosen for that purpose. The first one is very good solvent of calixarenes and the second one is able to disperse silica particles (charged and hydrophobic). The process was monitored by light-scattering measurements in order to detect aggregates formation. The ability of silica colloids for cesium complexation was studied during the contact of dispersed colloids in chloroform and cesium chloride water solution. According to the results, it was proved that the modified calix[4]arene-crown-6 was stable during grafting process i. e. in the temperature range 140-160°C.

When considering silica particles, commercial Ludox ones and Stöber spheres were used. It was observed that silica was partly covered with solvent triethyl phosphate giving good colloidal stability but lower grafting by receptors. In case of another solvent, the percentage of grafting was much higher but Ludox silica has a tendency to flocculate, which was not observed for Stöber spheres.

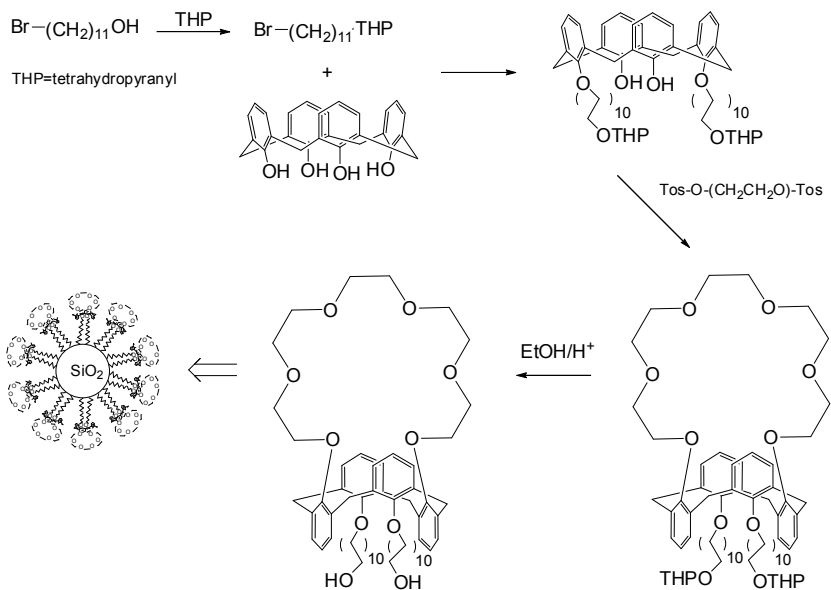


Figure 3. Synthesis of silica spheres coated with calixarene derivative having two long alkyl chains

Research group of Arena [14-16] focused on the synthesis of calixcrowns, characterized by different cavity of crown ether, immobilized on silica gel. According to the scheme presented in Figure 4, the synthesis procedure of macrocycles A was started from 1,3-diallylcalix[4]arene, through alkylation of hydroxyl groups, Claisen rearrangement and transformation of upper part into the crowns. The macrocycles obtained were then linked to silica gel by heating with triethoxysilane and used as stationary phases in chromatographic columns. As expected the macrocycle having smaller cavity of crown ether unit showed good selectivity for potassium ions and the second one-for cesium ions. Unfortunately, long-term usage of the column takes effect in its efficiency decreasing and the removal of e.g. cesium in the presence of other alkali metals

is no more sufficient. However, it can be easily improved by a column cleaning with acidic aqueous solutions.

In the following studies the same research group compared the properties of three chromatographic stationary phases (Figure 4, A (n=1 or 2) and B). They focused on the role of a length of the attaching arm on the column behaviour. They applied X-ray photoelectron spectroscopy (XPS) in order to estimate the degree of coverage of the activated silica-gel surface. Compared with elemental analysis, this is more convenient technique for that purpose. It was proved that the coverage calculated by elemental analysis data was lower than the one determined via XPS. It results from the fact that the elemental analysis data include not only the macrocycle but also other sources of carbon (contamination). As it was demonstrated in previous paper, smaller crown cavity takes effect in higher efficiency towards potassium ions than cesium ones. Two other discussed phases contain the same macrocyclic receptor-calixcrown-6 and both demonstrated the ability of total separation of cesium in the presence of sodium and potassium ions. The degree of silica gel surface coverage was a bit higher (10-15%) when the attaching arm was shorter.

Several papers of Zhang [17-19] describe the application of another silica based adsorbent. They used 1,3-[(2,4-diethylheptylethoxy)oxy]-2,4-crown-6-Calix[4]-arene (Calix[4]arene-R14; Figure 5) as supramolecular recognition agent that should be potentially responsible for the complexation of alkali and alkaline-earth metal ions. Firstly supramolecular compound was modified with Methyl-octyl-2-dimethylbutanamide (MOBD). Then calix[4]-arene and MOBD were impregnated and immobilized into the pores of SiO₂-P particles (P: styrene-divinylbenzene copolymer obtained after the polymerization reaction inside the macroporous SiO₂) and (Calix[4] + MOBD)/SiO₂-P was obtained.

Several alkali metals (potassium, rubidium, cesium) and alkaline-earth metals (strontium, barium) are fission products are present in HLW that results from nuclear spent fuel reprocessing process. The presence of sodium in HLW is due its addition (sodium nitrate(III)) during the process. The adsorption studies of mentioned metals on the support studied were carried out for different contact time. It was observed that Na(I), K(I), Sr(II) and Ba(II) were adsorbed insignificantly when the contact time increased. However, such a tendency was not demonstrated by Rb(I). On the other hand, the adsorption of Cs(I) shows the opposite tendency as it increases with increasing contact time. Generally, the composite support demonstrates high selectivity for heat-emitting nuclide Cs(I) with the exception of rubidium(I). Another important item that favours the support is extremely low adsorption of other heat-emitting nuclide-strontium(II).

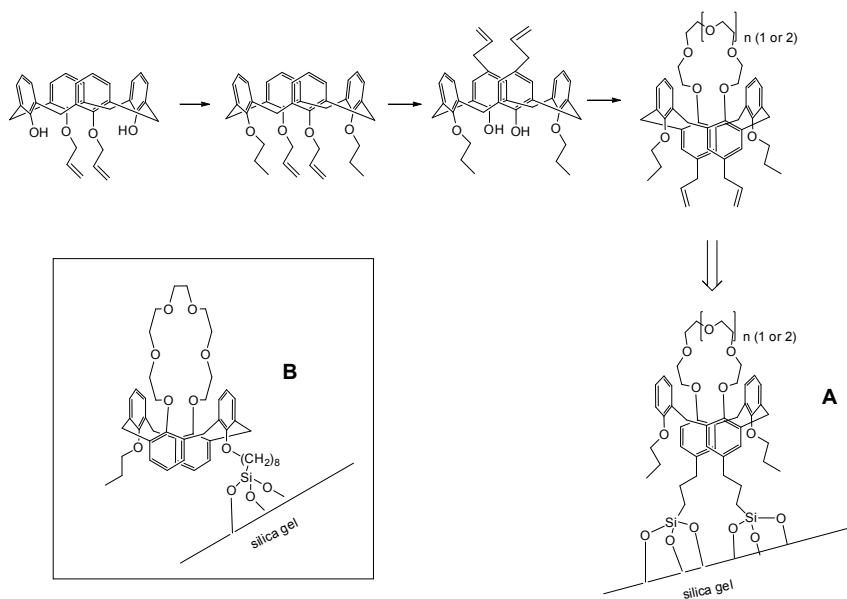


Figure 4. Synthesis of immobilized calixcrowns for different cations removal.

The adsorption studies were carried out in nitric acid of different concentration (0.3-7.0 mol dm⁻³). Typically, nuclear spent fuel reprocessing is conducted using 3.0 mol dm³ HNO₃. Therefore, the results were predictable to a certain degree. The adsorption abilities increased starting from 0.3 till 3.0 mol dm³ and then decreased from 3.0 to 7.0 mol dm³ nitric acid solution. It was explained by the effective complexation of cesium in lower (below 3.0) acid concentration or the protonation of calix[4]arene-R14 with HNO₃ in higher (above 3.0) one.

The mechanism of cesium sorption is chemisorption therefore it was important to investigate also the influence of the temperature (293-333 K). It was proved that the adsorption process was exothermic as it decreased with increased temperature. According to the calculated thermodynamic parameters it was stated that the adsorption process is spontaneous and is favorable at lower temperature.

The only defect of the composite polymeric material is co-adsorption of rubidium(I), which should be separated from cesium(I). The authors suggested that it could be achieved by using other silica-based composite bearing Ar-OH functional groups.

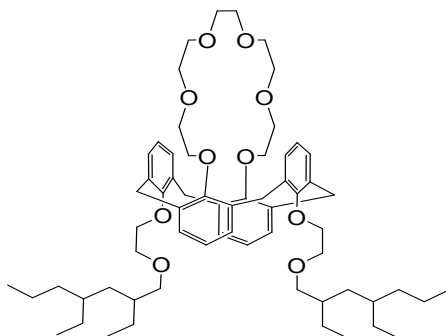


Figure 5. Structure of 1,3-[(2,4-diethylheptylethoxy)oxy]-2,4-crown-6-Calix[4]-arene; Calix[4]arene-R14.

In another paper, the same research group broadened their studies in order to estimate the adsorption of other typical fission products (molybdenum, palladium, lanthanum, yttrium, ruthenium, rhodium, and zirconium) on the composite material Calix[4] + MOBD)/SiO₂-P. The research studies were result of complex composition of HLW, i.e. it was reported that it contained about 30 elements that could influence unfavorably elimination of cesium(I). Again, it was proved that the tested metals were not adsorbed onto polymeric composite with increasing contact time but the situation was exactly opposite in case of cesium(I). In other words, other fission products do not have any influence on the adsorption of Cs(I). Analogous conclusions, with reference to previous paper, were described, i.e. chemical nature of the cesium(I) adsorption process, optimal sorption of the desired ion in 3.0 M HNO₃.

The molecular modification of calix[4]arene-R14 with MOBD resulted from some disadvantages of the calixcrown in selective complexation of cesium(I). The lipophilic nature of calix[4]arene and hydrophilic one of crown ether made the synthesis unsatisfactory. Moreover, the optimal concentration of nitric acid for cesium ions separation by extraction chromatography was different than that of HLW. In order to evaluate the influence of different modifier M, the authors decided to compare the properties of the composite material by the modification of calix[4]arene-R14 with tri-n-butyl phosphate (TBP), octanol (Oct) and previously discussed methyloctyl-2-dimethylbutanemide (MOBD). The chromatographic partitioning was carried out in the presence of some typical fission and nonfission products, including uranium(VI), strontium(II) and cesium(I), in nitric acid solution. Most of uranium (more than 99%) is separated by liquid-liquid solvent extraction but a small quantity is still present in HLW

and it is important to test if it has any impact on the separation of Cs(I). However, it was shown that uranium adsorption was weak, slightly better than strontium.

The presence of varied modifiers, having different functional groups, should result in different adsorption properties. The first distinction was observed when comparing the adsorption capacity in nitric acid concentration range 0.3-7.0 M. In case of the modifiers Oct and TBD the optimal adsorption was achieved for 4.0 M HNO_3 , while for MODB - 3.0 M. In the optimal conditions, the highest distribution coefficient was obtained by (Calix[4] + Oct)/ $\text{SiO}_2\text{-P}$, that was interpreted by several factors (matching of size between cavity and cesium, π -bonding interactions with arene groups, molecule reorganization). According to the authors, the mechanism of adsorption and elution of cesium(I) in chromatographic partitioning by the composite materials discussed is as following (Figure 6).

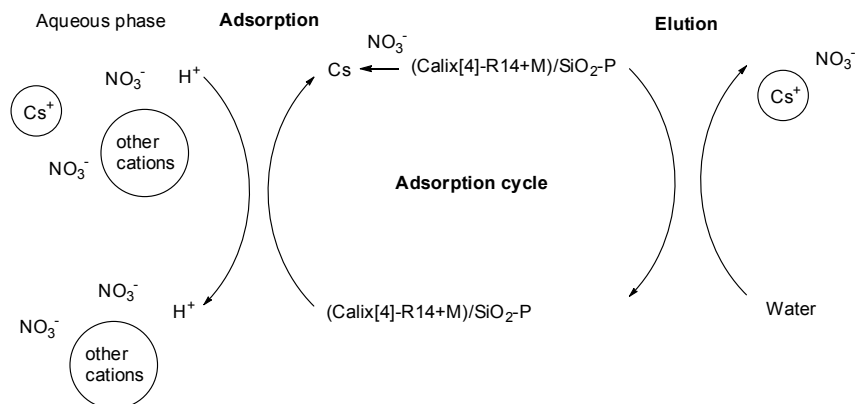


Figure 6. Mechanism of cesium(I) adsorption and elution in partitioning by the composite materials.

Another version of Calix[4]arene-R14 modification was described by Wu et al. [20]. This time the supramolecular system was modified with dodecanol to form (Calix[4] + Dodecanol)/ $\text{SiO}_2\text{-P}$. The results obtained were similar with the previous studies as the material demonstrated an excellent adsorption ability of cesium(I) and the maximum separation was observed for 4 M nitric acid solution.

It seems that composite matrices, having calixcrowns as molecular receptors for cesium(I) complexation, are very promising tool for Cs(I) separation from highly active liquid waste. In optimal conditions, they are able to eliminate selectively the desired cation in the presence of great number of other ones.

Unfortunately, the synthesis cost could exclude it from a practical application because of economical aspects.

References

1. S. Gaur, "Determination of Cs-137 in environmental water by ion-exchange chromatography", *J. Chromatogr. A*, 733, 57-71 (1996);
2. M.S. Devarakonda, M.C. Seiler, „Radioactive wastes”, *Water. Environ. Res.*, 67, 585-596 (1995);
3. D. Copplestone, M.E. Toal, M.S. Johnson, D. Jackson, S.R. Jones, "Environmental effects of radionuclides—observations on natural ecosystems", *J. Radiol. Prot.*, 20, 29–40 (2000);
4. M. Dubourg, "Review of advanced methods for treating radioactive contaminated water", *Radioprotection*, 33, 35-46 (1998);
5. M.S.H. Bader, "Separation of critical radioactive and non-radioactive species from aqueous waste streams", *J. Hazard. Mater.*, B82, 139–182 (2001);
6. B. Hua, B. Deng, "Radioactive wastes", *Water Environ. Res.*, 78, 1856-1882 (2006);
7. L. Cecille Ed., "Radioactive waste management and disposal", Elsevier Science, New York, 1991, ISBN 1851666575 9781851666577;
8. E. Bascetin, H. Haznedaroglu, A.Y. Erkol, "The adsorption behaviour of cesium on silica gel", *Appl. Radiat. Isot.*, 59, 5-9 (2003);
9. J. Orechwoská, P. Rajec, "Sorption of cesium on composite sorbents based on nickel ferrocyanide", *J. Radioanal. Nucl. Chem.*, 242, 387-390 (1999);
10. P. Rajec, J. Orechwoská, I. Novák, "NIFSIL: A new composite sorbent for cesium", *J. Radioanal. Nucl. Chem.*, 245, 317-321 (2000);
11. P.K. Mohapatra, S.A. Ansari, A. Sarakar, A. Bhattacharyya, V.K. Marchanda, „Evaluation of calix-crown ionophores for selective separation of radio-cesium from acidic nuclear waste solution", *Anal. Chim. Acta*, 571, 308-314 (2006);
12. X. Hao, S. Tan, W. Deng, "The studies on adsorption behaviour of calix[4]-bis-crown-6 chromatographic resin and its application to the separation of HLW", *J. Radioanal. Nucl. Chem.*, 292, 1291-1296 (2012);
13. A.M. Nechifor, A.P. Philipse, F. de Jong, J.P.M. van Duynhoven, R.J.M. Egberink, D.N. Reinhoudt, "Preparation and properties of organic dispersions of monodisperse silica receptor colloids grafted with calixarene derivatives or alkyl chains", *Langmuir*, 12, 3844-3854

- (1996);
14. G. Arena, A. Casnati, A. Contino, L. Mirone, D. Sciotto, R. Ungaro, "Synthesis of new calixcrowns and their anchoring to silica gel for the selective separation of Cs⁺ and K⁺", *Chem. Commun.*, 2277-22780 (1996);
 15. G. Arena, A. Contino, A. Magri, D. Sciotto, G. Spoto, A. Torrisi, "Strategies based on calixcrowns for the detection and removal of cesium ions from alkali-containing solutions", *Ind. Eng. Chem. Res.*, 39, 3605-3610 (2000);
 16. G. Arena, A. Contino, E. Longo, D. Sciotto, G. Spoto, A. Torrisi, "Two calix-crown based stationary phases. Synthesis, chromatographic performance and X-ray photoelectron spectroscopy investigation", *J. Supramol. Chem.*, 2, 521-531 (2002);
 17. A. Zhang, Q. Hu, Z. Chai, "Synthesis of a novel macroporous silica-calix[4]arene-crown polymeric composite and its adsorption for alkali metals and alkaline-earth metals", *Ind. Eng. Chem. Res.*, 49, 2047-2054 (2010);
 18. A. Zhang, Q. Hu, "Adsorption of cesium and some typical coexistent elements onto a modified macroporous silica-based supramolecular recognition material", *Chem. Eng. J.*, 159, 59-66 (2010);
 19. A. Zhang, Z. Chai, "Adsorption properties of cesium onto modified macroporous silica-calix[4]arene-crown based supramolecular recognition materials", *Ind. Eng. Chem. Res.*, 51, 6196-6204 (2012);
 20. Y. Wu, S.-Y. Kim, D. Tozawa, T. Ito, T. Tada, K. Hitomi, E. Kuraka, H. Yamazaki, K. Ishii, "Study on selective separation of cesium from high level liquid waste using a macroporous silica-based supramolecular recognition absorbent", *J. Radioanal. Nucl. Chem.*, 293, 13-20 (2012).

Chapter 19

Algae and their chelating properties

Joanna Fabrowska and Bogusława Łęska
*Adam Mickiewicz University in Poznań, Faculty of Chemistry,
Umultowska 89b, 61-614 Poznań, Poland*

1. Introduction

Algae are differential group of organisms, which consist of both unicellular microalgae (e.g. *Spirulina*, *Chlorella*) and multicellular macroalgae (e.g. *Ulva*, *Fucus*). However, they have several common features, as a existence in aquatic habitat or their simple morphology. Due to their chemical diversity and unique properties, algae have been the subject of many studies and they are widely used in pharmaceutical, cosmetic and agricultural industry. The algae are common on all seashores and can produce in time an important amount of biomass in nutrient-enriched waters. They are characterized by chelating properties and they are able to form complexes with cations. The problem of finding compounds to capable complex formation is also one of the main subject of supramolecular chemistry.

The term “ulvan” refers to the anionic polysaccharides found in the cell wall of green seaweeds belonging to the genus *Ulva* (Chlorophyta), in which it represents from 8 to 29% of the dryweight. Ulvan is a complex anionic sulfated polysaccharide extracted from the cell-walls of green sea weeds.

Algal cell walls are freely permeable to low molecular-weight constituents such as water, ions, gases, and other species [1]. Hence, marine algae (e.g. *Fucusvesiculosus*) are characterized by high concentration of e.g. iodine, chlorine or potassium in their cell walls by contrast to algae, which exists in fresh waters. Furthermore, algae are able to uptake biogenic elements such as nitrogen and phosphorus from surfacewaters. This process is widely studied for using in water treatment because of algae potential as biofilters [2-4]. Moreover, in recent years algae have received increasing attention for heavy metal removal [1]. This organisms can absorb various metals, especially heavy metals such as: Cd, Cu, Zn, Pb, Cr, Hg, Fe, Ni, Co, Au. Therefore, algae are used as bioindicators and biosorbents [5]. They can be also potentially applied in rare metal recovery

from water, e.g. gold [6].

The accumulation of metals in algal biomass is the result of the presence of specific compounds, which generally bond metal ions by chelation. There are several functional groups responsible for coordination bond formation with metal ions, e.g. hydroxyl, carboxyl, amino, ester. The major chemical components in algae, which contain these functional groups are polysaccharides (alginic acid and alginates, cellulose, xylans, ulvans, fucoidan), proteins and lipids [1,5]. Depending on species of algae the composition of individual compounds can be different in a biomass. As a result, particular groups of algae have distinct chelating properties due to differences in composition of chelators. For example, the cell walls of brown algae (*Phaeophyta*) generally containsuch components as cellulose, alginic acid and the corresponding salts of sodium, potassium, magnesium and calcium and sulphated polysaccharides (fucoidan). The red algae (*Rhodophyta*) also contain cellulose, but the main compounds responsible for chelation of metals are sulphated polysaccharides made of galactanes (agar and carragenates). Finally, green algae (*Chlorophyta*) mainly consist of cellulose and proteins bonded to polysaccharidesto form glycoproteins [7,8]. The Table 1 shows the main cell wall components occurring in green, brown and red algae.

Table 1. The major classes of chemical components present in different groups of algae[8].

Group of algae	Cell wall component
Green algae	Cellulose, hydroxyproline glucosides, xylans, mannan
Brown algae	Cellulose, alginic acid, sulfated mucopolisaccharidies (fucoidan)
Red algae	Cellulose, xylans, sulfated polysaccharidies (galactanes)

On the basis of a number of studies it was found that brown algae have the greatest ability to accumulation of heavy metals than green or red algae. Brown algae have also higher uptake capacity and they offer better sorption of metal ions [5,9,10]. This fact is probably caused by higher amount of alginates and fucoidans in cell walls of brown algae, which are responsible for bioaccumulation process [5]. In the Table 2 this is evident that brown algae are the best biosorbents due to the highest values of maximum biosorption capacity.

Table 2, The value of maximum biosorption capacity [mmol/g biomass] for brown, red and green algae[7].

Metal ions	Brown alga	Red alga	Green alga	Average value
Cd	0.930	0.260	0.598	0.812
Ni	0.865	0.272	0.515	0.734
Zn	0.676	-	0.370	0.213
Cu	1.017	-	0.504	0.909
Pb	1.239	0.651	0.813	1.127

Moreover, the efficiency of absorption of metal ions depends on species of algae. There are many researches shows that various species of algae are characterized by different uptake capacity of heavy metals. Romera et al. studied the sorption capacity of six different species of algae (*Codium vermilara*, *Spirogyra insignis*, *Asparagopsis armata*, *Chondrus crispus*, *Fucus spiralis*, *Ascophyllum nodosum*) in the recovery of Cd, Ni, Zn, Cu and Pb. The best results were obtained with *Fucus spiralis*[11]. Baran et al. reported that the maximum sorption capacity of *Halimeda tuna*, *Sargassum vulgare*, *Pterocladia capillacea*, *Hypnea musciformis*, *Laurencia papillosa* for Cr(VI) were 2.3; 33.0; 6.6; 4.7 and 5.3 mg/g, respectively. The results showed that *Sargassum vulgare* was suitable for removing chromium from aqueous solution [12]. Łęska et al. proved that freshwater *Ulva* species were characterized by high ability to uptake cadmium and lead ions. As a result *Ulva* spp. can potentially be used as a biosorbent of this ions [13]. However, the same research group examined freshwater populations of *Ulva*, which exhibited a greater efficiency to bioaccumulate nickel as compared to species derived from marine ecosystems. That is why *Ulva* maybe also used as bioaccumulator for Ni [14]. Murphy et al. investigated several species of the marine macroalgae: *Fucus spiralis*, *Fucus vesiculosus*, *Ulva linza*, *Ulva compressa*, *Ulva intestinalis*, *Ulva lactuca*, *Polysiphonia palmata* and *Polysiphonia lanosa*, in terms of their Cu(II) biosorption performance. Consequently, *Ulva* spp. performed extremely efficiently in sequestering copper ions (0.326 mmol/g biomass) [15].

2. Alginates

One of the most essential group of compounds, which enables algae to chelate heavy metal ions is alginic acid and alginates – its sodium, potassium, magnesium, calcium or ammonium salts. Generally this components occur in brown algae [5]. They are derived by extraction with diluted alkaline solution from such species as: *Laminaria*, *Lessonia*, *Macrocystis*, *Ascophyllum*, *Durvillea* [16, 17].

Alginic acid and alginates are reclassified as polysaccharides and they are polymers of β -D-mannuronic acid and α -L-guluronic acid. β -D-mannuronic acid creates M-blocks in alginate chain and α -L-guluronic acid creates G-blocks, which have different spatial conformation [5]. Thanks to presence of carboxyl or hydroxyl groups they are able to create complexes with metal ions. The Figure 1 presents the structure of alginic acid.

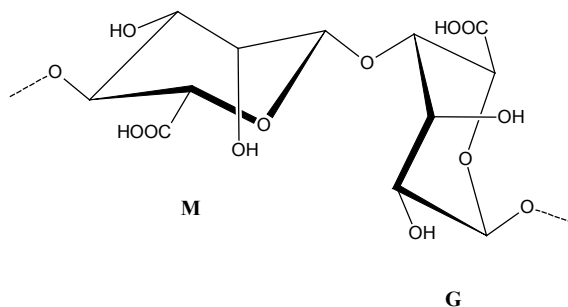


Fig. 1. Structure of alginic acid [18].

Blocks M and G occur in various location and ratio in alginic chain. There are three possible types of location of M and G blocks: homopolymeric blocks of guluronate (GGGG), homopolymeric blocks of mannuronate (MMMM) or the blocks with alternating sequence (MGMG) [19]. It was found that the structure of alginates depends on species of algae, their geographical location and climatic conditions. For example, alginates extracted from *Laminaria hyperborea* are characterized by a high amount of G-blocks, in contrast to *Laminaria japonica*, which contains alginates with a small amount of G-blocks [20].

Hence, individual types of alginate chains represent different capacity to metals binding. The most favourable structure of alginic chain is the GGGG type of structure. The reason why this structure provides the most efficient metal chelation must be due to suitable geometry of the particle. There are specific cavities between G-blocks, which offer convenient places for metal ion because of the possibility of interactions between metal ion and functional groups from alginates. The GGGG type of alginate creates zigzag structure, which enables the stronger impact of metal cation and its more stable connection with alginate. By contrast, the MMMM structure do not offer such effective geometry for stable chelation of metal ions. As a result, the homopolymeric blocks of guluronate shows a better specificity for cations bonding and represents well-defined

chelate spaces. The consequence of this fact is that higher amount of the GGGG blocks in alginate allows the highest values of maximum biosorption capacity. The interaction between poliguluronate blocks and metal cation is described by the “egg-box” model, where homopolymeric G-blocks form three-dimensional structures, in which metal ions are embedded like eggs in a cardboard egg-box [21, 22]. The structure of alginic chain can be regulated with action of the enzyme - alginate C5-epimerase [23]. The Figure 2 shows three types of blocks in alginic chain.

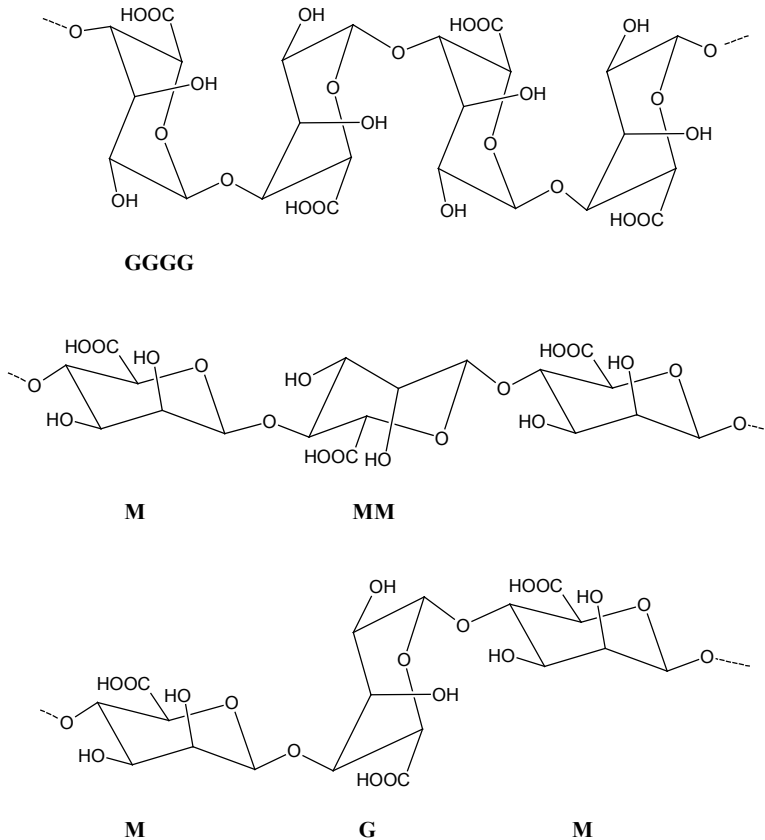


Fig. 2. Types of blocks in alginic chain [16].

The interactions of alginic acid with diverse bivalent cations, particularly with Ca^{2+} ions, have been studied frequently. This ions readily links between GGGG blocks in alginic acid thanks to creating chelating bonds comes from carboxyl and hydroxyl groups. In the presence of calcium ions alginates create gel, which is additionally stabilised by intermolecular hydrogen bonds [23]. These gels are used in preparing active dressings. If alginic dressing consist of high amount of GGGG blocks there are obtain high-apsorptive compact gels with efficiently bonded calcium ions. On the contrary, if we use alginic acid with small amount of polyguluronate blocks there we obtain more liquid and less-apsorptive gels [24]. Also manganese ions prefer to link with polyguluronate chain, by contrast to polymannuronate blocks, which do not form stable complexes with Mn^{2+} ions. However, there were observed impacts between carboxyl carbon C_6 and carbon C_5 comes from polyguluronate blocks and Mn^{2+} ion [25].

3. Ulvan

Another interesting group of chelators in algae classified to polysaccharides are ulvans. This compounds were discovered and extracted from *Ulva* species, so they are characteristic for this green algae. Ulvans are extracted e.g. from *Ulva armoricana*, *Ulva lactuca*, *Ulva rotundata*, *Ulva rigida* or *Ulva mutabilis* with hot water containing a divalent cation chelator such as ammonium oxalate. Recovery of ulvan is generally done by precipitation by adding an alcohol or a quaternary ammonium salt [26,27]. An alternative extraction can be sequential extraction on AIR (alcohol insoluble residue) e.g. AIR extraction with hot HCl or AIR extraction with acidified ammonium oxalate [28].

Ulvans are water-soluble sulfated polysaccharides, in general consist of rhamnose, xylose and glucuronic acid. The other constituents of ulvans could be mannose, galactose or arabinose. However, it is difficult to determine the sugar composition in ulvans due to changes in the composition with seasons, environmental conditions and ecophysiological growth conditions of algae [26]. The Figure 3 presents the main disaccharides occurring in ulvan.

Ulvans are able to form chelate complexes with metal ions and to create gels. The mechanism of gel formation is complex and not fully explained. Actually, conditions, in which the gel is formed with ulvans, are following: a presence of boric acid, calcium ions and pH between 7.5-8 [29]. However, increasing elastic modulus in the gel were obtained with $\text{Cu} > \text{Zn} > \text{Mn} > \text{Ca}$ for *Ulva armoricana* ulvans, but no gel was obtained with Mg ions [26]. In normal conditions ulvans have linear structure. In the presence of boric acid and metal ion (e.g. Ca^{2+}) they form spherical-shaped structures, which have diameter of about 10 nm. Afterwards this spherical-shaped structures can associate with each other and

create grouping of associates with diameter of 500-1200 nm, which look like raspberry fruit (bead-like structures). Subsequently bead-like structures link with each other by linear fibers (fiber-like materials) thanks to ionic interactions. Probably fiber-like materials can consist of protein chains, glucuronic acid or ulvans, which do not create spherical-shaped structures. As a result, there is formed three-dimensional structure, characteristic for ulvans. There are creating specific zones between spherical-shaped structures, in which metal ion can be embedded and complexed [27]. The Figure 4 shows the three-dimensional structure formed by ulvans in the presence of boric acid and bivalent metal ion.

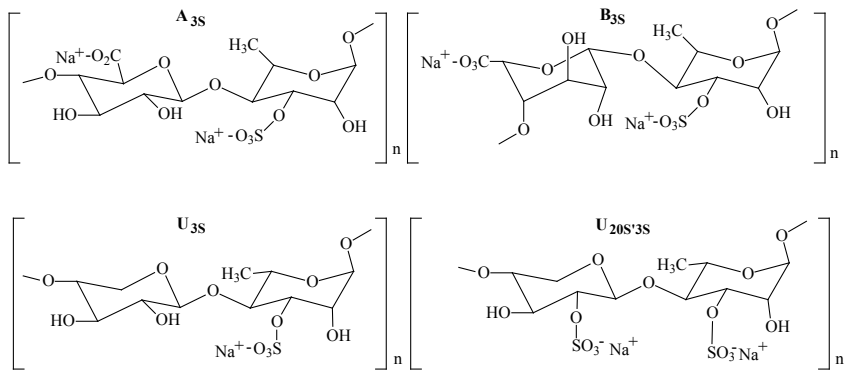


Fig. 3. Structure of the main disaccharides occurring in ulvan: ulvanobiuronic acids A_{3S} and B_{3S} and ulvanobioses U_{3S} and U_{20S3S} [27].

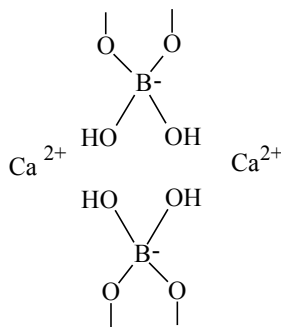


Fig. 4. Structure formed by ulvans in water solution in the presence of boric acid and bivalent cation [27].

There are several proposed interactions between ulvans and metal ions. One of the proposed mechanisms explains that few borate esters are formed with the cisdiol functions of unsulfated rhamnose residues to cross-link ulvan chains (Figure 5. I). Calcium ions can bridge complexes and stabilize the borate esters. On the other hand, direct ulvan cross-links by borate esters are unlikely (Figure 5. II). Finally, sulfate and carboxylic acid groups from ulvans are able to coordinate metal ions (Figure 5. III, IV) [26].

So far, it was proved that ulvans extracted from *Ulva armoricana* have had the most applicable gelling properties. Ulvans from this species showed an affinity for chelating metal ions in the following order: Al > Cu > Pb > Zn > Cd = Mn > Sr > Mg = Ca [26].

4. Use of the chelating properties of algae

Due to chelating properties of algae there are a range of applications in various industries of this water organisms. First of all, algae may be used as biosorbents due to their ability to accumulation of heavy metal ions [1,5,7,9]. Biosorption is an innovative technology, which uses inactive and dead biomass for the recovery of heavy metals from aqueous solutions. Because of high values of biosorption capacity obtained for many species of algae, especially for brown algae [11,12,15], biosorption seems to be a promising alternative to traditional methods of water treatment. Apart from high yield of metal chelation, algae present other advantages, e.g.: rapid increase in biomass in a short time, low nutritional requirements (water, light, CO₂), environmentally friendly production of algae biomass [5,11]. There are available researches showing that algae can be competitive biosorbents with other types. For example, it was found that *Fucus vesiculosus* presents higher maximum biosorption capacity for lead than bacterias, fungi or natural zeolite [10]. The comparison of the value of maximum biosorption capacity is showed at Table 3. What is more, algae can be potentially used as bioindicators of metal contamination in aquatic environments [3,13,14].

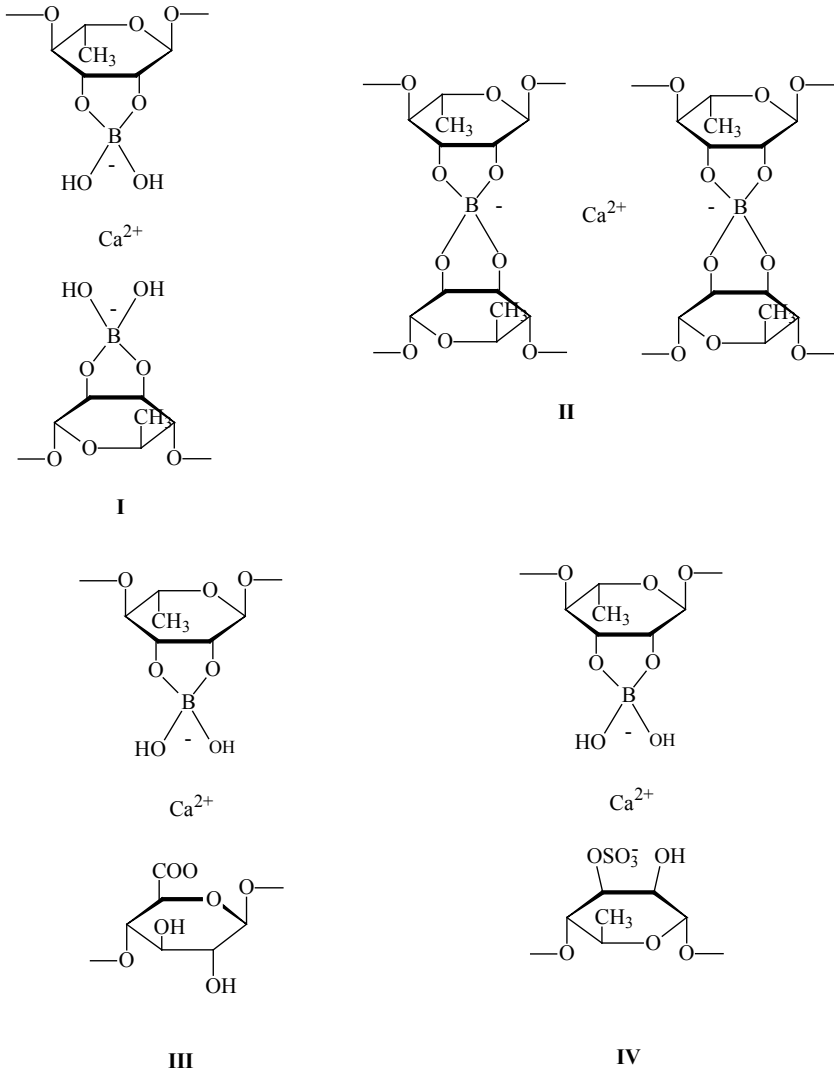


Fig. 5. Proposed interactions between ulvans and calcium ion [26].

Table 3. Comparison of the value of maximum biosorption capacity [mmol/g mass] for different types of sorbents [10].

Sorbents	Pb	Cu	Cr
<i>Fucus vesiculosus</i> (alga)	1.04	0.97	1.12
<i>Pseudomonas aeruginosa</i> (bacteria)	0.33	0.29	-
<i>Rhizopus arrhizus</i> (fungus)	0.50	0.25	0.27
Natural zeolite	0.18	-	-
Ion exchange resin	1.37	-	0.59

Secondly, algae are also able to accumulate radioactive ions. Oszczak et al. investigated the sorption of U^{6+} , Eu^{3+} and Am^{3+} with using calcium alginate as a biosorbent. It was found that all of the radionuclides used were removed efficiently [30]. Another research concerned of identification of the level of ^{137}Cs concentrations in three macroalgae species: *Polysiphonia fucooides*, *Furcellaria lumbricalis* and *Cladophora glomerata* coming from Puck Bay. *Polysiphonia fucooides* turned out to be the best bioindicator for the monitoring of ^{137}Cs contamination due to the high efficiency of bioaccumulation [31]. Therefore, algae may be potentially used in removal of radionuclides from liquid radioactive waste. They also can be applied in study of the marine environment as a bioindicators of the presence of transuranic elements and products of fission of nuclear fuel. Furthermore, algae are considered as potential reference organisms to be used in models for assessing the radiological consequences of radioactive releases, arising both from the routine operation of nuclear facilities [32] and from accidental situations [33].

Moreover, chelating properties of algae are widely used in medicine. Their ability to removing heavy metals is applied in detoxify a body from this metals, e.g. *Spirulina platensis* is used in this respect [34]. Algae are usually applied for this purpose in the form of tablets, capsules or solutions [35]. Nowadays, different kinds of biomaterials, such as alginate fibers, become more and more popular in medical applications as a modern active dressings. There are many types of alginate fibers, which are made from: alginic acid, zinc alginate, copper alginate, sodium alginate, calcium alginate, calcium alginate with nanosilica. Generally, in the case of calcium alginate the mechanism of action is that calcium

ions from dressing are converted to sodium ions from the wound exudate [36]. In addition, Ca^{2+} ions are able to activate thrombocytes. Hence, this ions have hemostatic properties and they accelerate blood clotting and wound healing when they are released into the wound [37]. Additionally, in case of zinc and copper alginate fibers application, dressings is achieved with bacteriostatic and antifungal properties [5]. The sorption properties of active dressings depends on the structure of alginate contained in the material. In the presence of high amount of GGGG blocks in an alginate there is possible 'egg-box' structure, which allows for the absorption of larger amounts of secretions from the wound [24]. Also ulvans can be proposed for the applications as wound dressings. What is more, ulvans were investigated in the release of dexamethasone from ulvan membranes. Results showed that these membranes may be potentially used as a drug delivery systems [38]. There are many others researches which proves the ability of algae materials, e.g. ulvans and alginates, to drug release [39,40,41].

Furthermore, there is still increasing interest in algae as a very attractive natural products used in cosmetics. Thanks to contents of a range of bioactive agents especially in marine algae, e.g. polysaccharides, proteins, fatty acids, vitamins, polyphenols, micro- and macroelements, algae have multifunctional applications and activity in cosmetics industry. Therefore, algae are able to hydrate the skin, cure acne and cellulite, and they also have anti-inflammatory, anti-irritant, anti-ageing or UVB-photoprotective activities [5,42-45]. However, in recent years the attention was focused mainly on antioxidative properties of algae [44,46]. Free radicals (ROS – reactive oxygen species) are largely responsible for destruction of DNA and other components of the skin, and – as a result – for skin aging. One of the mechanisms of formation of ROS is catalysis of this process by traces of heavy metals, e.g. iron [42]. Because algae contain chelators, such as alginates and ulvans, they are able to chelate heavy metals cations into complexes. Consequently, algae are used in cosmetics as a free radical scavengers to prevent skin aging. The antioxidant activities of algae have been investigated in many researches. Gómez-Ordóñez et al. examined the antioxidant activity of red alga *Mastocarpus stellatus* by FRAP (ferric reducing ability of plasma) method. The antioxidant status improvement in caecum of rats was observed, probably because of presence of sulphated-galactans [46]. Moreover, Ngo et al. determined the antioxidant activities of micro- and macroalgae with DPPH (1,1-diphenyl-2-picrylhydrazyl), hydroxyl radical, hydrogen peroxide and superoxide anion scavenging methods [47]. Apart from alginates and ulvanes, there are numerous others antioxidants having chelating properties in algae, such as polyphenols, e.g. fucols, phlorethols, fucophlorethols [43]. In addition, the red alga *Ancanthophora delilei* has been described as a

source of carnosine (β -alanyl-L-histidine), a histidyl peptide with an antioxidant activity as well as is associated the ability of chelate transition metals [48]. Hence, algae are very useful in preparing functional cosmetics.

Last but not least, various preparations based on algae are applied in organic farming. They may be used successfully as fertilizers [49], plant protection measures [50] or biostimulators [51], which are more environmentally friendly than measures used in traditional agriculture. In studies of AlgaminoPlant (a biostimulator consisting of *Sargassum* spp.) it was found that this measure improved germination and growth of carrots and parsley, and also it resulted in a decrease of nitrate and increase of carotenoid [52]. What is more, algae are an attractive material for the production of animal feed. Because of their chelating properties, algae are able to accumulate micro- and macroelements in their biomass. Therefore, such microelements as Zn, Cu, I, Fe, Mg or Mn occur in algae in the form of organometallic compounds or complexes, which are particularly well absorbed by animal organisms, much better than the individual micronutrients [5,53]. Also macroelements such as N, P, K, Na occurring in feed based on algae biomass turned out to be better absorbed than in inorganic form [54]. Furthermore, in the literature there are described attempts to enrich the biomass of *Spirulina platensis* in iodine and selenium [55,56]. Thanks to ability of algae to bioaccumulation they can be enriched in micro- and macronutrients, and – as a result – they may solve the problem of deficiency of important nutrients in the diet of farm animals (fish, poultry, cattle, pigs) [53].

5. Conclusion

To sum up, both microalgae and macroalgae are currently the subject of many studies. This is probably because of the range of various compounds occurring in algae, which are responsible for their unique properties. One of the most unusual compounds in algae are chelators such as alginic acid, alginates [5], ulvans [26], but also fucols, phlorethols, fucophlorethols [43] and carnosine [48]. Due to chelating properties and the bioaccumulation process algae may be applied in many areas. With regard to heavy metals chelation, numerous species of algae are considered for applications as cleaning agents in aqueous reservoirs [1,5], bioindicators for monitoring of aquatic environments [3,13,14], in medicine as antidotes in heavy metal poisonings [34] and active dressings [36] or antioxidants in cosmetics [44,46]. Because of ability of algae to absorbing of micro- and macroelements they are widely used in production of valuable cosmetics [5,42], supplements and farm animal feed [53]. However, the bioaccumulation process is determined by different factors, e.g.: temperature, light conditions, water motion, salinity, species of algae and their morphology

and physiology, nature and content of the chelating agents occurring in algae, concentration of absorbed elements and their physical and chemical form [31]. Nevertheless, algae seems to be very efficient biosorbents [10] and they may be successfully used in various industries as very attractive and useful natural products.

Acknowledgements

The author thanks the NCBiR for financial support under Grants No. 176892, titled: “Innowacyjna technologia ekstraktów glonowych – komponentów nawozów, pasz i kosmetyków”.

References

1. Wang J., Chen C. (2009), Biosorbents for heavy metals removal and their future, *Biotechnology Advances*, 27: 195–226.
2. Copertino M.D.S., Tormena T., Seeliger U. (2009), Biofiltering efficiency, uptake and assimilation rates of *Ulvaclathrata* (Roth) J. Agardh (Clorophyceae) cultivated in shrimp aquaculture waste water, *Journal of Applied Phycology*, 21: 31–45.
3. Yokoyama H., Ishihi Y. (2010), Bioindicator and biofilter function of *Ulva* spp. (Clorophyta) for dissolved inorganic nitrogen discharged from a coastal fish farm – potential role in integrated multi-trophic aquaculture, *Aquaculture*, 3: 74–83.
4. Habaki H., Tajiri S., Egashira R., Sato K. (2011), Uptake rate of ammonia-nitrogen with sterile *Ulva* sp. for water quality control in sensitive shrimp culture ponds in developing countries, *Chemical and Biochemical Engineering Quarterly*, 25: 341–349.
5. Pieleś A. (2010), Algi i alginiany – leczenie, zdrowie i uroda, E-book.
6. Mata Y.N., Blazquez M.L., Ballester A., Gonzalez F., Munoz J.A. (2008), Gold (III) biosorption and bioreduction with the brown alga *Fucusvesiculosus*, *Journal of Hazardous Materials*, 166: 612–618.
7. Romera E., Gonzalez F., Ballester A., Blazquez M.L., Munoz J.A. (2006), Biosorption with algae: a statistical review, *Critical Reviews in Biotechnology*, 26: 223–35.
8. Davis T.A., Volesky B., Mucci A. (2003), A review of the biochemistry of heavy metal biosorption by brown algae, *Water Research*, 37: 4311–4330.
9. Brinza L., Dring M.J., Gavrilescu M. (2007), Marine micro- and macro-algal species as biosorbents for heavy metals, *Environmental*

- Engineering and Management Journal*, 6: 237–51.
10. Rincon J., Gonzalez F., Ballester A., Blazquez M.L., Munoz J.A. (2005), Biosorption of heavy metals by chemically-activated alga *Fucusvesiculosus*, *Journal of Chemical Technology and Biotechnology*, 80: 1403–7.
 11. Romera E., Gonzalez F., Ballester A., Blazquez M.L., Munoz J.A. (2007), Comparative study of biosorption of heavy metals using different types of algae, *Bioresource Technology*, 98: 3344–3353.
 12. Baran A., Baysal S.H., Sukatar A. (2005), Removal of Cr⁶⁺ from aqueous solution by some algae, *Journal of Environmental Biology*, 26: 329–33.
 13. Łęska B., Ptaszkiewicz M., Messyasz B., Rybak A. (2010), Metale ciężkie w wodzie oraz w plechach zielenicy *Ulva* (Ulvophyceae, Chlorophyta), in: G. Schroeder (Ed.), *Środowisko i Przemysł*, Cursiva, Poznań, 9-41.
 14. Rybak A., Messyasz B., Łęska B. (2012), Freshwater *Ulva* (Chlorophyta) as a bioaccumulator of selected heavy metals (Cd, Ni and Pb) and alkaline earth metals (Ca and Mg), *Chemosphere*, 89: 1066-1076.
 15. Murphy V., Hughes H., McLoughlin P. (2007), Cu(II) binding by dried biomass of red, green and brown macroalgae, *Water Research*, 41: 731–40.
 16. Tonnesen H.H., Karlsen J. (2002), Alginate in drug delivery system, *Drug Development and Industrial Pharmacy*, 28: 621-630.
 17. McHugh D.J. (2002), Prospects for seaweed production in developing countries, Food and Agriculture Organization of the United Nations, in: <http://www.fao.org/>.
 18. Khalil S. El D. (2005), Deposition and structural formation of 3D alginate tissue scaffolds., A Thesis Submitted to the Faculty of Drexel University, in: <http://dspace.library.drexel.edu/>.
 19. Holte O., Onsoyen E., Myrvold R., Karlsen J. (2003), Sustained release of water-soluble drug from directly compressed alginate tablets, *European Journal of Pharmaceutical Sciences*, 20: 403-407.
 20. Draget K.I, Smidsrod O., Skjak-Braek G. (2005), Polysaccharides and polyamides in the food industry, properties, production and patents, chapter 1, vol 1, *Alginates from Algae*, in: Wiley-VCH.
 21. Yalpani M. (1988), *Polysaccharides: synthesis, modifications and structure/property relations*, Amsterdam: Elsevier Science Publishers.
 22. Powell D.A. (1979), Structure, solution properties and biological interactions of some microbial extracellular polysaccharides, in: Berkeley RCW, Gooday GW, Ellwood DC, editors, *Microbial*

- polysaccharides and polysaccharases, London: Academic Press, p. 117.
23. Draget K.I., Skjak-Braek G., Stokke B.T. (2006), Similarities and differences between alginic acid gels and ionically crosslinked alginate gels, *Food Hydrocolloids*, 20: 170–175.
 24. Mikołajczyk T., Wołowska-Czapik D., Boguń M. (2008), A new generation of fibers from alginic acid for dressing materials, *Journal of Applied Polymer Science*, 107: 1670-1677.
 25. Emmerichs N., Wingender J., Flemming H.C., Mayera C. (2004), Interaction between alginates and manganese cations: identification of preferred cation binding sites, *International Journal of Biological Macromolecules*, 34: 73–79.
 26. Robic A., Lahaye M. (2007), Structure and functional properties of ulvan, a polysaccharide from green seaweeds, *Biomacromolecules*, 6: 1765-1774.
 27. Robic A., Gaillard C., Sassi J.F., Lerat Y., Lahaye M. (2009), Ultrastructure of Ulvan: a polysaccharide from green seaweeds, *Biopolymers*, 8: 654-664.
 28. Robic A., Rondeau-Mouro C., Sassi J.F., Lerat Y., Lahaye M. (2009), Structure and interactions of ulvan in the cell wall of the marine green algae *Ulvarotundata* (Ulvales, Chlorophyceae), *Carbohydrate Polymers*, 77: 206–216.
 29. Haug A. (1976), The influence of borate and calcium on the gel formation of a sulphated polysaccharide from *Ulvalactuca*, *Acta Chemica Scandinavica*, B30, 562-566.
 30. Oszczak A., Fuks L. (2011), Sorpcja na alginianie wapnia wybranych radionuklidów występujących w odpadach promieniotwórczych, in: <http://www.profuturo.agh.edu.pl/>.
 31. Zalewska T. (2012), Distribution of ¹³⁷Cs in benthic plants along depth profiles in the outer Puck Bay (Baltic Sea), *Journal of Radioanalytical and Nuclear Chemistry*, 293:679-688.
 32. Kumblad L., Kautsky U., Naesslund B. (2006,) Transport and fate of radionuclides in aquatic environments—the use of ecosystem modelling for exposure assessments of nuclear facilities, *Journal of Environmental Radioactivity*, 87:107–129.
 33. Lepicard S., Heling R., Maderich V. (2004), POSEIDON/RODOS models for radiological assessment of marine environment after accidental releases: application to coastal areas of the Baltic, Black and North Seas, *Journal of Environmental Radioactivity*, 72:153–161.
 34. <http://www.spirulina.pl/>

35. Spolaore P., Claire J.-C., Elie D., Arsene I. (2006), Commercial applications of microalgae, *Journal of Bioscience and Bioengineering*, 101: 87-96.
36. Qiun Y., Gilding D.K. (1996), Alginate fibers and wound dressings, *Medical Device Technology*, 7: 32-41.
37. Szewczyk M. T., Jawień A., Cwajda J., Cierzniakowska K. (2005), Miejscowe leczenie owrzodzeń żylnych – zasady wyboru opatrunków, *Zakażenia*, 1: 80–88.
38. Alvesa A., Pinhoa E.D., Nevesa N.M., Sousaa R.A., Reisa R.L. (2012), Processing ulvan into 2D structures: Cross-linked ulvan membranes as new biomaterials for drug delivery applications, *International Journal of Pharmaceutics*, 426: 76–81.
39. Maticardi P., Di Meo C., Coviello T., Alhaique F. (2008), Recent advances and perspectives on coated alginate microspheres for modified drug delivery, *Expert Opin., Journal of Drug Delivery*, 5: 417-425.
40. Barrias C.C., Lamghari M., Granja P.L., Sa Miranda M.C., Barbosa M.A. (2005), Biological evaluation of calcium alginate microspheres as a vehicle for the localized delivery of a therapeutic enzyme, *Wiley Periodicals, Inc.*
41. Meera G., Abraham E. (2006), Polyionic hydrocolloids for the intestinal delivery of protein drugs: Alginate and chitosan – a review, *Journal of Controlled Release*, 114: 1-14.
42. Molski M. (2010), *Chemia piękna*, Wydawnictwo Naukowe PWN, Warszawa.
43. Czerpak R., Jabłońska-Trypuć A. (2008), *Roślinne surowce kosmetyczne*, MedPharm Polska, Wrocław.
44. Samarkoon K., Jeon Y.-J. (2012), Bio-functionalities of proteins derived from marine algae – A review, *Food Research International*, 48: 948–960.
45. Guinea M., Franco V., Araujo-Bazan L., Rodriguez-Martin I., Gonzalez S. (2012), In vivo UVB-photoprotective activity of extracts from commercial marine macroalgae, *Food and Chemical Toxicology*, 50: 1109–1117.
46. Gómez-Ordóñez E., Jiménez-Escrig A., Rupérez P. (2012), Effect of the red seaweed *Mastocarpus stellatus* intake on lipid metabolism and antioxidant status in healthy Wistar rats, *Food Chemistry*, 135: 806–811.
47. Ngo, D.H., Wijesekara I., Vo T.S., Ta Q.V., Kim S.K. (2011), Marine food-derived functional ingredients as potential antioxidants in the food industry: An overview, *Food Research International*, 44: 523–529.

48. Fleurence J. (2004), Seaweed proteins, in: Yada R.Y. (Ed.), Proteins in food processing (pp. 197–213), Cambridge, UK: Woodhead publishing limited.
49. Matysiak K., Adamczewski K. (2009), Regulatory wzrostu i rozwoju roślin – kierunki badań w Polsce i na świecie, *Progress in Plant Protection*, 49: 1810-1816.
50. Horoszkiewicz-Janka J., Jajor E. (2006), Wpływ zaprawiania nasion na zdrowotność roślin jęczmienia, pszenicy i rzepaku w początkowych fazach rozwoju, *Journal of Research and Applications in Agricultural Engineering*, 51: 47-53.
51. Hong D.D., Hien H.M., Son P.N. (2007), Seaweeds from Vietnam used for functional food, medicine and fertilizer, *Journal of Applied Phycology*, 19: 817-826.
52. Dobrzański A., Anyszka Z., Elkner K. (2008), Reakcjamarchwinaekstrakty pochodzenia naturalnego z alg z rodzaju Sargassum – AlgaminoPlanti z Leonardytu – HumiPlant, *Journal of Research and Applications in Agricultural Engineering*, 53: 53-58.
53. Chojnacka K., Saeid A., Michalak I. (2012), Possibilities of using algae biomass in agriculture, *Chemik*, 66: 1235-1248.
54. Caiozzi M., Peirano P., Rauch E., Zunino H. (1968), Effect of seaweed on the levels of available phosphorus and nitrogen in calcareous soli, *Agronomy Journal*, 60: 324-326.
55. Mosulishvili L.M., Kirkeasali E.I., Belokobylsky A.I., Khizanishvili A.I., Frontasyeva M.V. (2002), Experimental substantiation of the possibility of developing selenium – and iodine – containing pharmaceutical based on blue-green algae *Spirulina platensis*, *Journal of Pharmaceutical and Biochemical Analysis*, 30: 87-97.
56. Li Z.Y., Guo S.Y., Li L. (2003), Bioeffects of selenite on growth of *Spirulina platensis* and its biotransformation, *Bioresource Technology*, 89: 171-176.

Chapter 20

Decontamination systems on the basis of hydrogen peroxide: decomposition of ecotoxic substrates

Lyubov Vakhitova

*L.M. Litvinenko Institute of Physical Organic Chemistry & Coal
Chemistry, National Academy of Sciences of Ukraine. 83-114,
R. Luxemburg St., 70, Donetsk, Ukraine*

In recent years, decomposition of highly toxic chemical products becomes pressing problem due to a great amount of ecotoxicants and chemical warfare agents (CWA) accumulated throughout the world [1-6]. Decontamination (detoxication) of such environmentally hazardous compounds can be performed by a variety of chemical, thermal and biological techniques.

Chemical decontamination of ecotoxicants sends one in search of innovative technologies to meet the following requirements:

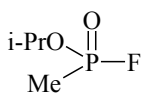
- commercial availability and high reactivity of the reagents;
- versatility of decontamination system toward a wide diversity of chemical warfare agents;
- freedom from special conditions for use;
- high degree of environmental safety both of chemical composition of the decontamination system and the resulting decomposition products;
- possibility to remove the toxic agents from the human skin surface
- chemical stability of the decontamination system during storage and transportation.

Of great importance are high decontamination efficiency and manageability of the decontamination process.

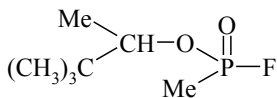
Hydrogen peroxide as a component of oxidative-nucleophilic decontamination systems

The most common chemical warfare agents can be divided into three groups

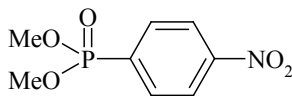
1. Neurotoxins – organophosphorus esters and structurally related pesticides:



GB

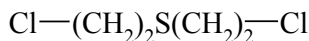


GD



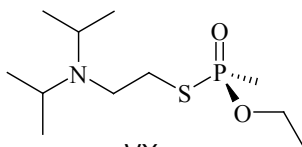
metaphos

2. Blister chemical agents – organic sulfur compounds:



HD

3. Nerve chemical agents (V gases) - compounds of the combined effects:



VX

The main technological processes in chemical decomposition of organophosphorus compounds are aqueous alkaline hydrolysis, oxidative chlorination by the mixture of chlorinated lime and calcium hypochlorite, alcoholysis by monoethanol amine or potassium butylate [7–10] followed by thermal bituminization of the salt concentrates. On the other hand, decomposition of sulfur organic compounds involves reactions of selective oxidation [11–14]. The drawbacks to the above methods of chemical detoxication are occasional use, significant corrosion attack on the equipment due to aggressive decontamination media, and considerable sewage pollution. It should be noted also that industrially used reagents (alkalies, alkali metal alcoholates and monoethanol amine) not-too reactive toward the esters of phosphoric and phosphonic acids.

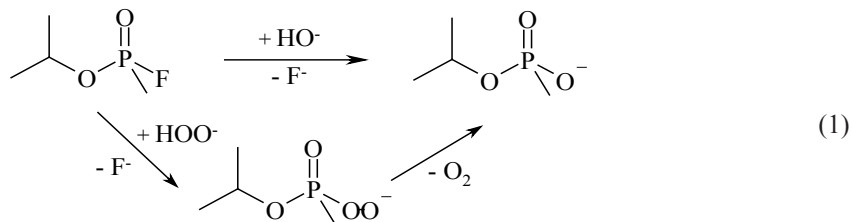
In view of hydrophobic properties of the toxic substances an optimum decontamination system must provide both solubilization and high decomposition rates of the toxic agents. That is why the most promising guidelines in the development of environmentally friendly systems is the use of organized nano-systems – micellar solutions and microemulsions (ME) [11, 12, 15–21]. Such systems provide reagents concentrating at the interphase boundary micelle (oil drop)/water and favorable conditions for nucleophilic attack on the electrophilic

centers in the ecotoxic substrates [21, 22].

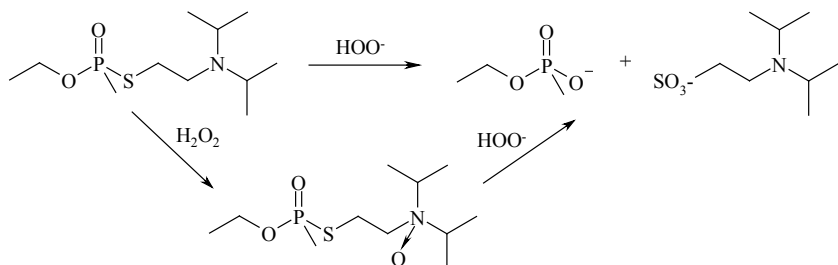
In a search for chemically active components for rapid and irreversible decomposition of the ecotoxicants, the emphasis is on the versatile oxidative-nucleophilic systems for destruction of a large variety of CWA. Thus, nucleophiles are efficient in decomposition of organophosphorus acid esters and halides (GB) [23, 24], oxidizers are the most reactive toward dialkyl sulfides like mustard gas (HD) [16, 25], whereas efficient decomposition of VX or the mixtures of the three types of the toxic substances (GB, HD and VX) requires oxidative-nucleophilic systems involved the pair HOX-OX^- (where $\text{X} = \text{OH}$, Hal and others) [1, 20]. In this connection hydrogen peroxide - due to its dual nature as an efficient oxidizer toward the mustard gas analogs and reactive α -nucleophile for nucleophilic substitution in organophosphorus esters - can be considered as multi-function agent in the development of the soft and environmentally safe decontamination systems.

Versatility of hydrogen peroxide and its derivatives as an oxidizers and nucleophilic agents was used in design of decontaminating compositions for materials polluted by toxic compounds, in particular, organophosphorus esters and organic sulfur compounds like paraoxon, parathion and mustard gas [26, 27]. Such compositions involve aqueous solutions of hydrogen peroxide, *tert*-butyl hydroperoxides, perborates and peroxy acids [28], and surfactant (usually quaternary ammonium salts). Although aqueous micellar systems on the basis of peroxides and peroxy acids feature relatively high reactivity toward paraoxon, mustard gas and its analogs, they are extremely unstable.

Studies on the reactions involving α -nucleophiles and recommendations on the development of the nucleophile-based formulations for decomposition of the chemical warfare agents were reported in [28–31]. It was shown that GB undergo rapid decomposition due to nucleophilic attack of hydroperoxide and hydroxide ions at phosphorus atom to form peroxy acids followed by their irreversible decomposition to the corresponding phosphonic acids [29-31]:



Under these conditions, peroxyhydrolysis of VX proceeds by the Scheme



to form ethyl methyl phosphonic acid and VX N-oxide followed by nucleophilic attack of the latter to form acid. Then the resulting thiol undergoes oxidation to sulfonate [5].

It is known that hydrogen peroxide oxidizes mustard gas and V-gases in the neutral and acid media. Addition of the activators (carbonates, borates, molybdates, phthalates, etc.) into the oxidizing system gives rise to a significant increase in the rate of oxidation due to formation of the efficient oxidizers – peroxy anions [15, 25, 32]. However, this is incomplete solving the problem of chemical warfare agents decontamination by combining oxidation processes with nucleophilic destruction since peroxyanions are reactive at $\text{pH} \leq 9$. Nucleophilic reactions with the participation of HOO^- ion require more alkaline media since acid dissociation constant of hydrogen peroxide amounts to $\text{pK}_a = 11,6$ [1], i.e. only 0,03-0,3% of hydrogen peroxide exists as a reactive ionic species HOO^- .

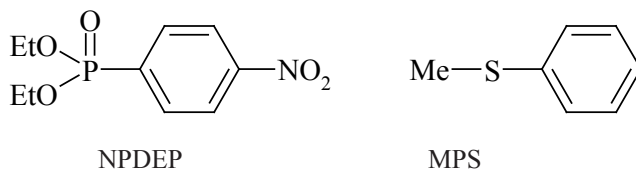
Thus, the essential restrictions to the use of such versatile agent as H_2O_2 in decomposition of ecotoxic substrates are as follows:

1. Extremely low solubility of hydrophobic substrates in aqueous media (the most favorable to meet the “green” technologies), and low reactivity of both H_2O_2 as an oxidizer and HOO^- as α -nucleophile;
2. Differences in the acidity of the reaction medium, necessary for maximum rates of oxidation and nucleophilic substitution;
3. Insufficient chemical stability of aqueous reactive systems with the participation of hydrogen peroxide and its derivatives.

For this reason combined oxidative-nucleophilic reactions, especially in the presence of the activators, require additional studies for determination of the optimum pH, that provide maximum reaction rates both for oxidation and nucleophilic substitution in the microorganized catalytic systems with high solubilizing ability toward the various ecotoxic substrates. Potentialities of the

alternative source of hydrogen peroxide, e.g., hydroperit [33] will be considered as well. Hydroperit (urea-hydrogen peroxide, UHP), an adduct of hydrogen peroxide with urea ($\text{H}_2\text{O}_2 \cdot \text{CO}(\text{NH}_2)_2$) is commercially available compound, non-toxic and stable in storage. Dry mixtures of UHP with the solid activators and detergents are of interest as efficient and long-term storage decontamination systems, as opposed to aqueous solutions on the basis of hydrogen peroxide whose long-term oxidative ability is restricted due to acid-base transformations of the reactive peroxyanions [33, 34].

In this paper 4-nitrophenyl ester of diethyl phosphoric acid (paraoxon, NPDEP), an analog of nerve gases and organophosphorus pesticides, and methylphenyl sulfide (MPS) as a close analog of mustard gas in reactivity and hydrophobic properties were studied as model substrates:

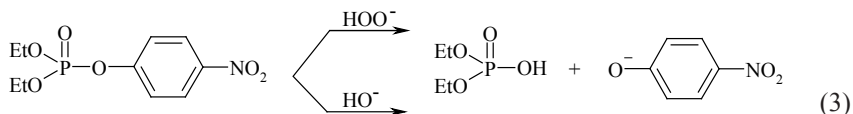


The main decontamination agents were hydrogen peroxide H_2O_2 and hydroperit. It is known, that their anionic species HOO^- exhibit supernucleophilic activity toward phosphorus acid esters and their neutral species are soft, environmentally friendly oxidizers of mustard gas analogs. Oxidizing properties of H_2O_2 were enhanced by addition of activators - ammonium hydrocarbonate NH_4HCO_3 and boric acid $\text{B}(\text{OH})_3$ [15, 19, 25, 35, 36].

In order to increase the solubility of the substrates, decomposition of NPDEP and MPS was carried out in the nano-sized polycomponent systems (Table 1): microemulsions (ME), micelles of various nature and aqueous alcohols with and without detergents added. Cationic cetyltrimethyl ammonium bromide (CTABr) was used as a detergent, since anionic detergents decelerate reactions in the system under studied [37–39], whereas the rates of the chemical transformations in such systems are unaffected by the neutral detergents.

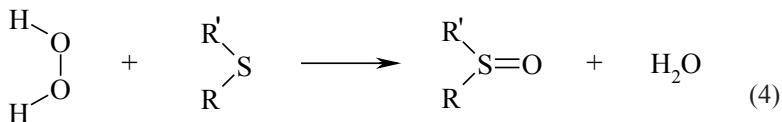
General characteristic of the nucleophilic and oxidative systems

Transformations of paraoxon in the solution of $\text{H}_2\text{O}_2\text{--HO}^-$ in the media under study proceed mainly in two directions: perhydrolysis with the participation of the resulting HOO^- anion ($\text{H}_2\text{O}_2 + \text{HO}^- \rightleftharpoons \text{H}_2\text{O} + \text{HOO}^-$) and alkaline hydrolysis by HO^- anion:



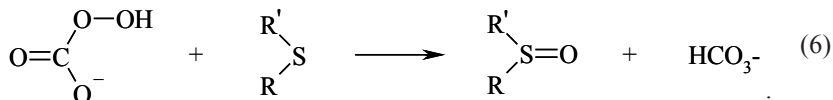
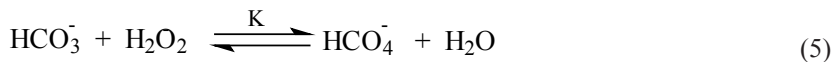
In this case a contribution from alkaline hydrolysis is minimal and does not exceed 1-5 % that from the overall rate of substrate loss [40]. According to kinetic and spectroscopic measurements, pK_a of hydrogen peroxide in water was calculated to be 11.6. This suggests that the considerable amounts of HOO^- anion are formed at high pH (Figure 1, curves a).

As was shown by gas chromatography technique, the only oxidation product under conditions of MPS oxidation by hydrogen peroxide at $[\text{MPS}] = 2.0 \times 10^{-3}$, $[\text{H}_2\text{O}_2] = 1.1 \text{ mol} \cdot \text{l}^{-1}$, and $[\text{NH}_4\text{HCO}_3] = 0.5 \text{ mol} \cdot \text{l}^{-1}$ is methylphenyl sulfoxide [39].



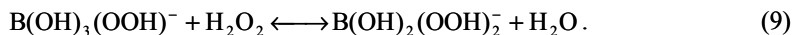
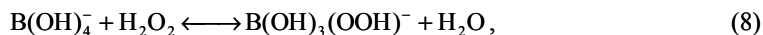
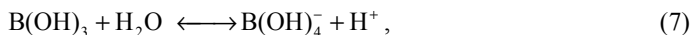
Further oxidation of sulfoxide to more toxic sulfone was not detected during at least 24 hours from the onset of MPS oxidation.

In H_2O_2 - NH_4HCO_3 system the activating effect of HCO_3^- in oxidation of sulfides with hydrogen peroxide is caused by the formation of peroxyhydrocarbonate anion HCO_4^- which exhibits higher oxidative ability than hydrogen peroxide [15, 25, 39, 40]:



Equilibrium (5) is established relatively rapidly (from ~ 5 to 30 min at pH 8-9) [15]. In this case the acid-base dissociation of HCO_3^- anions ($\text{pK}_a = 10.3$ [25]) and HCO_4^- can be neglected [39].

In the solutions of $\text{H}_2\text{O}_2\text{-B(OH)}_3$ peroxoborates are predominantly formed [41, 42]:



A ratio between the resulting peroxoborates depends on pH and proportion of the initial concentrations of B(OH)_3 and H_2O_2 [42]. At relatively low concentrations of B(OH)_3 , H_2O_2 ($< 1 \text{ mol}\cdot\text{L}^{-1}$) and pH 6–14 the main reaction products are monoperoxoborate $\text{B(OH)}_3(\text{OOH})^-$ and diperoxoborate $\text{B(OH)}_2(\text{OOH})_2^-$ anions, whereas at the higher reagent concentrations those are polyperoxoborates

Table 1. Composition of reaction media (wt %)

No.	Medium	Water	CTABr	<i>i</i> -propanol	<i>n</i> -butanol	Ethylene glycol	Hexane
1	Water	100					
2	Water/alcohol	74.8		25.2			
3		74.7			25.3		
4		67.7				32.3	
5	Water/alcohol/detergent	70	5	25			
6		68.8	1.8			29.4	
8	Micellar solution	99.73-99.45	0.27-0.55				
9	Microemulsion	88	5		5		2

$\text{B}_2(\text{O}_2)_2(\text{O}_2\text{H})_n(\text{OH})_{4-n}$ ($n = 0, 2$ or 4). Therefore, the strict separation of the oxidation routes combined with the determination of reactivity of the peroxoborates meets with difficulties. Nevertheless, an enhancement in reaction rates of sulfides with H_2O_2 in the presence of B(OH)_3 , as against the oxidation only by hydrogen peroxide, is unquestionable fact [35, 41].

It should be noted that there is no literature data on the nucleophilic reactivity of peroxoborates. It is known, however, that peroxyanions HCO_4^- and CO_4^{2-} can serve as typical nucleophilic reagents [36]. In aqueous media the second-order rate constants for reactions of HCO_4^- and CO_4^{2-} with 4-nitrophenyl esters of diethyl phosphonic acid were calculated to be $0.01 \text{ l} \times (\text{mol}^{-1} \cdot \text{s}^{-1})$ and $0.105 \text{ l} \times (\text{mol}^{-1} \cdot \text{s}^{-1})$, respectively. On this basis it is reasonable to expect that the activation of H_2O_2 by borates and hydrocarbonates can provide additional routes in decomposition of organophosphorus compounds by nucleophilic mechanism with the participation of peroxy anions formed in systems $\text{B}(\text{OH})_3/\text{H}_2\text{O}_2$ and $\text{NH}_4\text{HCO}_3/\text{H}_2\text{O}_2$.

Effects of pH

Changes in the observed rate constants in decomposition of NPDEP and MPS by hydrogen peroxide vs pH with and without activators are shown in Figure 1.

A general trend for the above reaction profiles is a drastic decrease in oxidation rate of MPS by hydrogen peroxide (Figures 1.1 and 1.2, (b)) and peroxy mono carbonate HCO_4^- (Figures 1.3 and 1.4, (b)) with increasing alkaline properties ($\text{pH} > 9.5$). Such a behavior can be explained on the basis of participation of two species of hydrogen peroxide (H_2O_2 and HO_2^- in oxidation. Anionic species, whose amount increases in alkaline media, are more reactive than the neutral molecule [36, 43]. At increased pH the concentration of the active species of oxidizer is decreased due to dissociation of HCO_4^- anion to CO_4^{2-} . The latter, as is the case with HO_2^- , exhibits a lesser oxidation ability than that of its protonated species [36, 44].

Addition of $\text{B}(\text{OH})_3$ into the system with hydrogen peroxide results in a maximum in the plot of observed rate constants in oxidation of MPS at $\text{pH} \approx 10$ (Figure 1.5. (b)). This is in agreement with the concentration changes (at a varied pH) of the active anions – monoperoxoborate $\text{B}(\text{OH})_3(\text{OOH})^-$ and diperoxoborate $\text{B}(\text{OH})_2(\text{OOH})_2^-$ – calculated from Eqns. (8) and (9) [35].

Table 2. gives the data on the reactivity of hydrogen peroxide ($k_{\text{H}_2\text{O}_2}$), peroxy moncarbonate anion ($k_{\text{HCO}_4^-}$), monoperoxoborate (k_1) and diperoxoborate (k_2) in oxidation of MPS in water and aqueous alcohol with the use of hydrogen peroxide and its complex with carbamide (UPH) as a source of oxidizers. Maximum observed rate enhancements due to the formation of peroxyanions are up to 200 times in activation by NH_4HCO_3 at pH 9 and 300 times for activation by $\text{B}(\text{OH})_3$ at pH 10.

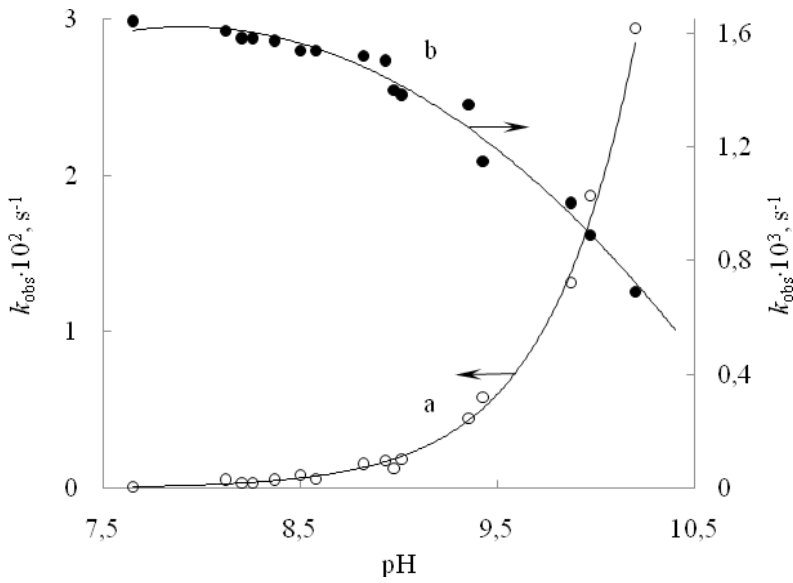


Figure 1.1

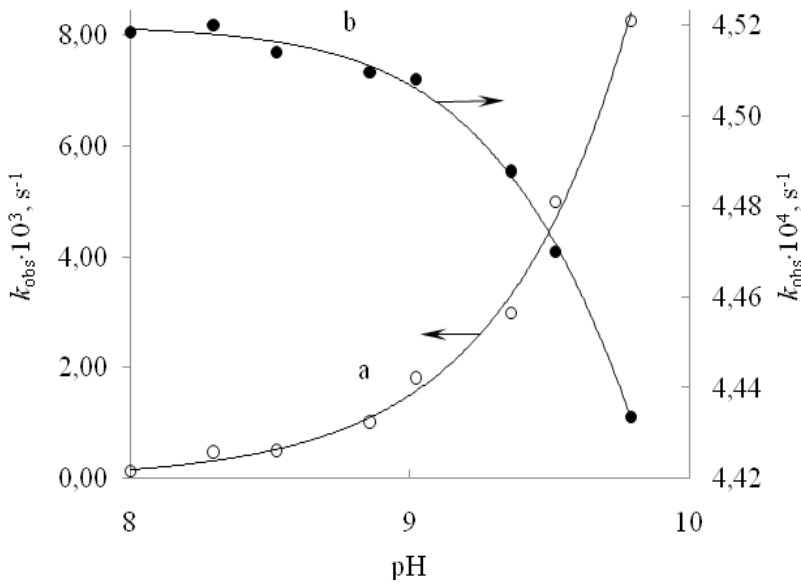


Figure 1.2

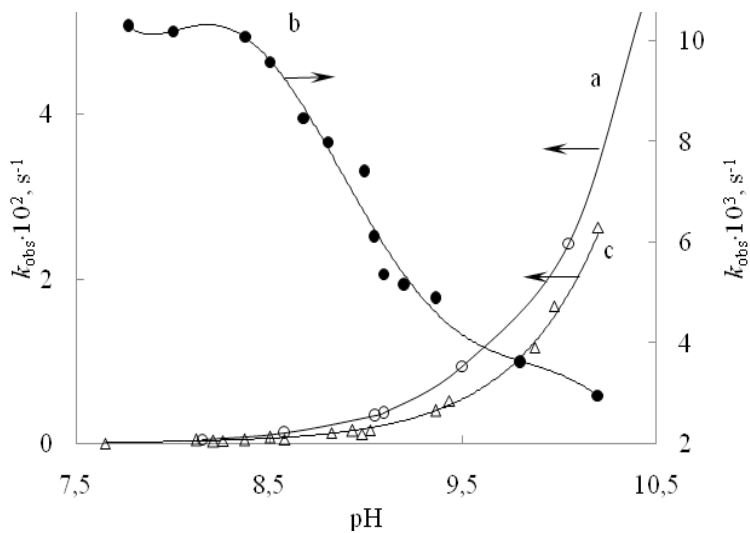


Figure 1.3

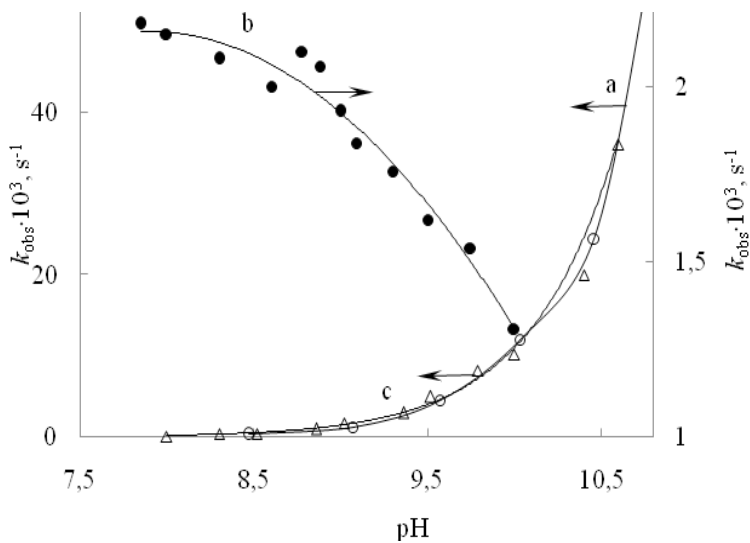


Figure 1.4

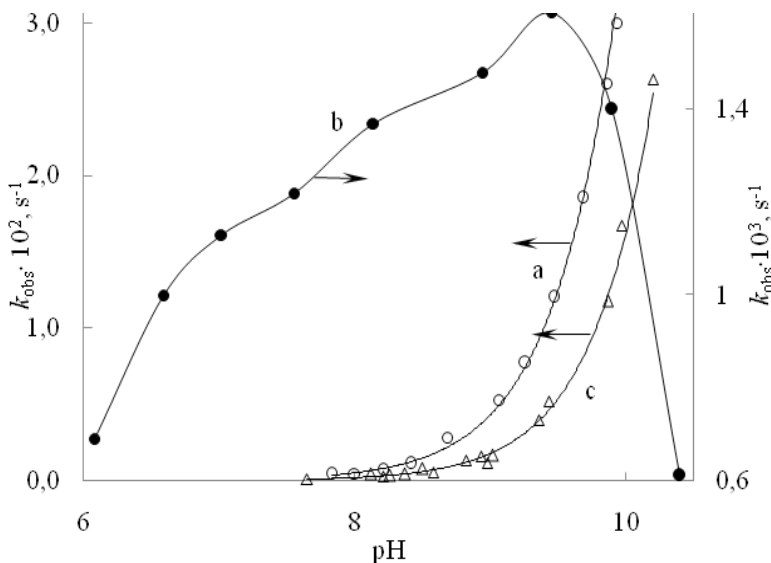


Figure. 1.5

Figure 1. Observed rate constants vs pH in nucleophilic substitution in paraoxon (a, c) and oxidation of methylphenyl sulfide (b) by hydrogen peroxide with and without activators at 25 °C.

- 1.1. water, phosphate buffer: a – $[H_2O_2]_o = 1.12 \text{ mol}\times\text{l}^{-1}$; b – $[H_2O_2]_o = 1.12 \text{ mol}\times\text{l}^{-1}$;
- 1.2. water/IPA (74.8/25.2 wt %): a – $[H_2O_2]_o = 1 \text{ mol}\times\text{l}^{-1}$; b – $[H_2O_2]_o = 1.13 \text{ mol}\times\text{l}^{-1}$;
- 1.3. water: a – $[H_2O_2]_o = 1 \text{ mol}\times\text{l}^{-1}$, $[NH_4HCO_3] = 0.1 \text{ mol}\times\text{l}^{-1}$; b – $[H_2O_2]_o = 1.13 \text{ mol}\times\text{l}^{-1}$, $[NH_4HCO_3] = 0.066 \text{ mol}\times\text{l}^{-1}$; c – $[H_2O_2]_o = 1 \text{ mol}\times\text{l}^{-1}$;
- 1.4. water/IPA (74.8/25.2 wt %): a – $[H_2O_2]_o = 1 \text{ mol}\times\text{l}^{-1}$, $[NH_4HCO_3] = 0.066 \text{ mol}\times\text{l}^{-1}$; b – $[H_2O_2]_o = 1.13 \text{ mol}\times\text{l}^{-1}$; $[NH_4HCO_3] = 0.066 \text{ mol}\times\text{l}^{-1}$; c – $[H_2O_2]_o = 1.13 \text{ mol}\times\text{l}^{-1}$;
- 1.5. water: a – $[H_2O_2]_o = 1 \text{ mol}\times\text{l}^{-1}$, $[B(OH)_3] = 0.1 \text{ mol}\times\text{l}^{-1}$; b – $[H_2O_2]_o = 1 \text{ mol}\times\text{l}^{-1}$, $[B(OH)_3] = 0.1 \text{ mol}\times\text{l}^{-1}$; c – $[H_2O_2]_o = 1 \text{ mol}\times\text{l}^{-1}$.

Table 2. Second-order reaction rates in oxidation of methyl phenyl sulfide by hydrogen peroxide and hydroperite ($k_{\text{H}_2\text{O}_2}$), hydroperoxocarbonate- (k_{HCO_4}), monoperoxoborate- (k_1) and diperoxoborate (k_2) anions at 25 °C

Solvent	Oxidizer	$k_{\text{H}_2\text{O}_2} \times 10^4$, l×(mol ⁻¹ ×s ⁻¹)	$k_{\text{HCO}_4} \times 10^2$, l×(mol ⁻¹ ×s ⁻¹)	$k_1 \times 10^2$, l×(mol ⁻¹ ×s ⁻¹)	$k_2 \times 10^2$, l×(mol ⁻¹ ×s ⁻¹)
Water	H ₂ O ₂	14.3 ± 0.2	25.6 ± 0.3	2.10±0.11	40.0±0.9
	UHP	16.0 ± 0.3	24.4 ± 0.4	2.20±0.34	51.0±1.2
Water/IPA	H ₂ O ₂	4.00 ± 0.12	5.67 ± 0.16	0.40±0.02	29.1±0.8
	UHP	4.06 ± 0.08	6.80 ± 0.15	0.35±0.02	31.6±1.3

Effects of pH on the observed rates in decomposition of NPDEP by peroxide anion with and without activators in water and aqueous alcohols are conventional: appearance of more or less significant route of nucleophilic substitution at pH ≥ 10 and further rate increase with alkalinity of medium (Figures 1.1–1.5, (a)). We failed to detect a high nucleophilic reactivity of peroxy anions toward paraoxon, as is the case in oxidation of MPS (Table 2). However, near two-fold acceleration of the nucleophilic reaction in activation of hydrogen peroxide by B(OH)₃ (Figure 1.5, cf. (a) and (c)) and that of 1.3 times in activation by NH₄HCO₃ (Figure. 1.3 (a)) was found in comparison with the corresponding reaction rates in the absence of activator (Figure 1.3 (c)). The only explanation of the observed gains in the decomposition rates of NPDEP is the participation of peroxy anions (HCO₄⁻, B(OH)₃(OOH)⁻, B(OH)₂(OOH)₂⁻, etc.) in nucleophilic substitution. In other words, peroxy carbonate and peroxy borate anions exhibit dual oxidative-nucleophilic properties, thus providing additional prospects (besides those of economical and ecological) in the development of multi-purpose decontamination systems.

All the above shows unambiguously that the main criterion for the development of oxidative-nucleophilic systems on the basis of hydrogen peroxide is a selection of activating agent and acidity of medium to provide maximum decomposition rates of NPDEP in combination with the maintenance of maximum oxidation rate of MPS.

Nano-sized systems

The use of the micellar aqueous solutions and microemulsions of the “water-

oil” type on the basis of cationic detergents is the conventional approach to increase the solubility of hydrophobic substrates in decontamination systems.

Figure 2 gives the results of the kinetic studies of decomposition of NPDEP in system $H_2O_2-HO^-$ -CTABr at pH 8.5–12.5, constant $[HOO^-]$, and a varying concentration of CTABr. The data demonstrate clear tendency for more than two-fold increase in absolute value of the observed micellar effect with decreasing pH from 12.5 to 8.5. A shift in pK_a of hydrogen peroxide under micellar conditions [45], especially pronounced at weakly alkaline media, at pH 8.5 and jointly with catalytic effect of micelle can provide a reaction rate of nucleophilic decomposition of substrate commensurable with those at $pH \approx 10.2$ and constant $[H_2O_2]$.

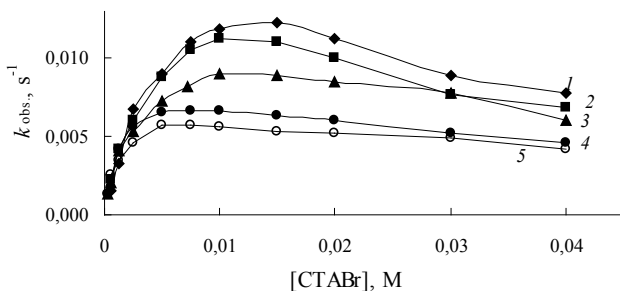


Figure 2. Effect of CTABr on decomposition rate of NPDEP in system $H_2O_2-HO^-$ at pH 8.5 (1), 9.5 (2), 10.5 (3), 11.5 (4), 12.0 (5); $[HOO^-] = 0.002 \text{ mol/l}$; 25°C .

Micellar effects in oxidation of MPS by hydrogen peroxide and peroxy-monocarbonate HCO_4^- were reported in [44]. Comparison examination of the micelle-catalyzed oxidation of MPS by hydrogen peroxide and HCO_4^- anion at pH 9 showed an increase both in reaction rates in the micelles (near 6-fold) and binding constant of the substrate K_S when passing to the system containing HCO_3^- anion. Generally a degree of binding of MPS with micelles is increased in the presence of anionic species (HCO_3^- , OH^- , HCO_4^-) in the micellar system. The same is true for micellar oxidation of MPS in the presence of $B(OH)_3$.

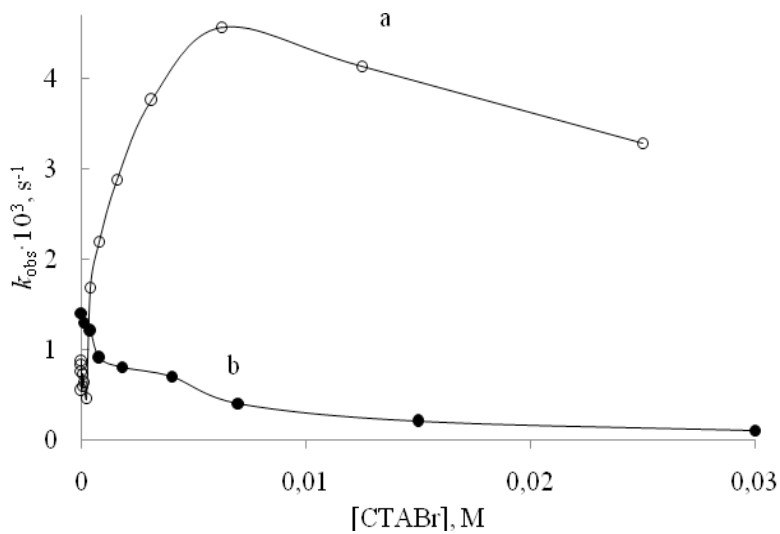


Figure 3.1

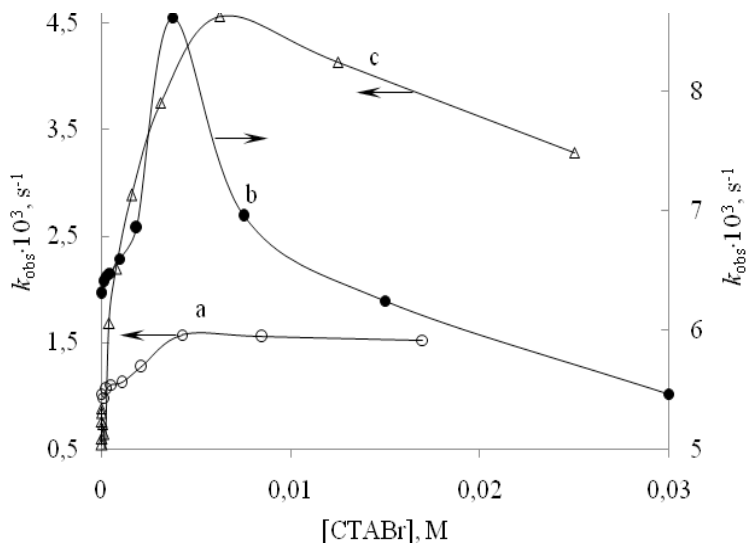


Figure 3.2

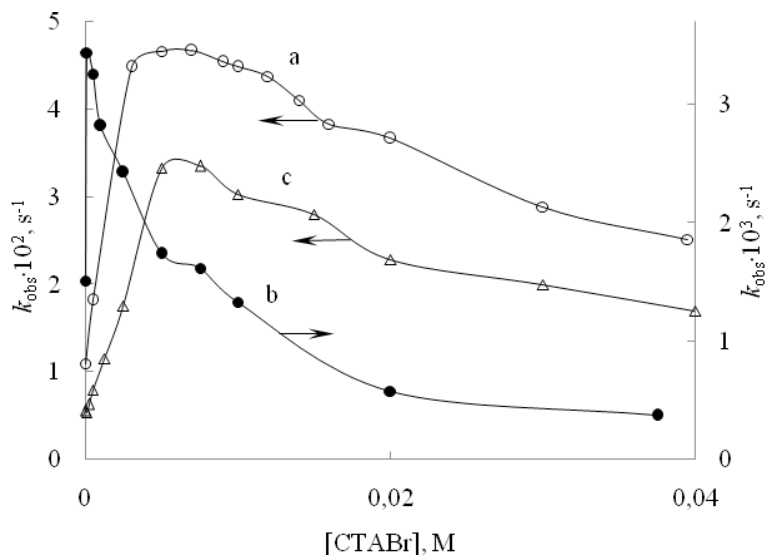


Figure 3.3

Figure 3. Effect of CTABr on the observed rate constants for nucleophilic substitution in MPDEP (a) and oxidation of MPS (b) by hydrogen peroxide with and without activators at 25 °C.

3.1. water/CTABr: a – $[H_2O_2]_o = 1 \text{ mol} \times l^{-1}$, $pH = 8.5$; b – $[H_2O_2]_o = 1 \text{ mol} \times l^{-1}$, $pH = 8.2$;
 3.2. water/CTABr: a – $[H_2O_2]_o = 1 \text{ mol} \times l^{-1}$, $[NH_4HCO_3] = 0.5 \text{ mol} \times l^{-1}$, $pH = 8.5$; b – $[H_2O_2]_o = 1.14 \text{ mol} \times l^{-1}$; $[NH_4HCO_3] = 0.083 \text{ mol} \times l^{-1}$, $pH = 8.5$; c – $[H_2O_2]_o = 1 \text{ mol} \times l^{-1}$;
 3.3. water/CTABr: a – $[H_2O_2]_o = 1 \text{ mol} \times l^{-1}$, $[B(OH)_3] = 0.1 \text{ mol} \times l^{-1}$, $pH = 9.5$; b – $[H_2O_2]_o = 1 \text{ mol} \times l^{-1}$, $[B(OH)_3] = 0.1 \text{ mol} \times l^{-1}$, $pH = 9.5$; c – $[H_2O_2]_o = 1 \text{ mol} \times l^{-1}$, $pH = 9.5$.

Studies on decomposition of MPDEP and MPS in micellar systems H_2O_2 –CTABr (Figure 3.1), H_2O_2 – NH_4HCO_3 –CTABr (Figure 3.2), H_2O_2 – $B(OH)_3$ (Figure 3.3) made it possible to draw some preliminary conclusions:

- micellar catalysis is efficient in nucleophilic and oxidative reactions with the participation of anionic species (HOO^- , HCO_4^- , $B(OH)_3(OOH)^-$ and $B(OH)_2(OOH)_2$ in the presence of cationic detergent CTABr at low pH (8.5–9.5) (Figures 3.1 – 3.3).
- activation of hydrogen peroxide by $B(OH)_3$ in decomposition of MPDEP causes near 1.5 fold increase of the micellar effect decomposition of NPDEP (Figure 3.3, cf. (a) and (c)), whereas NH_4HCO_3 decreases the catalytic effect of CTABr (Figure 3.2, cf. (a) and (c)).

Hydroperit in decomposition of paraoxon and oxidation of methylphenyl sulfide

Comparison studies on the reactivity of hydrogen peroxide (H_2O_2) and hydroperite (UHP) in reactions (3) and (4) were reported in [33, 34]. Kinetic parameters of oxidation of MPS by alternative sources of H_2O_2 (Table 2) and nucleophilic substitution in MPDEP (Table 3) are indicative of complete dissociation of the complex $\text{H}_2\text{O}_2 \cdot \text{CO}(\text{NH}_2)_2$ into the starting compounds without any assistance from carbamide to the processes under study.

Table 3. Second-order rate constants (k_{HOO^-}) of perhydrolysis of 4-nitrophenyl ester of diethylphosphoric acid at 25 °C

No.	Medium	k_{HOO^-} , l·(mol ⁻¹ ·s ⁻¹)	
		H_2O_2	UHP
1	H_2O	0.54 ± 0.02	0.58 ± 0.07
2	H_2O -IPA	0.35 ± 0.02	0.23 ± 0.01
3	H_2O -CTABr	2.30	8.2
4	ME	0.77 ± 0.03	0.81 ± 0.06

Data on the kinetic of decomposition of paraoxon in the micellar systems $\text{H}_2\text{O}_2/\text{HO}^-/\text{CTABr}$ (No. 3, Table 3) at a constant pH 10, concentration of HOO^- anion in aqueous phase ($[\text{HOO}^-]_{\text{w}} = 0.002 \text{ mol} \cdot \text{l}^{-1}$) and variable concentration of CTABr (0 – 0.4 mol·l⁻¹) should be considered separately. Figure 4 shows that rates of hydrolysis of paraoxon in the micelles of CTABr differ markedly from those for sources of nucleophile HOO^- – solution of hydrogen peroxide or hydroperit. In the case of the formation of HOO^- anion from hydroperit (Figure 4, curve 2) micellar effect increased to a maximum in comparison with the reaction in solution of H_2O_2 (Figure 4, curve 1). Taking into account that the reactivity of HOO^- anion in the system UHP/ HO^-/CTABr remains unchanged ($k_{\text{HOO},\text{m}} = 0.071 \text{ l} \cdot \text{mol}^{-1} \cdot \text{s}^{-1}$ is similar to that reported in [9]), a decrease in size of the micelles and, therefore, an increase in surface area of the chemical interaction, is mainly responsible for abnormal micellar acceleration in the presence of carbamide.

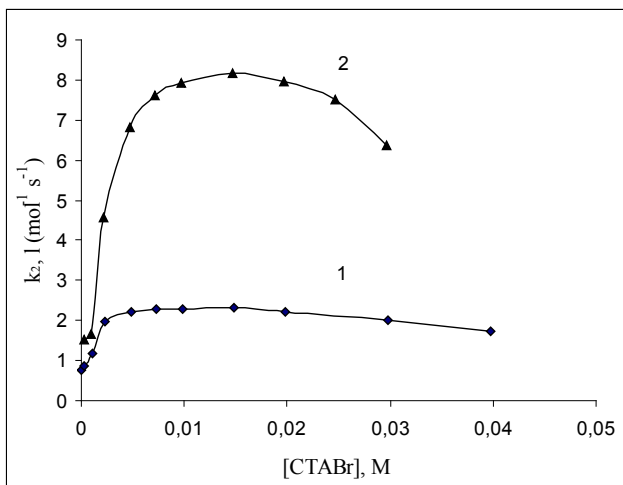


Figure 4. Effect of CTABr on the rate of nucleophilic substitution in 4-nitrophenyl diethylphosphate in systems $H_2O_2/HO/CTABr$ (1), $UHP/HO/CTABr$ (2) at $pH = 10$, $[HOO^-] = 0,002 \text{ mol}\cdot\text{l}^{-1}$, 25°C .

Thus, hydroperit can be used in decontamination of organophosphorus acids and mustard gas analogs. Moreover, hydroperit has some advantages in its use as a solid carrier of hydrogen peroxide in the micellar reactions. It is clear that the mixtures of water-free sources of hydrogen peroxide with a certain amount of the solid components (activators and detergents) can be recommended as efficient, long-term storage systems for mild and environmentally safe decomposition of highly toxic compounds

Comparison of the efficiency of decontamination systems

Table 4 gives the apparent second-order rate constants for oxidation of MPS (k_{app}^{2o} , $\text{l}\cdot(\text{mol}^{-1}\cdot\text{s}^{-1})$) and nucleophilic substitution in MPDEP (k_{app}^{2n} , $\text{l}\cdot(\text{mol}^{-1}\cdot\text{s}^{-1})$) by hydrogen peroxide with and without activators of hydrogen peroxide, NH_4HCO_3 and $\text{B}(\text{OH})_3$, at pH 9. These were calculated starting from total concentrations of H_2O_2 (for oxidation) and HOO^- anion (for nucleophilic substitution) in the system without regard for their distribution over the pseudophases (in the micelle of the detergent or drop of “oil”) and contributions from the reaction routes with the participation of peroxyanions formed according to Eqns. (6), (8) and (9). In our opinion, such an approach is more informative in comparison of decomposition rates of the substrates in the dynamic media

which are prone to the phase and aggregation transitions and exhibit different solubilization properties toward the hydrophobic substrate. Relative values $i^{o(nu)}$ – the ratio of k_{app}^o ($k_{app}^{2, n}$) for all systems under study to the apparent rate constants in water in the absence of activators - are also given in Table 4 (No. 1). The values of $i^{o(nu)}$ were taken as a measure of the efficiency of the oxidative (nucleophilic) system in going from aqueous to nano-sized and/or activated media. The products ($i^o \cdot i^{nu}$) were considered as a quantitative measure of the efficiency of versatile system for oxidation of MPS together with decomposition of MPDEP.

Table 4. Apparent second-order rate constants (k_{app}^2 , $l/(mol \cdot s)$) of oxidation of MPS and nucleophilic substitution in NPDEP by H_2O_2

No.	Medium	Activator	Oxidation		Nucleophilic substitution		$i^o \cdot i^{nu}$
			$k_{app}^2 \cdot 10^4$, $l \times (mol^{-1} \cdot s^{-1})$	i^o	$k_{app}^2 \cdot 10^3$, $l \times (mol^{-1} \cdot s^{-1})$	i^{nu}	
1	H ₂ O (1) ^a	-	14.3	1	53.0	1	1
2	H ₂ O (1)	NH ₄ HCO ₃	85.8	8	95.6	1.8	14
3	H ₂ O (1)	B(OH) ₃	170	12	132	2.5	30
4	H ₂ O-IPA (2)	-	4.00	0.3	41.0	0.8	0.2
5	H ₂ O- IPA (2)	NH ₄ HCO ₃	20.5	1.4	35.1	0.7	1
6	H ₂ O-TBA (3)	-	2.00	0.14	43.4	0.8	0.1
7	H ₂ O-TBA (3)	NH ₄ HCO ₃	10.6	0.7	38.8	0.7	0.5
8	H ₂ O-EG (4)	-	8.32	0.6	32.0	0.6	0.4
9	H ₂ O-EG (4)	NH ₄ HCO ₃	40.6	2.8	30.1	0.6	2
10	H ₂ O- IPA -CTABr (5)	-	2.00	0.1	39.3	0.7	0.1
11	H ₂ O- IPA - CTABr (5)	NH ₄ HCO ₃	50.1	3.5	68.5	1.3	5

12	H ₂ OEG- CTABr (6)	-	20.2	1.4	86.4	1.6	2
13	H ₂ O-EG- CTABr (6)	NH ₄ HCO ₃	94.4	6.6	100	1.9	13
14	H ₂ O-EG- CTABr (6)	B(OH) ₃	67	5	250	4.7	25
15	H ₂ O- CTABr (8)	-	6.77	0.5	602	11	6
16	H ₂ O- CTABr (8)	NH ₄ HCO ₃	75.5	5.3	142	2.7	14
17	H ₂ O- CTABr (8)	B(OH) ₃	165	11.5	721	14	161
18	ME (9)	-	4.72	0.3	74	1.4	0.4
19	ME (9)	NH ₄ HCO ₃	6.23	0.4	34	0.6	0.2
20	ME (9)	B(OH) ₃	4.68	0.3	21	0.4	0.1

^a Enumerated as in Table 1.

Table 4 reveals that there are no strict regularities between the properties of the medium and the reactivity of the main decontamination agents both in oxidation of MPS and nucleophilic decomposition of MPDEP in the absence (H₂O₂, HOO⁻) and in the presence (H₂O₂, HOO⁻, HCO₃⁻, B(OH)₃(OOH)⁻ and B(OH)₂(OOH)₂⁻) as activators. Nevertheless, the main general tendencies for a change in efficiency of the systems with participation of hydrogen peroxide in going from aqueous media to aqueous alcohols and organized media and the reactivity rating of the decontamination systems under study can be established. Thus the activation of hydrogen peroxide by ammonium hydrocarbonate and boric acid increases the oxidation rate of MPS no less than an order of magnitude and decomposition rate of NPDEP by a factor of 1.5–2 (Nos. 2, 3, 13, 14, and 17 in Table 4). The use of B(OH)₃ as an activator is more favorable than NH₄HCO₃ since the maximum oxidation activity of peroxoborates at pH 10 remains unchanged at a similar acceleration of the two processes, whereas peroxycarbonate anion is active at pH 7–9.

A comparison of the products $i^0 \cdot i^{nu}$ for Nos. 2 and 16, 5 and 11, 9 and 13 in Table 4 shows that cationic detergent (CTABr) in the activated media increases decontamination efficiency of the system. Moreover, in this case micelles and aqueous alcohols, especially in the presence of salt activators, cause significant increase in solubility of the substrates (Table 5). This is the main advantage of such reaction media in the development of oxidative-nucleophilic formulations for

decomposition of ecotoxicants. The most efficient and versatile decontamination system on the basis of hydrogen peroxide is the micellar solution of CTABr in the presence of $B(OH)_3$ (No. 17, Table 4). This system exhibits the highest reactivity of anions in oxidative-nucleophilic reactions and high binding constant K_s (No. 3, Table 5) of both substrates (MPS and NPDEP) by the micelles of CTABr.

Table 5. Binding constants (K_s , l/mol) of MPS and MPDEP

No.	Medium	$K_s, \text{l}\cdot\text{mol}^{-1}$	
		MPS	NPDEP
1	H_2O -CTABr	400	350
2	H_2O -CTABr- NH_4HCO_3	900	700
3	H_2O -CTABr- $B(OH)_3$	300	500
4	H_2O -EG-CTABr	150	50
5	H_2O -EG-CTABr- NH_4HCO_3	250	90
6	ME	300	250

Despite the attractiveness of ME as a media of high solubilizing ability (No. 6, Table 5), their use for oxidative-nucleophilic reactions have a number of disadvantages. In the first place, ME are multi-component systems with a compulsory presence of toxic organic solvents served as an oil. This reduces ecological safety of the reaction medium. Secondly, as evidenced by the data in Table 4 (Nos. 18–20) both oxidative and nucleophilic reactions in ME proceed at lower rates than those in water, aqueous alcohols, and micellar systems at similar K_s for both substrates (Cf. Nos. 1 and 6 in Table 5).

To summarize, water and aqueous alcohols containing hydrogen peroxide, cationic detergent and activator provide a high degree of substrate solubilization, an increase in reactivity of oxidizers and nucleophiles at pH 8–9 (in comparison with pure water as a solvent). The mixtures are simple in preparation and exhibit environmentally friendly properties. This gives grounds to consider the above media as promising components in oxidative-nucleophilic decomposition of ecotoxic compounds.

References

1. Savyolova V.A., Popov A.F., Vakhitova L.N., Solomoichenko T.N., Sadovkii Yu.S., Prokop'eva T.M., Skrypka A.V., Panchenko B.V. *J. Org. Chem.* 2005; 41: 810.
2. Petrov S.V. *Ross. khim. zh.* 1993; 37: 5.
3. Agadzhanov G.L., Konovalov E.N., Kushnir P.F., Nikulin A.V. *Ross. khim. Zh.* 1993; 37: 8.
4. Udaltsova G.Yu., Tankovich N.A., Lyangasov L.P. *Ross. khim. Zh.* 1993; 37: 17.
5. Protocol for the Prohibition of the Use of Asphyxiating, Poisonous or Other Gases, and of Bacteriological Methods of Warfare. Geneva, 17 June 1925.
6. Convention on the prohibition of the development, production, stockpiling and use of chemical weapons and on their destruction. Paris, 13 January 1993.
7. Zhdanov V.A., Koshelev V.M., Novikov V.K., Shuvalov A.A. *Ross. khim. Zh.* 1993; 37: 22.
8. S. Franke, P. Franz, W. Warnke. *Lehrbuch der Militarchemie.* Berlin, 1967., 437 p
9. Umyarov I.A., Kuznetsov B.A., Krotovich I.N., Kholstov V.I., Solovyov V.K. *Ross. khim. Zh.* 1993; 37: 25.
10. Beker S., Derre P., Shtelt E. *Ross. khim. Zh.* 1993; 37: 29.
11. Latt A., Rico-Latt I., Perez E., Krutikov V.I., Amada B. *Ross. khim. Zh.* 2007; 51: 36.
12. Yang Y.C., Baker J.A., Ward J.R. *Chem. Rev.* 1992; 92: 1729.
13. Gonzaga F., Perez E., Rico-Lattes I., Lattes A. *C.R. Acad. Sci. Sér. II C Chem.* 1998: 209.
14. Gonzaga F., Perez F., Rico-Lattes I., Lattes A. *New J. Chem.* 2001: 151.
15. Yao H., Richardson D.E. *J. Am. Chem. Soc.* 2003; 125: 6211.
16. Wagner G.W., Procell L.R., Yang Y.-C., Bunton C.A. *Langmuir.* 2001; 17: 4809.
17. Chiarini M., Gillitt N.D., Bunton C. A. *Langmuir.* 2002; 18: 3836.
18. Chiarini M., Bunton C.A. *Langmuir.* 2002; 18: 8806.
19. Lobachev V.L., Prokop'eva T.M., Savyolova V.A. *Teor. Exp. Chem.* 2004; 40: 368.
20. Menger F.M., Rourk M.J. *Langmuir.* 1999; 15: 309.
21. Tishkova E.P., Kudryavtseva L.A. *Bull. Russ. Acad. Sci. Chem.* 1996; 60: 298.
22. Zakharova L.Ya., Mirgorodskaya A.B., Zhiltsova E.P., Kudryavtseva

- L.A., Konovalov A.I. *Bull. Russ. Acad. Sci. Chem.* 2004: 1331.
23. Segues B., Perez E., Rico-Lattes I., Riviere M., Lattes A. *Bull. Soc. Chim.* 1996; 133: 925.
 24. Simanenکو Yu.S., Popov A.F., Prokop'eva T.M., Karpichev Eu.A., Savyolova V.A., Suprun I.P., Bunton K.A. *J. Org. Chem.* 2002; 38: 1341.
 25. Richardson D.E., Huirong Y., Frank K.M., Bennet D.A. *J. Am. Chem. Soc.* 2000; 122: 1729.
 26. Lion C., Charvy C. Patent US 6143088 (2000).
 27. Carnes C. L., Klabunde K.J. / Patent US 682776682 B2 (2004).
 28. Talmage S.S., Watson A.P., Hauschild V., Munro N.B., King J. *Current Org. Chem.* 2007; 11: 285.
 29. Wagner G.W., Sorrick D.C., Procell L.R., Brickhouse M.D., Mcvey I.F., Schwartz L.I. *Langmuir.* 2007; 23: 1178.
 30. Cassgne T., Cristau H.-J., Delmas G., Desgranges M., Lion C., Magnaud G., Torrelles E., Virieux D. *Heteroatom Chem.* 2001; 12: 485.
 31. Davies D.M., Deary M.E., Quill K., Smith R.A. *Chem. Eur. J.* 2005; 11: 3552.
 32. Aubry, J.-M.; Bouttemy, S. *J. Am. Chem. Soc.* 1997; 119: 5286.
 33. Vakhitova L.N., Lakhtarenko N.V., Skrypka A.V., Matvienko K.V., Taran N.A., Popov A.F. *Teor. Exp. Chem.* 2010; 46: 308.
 34. Vakhitova L.N., Lakhtarenko N.V., Skrypka A.V., Kaida E.Yu., Taran N.A., Popov A.F. *Teor. Exp. Chem.* 2011; 47: 217.
 35. Lobachev V.L., Zimtseva G.P., Matvienko Ya.V., Rudakov E.S. *Teor. Exp. Chem.* 2007; 43: 38.
 36. Savyolova V.A., Sadovkii Yu.S., Solomoichenko T.N., Prokop'eva T.M., Kosmynin V.V., Piskunova Zh.P., Bunton K.A., Popov A.F. *Teor. Exp. Chem.* 2008; 44: 98.
 37. Micelle formation, solubilization and microemulsions / K.L. Mitell, Ed. M.: Mir, 1980: 598.
 38. Vakhitova L.N., Skrypka A.V., Bogutskaya K.V., Taran N.A., Popov A.F. *Teor. Exp. Chem.* 2007; 43: 358.
 39. Vakhitova L.N., Skrypka A.V., Savyolova V.A., Popov A.F., Panchenko B.V. *Teor. Exp. Chem.* 2005; 41: 94.
 40. Bennet D.A., Yao H., Richardson D.E. *Inorg. Chem.* 2001; 40: 2996.
 41. Davies D.M., Deary M.E., Quill K., Smith R.A. *Chem. Eur. J.* 2005; 11: 3552.
 42. Pizer R., Tihal C. *Inorg. Chem.* 1987; 26: 3639.
 43. Herriott A.W., Picker D. *Synthesis.* 1975: 447.

44. Vakhitova L.N., Zhiltsova S.V., Skrypka A.V., Razumova N.G., Taran N.A., Savyolova V.A., Popov A.F. *Teor. Exp. Chem.* 2006; 42: 281.
45. Vakhitova L.N., Bogutskaya K.V., Taran N.A., Razumova N.G., Savyolova V.A., Popov A.F. *Teor. Exp. Chem.* 2008; 44: 83.

Наукове видання

ВІД МОЛЕКУЛ ДО ФУНКЦІОНАЛЬНОЇ АРХИТЕКТУРИ
СУПРАМОЛЕКУЛЯРНІ ВЗАЄМОДІЇ

(англійською мовою)

Збірник наукових праць

Підписано до друку 27.12.2012. Формат 60x84/16. Папір офісний.

Гарнітура Times New Roman. Друк-лазерний. Ум.друк.арк. 24.

Обл.-вид.арк. 25. Тираж 300.

Видавниче підприємство «Східний видавничий дім»
(Державне свідоцтво № ДК 697 від 30.11.2001)
83086, г. Донецьк, вул. Артема, 45
тел./факс (062) 338-06-97, 337-04-80
e-mail: svd@stels.net

О 80 Від молекул до функціональної архітектури:
Супрамолекулярні взаємодії/ [collected research papers]
Edited by V.I. Rybachenko.
Donetsk : «East Publisher House»
Ltd, 2012. – 538 с.

ISBN 978-966-317-108-1

The supramolecular interaction and self-organization of molecules leads to a material and is responsible for their function. The monograph presents various methods for the preparation and use of functional materials.

Супрамолекулярна взаємодія і самоорганізація молекул призводять до матеріалів і відповідають за їх функції. Монографія представляє різні методи отримання, вивчення і використання функціоналізованих матеріалів.

УДК 541.1+547

О 80

